Ondes et turbulence à la tropopause tropicale et impacts sur les cirrus

Aurélien Podglajen

THÈSE DE DOCTORAT

de l'Université de recherche Paris Sciences et Lettres
PSL Research University

Préparée à l'Ecole Normale Supérieure

Ondes et turbulence à la tropopause tropicale et impacts sur les cirrus

Waves and turbulence at the tropical tropopause and their impacts on tropical tropopause layer cirrus

Ecole doctorale n°129

SCIENCES DE L'ENVIRONNEMENT D'ILE-DE-FRANCE

Spécialité METEOROLOGIE, OCEANOGRAPHIE,
PHYSIQUE DE L'ENVIRONNEMENT

COMPOSITION DU JURY :

M. François LOTT
CNRS/Ecole Normale Supérieure,
Président du jury

Mme. Martina KRÄMER
Forschungzentrum Jülich
Rapporteur

M. Jean-Pierre CHABOUREAU
Observatoire Midi-Pyrénées
Rapporteur

M. Gwenaël BERTHET
CNRS/Université d'Orléans
Membre du jury

M. Bernard LEGRAS
CNRS/Ecole Normale Supérieure
Membre du jury

M. Emmanuel RIVIERE
Université de Reims-Champagne - Ardennes
Membre du jury

M. Riwal PLOUGONVEN
Ecole Polytechnique
Directeur de thèse

M. Albert HERTZOG
Université Pierre et Marie Curie
Co-directeur de thèse

Soutenue par Aurélien PODGLAJEN
le 30 juin 2017

Dirigée par **Riwal PLOUGONVEN**
et **Albert HERTZOG**

ENS ÉCOLE NORMALE SUPÉRIEURE

PSL RESEARCH UNIVERSITY PARIS

Remerciements

Je voudrais avant tout remercier chaleureusement mes directeurs de thèse, Riwal Plougonven et Albert Hertzog. Je les remercie d'abord de m'avoir entraîné dans ces thématiques captivantes : Riwal, merci de m'avoir envoyé en stage sur la TTL à Boulder alors que j'étais étudiant de M1 ; Albert, merci de m'avoir fait découvrir et converti aux observations ballon en stage de master 2. Je voudrais également les remercier pour les échanges scientifiques que nous avons eus mais aussi pour leur enthousiasme, leur confiance et leur soutien tout au long de la thèse. Grâce à eux, j'ai pu apprécier pleinement cette expérience.

Je tiens également à remercier Gwenaël Berthet, Jean-Pierre Chaboureau, Martina Krämer, François Lott, Bernard Legras et Emmanuel Rivière de m'avoir fait l'honneur de participer à mon jury de thèse, et pour leurs questions et leur regard sur mon travail. Merci en particulier à Jean-Pierre Chaboureau et à Martina Krämer qui ont accepté la charge supplémentaire de rapporteurs. Un grand merci à Bernard Legras pour ses conseils et les critiques constructives tout au long de la thèse, et pour les perspectives ouvertes lors de nos discussions.

Je remercie les personnes avec qui j'ai eu la chance de collaborer et d'interagir. Many thanks in particular to Eric Jensen, Bill Randel and Joan Alexander for their continuous advice and their guidance. I learnt a lot from them. Thanks to Bill also for welcoming me in Colorado once again. Merci à Tra Dinh pour son enthousiasme et les discussions fructueuses sur la microphysique. Merci à tous les membres de l'équipe cirrus, en particulier à Claudia Stubenrauch d'avoir suivi mon travail au sein des comités de thèse et à Pasquale Sellitto pour les discussions, scientifiques ou autre, autour d'un burrito. Merci enfin à ceux avec qui j'ai eu la chance d'échanger au cours de la thèse, en particulier Lenny Pfister, Rei Ueyama, Bernd Kärcher, Jens-Uwe Grooß, Felix Plöger, Inès Tritscher, Geneviève Sèze, Julio Bacmeister, John Bergman, Mark Schoeberl, Hector Teitelbaum, Hölger Vömel, et bien d'autres. Merci à Kuni Kodera de m'avoir fait visiter Kyoto.

Je suis reconnaissant envers Sabrina Speich, Pasquale Sellitto, François Lott, Bernard Legras, Caroline Müller, Guillaume Lapeyre, Vladimir Zeitlin, Xavier Capet, Julie Deshayes, Lionel Guez et Gwendal Rivière pour la confiance qu'ils m'ont accordé pour les enseignements. Merci aussi aux étudiants du département de géosciences de l'ENS pour leur curiosité.

Mes remerciements s'adressent également à ceux qui, par leur bonne humeur, ont contribué à la réussite de cette thèse. Merci à Valérian, Jean-Sébastien, Marine, Noé, Xavier, Loïc. Merci à mes collègues du préfa à l'X : Julien, Sophie, Karim, Nathalie, Briac, Olivier, Jean-François, Marie, Pauline, André, Patrick, Chantal, Michel, et tous les autres. Merci à Julien et Karim pour leur aide informatique, à Sophie pour les rapatriements de données sur demande. Un merci spécial à Michel pour m'avoir appris à calculer la date de Pâques et à Chantal pour m'avoir fait découvrir les *polar lows*. Merci aux équipes administratives du LMD, du département de Géosciences de l'ENS et de l'école doctorale pour leur aide dans toutes les démarches qui jalonnent la vie d'un doctorant. Un grand merci à mes coburaux successifs : Thomas, Yoann, Lluis et Estelle pour m'avoir supporté avec humour et bonne humeur. Merci à tous d'avoir participé aux pronostics d'événements sportifs (comme on dit participer c'est le plus important). Thanks also to : Marta, Alvaro, Mathias, Patrick, Falko, Mike, Fabio and the others, and to my housemates Rebecca, Jeremy, Ganesh and Leo.

Enfin, je remercie Marine, ma famille et mes amis.

RÉSUMÉ

Cette thèse s'intéresse aux ondes de gravité et à la turbulence dans la région de la tropopause tropicale (TTL pour Tropical Tropopause Layer, entre 14 et 18 km d'altitude), et à leurs impacts sur les cirrus.

Dans un premier temps, les fluctuations de température et de vent vertical induites par les ondes de gravité sont caractérisées à partir de mesures provenant de ballons stratosphériques longue durée. Les perturbations observées sont comparées à celles résolues par différents modèles atmosphériques globaux. À la lumière de ces observations, différentes méthodes de paramétrisation des fluctuations de température sont discutées.

Dans un second temps, l'influence des ondes équatoriales et de gravité sur la microphysique des cirrus est étudiée. On considère d'abord l'impact des ondes de gravité de haute fréquence sur la nucléation des cristaux de glace. Ensuite, l'effet des ondes de basse fréquence sur le transport de la glace est examiné, puis quantifié à l'aide d'observations in situ. Enfin, on étudie la formation et l'évolution d'un cirrus de grande échelle à l'aide de simulations numériques. Parmi les différents processus en jeu, on montre l'importance d'une onde équatoriale de grande échelle dans la structuration du champ nuageux.

Dans une dernière partie, les fluctuations de vent de petite échelle, interprétées comme de la turbulence, sont étudiées à partir des observations avion de la campagne ATTREX dans la TTL au-dessus de l'océan Pacifique. Leur impact sur le transport vertical de différents traceurs est quantifié. Il est inférieur à l'impact de l'upwelling équatorial de grande échelle mais néanmoins significatif.

ABSTRACT

Atmospheric waves and turbulence and their impacts on cirrus clouds in the Tropical Tropopause Layer (TTL, 14-18 km above sea level) are studied using in situ observations, numerical simulations and theoretical approaches.

First, long-duration stratospheric balloon measurements are used to analyze Lagrangian temperature and vertical wind fluctuations induced by gravity waves at the tropical tropopause. The amplitude and intermittency of wave fluctuations are assessed, and the observations are compared with resolved wave fluctuations in atmospheric models. Methods to parameterize Lagrangian temperature fluctuations are then discussed.

Then, some impacts of waves on cirrus cloud microphysics are examined. We first consider the influence of high-frequency gravity waves on the ice nucleation process. Next, we explore the interplay between the sedimentation of the ice crystals and their advection by wave-induced wind perturbations. Last, we use numerical simulations to investigate the formation of a large-scale cirrus in the TTL. We demonstrate the role of large-scale equatorial waves and quantify the impact of different processes (dynamics, radiative heating, microphysics) on the cloud field.

Finally, small-scale wind fluctuations, interpreted as turbulent bursts, are characterized using aircraft measurements from the ATTREX campaign in the tropical Pacific. The impact of the fluctuations on vertical mixing and on the TTL tracer budget is quantified. The vertical transport induced by turbulent mixing is found to be smaller than the one induced by mean tropical upwelling, but nonetheless significant.

Introduction générale

L'interface entre troposphère et stratosphère tropicales (TTL dans la suite du manuscrit pour Tropical Tropopause Layer en anglais) est une région clef du système climatique.

En effet, siège d'une ascendance de grande échelle, la TTL est « **la porte d'entrée de la stratosphère** » pour de nombreuses espèces chimiques, comme la vapeur d'eau ou certains gaz à effet de serre. Les processus s'y produisant ont donc un impact sur la composition de l'ensemble de la stratosphère. En particulier, les très basses températures rencontrées à la tropopause tropicale (inférieures à 185 K) sont responsables du faible contenu en vapeur d'eau de la stratosphère, via la formation de cirrus et la sédimentation des cristaux de glace qui entraînent un assèchement progressif des masses d'air. Les anomalies de vapeur d'eau naissant dans la TTL se propagent ensuite verticalement et horizontalement dans toute la stratosphère (*Brewer*, 1949), ce qui a des effets importants sur le climat. À l'échelle de la décennie, les variations du contenu en vapeur d'eau de la stratosphère ont d'ailleurs un impact climatique comparable à celui des émissions anthropiques de gaz à effet de serre (*Solomon et al.*, 2010). Après transport vers les pôles par la circulation de Brewer-Dobson, le contenu des masses d'air stratosphériques en vapeur d'eau va également influencer la température de formation des nuages stratosphériques polaires et affecter ainsi le cycle catalytique aboutissant à la destruction de l'ozone stratosphérique.

De plus, la composition de la TTL a un **impact direct sur le climat**. Sa très faible température, associée à la très haute température de la surface dans les tropiques, fait de la tropopause tropicale une zone de grande sensibilité pour le forçage radiatif associé aux gaz à effet de serre (par exemple CO_2, CH_4, *Riese et al.*, 2012), mais aussi aux aérosols et aux cirrus.

Cependant, malgré leur importance, les processus en jeu dans la TTL et leur évolution dans le cadre du changement climatique sont mal contraints et mal représentés dans les modèles atmosphériques (*Randel and Jensen*, 2013; *Hardiman et al.*, 2015). Par exemple, les variations observées du contenu en vapeur d'eau de la TTL et de la stratosphère restent en partie inexpliquées (*Randel and Jensen*, 2013). Le bilan thermique de la TTL et notamment la contribution des nuages aux taux de chauffage radiatifs sont également très mal connus (*Wright and Fueglistaler*, 2013). Un des obstacles principaux à une représentation réaliste de la TTL est la difficulté d'appréhender les processus sous-maille dans les modèles. Cela concerne la convection profonde mais aussi la chimie, la microphysique des aérosols et des nuages de glace formés *in situ*, et les **processus dynamiques** que sont les ondes et la turbulence.

En effet, si la théorie et les premières observations des ondes équatoriales datent des années 1960 (*Matsuno*, 1966; *Holton and Lindzen*, 1968; *Wallace and Kousky*, 1968), la variabilité associée à celles-ci et aux ondes de gravité reste relativement mal quantifiée. Ceci est en partie dû aux échelles impliquées, qui peuvent être fines verticalement ($\sim$1 km) comme horizontalement ($<$10 km), compliquant à la fois l'observation et la modélisation des ondes. À des échelles plus petites encore, la turbulence tridimensionnelle, son amplitude, sa répartition géographique sont largement inconnues.

Il ne fait néanmoins aucun doute qu'ondes et turbulence jouent des rôles clefs dans la TTL. Par exemple, les interactions ondes-écoulement moyen forcent l'oscillation quasi-biennale (QBO) du vent moyen dans la stratosphère équatoriale ; les ondes de Rossby équatoriales et extra-tropicales affectent l'upwelling équatorial associé à la circulation de Brewer-Dobson. Outre ces effets sur la dynamique à grande échelle, les ondes et la turbulence influencent également les processus microphysiques et le transport d'espèces chimiques. Les ondes induisent des fluctuations de température qui affectent la formation et l'évolution des cristaux de glace et des aérosols. La turbulence de petite échelle, quant à elle, contribue au brassage vertical des masses d'air et contrôle le mélange des espèces chimiques.

Dans ce contexte, cette thèse vise à mieux caractériser les processus dynamiques de méso et petite échelle à la tropopause tropicale, ainsi qu'à comprendre et quantifier leurs impacts sur les processus microphysiques et le transport d'espèces chimiques. Un accent particulier est mis sur l'influence des ondes sur les cirrus au cours de leur cycle de vie. Le travail s'appuie principalement sur l'analyse d'observations in situ, et utilise également des approches théoriques et de modélisation numérique.

Contents

Liste des figures

List of Tables

Chapitre 1

Processus dynamiques à la tropopause tropicale

Sommaire

1.1 La tropopause tropicale : historique et panorama dans le système climatique

1.1.1 Définition de la tropopause

Découverte de la tropopause Lorsqu'à la fin du XIX$^{\text{ième}}$ siècle les premiers radiosondages atteignant ces altitudes ont indiqué une rupture de la *loi de décroissance de la température* vers 10 km, on a incriminé des erreurs instrumentales. Il a fallu attendre le rapport de Teisserenc de Bort à l'académie des Sciences en 1902 pour que soit admise l'existence de deux couches dans l'atmosphère : la première, de la surface à environ 10 km d'altitude, caractérisée par un gradient de température négatif $\left(\frac{\mathrm{d}\bar{T}}{\mathrm{d}z} < 0\right)$; la seconde surplombant la première avec un arrêt de cette décroissance de la température. Teisserenc de Bort a baptisé la première couche troposphère (du grec « tropos », « tour »), en référence aux mouvements verticaux (convection ou turbulence) responsables, via la détente adiabatique des particules d'air, du gradient de température négatif observé. La seconde couche a, elle, été nommée stratosphère en raison de la suppression de ces mouvements verticaux supposée expliquer l'arrêt de la décroissance de la température, et donc l'existence de strates horizontales. En réalité, la température croît avec l'altitude dans cette seconde couche $\left(\frac{\mathrm{d}\bar{T}}{\mathrm{d}z} > 0\right)$, ainsi que l'indiquaient déjà les observations.

A l'interface entre les deux couches $\left(\frac{\mathrm{d}\bar{T}}{\mathrm{d}z} < 0 \text{ et } \frac{\mathrm{d}\bar{T}}{\mathrm{d}z} > 0\right)$ se trouve un minimum local de température sur la verticale : la tropopause. Ce terme désigne ainsi le premier minimum de température rencontré sur la verticale, et nous prendrons pour définition de la tropopause celle du point le plus froid entre 5 et 25 km d'altitude [1]. Elle se situe vers 18 km dans les tropiques[2], contre 10 km environ aux latitudes moyennes.

Définition de la couche de la tropopause tropicale Si on considère les caractéristiques dynamiques (vorticité potentielle) et physico-chimiques (vapeur d'eau, ozone), la transition entre troposphère et stratosphère est en fait progressive. La région de transition, généralement nommée haute troposphère-basse stratosphère (*Upper Troposphere-Lower Stratosphere* ou UTLS en anglais), est appélée TTL pour *Tropical Tropopause Layer* dans les tropiques. Cette région a été définie par *Fueglistaler et al.* (2009) comme s'étendant entre les altitudes 150 hPa (355 K en température potentielle ou 14 km en altitude) et 70 hPa (425 K ou 18,5 km). En latitude, elle est limitée par les jets subtropicaux qui constituent une frontière relativement hermétique aux mouvements horizontaux, frontière associée au fort gradient de vorticité potentielle à travers ces jets [3].

Les limites verticales de la TTL choisies par *Fueglistaler et al.* (2009) se rapportent à l'influence décroissante de la convection profonde qui brasse la troposphère tropicale. La base de la TTL est ainsi juste au-dessus du niveau de détrainement le plus fréquent des nuages convectifs, alors que son sommet correspond à l'altitude généralement atteinte par les plus hauts d'entre ceux-ci.

[1] D'autres définitions, comme celle de la WMO, considèrent le gradient de température vertical pour définir la tropopause. Les différentes définitions ne sont pas strictement équivalentes.

[2] En tous cas en hiver boréal, elle est en général plus basse en été boréal (autour de 17 km).

[3] La diffusivité horizontale effective a ainsi un minimum local au niveau de ces jets subtropicaux (*Haynes and Shuckburgh*, 2000)

Rôle particulier de la tropopause tropicale La place importante de la tropopause tropicale dans les échanges stratosphère-troposphère a été suggérée par *Brewer* (1949). Il s'est appuyé sur des observations de vapeur d'eau et d'hélium dans la stratosphère au-dessus de l'Angleterre et sur un raisonnement poussé, qu'il est intéressant de rappeler.

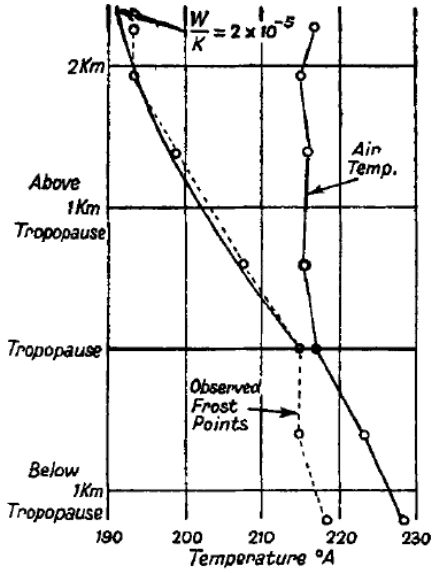

FIG. 2. 25 April 1945. Tropopause ht 34,000 ft.

FIGURE 1.1 – Température et température du point de givre mesurées lors de sondages effectués en 1945 au-dessus de l'Angleterre. Extrait de *Brewer* (1949).

Brewer (1949) avait remarqué que la température du point de givre était très faible juste au-dessus de la tropopause (de l'ordre de 195 K, c'est-à-dire des concentrations en vapeur d'eau de l'ordre de quelques ppmv), bien plus faible que le minimum de température rencontré à la tropopause dans le même profil (figure 1.1). Par ailleurs, des études précédentes avaient montré que l'hélium présentait un rapport de mélange quasi-constant avec l'altitude, jusqu'à des altitudes de 20 km au moins.

L' hélium est une molécule très légère. En l'absence de mouvements verticaux, maintenir un rapport de mélange constant d'hélium contre le tri gravitationnel implique des diffusivités verticales turbulentes importantes, en tous cas si l'état d'équilibre est atteint. Les mêmes diffusivités turbulentes appliquées au rapport de mélange de vapeur d'eau conduiraient rapidement à un air bien plus humide que celui que Brewer observe. Sachant qu'aucun puits de vapeur d'eau n'est présent en stratosphère, d'où provient donc cet air si sec ?

Brewer sait que dans les tropiques (30°N-30°S), la tropopause est plus haute et surtout plus froide qu'aux moyennes latitudes. Les températures peuvent y atteindre moins de 185 K et assécher l'air efficacement. L'air qu'il observe dans la stratosphère des moyennes latitudes provient donc probablement des tropiques, plus précisément de régions proches de la tropopause. Cependant, la tropopause est bien plus haute aux tropiques qu'aux moyennes latitudes. Il est donc impossible que les faibles rapports de mélange en vapeur d'eau soient le fait uniquement de l'advection horizontale. Brewer met ainsi en contradiction ses observations avec le paradigme prévalent à l'époque, c'est-à-dire l'idée d'une stratosphère à l'équilibre radiatif, sans mouvements verticaux. La seule explication plausible qu'il trouve pour expliquer ses

observations est l'existence d'une circulation verticale près de la tropopause aux moyennes latitudes, qui ferait descendre de l'air sec de plus haut dans la stratosphère. Cet air sec de haute altitude proviendrait lui des tropiques, de la tropopause tropicale où se tiendrait une ascension compensatoire à la subsidence des latitudes moyennes ou polaires. L'existence de cette circulation permet d'expliquer les observations de vapeur d'eau mais aussi celles d'ozone de Dobson.

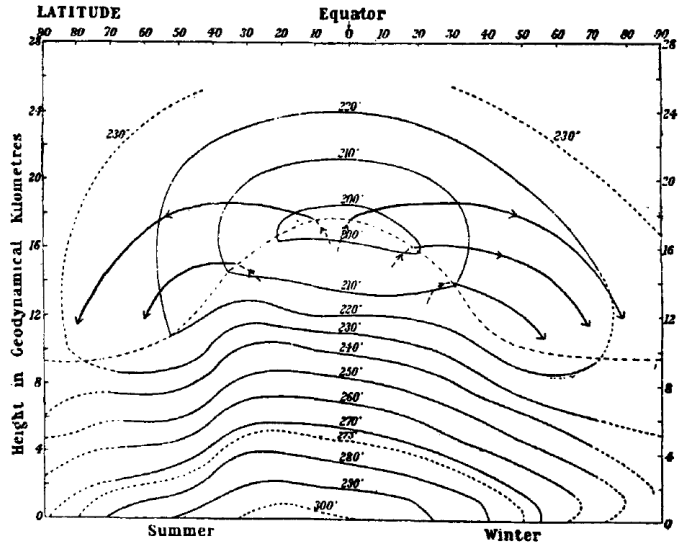

FIG. 5. A supply of dry air is maintained by a slow mean circulation from the equatorial tropopause.

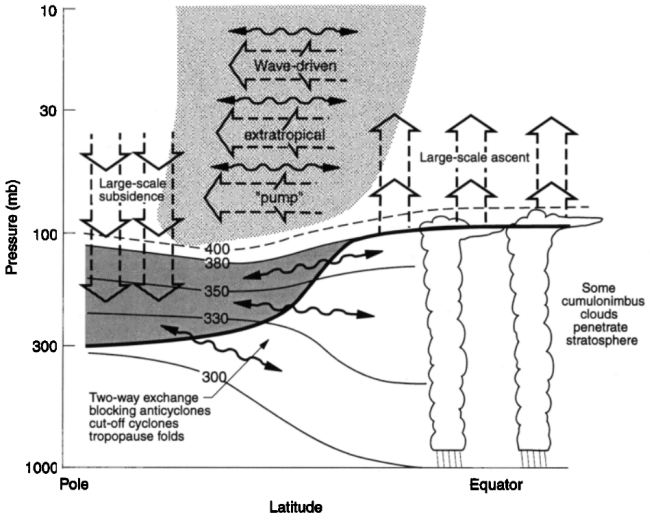

FIGURE 1.2 – Représentations schématiques de la circulation de Brewer-Dobson. Extrait de *Brewer* (1949) et de *Holton et al.* (1995).

La circulation supposée par Brewer, dite circulation de Brewer-Dobson, est représentée schématiquement sur la figure 1.2. Elle est en fait forcée par les interactions ondes-écoulement moyen aux moyennes latitudes. Elle fait de la tropopause tropicale la porte d'entrée de la stratosphère, une région où les processus physico-chimiques viennent impacter la composition de toute la stratosphère.

La tropopause tropicale est aussi une composante majeure du système climatique du fait

de sa très basse température. En règle générale, les gaz à effet de serre ont un impact d'autant plus grand qu'ils sont injectés dans des couches atmosphériques dont la température est plus basse que celle du sol. Aux tropiques, la différence de température entre le sol et la surface est de plus de 100 K, ce qui fait qu'une modification même faible de la composition chimique dans ces régions peut avoir un impact important sur le climat (*Forster and Shine*, 2002; *Solomon et al.*, 2010; *Riese et al.*, 2012). La figure 1.3 illustre le rôle primordial de la tropopause tropicale dans le bilan radiatif du système Terre. Elle représente l'effet sur la température de surface du changement de concentration de différents gaz à effet de serre en fonction de l'altitude et de la latitude. Les résultats, obtenus à l'aide d'un modèle de transfert radiatif, montrent l'importance disproportionnée des changements de concentration de gaz à effet de serre à la tropopause tropicale par rapport à d'autres régions de l'atmosphère.

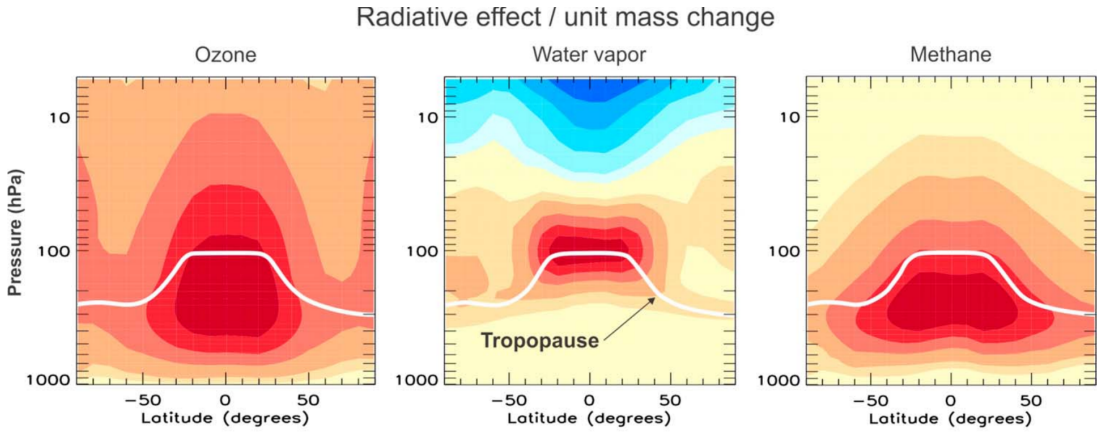

FIGURE 1.3 – Forçage radiatif dû à différents gaz, obtenu en faisant varier leur concentration à différentes altitudes et latitudes (forçage mesuré en unité de variation de la température à la surface par unité de changement de masse de la concentration du gaz à effet de serre). Résultats obtenus avec un modèle de transfert radiatif, les concentrations sont variées autour de l'état moyen actuel. Extrait de *Riese et al.* (2012).

À cet impact important des gaz à effet de serre s'ajoute l'impact radiatif des nuages hauts sur la température de surface. Le signe de la rétroaction de la couverture des cirrus tropicaux dans le cadre du changement climatique est encore incertain et débattu (*Lindzen et al.*, 2001; *Zelinka and Hartmann*, 2010; *Bony et al.*, 2016), mais leur importance pour le climat ne fait pas de doute.

1.1.2 Caractéristiques de la tropopause tropicale

La tropopause tropicale occupe donc une place très importante au sein du système climatique. La figure 1.4, tirée de *Fueglistaler et al.* (2009), résume les caractéristiques de cette région de l'atmosphère, qui combine des caractères troposphériques et stratosphériques. C'est une zone de forts gradients verticaux pour de nombreux traceurs troposphériques (CO, H_2O,...) et stratosphériques (ozone). Dynamiquement, les circulations de grande échelle de la haute troposphère, notamment la cellule de Walker ou les anticyclones de mousson, y sont très actifs ; l'impact de l'oscillation quasi-biennale du vent zonal dans la stratosphère tropicale se fait sentir dans la partie supérieure de la TTL.

La convection, active dans la partie inférieure de la TTL, y impose un profil de température proche d'une adiabatique humide. À ces basses températures et faibles rapports de

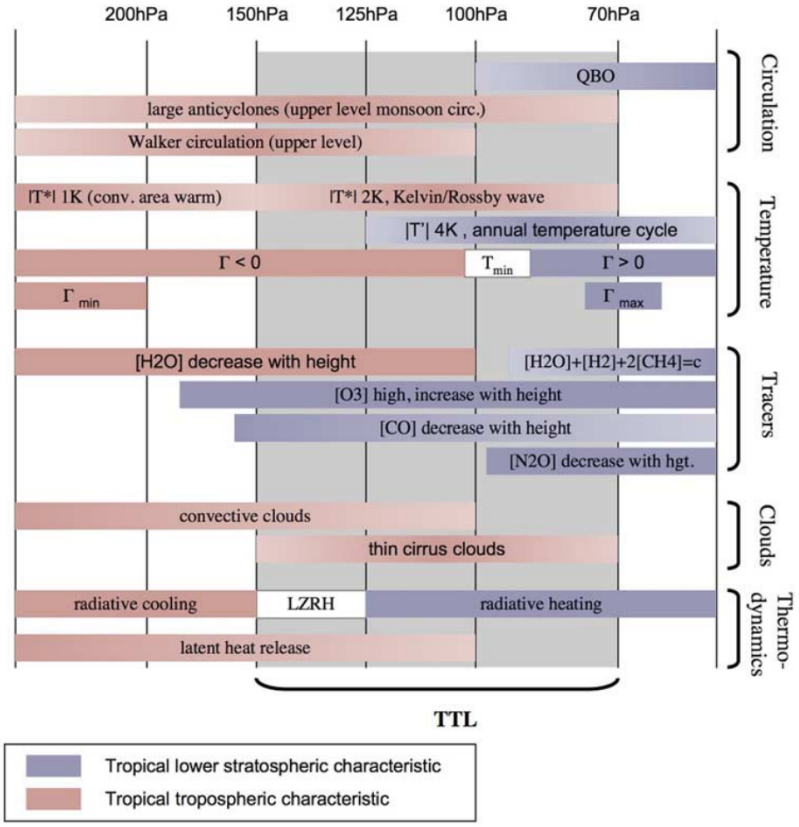

Figure 14. Summary of tropospheric/stratospheric characteristics and transitions thereof (symbolically shown as fade out of colored pattern). Γ, temperature lapse rate; T_{min}, temperature minimum of profile; $|T^*|$, amplitude of quasi-stationary zonal temperature anomaly; $|T'|$, amplitude of tropical mean temperature seasonal cycle; QBO, quasi-biennial oscillation.

FIGURE 1.4 – Caractéristiques de la tropopause tropicale. $\Gamma = \frac{\mathrm{d}\bar{T}}{\mathrm{d}z}$, $|T^*|$ est l'amplitude des anomalies zonales de température quasi-stationnaires. QBO : l'oscillation quasi-biennale (*Baldwin et al.*, 2001) ; LZRH : niveau de chauffage (radiatif) nul (Level of Zero Radiative Heating). Extrait de *Fueglistaler et al.* (2009).

mélange de vapeur d'eau, les dégagements de chaleur latente par condensation sont relativement faibles et l'adiabatique humide est en fait très proche de l'adiabatique sèche. La base de la TTL est donc caractérisée par une faible stabilité (faible $\frac{\partial\theta}{\partial z}$). Au contraire, l'augmentation de la température avec l'altitude dans la partie supérieure de la TTL fait que son sommet est très stable. Bien que la TTL soit une région de transition progressive, ce changement de stabilité reste relativement abrupt.

Concernant les échanges thermiques qui participent à contrôler le profil moyen de température et de stabilité, ils sont supposés être surtout radiatifs. En général, le dégagement chaleur latente (par sublimation de glace par exemple) est négligeable, car les quantités de condensats considérées sont faibles. Le bilan de chaleur est donc essentiellement contrôlé par l'équilibre entre chauffage radiatif et ascension lente. Les nuages, s'ils ne jouent que peu via la chaleur latente, ont un impact radiatif de premier ordre (*Corti et al.*, 2006).

L'absence de dégagement de chaleur latente fait de la dynamique de la TTL une dynamique « sèche ». Cependant, si l'influence directe de la convection profonde décroît avec l'altitude, une influence indirecte persiste, notamment via la génération d'ondes équatoriales

et d'ondes de gravité, et la turbulence qui peut leur être associée. Ces processus dynamiques sont présentés dans les sections suivantes.

1.2 Ondes équatoriales et ondes de gravité à la tropopause tropicale

Cette section présente la dynamique en région équatoriale, d'un point de vue théorique et observationnel. L'accent est mis sur les propriétés dynamiques des ondes équatoriales et des ondes de gravité. On insiste en particulier sur les échelles des fluctuations de température associées à ces ondes. On fait également quelques liens entre la variabilité observée et la théorie des ondes de gravité.

1.2.1 Ondes sur le plan β équatorial

Obtention des ondes équatoriales La théorie des ondes équatoriales a été développée par *Matsuno* (1966) sur le plan β. Les propriétés dynamiques sont très similaires sur la sphère et sur le plan β pour ces ondes, et il est intéressant et instructif de rappeler leur provenance.

Les relations analytiques des ondes équatoriales s'obtiennent par la linéarisation des équations de la dynamique sur le plan β équatorial. On utilise la coordonnée verticale altitude log-pression ($z_p = H \ln\left(\frac{P_S}{P}\right)$, H étant la hauteur d'échelle, P la pression et P_S une pression de référence ; $H = 7\,\mathrm{km} \simeq \left(-\frac{1}{\rho_0}\frac{\mathrm{d}\rho_0}{\mathrm{d}z}\right)^{-1}$ avec ρ_0 la densité[4] de référence). En négligeant les termes diabatiques et de dissipation, on obtient la linéarisation autour d'un vent moyen zonal $\bar{u}$:

$$\begin{aligned}
&\frac{\partial u}{\partial t} + \bar{u}\frac{\partial u}{\partial x} - \beta y v = -\frac{\partial \Phi}{\partial x} \\
&\frac{\partial v}{\partial t} + \bar{u}\frac{\partial v}{\partial x} + \beta y u = -\frac{\partial \Phi}{\partial y} \\
&\frac{\partial u}{\partial x} + \frac{\partial v}{\partial y} + \rho_0^{-1}\frac{\partial \rho_0 w}{\partial z_p} = 0 \\
&\frac{\partial \Phi_{z_p}}{\partial t} + \bar{u}\frac{\partial \Phi_{z_p}}{\partial x} + N_p^2 w = 0, \quad \Phi_{z_p} = \frac{RT}{H}
\end{aligned} \tag{1.1}$$

Ici, $\beta = \frac{\mathrm{d}f}{\mathrm{d}y}(y=0) = 2.3\,10^{-11}\ \mathrm{m^{-1}\,s^{-1}}$, R=287 J/K/kg est la constante des gaz parfaits pour l'air sec, N_p est la fréquence de Brunt-Väisälä en coordonnées log-pression : $N_p^2 = \frac{R}{H}\left(\frac{\mathrm{d}\bar{T}}{\mathrm{d}z_p} + \frac{\kappa\bar{T}}{H}\right)$ ($\kappa = \frac{R}{C_p}$ où C_p=1004 J/K/kg est la capacité thermique massique de l'air à pression constante), Φ le géopotentiel, u et v les vents zonal et méridien. Avec la condition de radiation à la limite supérieure, des solutions onde existent sous la forme

$$(u, v, T) = \left(\hat{u}(y), \hat{v}(y), \hat{T}(y)\right) e^{\frac{z}{2H}} \mathrm{Re}\left(e^{i(kx+mz-\omega t)}\right) \tag{1.2}$$

où k est le nombre d'onde zonal et m le nombre d'onde vertical. Parmi ces solutions, on distingue un mode sans vitesse méridienne ($\hat{v}(y) = 0$), l'onde de Kelvin, caractérisée par la relation de dispersion :

$$\hat{\omega} = \frac{Nk}{|M|} \tag{1.3}$$

[4]Ou la masse volumique. Dans cette introduction, on utilisera l'anglicisme courant qui consiste à désigner par densité la masse volumique.

avec $M = im + \frac{1}{2H}$ et $\hat{\omega} = \omega - k\bar{u}$ la pulsation intrinsèque des ondes, c'est-à-dire la fréquence ressentie par un observateur se déplaçant avec l'écoulement moyen zonal $\bar{u}$. Cette relation de dispersion est la même que celle d'une onde de gravité de fréquence intermédiaire, sans rotation, qui sera explicitée dans la section suivante ; dans le plan équatorial $x - z$, les ondes de Kelvin ne ressentent pas la force de Coriolis qui n'intervient qu'en limitant leur extension méridienne. Les signatures des ondes de Kelvin en température et en vent zonal s'écrivent :

$$(\hat{u}, \hat{T}) = \hat{u}_0 \mathrm{Re}\left(1, \frac{H}{R}\left(im + \frac{1}{2H}\right)\frac{\hat{\omega}}{k}\right) \exp\left(-\frac{\beta|M|y^2}{2N}\right)$$

On notera la quasi-quadrature entre signature en vent zonal et en température, et l'équipartition entre énergie potentielle par unité de masse

$$E_p = \frac{1}{2}\frac{\overline{\Phi'^2_{z_p}}}{N^2} = \frac{1}{2}\frac{R}{H}\frac{\overline{T'^2}}{N^2} \tag{1.4}$$

et énergie cinétique horizontale par unité de masse $E_{k_h} = \frac{1}{2}\overline{u'^2}$. En particulier, cela signifie que la signature en température de ces ondes est aussi importante que celle en vent. La validité de ces relations linéaires n'est limitée en fréquence que par la validité de l'approximation hydrostatique (invalide à haute fréquence).

En plus de l'onde de Kelvin, d'autres modes existent et ont une vitesse méridienne non nulle dont la structure méridienne vérifie l'équation :

$$\frac{\mathrm{d}^2\hat{v}}{\mathrm{d}y} + \left(\frac{\hat{\omega^2}}{c^2} - k^2 - \frac{\beta k}{\hat{\omega}} - \frac{\beta^2 y^2}{c^2}\right)\hat{v} = 0 \tag{1.5}$$

où $c^2 = \frac{N}{|M|}$.

La solution de cette équation en fonction de y est donnée par :

$$\hat{v}(y) = \hat{V}_0 \exp\left(\frac{-\beta|M|}{2N}y\right) H_n\left(\sqrt{\frac{\beta|M|}{N}}y\right) \tag{1.6}$$

où H_n sont les polynômes de Hermite (n pair ou impair correspondent respectivement à des modes symétriques ou antisymétriques). La relation de dispersion de ces ondes est donnée par :

$$\frac{|M|^2\hat{\omega}^2}{N^2} - k^2 - \frac{\beta k}{\hat{\omega}} = (2n+1)\frac{\beta|M|}{N} \tag{1.7}$$

Le diagramme de dispersion correspondant (pour une longueur d'onde verticale ou structure verticale donnée) est présenté sur la figure 1.5. L'équation étant cubique en $\hat{\omega}$, à chaque triplet $(n, k, |M|)$ correspond trois $\hat{\omega}$, représentés sur la figure. Ainsi qu'indiqué sur la figure, ces trois solutions correspondent à deux branches pour chaque mode $n \geq 1$: une branche *basse fréquence* (pour laquelle $\hat{\omega}^3 \ll \frac{\beta k N^2}{|M|^2}$) suivant approximativement la relation de dispersion :

$$\hat{\omega} = -\frac{\beta k}{k^2 + (2n+1)\frac{\beta|M|}{N}} \tag{1.8}$$

Cette branche est celle des ondes de Rossby équatoriales qui ne se propagent que vers l'ouest

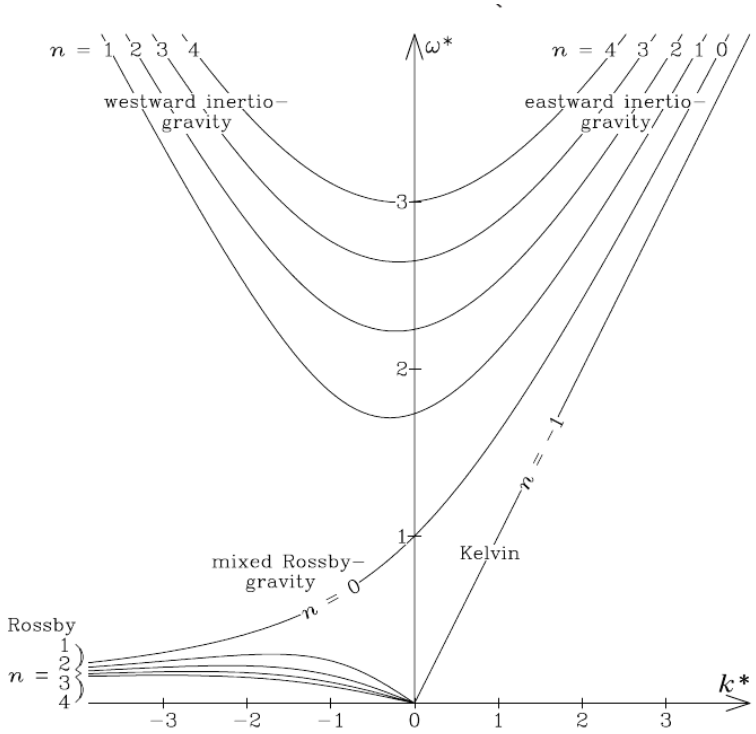

FIGURE 1.5 – Diagramme de dispersion des ondes équatoriales, où $\omega^* = \frac{\hat{\omega}}{\left(\beta\frac{N}{|M|}\right)^{\frac{1}{2}}}$ et $k^* = k\left(\frac{N}{|M|\beta^{\frac{1}{2}}}\right)^{\frac{1}{2}}$. Ces relations sont les solutions de l'équation (1.7) pour $n \leq 4$. Seules les solutions avec $\omega^* > 0$ sont représentées, mais les branches $\omega^* < 0$ peuvent être obtenues via une symétrie de centre (0,0). Extrait de *Kiladis et al.* (2009).

par rapport à l'écoulement moyen. Les deux branches *haute fréquence* ($\hat{\omega}^3 \gg \frac{\beta k N^2}{|M|^2}$) sont celles des ondes d'inertie-gravité équatoriales, de relation de dispersion proche de :

$$\hat{\omega}^2 = N^2\frac{k^2 + (2n+1)\frac{\beta|M|}{N}}{|M|^2} = N^2\frac{k^2}{|M|^2} + (2n+1)\frac{\beta N}{|M|} \tag{1.9}$$

Cette relation est similaire à celle des ondes de gravité classiques sur le plan f ou sans rotation, que nous discuterons dans la suite. Pour les deux branches de haute fréquence et comme pour la branche de basse fréquence, on note que l'échelle méridienne des ondes, donnée par $(2n+1)\frac{\beta|M|}{N}$ joue le rôle du nombre d'onde méridien. Alternativement, pour les ondes d'inertie-gravité, ce terme peut être vu comme un terme de « rotation effective », le f effectif ressenti par les ondes de mode n. Le mode $n = 0$ est intéressant car pour celui-ci il n'y a qu'une seule branche continue entre les ondes de Rossby et les ondes de gravité (en réalité il y aurait une seconde branche de la relation de dispersion mais il s'agit en fait de l'onde de Kelvin déjà discutée) ; il est appelé mode de Yanai ou mixte Rossby-gravité.

Bilan d'action pour les ondes de Kelvin équatoriales et échelles des fluctuations de température L'évolution de l'amplitude des ondes linéaires est donnée par le bilan d'action $A = \frac{E_{tot}}{\hat{\omega}} = \frac{E_p + E_k}{\hat{\omega}}$; dans l'approximation du milieu lentement variable (ou approximation

WKBJ[5], stipulant que l'amplitude de l'onde et le milieu dans lequel elle se propage varient peu sur une période ou sur une longueur d'onde), on a, en négligeant la dissipation :

$$\begin{aligned} &\frac{\partial A}{\partial t} + \nabla \cdot A\,\mathbf{c_g} = 0 \\ &\mathbf{c_g} = \frac{\partial \Omega}{\partial \mathbf{k}} \end{aligned} \tag{1.10}$$

$\mathbf{c_g}$ est la vitesse de groupe, $\mathbf{k} = (k, m)$ et Ω est une fonction de dispersion, définie par $\omega = \Omega(k, m, x, z, t)$. Il est commun et commode de résoudre le système précédent le long de sa caractéristique, le rayon d'énergie :

$$\begin{aligned} &\frac{\mathrm{d}_g \omega}{\mathrm{d}t} - \frac{\partial \Omega}{\partial t} = 0 \\ &\frac{\mathrm{d}_g \mathbf{k}}{\mathrm{d}t} + \frac{\partial \Omega}{\partial \mathbf{x}} = 0 \\ &\frac{\mathrm{d}_g A}{\mathrm{d}t} + A \nabla \cdot \mathbf{c_g} = 0 \end{aligned} \tag{1.11}$$

en définissant $\frac{\mathrm{d}_g}{\mathrm{d}t} = \frac{\partial}{\partial t} + \mathbf{c_g}\nabla$ et $\mathbf{x} = (x, y)$.

Flannaghan and Fueglistaler (2013) ont résolu ce système d'équations dans la TTL, et ont montré l'importance des champs de vent pour comprendre la réfraction des rayons d'énergie et la répartition de l'activité des ondes de Kelvin. Il est instructif, pour guider l'intuition, de considérer l'évolution d'un paquet d'onde dans un milieu ne variant que verticalement (k et ω sont alors constants au cours de la propagation du paquet d'onde). Pour une onde se propageant vers le haut (et en négligeant $\frac{1}{2H}$ par rapport à m), $\Omega = -\frac{Nk}{m} + k\bar{u}$ et $c_{g_z} = \frac{Nk}{m^2}$. On a alors :

$$\mathrm{d}_z \left(\frac{E_{tot}}{m} \right) = 0 \tag{1.12}$$

Ainsi, au cours d'une propagation conservative (sans dissipation), on s'attend à ce que les ondes deviennent plus « énergétiques » à mesure que leur longueur d'onde verticale $\lambda_z = \frac{2\pi}{m}$ s'amenuise. Cela est vrai en particulier pour l'énergie potentielle puisque pour les ondes de Kelvin il y a équipartition entre énergie potentielle et cinétique. Ainsi,

$$E_p \propto E_{tot} \propto m \propto \frac{1}{\lambda_z} \tag{1.13}$$

D'après ces propriétés de propagation, on s'attend donc à ce que les ondes de petite longueur d'onde verticale, proches de leur niveau critique [6] défini par $\hat{\omega} = 0$, aient une forte signature en température [7]. En effet, *Kim and Alexander* (2013) ont remarqué que les profils de température donnés par les radiosondes montraient de nombreuses occurrences d'ondes de fine échelle verticale, ainsi que le montre la figure 1.6. L'amplitude de ces ondes de fine échelle verticale est souvent sous-estimée dans les réanalyses atmosphériques. Ainsi, *Podglajen et al.* (2014) ont observé des paquets d'onde de Kelvin de grande échelle absents des réanalyses ERA interim et MERRA, et de l'analyse opérationnelle du centre européen, avec des amplitudes

[5] En hommage aux physiciens Léon Brillouin, Hendrik Anthony Kramers et Gregor Wentzel et au mathématicien Harold Jeffreys

[6] Car $|m| = \frac{Nk}{\hat{\omega}}$.

[7] Du moins jusqu'à ce que la saturation soit atteinte et qu'elles ne commencent à déferler.

de plus de 10 $\mathrm{m\,s^{-1}}$ en vent zonal.

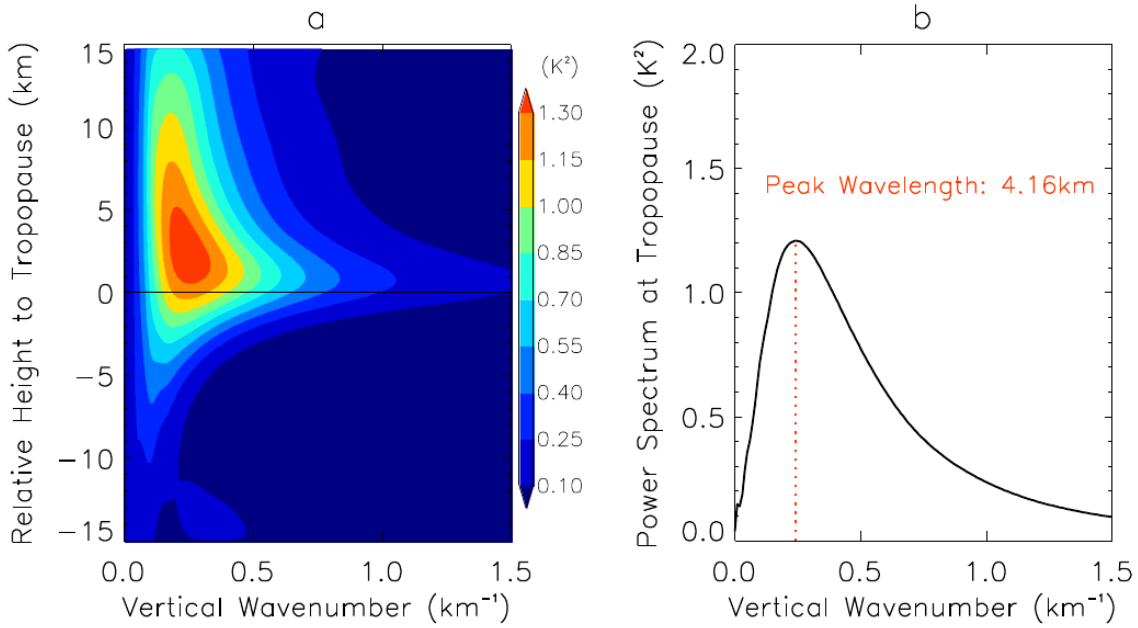

FIGURE 1.6 – (A gauche) Transformée de Fourier S verticale des anomalies de température eulériennes à la tropopause tropicale, en fonction de l'altitude relative à la tropopause. À droite, le spectre de température en fonction de l'échelle verticale à la tropopause. Noter la longue queue de spectre pour les hauts nombres d'onde (les petites longueurs d'onde verticales). Extrait de *Kim and Alexander* (2015).

1.2.2 Ondes de gravité de mésoéchelle dans la haute troposphère-basse stratosphère tropicale

Equations des ondes de gravité Comme pour les ondes équatoriales, les équations décrivant les ondes de gravité peuvent être obtenues à partir des équations du mouvement linéarisées [8] par rapport à un écoulement moyen $\bar{u}$, $\bar{v}$ uniforme, en négligeant les termes diabatiques et de dissipation. Contrairement aux ondes équatoriales, mouvements de grande échelle et proches de l'équilibre hydrostatique, il n'est pas approprié pour les ondes de gravité de travailler en coordonnées log-pression, et les relations sont obtenues en coordonnée altitude. Elles sont résumées, par exemple, par *Fritts and Alexander* (2003). Dans une onde interne de gravité monochromatique, les champs dynamiques, par exemple celui de vent vertical w, sont de la forme :

$$w(x,y,z,t) = e^{\frac{z}{2H}} Re\left(\hat{w} e^{i(kx+ly+mz-\omega t)}\right) \tag{1.14}$$

où $\mathbf{k} = (k,l,m)$ est le nombre d'onde, ω la pulsation et $H = \left(-\frac{1}{\bar{\rho}}\frac{\mathrm{d}\bar{\rho}}{\mathrm{d}z}\right)^{-1} \simeq 7$ km la hauteur d'échelle. On note que l'amplitude des ondes croît exponentiellement avec l'altitude, en lien avec la décroissance exponentielle de la densité. La relation de dispersion reliant fréquence et

[8] Sur le plan f

nombres d'onde s'écrit :

$$\hat{\omega}^2 = \frac{N^2 k_h^2 + f^2 \left(m^2 + \frac{1}{4H^2}\right)}{k_h^2 + \left(m^2 + \frac{1}{4H^2}\right)} \tag{1.15}$$

où $\hat{\omega} = \omega - k\bar{u} - l\bar{v}$ est à nouveau la pulsation intrinsèque (en suivant l'écoulement), N la fréquence de Brunt-Väisälä, $N^2 = \frac{g}{\bar{\theta}} \frac{\mathrm{d}\bar{\theta}}{\mathrm{d}z}$, et $k_h^2 = k^2 + l^2$. Cette équation indique que les ondes internes n'existent que dans une gamme de fréquences limitée par la fréquence de Coriolis f et par la fréquence de Brunt-Väisälä N. Comme souligné dans la section précédente, $f \to 0$ à l'équateur de telle sorte que les ondes de gravité peuvent y être de très basses fréquence, bien que l'effet β du guide d'onde équatorial soit ressenti par ces ondes à partir de longueurs d'onde méridiennes suffisantes (c'est-à-dire l suffisamment petit ; ce sont alors des ondes d'inertie gravité équatoriales). À haute et moyenne fréquence, au contraire, l'effet de la rotation peut être négligé (on prend $f = 0$).

La fréquence de Brunt-Väisälä N[9] correspond à la limite supérieure du domaine des ondes de gravité. Pour $\hat{\omega} > N$, les modes associés aux ondes de gravité sont évanescents et leur amplitude décroît avec l'altitude. Les sources (en tous cas les plus efficaces) étant principalement situées en troposphère, ces ondes évanescentes sont peu présentes en haute troposphère et basse troposphère. Cela fixe une limite aux échelles de temps courtes en-dessous de laquelle les fluctuations associées aux ondes de gravité sont peu intenses car les paquets d'ondes associés ne peuvent se propager loin de leurs sources troposphériques.

Génération d'ondes de gravité Les principales sources d'ondes de gravité de moyenne et haute fréquence intrinsèque ($\hat{\omega} \gg f$) dans l'atmosphère sont la topographie et la convection. D'autres sources, comme l'ajustement géostrophique, agissent surtout à plus basse fréquence ou, comme les instabilités de cisaillement ou la turbulence, sont moins efficaces. Ces deux sources principales, convective et topographique, sont localisées en troposphère et les ondes se propagent verticalement jusqu'en basse stratosphère.

Concernant les ondes topographiques, elles sont principalement dues au déplacement des surfaces isentropes associé au fait que l'écoulement évite verticalement la montagne. Dans le manuscrit, on discutera des régions polaires de l'hémisphère sud, où l'orographie est une source importante d'ondes. Cependant, à cause du nombre limité de chaînes de montagne et de vents moyens relativement faibles, la génération d'ondes par effets topographiques est assez peu fréquente en région tropicale, et c'est la convection qui est la source majeure des ondes de gravité.

Il n'existe pas à l'heure actuelle de consensus quant à l'importance relative des différents processus impliqués dans la génération des ondes de gravité convectives. Pour étudier cette question, inspiré par les travaux de Lighthill sur la génération d'ondes acoustiques par la turbulence, *Lane et al.* (2001) ont introduit un réarrangement des équations du mouvement mettant en évidence le forçage d'ondes et de termes linéaires par les composantes non linéaires de l'écoulement, le chauffage diabatique, et le cisaillement du vent moyen. L'équation de forçage pour le vent vertical w dans ce système est :

$$\bar{D}_{tt}\left(\nabla^2 w - \left(\frac{w}{H}\right)_z\right) - \bar{D}_t\left(\mathbf{U}_z \nabla \frac{w}{H} + \mathbf{U}_{zz} \nabla w\right) + N^2 \nabla_h^2 w = \mathcal{F} \tag{1.16}$$

[9] Pulsation de Brunt-Väisälä à strictement parler.

où $\bar{D}_t$ est la dérivée lagrangienne en suivant l'écoulement moyen U, V, cisaillé verticalement. Le terme de forçage $\mathcal{F}$ peut être décomposé en un terme « advectif » $\mathcal{F}_a$ (les termes inertiels non linéaires des équations de conservation du mouvement), un terme lié aux processus diabatiques $\mathcal{F}_h$, et un terme lié au cisaillement du vent moyen $\mathcal{F}_s$:

$$\mathcal{F} = \mathcal{F}_a + \mathcal{F}_h + \mathcal{F}_s \tag{1.17}$$

Ce formalisme permet de distinguer au niveau de la « source » les différents processus intervenant dans la génération des ondes de gravité ; il est particulièrement adapté au cas des nuages convectifs.

Il est généralement admis que les ondes longues (équatoriales et de gravité) sont le produit du terme diabatique $\mathcal{F}_h = \nabla_h^2 \frac{g\dot{\theta}}{\bar{\theta}}$ (*Beres et al.*, 2004). Dans ce cas, *Salby and Garcia* (1987) ont montré que les longueurs d'onde verticales des ondes générées étaient de l'ordre de deux fois la profondeur du chauffage, et dépendaient peu du détail de ce profil. Cette longueur d'onde verticale privilégiée est celle sur laquelle le chauffage convectif se projette le plus ; elle est généralement divisée par deux par réfraction au passage de la tropopause. Ainsi, la longueur d'onde verticale des ondes en stratosphère est finalement proche de la profondeur du chauffage en troposphère. Bien qu'intuitif, ce dernier résultat, n'est en fait valable que si l'on considère des chauffage de relativement basse fréquence et d'extension horizontale limitée. Pour des ondes de plus haute fréquence ou de plus large extension horizontale, la relation de dispersion impose en fait une limite à l'applicabilité du résultat précédent ; les longueurs d'onde verticales excitées sont en général plus grandes, jusqu'à 4 fois la profondeur du chauffage (*Holton et al.*, 2002). En effet, en l'absence de cisaillement de vent, la relation de dispersion impose les longueurs d'onde verticales excitées en fonction des fréquences $\hat{\omega}$ et des nombres d'onde horizontaux k_h :

$$m^2 = \frac{N^2 - \hat{\omega}^2}{\hat{\omega}^2 - f^2} k_h^2 - \frac{1}{4H^2} \tag{1.18}$$

Ainsi, si l'efficacité de la projection sur les modes d'onde de gravité propagatifs est maximisée lorsque la longueur d'onde verticale associée est proche du double de la profondeur du chauffage, cette relation n'est pas systématique.

La génération d'ondes de gravité par le terme de chauffage diabatique peut être étudiée plus précisément en prenant en compte les différents profils de chauffage, de type stratiforme ou convectif (*Ortland et al.*, 2011). Des études de modélisation récentes ont mis à profit les observations haute fréquence de taux de précipitations ainsi que de sommets nuageux pour en déduire une distribution des taux de chauffage convectifs et stratiformes et quantifier les ondes générées par ce processus (*Alexander et al.*, 2017). Cependant, malgré son importance, le terme diabatique n'est pas le seul en lice pour expliquer la génération d'ondes de gravité convectives. *Lane et al.* (2001) ont montré que, dans les nuages convectifs, les termes advectifs non linéaires pouvaient dépasser en amplitude ceux associés aux taux de chauffage.

Une autre approche conceptuelle du problème de la génération des ondes de gravité est celle dite de l'« oscillateur mécanique » (*Fovell et al.*, 1992). Plutôt que de s'intéresser directement à la source des ondes, cette approche consiste à considérer les oscillations d'une surface isentrope au-dessus du niveau où les termes de forçages sont les plus forts, typiquement au-dessus du niveau de flottabilité neutre. La distribution spatio-temporelle des ascendances

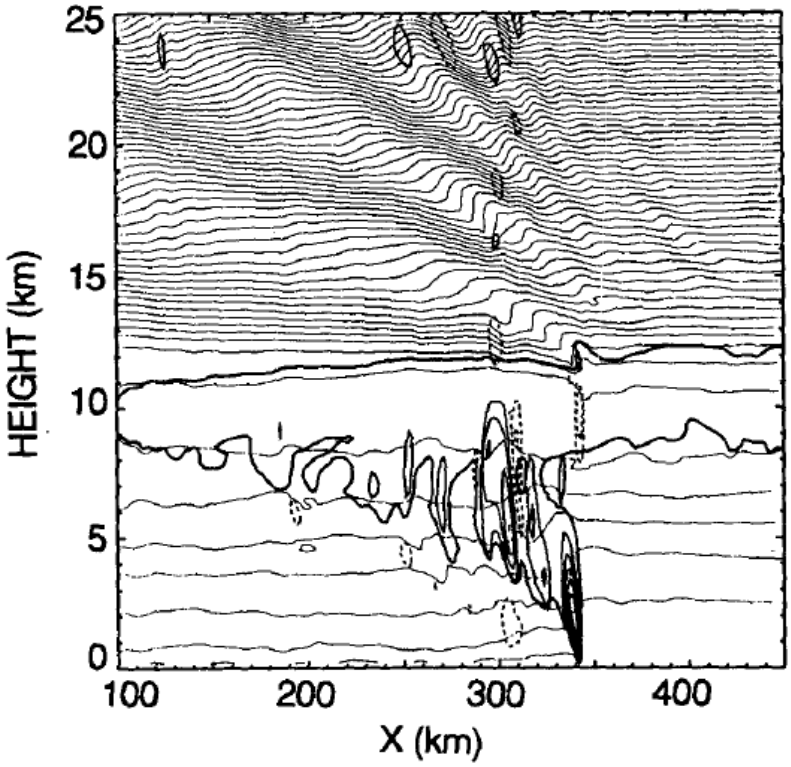

FIGURE 1.7 – Coupe du champ de température potentielle (traits fins) et de vitesse verticale (traits épais) dans une simulation numérique au-dessus d'une ligne de grain convective. Des ondes de gravité convectives d'amplitude importante peuvent être observées dans la stratosphère, via les déformations des surfaces isentropes (au-dessus de 10 km). Les lignes de phase de ces ondes sont inclinées vers l'est, ce qui indique (voir équation (1.20)) que les paquets d'ondes remontent le vent moyen dans cette simulation où celui-ci est de +8 m/s dans la stratosphère. Extrait de *Fovell et al.* (1992).

traversant le niveau de flottabilité neutre (les « overshoots ») induit des déflexions des isentropes et sert de condition aux limites inférieure pour les équations linéaires sans forçage. Cette approche est particulièrement adaptée pour décrire les ondes de haute fréquence, générées par les overshoots près de la fréquence de Brunt-Väisälä. Le problème est ainsi similaire à celui d'une génération topographique, sauf que la montagne dans ce cas peut osciller, et se déplacer par rapport au sol mais aussi par rapport aux masses d'air en altitude à cause du cisaillement de vent (*Pfister et al.*, 1993).

Propagation et dissipation des ondes de gravité Une fois générées, les ondes de gravité se propagent loin de leurs sources. Leurs caractéristiques évoluent au cours de cette propagation. Comme pour les ondes de Kelvin, un moyen d'étudier l'évolution des paquets d'onde au cours de leur propagation est de considérer le bilan d'action d'une onde linéaire, qui s'écrit :

$$\frac{\partial A}{\partial t} + \nabla \cdot \mathbf{c_g} A = D \tag{1.19}$$

où $\mathbf{c_g}A$ est le flux d'action ($\mathbf{c_g}$ étant la vitesse de groupe) et D représente les termes dissipatifs-diabatiques (parfois paramétrés comme proportionnels à A). Le flux d'action peut-être relié aux flux d'Eliassen-Palm responsables du forçage de l'écoulement moyen $\mathbf{F_u} = (\mathbf{c_g} - \bar{\mathbf{u}})kA = (\mathbf{c_g} - \bar{\mathbf{u}})p_x$ et $\mathbf{F_v} = (\mathbf{c_g} - \bar{\mathbf{u}})lA = (\mathbf{c_g} - \bar{\mathbf{u}})p_y$, $\mathbf{p} = \mathbf{k}A$ étant le pseudo-moment. Pour des

ondes linéaires, $A = \frac{E_p+E_k}{\hat{\omega}}$. La vitesse de groupe des ondes de gravité est donnée par *Fritts and Alexander* (2003) :

$$(c_{g_x}, c_{g_y}, c_{g_z}) = \left(\frac{\partial\Omega}{\partial k}, \frac{\partial\Omega}{\partial l}, \frac{\partial\Omega}{\partial m}\right) = \bar{\mathbf{u}} + \frac{(k(N^2-\hat{\omega}^2), l(N^2-\hat{\omega}^2), -m(\hat{\omega}^2-f^2))}{\left(k^2+l^2+m^2+\frac{1}{4H^2}\right)\hat{\omega}} \tag{1.20}$$

Dissipation des ondes de gravité et déferlement Dans le cas des ondes de gravité comme dans celui des ondes équatoriales, le terme dissipatif D de l'équation de bilan d'action (1.19) peut être associé à deux processus : le déferlement via les instabilités hydrodynamiques et la relaxation radiative. Ces deux mécanismes sont favorisés par l'augmentation des gradients verticaux de température et de vent lorsque l'amplitude de l'onde augmente et/ou que son échelle verticale se réduit, comme c'est le cas à l'approche d'un niveau critique ($\hat{\omega} \to 0$ (ou f)).

Le mécanisme de relaxation radiative est associé aux fluctuations de température induites par l'onde, qui éloignent l'atmosphère du profil d'équilibre radiatif. Les phases de température positive de l'onde émettent plus de flux infrarouge qu'elles n'en reçoivent et se refroidissent donc radiativement, et inversement pour les phases négatives. Ceci résulte en une atténuation des anomalies de température et donc de l'amplitude de l'onde. *Schoeberl et al.* (1983) et *Fels* (1984) ont discuté ce mécanisme pour les ondes en mésosphère, où les anomalies de température sont les plus importantes. Dans ces régions de la haute atmosphère où la décroissance de la densité augmente l'amplitude des ondes, cet effet pourrait dominer face au déferlement.

Néanmoins, à plus basse altitude, le mécanisme le plus actif est probablement celui des instabilités hydrodynamiques dues au cisaillement ou à l'instabilité statique (*Fritts and Alexander*, 2003). Pour ce dernier cas, l'instabilité statique est rencontrée lorsque le critère :

$$\frac{\mathrm{d}\bar{\theta}}{\mathrm{d}z} + \frac{\partial\theta'}{\partial z} < 0 \tag{1.21}$$

est vérifié, où $\bar{\theta}$ est la température potentielle de l'état moyen et θ' l'anomalie de température potentielle due à l'onde. S'inspirant de l'étude de *Lindzen* (1981), *Alexander and Dunkerton* (1999) définissent l'altitude de déferlement z_b comme l'altitude à laquelle le flux d'Eliassen-Palm vertical (flux de pseudo-moment) $(F_u)_z = kc_{g_z}A = \bar{\rho}\overline{u'w'}\left(1-\frac{f^2}{\hat{\omega}^2}\right)$ atteint la valeur de saturation, pour laquelle $\frac{\mathrm{d}\bar{\theta}}{\mathrm{d}z} + \frac{\partial\theta'}{\partial z} = 0$[10]. L'altitude z_b est donnée par :

$$(F_u)_z = \left[\frac{\bar{\rho}(z)k}{2N(z)}(c-\bar{u}(z))^3)\right]_{z=z_b} \tag{1.22}$$

où $c = \frac{\omega}{k}$ est la vitesse de phase de l'onde. Pour une vitesse de phase c donnée, les ondes de plus grandes longueurs d'onde (petits k) rencontrent leur niveau de déferlement à plus basse altitude, toutes choses étant égales par ailleurs. C'est en particulier le cas des ondes orographiques (pour lesquelles $c = 0$), qui déferlent d'autant plus bas par rapport à leur niveau critique[11] qu'elles sont de grande échelle. Pour les ondes convectives, souvent de haute fréquence, il peut être plus avantageux de réexprimer l'équation précédente en fonction de la

[10] La conservation du flux d'action impose la conservation de $(F_u)_z$ dans sa propagation verticale jusqu'à z_b.
[11] Caractérisé par $\bar{u} = c = 0$.

pulsation de l'onde ω :

$$(F_u)_z = \left[\frac{\bar{\rho}(z)}{2N(z)} \frac{(\omega - k\bar{u}(z))^3)}{k^2} \right]_{z=z_b} \tag{1.23}$$

ce qui indique que pour une pulsation ω telle que $|\omega| > |k\bar{u}(0)|$ donnée, ce sont au contraire les ondes de plus petites longueurs d'onde qui ont généralement leur niveau de déferlement à plus basse altitude.

1.2.3 Observations d'ondes de gravité dans les tropiques

Variabilité de la température L'étude des propriétés de propagation des ondes à la section précédente a montré une différence importante entre les tropiques et les moyennes latitudes : aux tropiques, l'effet limité de la rotation ($f \to 0$) permet la présence d'ondes de bien plus basses fréquences (les ondes de Kelvin et de Yanai notamment peuvent être de très basse fréquence) et évite le transfert d'énergie potentielle (des fluctuations de température) en énergie cinétique (des fluctuations de vent) qui se passe aux moyennes latitudes pour les ondes inertielles. Ainsi, de par le spectre d'ondes admises et les relations de polarisation, les fluctuations de température sont plus intenses aux tropiques, surtout pour les ondes de petite longueur d'onde verticale. Ceci a été observé par *Alexander et al.* (2002) et la figure 1.8 illustre cette propriété.

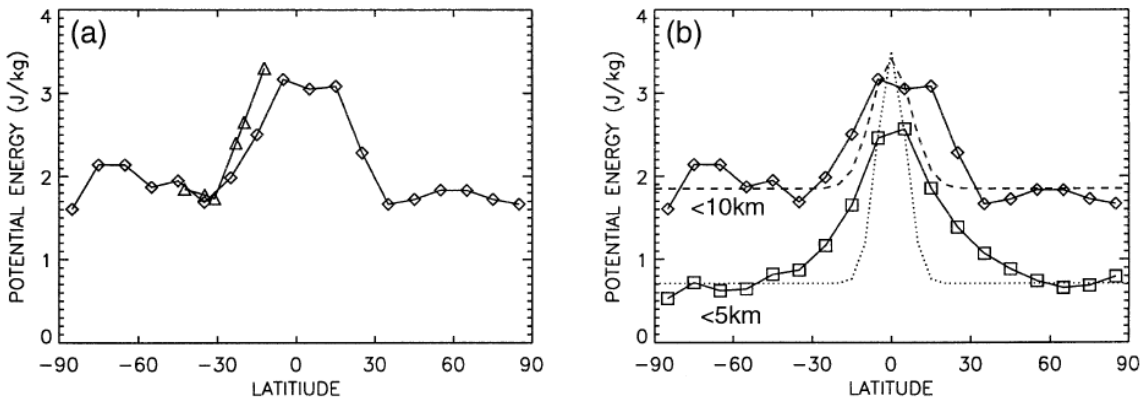

FIGURE 1.8 – Variabilité de l'énergie potentielle $E_p = \frac{1}{2}\frac{g^2\overline{T'^2}}{\bar{T}^2 N^2}$ associée aux ondes de gravité en fonction la latitude dans la basse stratosphère (18-25 km), d'après des observations satellites. Noter l'augmentation de E_p dans les tropiques. Extrait de *Alexander et al.* (2002).

Sources des ondes de gravité d'après les observations Les observations lors de campagnes dédiées tendent à indiquer que la convection, profonde ou peu profonde, est la source majeure des ondes de gravité dans les tropiques. Concernant les ondes d'inertie-gravité de basse fréquence, *Pfister et al.* (1993); *Lane et al.* (2003b); *Hankinson et al.* (2014a) par exemple ont montré que la convection pouvait en être une source importante. Les simulations numériques de *Evan et al.* (2012) suggèrent également une origine convective à des paquets ondes d'inertie-gravité observés lors de sondages en basse stratosphère au-dessus de l'Australie.

Pour ce qui est des ondes de haute fréquence, les études de *Alexander et al.* (2000); *Hertzog et al.* (2002); *Hankinson et al.* (2014b) suggèrent que l'activité convective ait un rôle dans

leur modulation. En particulier, *Hankinson et al.* (2014b) ont noté dans des radiosondages la corrélation entre l'observation de paquets d'ondes de haute fréquence et l'occurrence de convection profonde. Les observations avion d'*Alexander et al.* (2000) ont montré des flux de quantité de mouvement associés aux ondes de gravité plus importants au-dessus des nuages convectifs. À partir de mesures de ballons longue durée, *Hertzog et al.* (2002) ont mis en évidence une bonne correspondance entre les occurrences d'activité ondulatoire haute fréquence et les périodes où le ballon survolait des régions de faible flux infrarouge sortant (OLR pour *Outgoing Longwave Radiation*), correspondant au survol de régions convectives. Au contraire, dans cette même étude, les ondes de plus basses fréquence étaient moins distinctement reliées à l'activité convective locale. Cette dernière observation peut être reliée à la vitesse de groupe des ondes. En effet, la pente $\left|\frac{\mathrm{d}z}{\mathrm{d}x}\right|_r$ du rayon d'énergie le long duquel se propage le paquet d'onde est égale au rapport de la vitesse de groupe verticale sur la vitesse de groupe horizontale. En négligeant le vent moyen (ou en prenant la vitesse de groupe intrinsèque), ce rapport s'écrit (voir aussi équation (1.20)) :

$$\left|\frac{\mathrm{d}z}{\mathrm{d}x}\right|_r = \sqrt{\frac{c_{g_z}^2}{c_{g_h}^2}} = \sqrt{\frac{\hat{\omega}^2 - f^2}{N^2 - \hat{\omega}^2}\left(1 - \frac{1}{4H^2k_h^2}\frac{\hat{\omega}^2 - f^2}{N^2 - \hat{\omega}^2}\right)} \tag{1.24}$$

Qualitativement, ceci indiquerait que les paquets d'ondes de plus basse fréquence ($\hat{\omega} \to f$) se propagent plus horizontalement que ceux de haute fréquence ($\hat{\omega} \to N$), et sont donc observés à des distances plus importantes de la convection. Au contraire, les paquets d'ondes de haute fréquence tendent à rester confiner près des zones convectives, en accord avec les observations de *Hertzog et al.* (2002). Une corrélation avec leurs sources est ainsi attendue pour les ondes de haute fréquence.

1.3 Ondes, cirrus et vapeur d'eau à la tropopause tropicale

Les ondes, notamment celles présentées dans la section précédente, ont un rôle important dans la TTL, en particulier à cause de leurs impacts sur les cirrus. Elles forcent la circulation résiduelle et l'upwelling (ascendance) tropical associé, ce qui module la température en moyenne zonale. Elles provoquent des déplacements verticaux des masses d'air qui induisent des variations de température lors des compressions-décompressions adiabatiques. L'essentiel des impacts des ondes sur les cirrus se fait via ces impacts sur la température. En effet, la formule de Clausius-Clapeyron impose un lien étroit entre la température T et la pression de vapeur saturante par rapport à la glace e_{sat} :

$$\frac{1}{e_{sat}(T)}\frac{\mathrm{d}e_{sat}(T)}{\mathrm{d}T} = \frac{L_s}{R_v T^2} \tag{1.25}$$

où R_v est la constante des gaz parfaits pour la vapeur d'eau et $L_s > 0$ la chaleur latente de sublimation de la glace. Une expression de e_{sat} pour la glace hexagonale, prenant en compte les variations de L_s en fonction de la température et obtenue à partir de données expérimentales, est proposée par *Murphy and Koop* (2005). Néanmoins, en supposant L_s constant, la relation de Clausius Clapeyron permet d'appréhender la grande dépendance de e_{sat} à la température. Cette dépendance est telle qu'on observe une correspondance presque exacte entre les anomalies froides de température et les nuages de glace (cirrus) observés à

grande échelle, comme le montre la figure 1.9 pour l'hiver boréal. À plus courte échelle de temps, la corrélation entre des anomalies de températures négatives et la présence de cirrus a aussi été remarquée dans les observations (e.g. *Taylor et al.*, 2011). Différentes études ont montré que la température seule (et les anomalies négatives de celle-ci) était un excellent prédicteur de la présence de cirrus (*Bergman et al.*, 2014).

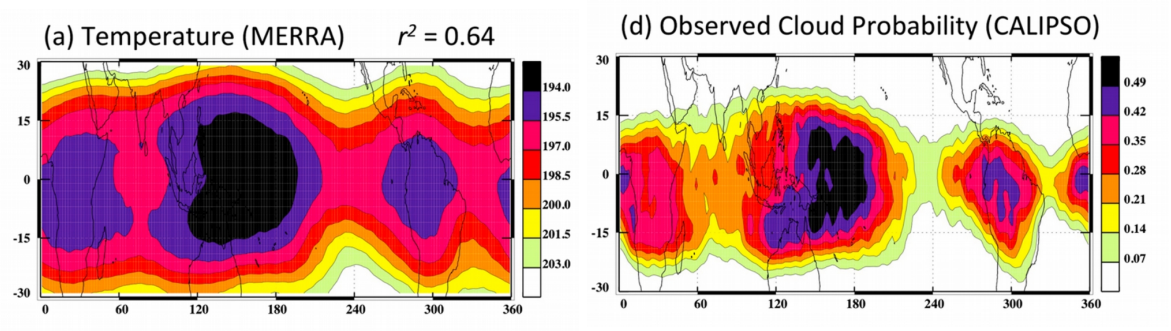

FIGURE 1.9 – Température dans la TTL, autour de 100 hPa, dans la réanalyse MERRA (à gauche) et probabilité d'observation de cirrus par le lidar CALIPSO (à droite). Il s'agit de moyennes pour les mois de janvier-février. Extrait de *Bergman et al.* (2014).

Partant de ce constat, des modèles simples représentant le transport de la vapeur d'eau depuis la TTL vers la stratosphère (e.g. *Bonazzola and Haynes*, 2004; *Fueglistaler et al.*, 2005) ont été développés. Ces modèles, lagrangiens, suivent les trajectoires des particules d'air et supposent que toute la vapeur d'eau en excès du rapport de mélange saturant $r_{sat} = \frac{e_{sat}}{P}$ (où P est la pression) est instantanément et irrémédiablement retirée de celles-ci.

Cette vision simplifiée du processus de déshydratation considère donc que la vitesse de croissance et de chute des cristaux de glace est infinie, et suppose que de la glace est toujours présente pour consommer la vapeur d'eau si $r > r_{sat}$. Sous ces hypothèses, la quantité de vapeur d'eau dans la stratosphère est uniquement contrôlée par le minimum de $(r_{sat})_{min}$ rencontré le long de la trajectoire des particules d'air. A priori, r_{sat} dépend à la fois de la température et de la pression ; cependant, étant donné la forte dépendance de e_{sat} en la température, le minimum de rapport de mélange saturant est en pratique très proche spatialement du minimum de température, i.e. du point le plus froid rencontré le long de la trajectoire : $(r_{sat})_{min} \simeq r_{sat}(T_{min})$. Pour des trajectoires essentiellement ascendantes dans la TTL, le minimum de température sur la verticale (ou point froid, « cold point tropopause » ou CPT en anglais) est potentiellement le point le plus froid (T_{min}) et joue donc un rôle très important. Le transport horizontal des masses d'air dans des régions plus froides de la TTL, comme le Pacifique occidental, contribue à diminuer encore $(r_{sat})_{min}$ (le « cold trap » de *Holton and Gettelman*, 2001).

Intuitivement, on s'attend donc à ce que les variations de température causées par les ondes aient un impact important sur les cirrus. Cette section présente une revue des effets suggérés ou observés des ondes sur les cirrus.

1.3.1 À basse fréquence et en moyenne zonale : les ondes contrôlent la variabilité de la température associée à la QBO et à l'upwelling de la circulation de Brewer-Dobson

Le cycle annuel associé à la circulation de Brewer-Dobson Dans le formalisme de la moyenne eulérienne transformée (TEM pour Transformed Eulerian Mean), l'évolution temporelle de la moyenne zonale de la température à la tropopause tropicale $\bar{T}_t$ s'écrit (*Andrews et al.*, 1987, p 128, équation 3.5.2.e) :

$$\bar{T}_t = -\bar{w}^* S - \bar{v}^* \frac{\bar{T}_\phi}{a} + \bar{Q} - \frac{1}{\rho_0}\left[\rho_0 \left(\overline{v'T'}\frac{\frac{\bar{T}_\phi}{a}}{S} + \overline{w'T'}\right)\right]_{z_p} - \frac{\kappa}{H}\left(\overline{v'T'}\frac{\frac{\bar{T}_\phi}{a}}{S} + \overline{w'T'}\right) \tag{1.26}$$

où $z_p = H \ln \frac{P_s}{P}$ ($H = \frac{RT_s}{g} \sim 7$ km) est l'altitude log-pression, $\rho_0 = \rho_s e^{-z/H}$, $S = N_p^2 H/R$ est un paramètre de stabilité, $\bar{w}^* = \bar{w} + \frac{1}{a\cos\phi}\left(\cos\phi \frac{\overline{v'T'}}{S}\right)_\phi$ et $\bar{v}^* = \bar{v} - \frac{1}{\rho_0}\left(\rho_0 \frac{\overline{v'T'}}{S}\right)_{z_p}$ sont les deux composantes verticales et méridienne de la circulation résiduelle. Dans la TTL, aux échelles de temps longues (> quelques mois), l'équilibre dominant dans cette équation est entre le terme de chauffage radiatif $\bar{Q}$[12] et le terme $\bar{w}^* S$ qui représente l'upwelling associé à la circulation de Brewer-Dobson (*Randel et al.*, 2002). En écrivant le terme de chauffage radiatif sous la forme d'une relaxation newtonienne vers la température à l'équilibre radiatif T_{eq}, on obtient donc :

$$\bar{w}^* S = \frac{1}{\tau_{eq}}(\bar{T} - T_{eq}) \tag{1.27}$$

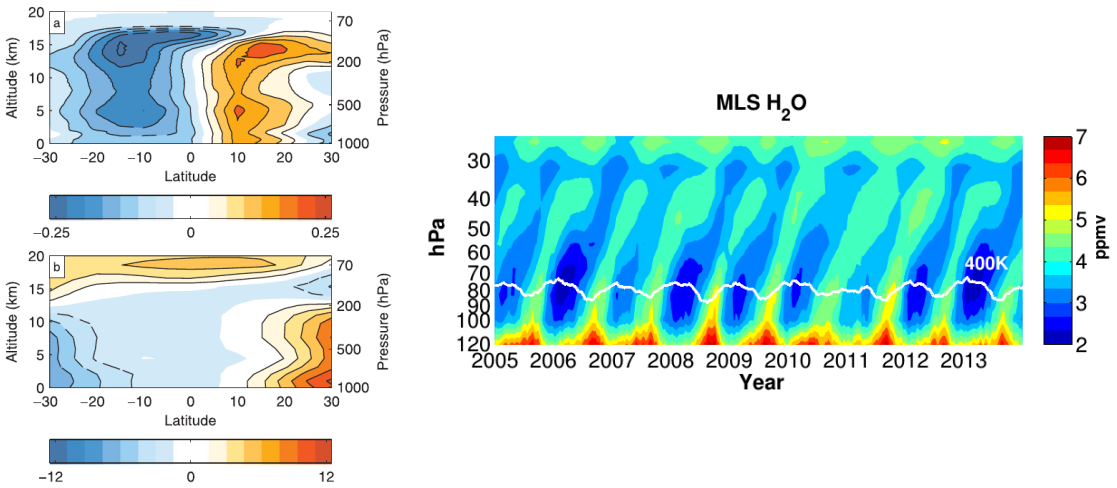

FIGURE 1.10 – A gauche : (en haut) différence de couverture nuageuse moyenne entre les mois de janvier et juillet d'après les observations CALIPSO et (en bas) différence de température entre les mois de janvier et juillet (tiré de *Virts and Wallace* (2010)). À droite : variabilité de la moyenne zonale en vapeur d'eau à la tropopause tropicale et propagation verticale dans la basse stratosphère tropicale (tiré de *Glanville and Birner* (2016))

Le temps de relaxation radiatif τ_{eq}, principalement associé à l'émission dans l'infrarouge

[12] A ces altitudes, $\bar{Q}$ représente essentiellement le chauffage dans l'infrarouge dû à la différence entre la température réelle et la température à l'équilibre radiatif T_{eq}.

de l'ozone et du CO_2, est d'environ 2 mois (*Randel et al.*, 2002). La branche mince de la circulation de Brewer-Dobson, qui contrôle $\bar{w}^* S$, est surtout forcée surtout par le déferlement des ondes de Rossby aux moyennes latitudes mais aussi par les ondes de Rossby équatoriales (*Ortland et al.*, 2011). L'upwelling tropical $\bar{w}^* S$, forcé par les ondes planétaires plus actives lors de l'hiver de l'hémisphère nord, a un cycle annuel, ce qui implique un cycle annuel en température. Ce dernier est d'environ 6 K pic à pic à 18 km d'altitude. Il entraîne une variation importante de e_{sat} et de la couverture nuageuse[13], comme illustré par la figure 1.10. Le panneau de droite de la figure 1.10 montre aussi que le cycle annuel de la température est responsable d'un cycle annuel du contenu en vapeur d'eau, cycle qui se propage à plus haute altitude : c'est le *tape recorder* (*Mote et al.*, 1996). Ainsi, la variabilité annuelle du déferlement des ondes de Rossby force le cycle annuel de l'upwelling tropical, ce qui modifie le contenu en vapeur d'eau et les cirrus.

La variabilité interannuelle associée à la QBO Un autre effet dynamique des ondes affectant la température en moyenne zonale est l'oscillation quasi-biennale (QBO *Baldwin et al.*, 2001). Cette oscillation, d'une période variable de 27 mois environ, se manifeste surtout en vent zonal. Elle a cependant également une signature en température[14] qui descend jusqu'au point froid de la tropopause, comme illustré par la figure 1.11. Étant donné que la QBO est forcée par les ondes équatoriales et de gravité, cette variabilité en température est en quelque sorte un effet indirect des ondes.

Cette variabilité en température est associée à une modification de la couverture nuageuse à haute altitude (*Davis et al.*, 2013) et de la concentration en vapeur d'eau (*Randel and Jensen*, 2013). La figure 1.11 illustre ces effets de l'oscillation quasi-biennale sur la température, l'impact sur la vapeur d'eau et la variabilité des nuages hauts.

La variabilité « rapide » en moyenne zonale : les réchauffements stratosphériques soudains (Sudden Stratospheric Warming SSW) Un dernier effet notable des ondes sur la température en moyenne zonale tropicale est celui associé aux réchauffements stratosphériques soudains. Ceux-ci sont provoqués par une accélération de la circulation résiduelle de Brewer-Dobson due à un déferlement accru d'ondes de Rossby extra-tropicales. L'accélération de la ciculation résiduelle implique davantage de subsidence aux pôles (d'où le réchauffement) et davantage d'upwelling aux tropiques. L'augmentation de l'upwelling entraîne un refroidissement de la TTL, ce qui génère une augmentation de la couverture nuageuse et de la déshydratation. Différentes études ont noté l'importance de ces processus (par exemple *Evan et al.*, 2015). L'impact de la circulation résiduelle forcée par les ondes sur l'upwelling et la température en moyenne zonale peut aussi s'exercer à des échelles de temps encore plus rapides (*Randel and Wu*, 2015), mais les effets deviennent négligeables par rapport aux fluctuations de température locales (i.e. sans signature sur la moyenne zonale) générées par les ondes elles-mêmes.

[13] Noter cependant qu'une partie du cycle annuel en couverture nuageuse doit être attribué à la variabilité de la convection.

[14] Via l'équilibre du vent thermique en région tropicale.

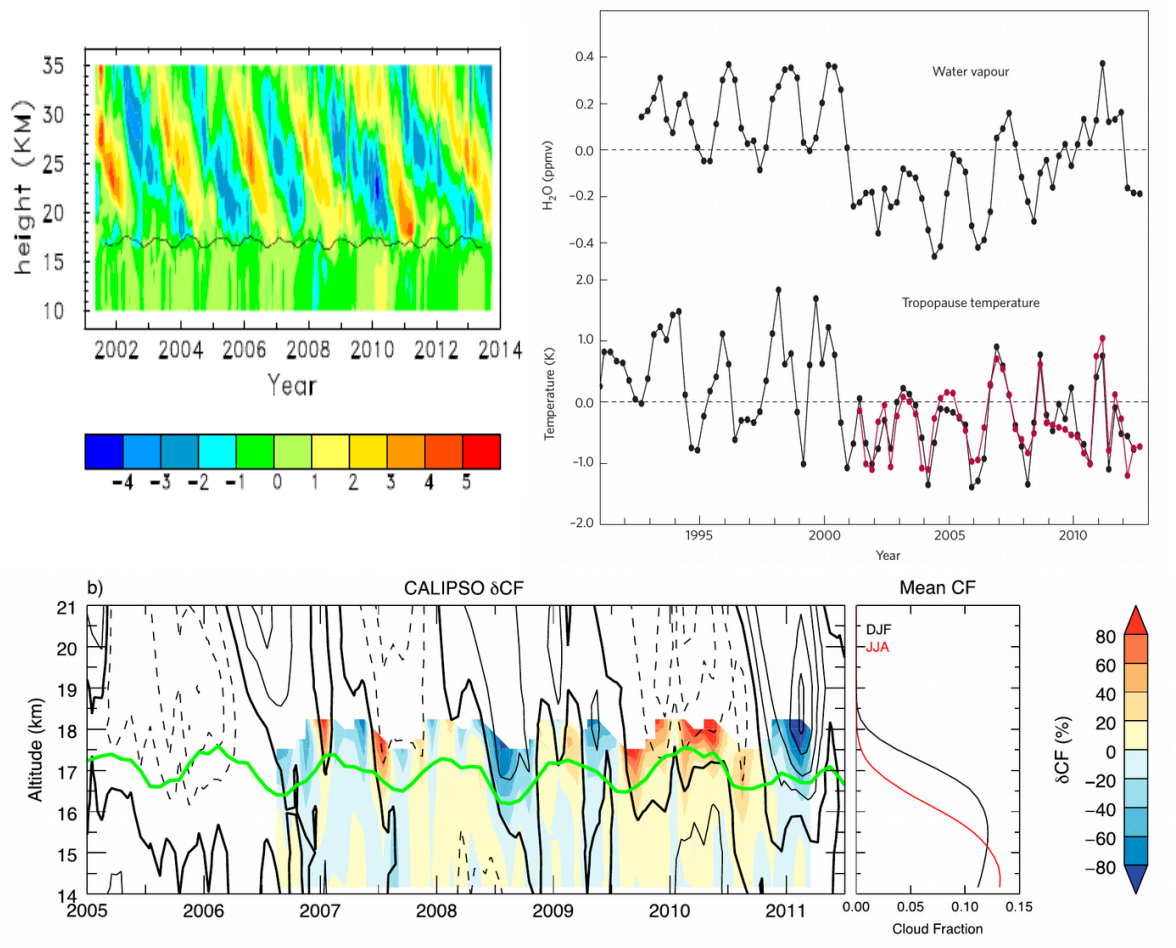

FIGURE 1.11 – En haut à gauche : diagramme de Hovmöller altitude-temps de la moyenne zonale tropicale de la température (*Randel and Wu*, 2005). En haut à droite : variabilité de la vapeur d'eau et de la température en moyenne zonale tropicale désaisonnalisée, tiré de (*Randel and Jensen*, 2013). En bas : diagramme de Hovmöller altitude-temps de la température dans la réanalyse MERRA (contours) et de la couverture en cirrus observée par l'instrument CALIOP (couleurs). Extrait de *Davis et al.* (2013).

1.3.2 Impact direct des ondes de basse et moyenne fréquence, avec structure zonale : favoriser la sursaturation et la formation des cirrus

Importance des ondes avec structure zonale et de la variabilité temporelle de la température On pourrait naïvement penser que seule la température en moyenne zonale influence la moyenne zonale de la concentration en vapeur d'eau et en glace de la TTL, les anomalies positives à la moyenne zonale étant compensées par des anomalies négatives. En fait ce raisonnement ne serait applicable qu'en cas d'équilibre thermodynamique entre vapeur et glace partout dans la TTL, c'est-à-dire si la TTL était entièrement à saturation et remplie de cirrus. Ce n'est évidemment pas le cas, la plus grande partie du volume de la TTL n'est pas nuageux et la sous-saturation par rapport à la glace y est majoritaire. À cause de l'existence d'un seuil en température pour la formation de glace[15], qui requiert que le rapport de mélange en vapeur d'eau soit au moins supérieur au rapport de mélange saturant $r_{sat}(T) < r_{H_2O}$, les

[15]Ce seuil n'est pas forcément le point de givre, ce peut aussi être le seuil de nucléation.

perturbations zonales et temporelles de température jouent un rôle important.

En particulier, si on suppose un lessivage complet de la vapeur d'eau en excès de la saturation, on a vu que la température au point froid de la tropopause T_{min}, minimum de température sur la verticale, jouait un rôle primordial. Sur cette température, les ondes ont un impact en moyenne zonale et temporelle qui est non négligeable[16] (voir la figure 1.12). *Kim and Alexander* (2015) ont quantifié cet impact à partir de radiosondes et ont trouvé que les ondes abaissaient en moyenne la température du point froid de 1,3 K ($\overline{T_{min}} - \overline{T}_{min} = -1,3$ K).

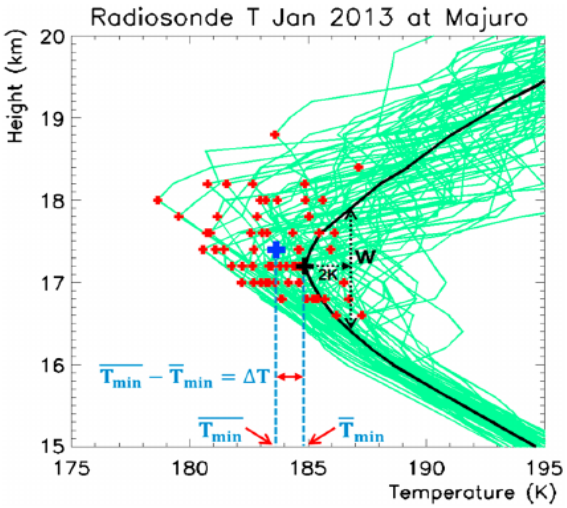

FIGURE 1.12 – Profils de température obtenus à partir de radiosondes à Majuro en janvier 2013, illustrant l'effet des ondes sur la température du point froid de la tropopause. Extrait de *Kim and Alexander* (2015).

Néanmoins, l'impact des ondes sur la déshydratation n'est pas nécessairement le même que celui le point froid. En effet, pour qu'il y ait déshydratation effective par un cirrus, il faut que les particules de glace sédimentent en dehors de leur zone de formation avant que la température ne réaugmente et ne provoque la sublimation des cristaux. À l'aide d'un modèle microphysique simplifié, *Fueglistaler and Baker* (2006) ont trouvé qu'à basse température ($<$ 210 K), le temps nécessaire pour une déshydratation efficace était de l'ordre de 10 heures. Les ondes de plus haute fréquence (intrinsèque) que 10 heures auraient donc un effet limité sur la déshydratation. Cela ne présume cependant en rien de leur effet sur la couverture nuageuse. De plus, comme présenté dans la section précédente, les ondes qui ont la plus forte signature en température sont les ondes de basse fréquence intrinsèque.

Observations et modélisation de la relation entre cirrus et ondes de « basse fréquence » En dehors des cirrus orographiques, une des premières observations de cirrus formé via des ondes de gravité est celle de *Fujita* (1982) qui décrit l'observations d'un « jumping cirrus » dans la stratosphère au dessus d'un complexe convectif. À l'aide de modélisation numérique, *Wang* (2004) interprète la formation de ce cirrus comme associée à des ondes de gravité convectives.

Dans la TTL, les études de modélisation de *Potter and Holton* (1995) ou de *Jensen et al.* (1996) ont été les premières à insister sur le rôle potentiel des ondes dans la formation des

[16] La moyenne temporelle ou spatiale des minima des profils verticaux de température est en effet inférieure (éventuellement égale) au minimum du profil de température moyen.

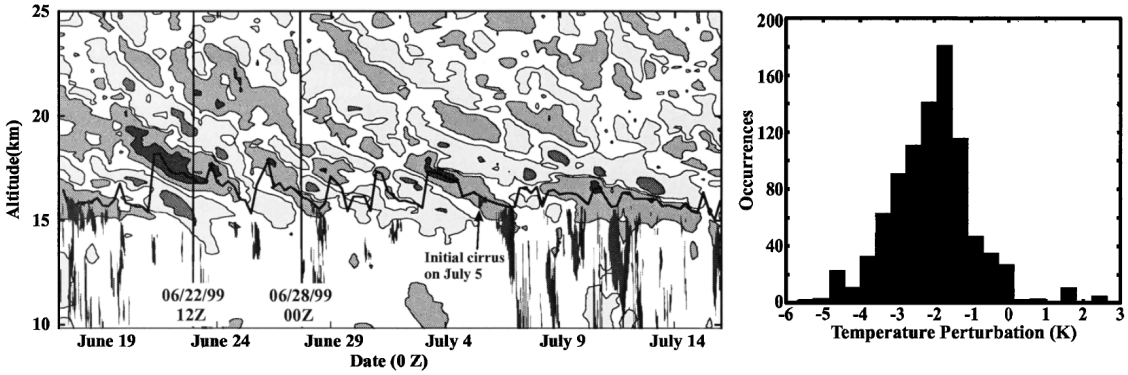

FIGURE 1.13 – A gauche : anomalies de température (contours grisés pour négatives, principalement associées à une onde de Kelvin) et observations lidar de nuage. À droite : occurrence de cirrus en fonction de l'amplitude de la perturbation de température. Extrait de *Boehm and Verlinde* (2000).

cirrus. De nombreuses observations ont par la suite confirmé ces prédictions. En particulier, la relation entre ondes de Kelvin et cirrus a été observée par différents auteurs (e.g. *Boehm and Verlinde*, 2000; *Immler et al.*, 2008; *Fujiwara et al.*, 2003, 2009). La figure 1.13 illustre les résultats de l'étude de *Boehm and Verlinde* (2000), qui montre essentiellement que les cirrus sont plus fréquents dans les anomalies froides de température causées par les ondes. *Pfister et al.* (2001) ont également noté la correspondance entre cirrus fin et phase de température froide d'une onde d'inertie gravité.

Concernant la modélisation, *Potter and Holton* (1995) ont été parmi les premiers à modéliser l'impact des ondes de gravité sur la déshydratation de la stratosphère. Leur étude a montré que les ondes de gravité convectives générées à proximité d'orages engendraient des fluctuations de température susceptibles de former des cirrus. Des études utilisant des modèles lagrangiens (*Jensen and Pfister*, 2004; *Ueyama et al.*, 2015; *Schoeberl et al.*, 2016) se sont également intéressées à l'impact des ondes de gravité sur les cirrus. En particulier, en accord avec les prédictions de *Fueglistaler and Baker* (2006), *Schoeberl et al.* (2016) ont montré que les ondes de gravité pouvaient accroître la fréquence d'occurrence des cirrus sans affecter la sédimentation et la déshydratation.

Récemment a eu lieu la campagne avion ATTREX (pour Airborne Tropical Tropopause Experiment) (voir figure 1.14), qui s'est déroulée en hiver boréal 2013-2014 dans le Pacifique tropical. Grâce à une série de vols longs couvrant plusieurs milliers de km, cette campagne a permis de mesurer la correspondance entre les anomalies de température négatives dues aux ondes et l'occurrence des cirrus à une échelle inédite jusqu'alors (*Kim et al.*, 2016). Sur la figure 1.14, tirée de *Kim et al.* (2016), on observe une très forte correspondance entre les anomalies de température froide et l'occurrence de cirrus dans le Pacifique Est et le Pacifique Ouest à haute altitude. À basse altitude dans le Pacifique Ouest, la correspondance est moins bonne, probablement à cause de l'effet direct de la convection. En effet, dans le Pacifique Ouest, région très convective en hiver boréal [17], les détrainements convectifs importants génèrent des enclumes et apportent de l'humidité, ce qui permettrait la formation de cirrus sans anomalie de température associée. Une autre possibilité est que le Pacifique Ouest, région climatologiquement très froide lors de l'hiver boréal (figure 1.9) constitue déjà une anomalie

[17] 2014 était une année ENSO neutre

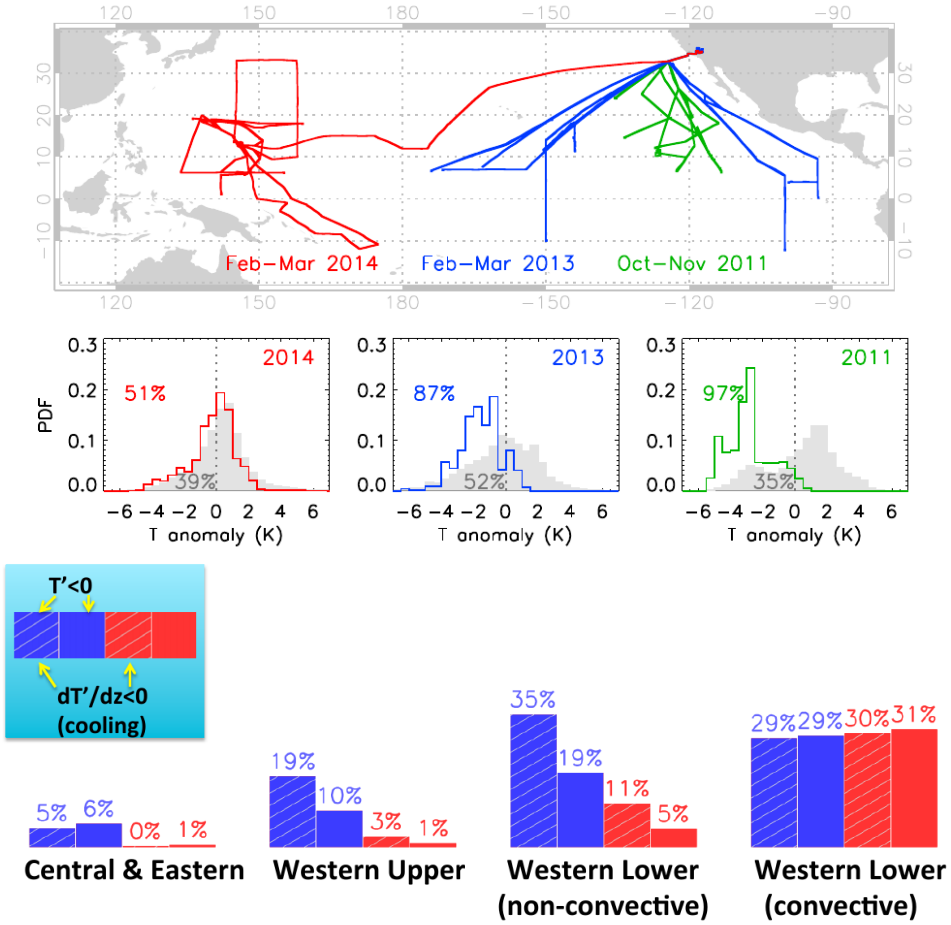

FIGURE 1.14 – Anomalies de température et de gradient vertical de température lors de l'occurrence de cirrus, d'après les données de la campagne ATTREX. Extrait de *Kim et al.* (2016).

lagrangienne de température pour les particules d'air advectées dans ces régions. D'ailleurs, d'un point de vue lagrangien, ceci peut aussi être vu comme un effet des ondes sur les nuages puisque les signatures de basses températures, en forme d'aile de papillon, observées dans le Pacifique Ouest sont souvent interprétées comme une réponse ondulatoire de grande échelle au chauffage convectif, suivant le modèle proposé par *Gill* (1980).

Structure verticale des ondes et cirrus Outre la relation avec la température, l'étude de *Kim et al.* (2016) observe également une **localisation préférentielle des cirrus sur les profils de température, dans les régions où les gradients verticaux d'anomalies de température dues aux ondes sont négatifs** $\frac{\mathrm{d}T'}{\mathrm{d}z}\left(=-\frac{m}{\hat{\omega}}\frac{\mathrm{d}T'}{\mathrm{d}t}\right) < 0$ [18]. Sachant que pour une onde se propageant vers le haut depuis la troposphère, $c_{g_z} > 0$ et donc $\frac{\hat{\omega}}{m} < 0$, la localisation préférentielle des cirrus dans les régions $\frac{\mathrm{d}T'}{\mathrm{d}z} < 0$ correspondrait ainsi à une formation préférentielle dans les régions de refroidissement $\frac{\mathrm{d}T'}{\mathrm{d}t} < 0$. Les cristaux formés sédimentent ensuite hors de leur région de formation initiale et en ont disparu lors de l'arrivée de la phase froide de l'onde, ce qui semblerait indiquer une irréversibilité du passage de l'onde et l'importance de la sédimentation. **Cette observation montre que les relations**

[18] En supposant une onde monochromatique.

entre ondes et cirrus vont au-delà de la simple corrélation avec les anomalies de température négatives, et appelle une explication théorique.

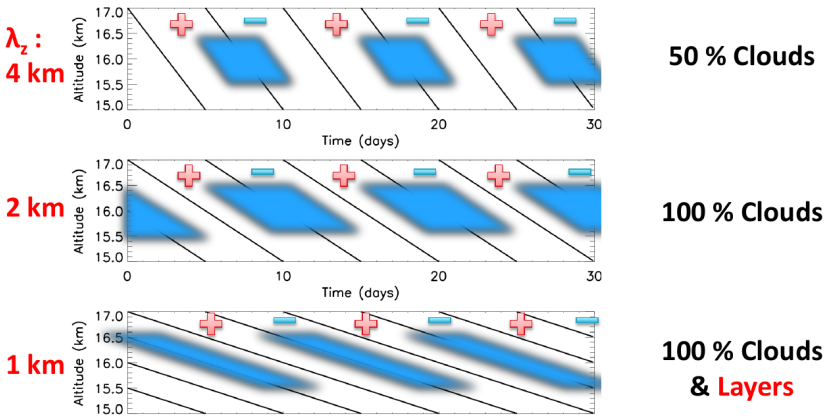

FIGURE 1.15 – Schémas représentant l'impact d'ondes de courte longueur d'onde verticale sur la couverture en cirrus. Extrait de *Kim et al.* (2016).

Conséquence des propriétés des ondes sur les cirrus Un des impacts des ondes de petite longueur d'onde verticale observées par *Kim and Alexander* (2013) sur les cirrus est de réduire leur épaisseur, tout en augmentant potentiellement la couverture nuageuse et donc leur impact radiatif. Ce phénomène est illustré par la figure 1.15.

1.3.3 Impact des ondes de haute fréquence sur les propriétés microphysiques des cirrus : nombre de cristaux de glace

Contrairement aux ondes de basse fréquence mentionnées précédemment, on s'attendrait à ce que les ondes de haute fréquence n'aient que peu d'impacts sur la déshydratation, d'abord parce que l'amplitude des fluctuations de température associées est limitée mais surtout parce que ces fluctuations ne durent pas assez longtemps pour qu'il y ait sédimentation de la glace.

Les ondes de haute fréquence jouent néanmoins un rôle important car elles dominent la variabilité des vitesses verticales, ce qui a un impact primordial sur la nucléation homogène des cristaux de glace à partir d'aérosols liquides (*Kärcher and Lohmann*, 2002; *Jensen et al.*, 1996). Pour comprendre cet effet, il convient d'expliquer en quelques mots le processus de formation des cristaux de glace dans la TTL. Il est évidemment question ici des cristaux de glace formés in situ et non de ceux détrainant de systèmes convectifs.

Deux principaux mécanismes sont débattus concernant la nucléation de la glace dans la haute troposphère-basse stratosphère. Le premier, et le moins bien connu, est la nucléation hétérogène : des aérosols solides, présents en faible quantité, nucléent lorsqu'une température et sursaturation critique par rapport à la glace sont atteintes. Les propriétés microphysiques des nuages, comme le nombre de cristaux, dépendent alors essentiellement des propriétés des aérosols solides sur lesquels se fait la nucléation et de leur concentration. Ce mécanisme de formation pourrait être dominant en basse TTL (*Cziczo et al.*, 2013).

Le second mécanisme en lice pour expliquer la formation in situ des cirrus est la nucléation dite homogène : des aérosols liquides aqueux (typiquement sulfatés) sont toujours présents en nombre important dans la TTL. Ils ont une certaine probabilité de nucléer en fonction

de leur taille, de la température et de la sursaturation ambiante par rapport à la glace. Contrairement à la nucléation hétérogène, ce processus est relativement bien contraint par la formule expérimentale de Koop (*Koop et al.*, 2000). En pratique, différentes études (e.g. *Jensen and Toon*, 1994; *Kärcher and Lohmann*, 2002) ont montré que le nombre de cristaux de glace formés par nucléation homogène était très sensible à la température T et au taux de refroidissement $\frac{\mathrm{d}T}{\mathrm{d}t}$ à l'instant de nucléation, taux de refroidissement qui de par l'hypothèse adiabatique sèche correspond à un facteur près à la vitesse verticale w[19]. La figure 1.16 montre le nombre de cristaux nucléés en fonction de w, pour différentes température de nucléation T. *Kärcher and Lohmann* (2002) proposent une formule reliant le nombre de cristaux nucléés N_i à la vitesse verticale, qui donne $N_i \propto w^{\frac{3}{2}}$. La figure 1.16 illustre cette loi d'échelle entre vitesse verticale et nombre de cristaux nucléés.

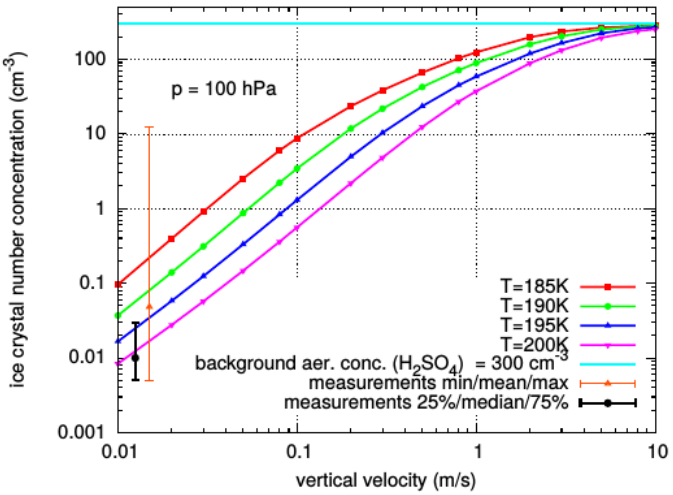

FIGURE 1.16 – Nombre de cristaux de glace N_i nucléés à partir d'aérosols aqueux suivant la formule de *Koop et al.* (2000) pour différentes vitesses d'updrafts w et différentes gammes de température T. Extrait de *Spichtinger and Krämer* (2013).

Néanmoins, ce type de relation entre w et N_i n'est valable que si w ne varie pas durant la nucléation. Une étude publiée peu de temps avant le début de la thèse (*Spichtinger and Krämer*, 2013) suggère qu'en présence d'ondes de gravité de haute fréquence, les variations significatives de w au cours de la nucléation limitent le nombre de cristaux formés [20]. Selon *Spichtinger and Krämer* (2013), ce type de processus pourrait expliquer les observation de faibles concentrations en cristaux de glace (10 #/L) faites dans les cirrus de la TTL (*Krämer et al.*, 2009), observations qui jusqu'à présent semblaient être en désaccord avec la théorie de la nucléation homogène. Cependant, l'étude de *Spichtinger and Krämer* (2013) est restée essentiellement illustrative à cause du manque de quantification des fluctuations de température et de vent vertical induites par les ondes de gravité.

Outre leur impact sur la microphysiques, les ondes influencent également la turbulence, sujet qui est abordé dans la section suivante.

[19] $\frac{\mathrm{d}T}{\mathrm{d}t} = -\frac{g}{C_p} w$ où $g = 10\,\mathrm{m\,s^{-2}}$ est l'accélération de la gravité et $C_p = 1004\,\mathrm{J/K/kg}$

[20] Via un réchauffement adiabatique qui viendrait stopper la nucléation.

1.4 Turbulence de petite échelle à la tropopause tropicale

La turbulence joue un rôle important dans la région de la haute troposphère-basse stratosphère (UTLS pour upper troposphere lower stratosphere). D'une part, elle contribue au mélange des constituants, aux échanges verticaux de chaleur et de matière. D'autre part, du fait des échelles impliquées, elle induit des réponses importantes dans le mouvement des avions qui volent principalement à ces altitudes, et représente un risque majeur pour le transport aérien (*Sharman and Lane*, 2016). Pour ces deux raisons, elle a fait l'objet de nombreuses études théoriques, de modélisation ou observationnelles. Ces études se sont surtout concentrées sur les moyennes latitudes, région où a lieu l'essentiel des vols long-courriers. La turbulence dans la TTL reste très mal connue.

1.4.1 Définition et origine de la turbulence dans l'UTLS

1.4.1.1 Tentative de définition

Turbulence est un terme vague, généralement associé dans notre imaginaire à l'idée de mouvement désordonné, chaotique, de tourbillons. Dans des introductions à la mécanique des fluides, le terme « turbulent » est généralement introduit pour un écoulement en opposition à celui de laminaire. Le nombre adimensionné distinguant ces deux régimes est le nombre de Reynolds Re, défini comme le rapport entre les termes non linéaires des équations de Navier-Stokes (les termes advectifs) et les termes diffusifs ; il peut s'écrire :

$$Re = \frac{LU}{\nu} \tag{1.28}$$

où L est une échelle caractéristique de l'écoulement, U une vitesse caractéristique et ν la viscosité cinématique du fluide. Un nombre de Reynolds très grand correspond à une dominance des termes d'advection de la quantité de mouvement par rapport aux termes de diffusion ; les équations de Navier-Stokes sont alors non linéaires. À l'inverse, pour $Re \ll 1$, les équations deviennent quasi-linéaires. La transition laminaire-turbulent est observée pour des nombres de Reynolds de l'ordre de 10^3. Si l'échelle caractéristique est facile à définir pour un écoulement observé autour d'un obstacle, le choix est moins évident dans l'atmosphère qui présente notamment des vitesses très variées selon l'échelle spatiale L. Un exemple pour un nombre de Reynolds « vertical » dans l'atmosphère est l'échelle de vitesse associée au vent vertical $U \sim 0,1\ \mathrm{m\,s^{-1}}$. Avec une viscosité cinématique $\nu \sim 10^{-4}\ \mathrm{m^2\,s^{-1}}$ en haute troposphère, on obtient des nombres de Reynolds supérieurs à 10^3 quelles que soient les échelles spatiales $L > 1$ m considérées.

Ainsi, en dynamique atmosphérique, le terme turbulence se réfère à un régime d'écoulement dans lequel on ne peut négliger les termes advectifs non linéaires qui permettent une interaction entre différentes échelles spatiales (une cascade d'énergie entre les échelles). Au sens strict, cela suppose une dominance des termes advectifs (verticaux ou horizontaux) par rapport à tout autre terme dans les équations du mouvement, donc par exemple un grand nombre de Reynolds mais un faible nombre de Froude (rapport entre la vitesse de l'écoulement et la vitesse des ondes). Dans un sens plus général, le terme turbulence peut s'appliquer à une superposition d'ondes quasi-linéaires, dans laquelle les termes non linéaires, bien que plus faibles et non dominants, interagissent les uns avec les autres entraînant une interaction entre

échelles. Le terme peut s'appliquer aussi à la turbulence quasi-géostrophique, pour laquelle le terme (linéaire) de Coriolis domine dans l'équation du mouvement mais la dynamique est contrôlée par les termes non linéaire. Ici, on s'intéresse à la turbulence de petite échelle (inférieure à quelques centaines de mètres), qui est souvent analysée comme de la turbulence stricto sensu, c'est-à-dire dans un régime dans lequel les termes advectifs dominent dans les équations du mouvement.

1.4.1.2 Origine de la turbulence dans la haute troposphère-basse stratosphère

Dans la couche limite, comme dans le cas de la convection profonde, ce sont principalement les instabilités convectives ou la génération mécanique à proximité de la surface qui donnent naissance à de la turbulence de petite échelle. Dans l'atmosphère libre, la mise en place de cette cascade d'énergie vers les petites échelles, qui connecte l'écoulement « moyen » et la dissipation, peut se faire via différents processus, générant des instabilités hydrodynamiques sèches ou humides, voir radiatives. Certains de ces processus sont examinés dans la suite.

Turbulence et onde de gravité L'un de ces processus générant de la turbulence est le déferlement d'ondes de gravité, évoqué à la section 1.2.2. La modification de l'amplitude des ondes à mesure de leur propagation dans des milieux de stabilité et de cisaillement variables, notamment la rencontre avec des niveaux critiques ou des niveaux de réflection, vient affecter le cisaillement $\sqrt{\frac{\partial u}{\partial z}^2 + \frac{\partial v}{\partial z}^2}$ et la stratification moyenne et peut déstabiliser l'écoulement. Ainsi, les ondes de gravité viennent modifier le nombre de Richardson Ri_g[21] :

$$Ri_g = \frac{N^2}{\left(\frac{\partial u}{\partial z}^2 + \frac{\partial v}{\partial z}^2\right)} = \frac{\frac{g}{\theta}\frac{\partial \theta}{\partial z}}{\left(\frac{\partial u}{\partial z}^2 + \frac{\partial v}{\partial z}^2\right)} \tag{1.29}$$

qui dans un fluide stratifié intervient dans le critère de déclenchement de l'instabilité de Kelvin-Helmholtz [22].

Pavelin et al. (2002) ou *Lane et al.* (2004) ont par exemple reporté des occurrences de turbulence associées à des ondes de gravité de plus ou moins grande amplitude à proximité de jets et fronts des moyennes latitudes. Combinées au cisaillement moyen de vent, ces ondes génèrent des nombres de Richardson plus forts et des instabilités. *Koch et al.* (2005) ont confirmé les résultats précédents et suggèrent l'existence d'une cascade d'énergie entre les échelles des ondes de gravité et la turbulence de petite échelle.

Dans des écoulements moyens complexes ou en présence de superpositions d'ondes, les ondes de gravité peuvent générer toutes une famille d'instabilité hydrodynamiques ou des processus de résonances entre ondes (incidente et réfléchie par exemple) qui peuvent amener à des cascades vers les plus petites échelles et à de la turbulence (*Fritts et al.*, 2009a,b).

En particulier, comme souligné dans la section 1.2, une source majeure d'ondes de gravité dans les tropiques est la convection profonde. De nombreuses études se sont intéressées aux ondes de gravité produites par les nuages convectifs et à la turbulence qu'elles pouvaient

[21] Il s'agit ici du nombre de Richardson de gradient.

[22] dont la condition nécessaire (en deux dimensions) est $Ri_g < \frac{1}{4}$.

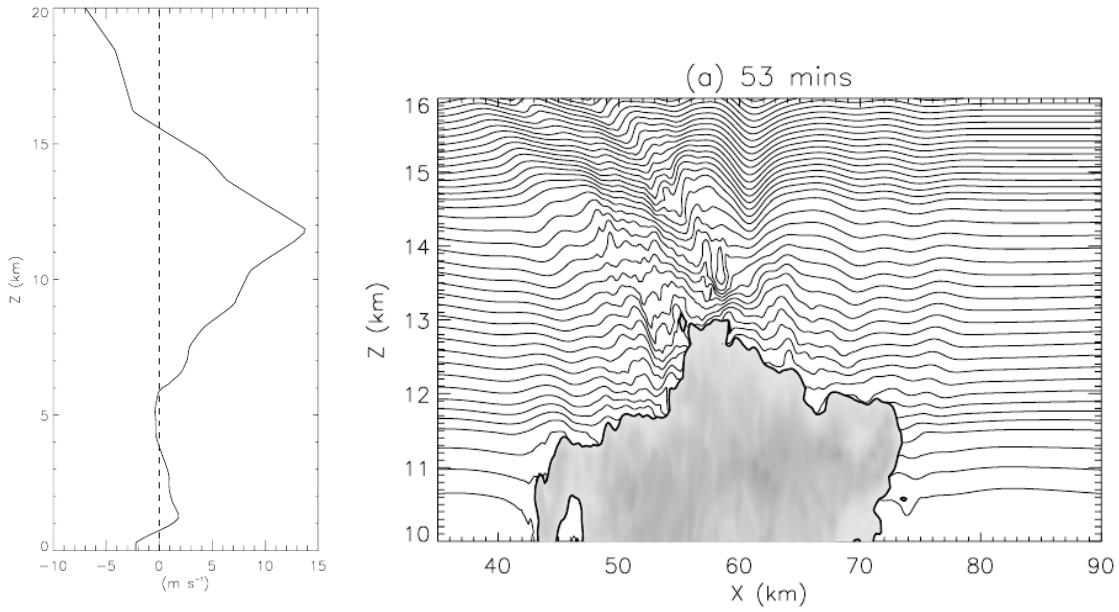

FIGURE 1.17 – Résultats de simulations d'ondes de gravité convectives déferlant à proximité de niveaux critiques et à l'origine de turbulence, tirées de *Lane and Sharman* (2006). À gauche, profil de vent moyen au début de la simulation. À droite, profil des isentropes au-dessus du nuage.

induire au cours de leur propagation. Par exemple, *Lane et al.* (2003a) ont montré que les ondes générées par la convection et se propageant suivant le cisaillement de vent pouvaient, en cas de cisaillement suffisamment forts, s'approcher de niveaux critiques. La figure 1.17 illustre les résultats de simulations numériques d'une étude similaire (*Lane and Sharman*, 2006) montrant ces processus à l'œuvre. Des ondes de gravité sont engendrées au-dessus d'un orage. Comme celles-ci sont de suffisamment petite échelle, le cisaillement au-dessus de l'orage est suffisant pour que $\omega - kU \rightarrow 0$ (f) et que l'onde se rapproche d'un niveau critique. Les ondes de petites échelles (grands k) sont plus sensibles à l'effet Doppler associé aux cisaillements de vent, qui modifie davantage leur fréquence intrinsèque par rapport aux ondes de grande longueur d'onde. Ces ondes de petite échelle ont donc tendance à déferler à plus basse altitude (voir aussi l'équation (1.23)). Ce type de simulation illustre ainsi le rôle des ondes de gravité convectives dans la formation de turbulence, ce qui est également suggéré par la répartition observée des poches de turbulence, plus fréquentes près des nuages convectifs (figure 1.18). Les simulations de *Lane and Sharman* (2006) illustrent également qualitativement l'impact que peut avoir le déferlement de ces ondes sur le mélange vertical de constituants, mais avec les limites du modèle : *While model simulations like this one are qualitatively useful, detailed observations of turbulence and the resultant transport are essential to obtain robust quantitative estimates of mixing.* (*Lane and Sharman*, 2006).

Enfin, comme présenté en début de chapitre, les circulations dans la TTL et la basse stratosphère sont dominées à grande échelle par des ondes équatoriales. Lorsque celles-ci sont proches de déferler, elles peuvent induire de la turbulence de façon significative. *Fujiwara et al.* (2003) prêchent ainsi en faveur de couches turbulentes induites par des ondes de Kelvin équatoriales.

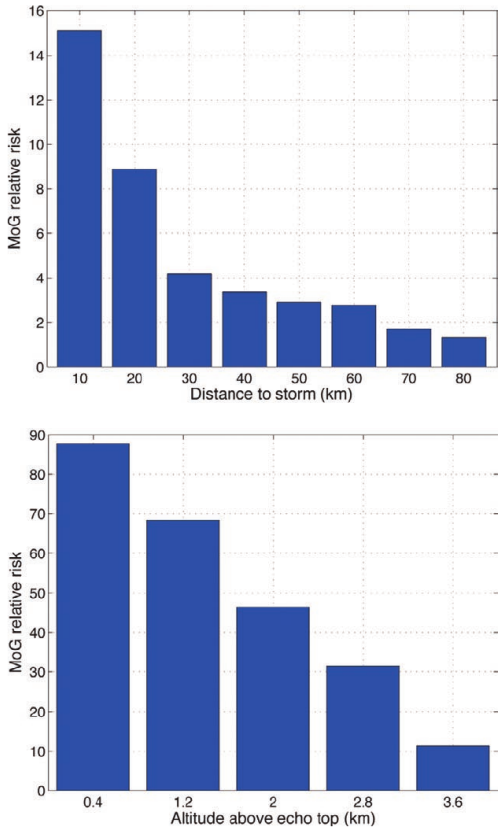

FIGURE 1.18 – Fréquence d'occurrence de turbulence en fonction de la distance à la convection (en haut) et de l'altitude au-dessus des nuages convectifs (en bas), pour des vols d'avions commerciaux au-dessus des États-Unis. Extrait de *Lane et al.* (2012).

Turbulence et cirrus Une autre source de turbulence dans l'UTLS est la présence de cirrus, nuages de glace. Ceux-ci, par dégagement de chaleur latente lors de la condensation ou de la sublimation, ou bien encore par effets radiatifs, peuvent contribuer à la mise en place de turbulence. Via des simulations numériques, *Dobbie and Jonas* (2001) ont étudié l'impact des processus radiatifs et de dégagement de chaleur latente sur l'évolution de cirrus dans des simulations numériques. Ils ont mis en évidence que le chauffage [23] contribuait à nourrir la variabilité des vitesses verticales et de la turbulence au sein du cirrus, et à augmenter son extension et sa durée de vie. L'effet radiatif est particulièrement marqué pour les cirrus d'enclumes, ainsi que l'ont montré les simulations numériques de *Fu et al.* (1995) : le chauffage différentiel (ondes longues) entre le sommet du nuage qui se refroidit vers l'espace et sa base chauffée par le sol, peut entraîner des instabilités convectives se développant dans le nuage. Les règles d'évitement de turbulence pour les avions de ligne spécifient d'ailleurs qu'il convient de rester en-dehors de ces cirrus d'enclumes. Différentes études basées sur des données d'observations in situ (par exemple *Gultepe and Starr*, 1995; *Chan et al.*, 1998) ont reporté des occurrences de turbulence plus fréquentes dans les cirrus qu'en ciel clair. En ce qui concerne les cirrus plus fins rencontrés à la tropopause tropicale, leur effet sur la turbulence est encore largement inconnu. Ces nuages sont suffisamment fins optiquement pour que leur présence ne soit associée qu'à un chauffage, et la mise en place éventuelle

[23] À la fois radiatif et par dégagement de chaleur latente.

de turbulence serait alors associée à des instabilités convectives au somment du nuage, qui est chauffé davantage que l'air le surplombant. Des études de modélisation récentes (e.g. *Dinh et al.*, 2010) suggèreraient que les chauffages radiatifs dans les cirrus tropicaux soient suffisants pour engendrer ce type de circulation au sein du nuage. Cependant, le réalisme de ces simulations très idéalisées pour le cas des cirrus de la tropopause tropicale est débattu (*Jensen et al.*, 2011). La question reste ouverte, faute d'observations.

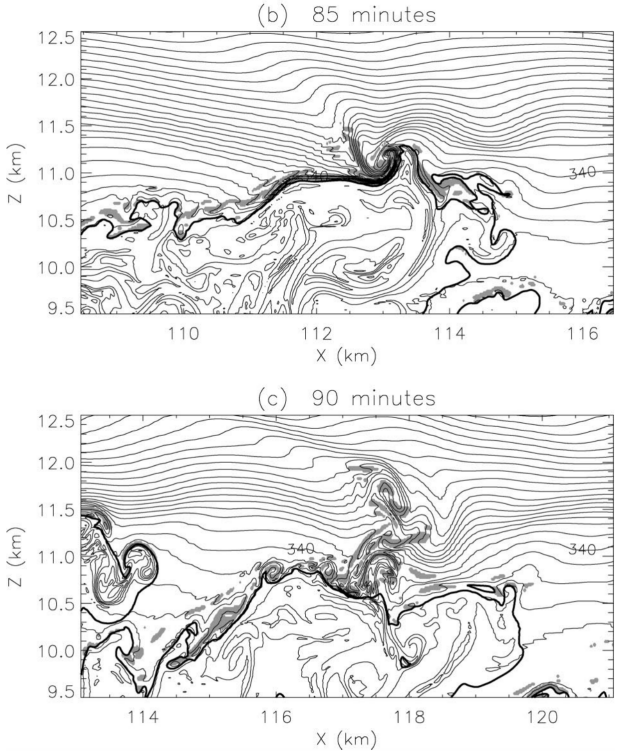

FIGURE 1.19 – Simulations numériques d'un overshoot et de la turbulence de petite échelle associée, tiré de *Lane et al.* (2003a). Les contours noirs sont les contours d'iso-température potentielle. Les limites du nuage sont représentées par les contours gras, alors que les zones turbulentes (d'après la paramétrisation sous-maille) sont représentées par les zones grisées.

Turbulence et nuages convectifs Outre via la génération d'ondes, la convection profonde, mouvement pleinement turbulent, peut étendre directement la turbulence dans la stratosphère via des overshoots, i.e. des bulles ou panaches nuageux dépassant le niveau de flottabilité neutre (souvent situé à la tropopause). La figure 1.19 montre une simulation d'un tel overshoot (à x=118 km, z= 11 km), ainsi que la turbulence associée. Celle-ci, limitée à la proximité immédiate du nuage dans un premier temps, s'étend ensuite dans la stratosphère avec la pénétration de l'overshoot.

Cette turbulence associée aux overshoots a reçu beaucoup d'attention, d'une part à cause des risques pour l'aviation, mais surtout à cause de son impact potentiel sur le mélange vertical.

1.4.2 Impacts de la turbulence à la tropopause tropicale sur le transport vertical

Transport via la turbulence convective et les overshoots Historiquement, le mélange vertical associé aux overshoots a reçu une attention particulière. Il a ainsi été suggéré que ce processus soit responsable de la sécheresse de la stratosphère (*Danielsen*, 1982). Le concept décrit dans le papier de Danielsen est illustré par la figure 1.20, panneau de droite. Les particules d'air dans les ascendances convectives s'élèvent dans l'atmosphère, accélérant verticalement à cause des forces de flottabilité, jusqu'à atteindre leur niveau de flottabilité neutre (LNB pour Level of Neutral Buoyancy), donné approximativement par le niveau où la température potentielle équivalente de la particule d'air est égale à la température de l'environnement. Ce niveau, qui est aussi le niveau de détrainement moyen des nuages convectifs, est en général situé sous la tropopause (voir panneau de gauche de la figure 1.20, mais aussi *Liu and Zipser* (2005)) ; il peut même être abaissé si les processus d'entrainement d'air non nuageux sont suffisants. Une fois que la particule d'air convectif atteint la tropopause, son inertie la transforme en overshoot. Sans mélange, celui-ci rejoint son niveau de flottabilité neutre et aucun échange ne se passe. Cependant, les processus dans les overshoots sont très non linéaires, et la turbulence générée entraîne un mélange entre cette ascendance et l'air stratosphérique, ce qui élève le niveau de flottabilité neutre. L'air nuageux s'étend au-dessus de la tropopause, dans une enclume de nuage de glace dans la stratosphère (voir figure 1.20). L'intuition suggérerait alors que le mélange de l'air convectif avec l'air stratosphérique sec entraîne l'évaporation rapide de la glace transportée avec l'overshoot, avant qu'elle ne puisse sédimenter, et donc in fine l'hydratation de la stratosphère. *Danielsen* (1982) prêche plutôt pour une déshydratation, via la mise en place de turbulence associée aux effets radiatifs des enclumes, qui maintiendrait le nuage et permettrait une sédimentation de la glace relativement à l'air environnant ; une machine à déshydrater selon ses termes. Cette théorie a été reprise dans son essence par différentes études (e.g. *Danielsen*, 1993; *Sherwood and Dessler*, 2000, 2001).

Cependant, depuis lors, des simulations numériques (e.g. *Jensen et al.*, 2007) ont montré que, si l'injection de glace par les overshoots était possible, les propriétés microphysiques des cristaux étaient telles qu'il semblait inenvisageable que ceux-ci puissent sédimenter sur des distances suffisantes avant leur sublimation complète pour produire une déshydratation de la stratosphère [24]. L'impact de ces overshoots serait donc plutôt une hydratation, contrairement à l'hypothèse originale de *Danielsen* (1982). Par contre, différentes observations ont suggéré la viabilité du mécanisme de détrainement des overshoots et de formation d'enclumes au-dessus du niveau de flottabilité neutre (et de la tropopause). *Corti et al.* (2008); *De Reus et al.* (2009) ont ainsi observé des cristaux de glace dans la stratosphère au-dessus d'*Hector the convector* célèbre orage des îles Tiwi au nord de l'Australie, et au-dessus d'orages au Brésil. Les concentrations en glace observées à de tels niveaux de température potentielle (>420 K, figure 1.20) sont telles que la seule explication[25] est une origine convective. Des études de modélisation idéalisée (e.g. *Hassim and Lane*, 2010) ou plus réalistes (e.g. *Chaboureau et al.*, 2007; *Frey et al.*, 2015; *Dauhut et al.*, 2016) montrent également un échange efficace entre overshoots et la stratosphère. En particulier, les simulations de *Frey et al.* (2015) ont montré

[24] En tous cas si la stratosphère est sous-saturée à l'origine, ce qui est le cas en général.

[25] Si l'on exclut les traînées de condensation (contrails) générées par l'avion d'observation.

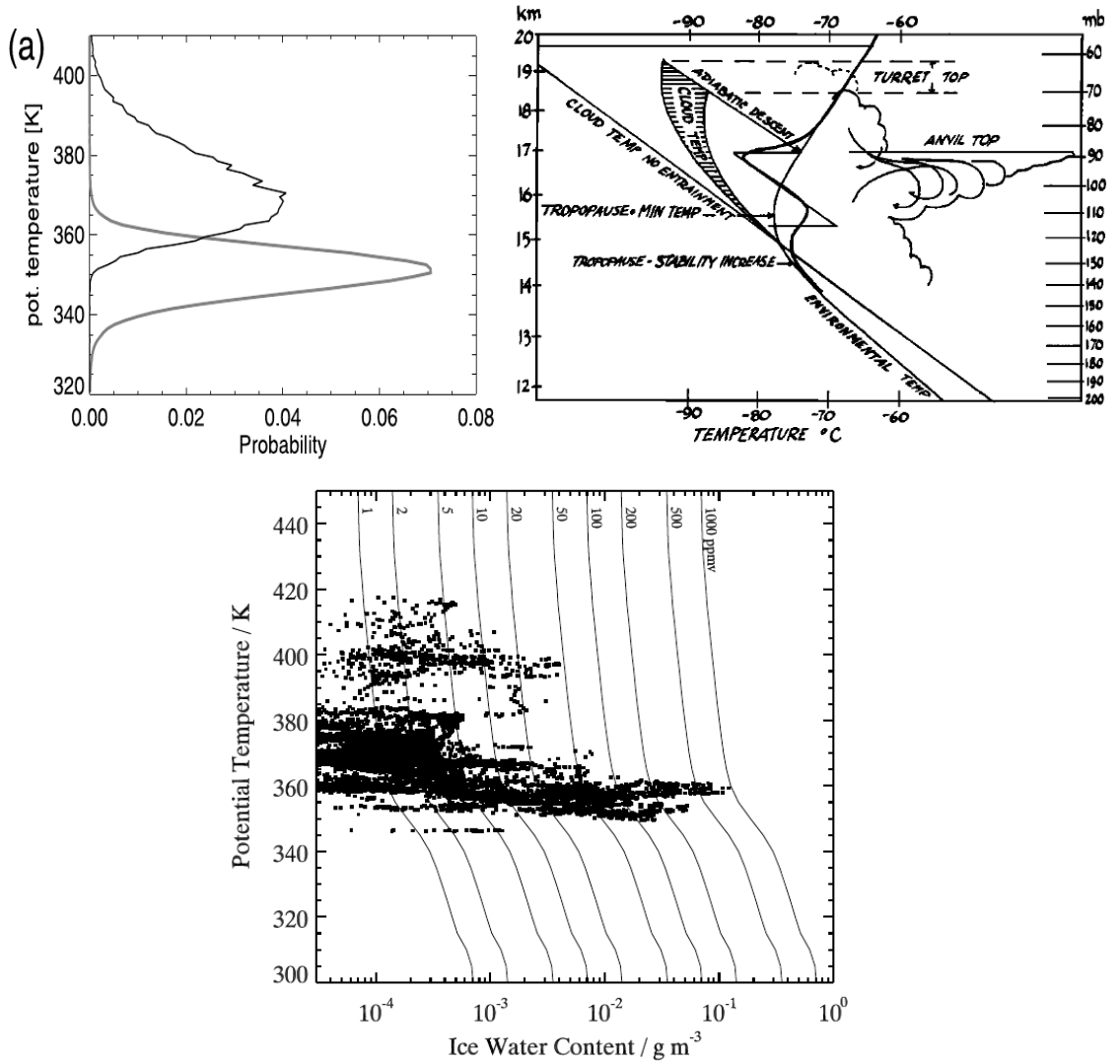

FIGURE 1.20 – En haut à gauche, distribution de probabilité de la température potentielle équivalente θ_e dans la couche limite et de la température potentielle à la tropopause (point froid) à Koror, Pacifique Ouest, d'après *Fueglistaler et al.* (2009). En haut à droite, schéma des processus aboutissant à la mises en place d'enclumes d'overshoots mélangeant de l'air de la couche limite avec l'air de la TTL, d'après *Danielsen* (1982). En bas, profils de rapport de mélange en glace en fonction de la température potentielle, observés in situ à proximité de nuages convectifs lors des campagnes SCOUT-O_3 et TROCCINOX, d'après *Corti et al.* (2008).

un transport irréversible (« à travers les isentropes ») de traceurs de la couche limite vers la stratosphère, illustrant le rôle potentiel du mélange des overshoots avec leur environnement. Les simulations de *Frey et al.* (2015) et *Dauhut et al.* (2016) illustrent également un transport irréversible d'air de la stratosphère-haute TTL vers les plus basses couches de la TTL, via les subsidences compensatoires aux ascendances des overshoots.

Du point de vue observationnel, outre l'échantillonnage de glace in situ à haute température potentielle, un second argument en faveur du détrainement et de l'échange overshoot-environnement au-dessus du niveau de flottabilité neutre est le profil d'isotopes stables de l'eau dans la phase vapeur. L'enrichissement en isotopes lourds dans la partie supérieure de la TTL (*Moyer et al.*, 1996; *Hanisco et al.*, 2007) suggère un apport de glace via un trans-

port vertical rapide, éventuellement via un mélange turbulent entre les overshoots et leur environnement. Néanmoins, étant donné le nombre de degrés de liberté impliqué pour une modélisation au niveau global, les observations in situ très ponctuelles et les incertitudes de la modélisation, l'efficacité du mélange et du transport par les overshoots reste à quantifier.

Transport via les poches de turbulence en air clair Bien que proches de la convection, les poches de turbulence en air clair induites par le déferlement d'ondes de gravité convectives n'ont probablement pas un impact direct aussi important que celui de la turbulence associée aux overshoots, car les masses d'air concernées ont connu moins de déplacements verticaux. Les simulations idéalisées de *Wang* (2004); *Lane and Sharman* (2006); *Hassim and Lane* (2010) ont montré la possibilité de mélange associée spécifiquement à la turbulence générée par le déferlement d'ondes de gravité convectives, en air clair, au-dessus de la convection. En dehors des régions convectives, dans le Pacifique Est par exemple, la turbulence associée aux ondes de gravité ou à des ondes équatoriales pourrait être active dans le mélange vertical. *Fujiwara et al.* (1998) rapportent par exemple une observation de transport vertical d'ozone associé au mélange induit par une onde de Kelvin déferlante [26]. Dans la même veine, *Fujiwara et al.* (2001) soulignent que le déferlement d'ondes équatoriales de Kelvin peut contribuer au transport irréversible de constituants, mais ces auteurs n'apportent pas de quantification de ce processus. Côté paramétrisations, *Flannaghan and Fueglistaler* (2011) ont montré que, dans un modèle météorologique global, les ondes de Kelvin équatoriales pouvaient induire une réponse de la paramétrisation du mélange turbulent et un transport vertical de chaleur important.

Impact du transport turbulent et de la diffusivité verticale induite par la turbulence en air clair L'impact de la turbulence sur le transport vertical est souvent représenté dans l'équation bilan d'un traceur sous la forme d'une diffusivité turbulente. En simplifiant les termes horizontaux, l'équation bilan en moyenne zonale tropicale du rapport de mélange d'un traceur χ peut s'écrire comme une simple équation d'advection-diffusion (*Mote et al.*, 1998) :

$$\bar{\chi}_t + \bar{w}\bar{\chi}_z = \frac{1}{\rho}(\rho K_{\text{eff}}\chi_z)_z - \alpha(\chi - \chi_{ML}) + S \tag{1.30}$$

où $\bar{w}$ est la composante verticale de la circulation, $\frac{1}{\rho}(\rho K_{\text{eff}}\chi_z)_z = \overline{w'\chi'}$ représente le transport turbulent, α est un coefficient de dilution dans l'air des moyennes latitudes de concentration χ_{ML} et S est le terme source. *Mote et al.* (1998) se sont servis de cette équation pour modéliser le bilan du *tape recorder* en vapeur d'eau dans la basse stratosphère tropicale (mis en évidence par *Mote et al.*, 1996). Le terme qui nous intéresse dans cette équation, i.e. $\frac{1}{\rho}(\rho K_{\text{eff}}\chi_z)_z$, représente le transport turbulent effectif. L'amplitude du mélange vertical turbulent est contrôlée par les gradients verticaux des différents traceurs et par le coefficient K_{eff}, appelé diffusivité verticale effective. Il est responsable, dans le cas du *tape recorder*, de la dilution du signal lors de sa propagation en stratosphère mais peut également selon le profil vertical contribuer au transport vertical moyen. La figure 1.21 représente le profil de K_{eff} déduit des observations satellites du *tape recorder* en vapeur d'eau ; des valeurs de K_{eff} de l'ordre de ~ 0.02 m^2/s sont déduites dans la TTL.

[26] Cependant, cette observation n'étant associée qu'à un unique profil d'ozone, sans signature en température potentielle, reste peu convaincante

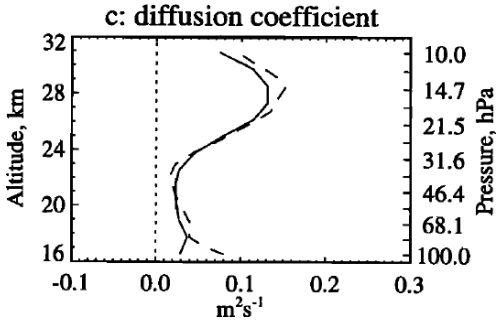

FIGURE 1.21 – Diffusivité turbulente verticale effective K_{eff} déduite par *Mote et al.* (1998) à partir d'observations satellites du *tape recorder* en vapeur d'eau.

Une forte incertitude entoure cette estimation de K_{eff} à partir d'observations satellites en moyenne zonale, à cause du nombre important de degrés de liberté. Les différents paramètres, comme $\bar{w}$, ont une variabilité importante, notamment saisonnière. Récemment, *Glanville and Birner* (2016) ont reproduit l'analyse de *Mote et al.* (1998) sur les données de vapeur d'eau du sondeur micro-onde aux limbes sur le satellite Aura (Aura-MLS) en incluant une variabilité saisonnière pour les différents termes ; ces auteurs obtiennent des valeurs de diffusivité estimées 3 à 4 fois supérieures à celles de *Mote et al.* (1998), mais ces résultats restent très incertains.

Il est donc souhaitable d'obtenir K_{eff} par d'autres approches. Une estimation de la diffusivité effective induite par un ensemble de poches turbulentes intermittentes sur le mélange vertical dans la stratosphère a été obtenue pour la première fois par *Dewan* (1981). Sans rentrer dans le détail des calculs, la méthode se base sur les observations des paramètres de couches turbulentes, notamment de leur épaisseur verticale. Elle considère le problème comme étant celui d'un ensemble de particules d'air se déplaçant lagrangiennement dans un écoulement laminaire, et rencontrant de façon intermittente mais régulière des poches turbulentes d'une certaine épaisseur. *Dewan* (1981) suppose les patchs parfaitement mélangés et une particule entrant dans un patch peut donc ressortir à n'importe quelle altitude. À cette marche aléatoire des particules d'air s'ajoute sur la verticale l'ascension moyenne, et l'ensemble peut être vu en moyenne comme un mouvement brownien avec dérive. L'effet de la turbulence peut donc, via l'équation de Fokker-Planck associée à ce mouvement brownien, être représentée par une diffusivité effective dépendant de la fraction turbulente de l'atmosphère (i.e. la fréquence de rencontre de patchs turbulents) et de leur épaisseur. Avec ces hypothèses, *Dewan* (1981) estimait $K_{\text{eff}} \simeq 0,2\,\text{m}^2/\text{s}$, bien supérieur à ce qu'indiquent les observations de traceurs dans les tropiques (*Mote et al.*, 1996). La théorie a été raffinée par *Alisse and Sidi* (2000); *Vanneste* (2004); *Osman et al.* (2016) pour inclure un mélange limité dans les poches de turbulence. Appliquée à des observations dans la stratosphère des moyennes latitudes, elle donne $K_{\text{eff}} \simeq 0.01\,\text{m}^2/\text{s}$. Aucune estimation équivalente n'est disponible pour la TTL, mais quelques observations de turbulence ont été obtenues en des régions précises.

1.4.3 Observations et paramétrisation de la turbulence à la tropopause tropicale et de son impact sur le transport

Observations de la turbulence à la tropopause tropicale L'essentiel des mesures de turbulence à la tropopause tropicale a été obtenu dans la région de l'Inde, à partir de données Radar (*Rao et al.*, 2001) ou de radiosondes appliquant la méthode de Thorpe « conventionnelle » (*Alappattu and Kunhikrishnan*, 2010; *Sunilkumar et al.*, 2015).

La figure 1.22 montre les profils de variance d'indice de réfraction C_n^2 et de diffusivité obtenus par *Rao et al.* (2001) sur le site de Gadanki au sud de l'Inde. On note un léger maximum local vers 18 km pour C_n^2, et surtout des diffusivité plus forte lors de la période de la mousson, en accord avec l'importance signalée précédemment des processus convectifs. On note également une décroissance légère de la diffusivité avec l'altitude dans la TTL.

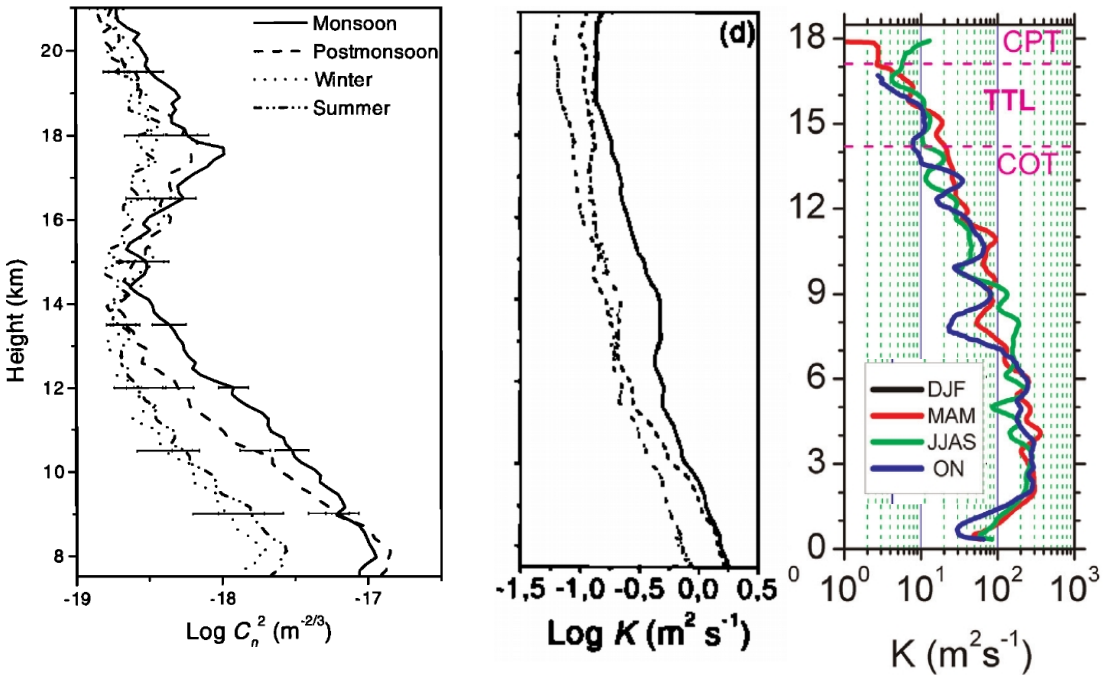

FIGURE 1.22 – (À gauche) Profils de variabilité d'indice de réfraction C_n^2, mesure de la turbulence à partir de Radar et (au centre) profils de diffusivité déduit de mesures Radar à Gadanki, Inde, tiré de *Rao et al.* (2001). Les différentes saisons (mousson,...) sont représentées par différents tiretés. Noter les diffusivités plus intenses lors de la mousson (traits pleins). À droite, profils de diffusivité obtenus à partir de radiosondes par *Sunilkumar et al.* (2015) en utilisant la méthode de Thorpe.

Le panneau de droite de la figure 1.22 montre le profil de diffusivité obtenu par l'analyse de radiosondes à partir de la méthode de Thorpe sur le même site de Gadanki que pour les observations Radar. Contrairement à celle de *Rao et al.* (2001), l'étude à partir de radiosondes de *Sunilkumar et al.* (2015) ne montre pas de variation saisonnière. Par contre, on observe un gradient d'un facteur 10 sur la diffusivité entre la base de la TTL (14-15 km) et son sommet (19 km). Les valeurs de K sont comprises entre 10^0 et 10^1 $m^2\,s^{-1}$ dans la TTL, plus d'un ordre de grandeur au-dessus de celles de *Rao et al.* (2001) aux mêmes altitudes. Il est important de noter que l'estimation de la diffusivité via la méthode de Thorpe est très indirecte (*Wilson et al.*, 2011), et donc les valeurs quantitatives apportées par cette étude ont probablement moins de valeur que les allures qualitatives des profils. Ces différentes études montrent une

grande disparité des estimations de diffusivité, qui varient de plusieurs ordres de grandeur selon la méthode employée. Cela provient essentiellement du caractère indirect des différentes mesures, mais ne rend pas la tâche aisée pour la paramétrisation de ces processus.

Paramétrisation de la turbulence dans les modèles atmosphériques Les paramétrisations qui servent de référence au forçage de l'écoulement moyen par la turbulence sont validées et tirées d'observations dans la couche limite atmosphérique. Les plaines du Kansas, si elles constituent un terrain de choix pour examiner les caractéristiques de la couche limite, n'ont que peu à voir avec la tropopause tropicale. L'impact de la turbulence en haute troposphère et stratosphère est ainsi un terme mal contraint dans les modèles météorologiques.

En effet, les paramétrisations de la turbulence utilisées dans les modèles atmosphériques sont essentiellement mises en place pour représenter les processus dans les basses couches, mais elles sont néanmoins en général utilisées dans toute l'atmosphère. L'effet de la turbulence dans la haute troposphère d'un modèle peut être grandement modifié lors d'un changement de paramétrisation de couche limite. Ainsi, *Bardeen et al.* (2013) ont noté que lors du passage à la version 5 du modèle de climat du NCAR, le changement du schéma de couche limite avait augmenté la diffusivité moyenne d'un facteur $\sim 10^2$ en haute troposphère (figure 1.23). Très inférieure dans CAM 4 aux estimations de *Alappattu and Kunhikrishnan* (2010), la diffusivité paramétrée dans CAM 5 était environ 5 à 10 fois supérieure à ces observations. Cela générait des problèmes majeurs pour la représentation des processus nuageux avec le modèle de microphysique détaillé CARMA : les flux verticaux de vapeur d'eau étaient tels que la déshydratation dans les nuages devenait insuffisante et la haute troposphère très humide, avec des effets de *run away greenhouse*. La diffusivité a été diminuée artificiellement pour pallier ce problème.

Flannaghan and Fueglistaler (2014) ont noté des différences similaires entre différentes versions du modèle du centre européen de prévision météorologiques à moyen terme (ECMWF). Le schéma de Louis modifié utilisé dans le modèle actuel (ECMWF IFS Cy43r1) et la réanalyse ERA interim (ECMWF IFS Cy31r2) d'une part, et le schéma type Monin-Obukhov qui a été utilisé dans une version intermédiaire (ECMWF IFS Cy33r1) d'autre part, produisent des diffusivités bien différentes, d'un facteur 1 à 10, selon la région et la période considérée. En comparant la vitesse verticale du *tape recorder* en vapeur d'eau dans les observations de Aura MLS et dans la réanalyse ERA interim, *Glanville and Birner* (2016) suggèrent une diffusion verticale environ 3 à 4 fois trop importante dans ERA-interim. Il est important de remarquer qu'une partie de la diffusion observée dans les modèles est d'origine numérique, ou pour les analyses peut provenir d'une dispersion excessive due à l'assimilation de données. Néanmoins, étant donné son importance et la plus faible magnitude de la diffusion numérique sur la verticale, il semble nécessaire d'évaluer et de caractériser la paramétrisation de la diffusion turbulente dans la haute troposphère-basse stratosphère tropicale.

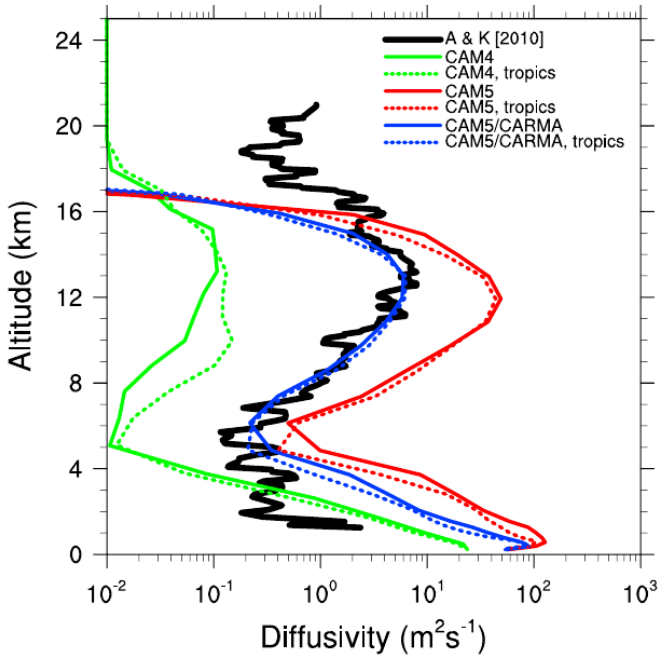

FIGURE 1.23 – Profils de diffusivité turbulente pour la chaleur K_h en moyenne tropicale (courbes pleines) et globale (courbes tiretées) telle que paramétrée dans le modèle du NCAR CAM, dans ses versions 4 (en vert) et 5 (en rouge). Les courbes bleues correspondent à la paramétrisation de la version 5 ajustée aux observations de *Alappattu and Kunhikrishnan* (2010) (en noir). Extrait de *Bardeen et al.* (2013).

1.5 Problématique, objectifs et méthodologie de la thèse

1.5.1 Problématique

Dans ce contexte, cette thèse vise à mieux quantifier et caractériser la dynamique à la tropopause tropicale et son impact sur les cirrus ou le mélange. Au sein de cette thématique générale, quatre grandes questions ont été abordées en combinant différentes approches :

1. **Fluctuations de température et de vitesse verticale** : Quelle est l'amplitude et la distribution en fréquence (spectre) des fluctuations de température et de vitesse verticale à la tropopause tropicale ? Comment expliquer le spectre des fluctuations observées ? Comment ces fluctuations sont-elles représentées dans les modèles à grande échelle ? Quelles caractéristiques doivent être paramétrées ? Comment l'intermittence du champ d'onde de gravité se traduit-elle pour ces fluctuations de température ?

2. **Effets des ondes sur la microphysique** : Quelles interactions peuvent exister entre les fluctuations dynamiques induites par les ondes et la microphysique ? En particulier, quel est l'impact des fluctuations rapides de vitesses verticales sur la **nucléation des cristaux de glace** et les propriétés microphysiques des cirrus ? Quel est l'**impact des ondes sur la sédimentation des cristaux** et la déshydratation des masses d'air ?

3. **Ondes équatoriales et cycle de vie des cirrus** : Des études basées sur les observations ont suggéré une forte corrélation entre les ondes et les occurrences de cirrus.

D'autres études ont souligné un impact potentiellement majeur des processus radiatifs sur la dynamique. Quels processus (dynamique des ondes, chauffages radiatifs) contrôlent le cycle de vie d'un cirrus ?

4. **Turbulence à la tropopause tropicale** : À quel point la TTL est-elle turbulente ? Qu'est-ce qui contrôle la mise en place et la répartition de cette turbulence ? Quel est l'importance du mélange turbulent (en ciel clair) sur le transport vertical à la tropopause tropicale ? Comment les paramétrisations utilisées dans les modèles à grande échelle se comparent-elles aux observations ?

1.5.2 Outils d'étude

Pour aborder ces questions, les études effectuées se sont en partie basées sur des approches théoriques et un modèle météorologique à mésoéchelle, le modèle WRF[27]. Ces outils seront introduits dans les chapitres concernés. Du fait de leur place centrale dans la thèse, on présente ici brièvement les mesures in situ acquises lors de campagnes d'observations récentes : la campagne ballon PréConcordiasi pilotée par le CNES[28], et la campagne ATTREX (Airborne Tropical Tropopause EXperiment) pilotée par la NASA[29].

Campagne PréConcordiasi La campagne, préparatoire à la campagne Concordiasi dans les régions polaires de l'hémisphère sud, a consisté en trois vols de ballons pressurisés d'environ trois mois dans la basse stratosphère équatoriale, juste au-dessus de la tropopause tropicale (vers 70-60 hPa, 19-20 km d'altitude). Les trajectoires des trois ballons, lâchés des Seychelles en février 2010, sont représentés dans la figure 1.24. Les ballons ont dérivé durant trois mois au gré des vents.

Lors de ces vols, des mesures de vents, température et pression ont été acquises à haute fréquence (1 minute pour les vents, 30 secondes pour la pression).

Campagne ATTREX Afin de mieux caractériser les processus de transport d'espèces chimiques et de formation et d'évolution des cirrus, la campagne ATTREX a mis en place plusieurs vols longue durée du Global Hawk lors des hivers (de l'hémisphère nord) 2013 et 2014. La figure 1.25 montre une photographie du Global Hawk, drone de 15 m de long et 35 m d'envergure volant à environ 180 $\mathrm{m\,s^{-1}}$.

De nombreux instruments étaient embarqués, parmi lesquels :

1. L'instrumentation MMS (pour *Meteorological Measurement System*) (*Scott et al.*, 1990) mesurant vent, pression et température à 20 Hz (environ 9 m de résolution le long de la trace de l'avion)

2. Des instruments de mesure de vapeur d'eau et d'eau totale (vapeur et glace) : le NOAA water (*Thornberry et al.*, 2015) avec une résolution de 1 Hz et le DLH (*Diode Laser Hygrometer*) avec une résolution nominale de 20 à 100 Hz

[27] Pour Weather Research and Forecast, modèle météorologique pour la recherche et la prévision, développé par le NCAR.

[28] Centre National d'Etudes Spatiales français

[29] National Aeronautics and Space Administration, en français l'Administration nationale de l'aéronautique et de l'espace

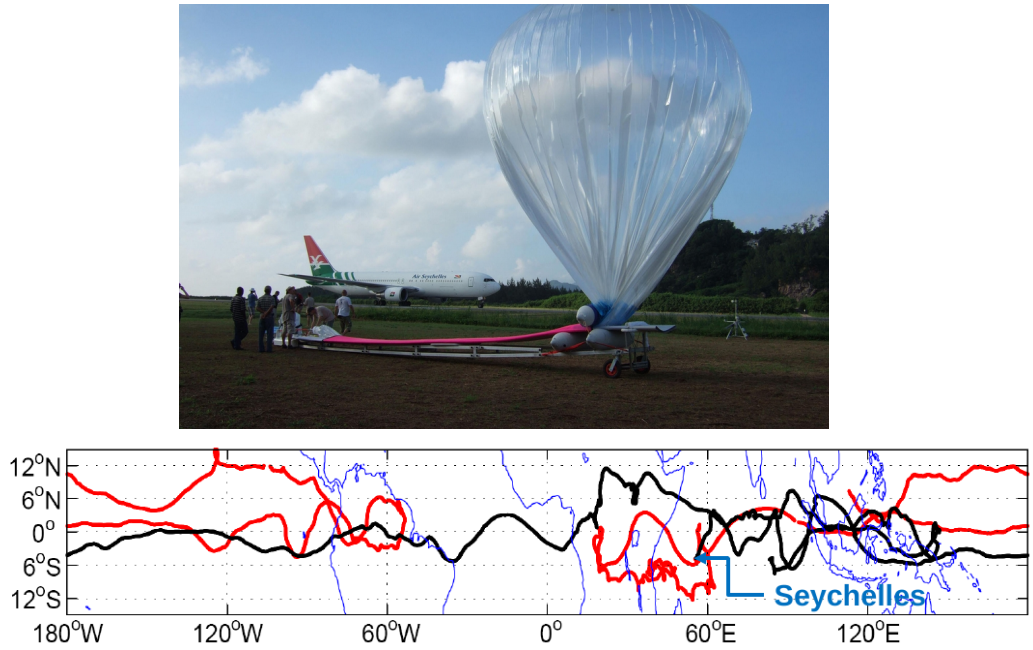

FIGURE 1.24 – (Au-dessus) Un ballon sur le point d'être lâché aux Seychelles lors de PréConcordiasi. (En-dessous) Trajectoire des ballons PréConcordiasi.

FIGURE 1.25 – Le drone NASA Global Hawk, plateforme d'observation utilisée lors de la campagne ATTREX.

3. Le FCDP (*Fast Cloud Droplet Probe*) imageur de particules nuageuses mesurant le nombre et la distribution en taille des cristaux de glace entre 1 et 50 micromètres.

Cette plateforme d'observations permet une description de la variabilité dynamique et de son lien avec la variabilité chimique et nuageuses.

1.5.3 Plan du manuscrit

Le développement du manuscrit s'articule en 4 chapitres.

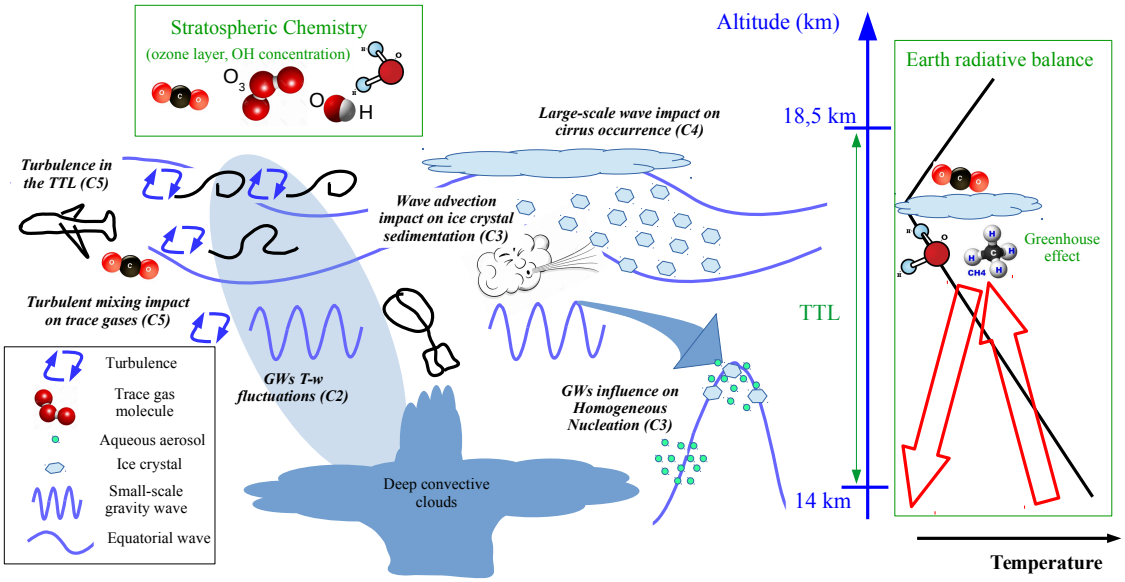

FIGURE 1.26 – Schéma des objets et processus abordés dans la thèse, des chapitres associés (Cn), ainsi que de leur contexte (cadrans verts).

Le **chapitre 2** présente les observations des fluctuations de température et de vitesses verticales par les ballons stratosphériques longue durée et les propriétés observées de ces fluctuations. Une attention particulière est accordée à leur *intermittence*, et à la forme du spectre des perturbations observées. Une comparaison est également effectuée avec des modèles de circulation générale et les observations de la campagne ATTREX.

Le **chapitre 3** s'intéresse à l'effet de ces fluctuations sur la microphysique des nuages de glace, notamment sur le processus de nucléation homogène et la sédimentation. Il décrit un nouveau régime de nucléation homogène en présence de fluctuations de haute fréquence dues aux ondes de gravité, et présente les possibles implications de l'existence de ce nouveau régime. Il s'intéresse également à l'impact des ondes et des anomalies de vent associées sur le transport des cristaux de glace. L'approche employée dans ce chapitre est de considérer les impacts des ondes sur les nuages de façon « lagrangienne », en considérant que l'on suit des particules d'air ou des cristaux de glace.

Au contraire, dans le **chapitre 4**, on utilise un modèle météorologique à mésoéchelle (eulérien), le modèle WRF (Weather Research Forecast), afin d'inclure les interactions entre différents processus (microphysiques, radiatifs, dynamiques). Le chapitre présente une étude de cas de la formation d'un cirrus de grande échelle dans le Pacifique Est, et examine les processus influençant la formation et le cycle de vie du cirrus ainsi que la sensibilité du champ nuageux simulé aux conditions initiales, à différentes hypothèses de modélisation microphysique ainsi qu'à l'impact radiatif des nuages.

Le **chapitre 5** explore « l'autre bout des échelles » : on y étudie l'occurrence des fluctuations de petite échelle (« la turbulence ») durant la campagne ATTREX et son impact sur le mélange des constituants.

L'ensemble des processus abordés dans la thèse interagissent entre eux et constituent

différentes facettes de la dynamique dans la TTL. La figure 1.26 représente schématiquement l'ensemble de ces thématiques ainsi que leur contexte plus vaste : impact sur le bilan radiatif de la planète et sur la chimie stratosphérique.

Chapter 2

Lagrangian temperature and vertical wind fluctuations at the tropical tropopause: observations and representation in large-scale models

Sommaire

2.1 Introduction

Wind, temperature and cooling rate fluctuations are of paramount importance for TTL microphysics and transport, and need to be represented or parameterized in atmospheric models. Yet, until recently, there had only been very few observational datasets providing constraints to validate or improve the models (e.g. *Hertzog et al.*, 2002; *Jensen et al.*, 2005). The two campaigns presented in the previous chapter, ATTREX and PreConcordiasi, changed the deal by largely increasing the amount of observations. This chapter is devoted to the study of those observations, focusing mainly on the balloons from PreConcordiasi. Some diagnostics and thoughts on the representation and parameterization of high frequency Lagrangian temperature and vertical wind fluctuations are also provided.

2.2 Inferring atmospheric motions from superpressure balloon (SPB) measurements

With the idea of future balloon campaigns performing high precision measurements at an increased frequency (pressure and temperature every 1 second), I find it useful to review the superpressure balloon (SPB) physics and our current understanding of its response to atmospheric motions. In particular, the following discussion reviews our current knowledge of the balloon response to the air motions, as well as the common approximations that are made. This will help the reader understand the remaining uncertainties associated with that platform.

2.2.1 Dynamics of the superpressure balloon platform

Figure 2.1 – Picture of a fully pressurized SPB similar to those used in this work.

What is a superpressure balloon ? SPB are closed, spherical balloons filled with a light gas (generally Helium). The light gas keeps a higher pressure than its environment, and is retained within a closed non extensible envelope, so that the volume occupied by the balloon is held fixed. A picture of a balloon similar to those used in this study is shown in Figure 2.1; those balloons are spherical at their equilibrium altitude level. Superpressure balloons have been first developed by NASA for scientific purpose, and have been used in a number of

meteorological campaigns, the larger ones starting in the 60s (e.g. American GHOST and TWERLE, French ÉOLE). The French Space Agency is currently one of the main users of those balloons in scientific applications, and has deployed them in various conditions to study polar ozone loss, and transport. Recently, a non scientific use has been under development by Google, the Loon project, in order to bring access to the internet in remote places. This has very significantly increased the total number of balloons launched since the first campaigns in the early 50s.

"Balloon equation" and simplifications The motion $\mathbf{v_b}$ of a spherical object (as is the superpressure balloon) in a fluid is given by:

$$M_b \frac{\mathrm{d}\mathbf{v_b}}{\mathrm{d}t} = \underbrace{-\eta M_a \left(\frac{\mathrm{d}\mathbf{v_b}}{\mathrm{d}t} - \frac{\mathrm{D}\mathbf{u}}{\mathrm{D}t} \right)}_{\text{added mass force}} \underbrace{-\frac{1}{2}\rho C_D A_b (\mathbf{v_b} - \mathbf{u})|\mathbf{v_b} - \mathbf{u}|}_{\text{drag force}} + \underbrace{M_a \frac{\mathrm{D}\mathbf{u}}{\mathrm{D}t}}_{\text{external forces (undisturbed flow)}} + \underbrace{(M_b - M_a)\mathbf{g}}_{\text{buoyancy force}} \quad (2.1)$$

The different variables are defined in Table 2.1, and $\frac{\mathrm{D}}{\mathrm{D}t} = \left(\frac{\partial}{\partial t} + \mathbf{u}\nabla \right)$ is the Lagrangian time derivative following a parcel of air, whereas $\frac{\mathrm{d}}{\mathrm{d}t} = \left(\frac{\partial}{\partial t} + \mathbf{v_b}\nabla \right)$ is the material derivative following the center of mass of the balloon system.

There are already approximations made to derive Equation (2.1). Among the neglected terms are:

- the atmospheric viscous stress and consistently the Basset history force associated with the development of the boundary layer around the balloon when it is accelerating relative to the surrounding flow

- small-scale turbulence acting at smaller scale than the balloon's diameter.

The second approximation, i.e. neglecting small-scale turbulence, is probably more limiting than the first, since the balloons may occasionally encounter turbulent layers. In that case, C_D could drop well below 0.5, even below 0.1, and a turbulent boundary layer may appear (Re gets above 10^5). We will nevertheless only consider Equation (2.1) in the remainder of the manuscript.

Horizontal motions After some reordering, Equation (2.1) reads:

$$(M_b + \eta M_a)\frac{\mathrm{d}\mathbf{v_b}}{\mathrm{d}t} = (1+\eta)M_a \frac{\mathrm{D}\mathbf{u}}{\mathrm{D}t} - \frac{1}{2}\rho C_D A_b (\mathbf{v_b} - \mathbf{u})|\mathbf{v_b} - \mathbf{u}| + (M_b - M_a)\mathbf{g} \quad (2.2)$$

Table 2.1 – Definition of the variables for the balloon equation, and typical values for the balloons used in this work, which will be referred to as CNES SPBs.

Symbol	Definition	Typical Value for CNES SPBs
ρ	air density	$\sim 0.1\,\mathrm{kg\,m^{-3}}$
μ	Dynamic viscosity of air	$1.3\,10^{-5}\,\mathrm{kg\,m^{-1}\,s^{-1}}$ (at 195 K)
D_b	balloon diameter	12 m
A_b	Cross-sectional area of the balloon	$\frac{\pi D_b^2}{4} \simeq 113$ m^2 (for a sphere)
V_b	volume of the balloon system	~ 1000 m^3
M_b	mass of the balloon system	~ 100 kg
$\mathbf{v_b}$	velocity of the balloon system	~ 20 m/s
M_a	mass of air moved by the balloon	$\rho V_b \simeq M_b \sim 100$ kg
η	added mass coefficient	$\frac{1}{2}$ (for a sphere)
$\mathbf{u}$	wind vector	$\sim \lvert\mathbf{v_b}\rvert \sim 20$ m/s
$\mathbf{g}$	acceleration of gravity	$9.81\,\mathrm{m\,s^{-2}}$
$Re = \frac{\rho D_b \lvert\mathbf{u}-\mathbf{v_b}\rvert}{\mu}$	Reynolds number	$\leq 5\,10^4$ (for $\lvert\mathbf{v_b}-\mathbf{u}\rvert \leq 0.5$ m/s)
C_D	drag coefficient	$\sim \frac{24}{Re} + 0.5$ (for a sphere and $Re \leq 10^5$)
ω_b	balloon oscillation frequency	$\omega_b = \sqrt{\frac{1}{1+\eta}\frac{g}{\bar{T}}\left(\frac{g}{R} + \frac{\mathrm{d}\bar{T}}{\mathrm{d}z}\right)} \simeq \frac{2\pi}{3-4\text{ min}}$
N	Brunt-Väisälä frequency	$N = \sqrt{\frac{g}{\bar{T}}\left(\frac{g}{C_P} + \frac{\mathrm{d}\bar{T}}{\mathrm{d}z}\right)} \simeq \frac{2\pi}{4-5\text{ min}}$

from which the following equation can be derived for the horizontal speed $\mathbf{v_h}$ of the balloon:

$$\underbrace{(M_b+\eta M_a)}_{\simeq(1+\eta)M_b}\frac{\mathrm{d}(\mathbf{v_h}-\mathbf{u_h})}{\mathrm{d}t} = \underbrace{(M_a-M_b)}_{\simeq 0\ (M_b\simeq M_a)}\frac{\mathrm{d}\mathbf{u_h}}{\mathrm{d}t} + \underbrace{(1+\eta)M_a}_{\simeq(1+\eta)M_b}((\mathbf{u}-\mathbf{v_b})\nabla)\mathbf{u_h} - \frac{1}{2}\rho\, C_D A_b(\mathbf{v_h}-\mathbf{u_h})\lvert\mathbf{v_b}-\mathbf{u}\rvert \quad (2.3)$$

where $M_b \simeq M_a$ if the balloon is near its equilibrium level. It is generally assumed that the drag term $\frac{1}{2}\rho C_D A_b(\mathbf{v_h}-\mathbf{u_h})|\mathbf{v_b}-\mathbf{u}|$ dominates the right-hand side. In that case, any difference in horizontal speeds is reduced to a third of its initial amplitude within $\Delta t \simeq \frac{2L_c}{|\mathbf{v_h}-\mathbf{u_h}|(0)}$ (*Vial et al.*, 2001), where $L_c = \frac{2(M_b+\eta M_a)}{\rho C_D A_b} \simeq \frac{3M_a}{\rho C_D A_b}$ ($L_c \simeq 50$ m for the CNES SPBs). However, the term $((\mathbf{u}-\mathbf{v_b})\nabla)\mathbf{u_h}$ is not always negligible, especially in the lower stratosphere where shears can be large ($|\partial_z \mathbf{u_h}| \simeq 10^{-2}$ s^{-1}). Strain and vorticity are generally much smaller than shear, so that the difference between the balloon velocity and the local air speed asymptotically tends to:

$$|\mathbf{v_h}-\mathbf{u_h}| \leq L_c|\partial_z \mathbf{u_h}| \simeq 0.5 \text{ m/s at the most} \quad (2.4)$$

Larger differences cannot be sustained and will decrease rapidly as just shown. Thus, the **horizontal speed of the balloon can be assumed close to the horizontal airspeed**

and the balloon horizontal motions relative to the air will be neglected in what follows:

$$\mathbf{v_h} \simeq \mathbf{u_h}. \tag{2.5}$$

However, depending on the ambient shear, this might become questionable at high frequencies.

Vertical motions Contrary to the horizontal one, the balloon vertical speed w_b is different from the vertical wind w. Indeed, the projection of Equation (2.2) on the vertical writes (*Nastrom*, 1980):

$$(M_b + \eta M_a)\frac{\mathrm{d}w_b}{\mathrm{d}t} = -g(M_b - M_a) + (1+\eta)M_a\frac{\mathrm{D}w}{\mathrm{D}t} - \frac{1}{2}\rho\, C_D A_b (w_b - w)|w_b - w| \tag{2.6}$$

It should be noted here that, in the drag term, we assume $|\mathbf{v_b} - \mathbf{u}| \simeq |w_b - w|$, since $\mathbf{v_h} \simeq \mathbf{u_h}$. Although consistent with the previous discussion, this becomes of limited applicability when the vertical winds are low[1].

Equation (2.6) shows that in an atmosphere at rest ($w = 0$), the equilibrium level of the balloon is given by $M_b = M_a$, i.e. $M_b = \rho V_b$. Introducing $\rho_b = \frac{M_b}{V_b}$, this is equivalent to $\rho_b = \rho$: the density of the balloon at rest is the same as the density of the air. Hence, the vertical equilibrium level of the balloon is called its Equilibrium Density Surface (EDS). It is an isopycnic (iso-density) surface, whose altitude $\zeta_\rho(\rho_b, x, y, t)$ generally depends on the horizontal position and time in the continuously stratified atmosphere.

Under superpressure, the balloon volume remains nearly constant as it moves vertically. Assuming small vertical displacements in a dominant vertical stratification, the density of the air surrounding the balloon varies as it moves in altitude, following at first order:

$$\rho \simeq \rho_b + (\zeta_b - \zeta_\rho(\rho_b))\frac{\mathrm{d}\bar{\rho}}{\mathrm{d}z} \tag{2.7}$$

where the altitude ζ_ρ of the isopycnic (iso density) surface is given by:

$$\rho' + \zeta_\rho \frac{\mathrm{d}\bar{\rho}}{\mathrm{d}z} \simeq 0. \tag{2.8}$$

ρ' being the density fluctuation at a fixed (Eulerian) location. To obtain Equations (2.7) and (2.8), a linearization has been undertaken and second order terms have been neglected. Since the density fluctuations remain small ($|\rho_b - \rho| \ll \rho_b$), second-order terms in ρ can be left in

[1]This should rarely happen.

Equation (2.6), which then reads (with $w_b = \frac{\mathrm{d}\zeta_b}{\mathrm{d}t}$ and $\bar{\rho} = \rho_b$):

$$\frac{\mathrm{d}^2\zeta_b}{\mathrm{d}t^2} = \underbrace{\left(\frac{1}{1+\eta}\right)\frac{g}{\bar{\rho}}\frac{\mathrm{d}\bar{\rho}}{\mathrm{d}z}}_{-\omega_b^2}(\zeta_b - \zeta_\rho(\rho_b)) + \left(1 + \underbrace{\frac{1}{1+\eta}\frac{1}{\bar{\rho}}\frac{\mathrm{d}\bar{\rho}}{\mathrm{d}z}(\zeta_b - \zeta_\rho(\rho_b))}_{B(\zeta_b - \zeta_\rho(\rho_b))}\right)\left[\frac{\mathrm{D}w}{\mathrm{D}t} - \underbrace{\frac{1}{2}\frac{C_D A_b}{(1+\eta)V_b}}_{A}\left(\frac{\mathrm{d}\zeta_b}{\mathrm{d}t} - w\right)\left|\frac{\mathrm{d}\zeta_b}{\mathrm{d}t} - w\right|\right] \quad (2.9)$$

In previous studies of balloon motions (*Nastrom*, 1980; *Vincent and Hertzog*, 2014), a simplification was made to neglect the $B(\zeta_b - \zeta_\rho(\rho_b)) \ll 1$ term. Following the notations of *Vincent and Hertzog* (2014), this leads to:

$$\frac{\mathrm{d}^2\zeta_b}{\mathrm{d}t^2} = -\omega_b^2(\zeta_b - \zeta_\rho(\rho_b)) + \frac{\mathrm{D}w}{\mathrm{D}t} - A\left(\frac{\mathrm{d}\zeta_b}{\mathrm{d}t} - w\right)\left|\frac{\mathrm{d}\zeta_b}{\mathrm{d}t} - w\right| \quad (2.10)$$

Considering the balloon to be a perfect sphere, $\eta = 0.5$ and $\frac{A_b}{V_b} = \frac{3}{4R_b}$ so that $A = \frac{C_D}{4R_b}$. Besides assuming the perfect sphere, the main approximation from Equation (2.6) to Equation (2.10) is the linearization of ρ and the drop of the B term. *Nastrom* (1980) showed that, for moderate fluctuations of the altitude of the isopycnic [2], those approximations generally lead to small differences with the solution of the full equation.

In the lower stratosphere, the parameters A and ω_b can be considered constant or slowly variable. The density ρ_b can also be assumed constant as long as the balloon volume is fixed (neglecting changes in superpressure and the elasticity of the balloon envelope). Hence, the balloon vertical motions respond to the 3 atmospheric forcing terms: the vertical wind acceleration $\frac{\mathrm{D}w}{\mathrm{D}t}$, the vertical wind w and the anomaly altitude of the isopycnic surface ζ_ρ. Considering once again small displacements and a dominant vertical stratification (compared to horizontal gradients), the altitude of the isentrope ζ_θ can be related to the potential temperature anomaly θ':

$$\theta' + \zeta_\theta \frac{\partial\bar{\theta}}{\partial z} = 0. \quad (2.11)$$

Neglecting compressibility effect, we have at first order $\frac{\theta'}{\bar{\theta}} = \frac{T'}{\bar{T}} = -\frac{\rho'}{\bar{\rho}}$ so that Equations (2.8) and (2.11) give:

$$\zeta_\rho = -\frac{\frac{1}{\bar{\theta}}\frac{\partial\bar{\theta}}{\partial z}}{\frac{1}{\bar{\rho}}\frac{\partial\bar{\rho}}{\partial z}}\zeta_\theta = \frac{\frac{g}{C_P} + \frac{\partial\bar{T}}{\partial z}}{\frac{g}{R} + \frac{\partial\bar{T}}{\partial z}}\zeta_\theta = \alpha\zeta_\theta \quad (2.12)$$

where $0 \leq \alpha \leq 1$ in a stable atmosphere. In the lower stratosphere, we have $\frac{R}{C_P} = 0.285 \leq \alpha \leq 0.40$, and typically $\alpha \simeq 0.33$. Assuming adiabatic motions, we have $w = \frac{\mathrm{D}\zeta_\theta}{\mathrm{D}t}$. Hence, the balloon vertical motions are forced by the vertical displacement of the isentropes, i.e. by $\frac{\mathrm{D}^2\zeta_\theta}{\mathrm{D}t^2}$, $\frac{\mathrm{D}\zeta_\theta}{\mathrm{D}t}$ and $\alpha\zeta_\theta$.

Another forcing comes from the fact that ρ_b is not constant but slightly varies along the

[2] smaller than the scale height $H \simeq 7$ km

diurnal cycle due to the balloon envelope being heated by the sun and expanding slightly the balloon volume during daytime. This causes vertical oscillation of the balloon, and prevents any use of the SPB data to study the diurnal tides.

2.2.2 Inferring Lagrangian atmospheric fluctuations from balloon motions

Under the reasonable assumption that $\mathbf{v_h} = \mathbf{u_h}$, the quasi-Lagrangian behavior of the balloon makes it ideal to follow air parcels. Indeed, for a quantity χ (e.g. mixing ratio of a given compound), the Lagrangian derivative can be related to the derivative following the balloon $\frac{\mathrm{d}}{\mathrm{d}t}$:

$$\frac{\mathrm{D}\chi}{\mathrm{D}t} = \frac{\mathrm{d}\chi}{\mathrm{d}t} + (w - w_b)\frac{\partial\chi}{\partial z} \tag{2.13}$$

Assuming that χ variations can be split into a background term $\bar{\chi}$ and a perturbation χ' and that there is no background vertical wind ($\bar{w} = 0$), one finds, by neglecting second order terms:

$$\frac{\mathrm{D}\chi}{\mathrm{D}t} = \frac{\mathrm{d}\chi}{\mathrm{d}t} + (w - w_b)\frac{\partial\bar{\chi}}{\partial z} \tag{2.14}$$

For the anomaly of the height of a given isentrope $\zeta_\theta(x, y, t)$, which has no vertical gradient, Equation (2.13) leads to:

$$\frac{\mathrm{D}\zeta_\theta}{\mathrm{D}t} = \frac{\mathrm{d}_b\zeta_\theta}{\mathrm{d}t} \tag{2.15}$$

Thus, time series of $\zeta_\theta \simeq \frac{1}{\alpha}\zeta_\rho$ estimated along the balloon trajectory are similar to Lagrangian fluctuations of ζ_θ, i.e. to Lagrangian fluctuations of an air parcel vertical position. This is what makes balloon measurement so attractive. The remaining difficulty however, is to estimate ζ_ρ from the balloon measurements. The balloon altitude ζ_b is known but differs from ζ_ρ or ζ_θ, due to a specific balloon response on the vertical.

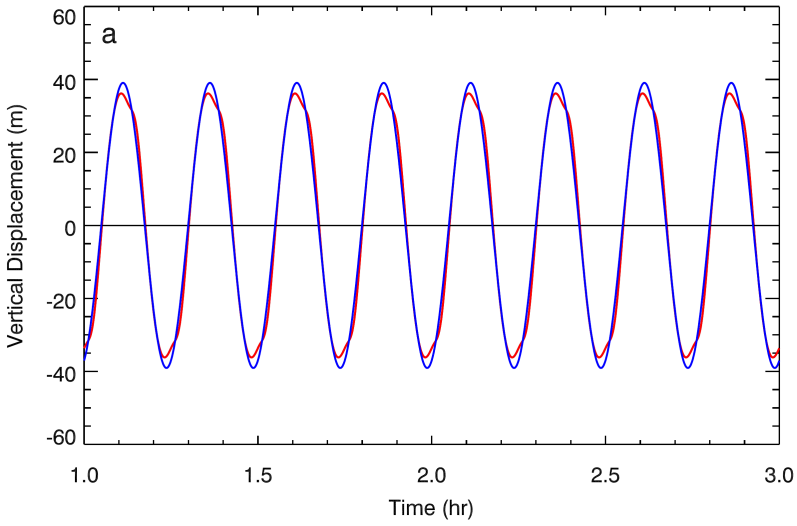

Figure 2.2 – Vertical displacements of a 12 m diameter superpressure balloon induced by a gravity wave with period 15 min and vertical wind amplitude of 1 m/s. Those results are obtained through a numerical integration of Equation (2.10), and they are plotted for the interval 1 to 3 h after the simulation was turned on to avoid transient effects near t = 0. From *Vincent and Hertzog* (2014).

Balloon response to gravity-wave fluctuations For a monochromatic gravity wave perturbation, the atmospheric forcing can be written as:

$$\zeta_\theta = \mathrm{Re}\left(\hat{\zeta}_0 e^{i\hat{\omega}t}\right), w = \mathrm{Re}\left(i\hat{\omega}\hat{\zeta}_0 e^{i\hat{\omega}t}\right), \frac{\mathrm{D}w}{\mathrm{D}t} = \mathrm{Re}\left(-\hat{\omega}^2\hat{\zeta}_0 e^{i\hat{\omega}t}\right) \tag{2.16}$$

where Re is the real part.

To determine the balloon response, one way to proceed is to use the simplified Equation (2.10). Simplified Equation (2.10) is nonlinear but numerical integrations (*Nastrom*, 1980) suggest that the response to a harmonic forcing from the atmosphere only excites odd harmonics[3], with the first harmonic strongly dominating (*Nastrom*, 1980; *Vincent and Hertzog*, 2014). Figure 2.2 illustrates that point, showing the result of a numerical integration of Equation (2.10) with a monochromatic gravity wave forcing. The quasi-harmonic response allows us to formally define a (complex) transfer function $\mathbf{Z_m}$ for the m^{th} harmonic (*Vincent and Hertzog*, 2014), and seek a solution for the balloon vertical displacement using an expansion into Fourier series:

$$\zeta_b = \mathrm{Re}\left(\sum_{m=1}^{+\infty} \hat{\zeta}_m e^{im\hat{\omega}t}\right) = \mathrm{Re}\left(\sum_{m=1}^{+\infty} \mathbf{Z_m}\hat{\zeta}_0 e^{im\hat{\omega}t}\right) \tag{2.17}$$

Guided by the numerical integrations, we can make progress by assuming that the first harmonic is dominant in the balloon response and neglecting higher harmonics (i.e. $|\mathbf{Z_m}| \ll |\mathbf{Z_1}|$ for $m \geq 2$) when estimating the nonlinear drag term:

$$\left(\frac{\mathrm{d}\zeta_b}{\mathrm{d}t} - w\right)\left|\frac{\mathrm{d}\zeta_b}{\mathrm{d}t} - w\right| \simeq Re(i\hat{\omega}(\mathbf{Z_1} - 1)\hat{\zeta}_0 e^{i\hat{\omega}t})|Re(i\hat{\omega}(\mathbf{Z_1} - 1)\hat{\zeta}_0 e^{i\hat{\omega}t})| \tag{2.18}$$

Expanding that term in Fourier series[4] and applying the principle of harmonic balance, Equation (2.10) leads to:

$$-\hat{\omega}^2\mathbf{Z_1} = -\omega_b^2\mathbf{Z_1} + \alpha\omega_b^2 - Ai\hat{\omega}|\hat{\omega}||\hat{\zeta}_0||\mathbf{Z_1} - 1|(\mathbf{Z_1} - 1)\frac{8}{3\pi} - \hat{\omega}^2 \tag{2.19}$$

for the first harmonic, which can be solved[5] first for $|\mathbf{Z_1} - 1|$ then for $\mathbf{Z_1}$, leading to[6]:

$$\mathbf{Z_1} = \frac{\alpha\omega_b^2 - \hat{\omega}^2 + i\frac{\mathrm{sign}(\hat{\omega})}{\sqrt{2}}\sqrt{\sqrt{\Delta} - (\omega_b^2 - \hat{\omega}^2)^2}}{\omega_b^2 - \hat{\omega}^2 + i\frac{\mathrm{sign}(\hat{\omega})}{\sqrt{2}}\sqrt{\sqrt{\Delta} - (\omega_b^2 - \hat{\omega}^2)^2}} \tag{2.20}$$

where $\Delta = (\omega_b^2 - \hat{\omega}^2)^4 + \left(\frac{16}{3\pi}\right)^2(1-\alpha)^2\omega_b^4 A^2\hat{\omega}^4|\hat{\zeta}_0|^2$.

As illustrated by figure 2.3, Relation (2.20) can be simplified for frequencies much lower than that of the balloon neutral oscillations, in which case one recovers the isopycnic displacement: $\mathbf{Z_1} \simeq \alpha$. There is no phase shift and just a change in amplitude between the balloon

[3] This is not the case for the more complete Equation (2.9), for which even harmonics are also excited due to the products with term B.

[4] given that the Fourier series expansion of $\sin(x)|\sin(x)| = \frac{8}{3\pi}\sin(x) - \frac{8}{15\pi}\sin(3x) + ... + \frac{8}{(2n+1)\pi(4-(2n+1)^2)}\sin((2n+1)x)$

[5] This was not noted by *Vincent and Hertzog* (2014), who used a numerical solution.

[6] The sign term is important to ensure that the same forcing written with two opposite $\hat{\omega}$ produces the same response

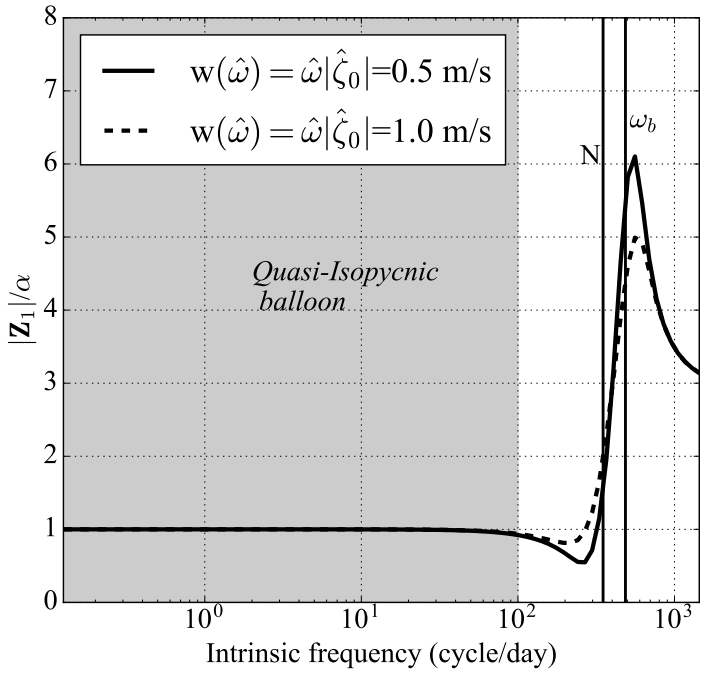

Figure 2.3 – Ratio of the first harmonic of the balloon vertical displacement over the isopycnic vertical displacement ($\frac{|\mathbf{Z_1}|}{\alpha}$ from Equation (2.20)) for an ideal gravity wave forcing, as a function of the wave intrinsic frequency. The dashed and continuous curves correspond to different amplitudes of the forcing gravity wave.

vertical displacement and the air parcel vertical motion. However, this approximation becomes questionable at higher frequencies approaching ω_b, for which the balloon response is non linear and the transfer function depends on the amplitude of the forcing. This "isopycnic approximation" $\mathbf{Z_1} \simeq \alpha$ was nevertheless used in the next section, both for the sake of simplicity and because at high frequencies (approaching ω_b) it appears inappropriate to consider a monochromatic wave, since low frequency motions can excite significant resonance at frequencies near ω_b, as shown below.

About the balloon oscillations As will be seen in the analysis presented later, observations suggest that the balloon oscillations at frequency $\omega_b \simeq \frac{2\pi}{3 \text{ min}}$ are not excited, and that the balloon is rather oscillating at frequencies close to the Brunt-Väisälä frequency. This is somehow surprising, and cannot be reconciled with the response model presented above. Indeed, solving (2.10) in Fourier series for the next harmonics, one finds $\mathbf{Z_{2n}} = 0$ for the even harmonics[7] (consistent with the simulations of *Nastrom*, 1980) and:

$$\mathbf{Z_{2n+1}} = i\frac{3}{\sqrt{2}(2n+1)((2n+1)^2-4)}\frac{\text{sign}(\hat{\omega})\sqrt{\sqrt{\Delta}-(\omega_b^2-\hat{\omega}^2)^2}}{(\omega_b^2-((2n+1)\hat{\omega})^2)}(\mathbf{Z_1}-1) \tag{2.21}$$

[7]However even terms are present in the solution to Equation (2.9).

for the odd harmonics ($n \geq 1$).[8]

Formula (2.21) illustrates that the assumption $|\mathbf{Z_n}| \ll |\mathbf{Z_1}|$ fails when ω_b is close to an odd harmonic of a forced frequency, which means that the response at the exciting frequency does not strongly dominate over the resonance near the neutral oscillation frequency. Given that gravity waves have intrinsic frequencies $\hat{\omega}$ in the range $f \leq \hat{\omega} \leq N$, one would expect that there are gravity waves whose odd harmonics can excite the balloon neutral oscillations at ω_b. As will be presented later, numerical simulations partly support that result, but also show that including a spectrum of gravity waves limits the resonance near ω_b.

It should also be mentioned that the issue of the balloon oscillations, artifact or atmospheric feature, is more complicated in the lower stratosphere than it is in the upper troposphere, which was the case considered by previous analyses (e.g. *Massman*, 1978): whereas in the troposphere there is a net distinction between ω_b and N, they are closer in the lower stratosphere, making the analyses of balloon motions more uncertain[9].

From displacement to temperature fluctuations Once the Lagrangian fluctuations of ζ_θ have been inferred from the balloon displacement, the Lagrangian fluctuations of temperature T_l can be estimated assuming small displacements, dry adiabatic transforms and conservation of the potential temperature θ:

$$T_l = \theta \left(\frac{p}{p_{ref}}\right)^{\kappa} = \bar{T}\left(1 + \frac{p'_l}{\bar{p}}\right)^{\kappa} \simeq \bar{T} + \frac{1}{C_P}\frac{p'_l}{\bar{\rho}} \tag{2.22}$$

For small displacements in the hydrostatic background atmosphere, $p'_l \simeq p' + \zeta_\theta \dfrac{\partial \bar{p}}{\partial z} = p' - \bar{\rho} g \zeta_\theta$ where p' is the Eulerian pressure perturbation. Assuming $p' \ll p'_l$ [10], one obtains:

$$T_l \simeq \bar{T} - \frac{g}{C_P}\zeta_\theta \tag{2.23}$$

It should be noted that this expression is valid in the UTLS where the assumption of dry transforms with little latent heat release is appropriate (away from deep convective clouds detraining sublimating ice). It could be simply adapted to include latent heat release as long as the condensate is transported with the parcel[11].

[8] For low harmonic frequency relative to ω_b (i.e. $(2n+1)\hat{\omega} \ll \omega_b$), the drag response spectrum has a slope in $((2n+1)\hat{\omega})^{-3}$, steeper than what is observed for the real atmospheric signal, which can hence be deduced from balloon motions.

[9] Especially if the value of the lapse rate and N^2 are not known exactly.

[10] from the dispersion and polarization relations for gravity waves (e.g. *Fritts and Alexander*, 2003), one can derive $\bar{\rho}^2 g^2 |\hat{\zeta_\theta}|^2 = \dfrac{g^2 k_h^2}{(\hat{\omega}^2 - f^2)(N^2 - \hat{\omega}^2)} |\hat{p}|^2$. The denominator's maximum is $\dfrac{N^4 + f^4}{4}$ (reached for $\hat{\omega} = \sqrt{\frac{N^2+f^2}{2}}$) so that with a typical $\lambda_h \leq 100$ km, one has $\bar{\rho} g |\hat{\zeta_\theta}| \geq 4|\hat{p}|$ in the worst case, and generally $\bar{\rho} g |\hat{\zeta_\theta}| \geq 10|\hat{p}|$

[11] $T_l \simeq \bar{T} - \frac{g}{C_P}\zeta_\theta + \frac{L_i}{C_P}(q_i(t) - q_i(0))$ where q_i the ice water content.

2.3 Letter: Lagrangian temperature and vertical velocity fluctuations due to gravity waves in the lower stratosphere

This section corresponds to a letter on the quantification and characterization of temperature fluctuations using superpressure balloon measurements. The paper was published in March 2016.

AGU PUBLICATIONS

Geophysical Research Letters

RESEARCH LETTER
10.1002/2016GL068148

Key Points:
- Long-duration balloon observations are used to characterize Lagrangian temperature fluctuations
- Intrinsic frequency spectra and PDFs are derived for temperature and cooling rates
- A parameterization of gravity wave temperature fluctuations in the lower stratosphere is developed

Supporting Information:
- Supporting Information S1

Correspondence to:
A. Podglajen,
apodgla@lmd.ens.fr

Citation:
Podglajen, A., A. Hertzog, R. Plougonven, and B. Legras (2016), Lagrangian temperature and vertical velocity fluctuations due to gravity waves in the lower stratosphere, *Geophys. Res. Lett.*, *43*, 3543–3553, doi:10.1002/2016GL068148.

Received 5 FEB 2016
Accepted 18 MAR 2016
Accepted article online 22 MAR 2016
Published online 9 APR 2016

Lagrangian temperature and vertical velocity fluctuations due to gravity waves in the lower stratosphere

Aurélien Podglajen[1], Albert Hertzog[2], Riwal Plougonven[1], and Bernard Legras[1]

[1]Laboratoire de Météorologie Dynamique, CNRS-UMR8539, Institut Pierre Simon Laplace, École Normale Supérieure, École polytechnique, Université Pierre et Marie Curie, Paris, France, [2]Laboratoire de Météorologie Dynamique/IPSL, UPMC Univ Paris 06, CNRS, Palaiseau, France

Abstract Wave-induced Lagrangian fluctuations of temperature and vertical velocity in the lower stratosphere are quantified using measurements from superpressure balloons (SPBs). Observations recorded every minute along SPB flights allow the whole gravity wave spectrum to be described and provide unprecedented information on both the intrinsic frequency spectrum and the probability distribution function of wave fluctuations. The data set has been collected during two campaigns coordinated by the French Space Agency in 2010, involving 19 balloons over Antarctica and 3 in the deep tropics. In both regions, the vertical velocity distributions depart significantly from a Gaussian behavior. Knowledge on such wave fluctuations is essential for modeling microphysical processes along Lagrangian trajectories. We propose a new simple parameterization that reproduces both the non-Gaussian distribution of vertical velocities (or heating/cooling rates) and their observed intrinsic frequency spectrum.

1. Introduction

Microphysical processes in the tropical upper troposphere control the characteristics of ice clouds in the tropical tropopause layer (TTL) and the amount of water vapor that enters the stratosphere, which has significant implications on global climate, circulation response to climate change, and stratospheric ozone chemistry [*Solomon et al.*, 2010; *Randel and Jensen*, 2013; *Voigt and Shaw*, 2015]. At high latitudes, the formation of polar stratospheric clouds (PSCs) and the nature of nucleated particles is a crucial step in the chain of processes that contribute to ozone depletion [*Solomon et al.*, 1986]. In both cases, modeling of microphysical processes along air parcel trajectories computed with reanalyzed winds and temperatures has allowed estimations of key quantities, e.g., water vapor transport across the tropical tropopause and ozone loss [*Fueglistaler and Haynes*, 2005; *Grooß and Müller*, 2007; *James et al.*, 2008]. Yet several studies have highlighted that mesoscale wave motions, which are unresolved in the large-scale fields used for these simulations, actually have a strong influence on cloud characteristics, such as ice crystal number and particle size distribution for instance [see, e.g., *Murphy and Gary*, 1995; *Tabazadeh et al.*, 1996; *Haag and Kärcher*, 2004; *Hoyle et al.*, 2005; *Jensen et al.*, 2012; *Spichtinger and Krämer*, 2013; *Kärcher et al.*, 2014]. Microphysical processes indeed strongly depend on temperature, generally in a highly nonlinear way (with thresholds) so that relatively small temperature fluctuations may have a strong impact on particle nucleation [e.g., *Jensen et al.*, 2010; *Murphy*, 2014; *Dinh et al.*, 2016]. In Lagrangian microphysical simulations, it is therefore required to parameterize the unresolved small-scale high-frequency temperature and heating/cooling rate (or vertical velocity) fluctuations [*Bacmeister et al.*, 1999; *Jensen and Pfister*, 2004; *Haag and Kärcher*, 2004; *Jensen et al.*, 2012]. However, there are few observational constraints on these Lagrangian disturbances.

In fact, among meteorological variables, vertical velocities are certainly the least known. This is not only due to their small-scale structure, tied to gravity waves and convection, but also mainly due to a lack of observations. Only a few observing platforms are actually able to provide reliable estimates of vertical motions in the upper troposphere-lower stratosphere: Doppler lidar and radar [*Gage et al.*, 1986], inertial navigation systems on board scientific aircraft (e.g., Meteorological Measurement System) [*Muhlbauer et al.*, 2014] and superpressure balloons (SPBs). While vertical profiles of vertical velocity are inferred from remote-sensing measurements (lidar and radar), in situ platforms (aircrafts and balloons) generally provide local observations at higher space/time resolution. Among all the systems, superpressure balloons are unique because they are advected by the winds like air parcels. This quasi-Lagrangian behavior provides direct estimates of

AGU Geophysical Research Letters 10.1002/2016GL068148

wave-induced temperature and cooling/heating rate disturbances. Another attractive feature of SPBs is that as they are passively advected in the lower stratosphere, their sampling is a priori unbiased so that the collected data set is representative of day/night, land/ocean, and convective/clear sky conditions.

In this study, we take advantage of measurements performed during such SPB flights to describe the statistical and spectral properties of gravity wave disturbances in the lower stratosphere. Our main focus is to provide details on the vertical displacement and vertical velocity perturbations, which are respectively associated with temperature and heating/cooling rate fluctuations felt by air parcels in the atmosphere. The analyzed data set was collected during two SPB campaigns in 2010: the first one took place in the deep tropics in February – May and involved the flight of three superpressure balloons [*Podglajen et al.*, 2014], while 19 balloon flights were performed during the second campaign that took place over Antarctica and the Austral ocean in September 2010 to January 2011 [*Rabier et al.*, 2010].

The paper is organized as follows. In section 2, the balloon observations and their relationship to air parcel disturbances are introduced. Section 3 presents a spectral analysis of the time series, and section 4 describes the probability distributions of vertical wind disturbances and Lagrangian displacement inferred from the observations. Section 5 discusses different methods to parameterize wave-induced temperature and cooling rate fluctuations in Lagrangian models and describes a new one. The last section summarizes our findings.

2. Long-Duration Balloon Observations

2.1. Superpressure Balloon Campaigns

During the 2010 equatorial and polar campaigns, respectively named PreConcordiasi and Concordiasi, the French Space Agency (Centre National d'Etudes Spatiales, CNES) deployed closed, spherical, 12 m diameter SPBs. They drifted for durations close to 3 months on nearly constant density (~0.1 kg/m^3) surfaces in the lower stratosphere, at about 19 km (PreConcordiasi) or 17 km (Concordiasi). Two of the three PreConcordiasi flights achieved circumterrestrial trajectories within 15° of the equator from February to May 2010 [*Podglajen et al.*, 2014], while the Concordiasi balloons flew from September to January and remained poleward of 60°S, within the decaying Southern Hemisphere stratospheric polar vortex.

The SPBs carried various instruments of interest for this study. All balloons were equipped with a GPS receiver, and the in situ horizontal winds were evaluated by finite differentiating the successive GPS positions, as in *Vial et al.* [2001]. In contrast to previous campaigns, positions were recorded every minute, giving access for the first time to the whole spectrum of gravity waves. The pressure measurements were performed every 30 s by the Thermodynamical SENsors meteorological package on board every balloon [*Hertzog et al.*, 2007]. Hence, as these measurements are performed in the frame of reference that moves with the wind (so-called intrinsic frame of reference), observations gathered during the 2010 SPB flights uniquely resolve the entire gravity wave spectrum, from the inertial (f) to the Brunt-Väisälä frequency (N). Regarding instrument performances, the estimated 1σ precisions of the GPS horizontal positions and pressure measurements, respectively, are 0.7 m and 0.1 Pa, and both measurement noises are assumed to behave as white noise processes.

2.2. Balloon Response to Air Motion

In order to correctly interpret the measured fluctuations, to understand their advantages and limitations, it is necessary to briefly discuss the response of the balloons to the surrounding air motions. Regarding horizontal motions, SPBs are advected by the horizontal wind, and their displacements therefore closely follow those of air parcels [*Massman*, 1978; *Vincent and Hertzog*, 2014]. Departures from the Lagrangian behavior in the horizontal are estimated to be within the uncertainty of GPS-derived winds [see, e.g., *Podglajen et al.*, 2014; *Vial et al.*, 2001].

The situation is different for the vertical motion of SPBs [e.g., *Massman*, 1978; *Nastrom*, 1980; *Vincent and Hertzog*, 2014]. While air parcels follow isentropes on timescales less than a few days in the lower stratosphere, superpressure balloons drift instead on isopycnic (constant density) surfaces as long as the wave-induced disturbances have intrinsic periods longer than twice the Brunt-Väisälä period ($2\pi/N$), i.e., longer than ~10 min at the balloon flight level. In this "low-frequency" range, the balloon vertical displacement ζ'_b and that of an isentropic air parcel ζ'_θ are linearly related:

$$\zeta'_b = \alpha \zeta'_\theta \tag{1}$$

with α of the order of 0.3 [see, e.g., *Vincent and Hertzog*, 2014; *Podglajen et al.*, 2014] so that the vertical displacement and velocity of air parcels can be easily inferred from SPB motions. At higher frequencies

AGU Geophysical Research Letters 10.1002/2016GL068148

(i.e., gravity waves with intrinsic frequencies close to N and turbulence), the accuracy of this linear relationship becomes more questionable for two reasons: the main limitation results from the neutral oscillations of the balloons around their equilibrium level which happen at a frequency $\omega_b > N$ (the associated period, $2\pi/\omega_b$, is typically 3 min). The second cause for departures from isopycnic behavior is the inertia of the balloon, which needs to be taken into account for frequencies close to N [*Vincent and Hertzog*, 2014]. Finally, there is also a deviation from isopycnic behavior associated with the diurnal cycle in the balloon density, which is due to the slight expansion of the balloon envelope when heated by the Sun and has a typical peak-to-peak amplitude of 100–150 m.

3. Intrinsic Frequency Spectra of Atmospheric Motions

A unique characteristic of SPB measurements is that they directly record the intrinsic frequency ($\hat{\omega}$) of atmospheric disturbances, i.e., the frequency felt by air parcels, in contrast with ground-based instruments that measure frequencies affected by Doppler shift [see, e.g., *Vincent and Eckermann*, 1990; *Fritts and Wang*, 1991]. This is used below to obtain intrinsic frequency spectra of horizontal kinetic energy (E_{k_h}) and potential energy (E_p) and to quantify the contributions from low-frequency (planetary) and gravity waves. The spectra of temperature and vertical velocity fluctuations are then derived, as these are the relevant quantities for microphysical modeling.

3.1. Kinetic and Potential Energy Spectra

The wave potential and kinetic energy per unit mass, E_p and E_{k_h}, are

$$E_p = \frac{1}{2}N^2\zeta_\theta'^2, \qquad E_{k_h} = \frac{1}{2}(u'^2 + v'^2), \tag{2}$$

with ζ_θ' the (isentropic) wave-induced vertical displacement and u' and v' the wave-induced disturbances in zonal and meridional velocities.

In this study, $E_{k_h}(\hat{\omega})$ and $E_p(\hat{\omega})$ are obtained from independent sensors: E_{k_h} is directly deduced from the balloon horizontal velocities, whereas E_p is estimated from the balloon vertical displacements with the help of equation (1). In the latter equation, we use the high-precision pressure measurements to estimate the balloon vertical displacements; i.e., we assume that the variance in the measured pressure perturbations is essentially due to the Lagrangian component $\zeta_b' d\overline{p}/dz$ (where $d\overline{p}/dz$ is the vertical gradient of the background pressure). We thus neglect the variance induced by the Eulerian pressure perturbations, which is smaller than its Lagrangian counterpart by a factor of 3 at the very least (and generally a factor of 10) in the gravity wave frequency range.

Although estimated from independent measurements, these two spectra should nonetheless be closely linked if the observed disturbances are caused by gravity waves. Namely, using gravity wave polarization relations [e.g., *Fritts and Alexander*, 2003], one obtains

$$E_p = \left(\frac{N^2}{N^2 - \hat{\omega}^2}\right)\left(\frac{\hat{\omega}^2 - f^2}{\hat{\omega}^2 + f^2}\right)E_{k_h} \tag{3}$$

where f and $\hat{\omega}$ are, respectively, the inertial and wave intrinsic frequencies. This relation holds in the gravity wave frequency range ($f < \hat{\omega} < N$).

Figure 1 presents the one-dimensional intrinsic frequency spectra, for both the polar and equatorial campaigns. They were estimated as the average of several periodograms calculated from sequences of consecutive 8 day observations with 4 day overlaps. In the equatorial flights, balloon depressurizations (occurring when the balloons fly over cold, deep convective systems at night) were discarded because of the complex balloon response to air motion during these brief episodes.

3.1.1. Low-Frequency and Midfrequency Range

In the midfrequency regime (i.e., $f \ll \hat{\omega} \ll N$), the observed spectra of E_p and E_{k_h} have similar magnitudes within the uncertainty associated with spectral estimation. This is in agreement with equation (3) and confirms the gravity wave nature of the disturbances observed in that frequency range. Moreover, the spectra exhibit a robust power law behavior of gravity wave energy over a large range of frequencies and geographical locations. Yet the spectral slopes seem slightly different between the tropical and polar regions (see Table 1): the tropical spectra suggest a $\hat{\omega}^{-2}$ power law, whereas the polar flights exhibit a slightly shallower $\hat{\omega}^{-1.8}$ slope.

AGU Geophysical Research Letters 10.1002/2016GL068148

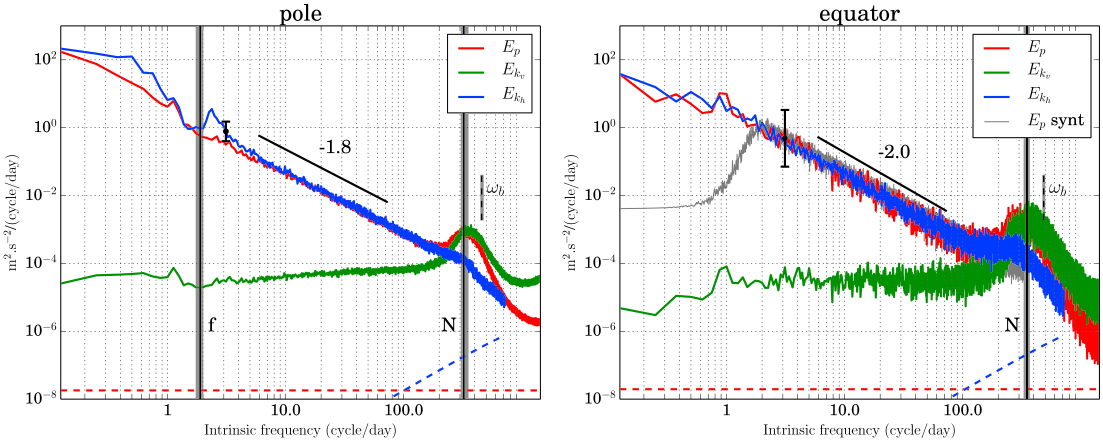

Figure 1. Spectra of potential (red), horizontal (blue), and vertical (green) kinetic energy, estimated from superpressure balloon observations collected during the 2010 (left) polar and (right) equatorial campaigns. On the right panel, the grey curve corresponds to the synthetic E_p signal described in section 5. The error bar indicates the confidence interval of the spectral estimates. The red and blue dashed lines correspond to the instrumental noise levels for potential and kinetic energy, respectively. The vertical black lines show the Coriolis frequency f for the polar flight and the Brünt-Väisälä frequency N (estimated from the European Centre for Medium-Range Weather Forecasts (ECMWF) operational analysis), the dashed line corresponds to the frequency of the balloon neutral oscillations ω_b (also estimated from the ECMWF operational analysis). The larger spectral uncertainty in the equatorial spectra is associated with a smaller number of flights during the PreConcordiasi campaign (3) than during the polar Concordiasi campaign (19).

It is known and expected that there is variability in spectral slopes, see for instance *Cho et al.* [1999a, 1999b] and *Dotzek and Gierens* [2008] for horizontal wave number wind and temperature spectra in the troposphere. Given the sampling available with our SPB measurements, the difference in slopes between the two regions appears statistically significant (see Table 1). However, at present, there is no theoretical argument to our knowledge that could attribute this difference to specific differences in wave sources or atmospheric structure between the polar and equatorial stratosphere.

Table 1. Major Characteristics of the Horizontal Kinetic Energy Spectra (Slope and 1σ Uncertainty), Lagrangian Temperature (or Vertical Displacements) and Vertical Velocity (or Heating/Cooling Rates) Disturbances Associated With Gravity Waves (GW) and Planetary Waves (PW) in the Superpressure Balloon Observations[a]

			Flights	
Spectral Characteristics	Motion	Frequency Range	Polar	Equatorial
E_{k_h} slope	GW	$2\pi/(4\,\text{h})-2\pi/(20\,\text{min})$	$-1.78(\pm0.01)$	$-1.96(\pm0.03)$
	GW	$2\pi/(12\,\text{min})-2\pi/(6\,\text{min})$	$-1.58(\pm0.02)$	$-0.48(\pm0.06)$
		$2\pi/(4\,\text{min})-2\pi/(2\,\text{min})$	$-3.36(\pm0.02)$	$-4.30(\pm0.03)$
$\sigma_{\zeta'}$ (m)/$\sigma_{T_l'}$ (K)	GW	f^b–N	66/0.64	110/1.07
	GW	$2f^c$–N	56/0.55	80/0.78
	PW	$2\pi/(20\,\text{day})-2\pi/(1.5\,\text{day})$	353/3.4	220/2.15
Kurtosis ζ'	GW	f^b–N	67	0.4
	GW	$2f^c$–N	112	0.8
$\sigma_{w'}$ (m s^{-1})/$\sigma_{\text{D}T_l'/\text{D}t}$ (K h^{-1})	GW	f^b–N	0.32/11.3	0.46/16.2
	GW	f^b–$N/2$	0.13/4.6	0.11/3.9
	PW	$2\pi/(20\,\text{day})-2\pi/(1.5\,\text{day})$	5×10^{-3}/0.18	3×10^{-3}/0.1
Kurtosis w'	GW	f^b–N	400	3.5
	GW	f^b–$N/2$	1310	5.8

[a]Normalized kurtosis values are all significantly different from 0, except the kurtosis of vertical displacements in equatorial flights.
[b]For the equatorial flights, we use a lower frequency bound of $2\pi/(1\,\text{day})$.
[c]For the equatorial flights, we use a lower frequency bound of $2\pi/(12\,\text{h})$.

AGU Geophysical Research Letters 10.1002/2016GL068148

At low frequencies, the polar E_{k_h} spectrum shows a distinct peak located close to the inertial frequency, which, in agreement with equation (3), has no equivalent in the potential energy spectrum. This low-frequency peak essentially remains an observational fact that has been already reported [e.g., *Hertzog et al.*, 2002]. The kinetic energy enhancement near f and the spectral gap between low-frequency planetary and inertia-gravity waves are striking characteristic of wave spectra at high latitudes. They are not seen in the equatorial spectra which, on the other hand, display a continuum of wave motions.

3.1.2. Higher-Frequency Range

At higher frequencies, the balloon observations suggest an interesting behavior near N with a local peak in potential energy, like a counterpart to the E_{k_h} peak at low frequencies in the polar flights. Caution is, however, needed in interpreting this peak, as the frequency of the balloon neutral oscillations ω_b is located close to N, and spurious (nonisopycnic) balloon vertical motions certainly contaminate the measurements at these high frequencies [*Vincent and Hertzog*, 2014].

We nevertheless argue in the supporting information that part of this high-frequency enhancement in E_p corresponds to real atmospheric motions. This rests on numerical simulations of SPB response to atmospheric motions, an alternative and independent determination of the E_p spectrum from the E_{k_h} one, and theoretical considerations on the expected evolution of vertical velocity disturbances along wave propagation. It is also worth noting that a similar peak near N has been previously reported in radar measurements in the troposphere, though with much smaller amplitudes [e.g., *Ecklund et al.*, 1985, 1986]. In any case, since the balloons overestimate the air parcel motions at frequencies close to N, further observations are needed to confirm the existence and assess the magnitude of this high-frequency peak in E_p.

On the other hand, a robust feature of E_p and E_{k_h} spectra is the sharp transition to much steeper slopes past N. In particular, the fact that the potential energy peak is located at N rather than at ω_b strongly supports the idea of weaker vertical motions at frequencies higher than N (cf. supporting information). This observed change of regime probably corresponds to the transition from gravity waves to isotropic turbulence. It is also noticed that this transition occurs at a slightly lower frequency than N on the equatorial E_{k_h} spectrum.

3.2. Vertical Velocity and Temperature Spectra

While considering energies emphasizes the agreement of balloon observations with gravity wave theory, the quantities that actually play a role in microphysical processes are the Lagrangian temperature disturbance and its temporal derivative along air parcel motions, the heating/cooling rate. The "Lagrangian" (adiabatic) temperature fluctuations are related to the wave-induced vertical displacement through

$$T'_l = -\frac{g}{C_p}\zeta'_\theta \tag{4}$$

in the dry adiabatic limit for a hydrostatic background atmosphere, where g and C_p are the gravity acceleration and the heat capacity of air at constant pressure, respectively. Hence, the spectrum of Lagrangian temperature disturbances follows

$$T'^2_l = 2\left(\frac{g}{C_p N}\right)^2 E_p. \tag{5}$$

It is worth noting here that this Lagrangian temperature disturbance differs from the Eulerian value (T'), which is estimated at constant altitude. The Eulerian temperature disturbance is indeed related to E_p through

$$T'^2 = \bar{T}^2\left(\frac{\theta'}{\bar{\theta}}\right)^2 = 2\,\bar{T}^2\left(\frac{N}{g}\right)^2 E_p. \tag{6}$$

This "Eulerian" temperature variance is the one usually evaluated from radiosonde observations or constant altitude aircraft flights. Equations (5) and (6) show not only that both Eulerian and Lagrangian temperature spectra have similar $\hat{\omega}$ dependence as $E_p(\hat{\omega})$ but also that they differ by their magnitudes. In particular, for a given vertical displacement ζ_θ, the variance of Eulerian temperature disturbances depends on the background atmospheric stability, unlike the Lagrangian disturbances (see Text S3 in the supporting information for further details on this effect).

AGU Geophysical Research Letters 10.1002/2016GL068148

Besides temperature, microphysical processes such as ice nucleation also strongly depend on cooling rates and their intrinsic frequency distribution [e.g., *Kärcher and Lohmann*, 2002; *Dinh et al.*, 2016]. For adiabatic motions, those cooling rates are simply linked to the vertical velocity disturbance (w'):

$$\frac{\mathrm{D}T_l'}{\mathrm{D}t} = -\frac{g}{C_p}w', \tag{7}$$

whose spectrum is itself related to the E_p spectrum through

$$w'^2 = 2E_{k_v} = 2\left(\frac{\hat{\omega}}{N}\right)^2 E_p, \tag{8}$$

with $E_{k_v}(\hat{\omega})$, the vertical kinetic energy. On Figure 1, the E_{k_v} spectra are also displayed. They show a flat (or slightly increasing) variation with intrinsic frequency that highlights the importance of high-frequency waves in the variance of vertical velocity or heating/cooling rates. These spectra also display a strong peak at N. As previously discussed, the balloon measurements suggest that a fraction of this peak corresponds to real atmospheric motions but do not allow a quantitative assessment of this enhancement (see Text S1 in the supporting information).

4. Probability Density Functions (PDFs) and Intermittency

Beyond the frequency spectra that provide information on the temporal autocorrelation of temperatures and heating/cooling rates, it is also worth paying attention to the statistical distribution of these signals. Indeed, gravity wave activity is known to be intermittent [*Alexander et al.*, 2010; *Hertzog et al.*, 2012], and the sporadic character of wave disturbances can impact microphysical processes because of their strong nonlinearities.

4.1. Vertical Displacement (or Temperature) Statistics

As most of the variability in temperature (or vertical displacement) is contained in the low frequencies, we have applied a fifth-order high-pass Butterworth filter [e.g., *Oppenheim et al.*, 1999] to the temperature time series to isolate the gravity wave contribution from longer planetary wave signals. Figures 2a and 2b display the probability density function of temperature perturbations obtained with two different values for the cutoff frequency: f and $2f$ for the polar flights and 1 day^{-1} and 2 day^{-1} for the equatorial flights. The polar temperature PDF is essentially not sensitive to this choice because of the spectral gap between gravity and planetary waves, while the variance of the equatorial temperature disturbances depends more significantly on it (yet not the shape of the PDF).

The equatorial and polar PDFs exhibit very different shapes. The equatorial vertical displacement PDF suggests a Gaussian distribution (note the log y axis in Figure 2), with normalized kurtosis close to 0. The associated standard deviation is of the order of 100 m (1 K). On the contrary, the polar temperature PDF exhibits long tails and a much higher normalized kurtosis (67–112). If the standard deviations are smaller in the polar time series (66 m or 0.7 K), there is a more substantial contribution of unfrequent large displacements [*Bacmeister et al.*, 1999]. *Gierens et al.* [2007] also found non-Gaussian PDFs of temperature perturbations in data sets gathered during commercial aircraft flights, which mainly took place in the extratropical Northern Hemisphere upper troposphere. In a subsequent paper, *Dotzek and Gierens* [2008] attribute the emergence of those shapes to intermittency in temperature disturbances, which was at least partly caused by the aircraft crossing the tropopause. In our data set, the intermittency of gravity wave activity is the primary reason for the non-Gaussian behavior [*Hertzog et al.*, 2012]. A geographic screening furthermore shows that the long tails of the polar PDFs are associated with mountain waves over the Antarctic Peninsula (see Figure S3 in the supporting information).

In Table 1, the standard deviations of temperature fluctuations associated with both gravity and planetary waves signals are presented. The temperature PDFs and the reported variances show that the gravity wave contribution accounts for a significant fraction of the total wave perturbations and should therefore not be neglected when modeling microphysical processes. In the tropics for instance, gravity wave temperature fluctuations will, together with other wave motions, lower the mean cold-point tropopause temperature as well as its minima, which has impacts on dehydration in the TTL [*Kim and Alexander*, 2015].

AGU Geophysical Research Letters 10.1002/2016GL068148

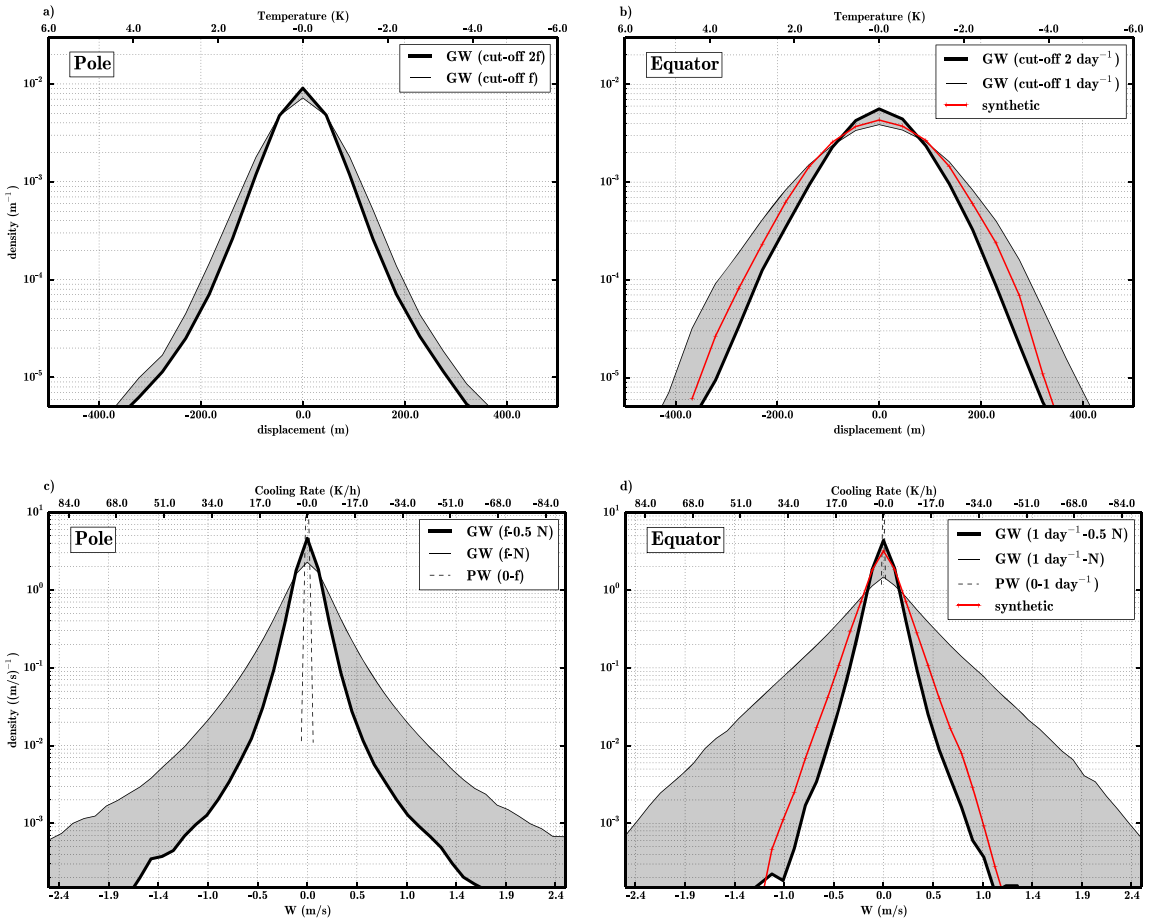

Figure 2. Probability density functions of (a, b) vertical displacements and (c, d) vertical velocities induced by gravity waves, for (Figures 2a and 2c) the polar and (Figures 2b and 2d) the equatorial balloon flights. For the vertical displacements (Figures 2a and 2b), two estimates that correspond to two different low cutoff frequencies (f and $2f$ in the polar flights, and 1 day^{-1} and 2 day^{-1} in the equatorial ones) are shown. The amplitude of the corresponding adiabatic temperature perturbations are shown on the upper x scale. For the (Figures 2c and 2d) vertical velocities, the two estimates correspond to two different high cutoff frequencies (N and $\frac{1}{2}N$) and the upper x scale shows the amplitude of the corresponding adiabatic cooling rates. The red curves in the Figures 2b and 2d correspond to the synthetic perturbations (see section 5).

4.2. Vertical Velocity (or Cooling Rates) Statistics

Unlike temperature fluctuations, most of the vertical velocity variance is associated with high-frequency motions. The frequencies of gravity waves extend to the Brunt-Väisälä frequency, but as previously mentioned the analysis of these high frequencies in the balloon measurements requires caution. In the following, we therefore show vertical velocity PDFs that have been obtained after applying a low-pass Kaiser filter [e.g., *Oppenheim et al.*, 1999] with cutoff frequencies located either at N or at $N/2$. The latter is a conservative choice (i.e., the spectral magnitude at this frequency is essentially void of any balloon-induced motions) that yields a lower bound for the total wave variance, since part of the full wave spectrum is omitted. The former, on the other hand, includes not only all wave motions but also some contributions associated with the balloon's own dynamics: it therefore corresponds to an upper bound of the wave variance.

The vertical velocity PDFs are displayed in Figures 2c and 2d for the two regions. In a more striking manner than for the vertical displacements, both tropical and high-latitude vertical velocity PDFs exhibit non-Gaussian shapes. The equatorial PDFs are close to a Laplace (double exponential) distribution. The polar PDFs even have distributions similar to double stretched exponentials. These shapes underline the important intermittency in the vertical velocity field, i.e., that the largest cooling rates are significantly more frequent than in a Gaussian distribution. They are likely to influence microphysical processes in the upper troposphere or lower stratosphere. For instance, the large tails that are primarily associated with mountain waves have a substantial impact on wave-driven PSC formation [e.g., *Carslaw et al.*, 1999].

AGU Geophysical Research Letters 10.1002/2016GL068148

We also show on Figures 2c and 2d the vertical velocity PDF associated with planetary waves, which are obtained by keeping only motions with intrinsic frequencies smaller than f (or 1 day^{-1}) in the balloon time series. Figure 2 highlights that the contribution of these low-frequency motions to the vertical velocities or cooling rates is very small, consistently with the slope of the corresponding spectrum. Almost all of the vertical velocity perturbations are due to gravity waves in the tropics and high latitudes, which once again supports the need to parameterize gravity wave fluctuations when modeling microphysical processes.

5. Parameterizations of Gravity Wave Fluctuations in Lagrangian Models

Lagrangian trajectory models targeting cloud or aerosol processes generally use large-scale analysis fields that are archived every few hours. In those models, different strategies have been used to represent shorter gravity wave temperature fluctuations and to reproduce either their spectra or their PDFs. In section 5.2, a new parameterization is proposed, which allows to reproduce both.

5.1. Existing Parameterizations

Aiming at simulating polar stratospheric clouds formation, *Bacmeister et al.* [1999] introduced a parameterization that consists in a discrete sum of harmonics with different frequencies, where the phase of each harmonic is attributed randomly while the amplitude is chosen to match prescribed spectral magnitudes. *Jensen and Pfister* [2004] used a similar approach for TTL cirrus clouds and constrained the harmonic amplitudes with measurements from long-duration balloon flights reported in *Hertzog and Vial* [2001]. This type of parameterization reproduces the observed slopes and magnitudes of the temperature and cooling rate spectra, but the use of random phases generates Gaussian PDFs. Such PDFs differ from observed cooling rate PDF in the tropics and from both temperature and cooling rate PDFs at high latitude.

Other methods to synthesize wave-induced fluctuations have included white noise [*Gary*, 2006] or multifractal random noise [*Murphy*, 2014] . If the use of white noise for temperature fluctuations easily allows the simulation of any PDF, it is in obvious contrast with the robust red spectra seen in the balloon observations. In fact, a white noise for cooling rate disturbances would be in closer agreement with the observations. *Murphy* [2003] and *Murphy* [2014] used multifractal random noise (using multiplicative cascades), for which one can control the spectral slope but did not provide any details on the temperature or cooling rate fluctuations PDFs.

Another approach for specific case studies is the use of a high-resolution nonhydrostatic model with output at high frequency, which can serve to compute trajectories resolving fast temperature fluctuations [*Kienast-Sjögren et al.*, 2015].

5.2. A New Parameterization for Temperature and Vertical Velocity Fluctuations

Based on the balloon observations, we propose an alternative way to parameterize wave-induced fluctuations by using a stochastic model. The synthetic time series generated by this parameterization agree with the balloon observations in the sense that they reproduce both the spectral shapes and the non-Gaussian cooling rate PDF. The tropical case is an especially favorable case, because the observed spectrum of temperature disturbances scales as $\hat{\omega}^{-2}$ and the associated PDF is nearly Gaussian. In this case, an autoregressive model of order 1, or Markov process, is sufficient to synthesize time series that resemble the observations. The displacement field ζ' is thus generated iteratively:

$$\zeta'_{t+dt} = \zeta'_t + W \cdot \mathrm{d}t\,, \tag{9}$$

where W is a white noise process that corresponds to the vertical velocity and follows a Laplace (double exponential) distribution. A 2 day^{-1} high-pass Butterworth filter is applied on the raw time series in order to remove its low-frequency component that should be resolved in the large-scale analysis. To match the balloon observations, the value of the free parameters are dt=2.2 min and the standard deviation of the Laplace white noise is 0.17 m/s. The Butterworth high-pass filter is of fifth order, and further details on the method are provided in the supplementary materials.

Figure 1 shows that the synthetized time series matches the slope and magnitude of the potential and kinetic energy spectra in the midfrequency range, up to $\frac{N}{2}$. Figures 2b and 2d illustrate that the PDFs of both temperature and vertical velocity can be reproduced. It should be noted that we take advantage of the flat vertical velocity spectrum, which easily allows us to match the observed cooling rate PDF. On the other hand, the Gaussian shape of the resulting temperature PDF results from the central limit theorem, and more sophisticated techniques would be needed to reproduce a non-Gaussian shape, as is observed over the pole (Figure 2).

Geophysical Research Letters 10.1002/2016GL068148

Since the tails of this polar temperature PDF are tied to mountain waves over specific regions (e.g., the Antarctic Peninsula), we agree with the suggestion of *Bacmeister et al.* [1999] that a dedicated parameterization of intermittent, intense orographic events is additionally required, as for instance done in *Carslaw et al.* [1999]. When the balloon data set is considered only over oceanic regions around Antarctica, the PDF of temperature fluctuations becomes more Gaussian, and our method succeeds in producing synthetic time series that mimic this perturbation background (see supporting information).

In the above example, the free parameters have been chosen to match SPB observations in the lower stratosphere. They would need to be adjusted to mimic temperature and vertical velocity fluctuations at a different time period (e.g., polar winter instead of spring) or at a different height (e.g., a few kilometers lower in the TTL). Such adjustment is described in the supporting information. Alternatively, the parameters may also be adjusted to reproduce the vertical velocity or Eulerian temperature statistics obtained from non-Lagrangian observations.

6. Summary

This letter has presented measurements of Lagrangian temperature and vertical velocity fluctuations in the tropical and polar lower stratosphere. The specificity of superpressure balloons and the high temporal resolution of the measurements gives an unprecedented opportunity to describe Lagrangian fluctuations tied to the entire wave spectrum, including gravity waves up to the Brunt-Väisälä frequency. The measurements were collected over specific regions during $\sim$ 3 month time periods: southern high latitudes during austral spring and deep tropics during boreal spring and easterly shear phase of the quasi-biennal oscillation. We note that seasonal variations of wave activity are expected to be important at high latitudes [e.g., *Geller et al.*, 2013]. In the tropics, on the other hand, the representativeness of the SPB data set is probably better because of the sampling of both clear skies and convection during the flights.

Our results confirm the $\hat{\omega}^{-2}$ power law behavior of potential and kinetic energy spectra in the midfrequency range ($f \ll \hat{\omega} \ll N$) for both the tropical and polar regions. Yet the observations also suggest a local enhancement of wave energy when N is approached, which may result from geophysical processes such as wave refraction and reflection or high-frequency wave sources (e.g., convection). Unfortunately, the amplitude of this local maximum near N cannot be assessed with current balloon observations because of the nonlinear response of SPBs to atmospheric motions with very high frequencies. On the other hand, the wave vertical velocity spectrum is essentially flat for $\hat{\omega} < N/2$, which is a direct consequence of the potential energy spectral slope and gravity wave polarization relations. Hence, high-frequency perturbations provide the major contribution to the whole wave vertical velocity variability.

Generally, the probability distributions of vertical velocity and temperature disturbances are not Gaussian, because of gravity wave intermittency. This is especially true in the polar flights that are affected by highly intermittent orographic sources, like over the Antarctic peninsula [*Hertzog et al.*, 2008]. In the tropical flights, the temperature perturbations are normally distributed but not the vertical velocity disturbances, which rather follow a Laplace distribution.

We propose a new parameterization of wave-induced temperature and heating/cooling rates in Lagrangian models. Crucially, this parameterization reproduces both the observed wave spectra and PDFs. Its simplicity makes it straightforward to implement in studies along air parcel trajectories, which address processes that depend on wave-induced fluctuations.

Acknowledgments
SPB data used in this study can be obtained upon request from A.H. (albert.hertzog@lmd.polytechnique.fr). Concordiasi is an international project, currently supported by the following agencies: Météo-France, CNES, CNRS/INSU, NSF, NCAR, University of Wyoming, Purdue University, University of Colorado, the Alfred Wegener Institute, the Met Office, and ECMWF. Concordiasi also benefits from logistic or financial support of the operational polar agencies (Institut Polaire Franais Paul Emile Victor) IPEV, Programma Nazionale di Ricerche in Antartide (PNRA), United States Antarctic Program (USAP) and (British Antarctic Survey) BAS, and from Baseline Surface Radiation Network (BSRN) measurements at Concordia. Concordiasi is part of The Observing System Research and Predictability Experiment International Polar Year (THORPEX-IPY) cluster within the International Polar Year effort. The authors acknowledge support from the StraDyVariUS project (ANR-13-BS06-0011-01) funded by ANR.

References

Alexander, M. J., et al. (2010), Recent developments in gravity-wave effects in climate models and the global distribution of gravity-wave momentum flux from observations and models, *Q. J. R. Meteorol. Soc.*, *136*(650), 1103–1124, doi:10.1002/qj.637.

Bacmeister, J. T., S. D. Eckermann, A. Tsias, K. S. Carslaw, and T. Peter (1999), Mesoscale temperature fluctuations induced by a spectrum of gravity waves: A comparison of parameterizations and their impact on stratospheric microphysics, *J. Atmos. Sci.*, *56*, 1913–1924, doi:10.1175/1520-0469.

Carslaw, K. S., T. Peter, J. T. Bacmeister, and S. D. Eckermann (1999), Widespread solid particle formation by mountain waves in the Arctic stratosphere, *J. Geophys. Res.*, *104*(D1), 1827–1836, doi:10.1029/1998JD100033.

Cho, J. Y. N., Y. Zhu, R. E. Newell, B. E. Anderson, J. D. Barrick, G. L. Gregory, G. W. Sachse, M. A. Carroll, and G. M. Albercook (1999a), Horizontal wavenumber spectra of winds, temperature, and trace gases during the Pacific Exploratory Missions: 1. Climatology, *J. Geophys. Res.*, *104*(D5), 5697–5716, doi:10.1029/98JD01825.

Cho, J. Y. N., R. E. Newell, and J. D. Barrick (1999b), Horizontal wavenumber spectra of winds, temperature, and trace gases during the Pacific Exploratory Missions: 2. Gravity waves, quasi-two-dimensional turbulence, and vortical modes, *J. Geophys. Res.*, *104*(D13), 16,297–16,308, doi:10.1029/1999JD900068.

AGU Geophysical Research Letters 10.1002/2016GL068148

Dinh, T., A. Podglajen, A. Hertzog, B. Legras, and R. Plougonven (2016), Effect of gravity wave temperature fluctuations on homogeneous ice nucleation in the tropical tropopause layer, *Atmos. Chem. Phys.*, *16*, 35–46, doi:10.5194/acp-16-35-2016.

Dotzek, N., and K. Gierens (2008), Instantaneous fluctuations of temperature and moisture in the upper troposphere and tropopause region. Part 2: Structure functions and intermittency, *Meteorol. Z.*, *17*(3), 323–337, doi:10.1127/0941-2948/2008/0292.

Ecklund, W. L., B. B. Balsley, D. A. Carter, A. C. Riddle, M. Crochet, and R. Garello (1985), Observations of vertical motions in the troposphere and lower stratosphere using three closely spaced ST radars, *Radio Sci.*, *20*(6), 1196–1206, doi:10.1029/RS020i006p01196.

Ecklund, W. L., K. S. Gage, G. D. Nastrom, and B. B. Balsley (1986), A preliminary climatology of the spectrum of vertical velocity observed by clear-air Doppler radar, *J. Clim. Appl. Meteorol.*, *25*(7), 885–892, doi:10.1175/1520-0450(1986)025<0885:APCOTS>2.0.CO;2.

Fritts, D. C., and M. J. Alexander (2003), Gravity wave dynamics and effects in the middle atmosphere, *Rev. Geophys.*, *41*(1), 1003, doi:10.1029/2001RG000106.

Fritts, D. C., and D.-Y. Wang (1991), Doppler-shifting effects on frequency spectra of gravity waves observed near the summer mesopause at high latitude, *J. Atmos. Sci.*, *48*(13), 1535–1544, doi:10.1175/1520-0469(1991)048<1535:DSEOFS>2.0.CO;2.

Fueglistaler, S., and P. H. Haynes (2005), Control of interannual and longer-term variability of stratospheric water vapor, *J. Geophys. Res.*, *110*, D24108, doi:10.1029/2005JD006019.

Gage, K. S., B. B. Balsley, and R. Garello (1986), Comparisons of horizontal and vertical velocity spectra in the mesosphere, stratosphere and troposphere: Observations and theory, *Geophys. Res. Lett.*, *13*(11), 1125–1128, doi:10.1029/GL013i011p01125.

Gary, B. L. (2006), Mesoscale temperature fluctuations in the stratosphere, *Atmos. Chem. Phys.*, *6*(12), 4577–4589, doi:10.5194/acp-6-4577-2006.

Geller, M. A., et al. (2013), A comparison between gravity wave momentum fluxes in observations and climate models, *J. Clim.*, *26*(17), 6383–6405, doi:10.1175/JCLI-D-12-00545.1.

Gierens, K., R. Kohlhepp, N. Dotzek, and H. G. Smit (2007), Instantaneous fluctuations of temperature and moisture in the upper troposphere and tropopause region. Part 1: Probability densities and their variability, *Meteorol. Z.*, *16*(2), 221–231, doi:10.1127/0941-2948/2007/0197.

Grooß, J.-U., and R. Müller (2007), Simulation of ozone loss in Arctic winter 2004/2005, *Geophys. Res. Lett.*, *34*, L05804, doi:10.1029/2006GL028901.

Haag, W., and B. Kärcher (2004), The impact of aerosols and gravity waves on cirrus clouds at midlatitudes, *J. Geophys. Res.*, *109*, D12202, doi:10.1029/2004JD004579.

Hertzog, A., and F. Vial (2001), A study of the dynamics of the equatorial lower stratosphere by use of ultra-long-duration balloons: 2. Gravity waves, *J. Geophys. Res.*, *106*(D19), 22,745–22,761, doi:10.1029/2000JD000242.

Hertzog, A., F. Vial, C. R. Mechoso, C. Basdevant, and P. Cocquerez (2002), Quasi-lagrangian measurements in the lower stratosphere reveal an energy peak associated with near-inertial waves, *Geophys. Res. Lett.*, *29*(8), 1229, doi:10.1029/2001GL014083.

Hertzog, A., et al. (2007), Stratéole/vorcore—Long-duration, superpressure balloons to study the Antarctic lower stratosphere during the 2005 winter, *J. Atmos. Oceanic Technol.*, *104*(D1), 2048–2061, doi:10.1175/2007JTECHA948.1.

Hertzog, A., G. Boccara, R. A. Vincent, F. Vial, and P. Cocquerez (2008), Estimation of gravity wave momentum flux and phase speeds from quasi-Lagrangian stratospheric balloon flights. Part II: Results from the Vorcore campaign in Antarctica, *J. Atmos. Sci.*, *65*(10), 3056–3070, doi:10.1175/2008JAS2710.1.

Hertzog, A., M. J. Alexander, and R. Plougonven (2012), On the intermittency of gravity wave momentum flux in the stratosphere, *J. Atmos. Sci.*, *69*(11), 3433–3448, doi:10.1175/JAS-D-12-09.1.

Hoyle, C. R., B. P. Luo, and T. Peter (2005), The origin of high ice crystal number densities in cirrus clouds, *J. Atmos. Sci.*, *62*, 2568–2579, doi:10.1175/JAS3487.1.

James, R., M. Bonazzola, B. Legras, K. Surbled, and S. Fueglistaler (2008), Water vapor transport and dehydration above convective outflow during Asian monsoon, *Geophys. Res. Lett.*, *35*, L20810, doi:10.1029/2008GL035441.

Jensen, E., and L. Pfister (2004), Transport and freeze-drying in the tropical tropopause layer, *J. Geophys. Res.*, *109*, D02207, doi:10.1029/2003JD004022.

Jensen, E. J., L. Pfister, T.-P. Bui, P. Lawson, and D. Baumgardner (2010), Ice nucleation and cloud microphysical properties in tropical tropopause layer cirrus, *Atmos. Chem. Phys.*, *10*(3), 1369–1384, doi:10.5194/acp-10-1369-2010.

Jensen, E. J., L. Pfister, and T. P. Bui (2012), Physical processes controlling ice concentrations in cold cirrus near the tropical tropopause, *J. Geophys. Res.*, *117*, D11205, doi:10.1029/2011JD017319.

Kärcher, B., and U. Lohmann (2002), A parameterization of cirrus cloud formation: Homogeneous freezing of supercooled aerosols, *J. Geophys. Res.*, *107*(D2), 4010, doi:10.1029/2001JD000470.

Kärcher, B., A. Dörnbrack, and I. Sölch (2014), Supersaturation variability and cirrus ice crystal size distributions, *J. Atmos. Sci.*, *71*, 2905–2926, doi:10.1175/JAS-D-13-0404.1.

Kienast-Sjögren, E., A. K. Miltenberger, B. P. Luo, and T. Peter (2015), Sensitivities of Lagrangian modeling of mid-latitude cirrus clouds to trajectory data quality, *Atmos. Chem. Phys. Discuss.*, *15*(5), 7535–7584, doi:10.5194/acpd-15-7535-2015.

Kim, J.-E., and M. J. Alexander (2015), Direct impacts of waves on tropical cold point tropopause temperature, *Geophys. Res. Lett.*, *42*, 1584–1592, doi:10.1002/2014GL062737.

Massman, W. J. (1978), On the nature of vertical oscillations of constant volume balloons, *J. Appl. Meteorol.*, *17*, 1351–1356, doi:10.1175/1520-0450(1978)017<1351:OTNOVO>2.0.CO;2.

Muhlbauer, A., H. Kalesse, and P. Kollias (2014), Vertical velocities and turbulence in midlatitude anvil cirrus: A comparison between in situ aircraft measurements and ground-based doppler cloud radar retrievals, *Geophys. Res. Lett.*, *41*, 7814–7821, doi:10.1002/2014GL062279.

Murphy, D. M. (2003), Dehydration in cold clouds is enhanced by a transition from cubic to hexagonal ice, *Geophys. Res. Lett.*, *30*(23), 2230, doi:10.1029/2003GL018566.

Murphy, D. M. (2014), Rare temperature histories and cirrus ice number density in a parcel and a one-dimensional model, *Atmos. Chem. Phys.*, *14*(23), 13,013–13,022, doi:10.5194/acp-14-13013-2014.

Murphy, D. M., and B. L. Gary (1995), Mesoscale temperature fluctuations and polar stratospheric clouds, *J. Atmos. Sci.*, *52*(10), 1753–1760, doi:10.1175/1520-0469.

Nastrom, G. D. (1980), The response of superpressure balloons to gravity waves, *J. Appl. Meteorol.*, *19*, 1013–1019, doi:10.1175/1520-0450(1980)019<1013:TROSBT>2.0.CO;2.

Oppenheim, A. V., R. W. Schafer, and J. R. Buck (1999), *Discrete-Time Signal Processing*, 1st ed., Prentice-Hall, Upper Saddle River, N. J.

Podglajen, A., A. Hertzog, R. Plougonven, and N. Žagar (2014), Assessment of the accuracy of (re)analyses in the equatorial lower stratosphere, *J. Geophys. Res. Atmos.*, *119*, 11,166–11,188, doi:10.1002/2014JD021849.

Rabier, F., et al. (2010), The Concordiasi project in Antarctica, *Bull. Am. Meteorol. Soc.*, *91*, 69–86, doi:10.1175/2009bams2764.1.

Randel, W. J., and E. J. Jensen (2013), Physical processes in the tropical tropopause layer and their roles in a changing climate, *Nat. Geosci.*, *6*(3), 169–176, doi:10.1038/ngeo1733.

Geophysical Research Letters 10.1002/2016GL068148

Solomon, S., R. R. Garcia, S. F. Rowland, and D. J. Wuebbles (1986), On the depletion of Antarctic ozone, *Nature*, *321*, 755–758, doi:10.1038/321755a0.

Solomon, S., K. H. Rosenlof, R. W. Portmann, J. S. Daniel, S. M. Davis, T. J. Sanford, and G.-K. Plattner (2010), Contributions of stratospheric water vapor to decadal changes in the rate of global warming, *Science*, *327*(5970), 1219–1223, doi:10.1126/science.1182488.

Spichtinger, P., and M. Krämer (2013), Tropical tropopause ice clouds: A dynamic approach to the mystery of low crystal numbers, *Atmos. Chem. Phys.*, *13*(19), 9801–9818, doi:10.5194/acp-13-9801-2013.

Tabazadeh, A., O. B. Toon, B. L. Gary, J. T. Bacmeister, and M. R. Schoeberl (1996), Observational constraints on the formation of type Ia polar stratospheric clouds, *Geophys. Res. Lett.*, *23*(16), 2109–2112, doi:10.1029/96GL01998.

Vial, F., A. Hertzog, C. R. Mechoso, C. Basdevant, P. Cocquerez, V. Dubourg, and F. Nouel (2001), A study of the dynamics of the equatorial lower stratosphere by use of ultra-long-duration balloons: 1. Planetary scales, *J. Geophys. Res.*, *106*(D19), 22,725–22,743, doi:10.1029/2000JD000241.

Vincent, R. A., and S. D. Eckermann (1990), VHF radar observations of mesoscale motions in the troposphere: Evidence for gravity wave Doppler shifting, *Radio Sci.*, *25*(5), 1019–1037, doi:10.1029/RS025i005p01019.

Vincent, R. A., and A. Hertzog (2014), The response of superpressure balloons to gravity wave motions, *Atmos. Meas. Tech.*, *7*, 1043–1055, doi:10.5194/amt-7-1043-2014.

Voigt, A., and T. A. Shaw (2015), Circulation response to warming shaped by radiative changes of clouds and water vapour, *Nat. Geosci.*, *8*, 102–106, doi:10.1038/ngeo2345.

2.4 Observed energy spectra and vertical velocity at the high frequencies

I develop here observational arguments that support the existence of a local maximum in gravity-wave vertical kinetic energy (and hence also an enhancement in potential energy) at high frequencies[12] in the lower stratosphere. This section inspires from the supplementary material of the letter, but also adds some discussions regarding the interpretation of the measurements at high frequency in terms of gravity wave properties. Finally, a tentative correction for the non-isopycnic response of the balloon at high frequency is proposed and the results are compared with independent aircraft measurements from ATTREX.

2.4.1 Polarization between zonal wind and vertical wind observations and wave reflection

Vertical wind from zonal wind using the polarization relations The first argument in favor of an E_p enhancement near N comes from the independent measurements of horizontal wind combined with the polarization relations. Using Equation (3) in the letter, which is derived from the polarization relations for linear gravity waves, we can compute an estimate of the wave E_p from the observed E_{k_h}. This E_{k_h}-based estimate is independent from the direct estimate of E_p, since it is first computed solely with the balloon horizontal positions provided by the GPS system, while E_p is obtained from the pressure measurements. Moreover, we have checked that the balloon-borne E_{k_h} spectrum is not influenced by the balloon vertical motions in a sheared environment ($\frac{\mathrm{d}\bar{u}}{\mathrm{d}z}$), in other words that the Lagrangian term $\zeta_b' \frac{\mathrm{d}\bar{u}}{\mathrm{d}z}$ can be neglected in front of the Eulerian wind disturbance u'. This remains true at all frequencies even for relatively large shear, i.e. $10^{-2}\,\mathrm{s}^{-1}$. The two estimates of E_p are displayed in Figure 2.4, and agree within 30% over almost the whole gravity-wave frequency range, namely when $1.05\,f < \hat{\omega} < 0.95\,N$. Larger discrepancies at both ends of the gravity-wave spectrum are likely associated with the finite resolution of the balloon-borne spectra and variations of f and N along the balloon flights, since E_{k_h} should theoretically vanish when $\hat{\omega} \to N$, and E_p when $\hat{\omega} \to f$. Yet the enhancement of the E_{k_h}-based estimate of E_p at $\hat{\omega} \lesssim N$ suggests an increase of wave activity at these frequencies.

Wave reflection and the limits of the polarization relations for $\hat{\omega} \to N$ The previous argument relied on the polarization relations. However, it should be mentioned that those relations might not hold, even if the measured perturbations were entirely caused by a superposition of linear gravity waves. This is due to the fact that balloon measurements are carried at a single altitude, so that there is a possibility of constructive interferences if a reflector were located just above that altitude. We explain the reason in the following.

Equation (3) of the letter is strictly valid only for a monochromatic linear gravity waves,

[12] In this work, high frequency usually means frequencies near N.

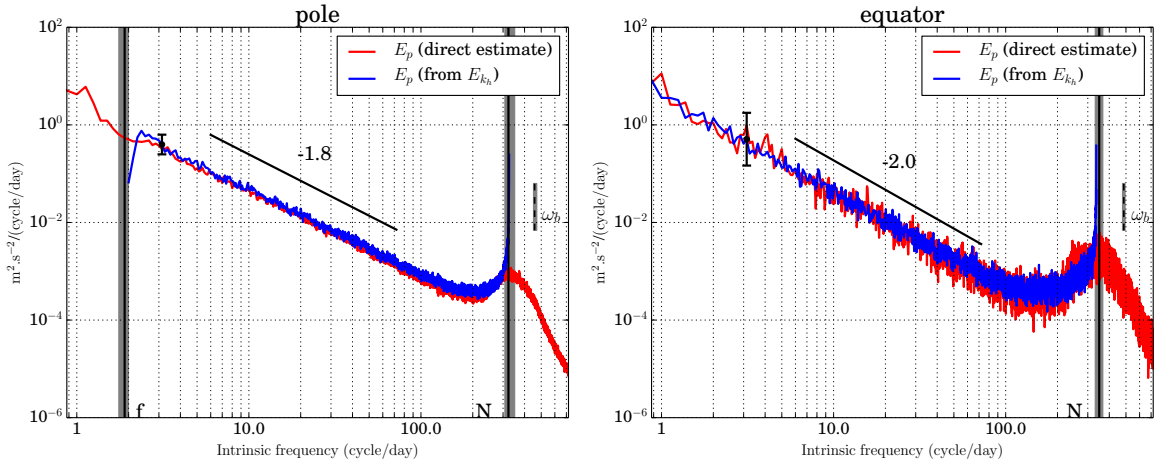

Figure 2.4 – Spectra of potential energy, estimated directly from the ballon vertical displacement (red) or from the kinetic energy spectra with the help of the wave polarization relation (blue, see equation (3) of the letter). Observations were made during the 2010 polar (left) and equatorial (right) campaigns. The vertical black lines show the Coriolis frequency f for the polar flight and the Brünt-Väisälä frequency N (estimated from the ECMWF operational analysis), the dashed line corresponds to the frequency of the balloon neutral oscillations ω_b . The larger spectral uncertainty in the equatorial spectra is associated with a smaller number of flights during the PreConcordiasi campaign (3) than during the polar Concordiasi campaign (19).

that is:

$$E_{k_h}(\hat{\omega},m) = \frac{N^2}{N^2-\hat{\omega}^2}\frac{\hat{\omega}^2-f^2}{\hat{\omega}^2+f^2}E_p(\hat{\omega},m) \text{ and}$$

$$|\hat{w}(\hat{\omega},m)|^2 = 2E_{k_v}(\hat{\omega},m) = 2\frac{N^2}{N^2-\hat{\omega}^2}\frac{\hat{\omega}^2-f^2}{\hat{\omega}^2+f^2}E_p(\hat{\omega},m) \quad (2.24)$$

are valid for each $\hat{\omega}$ and m (neglecting the horizontal dependency for simplicity). Integrating over vertical wavenumbers, the same relations apply for, e.g. $|\hat{W}_t(\hat{\omega})|^2 = \frac{1}{2\pi}\int_{-\infty}^{+\infty}|\hat{w}(\hat{\omega},m)|^2 \mathrm{d}m$, etc ... However, balloon measurements are obtained at a given altitude z so that they measure:

$$w(z,t) = \frac{1}{2\pi}\int_{\mathbb{R}}\left(\frac{1}{2\pi}\int_{\mathbb{R}}\hat{w}(\hat{\omega},m)e^{imz}\mathrm{d}m\right)e^{-i\hat{\omega}t}\mathrm{d}\hat{\omega} = \frac{1}{2\pi}\int_{\mathbb{R}}\hat{W}(\hat{\omega},z)e^{-i\hat{\omega}t}\mathrm{d}\hat{\omega} \quad (2.25)$$

By virtue of Parseval's formula, one also has: $|\hat{W}_t(\hat{\omega})|^2 = \int_{\mathbb{R}}|\hat{W}(\hat{\omega},z)|^2\mathrm{d}z$. However, the measurements are only acquired at one level, so that the balloon estimated spectra $|\hat{W}(\hat{\omega},z_b)|^2$ are actually given by:

$$|\hat{W}(\hat{\omega},z_b)|^2 = \frac{1}{4\pi^2}\iint_{\mathbb{R}^2}\hat{w}(\hat{\omega},m)\hat{w}^*(\hat{\omega},m_1)\,e^{i(m-m_1)z_b}\mathrm{d}m\,\mathrm{d}m_1 \quad (2.26)$$

$$= \frac{1}{4\pi^2}\iint_{\mathbb{R}^2}|\hat{w}(\hat{\omega},m)||\hat{w}(\hat{\omega},m_1)|\,e^{i((m-m_1)z_b+\varphi(m)-\varphi(m_1))}\mathrm{d}m\,\mathrm{d}m_1 \quad (2.27)$$

If the phases for different vertical wavenumbers are random and statistically uncorrelated, then ensemble averaging over multiple periodograms leads to: $\overline{|\hat{W}(\hat{\omega},z_b)|^2} = |\hat{W}_t(\hat{\omega})|^2$ since $\overline{e^{i(\varphi(m)-\varphi(m_1))}} = 0$ except for $m = m_1$. This consideration is the reason why we expect the polarization relations to be verified in the averaged spectra. Classical when examining waves,

it holds both for random wave and random wave packet superposition.

However, ensemble averaging will not be sufficient for the polarization relation to hold if different waves or wave packets with different wavenumbers have their phases systematically correlated. Then, interferences can occur. In particular, this will be the case if there are incident and reflected waves, near the altitude of reflection, in which case interferences will occur between $\hat{w}(\hat{\omega}, m)$ and $\hat{w}(\hat{\omega}, -m)$[13]. This case of reflected waves, tied to the presence of vertical heterogeneities in wind and stratification, is illustrated in details in the appendix A to this chapter. It shows that the polarization relations will not generally hold for all waves near a stratification jump (e.g. the tropopause) and for high frequency waves in a sheared environment. The first case is of little relevance for PreConcordiasi observations at 19-20 km, but the second is likely. Therefore, the polarization relation (Equation (3) of the letter) might not be strictly applicable at high frequency, even if the fluctuations are purely linear gravity waves. This limits the validity of the above argument, which deduced a N peak in potential energy E_p from the measured E_{k_h} and the polarization relations.

2.4.2 Non isopycnic balloon response at high frequencies

Another type of arguments supporting the existence of an E_p enhancement near N comes from estimating the non isopycnic response of the balloons. We have used two approaches: numerical simulations of the balloon response to different synthetic input atmospheric spectra, and an observational correction for the non isopycnic displacement using the temperature measurements. Both approaches have their own limitations.

Numerical simulations of the balloon response By solving Equation (2.10), we have numerically calculated the balloon response to various synthetic input spectra representative of atmospheric vertical-velocity disturbances. In Figure 2.5, we show the w' input spectrum and the corresponding spectrum in the simulated balloon observations (left panels), as well as the ratio of these two spectra (right panels). In the top panel, we have used a flat input spectrum up to the Brunt-Väisälä frequency. The associated balloon response spectrum displays a non-geophysical enhancement, but at frequencies higher than N. In fact, the balloon spectrum exhibits a decrease at frequencies slightly shorter than N, which contrasts with the spectra obtained with the real balloon measurements. On the other hand, if an increase in wave activity at $\hat{\omega} \lesssim N$ is already present in the synthetic input spectrum (lower panel), the simulated balloon spectrum displays an energy enhancement at frequencies close to N in better agreement with the observations. We also note that the balloon spectra tend to significantly overestimate the imposed increase of energy at frequencies higher than N, so that we cannot provide any quantitative estimation of this enhancement in atmospheric motions with current balloon measurements.

Correction for non-isopycnic behavior using observations of temperature Besides using numerical simulations, the uncertainty in the balloon response at high frequency can also be circumvented with direct measurements of the density ρ. Indeed, one can then derive

[13]For instance, for a total reflection at altitude z_0, $(\varphi(m) - \varphi(-m)) = \pi + 2mz_0$.

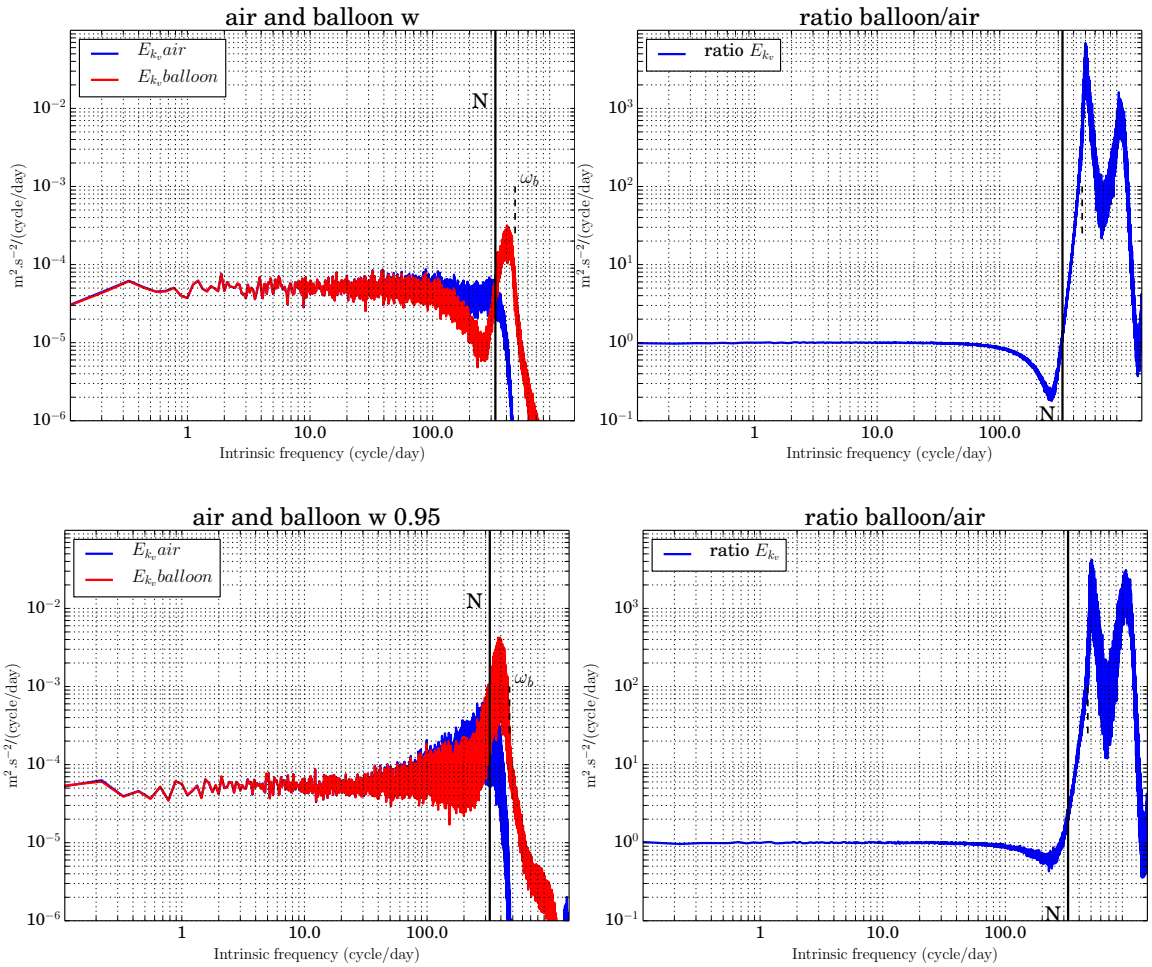

Figure 2.5 – (Left two rows) Spectra of the atmospheric vertical kinetic energy E_{k_v} used to force the balloon response simulations (in blue) and simulated spectra of the vertical kinetic energy that would be inferred from the balloon observations forced by the corresponding air spectrum (in red). (Right two rows) Ratio of the balloon estimated vertical velocity spectrum (assuming the balloon perfectly isopycnic over the "true" air vertical velocity spectrum (used ad forcing). This figure illustrates the non-linear response of the balloon at high frequencies.

the isopycnic displacement within the limits of the linearization in Equation (2.7):

$$\zeta_\rho \simeq \zeta_b + \frac{\rho_b - \rho}{\frac{\mathrm{d}\bar{\rho}}{\mathrm{d}z}} \text{ and then } \zeta_\theta = \frac{1}{\alpha}\zeta_\rho \tag{2.28}$$

This retrieval needs an external estimate of the lapse rate $\frac{\mathrm{d}\bar{T}}{\mathrm{d}z}$ (for the term $\frac{\mathrm{d}\bar{\rho}}{\mathrm{d}z}$), which can be obtained from a meteorological analysis. This makes the correction dependent on the quality of the analysis. ρ can be retrieved from T and p using the perfect gas law. The main limitations, however, are:

1. the noise in the temperature measurements at high frequency. This noise is most significant during day when the elements of the flight chain are heated by the sun. It is especially large when the sensors are in the wake of the balloon and sample air that has been in contact with elements of the flight chain.

2. the possibility of small time offsets between the temperature and pressure (or altitude)

measurements, since computing ζ_ρ at high frequency will be made through the difference of two very close terms[14].

Point (1) imposes that the correction can only be carried out at night.

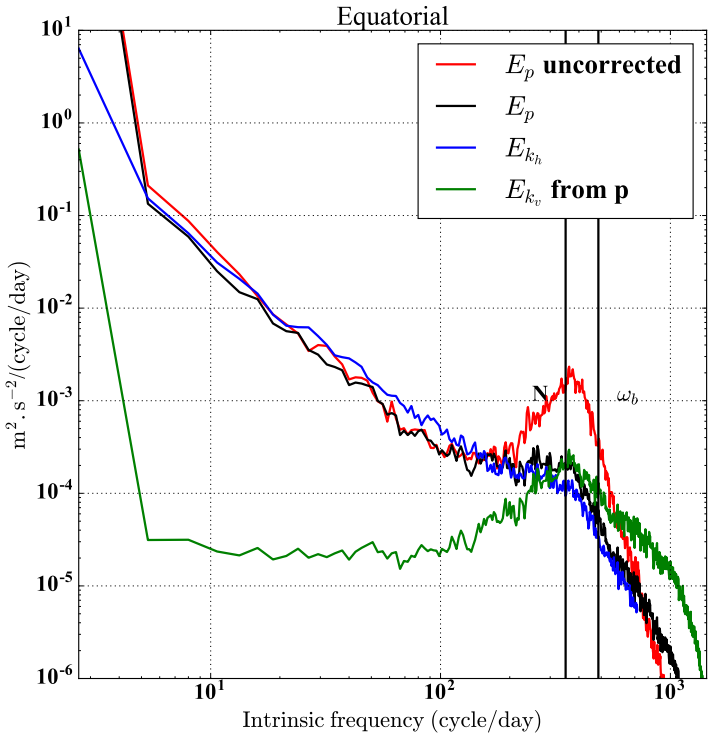

Figure 2.6 – Power spectral density of horizontal kinetic energy, potential energy uncorrected and corrected for the non isopycnic vertical motion, and of (corrected) vertical kinetic energy, as a function of intrinsic frequency. The background vertical density gradient needed for the correction is taken from the ECMWF operational analysis interpolated along the balloon trajectory.

Figure 2.6 shows the corrected spectra compared with the original, for the equatorial flights at night. The N peak in E_{k_v} remains but its amplitude is much reduced.

Comparison with aircraft observations Due to the limitations of the balloon measurements at high frequency, it is necessary to compare those with other datasets. Only a few other platforms measure vertical velocity and provide data in the tropics, and none are quasi-Lagrangian. However, the ATTREX aircraft data was obtained over a similar area (the tropical Pacific), and season (the end of boreal winter) as the PreConcordiasi balloon data. Although aircraft data is gathered in a Eulerian frame and the spectra cannot be compared, it is still possible to compare the statistics obtained.

Figure 2.7 compares the PDF of vertical velocity from ATTREX to that from the corrected balloon time series. The corrected time series show closer statistics to the aircraft observations than the uncorrected one, but a significant discrepancy remains. ATTREX observations were carried away from deep convection to limit the risks of damaging the Global Hawk. This is not the case for the balloons, and might explain part of the difference. However, most of it probably comes from remaining issues in the correction for non isopycnic behavior. At

[14]Since ζ_b is of the order of $\frac{\rho_b - \rho}{\frac{\mathrm{d}\bar{\rho}}{\mathrm{d}z}}$

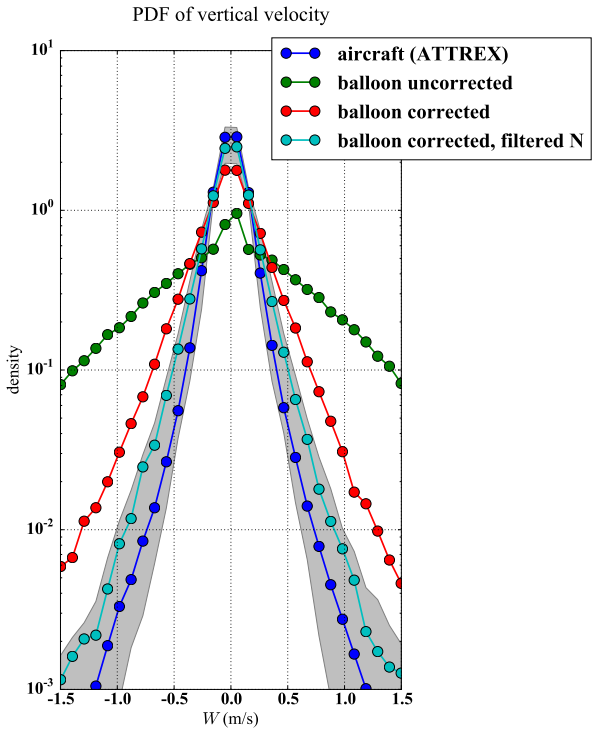

Figure 2.7 – Vertical wind probability distribution in the TTL from ATTREX Meteorological Measurement System observations above 17 km (blue line: average and shaded gray: variability from different flights) versus raw balloon observations (at 30 seconds), balloon observations corrected using the temperature measurements (red), and low-pass filtered version (at the Brunt-Väisälä frequency N) of the corrected time series.

high frequencies, even in the absence of balloon motions, the temperature sensor will be subject to noise which might overcome the weaker signal of the balloon displacement, so that the correction is actually degrading the signal at those frequencies. Indeed, it can be noticed in Figure 2.6 that the corrected spectrum gets above the uncorrected spectra for frequencies higher than $\sim \omega_b$. To quantify that impact, Figure 2.7 also shows a corrected time series filtered at the Brunt-Väisälä frequency, which is in good agreement with ATTREX observations.

Planned future balloon campaigns will include high resolution and precision measurements of temperature as well as direct measurements of the temperature lapse rate. This will allow to apply the technique demonstrated here to a fully observational datasets, and will help clarify the atmospheric variability at very high intrinsic frequencies (not relying on the reanalysis for the lapse rate).

2.5 Gravity wave Intermittency, Wave Sources and intrinsic frequency spectrum: insights from SPB measurements

One property of the gravity wave field that has been emphasized in the recent literature is its intermittency. The term intermittency comes from the field of turbulence where it refers to the irregular dissipation of kinetic energy, which is associated with heterogeneities in the small-scale variance of winds and temperature. For gravity waves, intermittency refers to

the fact that large amplitude wave packets are encountered in the atmosphere at specific time and locations, and that they account for most of the mean variance. In the following, a method of intermittency analysis is applied to SPB observations in the tropics. The results are preliminary and express an ongoing reflection. They are included because they provide further insights on one of the main question of the thesis: what is causing the temperature fluctuations and how to parameterize them?

2.5.1 Intermittency

Method of intermittency analysis In geophysics, two methods have been used to investigate intermittency in the energy spectra of wind and temperature fluctuations: multifractal analysis (*Davis et al.*, 1994) and continuous wavelet transforms (*Torrence and Compo*, 1998). In atmospheric dynamics, both have been extensively used, although each specific field has its habits. Generally, multifractal analysis is more common to the field of turbulence[15] whereas wavelet transforms are a common tool for analyzing gravity waves. Following previous works (e.g. *Hertzog et al.*, 2002), our analysis relies on the continuous wavelet transform.

Without getting into technical details about continuous wavelet analysis, which can be found in dedicated publications (e.g. *Torrence and Compo*, 1998), a few properties are important to keep in mind. First, the wavelet (complex) coefficients $W_m(s_j) = W(t_m, s_j)$ provide a time-frequency decomposition of the input signal (corresponding to different times t_m and scales s_j or frequency $\hat{\omega}_j$). Second, the time-average wavelet spectrum tends towards the traditional Fourier spectrum $\frac{\mathrm{d}\sigma^2}{\mathrm{d}\hat{\omega}}$:

$$\frac{\mathrm{d}\sigma^2}{\mathrm{d}\hat{\omega}}(\hat{\omega}_j) = \frac{1}{M}\sum_{m=1}^{M} |W_m(\hat{\omega}_j)|^2 \tag{2.29}$$

Hence, the coefficients $|W_m(\hat{\omega}_j)|^2$ indicate the "local"magnitude of the fluctuations at time t_m intrinsic frequency $\hat{\omega}_j$. Variability of $|W_m(\hat{\omega}_j)|^2$ with time (t_m here) indicates variable energy of the fluctuations at frequency $\hat{\omega}_j$. Formula (2.29) shows that wavelets can be used to investigate variability in, e.g., the horizontal kinetic energy spectrum E_{k_h}, by computing:

$$(E_{k_h})_m(\hat{\omega}_j) = \frac{1}{2}(|U_m(\hat{\omega}_j)|^2 + |V_m(\hat{\omega}_j)|^2) \tag{2.30}$$

where $U_m(\hat{\omega}_j)$ and $V_m(\hat{\omega}_j)$ are the wavelet coefficients associated with the zonal wind and meridional wind time series. Formula (2.29) implies that:

$$E_{k_h}(\hat{\omega}_j) = \frac{1}{M}\sum_{m=1}^{M} (E_{k_h})_m(\hat{\omega}_j) \tag{2.31}$$

$E_{k_h}(\hat{\omega}_j)$ is the mean of the energy spectrum, whereas the full time series of the $(E_{k_h})_m(\hat{\omega}_j)$ coefficients characterize its variability with time. The same calculation can be derived for potential energy E_p.

Different mother wavelets can be used for continuous wavelet analysis; I have used the

[15] This is probably related to the fact that exact formulas involving the structure functions have been proved in inertial range turbulence (*Monin and Yaglom*, 1977).

Morlet wavelet in the following. Its analytical expression is given by:

$$\Psi_M(t) = \pi^{-\frac{1}{4}} \left(e^{i\omega_0 t} - e^{-\frac{\omega_0^2}{2}} \right) e^{-\frac{t^2}{2}} \tag{2.32}$$

Choosing $\omega_0 = 6$ the second term in the parenthesis is about 10^{-8} and can be safely dropped. The Morlet wavelet is then just a harmonic with a Gaussian window.

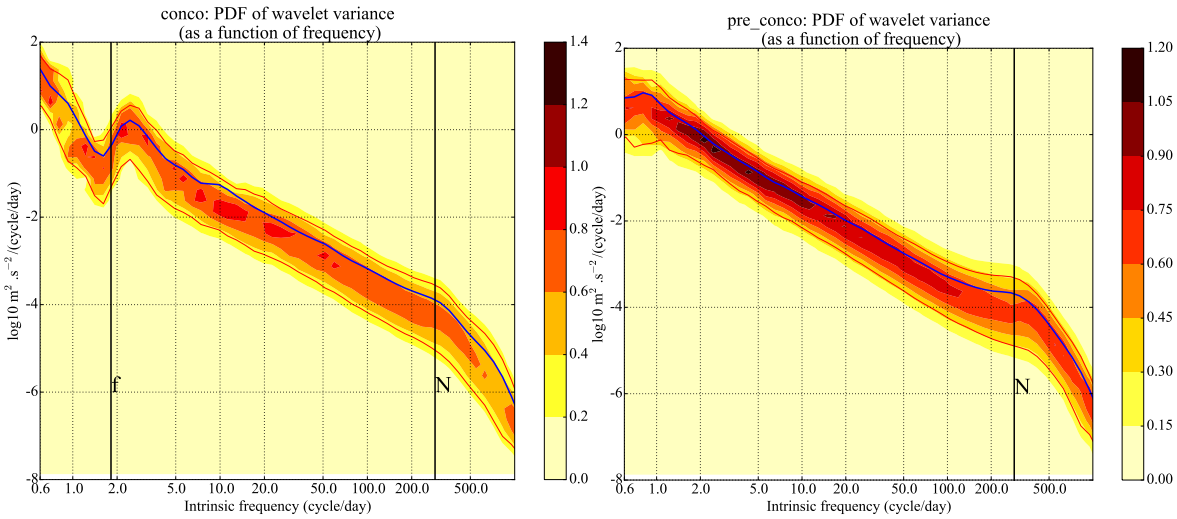

Figure 2.8 – Mean wavelet power spectrum (blue line) and distributions of wavelet coefficients (color scale) for horizontal kinetic energy E_{k_h} at different frequencies, for the balloon observations during the (left) polar and (right) equatorial campaigns.

Intermittency in the Lagrangian fluctuation spectrum Figure 2.8 shows the average wavelet kinetic energy spectrum E_{k_h} (power spectral density) for both campaigns, and the distribution of all wavelet power coefficients $(E_{k_h})_m$ (color scale). The average spectrum is the mean of variable wavelet coefficients, since the distribution is wide around the mode value. This behavior is expected both for a stationary background "noise"and for intermittent time series. However, there is a big difference between balloon observations and a stationary noise, which can be appreciated by comparing the distributions in figure 2.8 to the synthetic Gaussian background red noise distribution shown in Figure 2.9. In the background noise case (Figure 2.9), the mode of the distribution corresponds to the mean value at each frequency. On the contrary, for the observations (Figure 2.8) the mode of the distribution appears below the average spectrum. In other words, the most likely value of $(E_{k_h})_m(\hat{\omega}_j)$ is smaller than the mean value $E_{k_h}(\hat{\omega}_j)$. Thus, rare occurrences of large $(E_{k_h})_m$ above the mode dominate the mean spectrum: this is a signature of intermittency.

On Figure 2.8, it also appears that the mean and the mode of the spectrum get more separated from one another as frequency increases. To quantify this more precisely, we use one metric that quantifies inhomogeneity in a positive field, the Gini coefficient (*Gini*, 1921). Designed to diagnose inequalities of income, it has been previously used to study atmospheric gravity waves, in order to quantify variability the momentum flux carried by gravity waves

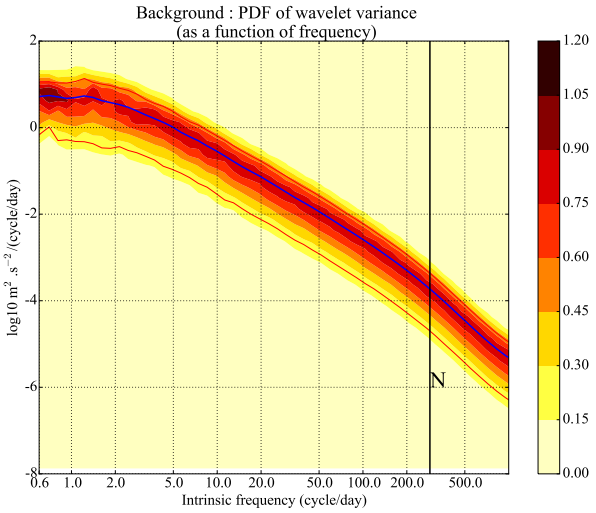

Figure 2.9 – Mean wavelet power spectrum (blue line) and distributions of wavelet coefficients (colorscale) for a synthetic Gaussian red noise time series.

to the stratosphere (*Plougonven et al.*, 2013). For, e.g. E_{k_h}, it is expressed as:

$$G_{E_{k_h}}(\hat{\omega}) = \frac{\sum_{n=1}^{M} \left(nE_{k_h}(\hat{\omega}) - \sum_{i=1}^{n} (E_{k_h})_n(\hat{\omega}) \right)}{\sum_{n=1}^{M} nE_{k_h}(\hat{\omega})} \tag{2.33}$$

where $(E_{k_h})_n(\hat{\omega})$ is the n sample from the wavelet series of squared wavelet coefficients $(E_{k_h})_m(\hat{\omega})$ measurements sorted in increasing order, and M is the total number of samples. $G_{E_{k_h}}(\hat{\omega})$ quantifies statistical dispersion in the kinetic energy at a given frequency, i.e. the relative importance of the tail of the Probability Density Function (PDF) of E_{k_h} relative to its average value. $G_{E_{k_h}} = 0$ corresponds to a constant $(E_{k_h})_m$ for which all measurements equally contribute to the sum, i.e. there is a constant amplitude wave of frequency $\hat{\omega}$. $G_{E_{k_h}} \to 1$ corresponds to a highly inhomogeneous wave field: a single measurement accounts for the total sum (all $(E_{k_h})_n(\hat{\omega}) = 0$, except $E_{k_h})_M(\hat{\omega}) > 0$). The Gini coefficient thus provides a quantitative measure of the relative contribution of the upper part of the $(E_{k_h})_m$ tail (the "extreme"values) to the average value.

The Gini coefficient as a function of frequency for the balloon data is shown in Figure 2.10 for the polar and equatorial flights, for different variables: potential energy E_p[16] and meridional wind V. The figures suggest that intermittency increases with frequency in the gravity wave frequency range, with more intermittent motions near N than near f. Although potential energy and meridional wind show comparable increase of the Gini coefficient with frequency, the values are not strictly the same for the two fields. This is surprising, from the polarization relations one would expect $G_{E_p}(\hat{\omega}) = G_{E_{k_h}}(\hat{\omega})$. This might be due to some artifact in the measurements although we have no clear explanation. Due to this uncertainty, we restrict ourselves to the interpretation of the robust features shared by the two variables.

One of those robust features over the Southern polar regions is the increased intermittency in the region of the Antarctic peninsula (Figure 2.10, upper panel). This can be seen as a peak in the potential energy and meridional wind Gini coefficients at frequencies between 10 and 40 cycles per day (periods of 30 minutes to 3 hours). This peak corresponds to mountain waves

[16] uncorrected

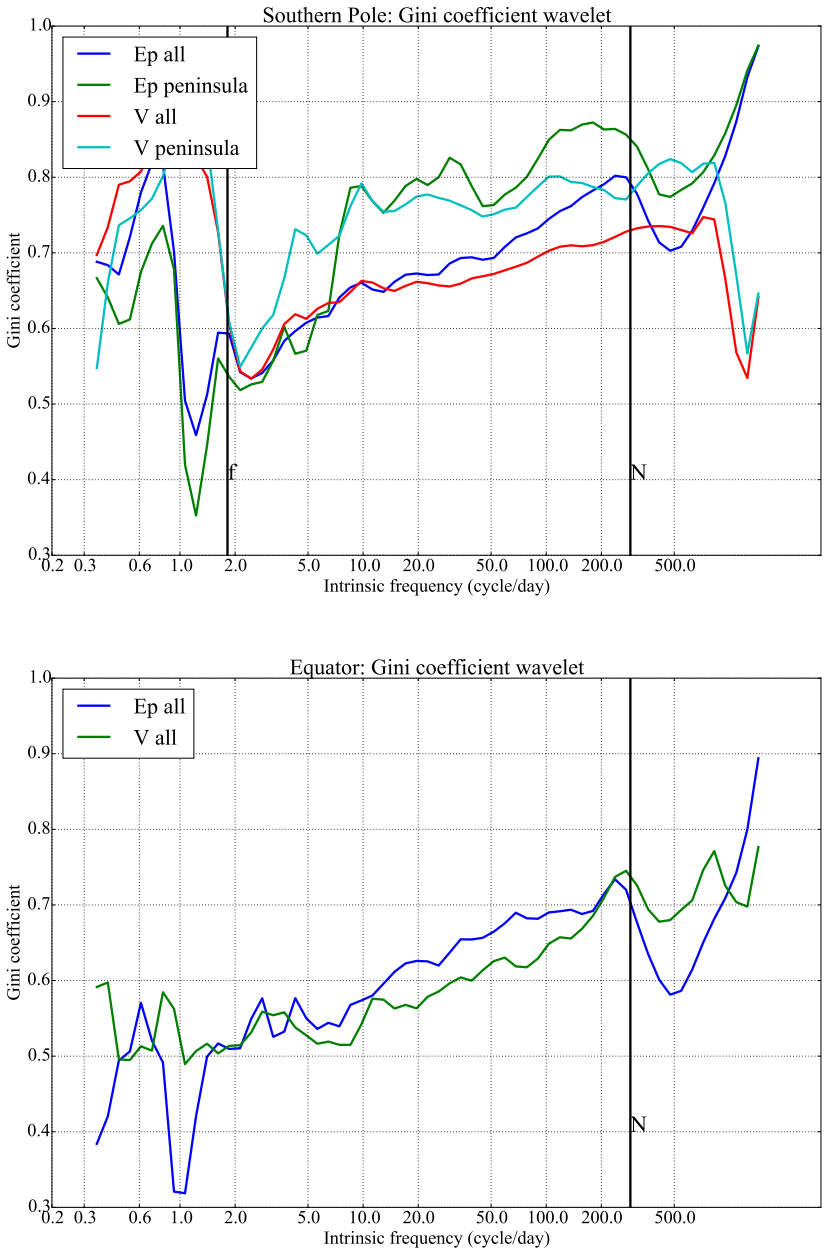

Figure 2.10 – Gini coefficient of the wavelet power time series as a function of frequency, for the (top) polar Concordiasi and (bottom) equatorial PreConcordiasi.

above the peninsula. Increased intermittency can also be noticed for high frequency waves near the Brunt-Väisälä frequency. This is probably associated with small-scale mountain waves.

Another robust feature in Figure 2.10 is the increase of the Gini coefficient with frequency in both the tropical and the polar regions. This increase of intermittency with frequency can probably be related to the propagation of gravity wave packets. As emphasized in the introductory chapter, the vertical group velocity and the angle of propagation with the horizontal both increase with frequency. As a consequence, high frequency wave packets tend to propagate smaller horizontal distances than low frequency ones. They tend to be more localized, tied to the sources, and more intermittent. On the contrary, low frequency waves

are more ubiquitous. We examine the relation between gravity wave activity at different frequencies and the environment in the following section.

2.5.2 Variability in fluctuations and environmental conditions in the tropics

Relationship with mean wind For conservative vertical propagation of stationary gravity waves, the vertical velocity variance is supposed to scale with the wind speed (see appendix A). Furthermore, horizontal refraction of wave packets can focus them in strong wind regions. This sort of relationship has been observed in extra tropical regions. Aircraft observations by *Bacmeister et al.* (1996) show enhanced vertical winds w'^2 in high wind regions ($|U| >$ 30 m/s). *Plougonven et al.* (2017) have reported a correspondence between large gravity wave momentum fluxes and high mean winds in the Concordiasi dataset. In the PreConcordiasi dataset, the range of mean wind is smaller since the campaign occurred during a transition phase of the QBO with prevailing weak winds ($|U| <$ 30 m/s). As a result, the dataset does not show any systematic relationship between vertical wind or high frequency potential energy activity and mean wind. If anything there would rather be an increase of energy at very high frequency near N for *low* winds, perhaps indicating less reflection.

Relationship with convection As emphasized in the introductory chapter, the main gravity wave source in the tropics is thought to be deep convection. We use the NOAA Climate Data Record (CDR) of Gridded Satellite Data from ISCCP B1 (GridSat-B1) Infrared Channel Brightness Temperature in the window channel (10.8 μm) to investigate the relationship with deep convection. GridSat-B1 provides 3-hourly global coverage of brightness temperature from geostationary satellites, at a pixel resolution of about 4 km. 3-hourly time resolution is rather limited given the quick development of deep convection, but this data nevertheless provides qualitative information on the position of the measurements relative to deep convection. Following *Liu and Zipser* (2005), we define deep convection using a 235 K brightness temperature threshold.

Figure 2.11 shows the average ratio of wavelet variance to the mean variance in various frequency bands as a function of distance to convection. Consistent with expectations, the variance is larger near deep convection and smaller away from it. This is also consistent with the study of *Alexander et al.* (2000), who found higher gravity wave momentum flux above cold convective clouds in aircraft measurements. Moreover, and interestingly, the contrast between convective and non convective environments becomes more and more abrupt with increasing intrinsic frequency. This is consistent with the wave propagation explanation mentioned earlier. The group velocity of gravity waves are:

$$(c_{g_x}, c_{g_y}, c_{g_z}) = \left(\frac{\partial\Omega}{\partial k}, \frac{\partial\Omega}{\partial l}, \frac{\partial\Omega}{\partial m}\right) = \bar{\mathbf{u}} + \frac{(k(N^2-\hat{\omega}^2), l(N^2-\hat{\omega}^2), -m(\hat{\omega}^2-f^2))}{\left(k^2+l^2+m^2+\frac{1}{4H^2}\right)\hat{\omega}} \tag{2.34}$$

so that low frequency waves $\hat{\omega} \ll N$ have slower vertical group velocity relative to horizontal group velocity (see also Chapter 1, Equation (1.24)). They travel larger horizontal distances than the high frequency waves and can disturb the atmosphere away from their source.

In agreement with that interpretation, Figure 2.12 shows that the increase in wavelet power near convection depends on the considered frequency. In particular, we note an increase

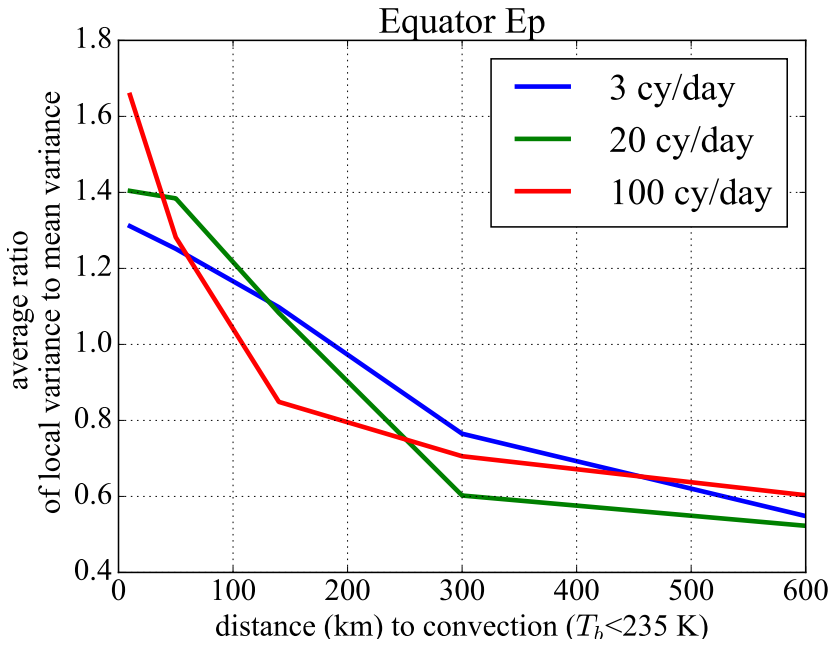

Figure 2.11 – Ratio of squared wavelet coefficient magnitude versus distance to convection (defined as pixel with $T_b < 235$ K), for 3 different frequencies.

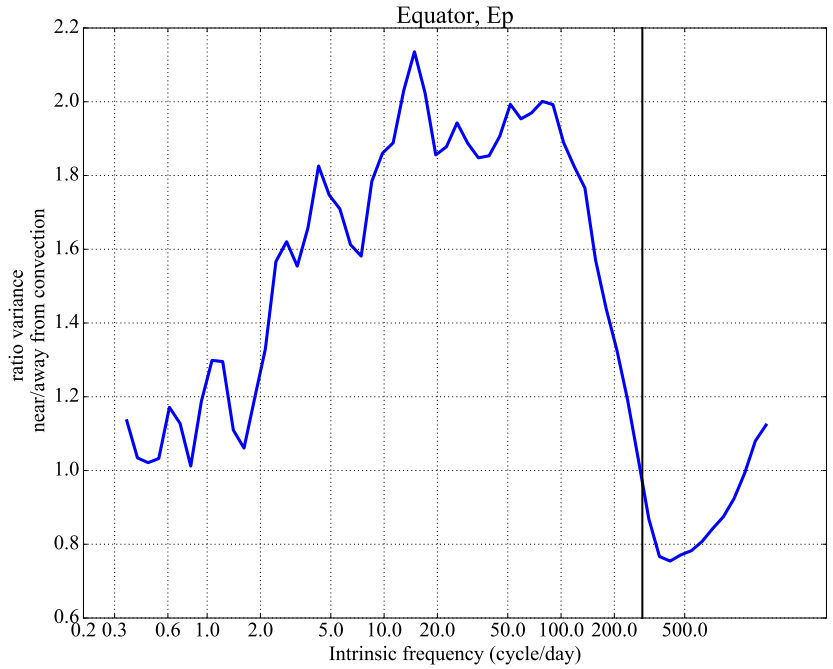

Figure 2.12 – Ratio of wavelet power between areas near (<100 km) and away (>100 km) from convection ($T_b < 235$ K).

with frequency of the contrast between convective and non convective environments. However, this difference starts to drop at higher frequencies near about $\frac{N}{2}$. At those frequencies, the balloon response might come at play and caution should be taken interpreting the results, especially since near N Gini coefficients were found higher for potential energy than for meridional wind. Furthermore, the 3-hourly Gridsat-B1 product is probably poorly suited for such high frequencies. Nevertheless, we note that the reduced influence of convection at

high frequencies might be related to the reduced vertical group velocity at high frequency. Indeed, for sufficiently small scale waves, c_{gz} is given by

$$c_{g_z}(\hat{\omega}, k_h) = \text{sign}(\hat{\omega}m)\frac{(\hat{\omega}^2 - f^2)^{\frac{3}{2}}(N^2 - \hat{\omega}^2)^{\frac{1}{2}}}{|\hat{\omega}||k_h|(N^2 - f^2)} \tag{2.35}$$

which tends towards 0 when $\hat{\omega} \to N$ (this is the turning point). Another possibility is that convectively gravity waves generated in the troposphere will mainly be limited to frequencies below $N_{\text{tropo}} = \frac{N_{\text{strato}}}{2}$. Hence, internal gravity waves populating the very high intrinsic frequency range of the stratospheric gravity wave spectrum are associated with Doppler shifting due to shear, which might distort the direct impact of deep convection.

Finally, although the observations show a correlation between high Gravity wave energy and convection for frequencies around 20 cycles/day, we emphasize that the associated variability in wave energy between different locations relative to convection remains somehow marginal compared to the variability in wave energy between different frequencies. Hence, deviations of instantaneous wavelet spectra from the statistical -2 slope are limited, with the slope generally in the -2.5 to -1.5 range. For the 1 cycle/day-5 minutes range examined here, convective regions show at most twice the variance shown in non convective areas (figures 2.11 and 2.12), which means a 50% difference in wave amplitude.

In a nutshell, this suggests that **the high-frequency waves are more tied to convection than low-frequency ones**. This is consistent with the previous section that showed higher intermittency at higher frequency, and with the different propagation properties of gravity wave packets.

2.5.3 Theories for the shape of the intrinsic frequency energy spectra

The energy spectra $E_{k_h}(\hat{\omega})$ and $E_p(\hat{\omega})$ are shown once again in figure 2.13, for the polar campaign[17]. They have the following main characteristics:

1. peak (of E_{k_h}) at the Coriolis frequency f
2. power law scaling with a -2 slope in the midfrequency range ($f \ll \hat{\omega} \ll N$). This is steeper than the $-\frac{5}{3}$ slope observed as a function of horizontal wavenumber at the mesoscale in the horizontal but shallower than the -3 spectral slope seen in the vertical
3. enhancement (mainly of E_{k_v}) when approaching N

To my knowledge, there is no consensual theory for the intrinsic frequency spectrum of Lagrangian wind and temperature fluctuations. Given the considered frequency range (f to N), it is highly plausible that the observed fluctuations are gravity waves, which is also consistent with the near equipartition between potential and kinetic energy and the spectral gap observed below f. A few approaches can be imagined to explain the intrinsic frequency spectrum: one relying on diffusion and wave damping (*Gardner*, 1994), one relying on wave-wave interaction, the cascade hypothesis (*Dewan*, 1997), and one relying on the propagation of the waves. The first idea, by *Gardner* (1994), does not seem to agree with our observations since the spectral magnitude is then expected to be somehow constant in space and time.

[17] To avoid $f \to 0$

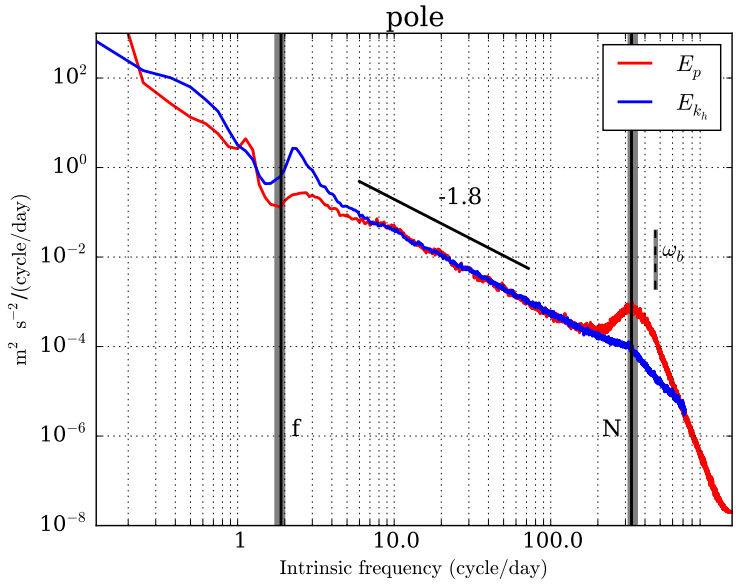

Figure 2.13 – $E_p(\hat{\omega})$ and $E_{k_h}(\hat{\omega})$ spectra from Concordiasi measurements.

In the following I explain the last two ideas and briefly discuss how they could relate to the observations.

Saturated cascade theory The saturated cascade theory has been mainly developed by *Dewan* (1997) and is partly inspired by theoretical considerations on the internal gravity wave spectra in the ocean. In that context, the spectra are supposed to depend only on $\hat{\omega}$, the intrinsic frequency, and the eddy dissipation rate ϵ_k. Then, the different terms have dimensions:

$$[\epsilon_k] = \frac{[L^2]}{[T^3]} \text{ and } [\hat{\omega}] = [T^{-1}] \text{ and } [E_{tot}(\hat{\omega})] = \frac{[L^2]}{[T]} \tag{2.36}$$

so that dimensional analysis gives

$$E_{tot}(\hat{\omega}) = C\epsilon_k \hat{\omega}^{-2} \tag{2.37}$$

with C a dimensionless constant that should be of order 1.

In the saturated cascade theory, I would expect the spectral slope to be maintained by low frequency waves cascading to larger frequencies. Statistically the variance should have the same relation with the sources at each frequencies. This seems to contradict Figure 2.10 and 2.12 which show that high frequencies are more tied to convection than lower frequencies. The cascade furthermore implies some downscaling flux of gravity wave action to feed the highest frequencies from lower ones. An alternative theory based on gravity wave propagation characteristics may explain the observed intrinsic frequency spectrum. It is described in the following.

Wave propagation theory Another approach is to examine the impact of wave propagation on the spectrum; it follows ideas developed by *Alexander et al.* (2002) and *Alexander and Barnet* (2007). The shape of the energy spectra can be tentatively examined using the

balance of wave action A under WKB assumption:

$$\frac{\partial A}{\partial t} + \nabla \cdot \mathbf{c_g} A = D \tag{2.38}$$

where $\mathbf{c_g}A$ is the wave action flux vector ($\mathbf{c_g}$ is the wave group velocity) and D represents dissipation terms (radiative damping, friction). For linear waves, one has $A = \frac{E_p + E_k}{\hat{\omega}}$ (the wave action).

Neglecting dissipation and wave breaking, this implies:

$$\frac{\mathrm{d}_g A}{\mathrm{d}t} + A \nabla \cdot \mathbf{c_g} = 0 \tag{2.39}$$

with $\frac{\mathrm{d}_g A}{\mathrm{d}t} = \frac{\partial_A}{\partial t} + \mathbf{c_g}\nabla$. To guide the intuition, we assume that the background flow and stability (N^2) are stationary and do not depend on x, y. Under those assumptions, horizontal wavenumber (k, l) and (ground relative) frequency ω are conserved during the propagation of the wave packet. With the hypothesis that gravity waves have their sources primarily at lower altitudes and propagate to the UTLS, Equation (2.39) can be solved along a ray, yielding:

$$A(\omega, k, l, Z, t) = A\left(\omega, k, l, z_0, t - \int_{z_0}^{Z} \frac{1}{c_{g_z}} \mathrm{d}z\right) \frac{c_{g_z 0}}{c_{g_z}} = A_0\left(\omega, k, l, t - \int_{z_0}^{Z} \frac{1}{c_{g_z}} \mathrm{d}z\right) \frac{c_{g_z 0}}{c_{g_z}} \tag{2.40}$$

where A_0 is the wave action at the source and z_0 some launching altitude for the waves. Equation (2.40) already suggests a dependence on c_{g_z}, but as it appears in a ratio of the group velocity at altitude z to the group velocity at the launching altitude $c_{g_z 0}$, the intrinsic frequency dependence is not obvious. Averaging (2.40) over time to obtain the mean action spectrum leads to:

$$\overline{A(\omega, k, l, Z)} = \overline{A(\omega, k, l, z_0) \frac{c_{g_z 0}}{c_{g_z}}} = \overline{A_0(\omega, k, l) \frac{c_{g_z 0}}{c_{g_z}}} \tag{2.41}$$

with $c_{g_z} = c_{g_z}(\omega, k, l, Z)$ and $c_{g_z 0} = c_{g_z}(\omega, k, l, z_0)$. Now, one property that has been emphasized regarding gravity waves is the intermittency of their emissions, which has consequences on the mean gravity wave field (*Alexander et al.*, 2002; *Bühler*, 2003). Sources do not continuously emit waves, there are rather pulse of wave packets emission. The mean spectrum is an average over those wave packets. This can be formally expressed as:

$$\overline{A_0(\omega, k, l) \frac{c_{g_z 0}}{c_{g_z}}} = \frac{1}{\Delta T} \sum_i \Delta t_i A_0^i(\omega, k, l) \frac{c_{g_z 0}}{c_{g_z}} \tag{2.42}$$

where ΔT is the duration of the time window, and the subscript i refers to wave packet i. *Bühler* (2003) implicitly preaches for some distribution of the pulse duration Δt_i that does not depend on $c_{g_z 0}$. On the contrary, *Alexander et al.* (2002) implicitly assume that regardless of their frequency and wavenumber the emitted wave packets will still have a comparable vertical extent of the envelope L_z (as imposed by the source). A wave packet instantly appears with vertical extent L_z^i. Then, the time Δt_i during which the wave packet is emitted will depend on $c_{g_z 0}$ the group velocity in the emission zone as $\Delta t_i = \frac{L_z^i}{c_{g_z 0}}$. It is arguably more realistic for atmospheric waves from orography, convection or fronts to assume

vertically constant "emission depth" rather than a pulse of definite duration (like a laser). That idea of a constant duration pulse may appear realistic on the horizontal but probably less on the vertical.

$$\overline{A\left(\omega,k,l,Z\right)}=\frac{1}{\Delta T}\sum_i\frac{L_z^i}{c_{g_z0}}A_0^i\left(\omega,k,l\right)\frac{c_{g_z0}}{c_{g_z}}=\frac{1}{c_{g_z}}\left(\frac{1}{\Delta T}\sum_i L_z^iA_0^i\left(\omega,k,l\right)\right) \tag{2.43}$$

Replacing the mean action by the energy, one obtains:

$$\overline{E_{tot}\left(\omega,k,l,Z\right)}=\frac{1}{c_{g_z}}\left(\frac{1}{\Delta T}\sum_i L_z^i\frac{\hat{\omega}}{\hat{\omega}_0^i}(E_{tot})_0^i\left(\omega,k,l\right)\right) \tag{2.44}$$

The sum is over all the rays of ω,k,l which have been able to propagate from z_0 to Z. Statistically, the variations of $\frac{\hat{\omega}}{\hat{\omega}_0^i}$ will cancel one another and one may hope little dependency of the term $\frac{1}{\Delta T}\sum_i L_z^i\frac{\hat{\omega}}{\hat{\omega}_0^i}(E_{tot})_0^i\left(\omega,k,l\right)$ on $\hat{\omega}$ [18]. In that case, the main dependence on $\hat{\omega}$ would be in the term c_{g_z}:

$$\overline{E_{tot}\left(\omega,k,l,Z\right)}\propto\frac{1}{c_{g_z}} \tag{2.45}$$

with:

$$c_{g_z}(\hat{\omega},k_h=\sqrt{k^2+l^2})=\mathrm{sign}(\hat{\omega}m)\frac{1}{k_h^2(N^2-f^2)}\frac{(\hat{\omega}^2-f^2)^2}{|\hat{\omega}|}\sqrt{\left(\frac{N^2-\hat{\omega}^2}{\hat{\omega}^2-f^2}k_h^2-\frac{1}{4H^2}\right)} \tag{2.46}$$

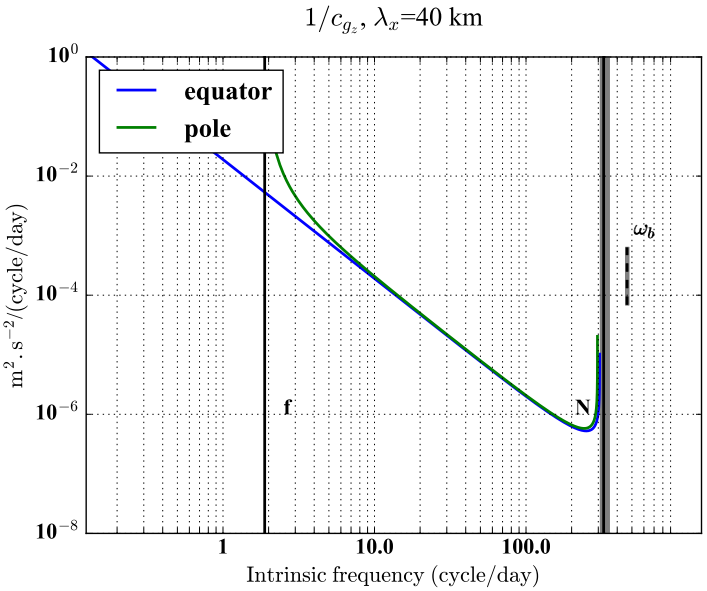

Figure 2.14 – Inverse vertical group velocity (probability of observation) for a wave of a given intrinsic frequency.

The dependence of $\frac{1}{c_{g_z}}$ on $\hat{\omega}$ is schematically depicted on Figure 2.14 for a given k_h. It exhibits the 3 main characteristics of the observed spectrum (enhancements at f and N, and power law slope close to -2).

In this framework, the shape of the intrinsic frequency spectrum is mainly controlled by

[18] Except if present in the sources amplitude $L_z^i(E_{tot})_0^i$.

the propagation characteristics of the waves (the residence time of a wave packet), and the imposed spectrum at the source and its intermittency. To reproduce the observed spectrum, the "source energy spectrum"would be rather flat. The spectrum has a $\hat{\omega}^{-2}$ shape because low frequency wave packets have a longer residence time than high frequency ones. This is very different from the cascade, in which low frequencies are generating high frequencies.

Note on cascades, propagation and the mesoscale energy spectrum The question of what is causing the shape of the intrinsic frequency energy spectrum is somehow similar and related to the question of the $k^{-5/3}$ mesoscale energy spectrum first reported by *Nastrom and Gage* (1985). As for the intrinsic frequency spectrum, a (burning) question on this subject is whether the mesoscale energy spectrum results from non linear interaction between modes at a given altitude or from perturbations vertically propagating. Different models provide different answers to that question (*Augier and Lindborg*, 2013) and this seems to depend on the parameterizations used (*Malardel and Wedi*, 2016).

2.6 Representation of the fluctuations of vertical wind and temperature in large-scale models

2.6.1 Resolved vertical velocity fluctuations in (re)analyses

As stated in the introductory chapter, the role of vertical wind and temperature fluctuations on microphysics has been reckoned for a long time, and different parameterizations for Lagrangian models have been developed. It is obvious that the resolution of current global models is not sufficient to fully resolve the vertical velocity variability. However, it is still interesting to investigate the resolved variability, in order to better quantify what is resolved and what should be parameterized. In the following, we present the variability in vertical velocity in the tropical UTLS as represented in three modern reanalyses systems (ERA interim, MERRA2 and JRA55) and in the ECMWF operational analysis during the time period of the PreConcordiasi balloon campaign. The resolution and model version for the (re)analyses used are summarized in Table 2.2.

Table 2.2 – Description of the resolution of the models presented in this section. For the spectral models, N corresponds to the reduced Gaussian grid, F to the full Gaussian grid, and an approximate resolution is given. For the horizontal grid, cs: cubed sphere; sp: spectral model. Further information on the reanalyses systems can be found in *Fujiwara et al.* (2017).

(Re)analysis	operational model version (if applicable)	horizontal grid type	Horizontal grid spacing	retrieved horizontal resolution
MERRA-2	GEOS 5.12.4 (2015)	CS	1/2° lat× 1/3° lon ∼ 60 km	native
JRA-55	JMA GSM (2009)	sp	N160(T319)∼ 55 km	F160
ERA interim	IFS Cy31r2 (2007)	sp	N128(T255)∼ 79 km	1°× 1°
op ECMWF	IFS Cy36r1 (2010)	sp	N640(T1279)∼ 16 km	1/8° ×1/8°

Some background *Jewtoukoff et al.* (2015) have shown that, if recent operational analyses represent part of the gravity wave spectrum observed by Concordiasi balloons, they still underestimate gravity wave momentum fluxes $\rho|\overline{\mathbf{u}'w'}|$ with respect to SPB observations. In particular, *Jewtoukoff et al.* (2015) showed that the ECMWF operational analysis underestimated the magnitude of $|\overline{\mathbf{u}'w'}|$ by a factor of 3-5. Since the horizontal power spectrum of u'^2 has a $k^{-5/3}$ shape whereas the power spectrum of w'^2 is flatter ($k^{\sim 0}$ up to wavelength around 10 km according to *Bacmeister et al.*, 1996), one would expect the discrepancy to be larger for w'^2 than for $|\overline{\mathbf{u}'w'}|$.

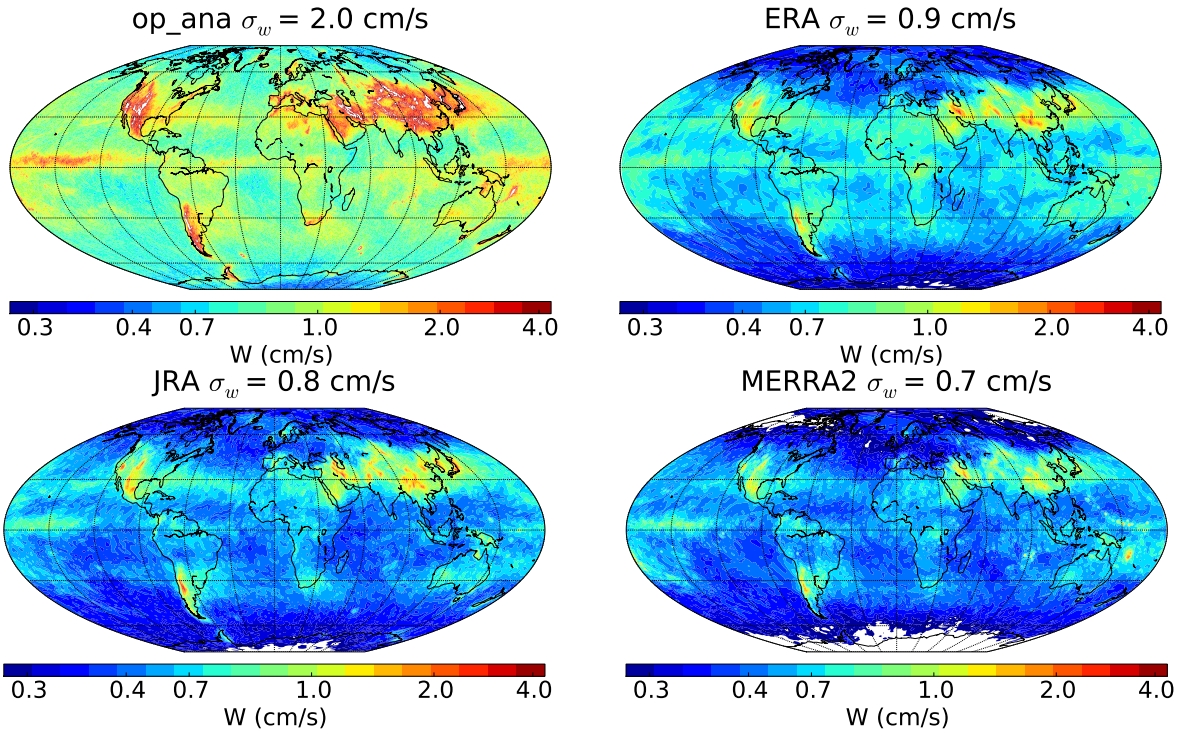

Figure 2.15 – Global maps of vertical velocity variance at 100 hPa in different reanalyses systems during the period of PreConcordiasi balloon flights (February-May 2010)

Comparison of different (re)analyses Figure 2.15 represents the geographic distribution of vertical velocity standard deviation σ_W at 100 hPa in a number of current reanalyses and one operational analysis system, during the period of the PreConcordiasi balloon campaign. Hot spots of high σ_W appear tied to orography and to a smaller extent convection near the Intertropical Convergence Zone (ITCZ). Much seasonal variability is actually present, e.g. an austral winter map would emphasize the southern hemisphere storm track. There is a good qualitative agreement between the different reanalyses regarding the geographic variability and the location of the hot spots.

However, there are quantitative differences between the (re)analyses. As expected, the magnitude of σ_W^2 is the largest in the ECMWF operational analysis, which has the highest resolution among all the systems presented. Then the second largest is ERA interim, which is somehow surprising given that it has the lowest nominal horizontal resolution. Furthermore, there are more contrasts between "active" and "inactive" areas in MERRA 2 and JRA 55 compared to ERA interim. Over the mountains or convective regions the amplitudes are

generally somehow similar, whereas oceanic and quiet regions have almost zero activity in JRA 55 and MERRA2 but show some activity in ERA interim. The Antarctic plateau in the polar southern hemisphere is the most striking example. This difference might be attributed to model physics, or to spurious waves generated in ERA interim during the course of a data assimilation cycle.

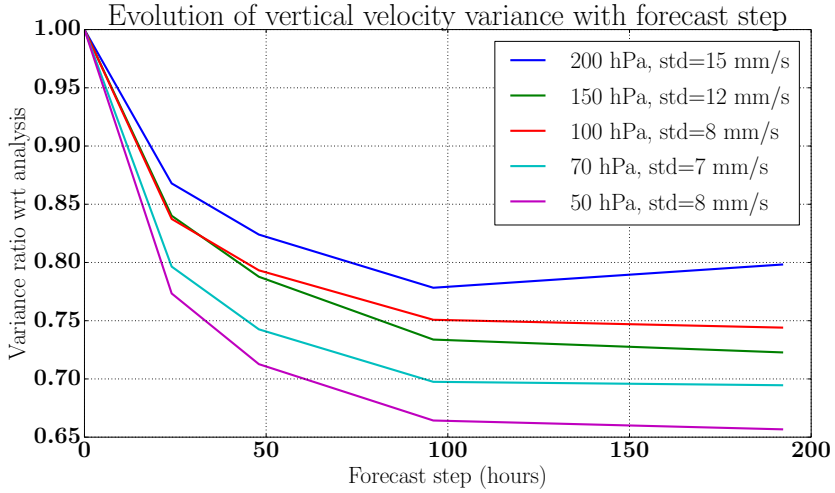

Figure 2.16 – Vertical velocity variance in ERA interim at different forecast steps, normalized by the analysis variance.

Figure 2.16 investigates the impact of the assimilation procedure in ERA interim by showing the vertical velocity variance as a function of forecast step at different model levels, the reference time corresponding to the analysis time[19]. A significant portion of the variance present in the analysis is absent from the forecast, and this fraction increases with decreasing pressure. Overall, this suggests that gravity waves are generated in the model at the analysis stage, which might be spurious or not. The fact that this fraction changes with altitude suggests that this process does not have the same magnitude at different altitudes. A possible reason is that more data is assimilated at lower altitude.

Further indication that different processes are taking place at different altitudes is provided in Figure 2.17, left panel, which shows the profile of zonal mean tropical mean σ_W during February-March 2010 in the reanalyses. According to Figure 2.17, all the analyses indicate a decrease of σ_W by a factor of 2 across the TTL, from 150 hPa to 80 hPa. As shown in appendix A to this chapter, this disagrees with conservative vertical propagation of hydrostatic waves, which would suggest an approximately constant σ_W. Wave saturation and breaking happen in the TTL and might cause this decrease and indeed the limited sampling achieved with ATTREX observations over the tropical Pacific (right panel) also shows a slight decrease of σ_W with altitude in the (convective) Western Pacific (Figure 2.17, right panel). However, in ATTREX observations, the decrease is limited to about 25% of the value at the bottom of the profiles (150 hPa), whereas it is 50% in the analyses. The reanalyses all show too strong a decrease of σ_W with altitude[20]. This decrease with altitude of the ratio of

[19] A similar figure could not be drawn for MERRA 2 and JRA, for lack of the long range forecast.

[20] Another possibility would be that the ATTREX dataset is biased towards lower σ_W at low altitudes because the aircraft was avoiding deep convection. However, the average in a non convective region for the operational analysis shows that the decrease, although smaller, is also larger that what is seen in ATTREX,

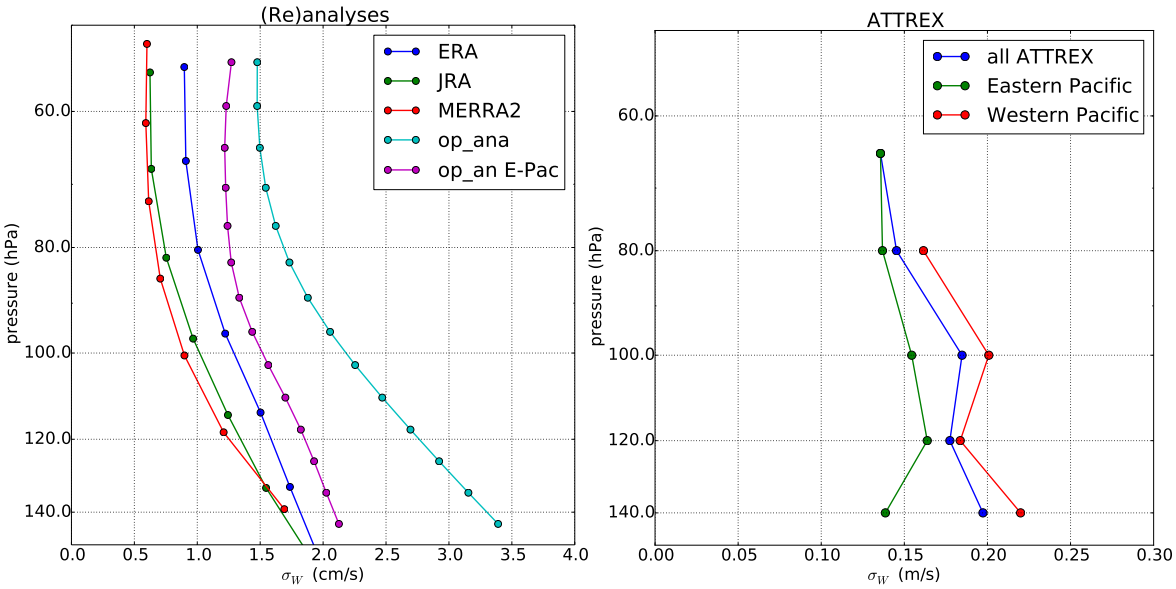

Figure 2.17 – (Left) Vertical profiles of vertical velocity standard deviation in a number of analyses systems in the whole tropics (30°S-30°N), and in the Eastern Pacific only (purple curve) and (right) vertical profiles of vertical velocity standard deviation in ATTREX aircraft observations in boreal winter 2013 and 2014.

analyzed to observed variance may also be seen in the temperature field, as shown in Figure 1 a of *Kim and Alexander* (2013)).

To try to better understand the reason for the difference between the reanalyses in the tropics, Figure 2.18 shows the zonal wavenumber spectra of vertical wind in those different analysis systems at 70 hPa. One limiting factor for the representation of w appears to be the resolution; since the vertical velocity spectrum is flat, its variance is contained in higher wavenumbers than for the horizontal wind, so that analyses with better resolution resolve a larger portion of the spectrum. However, this does not seem to be the only factor at play, since there are differences at small wavenumbers. The non systematic relation with resolution is also illustrated by the PDF of the vertical wind shown in the right panel of Figure 2.18. Although the extreme values in the tails appear to scale with the resolution, fluctuations of intermediate are more frequent in ERA interim. Accordingly, the kurtosis of the fluctuations increase with increased resolution (not shown).

Summary Even with the ∼10 km resolution now achieved, *modern reanalyses systems are far from resolving the vertical wind fluctuations present in the tropics*. They underestimate the variance of vertical wind observed by the balloons or the Global Hawk by a factor of 100 or so. This is due to resolution, but our analysis suggests that other factors are at play. For instance, for the highest frequencies, which have the strongest signature in vertical velocity, the hydrostatic approximation made in all the reanalyses is questionable. Furthermore, the structure of vertical velocity variability seen in the observations is different from that produced in the reanalyses, in particular the evolution with altitude. Hence, for processes sensitive to cooling rates $\frac{DT}{Dt} = -\frac{g}{C_P}w$, vertical velocity fluctuations and hence high fre-

especially over non convective regions.

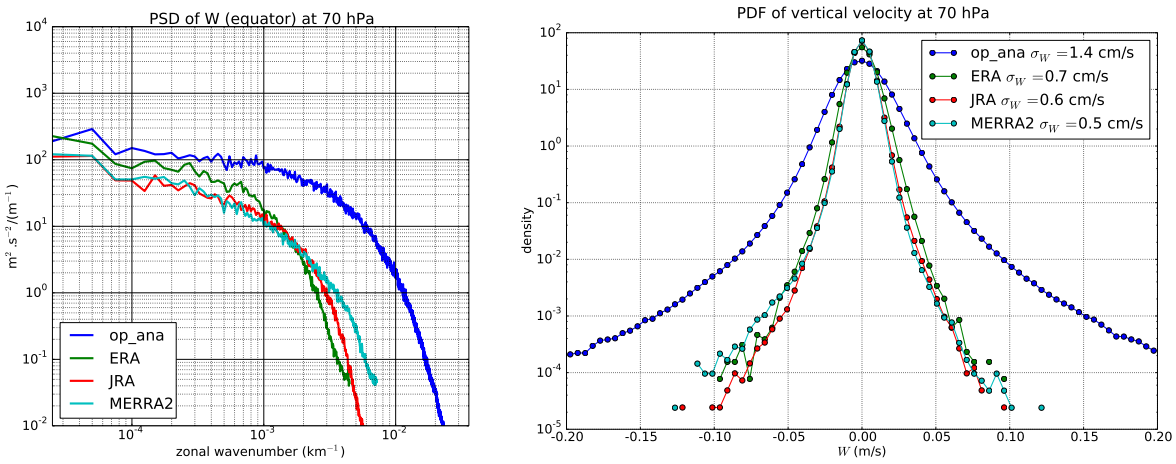

Figure 2.18 – (Left) Zonal wavenumber power spectrum of vertical velocity at the equator, during the period of the balloon flights (February-May 2010). (Right) PDF (Probability Density Function) of vertical wind at 70 hPa in different (re)analyses systems for one month starting February 15 2010 (ERA: ECMWF ERA interim and operational analysis, JRA: JRA 55, MERRA2 and the ECMWF operational analysis)

quency Lagrangian temperature fluctuations are absent from the reanalyses and need to be parameterized.

2.6.2 Parameterization

2.6.2.1 Proposed parameterization

For the sake of completeness, the parameterization proposed in the letter and its extension to other altitudes are described in the appendix to this chapter (appendix A). We just summarize here its main characteristics:

- the fluctuations are synthesized using a Markov process; they have the same slope as the observations (-2 for temperature, 0 for vertical wind).
- Their probability distributions is the same as in the observations, i.e. Laplace distribution in the tropics.

This parameterization is entirely stochastic and is not tied to convection or any wave source, although some influence is seen in the dataset, as described previously. For orographic waves, an additional dedicated treatment will be required. The most important space dependency that we suggest to include is on altitude, by imposing conservative wave propagation through the requirement:

$$\sigma_W(z)\sqrt{\rho(z)N(z)} \simeq \text{constant} \tag{2.47}$$

This relation, which neglects shear and assumes $\hat{\omega} \ll N$, is also derived in appendix A. Usually, in the literature of gravity wave drag parameterization, it is accompanied by a saturation constraint on the amplitude, e.g. keeping:

$$\sigma_W(\hat{\omega}, z)^2 \leq \frac{\hat{\omega}^4}{(N^2 - \hat{\omega}^2)(k^2 + l^2)} \tag{2.48}$$

Here the proposed parameterization does not allow to include those physical refinements. It is empirical, its strength is not in its accuracy in representing physical processes but in its simplicity and in the fact that it matches observations. A possible extension would be to take the needed σ_W from gravity wave drag parameterizations, but in that case that term needs to be carefully assessed. The reflected waves, which also induce significant vertical winds, are indeed not included in most parameterizations.

2.6.2.2 Discussion on other parameterizations and how to adapt them to match observations

Previous parameterizations in Lagrangian models Due to their impact on transport and microphysics, unresolved fluctuations have been parameterized in a number of Lagrangian models. Some are discussed in the letter, and we provide below a more extensive discussion to emphasize the uncertainties associated with the current procedures.

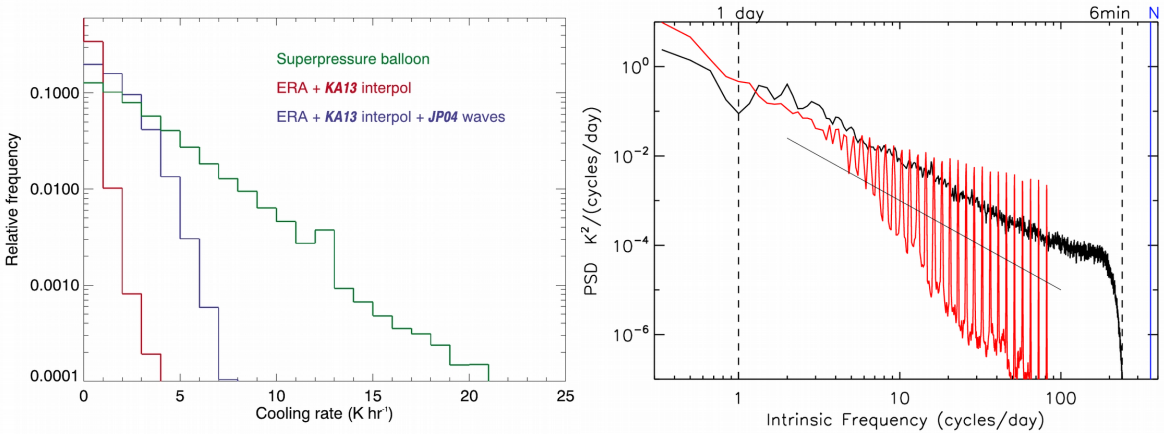

Figure 2.19 – (Left) PDF of cooling rates from Lagrangian trajectories in the TTL using only ERA interim resolved winds and temperature in red, with the parameterization of *Jensen and Pfister* (2004) (JP04) in blue, and with a version of the balloon time series low-pass filtered at $\frac{N}{2}$. (Right) Spectrum of Lagrangian temperature fluctuations in the TTL in the parameterization of *Jensen and Pfister* (2004) (red) and in balloon observations low-pass filtered at $\frac{N}{2}$ (black). Courtesy of E. Jensen and L. Pfister.

Inspired by the results of a previous balloon campaign (*Hertzog et al.*, 2002), *Jensen and Pfister* (2004) developed a wave parameterization consisting in a sum of harmonics at given frequencies whose amplitudes decrease following the observed $\hat{\omega}^{-2}$. For each trajectory, the temperature fluctuations T'_{JP04} are given by:

$$T'_{\mathrm{JP04}} = \sum_{j=1}^{n} A_j \cos\left(\hat{\omega}_j t + \Phi_j\right) \tag{2.49}$$

The right panel of Figure 2.19 shows the power spectral density of the parameterized temperature fluctuations from *Jensen and Pfister* (2004), and illustrates that the $\hat{\omega}_j$ are evenly space in $\ln\hat{\omega}$ and that the $A_j^2 \propto \hat{\omega}_j^{-1}$. This is consistent with the balloon observations who show that $A(\hat{\omega}) \propto \hat{\omega}^{-2}$ (but with $A(\hat{\omega})^2 = \frac{\mathrm{d}\sigma^2(\hat{\omega})}{\mathrm{d}\hat{\omega}}$, i.e. "evenly spaced in $\hat{\omega}$"). This parameterization is similar to the one proposed by *Bacmeister et al.* (1999).

Figure 2.19, left panel, shows the PDF of vertical wind fluctuations associated with the

parameterized temperature fluctuations of *Jensen and Pfister* (2004) compared with a version of the balloon observations filtered at $\frac{N}{2}$. Comparing the PDFs (left panel), it can be noticed that the cooling rates in the parameterization are normally distributed. This is a natural consequence of the random choice of the phase of the different harmonics [21], but disagrees with balloon observations which show larger tails. The figure also shows that the cooling rates are strongly underestimated compared to what observations suggest. The right panel of Figure 2.19 offers some explanations: the frequencies of the parameterized harmonics do not extend up to the tropospheric Brunt-Väisälä frequency at 144 cycles/day (10 minutes). Assuming a constant -2 spectral slope, the temperature perturbations associated with the fluctuations at the highest frequencies are small but they still dominate the cooling rates, and therefore need to be parameterized for processes sensitive to the cooling rates, such as ice nucleation.

Unresolved mesoscale wind fluctuations are also parameterized in Lagrangian trajectory models, since they introduce additional dispersion of the trajectories. In that case, the choice made in many models is to parameterize the additional fluctuations as a Markov process whose variance depends on the resolved wind variance. In FLEXPART (*Stohl et al.*, 2005), the unresolved vertical wind w' is taken to be:

$$w'(t+\delta t) = \alpha w'(t) + \sqrt{(1-\alpha)\sigma_W^2}W \tag{2.50}$$

where W is a Gaussian random white noise of variance 1, σ_W is the unresolved vertical wind variance and $\alpha = \exp(-\delta t/\tau)$ where τ is the Lagrangian autocorrelation time of the unresolved fluctuations which is generally taken to be half the time step at which the wind fields are available $\tau = \frac{\Delta_{t_m}}{2}$. σ_W^2 is proportional to the resolved variance from the closest available grid points and time points. The method is the same as the one used for the horizontal wind, and will leads to a $\hat{\omega}^{-2}$ spectrum which deviates from the observations. A better choice of τ for vertical wind would be $\tau = \frac{1}{N}$. Rather than a Markov process which imposes a -2 slope, *Bergman et al.* (2016) used the mid-point displacement method, which allows to reproduce any (constant) slope for the PSD of the fluctuations. In general, those studies did not recognized the special case of vertical wind compared to horizontal ones and assume an $\hat{\omega}^{-s}$ spectrum with $s \geq 1$. This might not matter for Lagrangian dispersion studies; however, for microphysics, it is key that appropriate spectra of vertical wind (flat, i.e. $s \simeq 0$ up to N) are included.

Parameterization in General circulation models Unresolved fluctuations need to be parameterized also in Eulerian General circulation models when their cirrus clouds parameterizations are aimed to resolve the nucleation process (as is the case for GEOS 5, WACCM, ECHAM, see for example *Barahona et al.*, 2014). In that context, the unresolved fluctuations variance σ_W^2 is decomposed between a turbulent and a gravity wave contribution:

$$\sigma_W^2 = (\sigma_W^2)_{\text{turb}} + (\sigma_W^2)_{\text{GW}} \tag{2.51}$$

where the turbulence contribution $(\sigma_W^2)_{\text{turb}}$ is estimated from the turbulent diffusivity in the mixing scheme (which is highly uncertain, see Chapter 5). In the absence of better alternative,

[21] This is a consequence of the central limit theorem.

the gravity wave contribution $(\sigma_W^2)_{\mathrm{GW}}$ amplitude is often related to that of the stationary mountain waves (This is the option used by *Joos et al.*, 2008). Applying Equation A.16 in appendix A assuming $\omega = 0$ ($\hat{\omega} = -kU$), one obtains:

$$(\sigma_W^2)_{\mathrm{GW}} = \frac{\rho_{\mathrm{surf}} N_{\mathrm{surf}} U}{\rho N U_{\mathrm{surf}}} (\sigma_W^2)_{\mathrm{surf}} \tag{2.52}$$

where $(\sigma_W^2)_{\mathrm{surf}}$ is the vertical velocity imposed near the surface imposed by the topography, U_{surf} the surface wind and ρ_{surf}. A saturation limit accounting for gravity wave breaking can be added (for instance following *Lindzen*, 1981). Although those considerations strictly apply only to stationary mountain waves, they have been applied in the tropics using the surface stress: $2k|\tau_s| = \frac{\rho_{\mathrm{surf}} N_{\mathrm{surf}}}{U_{\mathrm{surf}}} (\sigma_W^2)_{\mathrm{surf}}$ (*Barahona et al.*, 2014).

This discussion is just aimed to show the limits of current parameterizations when they are compared to observations. More realism in vertical velocity representation in TTL cirrus could be achieved by taking the parameterizations developed for Lagrangian models, such as the one presented in the letter.

2.7 Conclusion

Summary The main points of the chapter are summarized as follows:

- Superpressure balloons provide unprecedented information on Lagrangian temperature fluctuations at periods from 1 day to about 10 minutes. TTL temperature and vertical velocity fluctuations in that range have standard deviations of about 1 K and 0.2 m/s respectively. The vertical wind fluctuations have a white spectrum up to N whereas the temperature fluctuations follow a -2 spectrum. There seems to be some enhancement in buoyancy oscillations near the Brunt-Väisälä frequency, causing a local peak in vertical wind and cooling rate power.

- **Temperature fluctuations at low frequency (near 1 day) seem ubiquitous, whereas at higher frequencies they are more intermittent and tied to convection.** This could be due to the propagation properties of the gravity waves, with low frequency wave packets traveling larger horizontal distance and high frequencies being more tied to the convective sources. Overall, and keeping in mind the more limited balloon sampling, the tropical regions seem to show more ubiquitous variability than the polar ones.

- **As expected, current (re)analyses strongly underestimate the variability in vertical wind, especially at high altitude.** Although the limited resolution of the reanalyses is a key factor, others seem to be at play. Parameterizations are necessary even with the relatively high resolutions (13 km or less for current operational systems).

- Different parameterizations approaches are possible, but it appears that relying on the fields resolved by the reanalyses may overestimate the decrease of variability with altitude. A simple parameterization is proposed; it reproduces some the observed statistical and spectral properties and is a good first-order representation of Lagrangian temperature fluctuations in the upper TTL.

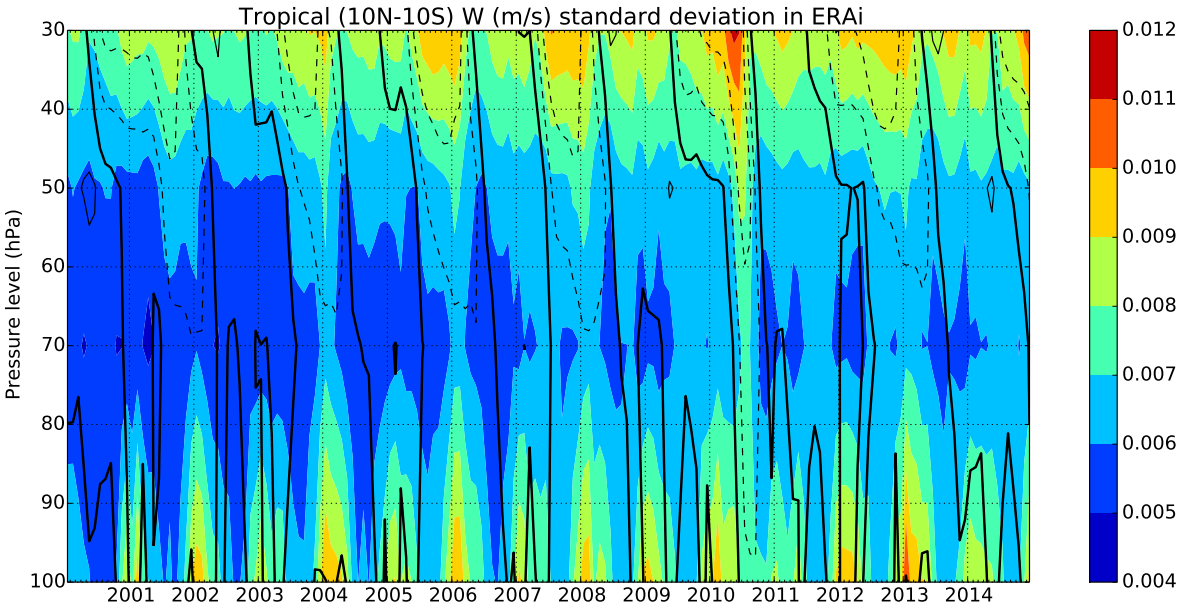

Figure 2.20 – Hoevmoller diagram of vertical wind standard deviation in the ERA interim reanalysis during the period 2000-2015 in the equatorial lower stratosphere. Seasonal cycle at 100 hPa and QBO cycle above are apparent.

Outlook In situ measurements during the PreConcordiasi and ATTREX campaigns have provided unprecedented constraints on vertical wind and temperature fluctuations, their characteristics and distributions. However, uncertainties remain, and the sampling was limited. In particular the datasets were limited to specific seasons and the interannual variability associated with ENSO or the QBO could not be studied. Variability in the convective sources or in the mean wind might cause important variability, and the analysis would go in that sense, as illustrated in Figure 2.20. In that respect, analysis of commercial datasets from the Google Loon project (*Schoeberl et al.*, 2017) and the future balloon campaign Stratéole 2 will help fill the gap. In particular, the Stratéole 2 payload will include several new instruments that will help constrain the analysis: in situ measurements will include the temperature lapse rate at the balloon level, which will allow to use the technique described in section 2.4. Given the uncertainty in the balloon response at high frequency, I have been preaching to include an instrument measuring the vertical wind relative to he balloon. This will allow to better constrain and apprehend the balloon dynamics at very high frequencies.

It will be interesting to confront those measurements to weather models which are continuously increasing their resolutions and changing their numerical integration techniques accordingly. For instance, since March 2016 and the implementation of cycle Cy41r2, the ECMWF operational model has seen a change in horizontal grid resolution (from ∼16 to ∼9 km) and geometry (from a linear gaussian grid to a cubic gaussian grid) (*Malardel et al.*, 2015-2016). This was accompanied by a roughening of the topography, a change in the distribution of precipitations (reduction of grid point storms), and a diminution of numerical filtering, which will have an impact on the distribution of vertical velocity and temperature fluctuations in the UTLS.

Besides an interesting scientific topic and a tool for evaluating the representation of small scales and gravity waves in models, the study of temperature and vertical velocity fluctuations

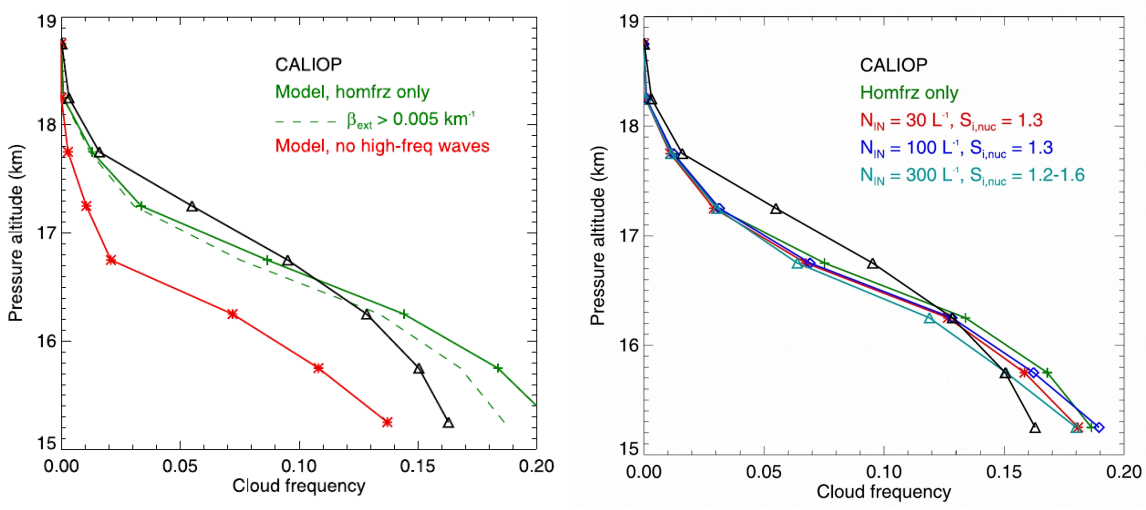

Figure 2.21 – (Left) Tropical-average cloud frequencies vs pressure altitude from CALIOP observations in January 2007 (black), Lagrangian cloud simulations with homogeneous freezing only and high-frequency waves included (green). (Right) Same as left, but for results showing the impact of changing aerosol abundance. The presence of aerosols increases TTL cirrus occurrence frequency, but the impact is minor compared to the impact indeuced by Lagrangian temperature (cooling rate) variability. From *Jensen et al.* (2016).

in the UTLS is of strong interest for our understanding of the climate system. An example is the aerosol indirect effect on ice clouds: since the cirrus radiative forcing effect is a balance between short wave cooling and long wave warming that nearly compensate one another, there is a significant uncertainty regarding the sign of the aerosol indirect forcing through ice clouds (*Penner et al.*, 2009; *Gettelman and Chen*, 2013). Vertical velocity has recently been suggested to play a key role in modulating the aerosol indirect effect (*Barahona et al.*, 2017). In particular, for the TTL, it has been suggested that the modulation of cloud cover induced by wave fluctuations far exceeds the effect of aerosol variability, as illustrated by Figure 2.21 (*Jensen et al.*, 2016). Indeed, for microphysical modeling, it is crucial to know the magnitude and intermittency of temperature fluctuations and their "intrinsic frequency distribution". The next chapter elaborates on that subject and treats of two impacts of the waves on cirrus microphysics.

Chapter 3

Some impacts of waves on cirrus cloud microphysics: homogeneous ice nucleation and ice crystal sedimentation

Sommaire

3.1 Introduction

This chapter examines some impacts of gravity waves on the microphysics of cirrus clouds in the TTL. We consider first the impact of high-frequency temperature fluctuations on homogeneous ice nucleation. In agreement with previous studies (*Spichtinger and Krämer*, 2013), we find that temperature fluctuations strongly influence the outcome of the ice nucleation process. In particular, they can be fast enough to stop homogeneous nucleation events. We argue that the existence of this nucleation regime explains some recent observations of small scale heterogeneities in TTL cirrus. However, the current theory is not sufficient to explain the overall microphysical properties of the observed TTL cirrus. In particular, it is still hard to reconcile the low ice crystal numbers generally observed in TTL cirrus with current homogeneous nucleation theory.

Then, we investigate the interaction between wave advection and ice crystal sedimentation and the impact on the transport of water by the falling ice crystals. The interactions described here might be responsible for the wave-cirrus relations observed in recent aircraft campaign (*Kim et al.*, 2016). We furthermore show, using aircraft observations, that there exists a systematic impact of wave advection on the dehydration efficiency of cirrus clouds. Tentative quantification of that impact suggests that wave advection diminishes the total sedimentation flux of water vapor leaving the TTL by an amount of about 10% at least.

3.2 Impact of high-frequency gravity waves on homogeneous ice nucleation

3.2.1 Homogeneous ice nucleation and TTL cirrus ice crystal numbers

Ice formation in the tropical upper troposphere Contrary to liquid water, for which supersaturation never exceeds 1%, ice formation in clear air is delayed and can occur at supersaturations of more than tens of %. At temperatures above the homogeneous freezing level of cloud droplets (about 235 K), ice and supercooled liquid water can coexist. Below 235 K is the cirrus domain, and only ice is present.

Many ice clouds in the upper troposphere may derive from mixed-phase clouds with the ice crystals originating from cloud droplets that homogeneously froze at about 235 K (*Krämer et al.*, 2016). However, an important part of the cirrus are formed *in situ*, i.e. directly from the gas phase. In that case, the formation of ice crystals can occur through either of two formation pathways:

- *heterogeneous nucleation*, i.e. nucleation involving a preexisting solid particle. The main processes that could be active at TTL temperature are deposition nucleation on dry particles (e.g., mineral dust or effloresced ammonium sulfate, *Froyd et al.*, 2010; *Jensen et al.*, 2010) or "immersion freezing"of aqueous aerosols from insoluble inclusions in liquid particles (e.g. glassy sulphuric aerosols containing organics, *Murray et al.*, 2010).

- homogeneous freezing of liquid solution droplets (aqueous sulphuric or nitric acid particles), often just called *homogeneous nucleation*.

Homogeneous nucleation Homogeneous nucleation is generally regarded and parameterized as a stochastic process: when the temperature is sufficiently low, each liquid aerosol particle has a certain probability P_r of freezing into ice during a time δt. P_r corresponds to

the probability of formation of an ice nucleus within the aerosol during δt. The formation of the nucleus can happen anywhere within the aerosol volume, and P_r writes:

$$P_r = 1 - \exp\left(-JV_{\mathrm{a}}\delta t\right) \tag{3.1}$$

where V_{a} is the aerosol volume and J in $\mathrm{m}^{-3}\,\mathrm{s}^{-1}$ is called the nucleation rate of the liquid aerosol particle. Laboratory experiments by *Koop et al.* (2000) suggest that J does not depend on the chemical composition of the liquid aerosol. Furthermore, according to *Koop et al.* (2000):

$$\log_{10} J = \mathbf{P}_3(a_w^d - a_w^i(T)) = \mathbf{P}_3(\Delta a_w) \tag{3.2}$$

where a_w^d is the water activity within the aerosol particle and $a_w^i(T)$ is the activity of a solution droplet in equilibrium with ice, which itself depends (only) on temperature T. $\mathbf{P}_3$ is a third order polynomial fit of the experimental results of *Koop et al.* (2000) [1]. Assuming that the aerosols are in equilibrium with their environment and neglecting surface tension effects, $a_w^d - a_w^i(T)$ rewrites:

$$\Delta a_w = a_w^d - a_w^i(T) = S_i\, a_w^i(T) - a_w^i(T) = (S_i - 1)\, a_w^i(T) \tag{3.3}$$

with $S_i = RH_i = \frac{e}{e_{\mathrm{sat}}(T)}$ the ice saturation ratio or relative humidity with respect to ice and $(S_i - 1)$ the supersaturation with respect to ice.

Nucleation may be formally defined to happen when the probability of nucleation exceeds a given threshold P_ϵ, i.e. $P_r \geq P_\epsilon$. The aerosol volume is nearly constant, so that nucleation happens when:

$$P_r \geq P_\epsilon \iff J \geq J_\epsilon \iff \Delta a_w \geq (\Delta a_w)_\epsilon \iff (S_i - 1)\, a_w^i(T) \geq (\Delta a_w)_\epsilon \tag{3.4}$$

Hence, the supersaturation $S_{\mathrm{nuc}} - 1$ required for an aerosol to nucleate with a given a probability P_ϵ during a certain duration δt is given by $(S_{\mathrm{nuc}} - 1)a_w^i(T) = (\Delta a_w)_\epsilon$.

Because $a_w^i(T)$ decreases with decreasing temperature, $S_{\mathrm{nuc}} = \dfrac{(\Delta a_w)_\epsilon}{a_w^i(T)} + 1$ increases with decreasing temperature. This is illustrated by Figure 3.1, which shows the supersaturation threshold required for the nucleation of ice within an aerosol of a given size, i.e. the threshold for which the probability of ice nucleation within that aerosol in 1 minute is 0.63. From this curve, one can see that *the critical supersaturation for homogeneous nucleation increases with decreasing temperature.*

When a population of N_a aerosols of volume V_{a} is initially present and susceptive to nucleate in N_i ice crystals, the rate of nucleation of the ice crystals $\frac{\mathrm{d}N_i}{\mathrm{d}t}$ is given by:

$$\frac{\mathrm{d}N_i}{\mathrm{d}t} = (N_a - N_i)JV_{\mathrm{a}} \tag{3.5}$$

where $(N_a - N_i)$ is the number of remaining aerosols after N_i ice crystals have formed. In practice, under atmospheric conditions, $N_a \gg N_i$.

A number of studies (e.g. *Jensen and Toon*, 1994; *Kärcher and Lohmann*, 2002; *Jensen et al.*, 2010; *Spichtinger and Krämer*, 2013) have shown that the *ice crystal number* N_i nucleated through homogeneous nucleation *mainly depends on the temperature and on the updraft speed at the nucleation time.* This dependence is illustrated by Figure 3.2, which displays simulation results using a parcel microphysics model solving homogeneous nucleation and growth and assuming a *constant updraft speed.* N_i increases exponentially with decreasing

[1] Note that $\mathbf{P}_3(\Delta a_w)$ increases with increasing Δa_w.

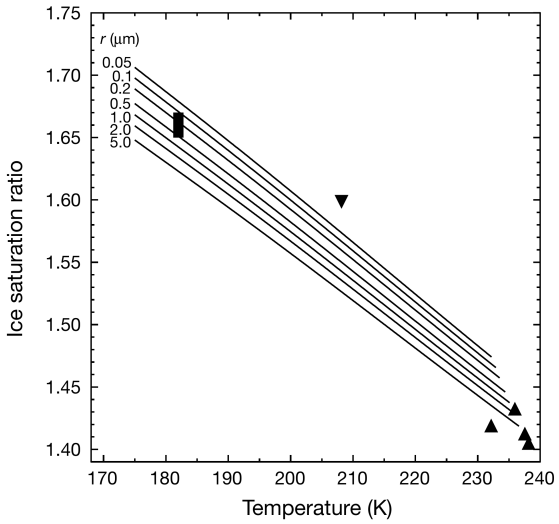

Figure 3.1 – Supersaturation threshold S_{nuc} for the nucleation of ice within an aerosol of a given size, i.e. saturation for which the probability of ice nucleation within the aerosol during $\delta t = 1$ minute is P_ϵ =0.63. The supersaturation threshold is shown as a function of temperature. From *Koop et al.* (2000).

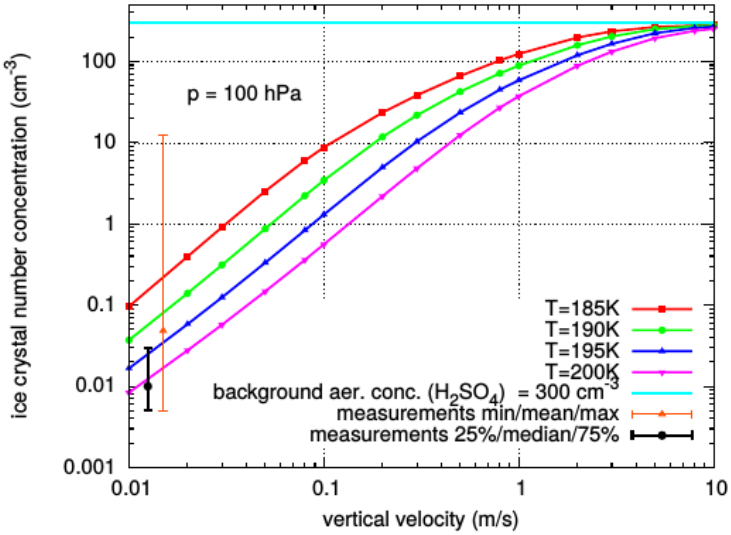

Figure 3.2 – Number of nucleated ice crystals per unit volume of air, as a function of the (constant) vertical velocity at the instant of nucleation, from a numerical model solving the homogeneous nucleation (*Koop et al.*, 2000) and growth equations of the ice crystals. The different colored curves correspond to different nucleation temperature. From *Spichtinger and Krämer* (2013).

temperature and as a power law of vertical velocity. The dependence on the aerosol size distribution and properties are weak. This makes homogeneous freezing the easiest to represent among the different ice nucleation processes. However, its relevance under TTL conditions has recently been a matter of debate in the literature.

The supersaturation and ice nucleation puzzles in the TTL Ice microphysics in the TTL has received special attention over the last decade, due to the surprisingly frequent occurrence of ice supersaturation there (*Peter et al.*, 2006), both in clear sky and inside clouds (e.g. *Jensen et al.*, 2005; *Krämer et al.*, 2009). Since then, it appears that some of the very high RH_i measurements reported in *Jensen et al.* (2005) (higher than 200%) may be artifacts caused by issues in instrument calibration (*Fahey et al.*, 2014; *Jensen et al.*, 2017). Recent measurements suggest near saturation relative humidity in cirrus (*Jensen et al.*, 2017). However, the occasional encounter of fairly high ice supersaturations inside cirrus still had to be explained. *Krämer et al.* (2009) have shown that *the low ice crystal numbers observed in TTL cirrus (see Figure 3.3) were responsible for the large supersaturations*: a smaller ice crystal number limits the size of the surface of interaction between the gas and solid phases, thus limiting the ability of ice crystals to dampen supersaturation. However, the problem now switches to: *why are there so few ice crystals in TTL cirrus?*

This question is especially puzzling because, for homogeneous ice nucleation, the ice crystal numbers nucleated at the low temperature of TTL cirrus should be larger than the ones nucleated at higher temperatures (see figures 3.2 and 3.3). Under commonly observed updraft speeds (which are of the order of 0.1 m/s, see the previous chapter), the nucleated ICN is expected to exceed by far the observations (Figure 3.3). Several explanations have been proposed to resolve the discrepancy, including the following:

- Heterogeneous nucleation dominates and limits the ICN to the number of available ice nuclei. This hypothesis is partly supported by in situ measurements of the residual particles remaining after ice crystal have sublimated (*Cziczo et al.*, 2013). Those measurements suggest that heterogeneous nucleation is prevalent in the subtropics and the tropics below TTL altitudes; however, the only TTL measurements to date suggest that ice crystals residuals are primarily a mixture of sulphates and organics (*Froyd et al.*, 2010), and that they are not so different from the background aerosol population (*Froyd et al.*, 2009). Heterogeneous formation scenarios could still be compatible with those observations, but more exotic microphysics would be involved (e.g; effloresced ammonium sulphate, *Jensen et al.*, 2010).

- Competition between homogeneous and heterogeneous nucleation results in a decrease of the nucleated ICN (*Spichtinger and Cziczo*, 2010).

- There is a slight composition dependency in the homogeneous nucleation rate J, compatible with the uncertainties in the measurements of *Koop et al.* (2000). *Murphy* (2014) has shown that this could reduce the ice crystal number nucleated by homogeneous nucleation.

- Ice sedimentation lowers the ICNs (e.g. *Barahona and Nenes*, 2011; *Jensen et al.*, 2012; *Murphy*, 2014) by extending the clouds away from their formation region

- The presence of high-frequency gravity waves quenches homogeneous nucleation events and limits the nucleated ICN (*Spichtinger and Krämer*, 2013). Indeed, the vertical velocity in the TTL is mainly due to high-frequency waves (see Chapter 2), for which the constant updraft speed approximation used to draw Figure 3.2 is not valid. The wave time scale can be sufficiently fast to interact with nucleation.

Among all those hypotheses, we have investigated further the last.

The impact of high-frequency waves that could quench a nucleation event and limit the nucleated ice crystal number was (probably) first reckoned by *Jensen et al.* (2010) for monochromatic waves. However, it was found insufficient to explain the observed ice crystal numbers

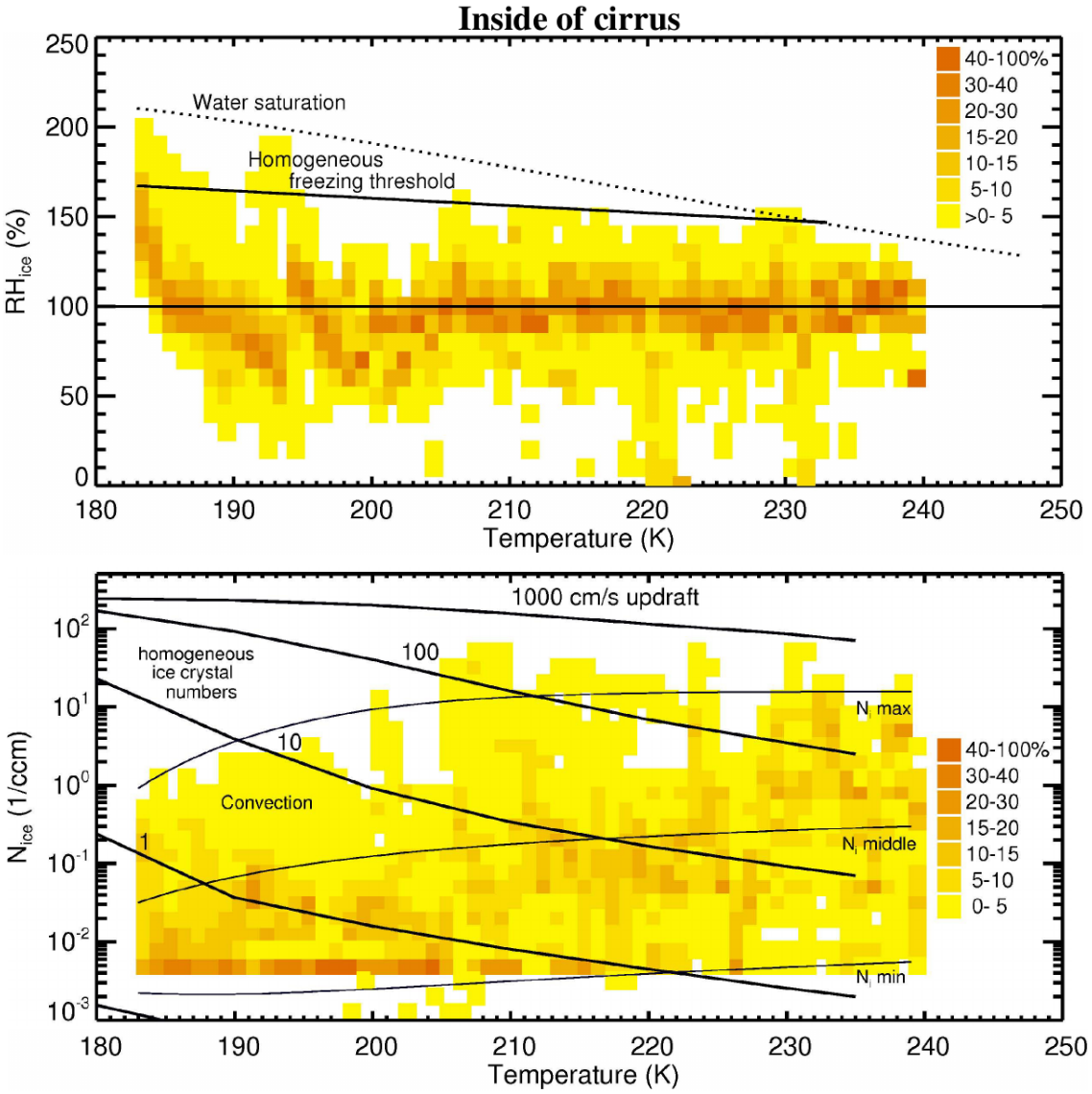

Figure 3.3 – (Top) Frequencies of occurrence of relative humidities over ice RHice vs. temperature from in situ measurements inside cirrus clouds. (Bottom) Frequencies of occurrence of ice crystal numbers N ice vs. temperature from the same dataset (thin solid lines: minimum, middle and maximum N ice; thick solid lines in top panel: nucleated ice crystal numbers arising for homogeneous freezing at different (constant) updraft velocities). From *Krämer et al.* (2009).

when the wave parameterization by *Jensen and Pfister* (2004) was included in the simulations. A variety of ice crystal numbers was obtained, but the statistics did not match the observations of low numbers[2]. In a different but still idealized set-up, *Spichtinger and Krämer* (2013) have found that high-frequency waves may explain the observed ICN distribution.

Both studies used idealized representations of the wave field. In this context, we have investigated the problem using realistic time series of Lagrangian temperature fluctuations, those presented in the previous chapter and derived from the superpressure balloon measurements. This article has been published in January 2016 in Atmospheric Chemistry and

[2]It is important to note that those results did not include ice sedimentation. However, *Jensen et al.* (2012) showed that with sedimentation, their simulations still did not agree with observations.

Physics: Dinh, T., Podglajen, A., Hertzog, A., Legras, B., and Plougonven, R.: Effect of gravity wave temperature fluctuations on homogeneous ice nucleation in the tropical tropopause layer, Atmos. Chem. Phys., 16, 35-46, doi:10.5194/acp-16-35-2016, 2016. This article is the product of a collaborative work between Dr Tra Dinh and our team. My personal contributions to the study were the development of the methodology used for the treatment of superpressure balloon data to infer Lagrangian temperature fluctuations (similar to the one developed in Chapter 2), the derivation of the analytical formula explaining the numerical results, and the highlight of their potential consequences. I also participated in the design of the simulations and of the sensitivity experiments, and in the method of analysis of the simulation results.

3.2.2 Article: Effect of gravity wave temperature fluctuations on homogeneous ice nucleation in the Tropical Tropopause Layer

Atmos. Chem. Phys., 16, 35–46, 2016
www.atmos-chem-phys.net/16/35/2016/
doi:10.5194/acp-16-35-2016

Atmospheric Chemistry and Physics Open Access EGU

Effect of gravity wave temperature fluctuations on homogeneous ice nucleation in the tropical tropopause layer

T. Dinh[1], A. Podglajen[2], A. Hertzog[2], B. Legras[3], and R. Plougonven[2]

[1]Program in Atmospheric and Oceanic Sciences, Princeton University, Princeton, New Jersey, USA
[2]Laboratoire de Météorologie Dynamique, École Polytechnique, Palaiseau, France
[3]Laboratoire de Météorologie Dynamique, École Normale Supérieure, Paris, France

Correspondence to: T. Dinh (tdinh@princeton.edu)

Received: 3 March 2015 – Published in Atmos. Chem. Phys. Discuss.: 24 March 2015
Revised: 5 November 2015 – Accepted: 24 November 2015 – Published: 14 January 2016

Abstract. The impact of high-frequency fluctuations of temperature on homogeneous nucleation of ice crystals in the vicinity of the tropical tropopause is investigated using a bin microphysics scheme for air parcels. The imposed temperature fluctuations come from measurements during isopycnic balloon flights near the tropical tropopause. The balloons collected data at high frequency, guaranteeing that gravity wave signals are well resolved.

With the observed temperature time series, the numerical simulations with homogeneous freezing show a full range of ice number concentration (INC) as previously observed in the tropical upper troposphere. In particular, a low INC may be obtained if the gravity wave perturbations produce a non-persistent cooling rate (even with large magnitude) such that the absolute change in temperature remains small during nucleation. This result is explained analytically by a dependence of the INC on the absolute drop in temperature (and not on the cooling rate). This work suggests that homogeneous ice nucleation is *not* necessarily inconsistent with observations of low INCs.

1 Introduction

Cirrus clouds have an important impact on the global radiative energy budget (Lohmann and Roeckner, 1995). In the tropical tropopause layer (TTL; Fueglistaler et al., 2009), cirrus clouds contribute to the radiative heating (Corti et al., 2006; Dinh and Fueglistaler, 2014a) and control the dehydration of the air before entry into the stratosphere (Brewer, 1949; Jensen et al., 1996; Dinh and Fueglistaler, 2014b). For all cirrus clouds, the radiative and climate impact, ability to modify water vapour, and cloud evolution are sensitive to the ice number concentration (e.g. Kärcher et al., 2014), which depends strongly on the nucleation process of ice crystals.

When evaluating the ice number concentration (INC) produced by nucleation, it has been often assumed that the relevant timescale is sufficiently short such that the vertical velocity and associated adiabatic cooling rate remain constant (e.g. Barahona and Nenes, 2008). For constant cooling rates, homogeneous freezing of aqueous aerosols produces higher INCs ($> 1000\,\mathrm{L}^{-1}$) than those commonly observed ($\lesssim 100\,\mathrm{L}^{-1}$) in cirrus clouds (Lawson et al., 2008; Krämer et al., 2009; Davis et al., 2010). Observations and calculations of INC based on homogeneous freezing can be reconciled only if very low vertical speeds ($w < 0.01\,\mathrm{m\,s}^{-1}$) are used in the simulations. This seems at odds with the ubiquitous presence of atmospheric gravity waves, which typically generate disturbances an order of magnitude larger in the vertical velocity. Therefore, it has been suggested that heterogeneous freezing (instead of homogeneous freezing) is the dominant nucleation mechanism for cirrus clouds in the upper troposphere (Jensen et al., 2010, 2012). The INC obtained by heterogeneous freezing is apparently limited by the availability of suitable ice nuclei (generally less than $100\,\mathrm{L}^{-1}$) in the upper troposphere (Chen et al., 1998; Rogers et al., 1998).

However, Spichtinger and Krämer (2013) pointed out that high-frequency variations in temperature and cooling rates can substantially decrease the INC produced during homogeneous nucleation compared to those obtained with constant updraft speeds. However, their numerical results are based

on ideally constructed temperature time series and so remain somewhat conceptual. The present work complements their study by using temperature time series data collected at high temporal resolution during long-duration balloon flights near the tropical tropopause. The observed temperatures contain perturbations from a spectrum of atmospheric waves, with periods ranging from days to minutes. Our numerical simulations based on these observed temperature time series confirm the earlier results of Spichtinger and Krämer (2013).

In addition to the numerical simulations using realistic temperature time series (as described above), our contribution is to provide a theoretical framework for characterising homogeneous nucleation while taking into account the temperature fluctuations due to gravity waves. The theoretical framework put forward here complements previous studies (see also Barahona and Nenes, 2011; Jensen et al., 2010, 2012; Murphy, 2014), where the effect of high-frequency temperature fluctuations on ice nucleation has been described but not explained analytically.

The article is organised as follows. Sections 2 and 3 describe the balloon data and the technical details of the model used here to simulate homogeneous ice nucleation. Section 4 presents the numerical results. Section 5 provides the theoretical basis explaining how the fluctuations in time of temperature may affect homogeneous ice nucleation. Section 6 contains the conclusions.

2 Balloon data descriptions

The temperature time series used in this study are derived from data collected by two long-duration, superpressure balloons launched by the French Space Agency from Seychelles Islands (55.5° E, 4.6° N) in February 2010 in the framework of the pre-Concordiasi campaign (Rabier et al., 2010). The balloons flew at an altitude of about 19 km and achieved circumterrestrial flights, therefore sampling the whole equatorial circle. Details on the balloon trajectories and large-scale atmospheric dynamics during the flights can be found in Podglajen et al. (2014). Superpressure balloons are advected by the wind on isopycnic (constant-density) surfaces and therefore behave as quasi-Lagrangian tracers of atmospheric motions. A further remarkable property of superpressure balloons is their sensitivity to atmospheric gravity waves (Massman, 1978; Nastrom, 1980; Boccara et al., 2008; Vincent and Hertzog, 2014). The sampling frequency of the balloon position, atmospheric pressure, and temperature during the campaign is every 30 s.

Here, we do not use the temperature observations gathered during the flights to constrain the nucleation simulations; these time series tend to be both too noisy and warm biased during daytime. Instead, we infer the temperature disturbances from the balloon vertical displacements ($\zeta'_{\rm b}$). The isentropic air parcel vertical displacement (ζ') is linked to that of the isopycnic balloon through

$$\zeta' = \frac{g/c_p + \partial\overline{T}/\partial z}{g/R_{\rm a} + \partial\overline{T}/\partial z}\zeta'_{\rm b} \quad (1)$$

(Boccara et al., 2008), where g is the gravitational acceleration, c_p is the specific heat at constant pressure, $R_{\rm a}$ is the gas constant for air, and $\partial\overline{T}/\partial z$ is the vertical gradient of the background temperature. We use the European Centre for Medium-range Weather Forecasts (ECMWF) operational analyses to diagnose $\partial\overline{T}/\partial z$ at the balloon position in the above equation. The isentropic vertical displacement is then converted to the Lagrangian temperature fluctuation (felt by the air parcel) at the balloon flight level (i.e. in the lower stratosphere) by

$$T'_{\rm LS} = -\frac{g}{c_p}\zeta'. \quad (2)$$

We must furthermore take into account that the balloons flew in the lower stratosphere rather than in the upper troposphere where most of the cirrus form. Because of the difference in stability of these two regions, the vertical displacements and hence temperature fluctuations induced by gravity waves are larger in the upper troposphere than in the lower stratosphere. For conservative wave propagation, it can be shown that

$$T'_{\rm UT} = \sqrt{\frac{N_{\rm LS}}{N_{\rm UT}}}\exp\left(-\frac{\Delta z}{2H}\right)T'_{\rm LS}, \quad (3)$$

where $N_{\rm UT}$ and $N_{\rm LS}$ respectively are the buoyancy frequencies in the upper troposphere and lower stratosphere, Δz is the difference between the balloon flight and cloud altitudes, H is the atmospheric scale height (~ 6 km in the TTL), and $T'_{\rm UT}$ is the temperature disturbance in the upper troposphere induced by the gravity wave packet observed at the balloon altitude. Typically, $N_{\rm LS} \sim 2N_{\rm UT}$, and $T'_{\rm UT} \sim T'_{\rm LS}$ if the cirrus forms 4 km below the balloon flight level.

The power spectrum of the temperature perturbation ($T'_{\rm UT}$) time series derived from the balloon vertical displacements is shown in Fig. 1. Notice that the balloon neutral oscillations due to the flight mechanics have a frequency of $0.25\,{\rm min}^{-1}$. Since the spectrum of gravity waves extends up to the Brunt–Väisälä frequency (typically less than $0.20\,{\rm min}^{-1}$ in the TTL), we expect that the balloon motions do not negatively affect the quality of gravity waves in the data set. Nevertheless, we applied a Butterworth band-stop filter to remove the balloon oscillations from the temperature time series (Fig. 1). We have also experimented filtering the data using a high cut-off frequency of 0.10 or $0.20\,{\rm min}^{-1}$ (not shown). Our results (Sect. 4) are not sensitive to the data filtering method.

3 Model configurations

We compute homogeneous freezing of aqueous aerosols following Koop et al. (2000) and depositional growth of ice

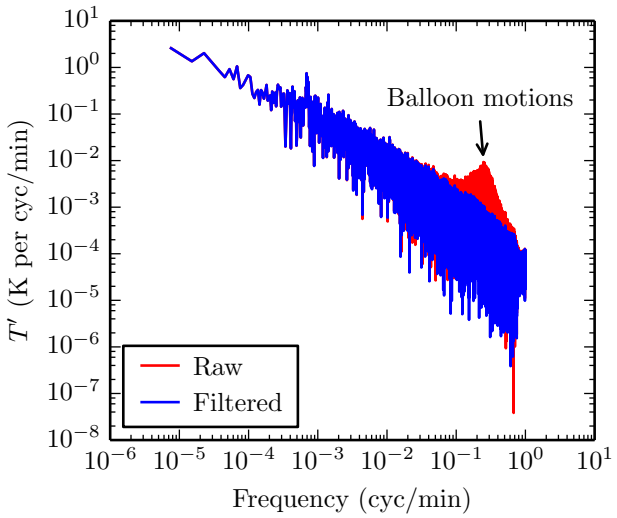

Figure 1. Power spectrum of the raw and filtered temperature perturbation time series derived from the balloon vertical displacements.

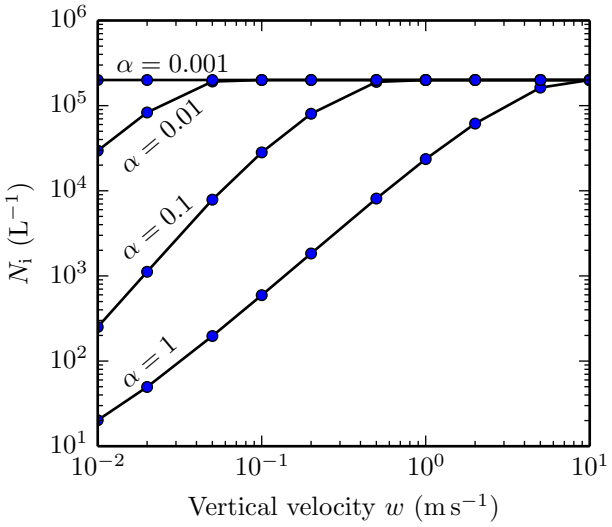

Figure 2. INC obtained from homogeneous nucleation at 195 K forced by constant vertical velocity w for different values of the deposition coefficient α.

crystals (see e.g. Pruppacher and Klett, 1978) using the bin scheme designed by Dinh and Durran (2012). The formula for the water activity has been revised following Koop and Zobrist (2009). The saturation water vapour pressure (over ice) is taken from Murphy and Koop (2005).

Ice crystals and aerosol particles that form ice crystals are assumed to be spherical. We use 20 bins to resolve the size distribution of ice crystals with radii up to 10 µm. The time step used in the simulations is 0.5 s. The numerical results do not change with more bins or smaller time step, i.e. the stated bin and time resolutions are sufficient to ensure accuracy.

The number concentration of the aerosol reservoir is $N_a = 200\,\mathrm{cm}^{-3}$, and aerosol particles are assumed to be monodispersed in size with a radius of 0.25 µm. These assumptions are within observed properties of aerosols in the upper troposphere (Chen et al., 1998; Hermann et al., 2003). Simulations with polydispersed aerosols up to 1 µm in size do not show qualitative differences, and so we retain a monodispersed distribution to simplify the analytical derivation in Sect. 5.

In addition, we do not consider ice sedimentation in order to focus solely on the nucleation process. Further, nucleation is calculated only for initially ice-free air parcels. The effect of pre-existing ice on nucleation has been discussed elsewhere (see Shi et al., 2015).

Currently, there is not yet a well-constrained limit on the deposition coefficient (also called accommodation coefficient). The deposition coefficient controls the number of gas molecules that effectively enter the condensed phase after a collision with the ice surface. Laboratory measurements of the deposition coefficient vary by as much as 3 orders of magnitude, between 0.001 and 1 (Magee et al., 2006; Skrotzki et al., 2013). Figure 2 illustrates the effect of varying the deposition coefficient α on the INC calculated using our model. For the same constant updraft, the INC obtained by homogeneous nucleation is smaller for larger α. In the following sections, we first present the simulations for $\alpha = 0.1$ and then discuss the sensitivity to α in Sects. 4.3.3 and 5.2.

4 Numerical simulations

For adiabatic motions, the effect of pressure variations on the water vapour mixing ratio (r) can be neglected compared with that due to temperature variations. Assuming constant air pressure, we prescribe an initial water vapour content for the air parcels such that nucleation occurs at a chosen temperature T_0. This is possible because the saturation ratio with respect to ice (S) at the threshold of nucleation (S_{nuc}) is a function of temperature (Koop et al., 2000; Kärcher and Lohmann, 2002; Ren and Mackenzie, 2005), and it is related to the initial water vapour mixing ratio of air parcels by

$$r_0 = \frac{e_{\mathrm{sat}}(T_0)\, S_{\mathrm{nuc}}(T_0)}{p} \frac{R_a}{R_v}, \tag{4}$$

where p is air pressure, e_{sat} is the saturation water vapour pressure over ice, and R_a and R_v are respectively the gas constants of air and water vapour. The notations $e_{\mathrm{sat}}(T_0)$ and $S_{\mathrm{nuc}}(T_0) \equiv S_0$ refer to respectively e_{sat} and S_{nuc} at T_0. Note that up to the nucleation time the vapour mixing ratio r is conserved ($r = r_0$ for $t \le t_0$). As illustrated in Fig. 3, every air parcel follows an isoline of constant water vapour mixing ratio ($r = r_0$) until crossing the $S_{\mathrm{nuc}}(T)$ curve, at which point ($t = t_0$) nucleation begins.

The simulations were first carried out for pressure $p = 100$ hPa, nucleation temperature $T_0 = 195$ K, and deposition coefficient $\alpha = 0.1$ (Sect. 4.1, 4.2, and 4.3.1). A nucleation

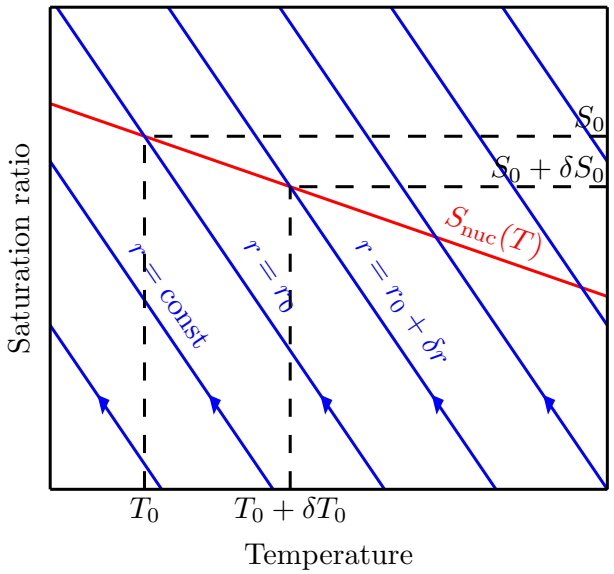

Figure 3. Diagram illustrating the initial conditions of the air parcels. Prior to nucleation air parcels follow isolines of water vapour mixing ratio r (shown here in blue) and approach the curve $S_{\rm nuc}(T)$ from below (as indicated by the arrows). Nucleation begins at the intersections of the r isolines with the curve $S_{\rm nuc}(T)$.

event may be formally defined to start when the rate of nucleation J exceeds a threshold J_ε ($J \geq J_\varepsilon$) and to end when it becomes less than J_ε ($J < J_\varepsilon$). For our simulations, choosing a threshold of $J_\varepsilon = 10^9\,\mathrm{L^{-1}\,s^{-1}}$, we have $S_0 = 1.553$ for $T_0 = 195\,\mathrm{K}$. Sensitivities to nucleation temperature T_0 in the range between 180 and 210 K and α in the range between 0.001 and 1 are discussed in Sect. 4.3.2 and 4.3.3. Time series of temperature is defined by

$$T(t) = \overline{T} + T'(t), \tag{5}$$

where $T'(t)$ are either idealised following temperature variations associated with constant and time-varying vertical velocities (Sect. 4.1 and 4.2), or taken from the balloon data (Sect. 4.3). The base temperature $\overline{T}$ is varied between 180 and 220 K, which allows us to explore a range of saturation ratio with respect to $\overline{T}$ ($0.8 \leq S(\overline{T}) \leq 1.2$) for a given nucleation temperature T_0. The results and conclusions presented below, including the analytical derivation in Sect. 5.1, do not depend on the choice of $\overline{T}$. The only requirement for $\overline{T}$ is that it is sufficiently low to allow for nucleation along the temperature time series, specifically $\overline{T} + T'(t) < T_0$ for at least some time (t) in the time series.

4.1 Constant vertical velocity

Here temperature is set to decrease with time due to adiabatic cooling at a constant vertical velocity in a hydrostatic background, i.e.

$$T'(t) = -\frac{g}{c_p} w t. \tag{6}$$

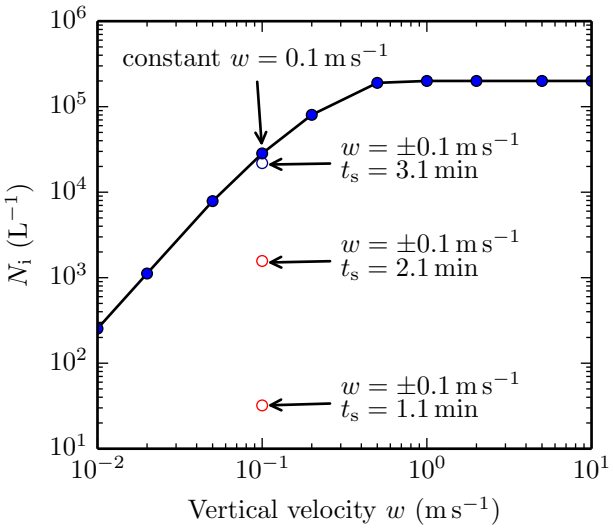

Figure 4. INCs obtained for $\alpha = 0.1$ with constant w (filled circles), and with $w = \pm 0.1\,\mathrm{m\,s^{-1}}$ (open circles), see Eq. (7). Vapour-limit events are shown in blue and temperature-limit events are shown in red.

For $\alpha = 0.1$, the number of ice crystals nucleated N_i increases with w if $w < 1\,\mathrm{m\,s^{-1}}$ (see Fig. 4). For $w \geq 1\,\mathrm{m\,s^{-1}}$, all aerosols particles form ice, hence $N_\mathrm{i} = N_\mathrm{a} = 200\,\mathrm{cm^{-3}}$. Figure 4 shows that if the vertical velocity and the cooling rate are constant during the nucleation events, w must be less than $0.01\,\mathrm{m\,s^{-1}}$ in order for $N_\mathrm{i} < 100\,\mathrm{L^{-1}}$. This result is consistent with previous studies (e.g. Krämer et al., 2009) of homogeneous freezing under constant vertical velocity.

4.2 Nonpersistent cooling

Now we vary w with time so that the rate of change of temperature $\frac{\mathrm{d}T}{\mathrm{d}t}$ is no longer constant with time. Specifically, we set

$$w(t) = \begin{cases} +0.1\,\mathrm{m\,s^{-1}} & \text{if } t - t_0 \leq t_\mathrm{s} \\ -0.1\,\mathrm{m\,s^{-1}} & \text{if } t - t_0 > t_\mathrm{s} \end{cases}. \tag{7}$$

The time t_s at which w switches signs is varied by setting $t_\mathrm{s} = \{1.10;\ 2.10;\ 3.10\}\,\mathrm{min}$. The dash lines in Fig. 5 show the evolution of the vertical velocity, temperature, saturation ratio, and INC during the nucleation events forced by $w = \pm 0.1\,\mathrm{m\,s^{-1}}$ as defined above.

In the event where w switches signs at $t_\mathrm{s} = 3.10\,\mathrm{min}$ (blue dash curves in Fig. 5), the saturation ratio (S) reaches a maximum (S_max) at $t^* = 3.05\,\mathrm{min}$, which is before the minimum temperature (T_min) is reached ($t^* < t_\mathrm{s}$). Here, S_max is controlled by the depletion of water vapour by depositional growth of ice crystals. The INC in this event is almost the same as that which would have been obtained if w were kept constant at $0.1\,\mathrm{m\,s^{-1}}$ (see also Fig. 4). We refer to this event and all cases with constant w as "vapour limit", indicating that N_i is limited by the depletion of water vapour.

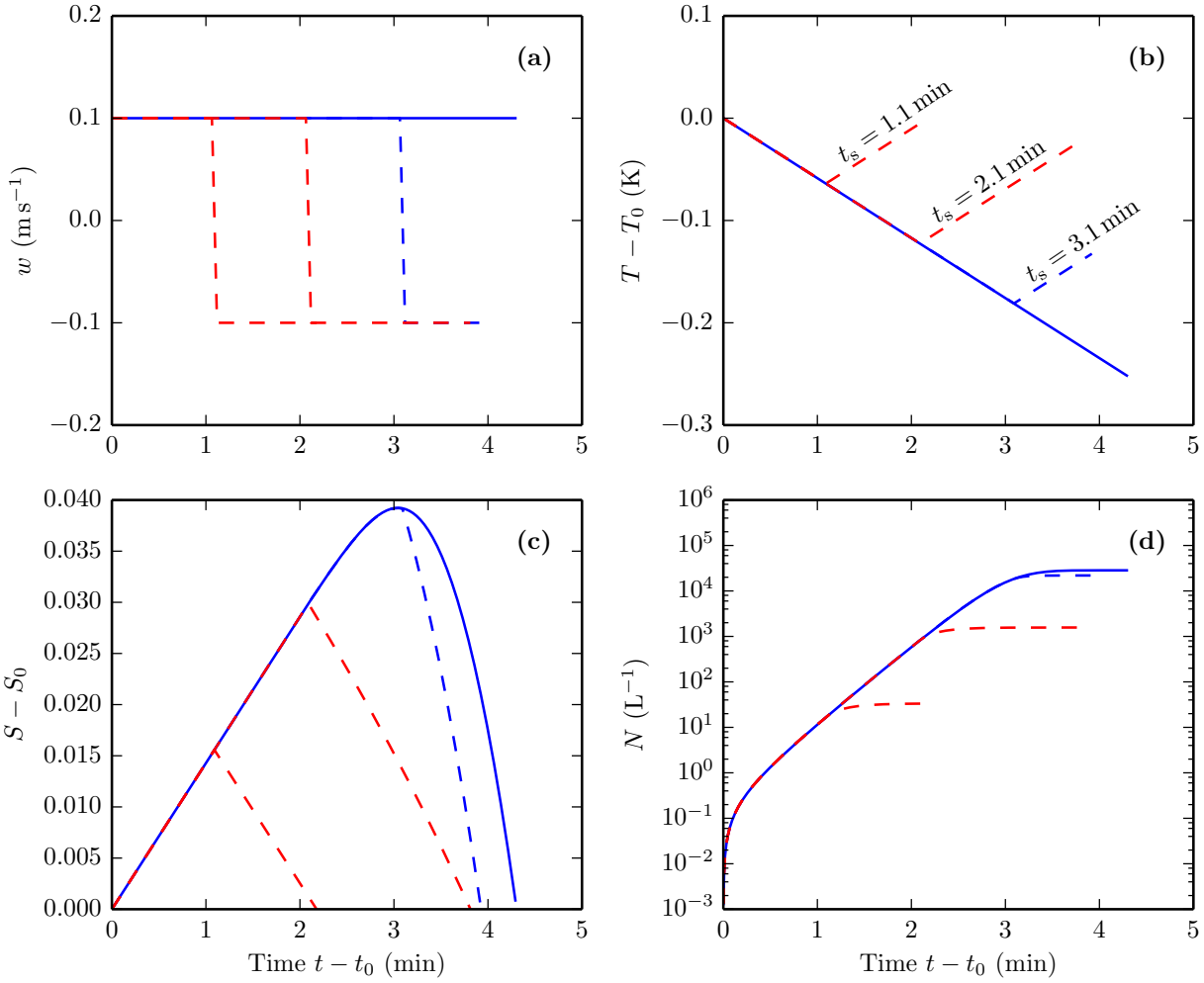

Figure 5. Evolution of vertical velocity **(a)**, temperature **(b)**, saturation ratio **(c)**, and INC **(d)** during nucleation events forced by constant $w = 0.1\,\mathrm{m\,s^{-1}}$ (solid) and by $w = \pm 0.1\,\mathrm{m\,s^{-1}}$ (dash) as defined by Eq. (7). Blue curves show vapour-limit events and red curves show temperature-limit events.

For the other two events in which w switches signs earlier at $t_s = 1.10$ and 2.10 min (red curves in Fig. 5 and red circles in Fig. 4), N_i is significantly smaller than that obtained for the vapour-limit event described above. For these two events, S_{max} and T_{min} occur at the same time ($t^* = t_s$). After S_{max} is reached, S decreases with time because temperature increases with time. We refer to these events as "temperature limit" because the minimum temperature determines S_{max} and hence N_i. The depletion of water vapour by ice depositional growth can be neglected because N_i is small.

The numerical results show that homogeneous nucleation may be cut off if the cooling that initiates nucleation does not persist sufficiently long into the nucleation events. As a consequence, low INCs can be obtained for temperature-limit events despite initially high vertical velocities and cooling rates. The results in this section are consistent with the simulations with similar setups that have been carried out previously by Spichtinger and Krämer (2013).

4.3 Balloon temperature time series

In contrast to the previous sections which used theoretically constructed temperature time series, the numerical simulations presented in this section were carried out using the balloon data. Below, for Sect. 4.3.1 we use $T_0 = 195\,\mathrm{K}$ and $\alpha = 0.1$ (same as previously in Sect. 4.1 and 4.2). In Sect. 4.3.2 and 4.3.3, we vary T_0 between 180 and 210 K and α between 0.001 and 1 to explore sensitivities to these parameters.

4.3.1 Control simulations with $T_0 = 195\,\mathrm{K}$ and $\alpha = 0.1$

The evolution of the vertical velocity, temperature, saturation ratio, and INC for representative nucleation events simulated using the balloon data is shown in Fig. 6. The plots in the figure are shown for an extended period of time before nucleation begins at t_0 to illustrate the background condition

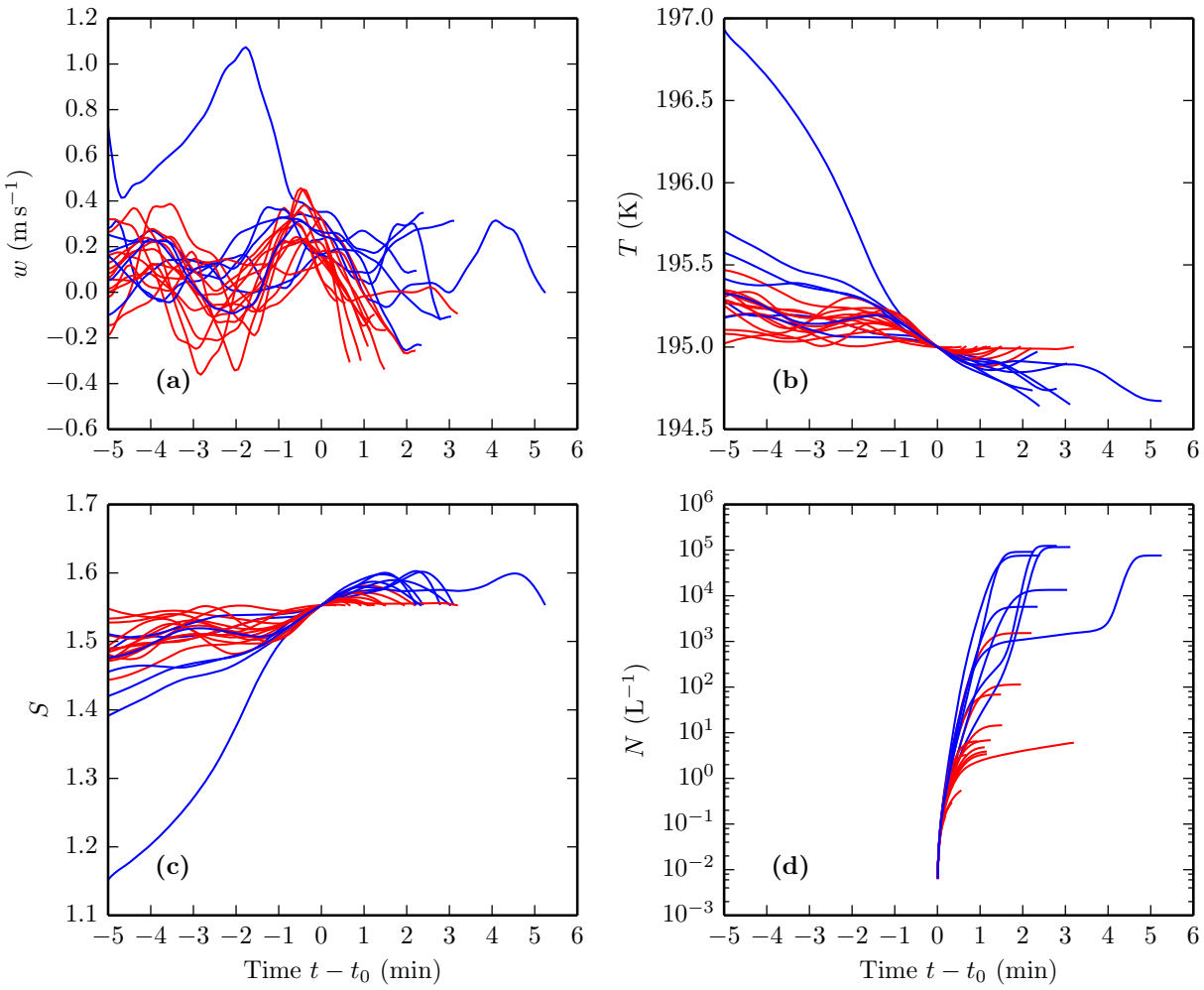

Figure 6. Evolution of vertical velocity **(a)**, temperature **(b)**, saturation ratio **(c)**, and INC **(d)** in the period immediately before and during representative nucleation events forced by the temperature perturbations derived from the balloon data. The plots are shown for an extended period of time before nucleation begins at t_0 to illustrate the background condition leading to nucleation. Blue curves show vapour-limit events and red curves show temperature-limit events.

leading to nucleation. However, we will show below that the INC obtained by nucleation is independent of the background condition prior to nucleation.

Figure 6 shows that the duration τ of the nucleation events (as formally defined by the period during which $J \geq J_\varepsilon$) is typically less than 5 min. However, during this short time period, the cooling rate is typically not constant because there are high-frequency fluctuations in the observed vertical velocity and temperature time series. Moreover, more than one local maximum and minimum in T and S may occur during one nucleation event. Nevertheless, it is possible to distinguish between

– vapour-limit events, for which the absolute maximum $S_{\max}$ is obtained before the absolute minimum $T_{\min}$ because of substantial vapour depletion – constant cooling rate is a special case of this type; and

– temperature-limit events, for which $S_{\max}$ is obtained at the same time as $T_{\min}$; i.e. temperature controls the cut-off of nucleation, and vapour depletion is negligible.

As shown in Fig. 7, the INCs nucleated during temperature-limit events are typically smaller than for vapour-limit events. The numerical results suggest that, for all nucleation events, $N_{\rm i}$ increases exponentially with the difference

$$\triangle S \equiv S_{\max} - S_0 \tag{8}$$

as long as $N_{\rm i} \ll N_{\rm a}$ (Fig. 7). For temperature-limit nucleation events, $N_{\rm i}$ increases exponentially with $|\triangle T|$, where

$$\triangle T \equiv T_{\min} - T_0. \tag{9}$$

In Sect. 5.1, we will prove analytically that the INC obtained by nucleation ($N_{\rm i}$) is indeed a function of $\triangle S$ (or a func-

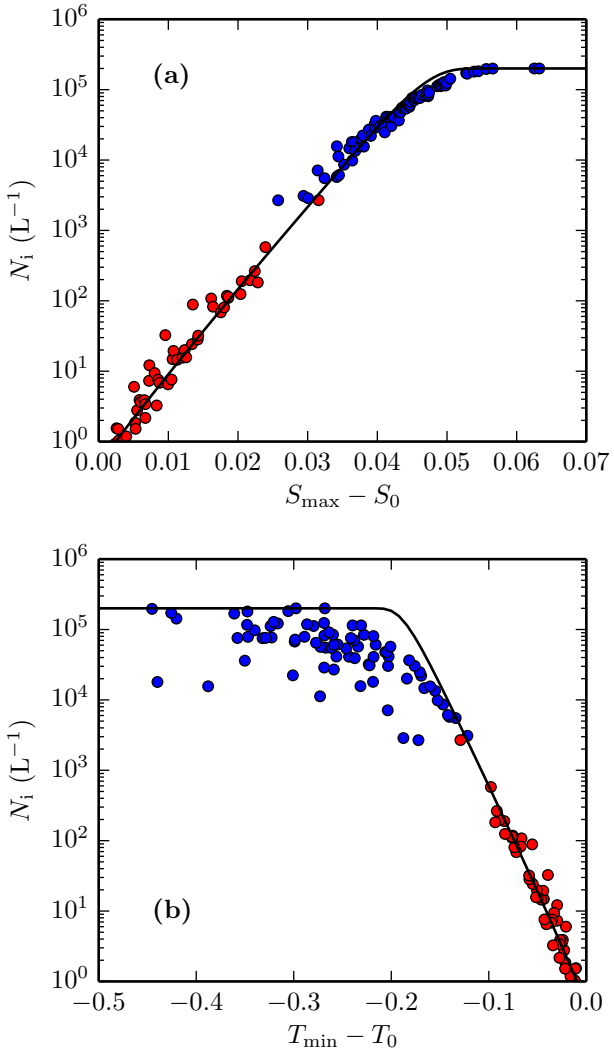

Figure 7. Number of ice crystals nucleated at $T_0 = 195\,\mathrm{K}$ for $\alpha = 0.1$ using the balloon temperature perturbation time series. Blue circles show vapour-limit nucleation events. Red circles show temperature-limit nucleation events. The solid curves are obtained from Eqs. (14)–(18) with $\mu = 0.05\,\mathrm{s}^{-1}$.

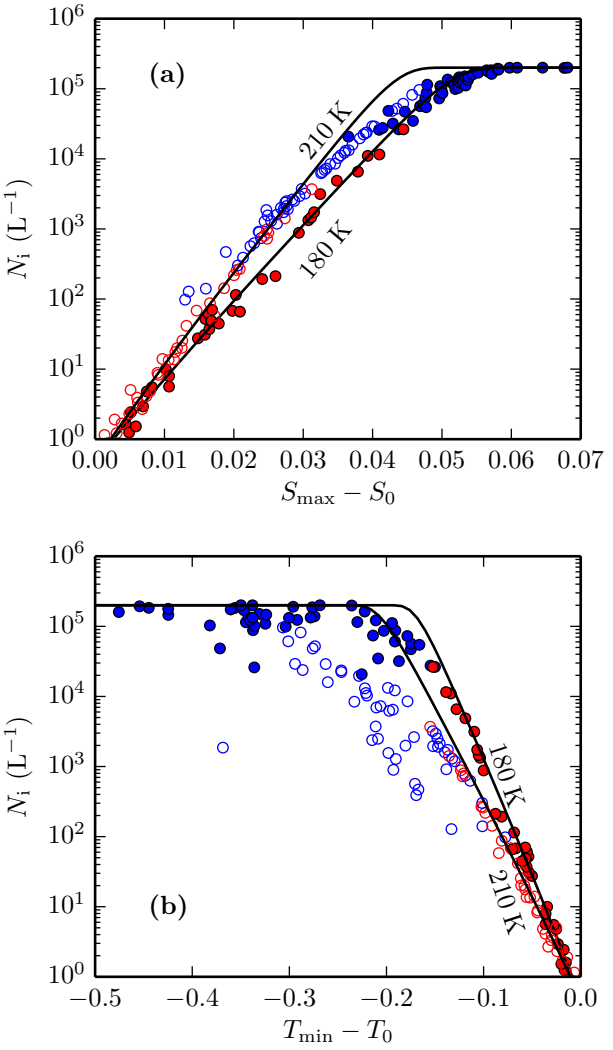

Figure 8. Same as Fig. 7 ($\alpha = 0.1$) but for $T_0 = 180\,\mathrm{K}$ (filled circles) and 210 K (empty circles).

tion of $\triangle T$ for temperature-limit events). These two quantities ($\triangle S$ and $\triangle T$) are characterisation of the fluctuations in water vapour and temperature during nucleation; they are defined exclusively within the period of nucleation and are independent of the background condition prior to nucleation.

4.3.2 Sensitivity of INC to nucleation temperature

Here, we prescribe the initial vapour content r_0 of the air parcels such that the nucleation temperature T_0 is either 180 or 210 K. In Fig. 3, this is equivalent to choosing another isoline of r and displacing accordingly the values of T_0 and S_0 at nucleation.

The number of ice crystals nucleated for $T_0 = 180$ and 210 K is shown in Fig. 8. The data for $T_0 = 195\,\mathrm{K}$ shown previously in Fig. 7 generally lie between the data points for $T_0 = 180$ and 210 K; that is, there is a monotonic relationship between N_i and T_0. For the same $\triangle S$, N_i is smaller for smaller T_0. Conversely, for the same $\triangle T$, N_i is smaller for larger T_0.

4.3.3 Sensitivity of INC to deposition coefficient

The number of ice crystals nucleated at $T_0 = 195\,\mathrm{K}$ for $\alpha = 0.001$ and $\alpha = 1$ is shown in Fig. 9. Notice that the transition from temperature-limit events to vapour-limit events occurs at lower INC for $\alpha = 1$ than $\alpha = 0.001$. This makes sense because ice crystals deplete water vapour at a faster rate in the case $\alpha = 1$, and so the number of ice crystals needed to significantly deplete water vapour is smaller.

For temperature-limit events, the functional dependence of N_i on $\triangle S$ (or $\triangle T$) is invariant for different values of α, i.e. N_i is independent of α. However, for vapour-limit events, N_i is

smaller for $\alpha = 1$ than $\alpha = 0.001$ for the same $\triangle S$ (or $\triangle T$). The sensitivity of vapour-limit events to the deposition coefficient is explained in the theory section below.

5 Theory and discussions

In this section we provide the theoretical basis that explains the numerical results shown previously in Sect. 4.

5.1 Formula for ice number concentration

The rate of nucleation of ice crystals during a nucleation event is given by

$$\frac{\mathrm{d}N}{\mathrm{d}t} = (N_\mathrm{a} - N)\, J\, V_\mathrm{a}, \tag{10}$$

where N_a is the aerosol particle number concentration, V_a is the volume of each aerosol particle, and J is the homogeneous nucleation rate given by Koop et al. (2000, their Eq. 7). By integrating Eq. (10) from the beginning ($t = t_0$) to end ($t = t_0 + \tau$) of the nucleation event we obtain

$$\begin{aligned}\ln\left(1 - \frac{N_\mathrm{i}}{N_\mathrm{a}}\right) &= -V_\mathrm{a} \int_{t_0}^{t_0+\tau} J\,\mathrm{d}t \\ &= -V_\mathrm{a} J_\mathrm{max} \int_{t_0}^{t_0+\tau} \exp\left(\ln(J) - \ln\left(J_\mathrm{max}\right)\right)\mathrm{d}t,\end{aligned} \tag{11}$$

where $J_\mathrm{max} \equiv J(t^*)$ is the maximum value of J during the nucleation event ($t_0 < t^* < t_0 + \tau$), and $N_\mathrm{i} \equiv N(t_0 + \tau)$ is the INC obtained at the end of the nucleation event. Following the steepest descent method, we obtain

$$\begin{aligned}&\ln\left(1 - \frac{N_\mathrm{i}}{N_\mathrm{a}}\right) \\ &\approx -V_\mathrm{a} J_\mathrm{max} \int_{t_0}^{t_0+\tau} \exp\left(\frac{1}{2}\frac{\mathrm{d}^2(\ln J)}{\mathrm{d}t^2}\left(t^*\right)\left(t - t^*\right)^2\right)\mathrm{d}t \\ &\approx -V_\mathrm{a} J_\mathrm{max} \int_{t_0-t^*}^{t_0+\tau-t^*} \exp\left(-\mu^2 t^2\right)\mathrm{d}t \\ &\approx -V_\mathrm{a} J_\mathrm{max} \int_{-\infty}^{\infty} \exp\left(-\mu^2 t^2\right)\mathrm{d}t \\ &\approx \sqrt{\pi} V_\mathrm{a} \frac{J_\mathrm{max}}{\mu},\end{aligned} \tag{12}$$

where

$$\mu^2 = -\frac{1}{2}\frac{\mathrm{d}^2(\ln J)}{\mathrm{d}t^2}\left(t^*\right) = -\frac{1}{2J_\mathrm{max}}\frac{\mathrm{d}^2 J}{\mathrm{d}t^2}\left(t^*\right). \tag{13}$$

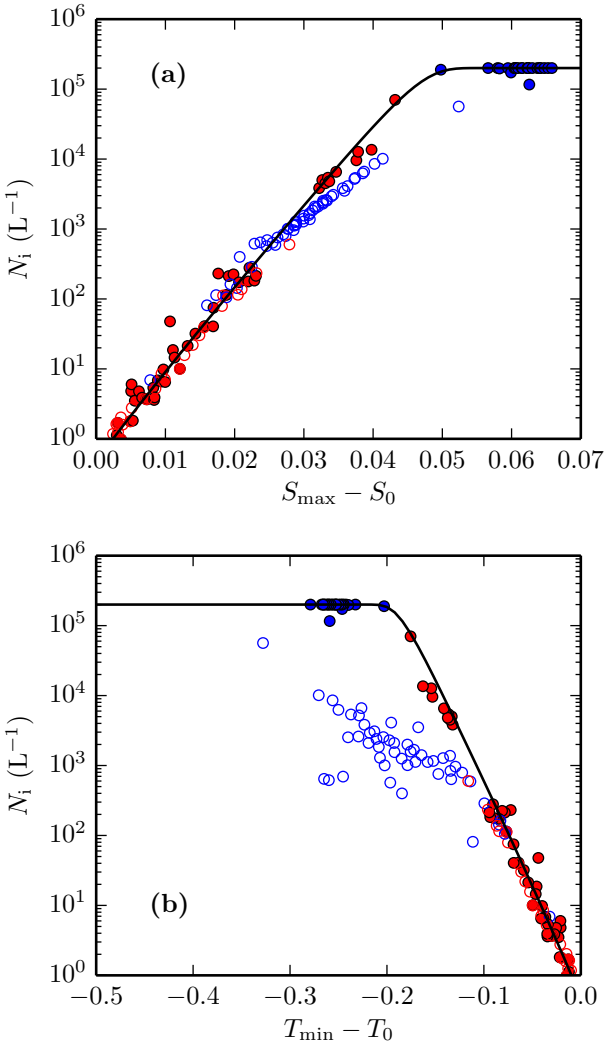

Figure 9. Same as Fig. 7 ($T_0 = 195$ K) but for $\alpha = 0.001$ (filled circles) and $\alpha = 1$ (empty circles).

The approximations used to derive Eq. (12) are appropriate if $t^* - t_0$ and $t_0 + \tau - t^*$ are both significantly larger than the e-folding timescale given by μ^{-1}. These criteria are well satisfied in our simulations. From Eq. (12) we obtain

$$N_\mathrm{i} \approx N_\mathrm{a}\left(1 - \exp\left(-\sqrt{\pi} V_\mathrm{a}\frac{J_\mathrm{max}}{\mu}\right)\right). \tag{14}$$

For homogeneous ice nucleation, J is given by (see Koop et al., 2000)

$$\log_{10}(J) = P_3\left((S-1)a_\mathrm{w}^\mathrm{i}\right), \tag{15}$$

where P_3 denotes a third-order polynomial, and a_w^i is the water activity of a solution in equilibrium with ice, which is independent of the nature of the solute (Koop et al., 2000). It

follows that

$$\log_{10}(J_{\max}) = P_3\left((S_{\max}-1)\,a_{\mathrm{w}}^{\mathrm{i}}\left(T\left(t^*\right)\right)\right) \approx P_3\left((S_0+\triangle S-1)\,a_{\mathrm{w}}^{\mathrm{i}}(T_0)\right), \quad (16)$$

where $\triangle S$ is the change in the saturation ratio during the nucleation event defined in Eq. (8). Since $a_{\mathrm{w}}^{\mathrm{i}}$ and S_0 are both functions of temperature, $J_{\max}$ is a function of $\triangle S$ and temperature. Therefore, Eqs. (14) and (16) indicate that N_{i} is a function of $\triangle S$, μ, and temperature. However, note that $\triangle S$, μ, and temperature are not exclusively independent variables. In fact, substituting Eqs. (15) and (16) into Eq. (13) we obtain

$$\mu^2 \approx f(\triangle S, T_0)\left(\frac{\mathrm{d}^2 S}{\mathrm{d}t^2}\left(t^*\right)\right) + h(\triangle S, T_0)\left(\frac{\mathrm{d}^2 T}{\mathrm{d}t^2}\left(t^*\right)\right), \quad (17)$$

where $f(\triangle S, T_0)$ and $h(\triangle S, T_0)$ are functions of $\triangle S$ and T_0, and we have made the approximation that $T \approx T_0$ because the perturbation T' is small compared with T and T_0. Equation (17) indicates that μ is a function of $\triangle S$, T_0, and the second-order time derivatives of S and T evaluated at t^*.

For the nucleation events at $T_0 = 195\,\mathrm{K}$ shown in Fig. 7, our calculations indicate that $0.01 < \mu < 0.1\,\mathrm{s}^{-1}$. From Eq. (14) we deduce that the large range of N_{i} (10^{-3} to $10^6\,\mathrm{L}^{-1}$) obtained for these nucleation events must be due to a large range in $J_{\max}$. If the differences in μ among the nucleation events can be ignored, at a chosen temperature N_{i} depends solely on $J_{\max}$, which depends solely on $\triangle S$. In fact, setting $\mu = 0.05\,\mathrm{s}^{-1}$ and $T_0 = 195\,\mathrm{K}$ in Eqs. (14) and (16) we obtain a functional dependence of N_{i} on $\triangle S$ (the solid curve in Fig. 7a) that fits the numerical data well. The error that results from assuming constant μ is further discussed in Sect. 5.2.

For the special case of a temperature-limit event, the partial pressure of water vapour can be approximated as constant during the nucleation event for $t_0 < t < t_0 + \tau$, and so

$$\triangle S \approx -\frac{S_0 L_{\mathrm{s}}}{R_{\mathrm{v}} T_0^2}\triangle T, \quad (18)$$

where $\triangle T$ is the change in temperature during the nucleation event defined in Eq. (9), L_{s} is the latent heat of sublimation, and R_{v} is the gas constant of water vapour. With $\mu = 0.05\,\mathrm{s}^{-1}$ and $T_0 = 195\,\mathrm{K}$, from Eqs. (14)–(18) we obtain the solid curve in Fig. 7b that captures the dependence of N_{i} on $\triangle T$ as suggested by the simulations of temperature-limit events.

5.2 Sensitivity of INC to nucleation temperature and deposition coefficient

Using the formulae derived in Sect. 5.1 we can now explain the sensitivity of the numerical results to T_0 and the deposition coefficient α. The analytic functions of N_{i}-versus-$\triangle S$ and N_{i}-versus-$\triangle T$ vary with T_0 (because $a_{\mathrm{w}}^{\mathrm{i}}$ depends on T_0, recall Eq. 16). If μ is assumed constant, the analytic functions are independent of the deposition coefficient α. As described further below, the assumption of constant μ gives consistent result with the numerical data for temperature-limit events but tends to overestimate INCs for vapour-limit events at larger T_0 and/or larger α.

For $\alpha = 0.1$, Fig. 8a shows that the analytic function of N_{i}-versus-$\triangle S$ is consistent with the numerical data, except for vapour-limit events at $T_0 = 210\,\mathrm{K}$ that produce more than $10^4\,\mathrm{L}^{-1}$ ice crystals. This error arises because μ has been assumed to be constant ($\mu = 0.05\,\mathrm{s}^{-1}$) and independent of $\triangle S$ in the calculation of the analytic curve. The error is larger for larger temperature.

For $\alpha = 1$, the analytic function of N_{i}-versus-$\triangle S$ also overestimates N_{i} for vapour-limit events (Fig. 9a). We again attribute this error to the assumption that μ is constant over the shown range of $\triangle S$. The deposition coefficient governs the growth rate of ice crystals and affects how the saturation ratio changes with time and how μ changes with $\triangle S$ (a consequence of Eq. 17). Our calculation indicates that the rate of change of μ with respect to $\triangle S$ increases with α. For larger values of α, calculation of N_{i} (especially for vapour-limit events) must account for the variations in μ as $\triangle S$ varies.

Let us now study the variation of N_{i} with respect to $\triangle T$ (Figs. 8b and 9b). Recall that the function of N_{i} with respect to $\triangle T$ is derived by neglecting the depletion of water vapour due to ice depositional growth (see Eq. 18). For all values of T_0 and α tested here, the analytic function with constant μ explains well the pattern of N_{i}-versus-$\triangle T$ for temperature-limit events. For vapour-limit events, the analytic curves in Figs. 8b and 9b overestimate the numerical solution because of (i) the neglect of water vapour depletion in Eq. (18) and (ii) the assumption of constant μ.

5.3 Dependence of INC on the initial water vapour mixing ratio

The temperature time series $T(t)$ along the trajectory of an air parcel (recall Eq. 5) and the initial water vapour content r_0 of the parcel are two independent conditions to be specified for the simulations. The initial water vapour content r_0 has a one-to-one relationship with the temperature at the threshold of nucleation T_0 via Eq. (4). In Sect. 4 we have studied how the INC varies with the various forms of $T(t)$ for a *given* r_0 and a corresponding T_0. Here, however, we discuss how the INC varies as r_0 and T_0 vary for a *given* $T(t)$.

Now, consider air parcels with slightly different initial water vapour mixing ratios: r_0 and $r_0 + \delta r_0$. The nucleation temperatures for these air parcels are respectively T_0 and $T_0 + \delta T_0$ (see illustration in Figs. 3 and 10). For constant pressure, δr_0 and δT_0 are related by

$$\frac{\delta r_0}{r_0} = \frac{\delta e_{\mathrm{sat}}}{e_{\mathrm{sat}}} + \frac{1}{S_0}\frac{\mathrm{d}S_0}{\mathrm{d}T_0}\delta T_0 = \frac{L_{\mathrm{s}}}{R_{\mathrm{v}} T_0^2}\delta T_0 + \frac{1}{S_0}\frac{\mathrm{d}S_0}{\mathrm{d}T_0}\delta T_0 \quad (19)$$

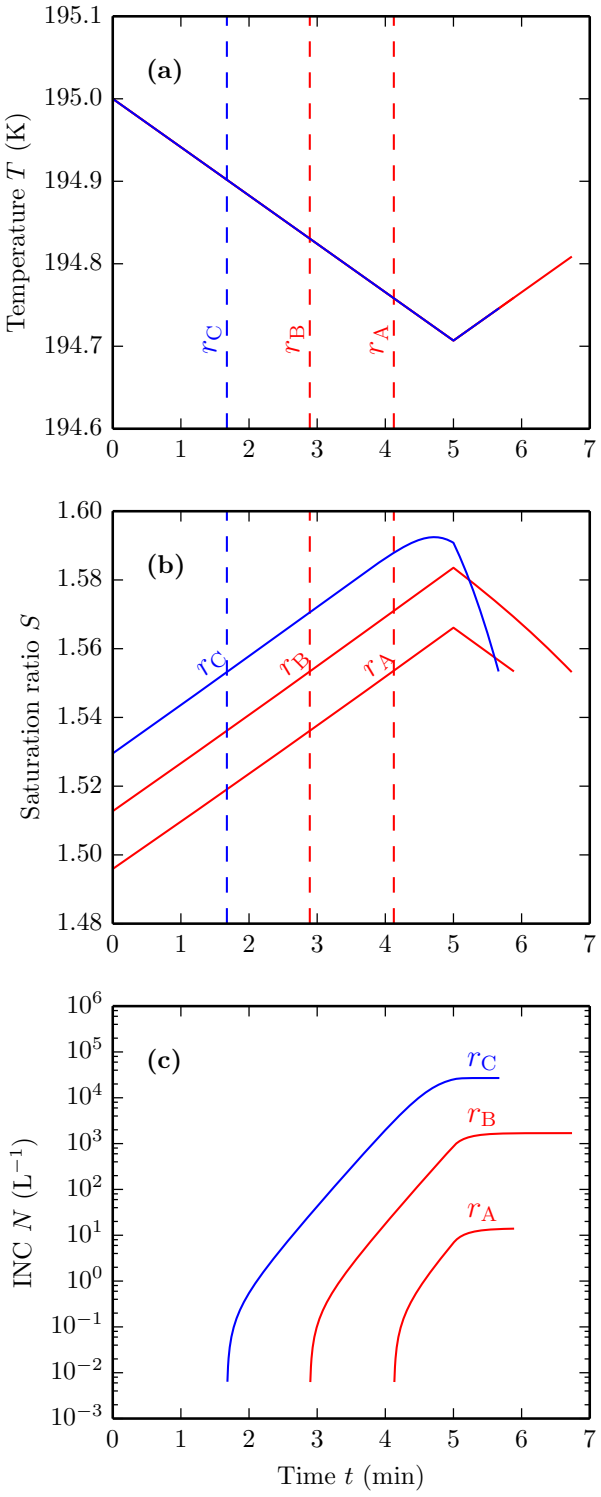

Figure 10. Evolution of temperature **(a)**, saturation ratio **(b)**, and INC **(c)** for three air parcels with slightly different initial water vapour mixing ratios: $\{r_A = 1.78;\ r_B = 1.80;\ r_C = 1.82\} \times 10^{-5}\,\mathrm{kg\,kg^{-1}}$. The parcels follow the same temperature time series as shown in **(a)**, but they begin nucleation at different times (indicated by the dash lines) and end up with widely different INCs.

by Eq. (4) and the Clausius–Clapeyron relation. The first term dominates the right-hand side of Eq. (19), from which we obtain

$$\frac{\mathrm{d}T_0}{\mathrm{d}r_0} \approx \frac{R_v T_0^2}{L_s r_0}, \tag{20}$$

which indicates that T_0 increases monotonically with r_0. For a given temperature time series $T(t)$, the minimum temperature $T_{\min}$ experienced by the parcels is the same (see Fig. 10). It follows that $|\triangle T| = T_0 - T_{\min}$ increases monotonically with r_0. For temperature-limit events, N_i increases exponentially with $|\triangle T|$ (recall Fig. 7 and Eq. 18), and so it must increase exponentially with r_0. As r_0 increases, N_i increases until reaching a limit above which the nucleation event must be vapour limit (see e.g. Fig. 7). Thus, for a given temperature time series, r_0 controls N_i and also determines whether the nucleation event is temperature or vapour limit.

For example, consider a temperature time series defined by a cooling rate associated with $w = +0.1\,\mathrm{m\,s^{-1}}$ between $t = 0$ and $t_s = 5\,\mathrm{min}$, and a warming rate associated with $w = -0.1\,\mathrm{m\,s^{-1}}$ after t_s (see Fig. 10). This temperature time series is similar to the profiles we have studied earlier in Sect. 4.2. Consider three air parcels following this temperature time series, but for which $r_0 = \{1.78;\ 1.80;\ 1.82\} \times 10^{-5}\,\mathrm{kg\,kg^{-1}}$. All three air parcels experience nucleation, and in all cases $T_{\min} = 194.71\,\mathrm{K}$ occurs during the nucleation periods. However, our calculations give $T_0 = \{194.76;\ 194.83;\ 194.90\}\,\mathrm{K}$ and $N_i = \{1.4 \times 10^1;\ 1.7 \times 10^3;\ 2.7 \times 10^4\}\,\mathrm{L^{-1}}$ respectively for the three parcels. Moreover, the two drier air parcels experience temperature-limit nucleation events (red lines in Fig. 10), whereas the moist air parcel experiences a vapour-limit event (blue line in Fig. 10). As illustrated here, small differences in r_0 result in many orders of magnitude changes in N_i. Such a strong dependence of N_i on r_0 could explain the large-amplitude, small-scale heterogeneities in the INC as observed in cirrus clouds by Jensen et al. (2013).

6 Conclusions

We have simulated homogeneous ice nucleation using temperature time series data collected at high frequency by long-duration balloon flights near the tropical tropopause. The simulated nucleation events can be conceptually categorised as either vapour limit or temperature limit. For vapour-limit events, nucleation is limited by the depletion of water vapour. In contrast, for temperature-limit events, nucleation is controlled by the fluctuations in temperature (while the depletion in water vapour is negligible). The INC obtained for temperature-limit events is typically smaller than that obtained for vapour-limit events.

Our calculations of temperature-limit events confirm the finding by Spichtinger and Krämer (2013) that high-frequency fluctuations in temperature may limit the INC obtained by homogeneous freezing. Indeed, a small INC is ob-

tained if the gravity waves produce large but non-persistent cooling rates such that the absolute drop in temperature (i.e. the difference between the temperature at the threshold of nucleation and the minimum temperature obtained during nucleation) remains small. This relationship between the INC and temperature has been illustrated here both numerically and analytically.

In addition to the fluctuations in temperature, small variations in the initial water vapour content of the air parcels can also lead to large variations in the INC obtained by nucleation. Moreover, post-nucleation processes acting during the cirrus life cycle contribute to modify the cloud original characteristics. Simulations of cirrus clouds in the TTL by Dinh et al. (2012, 2014) show that the INC decreases by several orders of magnitude as the cloud ages. For these reasons, we suggest that homogeneous ice nucleation (even acting alone in the absence of heterogeneous freezing) is not inconsistent with recent observations of cirrus clouds in the TTL that indicate generally low but highly variable INC (Jensen et al., 2013).

Finally, it is encouraging that the INC for temperature-limit events does not depend on the deposition coefficient, a parameter still poorly constrained by theoretical understanding as well as laboratory measurements and field observations.

Acknowledgements. The data used for simulations in this work were collected during the project "Concordiasi," which is supported by the following agencies: Météo-France, CNES, CNRS/INSU, NSF, NCAR, University of Wyoming, Purdue University, University of Colorado, Alfred Wegener Institute, Met Office, and ECMWF. Concordiasi also benefited from the logistic and financial support of the Institut polaire français Paul Emile Victor (IPEV), Programma Nazionale di Ricerche in Antartide (PNRA), United States Antarctic Program (USAP), British Antarctic Survey (BAS), and from measurements by the Baseline Surface Radiation Network (BSRN) at Concordia.

Tra Dinh acknowledges support from the NOAA Climate and Global Change Postdoctoral Fellowship Program and NSF grant AGS-1417659. This collaborative research emerged from Tra Dinh's visit to the Laboratoire de Météorologie Dynamique, which was supported by the "Tropical Cirrus" project of École Polytechnique's "Chaire pour le Développement Durable". Aurélien Podglajen, Albert Hertzog, Bernard Legras, and Riwal Plougonven received support from the ANR project "Stradyvarius" (ANR-13-BS06-0011-01). Additional support was provided by the EU 7th Framework Program under grant 603557 (StratoClim).

The authors would like to thank three anonymous reviewers and Martina Krämer, Bernd Kärcher, and Daniel Knopf for helpful questions and comments that led to significant improvements of this work.

Edited by: M. Krämer

References

Barahona, D. and Nenes, A.: Parameterization of cirrus cloud formation in large-scale models: Homogeneous nucleation, J. Geophys. Res., 113, D11211, doi:10.1029/2007JD009355, 2008.

Barahona, D. and Nenes, A.: Dynamical states of low temperature cirrus, Atmos. Chem. Phys., 11, 3757–3771, doi:10.5194/acp-11-3757-2011, 2011.

Boccara, G., Hertzog, A., Vincent, R. A., and Vial, F.: Estimation of gravity-wave momentum fluxes and phase speeds from quasi-Lagrangian stratospheric balloon flights. Part I: Theory and simulations, J. Atmos. Sci., 65, 3042–3055, doi:10.1175/2008JAS2709.1, 2008.

Brewer, A. W.: Evidence for a world circulation provided by the measurements of helium and water vapour distribution in the stratosphere, Q. J. Roy. Meteorol. Soc., 75, 351–363, doi:10.1002/qj.49707532603, 1949.

Chen, Y., Kreidenweis, S. M., McInnes, L. M., Rogers, D. C., and DeMott, P. J.: Single particle analyses of ice nucleating aerosols in the upper troposphere and lower stratosphere, Geophys. Res. Lett., 25, 1391–1394, doi:10.1029/97GL03261, 1998.

Corti, T., Luo, B. P., Fu, Q., Vömel, H., and Peter, T.: The impact of cirrus clouds on tropical troposphere-to-stratosphere transport, Atmos. Chem. Phys., 6, 2539–2547, doi:10.5194/acp-6-2539-2006, 2006.

Davis, S., Hlavka, D., Jensen, E., Rosenlof, K., Yang, Q., Schmidt, S., Borrmann, S., Frey, W., Lawson, P., Voemel, H., and Bui, T. P.: In situ and lidar observations of tropopause subvisible cirrus clouds during TC4, J. Geophys. Res., 115, D00J17, doi:10.1029/2009JD013093, 2010.

Dinh, T. and Durran, D. R.: A hybrid bin scheme to solve the condensation/evaporation equation using a cubic distribution function, Atmos. Chem. Phys., 12, 1003–1011, doi:10.5194/acp-12-1003-2012, 2012.

Dinh, T. and Fueglistaler, S.: Cirrus, Transport, and Mixing in the Tropical Upper Troposphere, J. Atmos. Sci., 71, 1339–1352, doi:10.1175/JAS-D-13-0147.1, 2014a.

Dinh, T. and Fueglistaler, S.: Microphysical, radiative and dynamical impacts of thin cirrus clouds on humidity in the tropical tropopause layer and stratosphere, Geophys. Res. Lett., 41, 6949–6955, doi:10.1002/2014GL061289, 2014b.

Dinh, T., Durran, D. R., and Ackerman, T.: Cirrus and water vapor transport in the tropical tropopause layer – Part 1: A specific case modeling study, Atmos. Chem. Phys., 12, 9799–9815, doi:10.5194/acp-12-9799-2012, 2012.

Dinh, T., Fueglistaler, S., Durran, D., and Ackerman, T.: Cirrus and water vapour transport in the tropical tropopause layer – Part 2: Roles of ice nucleation and sedimentation, cloud dynamics, and moisture conditions, Atmos. Chem. Phys., 14, 12225–12236, doi:10.5194/acp-14-12225-2014, 2014.

Fueglistaler, S., Dessler, A. E., Dunkerton, T. J., Folkins, I., Fu, Q., and Mote, P. W.: Tropical tropopause layer, Rev. Geophys., 47, RG1004, doi:10.1029/2008RG000267, 2009.

Hermann, M., Zahn, A., Heinrich, G., and Brenninkmeijer, C. A. M.: Meridional distributions of aerosol particle number concentrations in the upper troposphere and lower stratosphere obtained by Civil Aircraft for Regular Investigation of the Atmosphere Based on an Instrument Container (CARIBIC) flights, J. Geophys. Res., 108, 4114, doi:10.1029/2001JD001077, 2003.

Jensen, E. J., Toon, O. B., Pfister, L., and Selkirk, H. B.: Dehydration of the upper troposphere and lower stratosphere by subvisible cirrus clouds near the tropical tropopause, Geophys. Res. Lett., 23, 825–828, doi:10.1029/96GL00722, 1996.

Jensen, E. J., Pfister, L., Bui, T.-P., Lawson, P., and Baumgardner, D.: Ice nucleation and cloud microphysical properties in tropical tropopause layer cirrus, Atmos. Chem. Phys., 10, 1369–1384, doi:10.5194/acp-10-1369-2010, 2010.

Jensen, E. J., Pfister, L., and Bui, T. P.: Physical processes controlling ice concentrations in cold cirrus near the tropical tropopause, J. Geophys. Res., 117, D11205, doi:10.1029/2011JD017319, 2012.

Jensen, E. J., Diskin, G., Lawson, R. P., Lance, S., Bui, T. P., Hlavka, D., McGill, M., Pfister, L., Toon, O. B., and Gao, R.: Ice nucleation and dehydration in the Tropical Tropopause Layer, P. Natl. Acad. Sci., 110, 2041–2046, doi:10.1073/pnas.1217104110, 2013.

Kärcher, B. and Lohmann, U.: A parameterization of cirrus cloud formation: Homogeneous freezing of supercooled aerosols, J. Geophys. Res., 107, 4010, doi:10.1029/2001JD000470, 2002.

Kärcher, B., Dörnbrack, A., and Sölch, I.: Supersaturation Variability and Cirrus Ice Crystal Size Distributions, J. Atmos. Sci., 71, 2905–2926, doi:10.1175/JAS-D-13-0404.1, 2014.

Koop, T. and Zobrist, B.: Parameterizations for ice nucleation in biological and atmospheric systems, Phys. Chem. Chem. Phys., 11, 10839–10850, doi:10.1039/b914289d, 2009.

Koop, T., Luo, B., Tsias, A., and Peter, T.: Water activity as the determinant for homogeneous ice nucleation in aqueous solutions, Nature, 406, 611–614, doi:10.1038/35020537, 2000.

Krämer, M., Schiller, C., Afchine, A., Bauer, R., Gensch, I., Mangold, A., Schlicht, S., Spelten, N., Sitnikov, N., Borrmann, S., de Reus, M., and Spichtinger, P.: Ice supersaturations and cirrus cloud crystal numbers, Atmos. Chem. Phys., 9, 3505–3522, doi:10.5194/acp-9-3505-2009, 2009.

Lawson, R. P., Pilson, B., Baker, B., Mo, Q., Jensen, E., Pfister, L., and Bui, P.: Aircraft measurements of microphysical properties of subvisible cirrus in the tropical tropopause layer, Atmos. Chem. Phys., 8, 1609–1620, doi:10.5194/acp-8-1609-2008, 2008.

Lohmann, U. and Roeckner, E.: Influence of cirrus cloud radiative forcing on climate and climate sensitivity in a general circulation model, J. Geophys. Res., 100, 16305, doi:10.1029/95JD01383, 1995.

Magee, N., Moyle, A. M., and Lamb, D.: Experimental determination of the deposition coefficient of small cirrus-like ice crystals near −50 Celsius, Geophys. Res. Lett., 33, L17813, doi:10.1029/2006GL026665, 2006.

Massman, W. J.: On the nature of vertical oscillations of constant volume balloons, J. Appl. Meteorol., 17, 1351–1356, doi:10.1175/1520-0450(1978)017<1351:OTNOVO>2.0.CO;2, 1978.

Murphy, D. M.: Rare temperature histories and cirrus ice number density in a parcel and a one-dimensional model, Atmos. Chem. Phys., 14, 13013–13022, doi:10.5194/acp-14-13013-2014, 2014.

Murphy, D. M. and Koop, T.: Review of the vapour pressures of ice and supercooled water for atmospheric applications, Q. J. Roy. Meteorol. Soc., 131, 1539–1565, doi:10.1256/qj.04.94, 2005.

Nastrom, G. D.: The response of superpressure balloons to gravity waves, J. Appl. Meteorol., 19, 1013–1019, doi:10.1175/1520-0450(1980)019<1013:TROSBT>2.0.CO;2, 1980.

Podglajen, A., Hertzog, A., Plougonven, R., and Žagar, N.: Assessment of the accuracy of (re)analyses in the equatorial lower stratosphere, J. Geophys. Res., 119, 11,166–11,188, doi:10.1002/2014JD021849, 2014.

Pruppacher, H. R. and Klett, J. D.: Microphysics of clouds and precipitation, D. Reidel Publishing Company, Dordrecht, the Netherlands, 1978.

Rabier, F., Bouchard, A., Brun, E., Doerenbecher, A., Guedj, S., Guidard, V., Karbou, F., Peuch, V.-H., Amraoui, L. E., Puech, D., Genthon, C., Picard, G., Town, M., Hertzog, A., Vial, F., Cocquerez, P., Cohn, S. A., Hock, T., Fox, J., Cole, H., Parsons, D., Powers, J., Romberg, K., VanAndel, J., Deshler, T., Mercer, J., Haase, J. S., Avallone, L., Kalnajs, L., and Mechoso, C. R.: The Concordiasi project in Antarctica, B. Am. Meteorol. Soc., 91, 69–86, doi:10.1175/2009bams2764.1, 2010.

Ren, C. and Mackenzie, A. R.: Cirrus parametrization and the role of ice nuclei, Q. J. Roy. Meteorol. Soc., 131, 1585–1605, doi:10.1256/qj.04.126, 2005.

Rogers, D. C., Demott, P. J., Kreidenweis, S. M., and Chen, Y.: Measurements of ice nucleating aerosols during SUCCESS, Geophys. Res. Lett., 25, 1383–1386, doi:10.1029/97GL03478, 1998.

Shi, X., Liu, X., and Zhang, K.: Effects of preexisting ice crystals on cirrus clouds and comparison between different ice nucleation parameterizations with the Community Atmosphere Model (CAM5), Atmos. Chem. Phys., 15, 1503–1520, doi:10.5194/acp-15-1503-2015, 2015.

Skrotzki, J., Connolly, P., Schnaiter, M., Saathoff, H., Möhler, O., Wagner, R., Niemand, M., Ebert, V., and Leisner, T.: The accommodation coefficient of water molecules on ice – cirrus cloud studies at the AIDA simulation chamber, Atmos. Chem. Phys., 13, 4451–4466, doi:10.5194/acp-13-4451-2013, 2013.

Spichtinger, P. and Krämer, M.: Tropical tropopause ice clouds: a dynamic approach to the mystery of low crystal numbers, Atmos. Chem. Phys., 13, 9801–9818, doi:10.5194/acp-13-9801-2013, 2013.

Vincent, R. A. and Hertzog, A.: The response of superpressure balloons to gravity wave motions, Atmos. Meas. Tech., 7, 1043–1055, doi:10.5194/amt-7-1043-2014, 2014.

3.2.3 Discussion

Main results and limitations The paper clarified the role of high-frequency temperature fluctuations in the homogeneous nucleation process. It confirmed that *high-frequency waves* indeed had time scales comparable to the ice nucleation time scale, so that they can *quench nucleation events through the reincrease of temperature during nucleation.* An analytical formula was derived which could be used to parameterize that effect in models.

However, *the model set-up used did not include ice sedimentation.* As a consequence, no comparison with observed ICN (Ice Crystal Number) could be made, nor any assertion on the relevance of quenched nucleation events to explain ICN concentrations. Different studies (e.g. *Jensen et al.*, 2012; *Murphy*, 2014) have shown the major impact of sedimentation on ice concentration statistics. In particular, *Murphy* (2014) argued that *accounting for sedimentation could cancel the tendency of producing higher ice crystal numbers at lower temperature that is seen in the parcel models* and thus help reconcile simulations and observations. Figure 3.4, reproduced from *Murphy* (2014), illustrates this result. Those studies show that ignoring sedimentation renders impossible any direct comparison with observations of ICN.

Initially aimed at more realism through the use of observed fluctuations, our study was in the end limited to the analysis of the two nucleation regimes. Both were shown to occur in the TTL, but no quantitative inference on cirrus clouds microphysical properties could be made.

An insight to understand observations Nevertheless, the study provides insights to interpret observations. In particular, quenched nucleation events might explain the spikes of high ice crystal number concentration that were encountered in TTL cirrus during ATTREX. Figure 3.5, reproduced from *Jensen et al.* (2013), shows an aircraft encounter of those spikes. Over spatial scales of a few tens of meters, the ICNs are seen to vary by three order of magnitudes.

In appendix B.1, I examine different explanations for the very high gradients in ICN observed during ATTREX. From that analysis, the most plausible conclusion is that *quenched nucleation events combined with small heterogeneities in the water vapor content are responsible for the observed heterogeneities in ICN.* In that case, the spikes in ice crystal number concentration are an observational argument supporting the existence of quenched homogeneous nucleation events. As shown in *Dinh et al.* (2016), those quenched nucleation events may also generate low ICNs. However, testing the compatibility of homogeneous nucleation theories with ice concentration statistics requires a model including ice sedimentation.

Follow-up study After the study by *Dinh et al.* (2016), we participated in another study (*Jensen et al.*, 2016) who investigated the processes with a more realistic model set-up, including ice sedimentation. The model used solves the microphysics in a 1-D vertical curtain following a Lagrangian trajectory calculated at a given altitude. *Jensen et al.* (2016) used the same temperature fluctuations time series derived from the superpressure balloons. Figurhe 3.6 is taken from that study and shows the ice concentration statistics obtained from parcel model simulations using the balloons temperature fluctuations and the parameterization of *Jensen and Pfister* (2004). The balloons measurements were point measurements so they could not be directly incorporated in a 1-D set-up, but *Jensen and Pfister* (2004) parameterization is 1-D. Hence, the figure shows that:

- the simulations using balloon temperature time series (green curve) generate more ice crystals than those using *Jensen and Pfister* (2004) parameterization of T fluctuations

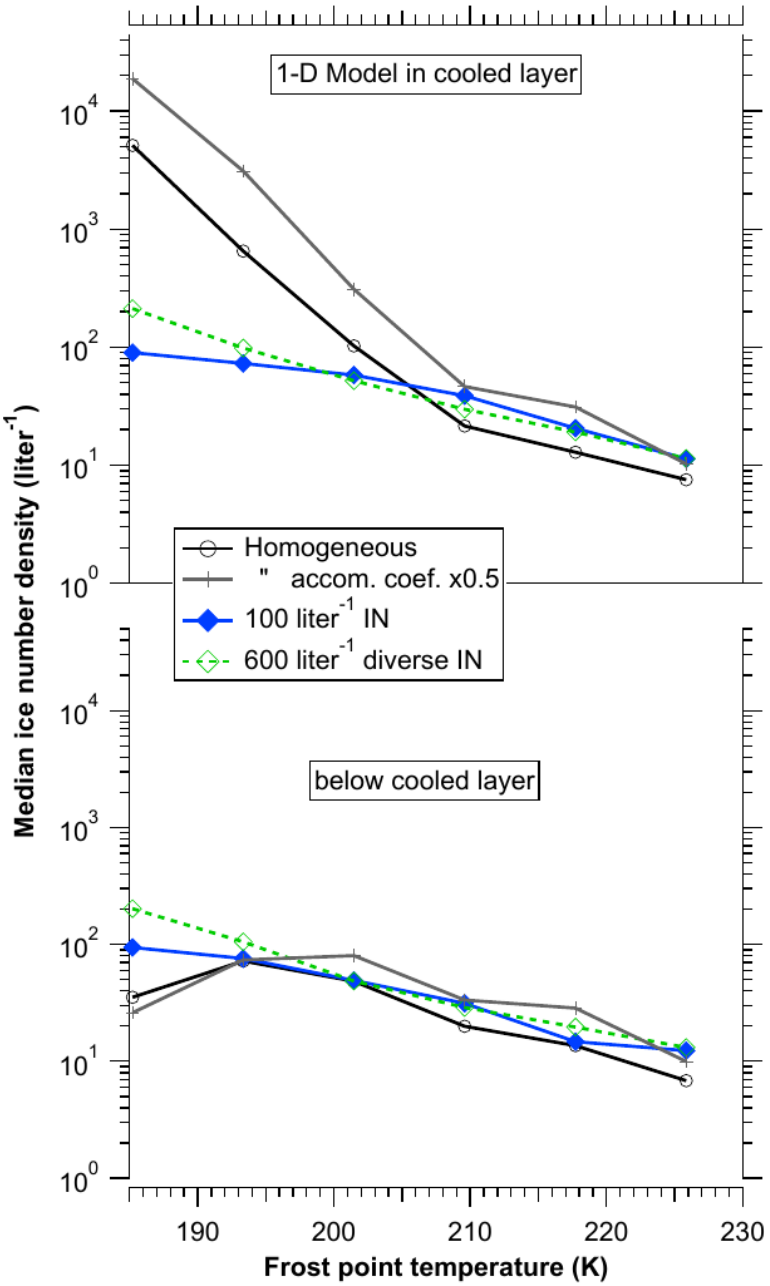

Figure 3.4 – Results from 1-dimensional microphysical simulations by *Murphy* (2014). The top panel shows the ICN statistics as a function of temperature in a region where temperature fluctuations are imposed and nucleation occurs. Simulations with homogeneous nucleation only, and homogeneous nucleation and heterogeneous nucleation with variable Ice Nuclei concentrations are shown, and the striking different behaviors with temperature can be identified. The bottom panel shows the ice concentration statistics in a region that does not experience nucleation but in which fall streaks from the cloud above sediment. In that region, the tendency (seen in the homogeneous only case) of the ICN to be larger at low temperature disappears, and the differences induced by the presence of ice nuclei are reduced.

(blue curve). This is consistent with the fact that higher w are found in observations than in the parameterization (as shown in the previous chapter).

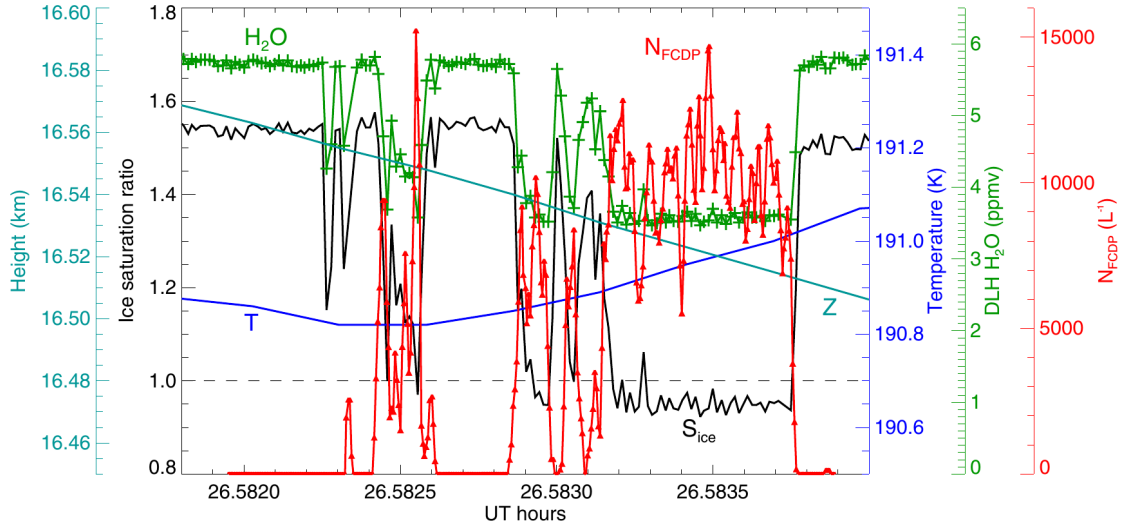

Figure 3.5 – In situ measurements of water vapor (green), temperature (blue), relative humidity (or ice saturation ratio, black) and cirrus ice crystal number (red) from aircraft observations in the TTL during ATTREX. Twenty-hertz water vapor and cloud particle concentration data are shown, such that every point on those curves is distant from the next one by less than 10 m. From *Jensen et al.* (2013).

- inclusion of ice sedimentation using *Jensen and Pfister* (2004) waves reduces the ICN (cyan curve versus blue curve) but not sufficiently to match the observed ice concentration statistics (black curve)

The most plausible implication is that realistic balloon time series combined with sedimentation would produce ice concentrations larger than those shown by the cyan curve and hence exceed by far the observations.

Although *Jensen et al.* (2016) did find occurrences of temperature limited (or quenched) nucleation events, the observed Ice Concentration Statistics are not compatible with simulations including only homogeneous nucleation and sedimentation. Quenched nucleation events are not sufficient to reconcile models and observations, and other processes probably need to be taken into account. However, the two studies both stress the importance of temperature fluctuations for microphysical modeling in the TTL, and the overwhelming impact of uncertainties in their parameterization.

Concluding remarks The problem of ice formation in the tropical UTLS is still unsettled. However, the study shows that:

- High-frequency temperature fluctuations due to gravity waves are among the key processes, and uncertainties in their parameterization induce first order uncertainties in modeling ice cloud microphysical properties.

- Quenched homogeneous nucleation is a relevant process and needs to be accounted for. However, other key phenomena are probably necessary to explain and model cirrus with realistic microphysical properties. Microphysical (heterogeneous nucleation or non conventional homogeneous nucleation) and dynamical processes (mixing, radiation, shear) are likely candidates.

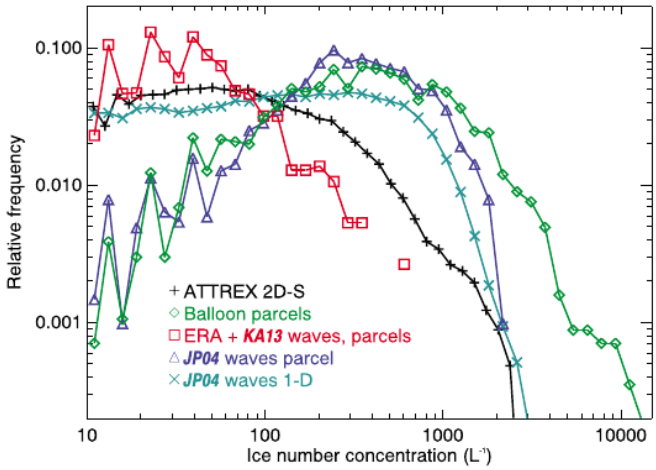

Figure 3.6 – TTL cirrus ice concentration frequency distributions from ATTREX 2D-S measurements (black curve); parcel model simulations using superpressure balloon temperature time series (green curve); parcel model simulations using ERA-interim trajectories (red curve); parcel model simulations with the *Jensen and Pfister* (2004) wave perturbations (blue curve), and one-dimensional simulations using ERA temperature curtains with *Jensen et al.* (2016) waves (cyan curve). From *Jensen et al.* (2016).

As we have seen in Chapters 1 and 2, gravity waves do not only induce temperature fluctuations, they also structure the wind. Hence, they can also have an influence on the advection and transport of ice crystals, potentially interacting with sedimentation. This problem is examined in the next section of the chapter.

3.3 Interaction between equatorial or gravity waves and sedimentation of ice crystals: impact on water transport

INTRODUCTION

Waves have long been reckoned to interact with cirrus clouds, in particular TTL cirrus, through temperature fluctuations. High frequency waves influence the cooling rates and cirrus formation. Low frequency waves influence the temperature and occurrence of supersaturation. Here, we examine the potential for a wave-induced transport of ice particles associated with wave vertical wind disturbances.

3.3.1 Theory

In general, the (irreversible) transport induced by linear waves is associated with the second-order Stokes drift (e.g. *Andrews et al.*, 1987). For internal gravity waves or for equatorial Kelvin waves under the Boussinesq approximation (neglecting the decrease of density with altitude), that Stokes drift term cancels out[3]. There is no mean transport of a purely Lagrangian tracer by a linear internal gravity wave. However, ice crystals (or aerosols) are *NOT* purely Lagrangian tracers. In the vertical, they fall relative to the surrounding air. Since the wave phase generally propagates downward (if the energy is to propagate up), the falling particles are moving in the same direction as the wave phase. If the particle falls at the same

[3]This is not the case when compressibility effects are not neglected (*Coy et al.*, 1986).

speed as the wave propagates downward, then there could be a systematic[4] effect of the wave presence on the mean particle motion.

In the following, we use a simple 2D framework with the wind and temperature structure of a monochromatic wave[5] to examine the potential effects of the wave on ice crystals transport.

3.3.1.1 Constant size particle

First, consider the case of a constant size particle (for instance an ice crystal in a 100% relative humidity environment), which is assumed horizontally Lagrangian but with a downward sedimentation speed $v_{sed} > 0$. The evolution of the particle's position X, Z is then given by:

$$\frac{\mathrm{d}X}{\mathrm{d}t} = U\cos(kX + mZ - \omega t + \phi) \tag{3.6}$$

$$\frac{\mathrm{d}Z}{\mathrm{d}t} = W\cos(kX + mZ - \omega t + \phi + \delta\phi) - v_{sed} \tag{3.7}$$

$$\tag{3.8}$$

where U and W are the amplitude of the wave in horizontal and vertical wind respectively, ω is the frequency, k the horizontal wavenumber, m the vertical wavenumber and ϕ the wave phase. For a gravity wave in the midfrequency range ($f \ll \omega \ll N$ with f the local Coriolis frequency and N the Brunt-Väisälä frequency), or in the vertical-zonal plane for an equatorial Kelvin wave, the polarization relations give:

$$W = -\frac{k}{m}U \text{ and } \delta\phi = 0. \tag{3.9}$$

Then, there is an analytical formula for the vertical trajectory $Z(t)$ of a particle with initial position X_0, Z_0:

$$Z(t) = \frac{W}{\omega + mv_{sed}}\left[\sin((\omega + mv_{sed})t)\cos(\phi_0) + \sin(\phi_0)(1 - \cos((\omega + mv_{sed})t))\right] - v_{sed}t + Z_0 \tag{3.10}$$

with $\phi_0 = kX_0 + mZ_0 + \phi$. This analytical solution highlights the difference with a no-wave case, which would simply give $Z_{\text{nowave}}(t) = -v_{sed}t + Z_0$, but also with a Lagrangian air parcel, whose vertical position is given by $Z_{\text{parcel}}(t) = \frac{W}{\omega}\sin(\omega t - (\phi + \phi_0)) + Z_0$.

Gravity waves in the upper troposphere mostly propagate upward from lower levels: their group velocity is positive, which implies that their vertical phase speed $c_{\phi_z} = \frac{\omega}{m}$ is negative (*Fritts and Alexander*, 2003). In the following, we take the convention $\omega > 0$ so that a negative vertical phase speed is associated with $m < 0$. Depending on the ratio between $\frac{\omega}{m}$ and v_{sed}, one sees that different cases may arise. If $|\frac{\omega}{m}| \gg v_{sed}$, the particles follow the air parcels and oscillate vertically. The particles are close to perfectly Lagrangian, and there is not net effect of the wave. If $|\frac{\omega}{m}| \ll v_{sed}$, the particles travel in a stationary wave field, i.e. through positive and negative wave phases, whose contributions cancel out. The interesting interaction appears when $\frac{\omega}{m}$ and v_{sed} are of the same order: then, as $\omega + mv_{sed} < \omega$ and $\omega + mv_{sed} > mv_{sed}$, the variations seen by the particles have longer periods than those seen by air parcels or by particles falling in a stationary wave field; this is due to the fact that the particles travel in the same direction as the wave phase. In particular, when $\frac{\omega}{m} \simeq -v_{sed}$, one has:

$$Z(t) \simeq (W\cos(\phi_0) - v_{sed})\,t + Z_0 \tag{3.11}$$

[4] i.e. an effect non reversible after one period.

[5] within an unsheared background $\frac{\mathrm{d}\bar{u}}{\mathrm{d}z} = 0$.

and thus the wave can bring a significant contribution to the displacement of the crystal, a contribution which does not cancel out after one wave period. Furthermore, such a configuration could significantly increase the lifetime of the ice crystals.

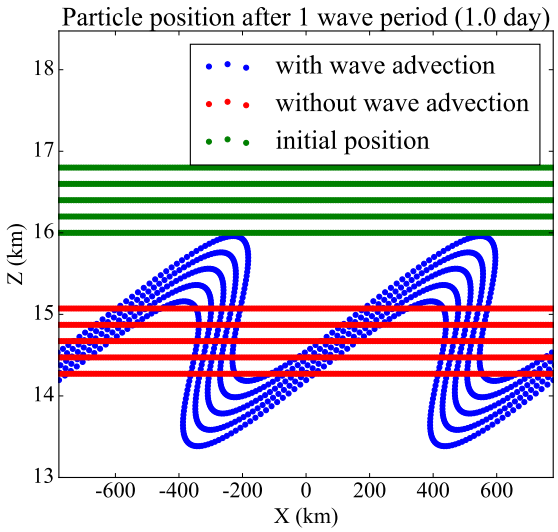

Figure 3.7 – Evolution of particle position after being advected by the wave field during one wave period. See text for details on the wave characteristics.

For illustration, we show the effect of a monochromatic wave on the vertical motion of the falling particles in a special configuration in Figure 3.7. We assume that the particles fall at a constant speed of 2 cm/s (equivalent to a $\simeq 20$ μm-diameter spherical ice particle). The wave is chosen with a period $T = \frac{2\pi}{\omega} \simeq 1$ day, a shallow vertical wavelength $\lambda_z = \frac{2\pi}{m} = 4$ km. The chosen squared Brunt-Väisälä frequency is $N^2 = 2 \cdot 10^{-4}$ rad^2/s^2, i.e. intermediate between stratosphere and the troposphere as expected for the transition region of the TTL. The horizontal wavelength is prescribed from the dispersion relation: $\lambda_x = \frac{2\pi}{k} = \frac{2\pi}{\frac{m\omega}{N}} \simeq 800$ km. The amplitude of the Eulerian temperature perturbation is $A_T = 1$ K, so that the vertical velocity amplitude is equal to:

$$W = \frac{g}{N^2}\omega\frac{A_T}{\bar{T}} \simeq 2 \text{ cm/s} \tag{3.12}$$

with $g = 9.81$ m s^{-2}, $\bar{T} = 185$ K, while $U = \frac{|m|}{k}W \simeq 3.7$ m/s. Overall, the chosen wave characteristics are similar to those of equatorial and gravity waves commonly observed in radiosondes in the tropical UTLS (e.g. *Kim and Alexander*, 2015). Figure 3.7 shows the position of the particles after one wave period, so that all meteorological fields have returned to their original value and air parcels to their original positions (green dots). On the contrary, particles have descended in altitude due to sedimentation. Without the wave, the particles would just have moved down at a constant speed (red dots). In the presence of the wave, however, they are significantly dispersed (blue dots) due to the advection by the vertical and horizontal winds. Thus, there can be a significant impact of the wave, although we did *not* select its characteristics to obtain it. In particular, it is worth noting that the wave amplitude is not overestimated: it is consistent with observations and we have also checked that the resulting monochromatic wave field is stable (see discussion in Appendix B.2).

Figure 3.7 shows that, if particles are of constant size, there is no mean effect of the wave on their downward transport. The only impact is to disperse the particles vertically:

while some particles fall more slowly due to the presence of the wave, others fall more rapidly. *Which of the two (increased or suppressed fall of the particles) will prevail when crystal growth is included?*

3.3.1.2 Growing and sublimating ice crystals

Statement of the problem and governing equations Now that we have explored the impact of wave advection on particle transport, we turn to the case of ice crystals which can grow and sublimate, exchanging water molecules with their environment. Assuming spherical shapes, the rate of growth of the crystal radius r is given by *Pruppacher and Klett* (1978):

$$\frac{\mathrm{d}r}{\mathrm{d}t} = \frac{G'(r,T)}{r}(RH_i - 1) \tag{3.13}$$

with $RH_i = \frac{q}{q_{\mathrm{sat}}}$ the relative humidity with respect to ice and $G'(r,T)$ the growth factor, a function of temperature and the crystal size r:

$$G'(r,T) = \frac{1}{\rho_{\mathrm{ice}}\left(\frac{R_v T}{e_{\mathrm{sat}}(T) D'_v(r,T)} + \frac{L_s}{T k'_a(r,T)}\left(\frac{L_s}{T R_v} - 1\right)\right)} \tag{3.14}$$

where $\rho_{\mathrm{ice}} \simeq 918$ kg/m^3 is the density of ice, D'_v is the modified diffusivity of water vapor in air, k'_a is the modified thermal conductivity of air, $R_v = 462$ J/K/kg is the perfect gas constant for water vapor and $L_s = 2.844 \cdot 10^6$ J/kg is the latent heat of sublimation of ice. The modified diffusivity D'_v can be expressed as the product of the diffusivity $D_v(T)$ and the ventilation (for large ice crystals) and non equilibrium correction (for small ice crystals) coefficients $f_{v,d}(r,T)$ and $f_{v,k}$. Similarly, the modified thermal conductivity k'_a is the product the conductivity $k_a(T)$ and the coefficients $f_{k,d}$ and $f_{k,k}$:

$$\begin{aligned} D'_v &= D_v(T) f_{v,d}(r,T) f_{v,k}(r,T;\alpha_d) \\ k'_a &= k_a(T) f_{k,d}(r,T) f_{k,k}(r,T;\alpha_d) \end{aligned} \tag{3.15}$$

Expressions for the f coefficients can be found in *Pruppacher and Klett* (1978). The coefficients $f_{.,k}$ depend not only on temperature and crystal size but also on the deposition coefficient α_d. α_d represents the fraction of water molecules colliding with the ice surface that effectively get incorporated into the ice crystal lattice. Its exact value is not known, and it could well depend on supersaturation and temperature and take any value from 0.001 to 1. Up to now, experimental studies have not been very helpful in constraining α_d (e.g. *Magee et al.*, 2006; *Skrotzki et al.*, 2013). However, atmospheric cloud observations are hard to reconcile with α_d values smaller than about 0.5 (e.g. *Kärcher and Lohmann*, 2002; *Kay and Wood*, 2008). In the following, we assume $\alpha_d = 0.5$. With such large deposition coefficients ($\alpha_d \geq 0.5$), one has $D'_v \simeq D_v(T)$ and $k'_a \simeq k_a(T)$ for intermediate crystal sizes ($r \simeq 5$ to 50 μm), so that G' is a function of T only.

Introducing $G = 2G'$, the rate of growth of the squared radius r^2, the governing equations for the evolution of the ice crystal size and position in the wave field are:

$$\begin{aligned} \frac{\mathrm{d}r^2}{\mathrm{d}t} &= G(r, T(X,Z,t))(RH_i(X,Z,t) - 1) \\ \frac{\mathrm{d}X}{\mathrm{d}t} &= U\cos(kX + mZ - \omega t + \phi) \\ \frac{\mathrm{d}Z}{\mathrm{d}t} &= W\cos(kX + mZ - \omega t + \phi) - v_{sed}(r) \end{aligned} \tag{3.16}$$

The trajectories of the crystals stop when r reaches 0 (total sublimation).

Since we still assume a monochromatic wave, the temperature is the sum of the equilibrium level temperature $\bar{Z}$ plus the temperature change due to adiabatic compression/decompression during the air vertical displacement Z_{wave}. It is given by:

$$T(x,z,t) = \underbrace{-\frac{g}{C_p} Z_{\text{wave}}(x,z,t)}_{\Delta T_{\text{wave}}} + \bar{T}(\bar{Z}(x,z,t)) \tag{3.17}$$

with

$$\begin{aligned} Z_{\text{wave}}(x,z,t) &= -\frac{W}{\omega}\sin(kx+mz-\omega t+\Phi) \\ \bar{Z}(x,z,t) &= z - Z_{\text{wave}}(x,z,t) \end{aligned} \tag{3.18}$$

For the pressure P, which is needed to evaluate the saturation mixing ratio $q_{\text{sat}} = \frac{e_{\text{sat}}(T)}{P}$, we assume hydrostatic equilibrium in the reference state $\bar{P}$ and neglect the pressure perturbations induced by the wave: $P(x,z,t) = \bar{P}(z)$.

Finally, the water vapor mixing ratio is estimated assuming that the crystals do *not* significantly deplete the water vapor content, which is conserved following the air parcel. This last assumption will allow to reveal the wave-sedimentation interactions more clearly. Although crude, it is not too unrealistic in TTL cirrus, where low ice crystal number clouds can occur[6] (*Krämer et al.*, 2009; *Jensen et al.*, 2013). Furthermore, we assume that in the reference state the water vapor mixing ratio depends only on the vertical position, so that the water vapor mixing ratio at any position and time is given by:

$$q(x,z,t) = \bar{q}(\bar{Z}(x,z,t)) \tag{3.19}$$

The previous set of equations are the base for the simulations presented in the next section. For the sedimentation speed v_{sed} of the spherical ice crystal, it can be expressed assuming Stokes flow:

$$v_{sed} = \underbrace{\frac{2}{9}\frac{\rho_{\text{ice}} g}{\mu}}_{\alpha_{\text{sed}(\bar{T})}} r^2. \tag{3.20}$$

This formula disregards Cunningham correction, which takes into account the non-continuum nature of the fluid for small particles and can be significant for particles smaller than about $5\,\mu$m. At the other end of the size spectrum, for particles larger than about 100 μm, the Stokes flow hypothesis is no longer valid and Equation (3.20) overestimates the sedimentation speed. In the full simulations, we use the formulas provided in *Pruppacher and Klett* (1978), which are based on dimensional analysis and experimental fits, to evaluate the Reynolds number from the Best number and then deduce the fall velocity of the particles. However, for the theoretical analysis presented below, we will use the Stokes formula (Equation (3.20)) in order to simplify the algebra.

System analysis Besides the above assumptions, for the theoretical analysis below, we consider a few additional simplifications. First, that the relative humidity of the reference state is constant with altitude, so that:

$$\bar{q}(z) = RH_{i_c}\, q_{\text{stat}}(\bar{T}(z), \bar{P}(z)) \tag{3.21}$$

[6] *Krämer et al.* (2009) have argued that the relaxation time for thin, low ICN TTL cirrus could be larger than a few hours

with $RH_{i_c}(z)$ taken as a constant RH_{i_c}. This allows to retain the main characteristic of water vapor variability in the TTL, i.e. its decrease with altitude due to the decrease in saturation vapor pressure. Second, we linearize the relative humidity term to retain only the essential oscillatory behavior (a strong assumption given the non linearity of the saturation vapor pressure, but enlightening):

$$RH_{i_{\text{wave}}}(x,z,t) \simeq RH_{i_c}(\bar{Z})\left(1 - \frac{L_s}{R_v\bar{T}^2}\Delta T_{\text{wave}} - \frac{g}{R_g\bar{T}}Z_{\text{wave}}\right) = RH_{i_c}(\bar{Z}) + RH_{i_c}(\bar{Z})\underbrace{\left(\frac{L_s}{R_v\bar{T}^2}\frac{g}{C_p} - \frac{g}{R_g\bar{T}}\right)}_{\beta_G,\text{ only dependent on }\bar{T}} Z_{\text{wave}} \quad (3.22)$$

Finally, we keep only the dependence on $\bar{T}(z)$ in G, which hence depends only on z. This might induce some quantitative change, but the qualitative impact will be marginal.

Under those approximations[7], System (3.16) can be rearranged into two ordinary differential equations for the wave phase $\Psi = kX + mZ - \omega t + \phi$ along the ice crystal trajectory and for the squared radius of the particle r^2, namely:

$$\begin{cases} \dfrac{\mathrm{d}r^2}{\mathrm{d}t} = G\left(\underbrace{-\dfrac{W}{\omega}\beta_G}_{\alpha_g} RH_{i_c}\sin(\Psi) + RH_{i_c} - 1\right) \\ \dfrac{\mathrm{d}\Psi}{\mathrm{d}t} = -(\omega + m\underbrace{v_{\text{sed}}}_{\alpha_{\text{sed}}r^2}) \end{cases} \quad (3.23)$$

This last set of equations reveals the simple properties of the system studied. It can be seen that the system has critical-fixed points provided that $\frac{\omega}{m} < 0$ [8] (since $v_{\text{sed}} > 0$) and that $(|\alpha_g| + 1)RH_{i_c} \geq 1$. Then, there are 1 or 2 fixed points (depending if it is an equality or a strict inequality in the previous equation), given by:

$$\begin{cases} r_f^2 = -\dfrac{\omega}{m\alpha_{\text{sed}}} \\ \sin(\Psi_f) = \dfrac{\omega}{W\beta_G}\dfrac{RH_{i_c}-1}{RH_{i_c}} = -\dfrac{1}{\alpha_g}\dfrac{RH_{i_c}-1}{RH_{i_c}} \end{cases} \quad (3.24)$$

Note that the second equation of this system corresponds to two possible fixed points in the wave phase space, since $\sin(\Psi_f) = \sin(\pi - \Psi_f)$. The Jacobian matrix at the critical points is:

$$J = \begin{pmatrix} 0 & -G\beta_G\frac{W}{\omega}RH_{i_c}\cos(\Psi_f) \\ -m\alpha_{\text{sed}} & 0 \end{pmatrix} \quad (3.25)$$

and its eigenvalues are:

$$\lambda^2 = \frac{W}{\frac{\omega}{m}}\alpha_{\text{sed}}\beta_G G\, RH_{i_c}\cos(\Psi_f) = \pm\frac{W}{\frac{\omega}{m}}\alpha_{\text{sed}}\beta_G G\, RH_{i_c}\sqrt{1 - \left(\frac{RH_{i_c}-1}{RH_{i_c}}\frac{\omega}{W\beta_G}\right)^2} \quad (3.26)$$

with the plus sign corresponding to the fixed point Ψ_f in $\left[-\frac{\pi}{2}, \frac{\pi}{2}\right]$, i.e. $\cos(\Psi_f) > 0$ whereas

[7] Given that $RH_{i_c}(\bar{Z}) = RH_{i_c}$

[8] This condition is satisfied for upward propagating wave packets, with $c_{g_z} > 0$.

Table 3.1 – Wave and background state characteristics assumed for the sedimentation-growth simulations reported in this section. $\bar{N}$: background Brunt-Väisälä frequency, $\frac{2\pi}{\omega}$: wave period, λ_z wave vertical wavelength, A_T: wave (Eulerian) temperature T amplitude, A_w: wave vertical wind W amplitude, A_u: wave zonal wind amplitude, $c_{\phi_z} = \frac{\omega}{m}$: wave vertical phase speed.

$\bar{N}^2$	$\frac{2\pi}{\omega}$	λ_z	A_T	A_w	A_u	c_{ϕ_z}
$2{\cdot}10^{-4}$ rad^2/s^2	2 days	4 km	$\sim$ 1.7 K	1.57 cm/s	6 m/s	-2.3 cm/s

the minus is for $\cos(\Psi_f) < 0$. The fixed point with $W\cos(\Psi_f) < 0$ (the phase during which $w < 0$) is associated with two opposite sign eigenvalues, and is hence a saddle point. On the contrary, the other fixed point (the one for which $w = W\cos(\Psi_f) > 0$) corresponds a cycle with two opposite imaginary parts.

Numerical analysis Figure 3.8 shows two numerical integrations of System (3.23) with different background relative humidity RH_{i_c}. To perform those, small crystals (from 1 to 10 microns) have been initialized at different initial positions (phases). The characteristics of the wave and of the background state that have been used in this simulation will also be assumed in the remainder of the study and are summarized in Table 3.1. Although the wave amplitude may seem large, it is consistent with the large events that regularly occur in the TTL, as observed by *Kim and Alexander* (2013). In particular, one specific wave event observed near Guam during ATTREX, which will be studied in Chapter 5, was observed to induce larger zonal wind and temperature fluctuations, with amplitude and period comparable to those of the wave chosen here.

In Figure 3.8, we note the "stable" fixed points and the existence of closed orbits near that fixed point, which also corresponds to the cooling phase of the wave. The crystals thus remain in a specific phase of the wave near the fixed point. Furthermore, the figure emphasizes that crystals initially placed in the negative temperature gradient region will tend to grow and leave that region to move into the negative temperature region, spending some time on the way in the cooling phase of the wave.

Physical understanding The existence of those two different fixed points can be easily understood physically. At the "cycle" (stable) fixed point, if ice crystals fall below the equilibrium point, they fall into subsaturated air and sublimate, which reduces their mass and their fall velocity. They fall more slowly and are caught up again by the equilibrium wave phase which is also descending. On the contrary, if ice crystals get lighter, they will fall more slowly than the wave phase and get transported into supersaturated regions where they grow, increasing their weight and fall speed and moving them back into the equilibrium phase. The trajectory of an ice crystals in altitude-time space around the "cycle" fixed point is shown in Figure 3.9, to illustrate the previous explanation.

At the "saddle" fixed point, the opposite feedback is acting with subsaturated air above and supersaturated air below, so that the crystals move further away from this equilibrium point.

We note that, given this tendency of some of the crystals to stay near the thermodynamic equilibrium phase of the wave ($RH_i = 100\%$), there is possibly a net impact of the wave on the particles' vertical displacement. Indeed, at the "stable" fixed point, those crystals will endure a constant wave-induced horizontal velocity $U\cos(\Psi_f)$ and a constant vertical velocity $W\cos(\Psi_f)$. Since the stable fixed point is the one for which $W\cos(\Psi_f) > 0$, the consequence is that sedimentation is slowed down by wave advection.

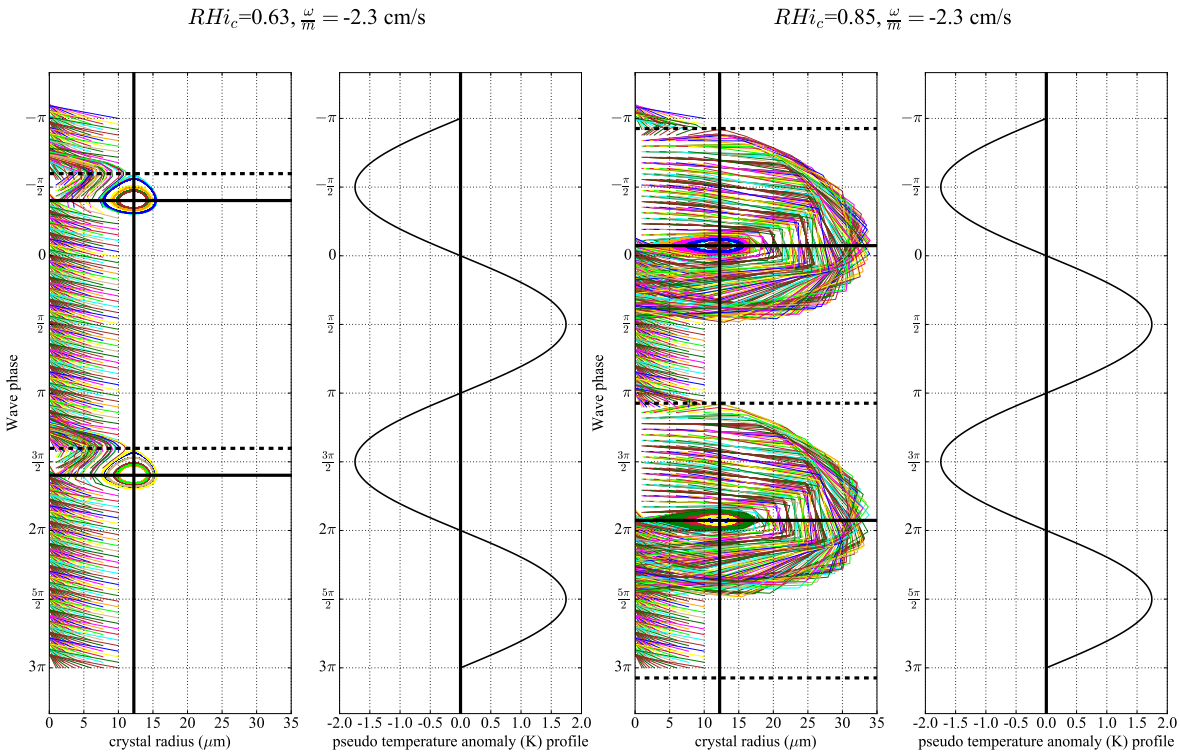

Figure 3.8 – Representation in the $\Psi - r$ phase space of numerical integrations of System (3.23), for a background state mean temperature $\bar{T} = 195$ K and mean pressure $\bar{P} = 120$ hPa. The figure shows results of the integrations for 2 different mean background relative humidities, a dry case on the left ($RH_{ic} = 0.63$) and a moister case ($RH_{ic} = 0.85$) on the right.

Moist versus dry environments Figure 3.8 displays numerical integrations for two background relative humidities, a moist and a dry scenario. The goal is here to identify geographic differences, motivated by observations. Indeed, as presented in the first chapter of this dissertation, a recent observational study by *Kim et al.* (2016) has shown that the relationship between TTL cirrus clouds and temperature anomalies during boreal winter time were different between the tropical Eastern and Western Pacific. In the Eastern Pacific, TTL cirrus are tied to the cold phases of the waves. In the Western Pacific, cirrus are more frequent in the negative temperature gradient phase, the supposed cooling phase of the waves in the upper TTL. However, results from the previous chapter using PreConcordiasi balloon observations suggest that the lower frequency waves responsible for the temperature fluctuations do not show a strong geographic variability within the equatorial region. *Kim et al.* (2016) also do not report a strong difference in the temperature variability between the Eastern and the Western Pacific. If the difference does not reside in wave amplitudes, another possible explanation would be that it is due to different mean relative humidities, the convective Western Pacific being moister on average than the dry Eastern Pacific.

I note that a simple explanation for the difference is that in a moist environment smaller temperature perturbations are required for ice nucleation than in a dry environment. Hence, ice formation may happen in the cooling phase of the wave in the moist regions while only the coldest wave phases provide sufficient supersaturation for nucleation in the dry Eastern Pacific. This explanation is not entirely satisfactory since it does not take into account the life cycle of the ice crystals. Figure 3.8 illustrates an alternative, related explanation accounting for the different wave-cirrus relationship in a different relative humidity environment. In the dry environment, the “stable” fixed point is located near the cold phase of the wave while

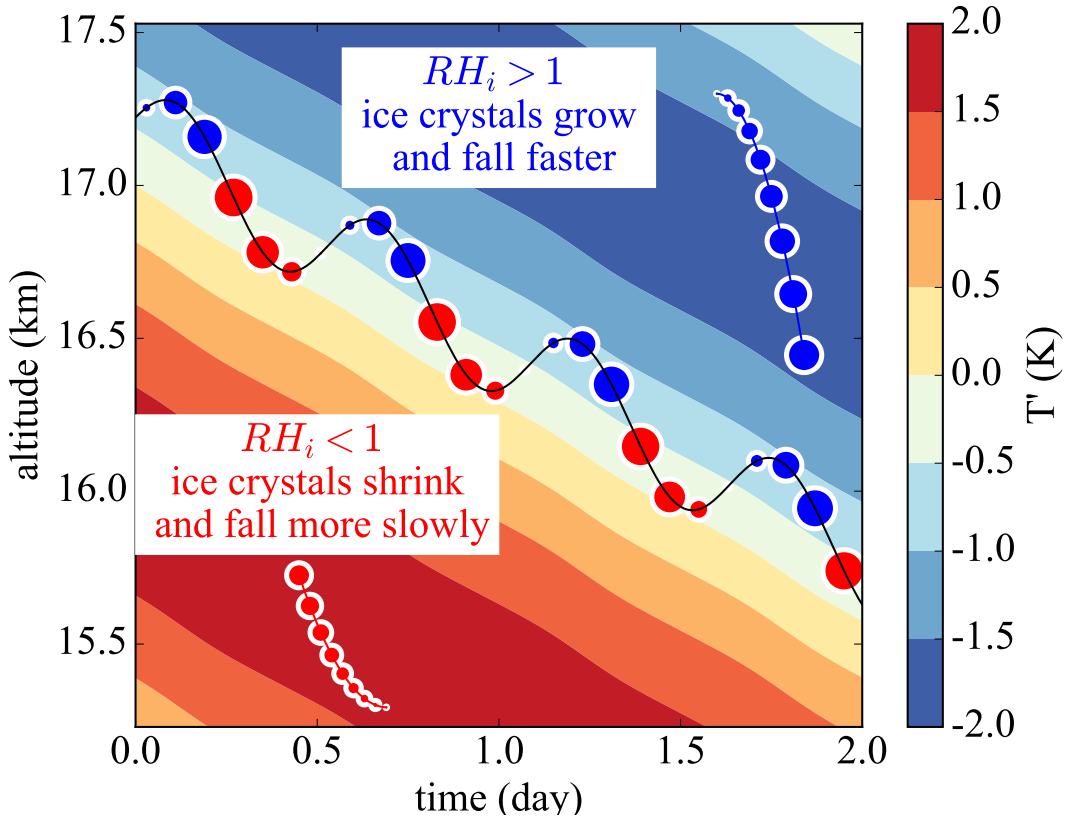

Figure 3.9 – Representation in altitude-time space of an ice crystal trajectory in the moist ($RH_{ic} = 0.85$) simulations. The colors correspond to the temperature anomalies induced by the wave, which also correspond to relative humidity anomalies. The black line corresponds to the ice crystal trajectory and the circular markers represent the ice crystal size. Blue circles indicate growing ice crystals ($RH_i > 1.$) whereas red circles indicate sublimating ice crystals. Idealized trajectories of growing (blue) and sublimating (red) crystals in constant RH_i backgrounds are also shown for a pedagogic purpose in the upper right and lower left corners.

in the moist environment it is in the cooling phase of the wave. This causes a preferential location of ice crystals and clouds, due to the interaction of sedimentation and growth with the wave field.

3.3.1.3 Full simulations

We now present numerical simulations of System 3.16. The set-up is the same as in the idealized system (constant background relative humidity and idealized wave). However, the full equations are solved, and the dependency of the microphysical parameters on the varying background temperature and pressure are included. We still assume that there are few ice crystals, i.e. there is no water consumption. The goal is to extend the analysis of the simplified system, to check whether the expected patterns of cloud occurrence in preferred wave phases appear, and to illustrate the impact of wave advection of transport. For that purpose, a population of ice crystals with radius 5 μm is initialized in all phases of the idealized wave. They then grow or sublimate depending on the environment relative humidity. Sublimated ice crystals are irremediably lost, while the others continue their trajectories down to the bottom of the domain.

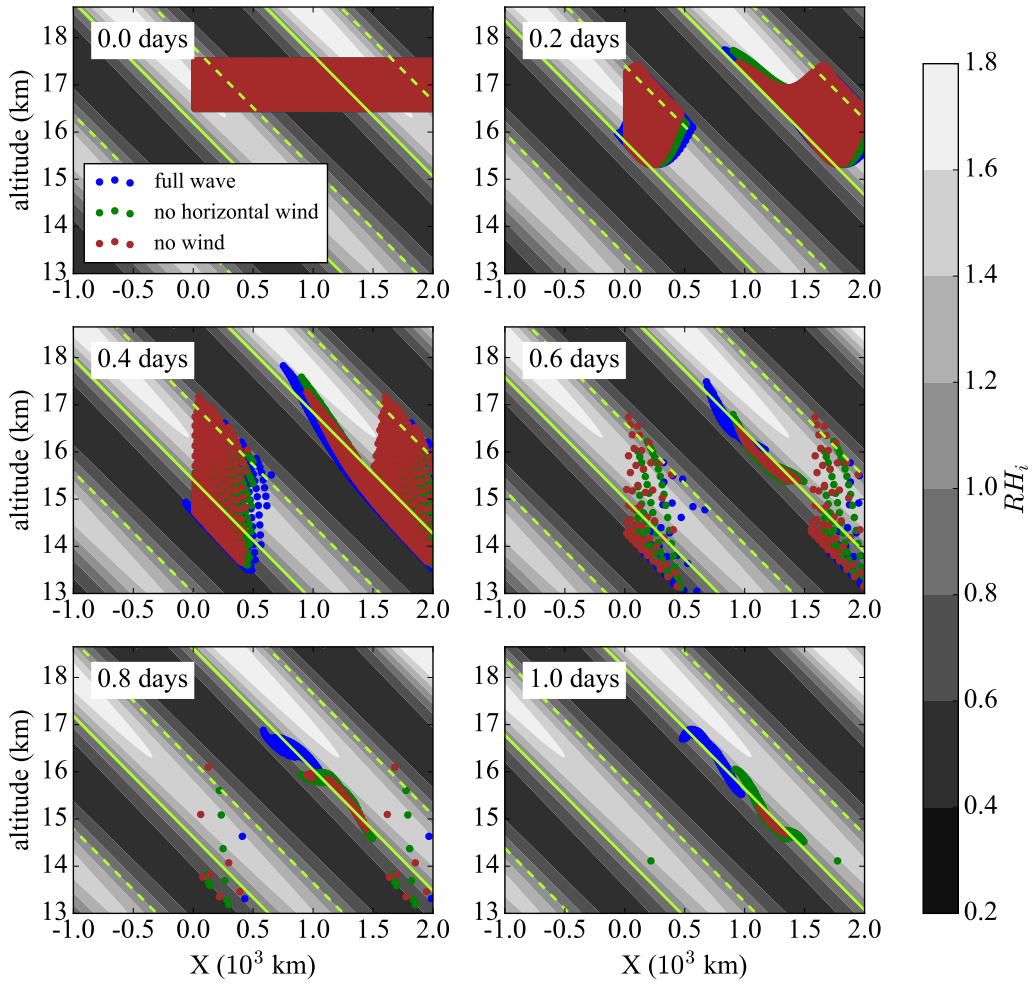

Figure 3.10 – Simulations of ice crystal growth and sedimentation in an idealized wave field at $RH_{i_c} = 85\%$. Different integration times are displayed, up to half a wave period, i.e. one day. The colored dots correspond to the position of the ice crystals. The different colors correspond to simulations with different processes (un)accounted for: the blue dots are the ice crystals' positions for the full simulation (wave advection and temperature fluctuations), for the green dots the horizontal wind of the wave has been neglected and for the maroon dots both the horizontal and vertical winds induced by the wave have been neglected. The light green lines correspond to the locations of the "stable" fixed points (continuous line) and the saddle points (dashed), for both of those $RH_i = 100\%$. The initial ice crystal radius used for all crystals is 5 μm.

Figure 3.10 displays the results of a simulation at $RH_{i_c} = 85\%$, integrated during one day. The ice crystals are initialized with a radius of 5 μm around 17 km in different horizontal positions spanning all the phases of the wave. The different colors correspond to simulations accounting for wave advection or not, and will be discussed later.

Consistent with the analysis of the simplified system in the previous section (see Figure 3.8), three types of behaviors of the ice crystals are evident in Figure 3.10:

- Ice crystals initialized in (highly) subsaturated regions ($RH_i < 70\%$, black in Fig-

ure 3.10) quickly sublimate.

- Ice crystals initialized in supersaturated regions below the saddle point grow and fall across the $RH_i = 100\%$ region (the "stable" fixed point) to sublimate below it, about half a vertical wavelength below their initial position.
- Ice crystals initialized near "stable" the fixed point ($RH_i \sim 100\%$) tend to stay in the same wave phase and fall more slowly.

The last group of ice crystals is interesting, since they remain in the TTL a significant amount of time after their formation. The qualitative behavior between the full ice crystals trajectories and the simplified system are similar, what about the sensitivity of the ice crystal population to the background relative humidity?

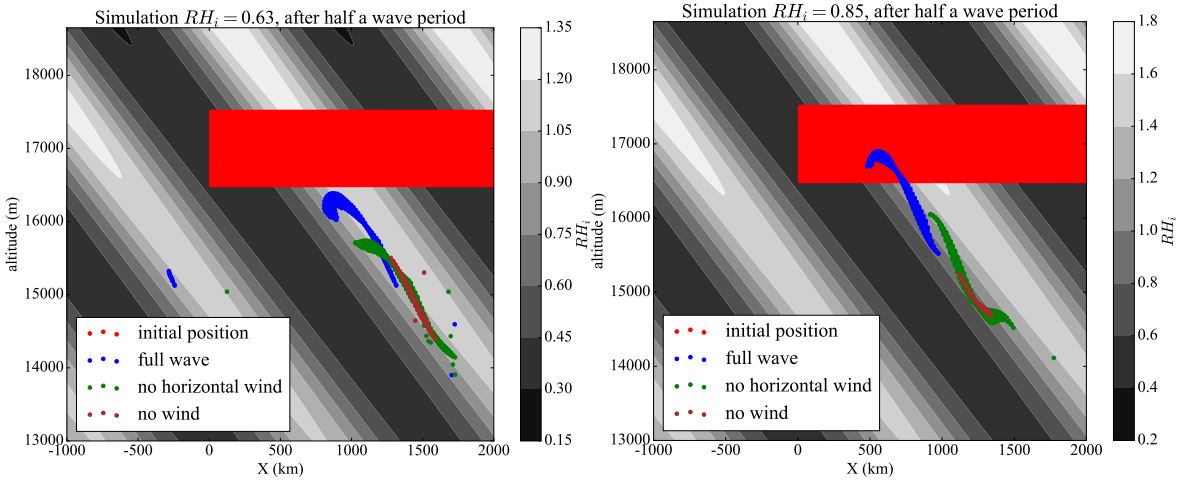

Figure 3.11 – Simulation of ice crystal growth and sedimentation in an idealized wave field at (left) RH_{i_c} = 63% and (right) RH_{i_c} = 85%, after half a wave period, i.e. one day. The colored dots correspond to the position of the ice crystals. The different colors correspond to simulations with different processes (un)accounted for: the blue dots are the ice crystals' positions for the full simulation (wave advection and temperature fluctuations), for the green dots the horizontal wind of the wave has been neglected and for the maroon dots both the horizontal and vertical winds induced by the wave have been neglected. The initial ice crystal radius used in both cases for all crystals is 5 μm. Note how the remaining crystals tend to be regrouped in the phase of the wave with RH_i=100%.

Figure 3.11 compares the results of the previous simulation ($RH_{i_c} = 85\%$) with the dry case ($RH_{i_c} = 63\%$) after one day of integration, i.e. half a wave period. The main characteristics described in the previous subsection can already be noticed, with the remaining ice crystals preferentially encountered in the 100% relative humidity phase of the wave. This equilibrium regime near $RH_i = 100\%$ is interesting because our system, without any consumption of water vapor, shows the same equilibrium properties as parcel cloud models with interactive vapor, for which $RH_i \to 100\%$ within clouds. However, this arises here for a different reason than the crystals forcing the vapor field towards thermodynamic equilibrium with the ice phase. Here, on the contrary, the relative humidity field is forcing the ice crystals towards the regions were thermodynamic equilibrium is achieved.

In the previous section, we emphasized that ice crystals may encounter significant wave advection when they are more frequent in specific wave phases. The feedback between sedimentation and growth presented above tends to localize the remaining ice crystals preferentially in a specific wave phase. Hence, we can expect a mean impact on the downward velocity of the ice crystals. To show that more precisely, we have also performed simulations

without the wave advection. The crystals just fall, seeing the relative humidity perturbations created by the wave, but not the horizontal wind or no winds at all. The end position of the ice crystals for the different simulations are represented in Figure 3.11 by the colored dots. For the low relative humidity case ($RH_{i_c} = 63\%$), the differences between the no wind and the full simulations remain limited, which is expected since $W \cos\Psi_f < W$ in that case. Contrasting the crystal positions between the no wind and no horizontal wind simulations nevertheless reveals a tendency of the remaining ice crystals to be present at higher altitude when full wave advection is accounted for. Furthermore, contrasting the no wind case with the others show that when the crystals are exposed to slightly larger vertical winds, more of them survive and do no sublimate. In the high relative humidity set-up, the differences between the full simulations and the no wind simulations already noticed for low RH_i are enhanced: the downward sedimentation velocity of the crystals has been slowed down by almost a factor of two, due to the crystals remaining in the phase $W \cos\Psi_f \simeq W$. This is in striking contrast with the no wind or no horizontal wind case.

The differences seen between these 3 simulations suggest that **the wave advection effect is important in understanding the impact of waves on ice clouds**. Especially, it appears that **wave advection slows the descent of the ice crystals**. This suggests a mean impact of wave advection on the average dehydration efficiency of ice crystals. The downward water mass flux needed to close the water budget of the TTL may be significantly affected by the waves. However, our simulations remain idealized. Hence, we investigate the potential effect in ATTREX aircraft observations in the following subsection.

3.3.2 Quantifying the impact of wave advection on the vertical transport using observations

Due to the lack of complete description of the wave-induced wind field in the observations, it is hard (almost impossible) to evaluate the wave advection impact directly using realistic crystal trajectories. However, it is possible to use observations to estimate the average impact of wave advection on the transport of ice crystals, even if those observations are not made following the ice crystals. To do so, rather than computing the average vertical motion of ice crystals $\overline{(w' - v_{sed})}_L$, one could estimate the average ice mass vertical flux F_{ice}, defined by:

$$F_{\text{ice}} = \overline{w'\rho_{\text{ice}}} - F_{\text{sed}} \tag{3.27}$$

where the sedimentation flux F_{sed} is given by

$$F_{\text{sed}} = \int_0^{+\infty} m(r)N(r)v_{sed}(r)\mathrm{d}r \tag{3.28}$$

Assuming spherical ice crystals, $m(r) = \frac{4}{3}\pi r^3$.

In practice, the method suggested by Equation (3.27) is difficult to apply to observations, since as emphasized in the previous chapter vertical velocities are dominated by high frequency waves whose mean impact cancels out ($\overline{w'\rho_{\text{ice}}}$=0) but who will add noise to the observational estimate. To overcome these issues, a common approach is to use isentropic coordinates. This acknowledges that the efficient, irreversible dehydration occurs when ice crystals cross isentropic surfaces. Switching to isentropic coordinates θ on the vertical, the ice crystal vertical speed becomes:

$$v_\theta = v_{sed}\frac{\partial\theta}{\partial z} \tag{3.29}$$

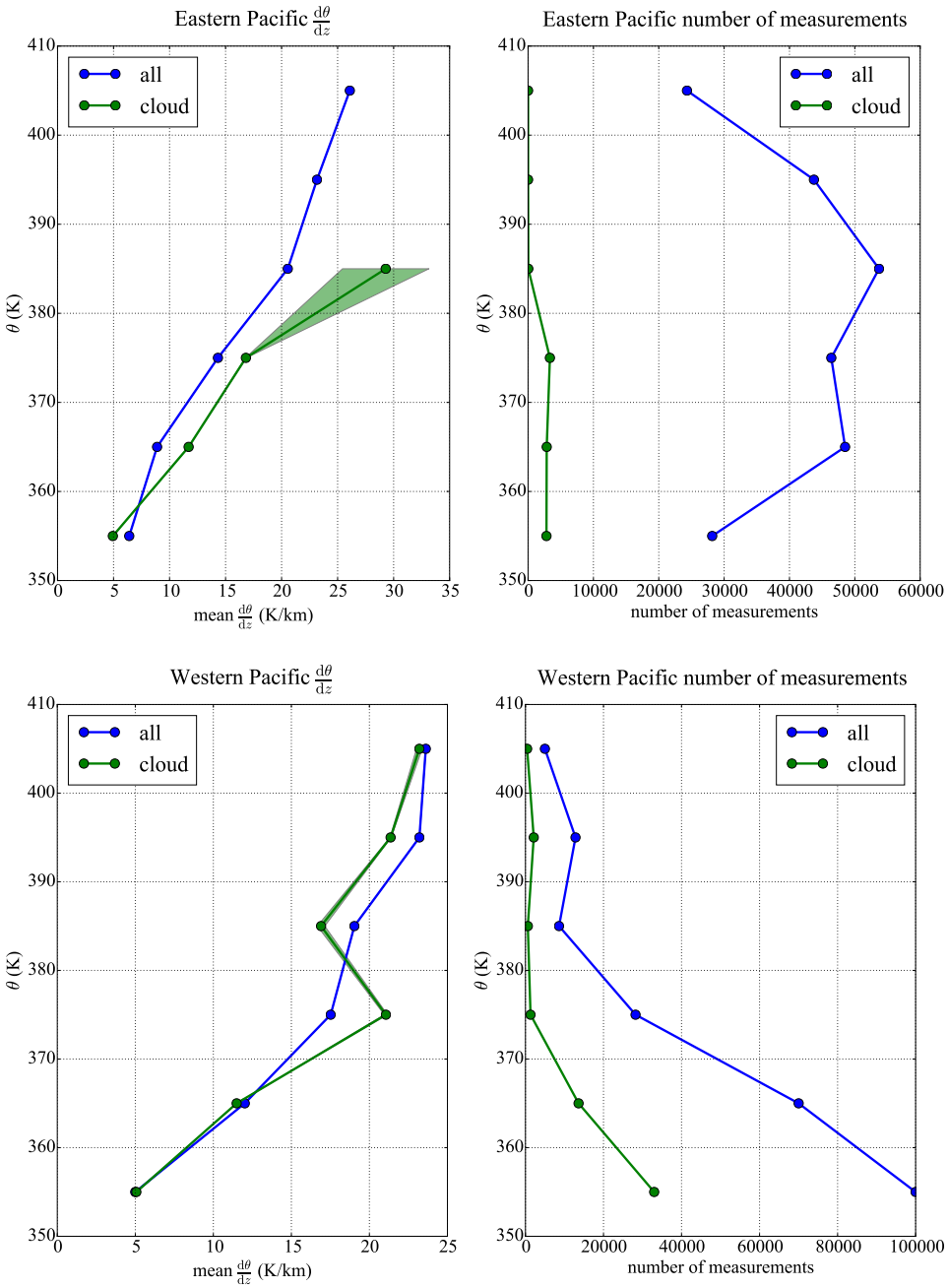

Figure 3.12 – (Left panels) Average potential temperature vertical gradient $\frac{d\theta}{dz}$ in cloudy and cloud-free air in the Eastern (top) and Western Pacific (bottom). The right panels show the total and in cloud number of measurements as a function of altitude. On the left panel, the $1-\sigma$ uncertainties are represented by shadings, but the amount of measurements is sufficient to make them indiscernible. This is nevertheless no statistical proof since the data come only from a few flights and are correlated.

The wave advection impact is then hidden in the stability impact of the wave

$$\frac{\partial\theta}{\partial z} = \underbrace{\frac{\partial\bar{\theta}}{\partial z}}_{\text{background}} + \underbrace{\frac{\partial\theta'}{\partial z}}_{\text{wave}} \tag{3.30}$$

and this can be readily computed directly from observations of vertical profiles of temperature

and ice crystals size, such as those from ATTREX campaign used by *Kim et al.* (2016).

In order to obtain an estimate of the impact of the advection of ice crystals on the vertical transport by waves, we thus turn to ATTREX observations. In both 2013 and 2014 the Global Hawk carried a Fast Cloud Droplet Probe which despite its name measured the size distribution and concentration of ice crystals from 1 to 50 microns diameter, and measured at about 1 Hz (180 m resolution). Temperature and pressure were provided at 1 Hz by the NASA Ames Meteorological Measurement System (MMS). Finally, of interest for this study, a Microwave Temperature Profiler provided estimates of the local temperature lapse rate with a resolution of about 3 km. The combination of those three instruments allows to contrast the average potential temperature vertical gradient between cloudy and cloud-free air in ATTREX observations.

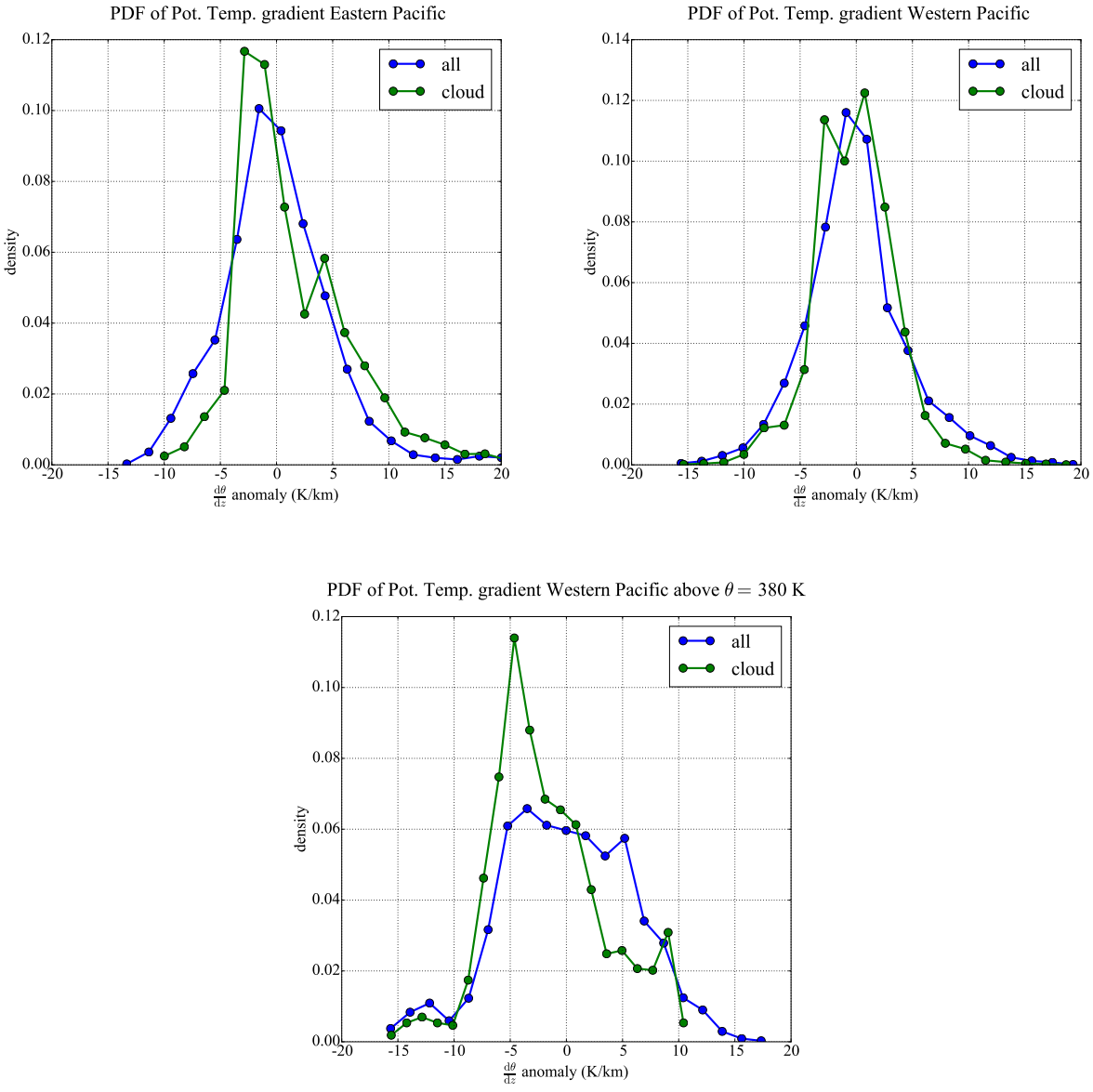

Figure 3.13 – Anomalies of stability $\left(\frac{\partial\theta}{\partial z}\right)$ distributions out of and within clouds from ATTREX observations in the (top left) Eastern Pacific, 2013 and (top right) Western Pacific, 2014. The lower panel also corresponds to the Western Pacific, but only data above the potential temperature level 380 K.

Figure 3.12 shows the mean lapse rate as a function of potential temperature, in and out of clouds. In the upper TTL (above 380 K or about 16.5 km) over the Western Pacific, the potential temperature lapse rate appears systematically lower within clouds compared to out of those, which is consistent with the results of *Kim et al.* (2016) who found anomalous negative lapse rate of wave temperature anomalies $\mathrm{d}T'/\mathrm{d}z$ within clouds. This difference between cloudy and cloud free air is robust, in particular it is larger than the vertical change of stability in the upper TTL, so that it is not due to clouds being more prevalent in the lower part of the bins where stability is weaker.

This relationship between clouds and stability is further analyzed in Figure 3.13, which presents the observed probability distribution of $\dfrac{\partial\theta'}{\partial z}$ for cloudy air versus clear air, in the Eastern and Western Pacific and in different potential temperature ranges. In the Eastern Pacific and in the Western Pacific above 380 K, Figure 3.13 shows a peak of the cloudy-air PDF in negative $\dfrac{\partial\theta'}{\partial z}$. The peak is shifted towards lower values of $\dfrac{\partial\theta'}{\partial z}$ in the Western Pacific above $\theta = 380\ K$ than in the Eastern Pacific, consistent with the results of *Kim et al.* (2016). Indeed, *Kim et al.* (2016) found that, in the Western Pacific above 15 km, most clouds were characterized by negative $\mathrm{d}T'/\mathrm{d}z$ whereas in the Eastern Pacific clouds were seen both in positive and negative $\mathrm{d}T'/\mathrm{d}z$ (see Figure 1.14 in Chapter 1). **The picture provided by Figure 3.13 is also consistent with the sensitivity to background moisture in the idealized and more realistic simulations results shown in Figures 3.8 and 3.11: in the dry Eastern Pacific, the ice crystals regroup in the minimum temperature,** $\mathrm{d}T'/\mathrm{d}z \simeq 0$ **phase of the wave. In the moister Western Pacific at high altitude, the ice crystals regroup in the** $\mathrm{d}T'/\mathrm{d}z < 0$ **phase of the wave.** In both cases, that phase is the phase where $RH_i \simeq 100\%$.

There is thus a systematic relationship between clouds and anomalies of $\dfrac{\partial\theta}{\partial z}$, which is consistent with the findings of *Kim et al.* (2016) who used a slightly different metric. This relationship suggests that there is a potential impact of wave advection. To quantify this more precisely, we use a relevant quantity for dehydration in isentropic coordinate, the cross-isentropic vertical mass flux of total water F_θ:

$$F_\theta = \rho_{\mathrm{H_2O}} \frac{\dot{\theta}}{\dfrac{\partial\theta}{\partial z}} - F_{\mathrm{sed}} = \frac{1}{\dfrac{\partial\theta}{\partial z}} \left[\rho_{\mathrm{H_2O}} \dot{\theta} - F_{\mathrm{sed}} \frac{\partial\bar{\theta}}{\partial z} - F_{\mathrm{sed}} \frac{\partial\theta'}{\partial z} \right] \tag{3.31}$$

with the term proportional to $\dot{\theta}$ corresponding to the cross-isentropic flux due to latent or radiative heating. We have here neglected eddy diffusion fluxes. *Permanent* dehydration due to cloud formation will be brought by this irreversible cross-isentropic water mass flux. The second part of the equality splits the sedimentation term into two terms, in order to emphasize its modulation by the waves through their stability impact. Strictly speaking, the impact is actually more on the radiatively driven mass flux than on the sedimentation flux. However, we apply this splitting for the purpose of illustration, since we have no estimate of the radiative heating.

Figure 3.14 represents the sedimentation flux for the whole ATTREX campaign, as well as for the Eastern and Western Pacific flights separately. It can be clearly seen that the downward flux due to sedimentation is stronger over the cold, convective Western Pacific than over the Eastern Pacific. Furthermore, the wave advection impact is represented by the black curves for the whole campaign. The full curve corresponds to the term $\left| F_{\mathrm{sed}} \dfrac{\partial\theta'}{\partial z} \Big/ \dfrac{\partial\theta}{\partial z} \right|$, which represents the wave advection impact on sedimentation. In the upper TTL, it is is on

average about 10% of the mean downward flux. This influence is not very large, but still significant. The wave advection impact might hence be worth taking into account.

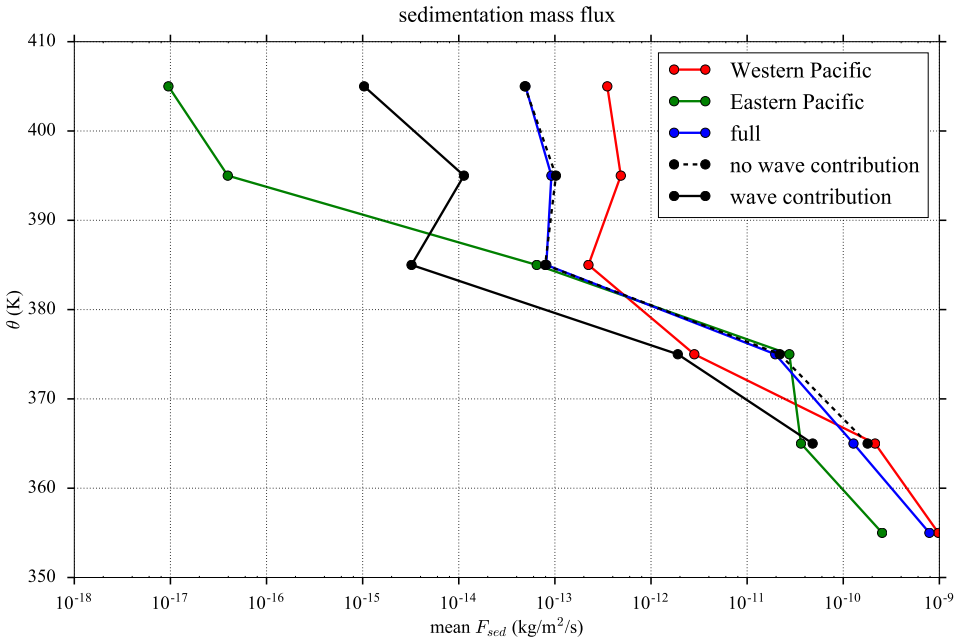

Figure 3.14 – Sedimentation water flux F_{sed} measured from ATTREX observations in the Eastern Pacific (2013), Western Pacific (2014) and for the whole campaign, as a function of potential temperature. The wave stability impact is illustrated for the whole campaign by the two black curves, the continuous curve corresponding to $F_{\text{sed}}\left(\frac{\partial\bar{\theta}}{\partial z}/\frac{\partial\theta}{\partial z}\right)$ while the dashed curve corresponds to $F_{\text{sed}}\left(\frac{\partial\theta'}{\partial z}/\frac{\partial\theta}{\partial z}\right)$. In the upper part of the TTL the wave stability impact reduces the sedimentation flux by about 10%.

3.3.3 Discussion

3.3.3.1 An alternative paradigm for the clear-sky and cloudy air relative humidity in the UTLS?

The numerical experiments and the analysis presented above are interesting because they suggest an alternative paradigm for the relative humidity distribution in the equatorial upper troposphere-lower stratosphere. Because it could apply to aerosols, polar stratospheric clouds (PSCs) or polar mesospheric clouds (PMCs), it is worth stating the alternative paradigm in more details, although we admit it is unlikely to hold for cirrus.

In the current paradigm, the variability in clear-sky relative humidity and the increased occurrence of high supersaturation encountered at low temperatures (*Krämer et al.*, 2009) is explained as follows. In clear sky environment, RH_i should not exceed the onset of homogeneous nucleation of aqueous aerosols. Meanwhile, the supersaturation required for the nucleation of those aerosols increases with decreasing temperature (see Figure 3.1). This "ice nucleation delay" is the reason for the increased occurrence of supersaturation with respect to ice in the TTL clear-sky environment and limits the dehydration efficiency of cold cirrus in the TTL (*Rollins et al.*, 2016).

Our alternative explanation for the increased occurrence of high supersaturations at low temperature and high altitude is the non-linearity of the Clausius-Clapeyron equation, combined with constant gravity wave temperature amplitude through the TTL. This process is

illustrated in Figure 3.11, where it can be seen that the amplitude of the RH_i oscillations increases with altitude whereas the wave displacement amplitude remains constant.

A second observational fact that has to be explained is that the relative humidity varies around 100% within cirrus. The most commonly invoked reason is that the presence of ice crystals, which absorb or release water molecules depending on the water supersaturation, dampens the relative humidity variations due to temperature fluctuations. Using a theoretical parcel model framework, *Korolev and Mazin* (2003) explain this by the relaxation towards a quasi equilibrium supersaturation state, near RH_i =100%. Using a stochastic parcel model framework driven by colored noise temperature variability, *Kärcher et al.* (2014) have also obtained a dampening of the initial mean supersaturation and a stabilization with fluctuations around a 100% relative humidity. In both cases, large excursions away from 100% were prevented by the stabilizing effect of the presence of the ice crystals. Consistent with *Krämer et al.* (2009), *Kärcher et al.* (2014) have argued that the high supersaturation within high altitude TTL cirrus compared to other cirrus was due to the small dampening time scale of supersaturation within those low ice crystal number clouds.

In the simulations presented above, the average in cloud relative humidity remains close to 100% also, but not because the water vapor content is dampened close to thermodynamic equilibrium due to exchange between the ice and vapor phase. In our set-up, the ice crystals grow, but they do not deplete the water vapor. Hence, they cannot regulate the vapor field to get $RH_i \simeq 100\%$. What happens on the contrary is that the position of the remaining ice crystals is dynamically constrained towards the regions of 100% relative humidity.

Of course, those considerations are not strictly applicable to the Earth cirrus clouds. Even for low ice crystal number TTL cirrus, the assumption of little water consumption is unrealistic. Dampening of the super and subsaturation by the moving ice crystals will broaden the equilibrium regions of $RH_i \simeq 100\%$. Our idealized examples may nonetheless point to a process overlooked up to now. This approach might be even more applicable for particles that only slowly affect the gas phase, such as the aerosol particles (unlikely to have sizes and fall speeds as large as those examined here) or particles in PSCs and PMCs.

Wave advection and ice crystal shape We have examined here the impact of wave advection assuming spherical crystal shape. However, even for relatively small size ice crystals, non spherical shape of the crystals can largely diminish the sedimentation speed. The largest ice crystals are the ones which can have the most non-spherical shapes shapes; they are also the ones that dominate the downward mass flux of water F_{sed}. Hence, the sedimentation flux may be more affected by the microphysical characteristics of the crystals (their shape,...) than by the wave advection effect, although ATTREX observations do suggest that that effect is present.

Another aspect that has only been briefly mentioned is that, besides regrouping the surviving crystal in specific wave phases, the theory presented above implies a narrow size distribution of the ice crystal so that their fall velocity is close to the wave vertical phase velocity. However, we would like to stress that ice crystals of different shapes may have different size but similar fall velocities, and this can widen the size range corresponding to a given fall velocity. For illustration, Figure 3.15 shows the different fall speeds for different ice crystal shapes but the same diameter (maximum dimension). The sizes can be increased by more than fifty percent and keep the same fall speed.

Impact on ice sedimentation and size distribution Because it depends on the fifth or fourth moment of the distribution (depending on the hydrodynamic regime in which the

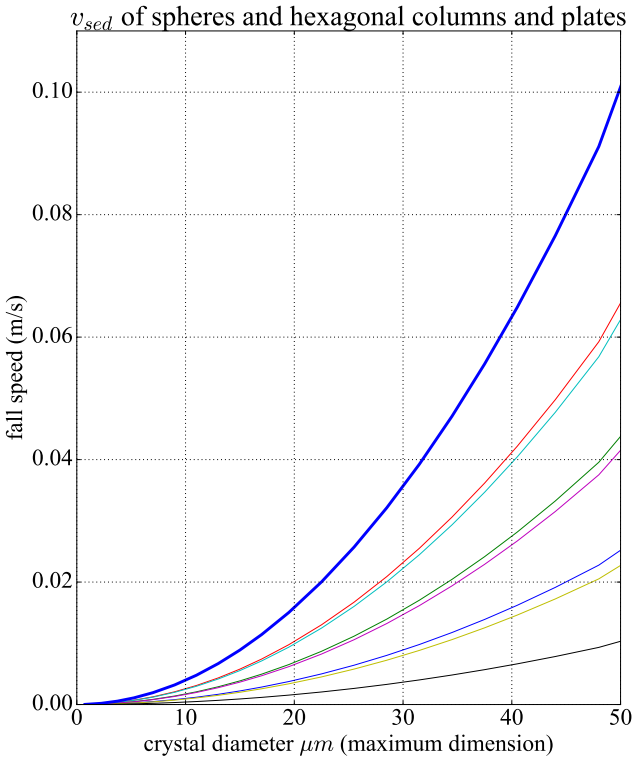

Figure 3.15 – Ice crystal fall speed for different crystal shapes and the same maximum dimension. The thick blue curve corresponds to the spheric shape, which has the largest fall speed.

crystals fall, see Equation (3.28)), F_{sed} is most sensitive to the largest ice crystals. The wave impact that we investigated is significant only when $v_{sed} \simeq |\frac{\omega}{m}|$, so that it would be negligible for water transport if the flux were dominated by large crystals for which $v_{sed} \gg |\frac{\omega}{m}|$.

Figure 3.16 shows the mean size distribution of the number, mass and mass flux of ice crystals from the ATTREX FCDP and 2DS during the 2014 field campaign. Small ice crystals of size of a few tens of microns diameter or less dominate the number distribution, with a peak around 10 μm corresponding to fall speeds around a few mm/s. However, larger ice crystals become more important when the mass distribution is considered, and even more for the mass flux distribution. Nevertheless, the observations suggest that in the TTL, at levels higher than θ =360 K, the mass flux is still dominated by crystals with maximum dimension smaller than 50 μm. In that case, the wave-sedimentation interaction described above will have an influence on the dehydration efficiency, since v_{sed} is not much larger than $|\frac{\omega}{m}|$.

3.3.3.2 Representation in models

Large-scale Eulerian models By diminishing the average downward speed of the ice crystals, the wave advection impact on TTL water is to limit the dehydration, and increase the average cloudiness. Climate models lack the vertical resolution to represent the fine vertical scale equatorial waves that have key interactions with sedimentation. For operational weather prediction, however, the situation is better. *Podglajen et al.* (2014) found that large disagreements could arise, but most of the wave packets are definitely well represented. That type of processes might hence be included in weather models.

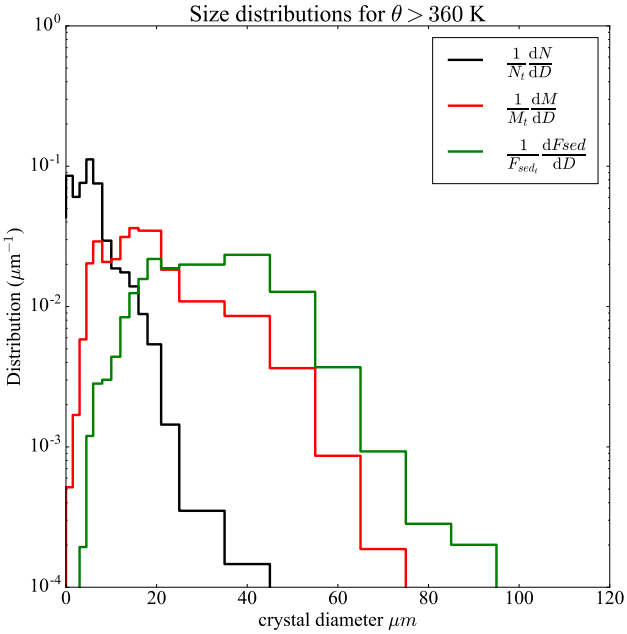

Figure 3.16 – Average ice crystal size distribution within cirrus clouds during ATTREX 2014 flights, above $\theta = 360$ K. In black, number distribution; in red, mass distribution; in green, mass flux distribution. The distributions shown are composites of 2DS and FCDP measurements. The size considered is the maximum dimension, the diameter for spherical particles. It should be mentioned that the size retrieved by the FCDP is not strictly exact because the retrieval of size distribution from scattered light assumes spherical particles. The sedimentation speed needed for the mass flux computation are computed using the formula of *Heymsfield and Westbrook* (2010).

Lagrangian models Full 3D ice crystal trajectories have been performed by *Jensen et al.* (2007) to elucidate the formation of large ice crystals in the TTL. However, the wave advection effect is essentially ignored in other Lagrangian parcel models which use a removal time for the falling ice (*Fueglistaler and Baker*, 2006; *Spichtinger and Cziczo*, 2010). Column models in isentropic coordinates, such as the one of *Jensen and Pfister* (2004); *Ueyama et al.* (2015), do partly include it, but they neglect horizontal wind vertical shear, which can significantly alter the results regarding the impact of the wave (see Figure 3.11). Most Lagrangian models do not include such effects, because they generally only follow air parcels and not particles. An exception is the Chemical Lagrangian Model of the Stratosphere (CLAMS) which has a particle following option which has been used to study polar stratospheric clouds and the denitrification of the polar stratosphere (*Grooßand Müller*, 2007).

3.4 Main points

We have examined two of the impacts of waves on microphysical processes in the UTLS: on nucleation and ice crystal transport. Those two examples show the paramount importance of gravity waves to accurately apprehend microphysics in a realistic TTL setting. The main points of the chapter are:

- *High-frequency gravity wave fluctuations in the TTL are fast enough to interact with homogeneous nucleation. Two limit regimes of homogeneous ice nucleation exist*: vapor-limit homogeneous nucleation, for which vertical velocities change little during nucle-

ation and water consumption by the newly formed ice crystals stops the nucleation event, and temperature-limit or quenched homogeneous nucleation, for which a temperature reincrease happens during the nucleation (due to wave oscillations) and quenches supersaturation before significant water consumption can occur. In the second regime, vertical velocity does not control the ice crystal number, which partly invalidates current approaches used in climate models.

- *In the vapor-limit nucleation regime, there is a very strong sensitivity of the nucleated Ice Crystal Number to the initial water vapor content, which might explain the fine scale structures of ICN observed recently in TTL cirrus.*

For low frequency waves (periods larger than half a day, up to a few days),

- In the absence of feedback on the vapor content, *the interactions between growth, sedimentation, wave temperature perturbations and wave advection make specific phases of the waves more favorable to the presence of ice crystals. The specific phase depends on the background relative humidity*: it is the cooling phase ($\frac{\mathrm{d}\theta'}{\mathrm{d}z}$ <0) for high background relative humidity and the cold phase in a drier environment. This is a possible explanation for recent in situ observations of wave-cirrus interactions in the Eastern (dry) and Western (moist) Pacific TTL (*Kim et al.*, 2016).

- *The preferred position of the ice crystals in the cooling phase of the wave* $\left(\frac{\mathrm{d}\theta'}{\mathrm{d}z} < 0\right)$ *diminishes the dehydrating downward ice flux.* From ATTREX observations, it seems that this effect can be detected and may be significant ($10 - 20\%$ of the total water flux).

Chapter 4

Large-scale TTL cirrus formation and life cycle: a numerical case study

Sommaire

4.1 Introduction

This chapter presents a modeling case study of cirrus formation in the Tropical Tropopause Layer over the Eastern Pacific. A mesoscale meteorological model, WRF[1], is used to simulate the cirrus field observed by satellite instruments (CALIOP). Such a configuration allows to investigate the relevance of different processes (dyncamics, radiation,...) in a realistic setting, and the simulations can be validated through comparison with the observations. However, real-case simulations of thin TTL cirrus are also challenging. For instance, small-scale waves have large impacts on cirrus (see Chapters 1 and 2), but might be poorly represented in the models and in the global analyses used for their initialization. It is also uncertain how well the model microphysics scheme will perform for the exotic TTL cirrus. In this context, the study presented below aims at:

- demonstrating the usefulness of mesoscale models for TTL cirrus studies
- identifying the main relevant processes influencing the simulated cloud field
- benchmarking the sensitivity of the modeled cirrus to model assumptions and parameterizations

To our knowledge, this is the first time a real-case simulation of a TTL cirrus is attempted with a mesoscale model.

4.2 Case-study of the formation of a large-scale cirrus in the tropical Eastern Pacific

4.2.1 Motivation for the choice of the case study and main results

Motivation Cirrus have long been reckoned to be extensive clouds (*Wang et al.*, 1996), and the spaceborne LiDAR CALIOP has provided repeated evidence of their large horizontal extent.

The case chosen was studied in CALIOP observations by *Taylor et al.* (2011). It might corresponds to the largest (on the horizontal) cirrus observed up to now. Figure 4.1 depicts the situation: the color points correspond to TTL cirrus cloud observations from CALIOP in the Eastern Pacific. The clouds appear very extensive along track. Especially, one of the green tracks shows a continuous cloud more than 3,000 km long.

Taylor et al. (2011) relate the formation of this extensive cloud to the presence of a cold temperature anomaly associated with a potential vorticity intrusion from the mid latitudes. The observations also suggest the presence of a cirrus cloud during about two days. Such a long duration seems hard to reconcile with the fact that ice crystals are sedimenting in subsaturated areas below the cloud, which should limit the cloud lifetime to less than a day. The explanation for this apparently long life time is a mystery, although different possibilities have been suggested by *Taylor et al.* (2011):

1. large-scale uplift maintaining the cloud
2. very small cloud particles that do not sediment

[1] the Weather Research and Forecast model

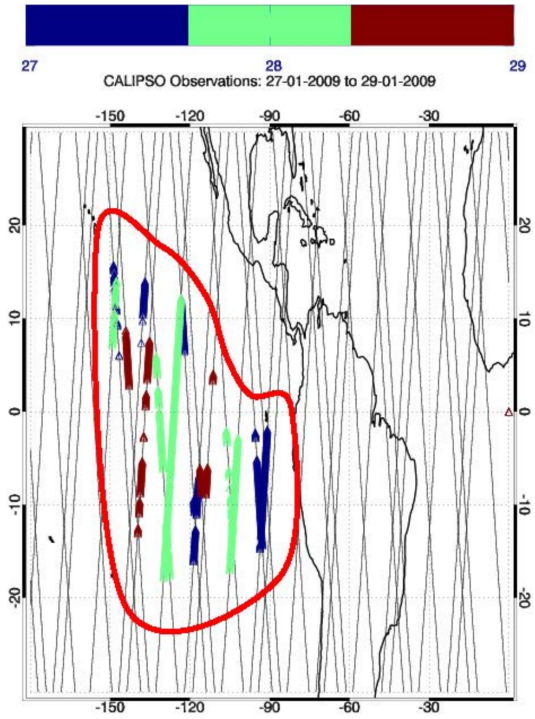

Figure 4.1 – Horizontal extent of the studied cirrus clouds in the 13-18 km altitude range from CALIPSO observations. The colors correspond to points where a cirrus was detected in the 13-18 km altitude range. From *Taylor et al.* (2011).

3. radiatively-induced circulation, due to in cloud long wave radiative heating

The third hypothesis is of special interest, since the existence and strength of radiatively induced circulations in TTL cirrus have been a matter of debate (*Durran et al.*, 2009; *Dinh et al.*, 2010; *Jensen et al.*, 2011). In this context, the science questions addressed by our study are:

1. *Is a mesoscale model using large scale analysis fields for initial and boundary conditions able to reproduce the observed cirrus ? What is the impact of analysis uncertainty and modeling uncertainties on the modeled fields ?*

2. *What dynamics cause the cirrus cloud formation ? Taylor et al.* (2011) emphasize the circulation as a stationary response to a potential vorticity anomaly, as explained by *Hoskins et al.* (1985). However, the relation between temperature and PV anomaly in *Hoskins et al.* (1985) was derived for constant Coriolis parameter f, and does not hold at the equator where f changes sign.

3. *What is the impact of the cloud field on circulation through radiative heating and on the dehydration of the TTL ?*

4.2.2 Article: A modeling case study of a large-scale cirrus in the tropical tropopause layer

This article was published in March 2016 in Atmospheric Chemistry and Physics (*Podglajen et al.*, 2016a).

Atmos. Chem. Phys., 16, 3881–3902, 2016
www.atmos-chem-phys.net/16/3881/2016/
doi:10.5194/acp-16-3881-2016

Atmospheric Chemistry and Physics Open Access EGU

A modelling case study of a large-scale cirrus in the tropical tropopause layer

Aurélien Podglajen, Riwal Plougonven, Albert Hertzog, and Bernard Legras

Laboratoire de Météorologie Dynamique (LMD), CNRS-UMR8539, Institut Pierre Simon Laplace, École Normale Supérieure, École Polytechnique, Université Pierre et Marie Curie, Paris, France

Correspondence to: Aurélien Podglajen (aurelien.podglajen@lmd.polytechnique.fr)

Received: 17 September 2015 – Published in Atmos. Chem. Phys. Discuss.: 6 November 2015
Revised: 13 February 2016 – Accepted: 28 February 2016 – Published: 23 March 2016

Abstract. We use the Weather Research and Forecast (WRF) model to simulate a large-scale tropical tropopause layer (TTL) cirrus in order to understand the formation and life cycle of the cloud. This cirrus event has been previously described through satellite observations by Taylor et al. (2011). Comparisons of the simulated and observed cirrus show a fair agreement and validate the reference simulation regarding cloud extension, location and life time. The validated simulation is used to understand the causes of cloud formation. It is shown that several cirrus clouds successively form in the region due to adiabatic cooling and large-scale uplift rather than from convective anvils. The structure of the uplift is tied to the equatorial response (equatorial wave excitation) to a potential vorticity intrusion from the midlatitudes.

Sensitivity tests are then performed to assess the relative importance of the choice of the microphysics parameterization and of the initial and boundary conditions. The initial dynamical conditions (wind and temperature) essentially control the horizontal location and area of the cloud. However, the choice of the microphysics scheme influences the ice water content and the cloud vertical position.

Last, the fair agreement with the observations allows to estimate the cloud impact in the TTL in the simulations. The cirrus clouds have a small but not negligible impact on the radiative budget of the local TTL. However, for this particular case, the cloud radiative heating does not significantly influence the simulated dynamics. This result is due to (1) the lifetime of air parcels in the cloud system, which is too short to significantly influence the dynamics, and (2) the fact that induced vertical motions would be comparable to or smaller than the typical mesoscale motions present. Finally, the simulation also provides an estimate of the vertical redistribution of water by the cloud and the results emphasize the importance in our case of both rehydration and dehydration in the vicinity of the cirrus.

1 Introduction

Cirrus are the most frequent type of clouds, covering about 30 to 50 % of the Earth surface (Stubenrauch et al., 2010). From remote-sensing observations, they seem nearly ubiquitous in the tropical tropopause layer (TTL; Wang et al., 1996; Fueglistaler et al., 2009) and radiative transfer calculations suggest that they strongly influence the heat balance of the TTL, potentially influencing its temperature and contributing to tropical upwelling (Corti et al., 2005). Furthermore, TTL cirrus are believed to control the dehydration of air masses and the amount of water vapour that enters the stratosphere (Jensen et al., 1996).

Despite the remarkable attention they have received for the last 20 years, the microphysical processes controlling the formation of TTL cirrus are still largely debated. More precisely, the respective importance of homogenous and heterogeneous nucleation remains unclear, although in situ observations suggest that both are active in the TTL (Jensen et al., 2013; Cziczo et al., 2013). Contrary to the microphysics, the dynamics leading to cirrus seems somehow better understood. The clouds result either from ice detrainment from convective towers or from in situ formation in supersaturated regions created by large- to mesoscale uplifts (Wang and Dessler, 2012). Nevertheless, the role of different waves with different scales in cirrus processes is still discussed, and

their impacts still require quantification (Kim and Alexander, 2015).

Processes in TTL cirrus have mainly been studied using a Lagrangian framework (parcel or single column models; Jensen and Pfister, 2004) or with idealized mesoscale simulations (e.g. Jensen et al., 2011; Dinh et al., 2012). There have been relatively few studies conducting meso- to large-scale modelling of real-case TTL cirrus. Different reasons may contribute to this: the fact that the typical spatial scale of TTL cirrus can go down to a few metres in the vertical, the many unknowns in the microphysics and the uncertainty regarding how detailed the microphysics modelling needs to be (bin or bulk). Despite these important limitations, simulations using a mesoscale model of tropical cirrus have nonetheless been carried out, but in a climatological perspective, i.e. using a moderate resolution and several months of simulations (Wu et al., 2012; Evan et al., 2013). Now, mesoscale simulations can also be used for case studies of individual clouds to address issues such as the dynamical causes of cloud formation. Such case studies will contribute to evaluating the realism of the macrophysical characteristics of the simulated cirrus (location, altitude, timing, extent). If these characteristics are successfully modelled, the simulation may serve to explore the cirrus evolution and its impact. Recently, Muhlbauer et al. (2014) used case studies with a mesoscale (cloud resolving) model to explore the sensitivity of different types of cirrus to modifications of the microphysical parameters and to modifications of the initial conditions. However, the mesoscale model tool has mainly been used to study midlatitude cirrus (e.g. Muhlbauer et al., 2015).

In this paper, we use the Advanced Research Weather Research and Forecast (ARW WRF; Skamarock et al., 2008) model to conduct a real-case study of an in situ formed TTL cirrus cloud. The case studied corresponds to a cloud having a very large spatial extent and occurring over the Eastern Pacific. Taylor et al. (2011) pointed out this cloud event and analysed it using satellite observations. In particular, they have shown that the cloud occurred within a large-scale low-temperature anomaly, which was itself probably related to a potential vorticity (PV) intrusion originating from the midlatitudes. The large-scale in situ formation of this cloud makes it suitable for a case study with a mesoscale model. Indeed, one can hope that the analyses used to force the model contain the necessary dynamical components to drive the cirrus formation, although the Eastern Pacific is a region where analyses may present significant errors due to the sparsity of observations (Podglajen et al., 2014). Finally, the choice of this cloud for the study is also motivated by the possibility to investigate dynamics–radiation interaction, which may have played a role in the cloud evolution for this case (Taylor et al., 2011).

The paper is organized as follows. In Sect. 2, the model set-up and an overview of the cirrus event in the simulations are presented. We show that despite uncertainties and crude assumptions in its microphysical parameterization, the model is able to reproduce the main characteristics of the observed cloud structure. In Sect. 3, we explain that this good agreement between observed and modelled clouds is tied to the well-represented large-scale dynamics. Section 4 illustrates several sensitivity studies and the strong dependence to the choice of the initial and boundary conditions. Finally, Sect. 5 discusses the modelled impact of the cloud in the tropical tropopause layer.

2 Model and observations

2.1 Case description

The study focuses on a cirrus cloud forming in the tropical Eastern Pacific in late January 2009. This case was highlighted as remarkable for its very large horizontal extent by Taylor et al. (2011), who analysed it using satellite observations. In measurements from the Cloud-Aerosol Lidar with Orthogonal Polarization (CALIOP, Winker et al., 2007), one can identify the large region covered by the cirrus through its intensified backscatter (Fig. 1, top left panel, similar to Fig. 1 of Taylor et al., 2011). In particular, the cloud seems to extend almost continuously over 3000 km along track, at an altitude between 15 and 16 km. In addition to this considerable spatial extent, Taylor et al. (2011) showed that high clouds were seen on CALIOP tracks during several days (27–29 January) and suggested that they could be portions of the same extensive cirrus. The cloud would then extend several thousand kilometres in the zonal direction as well and last a few days.

Regarding the atmospheric flow in the tropical Eastern Pacific region, where the cloud forms, climatological westerlies dominate at upper-tropospheric levels, as part of the Walker circulation. However, they can be strongly modulated at synoptic timescales by PV intrusions from the midlatitudes. This is the case at the time of our simulation, as we will see in Sect. 3.

2.2 Model description and set-up

To simulate the cirrus event, we use the WRF mesoscale model (Skamarock et al., 2008). The relevant elements of our reference set-up are described in the following, while the different sensitivity tests that were carried out will be the subject of Sect. 4.

Our spatial domain extends from 18° S to 18° N and from 148 to 112° W (i.e. about 4000×4000 km), and the nominal horizontal resolution is 10 km (i.e. 400×400 points). The domain was chosen to surround the cloud seen in CALIOP observations in Fig. 1. It is large enough that the development of the cirrus clouds at its centre is not much affected by the boundary conditions, according to trajectory analysis. In the vertical, there are 120 levels extending up to 8 hPa, with the last 7 km taken as a sponge layer to avoid spurious wave reflection. The resulting vertical resolution around

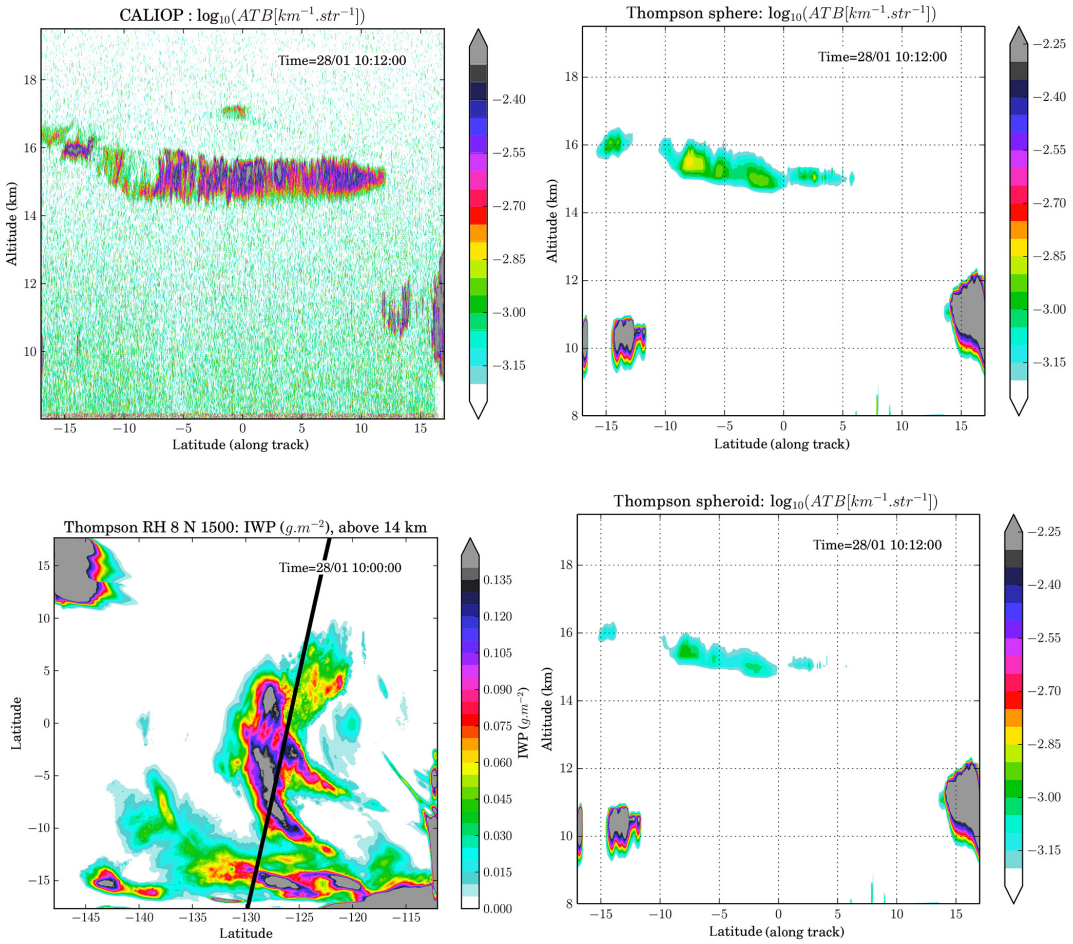

Figure 1. (Top two panels) Decimal logarithm of total attenuated backscatter (ATB) at 532 nm, from (left) CALIOP observations and (right) WRF reference simulation, using default Thompson microphysics and assuming spherical ice crystals. ATB in the simulation assuming non spherical crystals is also shown (bottom right). (Bottom left panel): total ice water path above 14 km in the reference simulation, at the time of CALIOP passage. The satellite track is highlighted by the black line.

15 km is approximately 300 m. The model is initialized on 27 July at 00:00 UTC. Although we performed a 4-day integration for the reference simulation, the paper is focused on the shorter period 27–29 July. One reason is that this time period includes the observations along CALIPSO track shown in Fig. 1. Another reason is that in longer simulations, at the altitudes considered (14–17 km), most of the air that was initially inside the domain has been advected out of it within 2 days or less, thus preventing the analysis with tracers initialized in the initial condition (see Sects. 3 and 5). In addition to this, the first 12 h of the simulation are regarded as spin-up and not shown. This is conservative: deep convection is very limited in our simulations, so little adjustment to latent heat release is expected, resulting in an effective spin-up time of only a few hours.

In the reference simulation, microphysical processes are treated with the bulk microphysics scheme of Thompson (Thompson et al., 2004, 2008; Thompson and Eidhammer, 2014), which has two moments for the ice class. The ice number concentration is assumed to follow an exponential distribution with respect to the diameter. The mass–diameter relationship adopted is $m(D) = \rho_i \frac{\Pi}{6} D^3$, with $\rho_i = 890\,\mathrm{kg\,m^{-3}}$ standing for ice density; i.e. the ice crystals are assumed to be spherical. With two moments for ice, differential sedimentation occurs in the scheme with different mass weighted and number weighted terminal fall speeds. The scheme allows for ice supersaturation and includes homogeneous nucleation (Koop et al., 2000) and an empirical treatment that could be considered as heterogeneous nucleation. Here, the heterogeneous ice nuclei are activated once a supersaturation threshold $S_{\mathrm{nuc}} = 8\,\%$ is reached, and their number N_{IN} follows the observations of Cooper (1986) above 233 K and are saturated to their value at 233 K (i.e. 1500 crystals per litre) below that. These values of N_{IN} and S_{nuc} may seem unlikely for heterogeneous ice nuclei concentrations and properties at 15–16 km in the TTL, although to our knowledge no direct measurements are available for compar-

ison in this region. We emphasize that, if one can interpret this ice-formation procedure as heterogeneous nucleation, it can also be better thought of as an empirical parameterization of the combined effect of heterogeneous and homogeneous nucleation triggered by resolved and unresolved perturbations inside the 10 km × 10 km × 300 m grid box. This explains the rather low supersaturation for ice formation that compensates for the fact that the box mean supersaturation is below the local maxima encountered within the grid box. To address the sensitivity to the nucleation-related parameters (N_{IN} and S_{nuc}), we have performed sensitivity tests that are described in Sect. 4 together with the sensitivity to the microphysics scheme. Moreover, we have also used the microphysical schemes of Morrison et al. (2005, hereafter Morrison) and Hong et al. (2004, hereafter WSM5), which handle nucleation at cold temperature in a similar way as Thompson scheme. Those experiments are also presented in Sect. 4. Our choice of the default Thompson scheme as reference among the many WRF microphysics schemes is a compromise between keeping acceptable computational costs and describing potentially important processes such as differential sedimentation; it is also motivated by the good comparison with observations obtained in this configuration, presented below.

Short- and long-wave radiative heating rates are calculated using the Rapid Radiative Transfer Model G (RRTMG; Iacono et al., 2008). RRTMG is fully coupled to the Thompson microphysics and accounts for the radiative effect of cloud particles through their mass and effective radius. In the radiative calculations, the values of well-mixed greenhouse gas concentrations and of the ozone mixing ratio are taken from the Community Atmosphere Model with Chemistry (CAM-chem) outputs, with monthly and latitudinal variations (see WRF user's guide). Finally, the initial and lateral boundary conditions come from the ECMWF operational analysis, which at that time had 91 vertical levels and a T1279 spectral resolution (corresponding to a horizontal resolution of about 0.125°).

2.3 Model validation against CALIPSO observations

In order to compare WRF outputs with CALIOP observations, we use the lidar simulator from the Cloud Feedback Model Intercomparison Project Observation Simulator Package (COSP; see Chepfer et al. (2008) for a description). Light scattering by ice particles is a complicated problem and in theory depends on the size distribution, shape and orientation of ice crystals on top of their concentration. In the COSP lidar simulator, only the dependences of the lidar signal to ice concentration and ice crystal effective radius are retained. Those two are calculated consistently between the different microphysical parameterization used and the lidar simulator.

For the comparison, we will mainly use the observed and simulated total attenuated backscatter (ATB) at 532 nm without any normalization. The ATB is an almost direct measurement, and the absence of normalization is appropriate as long as we are interested in one specific and limited altitude range. Figure 1 shows the along-track profiles of the ATB observed by CALIOP (top left) and simulated by WRF-COSP (top right) for the reference case on 28 January 2009. Despite the crude microphysical treatment of ice nucleation in the reference Thompson scheme, there is an overall good agreement between observed and simulated cirrus cloud location and extension (quantitative evaluation will be used in Sect. 4 to compare different choices for the simulations). The northern extension of the cloud field appears underestimated along CALIPSO track, but the simulation does show an extension beyond 5° N to the east of the track (see Fig. 1).

This agreement qualitatively validates the simulation of the general dynamics which led to cloud formation. However, the model visually seems to underestimate the backscatter by a factor of about 2. Possible reasons are the uncertainties associated with measurement noise (typically about 35–50 % of the measured ATB for our cloud) and approximations and uncertainties in the calculated backscatter from WRF outputs.

Shape assumptions is one source of such uncertainties. Here, the choice of the ATB for comparison implies that the hypothesis about ice crystal shapes are made in the COSP lidar simulator and not in the retrieval. Hence, we do not rely on the lidar ratio chosen in the CALIOP retrieval algorithm, contrary to what would have happened if we had used CALIOP's extinction coefficients for example (Mioche et al., 2010). This allows us to evaluate the sensitivity to shape assumptions directly by varying parameters in COSP. Among the choices available, we have tested for differences between spherical and non-spherical prolate shapes. The results for this experiment are illustrated in Fig. 1 (top right and bottom right panels). The strong difference in amplitude seen between the two panels agrees with results stressed for instance by Cirisan et al. (2014), who showed that changing the assumed aspect ratio of prolate spheroids by 20 % could modify the backscatter by a factor of 2. For our simulation, the best agreement in the signal amplitude is achieved assuming spherical crystals, which agrees with the shape assumption in the microphysics scheme and with observations of the shape of small TTL ice crystals (McFarquhar et al., 2000; Lawson et al., 2008). At last, beside shape assumptions, the type of ice crystal size distribution assumed also affects the simulated ATB; however, we did not test the sensitivity to this parameter to keep consistency with the microphysical parameterization, which assumes an exponential distribution. In light of the strong unknowns in the measurements and in the comparison procedure, the agreement found between the top left and right panels in Fig. 1 is very encouraging.

Nevertheless, in addition to the "comparison related" uncertainties mentioned above, the disagreement between the observed and simulated backscatter intensities may also be due to an underestimation of the ice water content (IWC). A number of factors could then be involved: inappropriate microphysics, too much diffusion of water vapour in the model,

Table 1. List of parameterizations and simulations used in this paper.

Simulation name	Microphysics	Radiation	Initial and boundary conditions
Thompson	Thompson	RRTMG	ECMWF op. an.
Thompson-ERAi	Thompson	RRTMG	ERA-Interim
Morrison	Morrison	RRTMG	ECMWF op. an.
Morrison-ERAi	Morrison	RRTMG	ERA-Interim
WSM5	WSM5	RRTMG	ECMWF op. an.
No heat	Thompson	RRTMG, no cloud radiative heating	ECMWF op. an.

ECMWF op. an. stands for the European Centre for Medium-Range Weather Forecast operational analysis; ERAi stands for the ECMWF ERA-Interim reanalysis.

Table 2. Bulk microphysical properties (ice water content, ice crystal number and effective radius, R_{eff}) of the simulated cirrus clouds at 15.5 km on January 28, at 10:00 and values reported from aircraft observations (Lawson et al., 2008).

	WRF simulation		Lawson et al. (2008)	
	mean	σ	mean	σ
Ice crystal number (L^{-1})	85.	131.	66.	31.
R_{eff} (microns)	10.4	1.8	8.8	2.4
Ice water content ($mg\,m^{-3}$)	0.10	0.17	0.06	0.1

underestimation of the water vapour content in the initialization or overestimation of the temperature. In fact, it is likely that several of those factors are at play and partly compensate, e.g. underestimation of both water vapour and supersaturation. In the absence of more constraining data, we do not attempt here any tuning of the initial conditions but we will provide some discussion on the sensitivity to those in Sect. 4. Due to the absence of in situ observational data for this case, it is also impossible to precisely evaluate the simulated microphysics. However, as shown in Table 2, we note that the simulated cloud microphysical properties are comparable to in situ observations by Lawson et al. (2008) and within the range of other observations from Krämer et al. (2009); Davis et al. (2010); Jensen et al. (2013).

Finally, one should add that the simulated and analysed temperature fields show significant local departures from one another, up to 3 K at 16 km, 36 h after initialization, though no systematic bias is noted. Those differences typically correspond to mesoscale structures of ~ 1000 km horizontal extent, yet they have small amplitudes (< 0.5 K) in the region with significant IWC. With these differences in absolute temperature, it may be rather surprising that the simulated cloud is so similar to observations. This arises because of the strong constraint provided by the large-scale dynamics leading to the cloud formation. This is the subject of Sect. 3, but first an overview of the cirrus evolution in the simulation is provided in the next subsection.

2.4 Simulated cirrus evolution

Figure 2 shows the evolution of the temperature and cirrus field in the simulation, at the potential temperature level $\theta = 360$ K. On those maps, we see that the correlation between the cloud field and low-temperature anomalies, as observed by Taylor et al. (2011), is reproduced in the WRF simulation. As expected due to the dependence of microphysical processes on relative humidity, which itself depends on temperature, the cloud development closely follows the evolution of low temperatures in the simulation.

The colour points on the figure illustrate individual air parcels positions initialized on 28 January, 10:00, at $\theta = 360$ K and at the horizontal position shown on the panel corresponding to this time in Fig. 2. The displacement of those air parcels comes from backward and forward (kinematic) Lagrangian trajectories calculated with the wind field in the simulation. Due to diabatic heating, the potential temperature level of those air parcels obviously changes during the time of the simulation. However, the trajectory calculations show that this change is limited to less than 1 K during the simulation, which is consistent with the value of diabatic heating rates. Hence the representation of those points on the isentrope $\theta = 360$ K does not introduce any qualitative bias.

One conclusion from those trajectories is that although the flow has a stagnation point and weak velocities at the centre of the domain (see the evolution of the blue and black point positions), air parcels nonetheless experience significant variations in temperature, partly due to the westward displacement of the cold-temperature anomaly. Moreover, aside from air parcels near the stagnation region, significant horizontal displacements are found (of the order of 1000 km per day). Different clouds are always present in the simulation but, due to the temperature variability along the trajectory (which is linked to different mesoscale perturbations), they do not follow air parcels and this limits the in-cloud residence time for each cloud (see also Sect. 5.2).

One last important property of this cloud field is that, despite its "patchy" feature, different clouds appear in the same regions, which suggest some large-scale forcing of the cloud. In the following Sect. 3, the causes of cloud formation in the simulation are examined more precisely.

3 Dynamical features leading to cloud formation

3.1 Cause of ice cloud formation

Cirrus clouds in the TTL can either form in situ through the cooling of ascending air masses or result from ice lofting from convective clouds (Fueglistaler et al., 2009). For our case, Taylor et al. (2011) argued that the latter was unlikely due to the horizontal extent of the cloud. Furthermore, there was no evidence of deep convection taking place in the region of interest at that time in CALIPSO observations. To

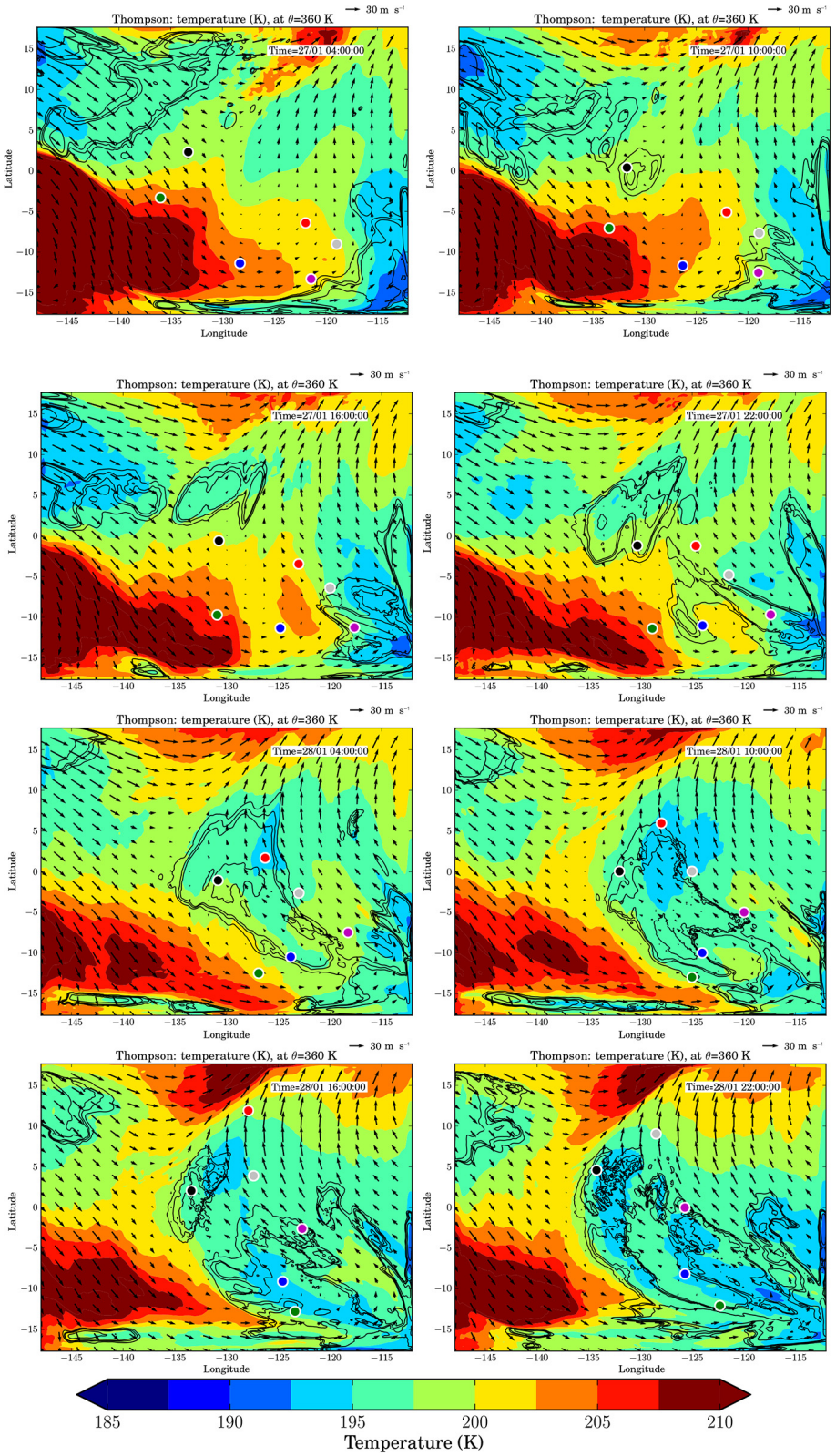

Figure 2. Successive maps of temperature at the potential temperature level $\theta = 360$ K for the reference simulation. The black contours correspond to contours of ice water content of 1×10^{-8}, 5×10^{-8}, 1×10^{-8} and 5×10^{-8} kg kg^{-1} respectively. They delimit the cirrus. The colour points represent the position of air parcels surrounding the cirrus on 28 January at 10:00 UTC; they were launched (backward and forward) at that date on the isentrope $\theta = 360$ K, at the horizontal positions shown by the colour points. They follow individual 3-D air-parcel trajectories and illustrate the air displacement in the region. The vectors represent the horizontal winds.

support their assertion, we have introduced passive tracers in the boundary layer at the beginning of the simulation (27 January 00:00 UTC). None of them had reached the cirrus altitude (> 14 km) at the end of the simulation.

Hence in situ formation prevails here, and it must happen through the cooling of ascending air masses. Using GPS radio-occultation temperature measurements, Taylor et al. (2011) showed that the synoptic situation in the cirrus region was associated with a cold-temperature anomaly in the TTL. The strong link of the cirrus clouds with low-temperature anomalies in the simulation can be seen in Fig. 2, where the cirrus, highlighted by the contours of the IWC, tend to be present in the coldest regions. One naturally thinks of cold-temperature anomalies as associated with strong constant upward vertical velocities because of the cooling associated with adiabatic expansion, which relates air parcels (Lagrangian) cooling rates $\frac{\mathrm{D}T}{\mathrm{D}t}$ and w through

$$\left(\frac{\mathrm{D}T}{\mathrm{D}t}\right)_{\text{adiabatic}} = -\frac{g}{C_\mathrm{p}}w,$$

where $g = 9.81\,\mathrm{m\,s^{-2}}$ is the gravitational acceleration and $C_\mathrm{p} = 1004\,\mathrm{J\,kg^{-1}\,K^{-1}}$ is the thermal capacity of dry air at constant pressure. However, there is no clear correlation between w and the cirrus cloud in most of our simulations (not shown). While this may seem puzzling at first, it simply reflects that the simulated clouds formed in wave-induced negative-temperature anomalies ΔT, which are related to upward vertical displacements ξ, i.e. time-integrated Lagrangian vertical velocity, rather than directly to upward velocities. Indeed, in the dry adiabatic limit,

$$\Delta T = -\frac{g}{C_\mathrm{p}}\xi = -\frac{g}{C_\mathrm{p}}\int_{\underline{X}} w(\underline{X}(t),t)\mathrm{d}t,$$

where $\int_{\underline{X}}$ is the integral following $\underline{X}(t)$, the air parcel position. Because of the horizontal velocity, uplift cannot be estimated directly with instantaneous w. A more appropriate quantity is the height of an isentropic surface, which is shown for instance for 28 January, 10:00 UTC, in Fig. 3, left panel. There is a good correlation of this height with the cirrus and temperature; however, the height of the isentrope is not computed following an air parcel and does not enable to quantify the uplift created by the dynamics in the simulation.

To quantify this uplift more precisely, we have computed Lagrangian trajectories in the WRF simulation. This also allows to evaluate the upward displacement in the more natural altitude coordinate, which is that of CALIOP observations. The deduced uplift, calculated since the start of the simulation, is shown in Fig. 4, left panel. Part of the figure is intentionally left blank, because the corresponding air was not in the domain at the initial time. The cirrus location is clearly associated with strong vertical uplifts, and the northern limit of the cloud corresponds to a reversal of the sign of the vertical displacement, which becomes negative in the northern part of the domain. To further show that the simulated relative humidity is actually controlled by the vertical displacement field and not directly by the initial conditions, we have also computed a ΔRH, which is defined as

$$\Delta\mathrm{RH} = \frac{q_\mathrm{vap}(\underline{X}(t),t) + q_\mathrm{ice}(\underline{X}(t),t)}{q_\mathrm{sat}(\underline{X}(t),t)} - \frac{q_\mathrm{vap}(\underline{X}(t_0),t_0) + q_\mathrm{ice}(\underline{X}(t_0),t_0)}{q_\mathrm{sat}(\underline{X}(t_0),t_0)}, \quad (1)$$

where $\underline{X}(t)$ indicates that we follow a Lagrangian trajectory, q_sat is the mass saturation mixing ratio with respect to ice, and q_vap and q_ice are the ice and vapour mass mixing ratios. Neglecting sedimentation and diffusion, the numerator of the two terms is the same (Lagrangian conservation of the total water). Hence, this quantity, which is shown in the right panel of Fig. 4, evolves in a Lagrangian manner because of the change of the denominator $q_\mathrm{sat}(\underline{X}(t),t)$, which is due to the vertical displacement and the associated adiabatic temperature change. It allows us to distinguish the contribution of the simulation's internal dynamics in driving a relative humidity increase from the initial conditions. The strong correlation of ΔRH with the cirrus location (shown by the black contours) confirms that in this case study the simulated cirrus forms because the upward vertical displacement caused an increase in the relative humidity and not because the relative humidity was already high enough in the initial conditions. Still, initial relative humidity, if too dry, can impact the cloud location because the ice formation threshold is not reached, as seen in the south-east part of the domain. Nonetheless, Fig. 4 shows that the dynamically induced vertical displacement exerts a strong control over the cloud structure.

3.2 Large-scale dynamics

A large-scale uplift thus explains the formation of the clouds, but the question of the cause of this uplift remains. Taylor et al. (2011) pointed out that the cold-temperature anomaly was most likely related to dynamical features originating in the extratropics. In particular, they showed a map of PV from NCEP reanalysis at 200 hPa (see their Fig. 9), illustrating intrusions of high PV anomalies extending in the region where the cirrus form. A comparable figure for our simulation is displayed in Fig. 3, right panel, which shows the PV at $\theta = 360$ K. A clear northern hemispheric PV intrusion can be identified in this figure and the large-scale dynamics in the simulation are likely strongly affected by this structure.

This kind of influence from the midlatitudes is common in the Eastern Pacific upper troposphere (Waugh and Polvani, 2000), where the average westerly winds associated with the Walker circulation enable inter-hemispheric interactions. Intruding in tropical regions, the midlatitude signals are expected to excite equatorial modes (Kiladis and Feldstein, 1994). We examined this using fields from the ERA-Interim. Figure 5 shows a Hovmöller diagram of the (left) symmetric

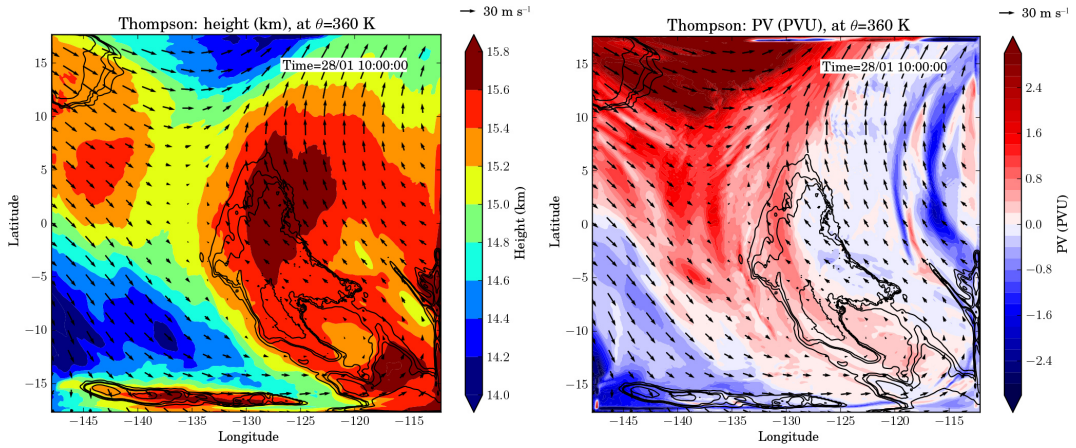

Figure 3. Fields from the reference simulation with Thompson microphysics, on the 360 K isentrope, showing (left) geopotential height (km, colours) and ice water content (1×10^{-8}, 5×10^{-8}, 1×10^{-8} and 5×10^{-8} kg kg^{-1}, black contours) and (right) potential vorticity (PVU, colours) and ice water content. Wind vectors are also displayed.

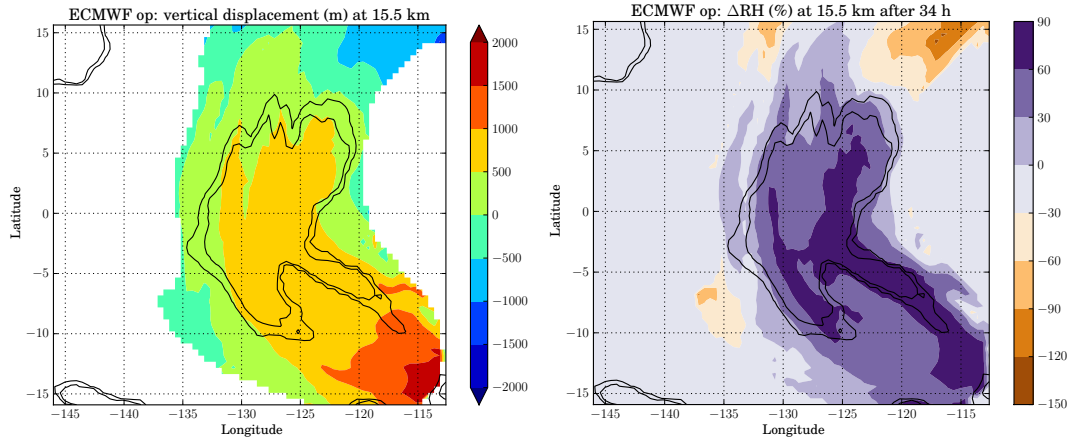

Figure 4. (Left) Lagrangian vertical displacement between the start of the simulation (27 January 2009, 00:00 UTC) and 28 January 2009, 10:00, after 34 h of simulation, displayed at the location of air parcels on 28 January, 10:00 UTC (altitude of 15.5 km). (Right) Contribution of vertical displacement to relative humidity change ΔRH along a Lagrangian trajectory; see text for details.

and (right) antisymmetric components of the 125 hPa temperature between 15° S and 15° N, with zonal wind contours added on the left panel and meridional wind contours on the right. The symmetric signal shows quasi-stationarity features, which could be the signature of an equatorial Rossby wave. In contrast, the antisymmetric signal clearly shows westward phase propagation, and antisymmetric temperature are in phase with the meridional wind component. This moving pattern is consistent with the signature of a Yanai (or mixed Rossby gravity) wave and explains the antisymmetric structure in which the cirrus forms that was seen in Fig. 3, left panel. The Yanai wave interpretation is also consistent with the quadrature phase PV and antisymmetric temperature anomalies (Fig. 3, both panels).

The onset of this "Yanai wave" perturbation in the domain and its vertical structure are depicted more clearly in Fig. 6, which shows a vertical Hovmöller diagram of antisymmetric temperature and symmetric meridional wind at 130° W. Meridional wind and antisymmetric temperature exhibit a downward phase propagation in the cirrus altitudes (in agreement with expectations for upward-propagating Yanai wave packets). It is worth noting that the "Yanai wave" perturbation seen here differs from the free-travelling Yanai waves observed in the equatorial lower stratosphere. Its period is longer (∼ 10 days versus 4–5 typically in the lower stratosphere) and its phase speed lower. This is probably due to several factors such as the low frequency of the PV perturbation that excites the wave-like response, Doppler shift, the interaction with the equatorial Rossby wave pattern and the complicated sheared wind structure (see Wang and Xie, 1996) over the Eastern Pacific at that time. Such long-period (6–10 days in our case) westward-propagating Yanai waves seem common in the westerly duct and have been observed in operational analyses by Randel (1992).

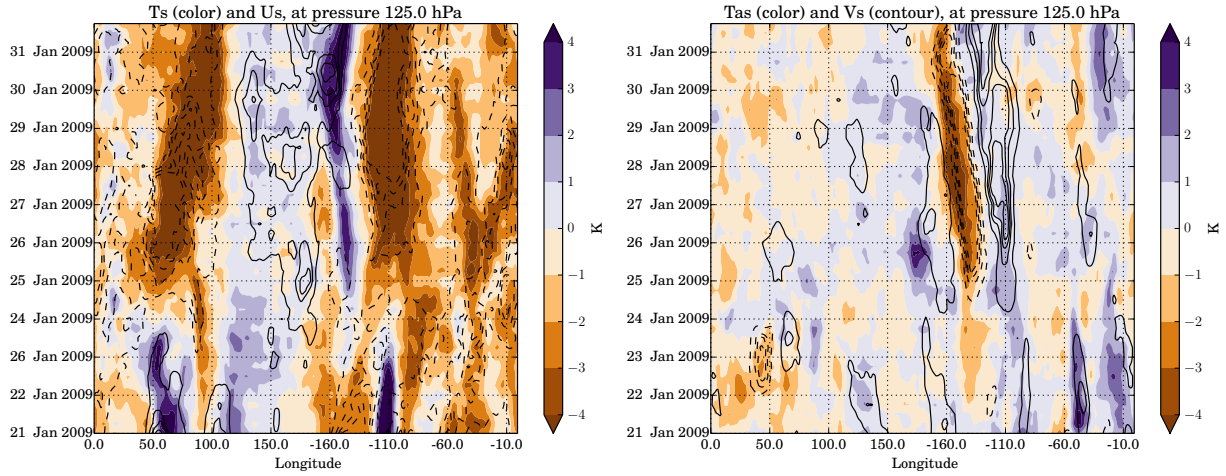

Figure 5. Hovmöller diagrams of (left) symmetric and (right) antisymmetric temperature anomalies in the ERA-Interim reanalysis. The averages are computed between 15° N/S and antisymmetric stands for antisymmetric relative to the equator. On the right panel, the black contours correspond to positive (continuous) and negative (dashed) symmetric meridional wind anomalies. On the left panel, they correspond to symmetric zonal wind anomalies.

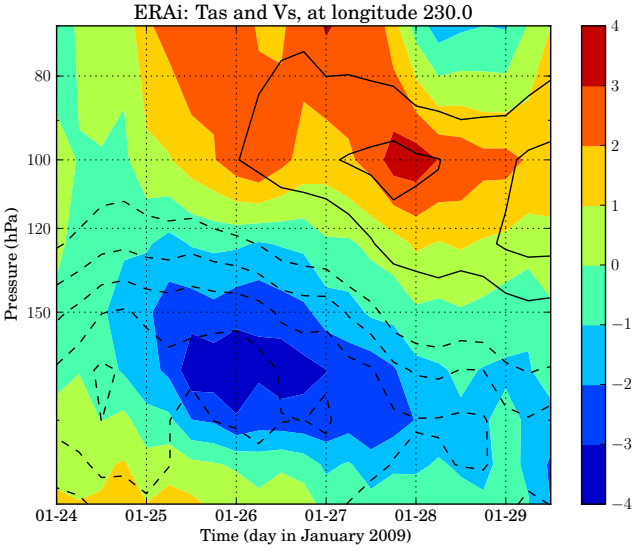

Figure 6. Hovmöller diagram of symmetric meridional wind (contours, dashed for negative values) and antisymmetric temperature anomalies (colour, K) in the ERA-Interim reanalysis, before and during the period of the simulation, at longitude 130° W. The averages are computed between 15° N/S and the antisymmetric stands for antisymmetric relative to the equator.

The combination of the symmetric and antisymmetric temperature signals creates negative temperature anomalies in the south-east part of the domain, which is also the region of strongest vertical displacements. Hence, the large-scale dynamics during the simulation is dominated by a PV intrusion originating from the midlatitudes that excites Yanai (and probably Rossby) equatorial wave modes, which are themselves responsible for the vertical displacements in the upper troposphere. These wave-induced vertical displacements are the necessary component to increase the supersaturation and cause the cirrus formation.

Although the main structure of the cirrus is dominated by the large-scale waves, other waves contributing to the vertical displacement might also have an impact on the temperature anomaly and may influence cirrus formation. However, for a given trajectory the spectrum of vertical displacements emphasizes more the contribution of motions with slower intrinsic frequencies. In the present case, where large-scale motions with significant vertical displacements are present, the contribution from smaller-scale motions (inertia gravity waves) to the vertical displacement needed to produce the cirrus clouds seems secondary to understand the cloud pattern.

4 Sensitivity of the simulated cirrus cloud

The large-scale uplift is thus a first-order element needed to produce the cirrus field. Accurate cirrus cloud simulations involve this and other components, ranging from a good description of the water vapour field to mesoscale gravity waves, as well as appropriate microphysics and radiative parameterizations. The sensitivity of the simulated cirrus to some of those components will be presented in the following subsections once the methodology for comparing the simulations is introduced. A summary of all simulations presented in this section can be found in Table 1.

4.1 Comparison methodology

Different characteristics of the cloud field should be compared between simulations and observations. Along a

CALIOP track, cloud location and extension ("cloud fraction") are important properties to be evaluated on top of the averaged returned backscatter. Their evaluation depends on subjectively chosen thresholds for the cloud limits but can nevertheless provide more objective insights into the differences than a visual comparison. Cloud location and amplitude will be used to determine how the different simulations compare with the observations.

On top of the comparison with the observations, it is also necessary to conduct comparisons of the simulations with one another in order to capture the spatial structure better than only with the along-track view provided by CALIOP. We have used maps of the simulated ice water path (IWP; vertically integrated IWC) above 14 km for this purpose. The (dis)similarity of the obtained maps is evaluated using standard correlations and the SAL metrics, which have been introduced by Wernli et al. (2008) and previously used to evaluate cirrus simulations by Kienast-Sjögren et al. (2015). The SAL consists in three components: structure (S), amplitude (A) and location (L). A perfect match between the fields (exactly similar) corresponds to the score 0 for structure, amplitude and location. More precisely, the structure and amplitude components take values between -2 and 2, while the location component is bounded by 0 and 2. The structure compares the shape of the two cloud fields (many small clouds versus one huge cloud). Positive values indicate a more dispersed cloud field than the reference. The amplitude compares the average IWP, positive values corresponding to an overestimation relatively to the reference. This A component takes no consideration on the spatial structure. The last component, L, summarizes the error in the spatial location of the field (the location of its centre of mass).

The comparisons of the different fields with observations are presented in Table 4, which reports the differences in the vertical and horizontal location of the centroid of the returned backscatter between observation and simulations, as well as the differences in the amplitude of the returned backscatter (calculated as the A component of the SAL). The maps of the IWP above 14 km are shown in Fig. 7 and the corresponding correlations with the reference set-up and SAL metrics are reported in Table 5.

4.2 Sensitivity to initial conditions

Previous studies have shown TTL cirrus modelling to be strongly sensitive to initial conditions, for instance the initial water vapour content (Dinh et al., 2016). To assess this sensitivity, we have carried out different sets of simulations varying the initial and the boundary conditions (see Table 1). With two different microphysics schemes (Morrison and Thompson), we have performed simulations with ERA-Interim and the ECMWF operational analysis initial and boundary conditions. The reference simulation uses the operational analysis for initialization and boundaries. We have also performed a nested model run with a coarser horizontal resolution (30 km), which was launched on January 25 over a larger domain (extending from 27.5 to 27.5° N and from 158 to 102° W) and initialized with the operational analysis. This simulation then served as initialization for another model run over our reference domain at 10 km resolution. This experiment can also be viewed as a sensitivity test to domain size. At last, we have conducted an additional simulation initialized with the operational analysis fields, but with a homogeneous 20 % increase in the initial water vapour content. This bias is in the range of observed disagreements between the ECMWF operational analysis and in situ observations (Kunz et al., 2014). We emphasize that all those experiments are mainly illustrative and may not span the uncertainty linked to initial and boundary conditions.

Table 4 shows that the reference simulation offers the best agreement with the observations in amplitude and a close centroid location. The centre of mass of the attenuated backscatter is about 300 m (less than one model level) lower in this simulation than in observations. All simulations put the cloud centroid too much to the south, which is linked to an along-track underestimation of the northward extension of the cloud compared to observations. All simulations also underestimate the intensity of the ATB, except the one with increased initial water vapour. The change in the initial condition mainly results in a change in the location of the cloud. While in the nested simulation the mean cloud location is comparable to the reference, in the simulation initialized with

Table 3. Average bulk microphysical properties (ice water content, ice crystal number and effective radius, R_{eff}) of the simulated cirrus clouds at 15.5 km on 28 January, at 10:00, for different choice of the microphysics parameters N_{IN} and S_{nuc}.

N_{IN} (L^{-1})	150			1500		
S_{nuc}	0.08	0.20	0.45	0.08	0.20	0.45
Ice crystal number (L^{-1})	72.	32.	9.	85.	41.	9.
R_{eff} (microns)	10.5	12.9	13.8	10.4	12.6	13.6
Ice water content ($\mathrm{mg\,m}^{-3}$)	0.09	0.07	0.03	0.10	0.07	0.03

Table 4. Differences in amplitude and in vertical and horizontal centroid location between the simulated and observed ATB (a proxy for cloud position), along CALIOP track on 28 January 2009, 10:00 h UTC.

Simulation name	Amplitude	Latitude along CALIOP track (degrees)	Altitude (m)
Thompson	−0.32	−2.71	−293.
Thompson-ERAi	−1.08	−7.4	80.
Thompson-nested	−1.13	−3.4	−39.
H2O+20 %	0.83	−2.9	−820.
Morrison	−0.94	−4.8	401.
Morrison-ERAi	−0.56	−7.1	257.

Table 5. Correlation and SAL (see text for details) for the ice water path above 14 km in WRF simulations compared to the reference simulation at 12:00 on 28 January 2009. The "cloud threshold" for SAL was chosen to be a fourth of the maximum ice water path (see Wernli et al., 2008).

Simulation name	Correlation	Amplitude	Structure	Location
Thompson-ERAi	0.54	0.26	−0.58	0.14
Thompson-nested	0.47	0.36	−1.46	0.20
H2O+20 %	0.93	0.34	0.34	0.02
No heat	0.97	0.04	0.29	0.02
WSM5	0.89	0.54	0.14	0.12
Morrison	0.85	0.54	0.46	0.10
Morrison-ERAi	0.62	0.87	1.04	0.08
Thompson-$S_{\mathrm{nuc}} = 0.08$, $N_{\mathrm{IN}} = 150$	0.99	0.036	0.046	0.004
Thompson-$S_{\mathrm{nuc}} = 0.20$, $N_{\mathrm{IN}} = 150$	0.96	−0.32	−0.31	0.02
Thompson-$S_{\mathrm{nuc}} = 0.20$, $N_{\mathrm{IN}} = 1500$	0.96	−0.33	−0.27	0.02
Thompson-$S_{\mathrm{nuc}} = 0.45$, $N_{\mathrm{IN}} = 1500$	0.64	−0.77	−1.30	0.11

the ERA-Interim the cloud is moved further southward (Table 4).

This effect of southward displacement of the cloud in the simulation with ERA-Interim is also shown in the IWP maps in Fig. 7. The cloud pattern is changed in the same way for the two microphysics schemes presented: the slightly different dynamics and water vapour in ERA-Interim simulations result in a cloud structure moved in the southern part of the domain. In terms of SAL metrics (Table 5), depending on the scheme, the amplitude in the ERA-Interim simulations are increased compared to those that use the operational analysis. This response is due to a moister initial condition in cirrus formation regions in the ERA-Interim simulations, and this prevails even though there are stronger uplifts in the northern part of the domain for simulations with the operational analysis. For the two schemes, the correlations with the reference are significantly decreased (below 0.65) when the ERA-Interim or the nested run are used for initialization. This mainly comes from a change in the location term. Finally, initial and boundary conditions are also the main factors affecting the S component of the SAL (Table 5).

We must emphasize that the sensitivity to the initial conditions refers in fact to both the initial dynamics of the simulation (e.g. initial distribution of the PV) and the initial relative humidity. To isolate one from the other, we have also performed a simulation with the ECMWF operational analysis initial and boundary winds and temperature, but with the ERA-Interim water vapour field (not shown). Our water vapour does not strongly affect the dynamics because of the limited occurrence of convection in the domain. The simulated cirrus is then very similar to the one obtained with the operational analysis fields in terms of location and structure; it shows higher IWC, consistently with the discussion above (moister ERA-Interim). This experiment highlights that, due to the importance of the uplifts and the strong vertical gradient of water vapour content, the cloud structure is controlled more by the dynamically induced vertical displacement than by the initial distribution of humidity. Consistently, a simulation with NCEP-CFSR winds and temperature conducted in early stages of this work led to a cirrus field with significant differences.

The specific effect of changing the initial relative humidity is also shown by the simulation with 20 % increase of the water content. It has little effect on the horizontal characteristics of the cloud field (see the correlation, location or structure in Table 5). However, its effect is not limited to increasing the IWC; it also tends to lower the cloud altitudes (see Table 4) by bringing regions below the cloud in the reference simulation to supersaturation and hence prolonging vertically the fall streaks generated by the initial cloud.

4.3 Some sensitivities to the microphysics

As stated in the Introduction, there has been much debate regarding microphysical pathways of cirrus cloud formation (Spichtinger and Krämer, 2013). Recent measurements and modelling studies suggest that strong variability may be present at scales as small as a few metres (e.g. Jensen et al., 2013; Murphy, 2014; Dinh et al., 2016), unreachable in our model set-up. Hence we do not attempt to delve into the details of the microphysics. We evaluate the sensitivity to some microphysical assumptions by two simple approaches. First, we just take advantage of the schemes available in WRF to test how sensitive the simulated cirrus clouds are to changes within a range of standard parameterizations. Then, inside the Thompson scheme, we modify the ad hoc parameters for nucleation at low temperature: number of ice nuclei N_{IN} and supersaturation threshold for ice nucleation S_{nuc}.

4.3.1 Sensitivity to the microphysical scheme in WRF

We performed tests with one single-moment scheme (WSM5) and two double-moment schemes, the Thompson and Morrison schemes. All those schemes use the same very empirical approaches of the nucleation at low temperature

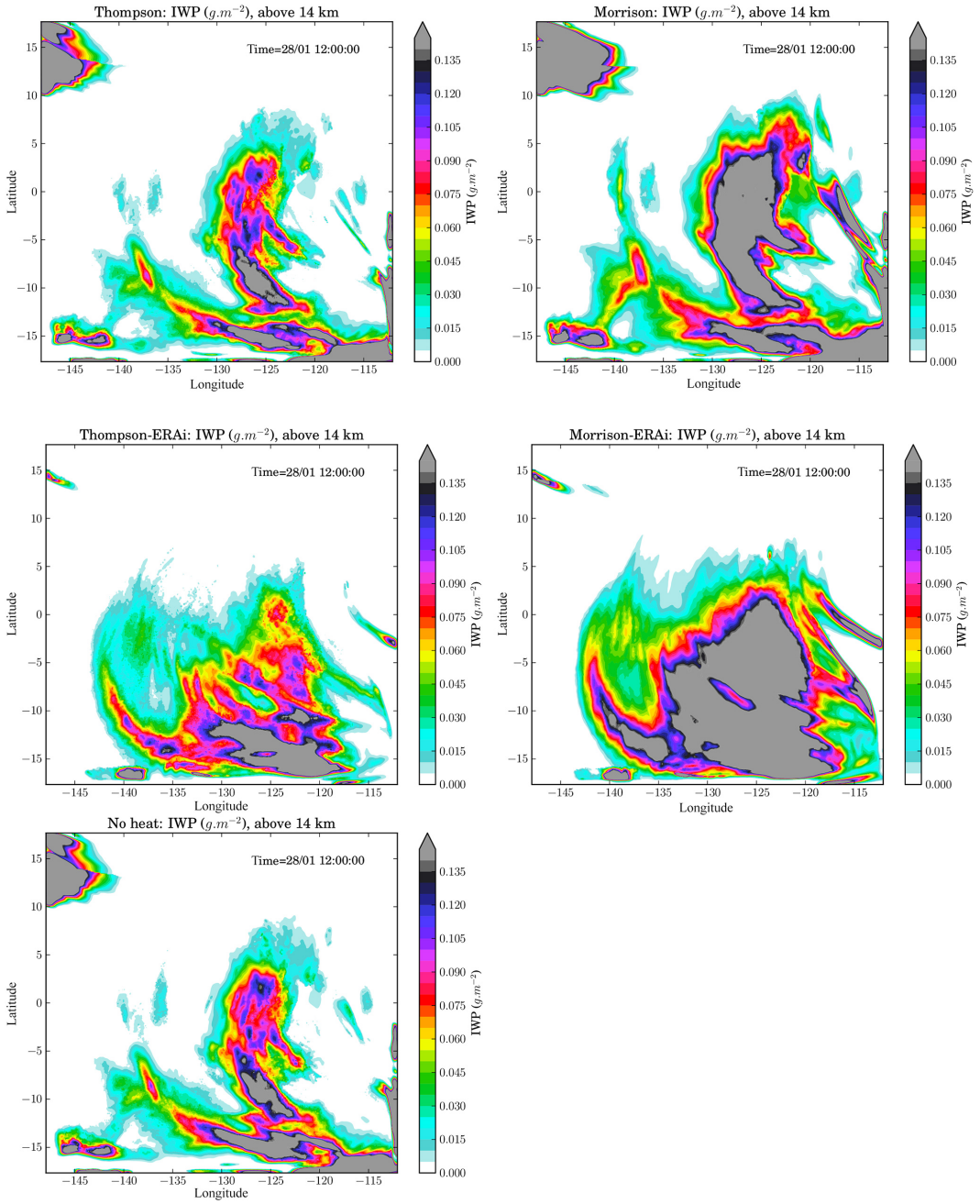

Figure 7. Maps of the ice water path above 14 km (vertically integrated ice water content) on 28 January 2009, at 12:00 UTC, in different simulations (see Table 1 for details): (top left) Thompson, (top right) Morrison, (middle left) Thompson-ERAi, (middle right) Morrison-ERAi and (bottom left) no heat.

as the Thompson scheme, but their different numerical treatments of sedimentation and growth lead to some sensitivity.

In Fig. 7, one can compare the IWP produced by the Thompson and Morrison schemes for the two initial and boundary conditions tested. The two schemes produce similar (correlated; see Table 5 for correlation with the reference) cloud fields, but their intensities differ. The Morrison simulation tends to have higher IWC than the Thompson simulation. The difference is mainly due to the integrated effect of sedimentation (it almost vanishes if sedimentation is suppressed), the Morrison scheme having a less efficient sedimentation (more details on the different treatments of sedimentation can be found in Appendix A). This lower downward flux of ice in the simulations with the Morrison scheme also explains that the cloud is higher in those compared to CALIPSO observations (see Table 4). Vertical profiles con-

firm this effect of higher IWC in the Morrison scheme (not shown).

In terms of SAL metrics, Table 5 shows that the main component affected by the different choice in microphysics is the amplitude, i.e. the mean value of the IWP. However, the correlations are higher, and the structure and location components are more similar between the different schemes than between different initial and boundary conditions. Also, it appears clearly in this table that the different choices made in the two-moment schemes make them as dissimilar from one another as from the WSM5 one-moment scheme.

4.3.2 Sensitivity to some bulk microphysics parameters: number of "ice nuclei" and supersaturation threshold for nucleation

In order to explore further the sensitivity to microphysical parameters, we have also run sensitivity simulations with different supersaturation thresholds S_{nuc} and "ice nuclei number" N_{IN}. Because our resolution is coarse relative to what is needed to resolve microphysical processes, we emphasize that the chosen supersaturation threshold is not meant to fit experimental data of homogeneous or heterogenous nucleation. Rather, it has to account for the fact that, within one model grid box, temperature and/or water vapour fluctuations will cause the relative humidity to rise above the actual (experimentally measured) threshold for the particles that are present, while the grid box average remains below this value (Kärcher and Burkhardt, 2008). However, the chosen value is ad hoc and the sensitivity to this parameter should be assessed. Besides the default value of 8 %, we have tested values for threshold supersaturation of 20, 30 and 45 %. As $N_{\mathrm{IN}} = 1500\,\mathrm{L}^{-1}$ may appear strong as a default value for the grid-box-mean effect of nucleation, we have tested reducing N_{IN} to $150\,\mathrm{L}^{-1}$.

Figure 8 shows maps of the IWP above 15 km for two simulations, with the Thompson scheme keeping the same $N_{\mathrm{IN}} = 1500\,\mathrm{L}^{-1}$ and varying the supersaturation threshold ($S_{\mathrm{nuc}} = 0.2$ and 0.45); these figures can also be compared to the reference simulation in the top left panel of Fig. 7. They show that, over some range of S_{nuc}, the large-scale cloud field is only weakly dependent on S_{nuc}: between $S_{\mathrm{nuc}} = 0.08$ and $S_{\mathrm{nuc}} = 0.2$, there is only a change in the absolute IWP value, which is diminished due to more grid point not experiencing nucleation and remaining ice free. This ice mass decrease can also be seen in Table 5 in the A component of the SAL. Despite the amplitude difference, the general cloud pattern is itself very similar between the simulations with $S_{\mathrm{nuc}} = 0.08$ and $S_{\mathrm{nuc}} = 0.2$, as confirmed by the strong correlation with the reference (Table 5). When a critical value for the threshold is exceeded, however, nucleation does not happen in some parts of the cloud and the pattern is much affected; this is the case for the experiment with $S_{\mathrm{nuc}} = 0.45$. Changing N_{IN} between $N_{\mathrm{IN}} = 150$ and $N_{\mathrm{IN}} = 1500\,\mathrm{L}^{-1}$ had only a minor impact on the large-scale properties of the simulated cloud field (Table 5), which may result from an increase in the portion of the cloud experiencing nucleation.

The overall bulk microphysical properties of the clouds are relatively weakly affected by the change, as reported in Table 3. We emphasize that this is very different from parcel model results, because the area covered by the clouds changes from a simulation to the other and because we select only cloudy air (i.e. with IWC bigger than $5 \times 10^{-1}\,\mathrm{kg\,kg}^{-1}$) to compute the statistics. N_{IN} has a limited impact. S_{nuc} variation creates much more substantial variability. However, this stays within the variability observed in TTL cirrus clouds, which scans several orders of magnitude (Jensen et al., 2013).

Overall, the results of those experiments show that there is robustness of the simulated cirrus large-scale and microphysical properties for a range of parameter values, which lie within reasonable values. This is reassuring given the uncertainty of those parameters in our simulation framework.

4.4 Sensitivity to radiation

Previous real-case studies have shown that interaction with radiation could have a strong influence on the high cloud field evolution for midlatitude cases (Gu et al., 2011). Idealized simulations suggest that this may also be the case for TTL cirrus, at least under specific environmental conditions (Dinh et al., 2010; Jensen et al., 2011). In Fig. 7, the IWP from simulations with (top) and without (bottom) cloud radiative effect included is displayed. There is little difference between the two simulations, and this is confirmed by the very high correlation (0.97) and the small amplitude component of the SAL metrics (Table 5). On this timescale (36 h after the beginning of the simulation), it seems that there is little impact on the cirrus field. We will discuss possible reasons for this negligible impact of the radiation in our case in Sect. 5.

4.5 Resolution

It should be noted that the results we present are for a specific resolution, which is probably too low to adequately simulate some of the processes at stake. Nevertheless, increasing the vertical resolution by a factor of 2 or the horizontal one by a factor of 2.5 created few quantitative changes to the simulated cirrus cloud field. This illustrates that in our set-up and with our typical resolution (a few kilometres in the horizontal and a few hundred metres in the vertical), sensitivity to resolution has not yet appeared. This is also linked to the relative lack of convection in the domain and to the first-order influence of the forcing provided by the large-scale dynamics.

4.6 Summary of sensitivities

For our cirrus case, the combination of the correlations and of the amplitude component of the SAL metrics in Table 5 allows some ranking of sensitivities. The dynamics are of

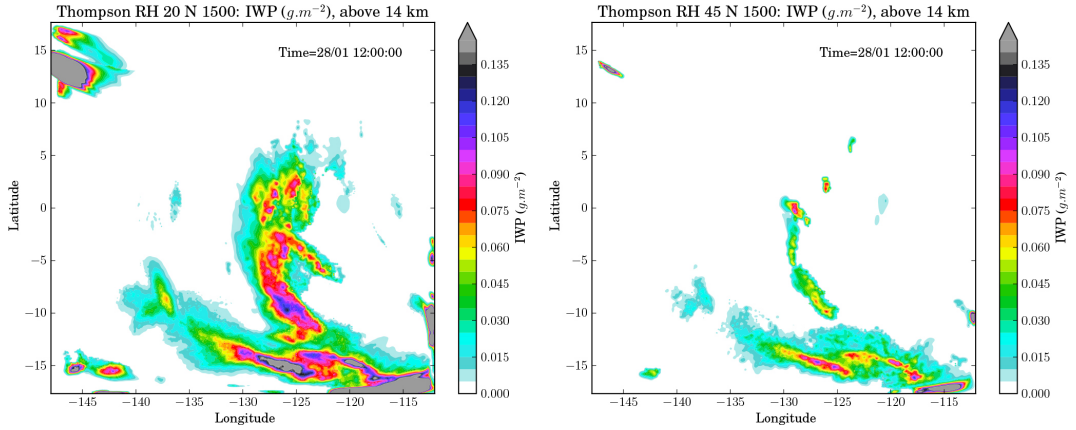

Figure 8. Maps of the ice water path above 14 km (vertically integrated ice water content) on 28 January 2009, at 12:00 UTC, in simulations using the Thompson scheme with different supersaturation threshold for ice formation (see Sect. 4.3.2 for details): (left) $S_{\text{nuc}} = 0.2$ and (right) $S_{\text{nuc}} = 0.45$.

first order, although after 36 h of simulation the impact of microphysics and initial water vapour are also important. The choices of the parameterization of microphysical processes and of the initial water content do not affect the cloud field in the same manner as dynamics; they mainly influence the cloud "amplitude" and vertical position. The "dry" dynamical initial and boundary conditions (winds and temperature), as well as the different dynamics and water vapour field they create through different advection, are more important to determine the cloud structure and location and have the strongest impact on correlations. The relatively moderate role of details in the water vapour field is reassuring because this quantity is poorly known at fine scale in the TTL. It explains why we obtain a good agreement with the observations without any tuning of the initial water vapour. Finally, Table 5 shows that, in our case, the cloud radiative effect results in much less sensitivity than the other factors because of the relatively low heating rates.

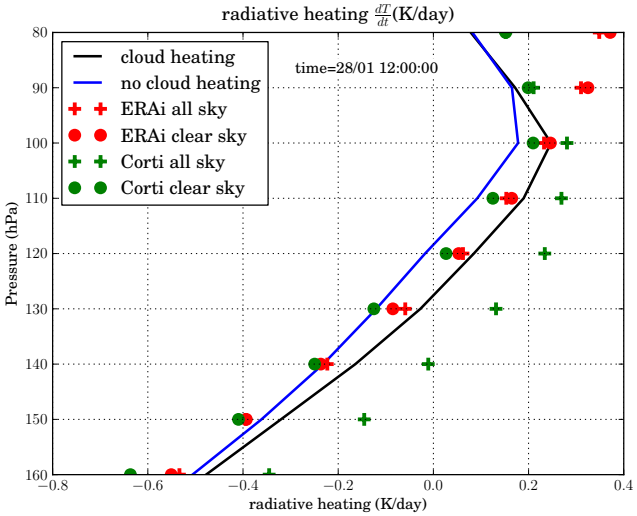

Figure 9. Profiles of radiative heating rates on 28 January 2009, 12:00 UTC, in the WRF domain, for the simulations with (black) and without (blue) cloud heating included. For comparison, the 3 h averaged clear-sky and all-sky radiative heating rates in the ERA-Interim reanalysis are shown in red, together with the estimates from Corti et al. (2006) for clear-sky and all regions in green.

5 Discussion

5.1 Evaluation of the cirrus radiative impact in the TTL

Cirrus clouds are believed to strongly influence the radiative budget of the TTL by increasing the radiative heating rates. In this region of low positive heating rates, even a small contribution from cirrus could significantly enhance the transport efficiency and strongly lower the transit time of ascending air parcels from the TTL to the stratosphere (Corti et al., 2006). Based on the satisfactory agreement with observations (see Sect. 2.3), our simulations allow us to provide a reliable estimate of the radiative impact of this specific cloud in the tropical tropopause layer. To evaluate this, we have performed simulations with the cloud radiative heating artificially turned off in the RRTMG scheme. The resulting profiles of radiative heating rates averaged over the domain are shown in Fig. 9. For comparison, the same profiles in the ECMWF ERA -Interim reanalysis and the zonal annual mean profiles calculated by Corti et al. (2006) are also displayed for clear and all-sky radiative heating rates. Note that the heating rates profiles displayed here are in actual temperature tendency and not in potential temperature tendency.

In the upper TTL (above 90 hPa), the WRF simulation seems to underestimate the heating rates compared to the ERA-Interim. They are in better agreement with Corti et al.

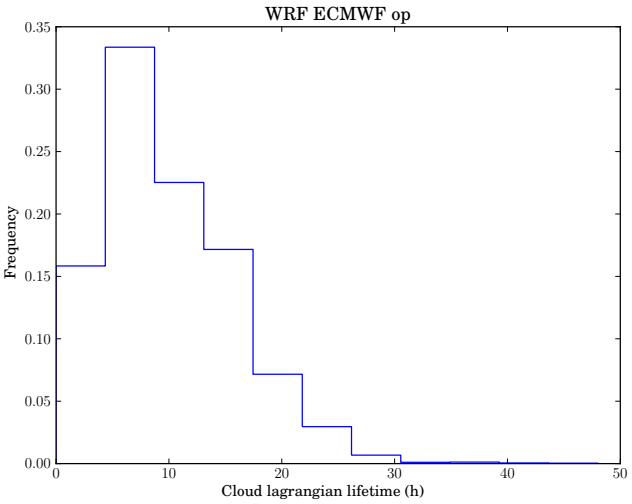

Figure 10. Distribution of in-cloud residence time for air parcels, estimated from Lagrangian trajectories launched on 28 January 2009, 12:00, in the reference simulation and calculated forward and backward. Parcels were considered in cloud when the ice water content was bigger than 1×10^{-8} kg kg^{-1}.

(2006). This disagreement mainly comes from long-wave differences and might be due to different ozone mixing ratios, but it was not investigated further as it is above the main levels of interest.

In the lower part of the TTL (below 90 hPa), there is a fair agreement between the heating rates in the ERA-Interim and in the WRF simulation, which use different versions of the same RRTMG scheme, as well as with those estimated by Corti et al. (2006). However, the difference between clear- and all-sky heating rates in the reanalysis is very limited, while there is a significant enhancement of the heating in the simulations even after averaging over the whole domain. From the difference between the WRF simulations with and without cloud radiative heating included, we estimate the domain-averaged cloud radiative effect to be of the order of 0.1 K day^{-1}. This contribution moves the level of zero radiative heating by about 10 hPa (i.e. about 500 m) below its clear-sky value. This is a factor of about 2–3 smaller than the estimates by Corti et al. (2006) for the whole tropics shown on the figure, which is probably due to geographic heterogeneities of the cloud field in the tropics with much colder and denser clouds in the Western Pacific boreal winter. We also emphasize that this is a domain average, but instantaneous values in the cloud can be much more substantial, reaching up to 1.5–2 K day^{-1}. This is comparable to estimates of the order of 1–3 K day^{-1} observed by Bucholtz et al. (2010) but higher than values in subvisible cirrus reported by Davis et al. (2010). This figure also stresses that a poor representation of the cirrus in the reanalysis probably leads to an underestimation of the additional heating rate induced by the cloud.

5.2 Absence of a cloud-scale (re)circulation and observed cloud duration

Recent studies (e.g. Dinh et al., 2012; Jensen et al., 2011) have examined how cloud-induced radiative heating could drive cloud-scale circulation in TTL cirrus. Among other results, the magnitude of wind shear was found to be an important factor affecting the buildup of cloud-scale circulations (Jensen et al., 2011).

We examined the dynamical impact of cloud radiative heating for our simulated cirrus by comparing the simulations with and without cloud radiative heating. Only minor differences were found for the cirrus evolution (see Table 5). Although the situation was a priori ideal for a cloud-scale circulation to build (cloud above the ocean, with little convection below), several factors can explain its absence in our simulations. First, our radiative heating rates are too low to generate such a circulation, although they are comparable to the lower values reported in the literature for modelling studies (e.g. Dinh et al., 2012). Then, our vertical resolution of 300 m may be too coarse to resolve this recirculation in the cloud and its surrounding. However, increasing the vertical resolution by a factor of 2 did not produce any significant change. Going back to physical reasons, Jensen et al. (2011) suggested that, in most cirrus, the Lagrangian temperature variability along an air parcel trajectory was such that it would limit the cloud lifetime, which would then be too short for a radiatively induced circulation to build. We estimated the in-cloud residence time using Lagrangian trajectories: forward and backward trajectories were calculated from initial positions within the cloud (IWC higher than 1×10^{-8} kg kg^{-1}), spaced every 1° in latitude and longitude and every 500 m in the vertical.

The resulting probability density functions for the in-cloud residence time of air parcels is displayed in Fig. 10. The typical lifetime is less than 10 h, which is probably too short for a radiative circulation to build and have significant impact on the cloud evolution. This result for our cirrus is in agreement with what was found for different TTL cirrus by Jensen et al. (2011).

On top of this cloud-lifetime limitation, there is another reason explaining the absence or at least the very limited impact of a cloud-scale (re-)circulation in our test case: the amplitude of this circulation. It will obviously depend on the background stability and heating efficiency, but idealized studies (Dinh et al., 2010, 2012) suggest that, in the most favourable cases and in a 2-D setting, those circulations will not exceed a few m s^{-1} in the horizontal and a few cm s^{-1} on the vertical. These velocities and the associated shears are at most comparable to and often smaller than the ambient velocities and shears (e.g. the amplitude of cirrus-induced wind shear in idealized simulations reaches at most 5 m s^{-1} km^{-1}; Dinh et al., 2012). In the vertical, typical large-scale to mesoscale motions which generate cirrus formation and cause cirrus dissipation can be of the order of

a few $\mathrm{cm\,s^{-1}}$. Hence, in cases such as ours, the radiatively induced vertical motions are not strong enough to come out relative to other motions present.

Finally, the set of simulations we have performed suggests that even if TTL cirrus appear to last several days, as suggested by Taylor et al. (2011), this can rather correspond to a succession of distinct clouds forming in a region of persistent favourable conditions. As for orographic lenticular clouds that can persist above mountains, the cloudy air parcels in the TTL cirrus clouds in our region are different through the cloud presence time. Cloud radiative heating seems not to have an important impact on the dynamics in our specific case and it is probably not required to explain the long duration of the cloud.

5.3 Cloud-induced vertical redistribution of water vapour

One major issue associated with TTL cirrus is the water vapour redistribution, which produces the irreversible dehydration (freeze-drying) experienced by air parcels that transit through the TTL before entering the stratosphere. Dinh et al. (2014) have used idealized simulations to illustrate that different scenarios for water vapour redistribution could arise depending on the cloud environment, with layers being dehydrated and others rehydrated. Similar estimates are not possible in our modelling configuration, because we do not use periodic boundary conditions. In our limited area simulations, there are air and water mass fluxes leaving and entering the domain through its boundaries. To nevertheless provide an estimate of the water redistribution due to the cloud field, we have introduced a passive water tracer in the simulations. The water tracer is advected and diffused using the same numerics as the moisture field (positive definite advection) but it is not subject to any physical, or more precisely microphysical, source nor sink. We evaluate the integrated impact of those microphysical sources and sinks, i.e. the vertical redistribution of water by the cloud, through the difference between the unaffected (advected only) water vapour field and the fully microphysically interactive water vapour.

Figure 11 shows the profile of the difference between microphysically passive and active water. To avoid being affected by the boundary conditions, we have introduced a second passive tracer for the "inner domain", i.e. the part of the domain whose air was inside the domain at the initial time. We have computed the difference only over this area, which depends on the altitude range considered due to wind vertical shear. Hence, the passive water is affected by exchange with air coming from the boundaries only in a limited "diffusion" range. This is less true for the active water due to the sheared vertical structure of our "inner domain" which, combined with ice sedimentation, may cause a water transfer due to ice falling from the "outer" into the "inner domain". That is why we can only provide a rough estimate of the vertical redistribution of water in the simulation. Here, three coloured curves are shown for three different simulations. The green curve corresponds to a "no sedimentation" test in which we artificially suppressed sedimentation for temperatures below 220 K (the cirrus regime); the consistency of our calculation is validated by the closeness of this curve to a 0 ppmv change in total water above 14 km. The blue curve shows the evaluation of redistribution for the Thompson scheme; with this scheme the cirrus dehydrates by about 0.5 ppmv above 15.5 km and rehydrates below this altitude (by about 0.5 ppmv). Finally, the red curve corresponds to a "maximum dehydration" simulation in which the microphysics in the cirrus regime has been replaced by a simple hypothesis of removal of all water above 100 % relative humidity with respect to ice (there is no ice for this simulation). Comparison of the red and blue curves illustrates the overestimation of dehydration and the missed rehydration made with this hypothesis, which is close to what has been used for Lagrangian trajectory modelling of stratospheric water vapour (e.g. Fueglistaler and Haynes, 2005).

We emphasize that the calculated redistributions are very dependent on the microphysical scheme and microphysical assumptions. Nevertheless, our simulations show the importance of the vertical redistribution of water associated with dehydration, which is known but may have been previously overlooked. Indeed, the dominant paradigm in calculations on dehydration along Lagrangian trajectories (e.g. Liu et al., 2010) is that the water vapour source is exclusively from below and that the last dehydration (i.e. coldest point along the trajectory) determines the water vapour concentration of air entering the stratosphere. This neglects the possibility of rehydration by sedimenting crystals, which constitutes another source of water vapour. Moreover, because of horizontal and vertical heterogeneities in the dehydration patterns, hydration by sedimenting ice crystals can modulate these patterns and the intensity of dehydration. In particular, Fueglistaler et al. (2014) recently illustrated that the stratospheric water response to a temperature drop associated with an increase in tropical upwelling would not follow the Clausius–Clapeyron scaling. By reducing the residence time of air in the TTL and thus the probability of air parcels to experience the coldest TTL temperatures (bounded in some geographic regions), the vertical velocity increase mitigates the temperature drop effect. If the TTL residence time indeed contributes to control dehydration, it is probable that rehydration (from in situ cirrus or anvil ice) does not fully cancel out before entering the stratosphere. In any case, limited (by microphysical processes) dehydration or rehydration (by sedimenting ice crystals) certainly contributes to influence the amount of water vapour and ice in the TTL.

6 Conclusions

We have performed a case study of large-scale cirrus clouds in the Eastern Pacific using a mesoscale model, the Weather

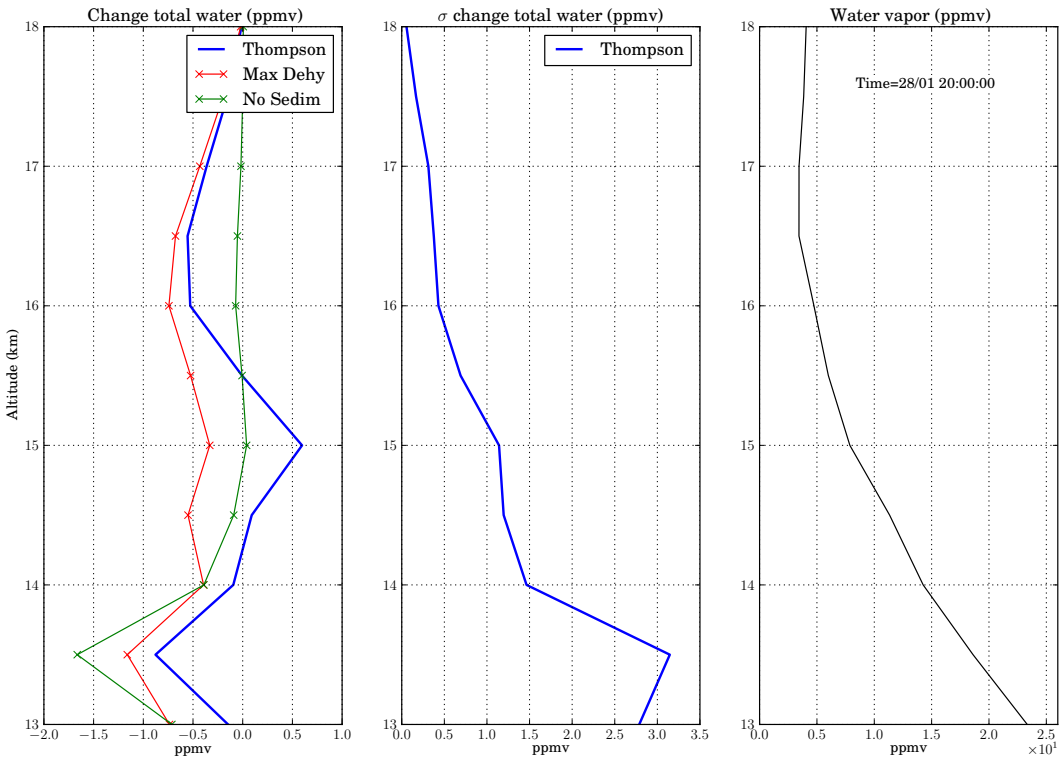

Figure 11. (Left) Change in water vapour between the start of the simulation (27 January 2009, 00:00) and 28 January 2009, 20:00, i.e. after 44 h of simulation, for three simulations: "Thompson" in blue (Thompson microphysics scheme), "Max Dehy" or "Maximum Dehydration" in red (removal of water vapour above 100 % relative humidity) and "No Sedim" or "no sedimentation" in green (sedimentation turned off for temperatures below 220 K). See text for details of the methodology of evaluation of the redistribution. (Middle) Standard deviation of the water redistribution for the "Thompson" full microphysics case; this emphasizes the variability and uncertainty in the estimate. (Right) Mean water vapour profile in the simulations.

Research and Forecast model (Skamarock et al., 2008). These simulations complement the previous study of the same case by Taylor et al. (2011), which was based on observations, and test the ability of the WRF model to reproduce cirrus clouds in the tropical tropopause layer. The simulations compare well with CALIPSO observations, suggesting that the dynamical processes leading to the cirrus formation are well captured by the model. They confirm that the cirrus forms in situ due to large-scale uplift associated with the response to a midlatitude potential vorticity intrusion. At the equator, this PV intrusion excites an equatorial wave response, mainly Yanai (mixed Rossby gravity) and equatorial Rossby modes that are modulated by faster inertio-gravity waves. The vertical displacements associated with this atmospheric flow are of the order of 1000 m in 30 h (equivalent to a mean cooling rate of $-8\,\mathrm{K\,day^{-1}}$) and generate an increase in the relative humidity which is responsible for the formation of the cirrus clouds. Although the cloud forms in regions of relatively weak winds and has a large horizontal extent (several hundreds to more than a thousand of kilometres), trajectory calculations show that air parcels transit through the cirrus on timescales of about half a day.

This study highlights the importance of dynamical forcing in TTL cirrus formation: large-scale uplift associated with low-frequency perturbations provides the necessary drop in temperature for the cloud to form. The presence of the cirrus is robust between the two analysis systems tested (the ECMWF ERA-Interim reanalysis and operational analysis), because they both resolve the PV intrusion, which is a large-scale feature. The simulated clouds are sensitive not only to the dynamics but also to the microphysical scheme and the distribution of water vapour, in different ways: differences in the dynamics affect the location, amplitude and structure of a cloud field, while the microphysics and water vapour mainly influence the intensity of the cloud and its vertical position and extent. The strong dependence to the dynamics, i.e. to the initial and boundary conditions provided by analyses, implies a serious difficulty for real-case simulations, because analyses notoriously have deficiencies in the description of winds in the TTL (Podglajen et al., 2014). In contrast to the sensitivity to dynamics and microphysics, the simulated cloud showed little sensitivity to radiation. More precisely, the simulations showed no evidence of a circulation on the scale of the cloud driven by radiative effects, likely because the cloud

residence times are short (half a day) and the radiatively induced heating rates are rather weak. As this result might be tied to the specific environment in which the cloud develops (e.g. its relatively warm temperature of about 190 K), more real-case simulations are needed in the future to evaluate the impact of cloud radiative heating on the dynamics in different environments.

Finally, the simulations illustrate the importance of dehydration and its associated rehydration in the TTL. This is important to understand not only the entry of stratospheric water vapour but also the water budget of the TTL itself. We emphasize that the latter is also of importance and has non-negligible impacts for the top of the atmosphere radiative fluxes (Riese et al., 2012).

Appendix A: Ice sedimentation in Thompson and Morrison schemes

In the version of the Thompson scheme used in this work, the sedimentation fall speed of a single ice crystal depends on its diameter D under the form

$$v(D) = \left(\frac{\rho_0}{\rho}\right)^{0.5} \alpha D^{\beta}. \quad \text{(A1)}$$

The coefficients are $\alpha = 1847.5$ and $\beta = 1$; they have been chosen to produce a smooth transition with the snow category (Thompson et al., 2008). In the Morrison scheme, ice sedimentation follows

$$v(D) = \left(\frac{\rho_0}{\rho}\right)^{0.35} a D^{b}, \quad \text{(A2)}$$

where $a = 700$ and $b = 1$; at the considered altitudes, there is a factor of 2 to 3 between the fall speeds in the Morrison and Thompson's schemes, which explains the higher IWC observed in the Thompson scheme.

Acknowledgements. The authors are grateful to Sophie Bastin, Marjolaine Chiriaco and Hélène Chepfer for help with the COSP. We thank Martina Krämer, Jens-Uwe Grooß, Joan Alexander, Eric Jensen and Bill Randel for helpful discussions, and Pasquale Sellitto and three anonymous reviewers for their insightful comments on the manuscript. Aurélien Podglajen and Riwal Plougonven received support from École Polytechnique's Chaire pour le Développement Durable (DDX). Riwal Plougonven, Albert Hertzog, Bernard Legras and Aurélien Podglajen acknowledge support from ANR project StraDyVariUS (Stratospheric Dynamics and Variability, ANR-13-BS06-0011-01) and from EU project StratoClim. The support of CNES through "Stratéole" project is also acknowledged.

Edited by: P. Haynes

References

Bucholtz, A., Hlavka, D. L., McGill, M. J., Schmidt, K. S., Pilewskie, P., Davis, S. M., Reid, E. A., and Walker, A. L.: Directly measured heating rates of a tropical subvisible cirrus cloud, J. Geophys. Res., 115, D00J09, doi:10.1029/2009JD013128, 2010.

Chepfer, H., Bony, S., Winker, D., Chiriaco, M., Dufresne, J.-L., and Sèze, G.: Use of CALIPSO lidar observations to evaluate the cloudiness simulated by a climate model, Geophys. Res. Lett., 35, 1944–8007, doi:10.1029/2008GL034207, 2008.

Cirisan, A., Luo, B. P., Engel, I., Wienhold, F. G., Sprenger, M., Krieger, U. K., Weers, U., Romanens, G., Levrat, G., Jeannet, P., Ruffieux, D., Philipona, R., Calpini, B., Spichtinger, P., and Peter, T.: Balloon-borne match measurements of midlatitude cirrus clouds, Atmos. Chem. Phys., 14, 7341–7365, doi:10.5194/acp-14-7341-2014, 2014.

Corti, T., Luo, B. P., Peter, T., Vömel, H., and Fu, Q.: Mean radiative energy balance and vertical mass fluxes in the equatorial upper troposphere and lower stratosphere, Geophys. Res. Lett., 32, L06802, doi:10.1029/2004GL021889, 2005.

Corti, T., Luo, B. P., Fu, Q., Vömel, H., and Peter, T.: The impact of cirrus clouds on tropical troposphere-to-stratosphere transport, Atmos. Chem. Phys., 6, 2539–2547, doi:10.5194/acp-6-2539-2006, 2006.

Cziczo, D. J., Froyd, K. D., Hoose, C., Jensen, E. J., Diao, M., Zondlo, M. A., Smith, J. B., Twohy, C. H., and Murphy, D. M.: Clarifying the dominant sources and mechanisms of cirrus cloud formation., Science, 340, 1320–1324, doi:10.1126/science.1234145, 2013.

Davis, S., Hlavka, D., Jensen, E., Rosenlof, K., Yang, Q., Schmidt, S., Borrmann, S., Frey, W., Lawson, P., Voemel, H., and Bui, T. P.: In situ and lidar observations of tropopause subvisible cirrus clouds during TC4, J. Geophys. Res., 115, D00J17, doi:10.1029/2009JD013093, 2010.

Dinh, T., Durran, D. R., and Ackerman, T.: Maintenance of tropical tropopause layer cirrus, J. Geophys. Res., 115, D02104, doi:10.1029/2009JD012735, 2010.

Dinh, T., Durran, D. R., and Ackerman, T.: Cirrus and water vapor transport in the tropical tropopause layer – Part 1: A specific case modeling study, Atmos. Chem. Phys., 12, 9799–9815, doi:10.5194/acp-12-9799-2012, 2012.

Dinh, T., Fueglistaler, S., Durran, D., and Ackerman, T.: Cirrus and water vapour transport in the tropical tropopause layer – Part 2: Roles of ice nucleation and sedimentation, cloud dynamics, and moisture conditions, Atmos. Chem. Phys., 14, 12225–12236, doi:10.5194/acp-14-12225-2014, 2014.

Dinh, T., Podglajen, A., Hertzog, A., Legras, B., and Plougonven, R.: Effect of gravity wave temperature fluctuations on homogeneous ice nucleation in the tropical tropopause layer, Atmos. Chem. Phys., 16, 35–46, doi:10.5194/acp-16-35-2016, 2016.

Evan, S., Rosenlof, K. H., Dudhia, J., Hassler, B., and Davis, S. M.: The reWater Vapor Measurement Biases in the Tropical Tropopause Layer: Aura Microwave Limb Sounder vs Frost Point Hygrometerspresentation of the TTL in a tropical channel version of the WRF model, J. Geophys. Res.-Atmos., 118, 2835–2848, doi:10.1002/jgrd.50288, 2013.

Fueglistaler, S. and Haynes, P. H.: Control of interannual and longer-term variability of stratospheric water vapor, J. Geophys. Res., 110, D24108, doi:10.1029/2005JD006019, 2005.

Fueglistaler, S., Dessler, A. E., Dunkerton, T. J., Folkins, I., Fu, Q., and Mote, P. W.: Tropical tropopause layer, Rev. Geophys., 47, RG1004, doi:10.1029/2008RG000267, 2009.

Fueglistaler, S., Liu, Y. S., Flannaghan, T. J., Ploeger, F., and Haynes, P. H.: Departure from Clausius-Clapeyron scaling of water entering the stratosphere in response to changes in tropical upwelling, J. Geophys. Res.-Atmos., 119, 1962–1972, doi:10.1002/2013JD020772, 2014.

Gu, Y., Liou, K. N., Ou, S. C., and Fovell, R.: Cirrus cloud simulations using WRF with improved radiation parameterization and increased vertical resolution, J. Geophys. Res.-Atmos., 116, 2156–2202, doi:10.1029/2010JD014574, 2011.

Hong, S.-Y., Dudhia, J., and Chen, S.-H.: A Revised Approach to Ice Microphysical Processes for the Bulk Parameterization of Clouds and Precipitation, Mon. Weather Rev., 132, 103–120, 2004.

Iacono, M. J., Delamere, J. S., Mlawer, E. J., Shephard, M. W., Clough, S. A., and Collins, W. D.: Radiative forcing by long-lived greenhouse gases: Calculations with the AER radiative transfer models, J. Geophys. Res.-Atmos., 113, 2156–2202, doi:10.1029/2008JD009944, 2008.

Jensen, E. and Pfister, L.: Transport and freeze-drying in the tropical tropopause layer, J. Geophys. Res., 109, D02207, doi:10.1029/2003JD004022, 2004.

Jensen, E. J., Toon, O. B., Pfister, L., and Selkirk, H. B.: Dehydration of the upper troposphere and lower stratosphere by subvisible cirrus clouds near the tropical tropopause, Geophys. Res. Lett., 23, 825–828, doi:10.1029/96GL00722, 1996.

Jensen, E. J., Pfister, L., and Toon, O. B.: Impact of radiative heating, wind shear, temperature variability, and microphysical processes on the structure and evolution of thin cirrus in the tropical tropopause layer, J. Geophys. Res., 116, 2156–2202, doi:10.1029/2010JD015417, 2011.

Jensen, E. J., Diskin, G., Lawson, R. P., Lance, S., Bui, T. P., Hlavka, D., McGill, M., Pfister, L., Toon, O. B., and Gao, R.: Ice nucleation and dehydration in the Tropical Tropopause Layer, P. Natl. Acad. Sci. USA, 110, 2041–2046, doi:10.1073/pnas.1217104110, 2013.

Kienast-Sjögren, E., Miltenberger, A. K., Luo, B. P., and Peter, T.: Sensitivities of Lagrangian modelling of mid-latitude cirrus

clouds to trajectory data quality, Atmos. Chem. Phys., 15, 7429–7447, doi:10.5194/acp-15-7429-2015, 2015.

Kiladis, G. and Feldstein, S.: Rossby wave propagation into the tropics in two GFDL general circulation models, Clim. Dynam., 9, 245–252, 1994.

Kim, J.-E. and Alexander, M. J.: Direct impacts of waves on tropical cold point tropopause temperature, Geophys. Res. Lett., 42, 1584–1592, doi:10.1002/2014GL062737, 2015.

Koop, T., Luo, B., Tsias, A., and Peter, T.: Water activity as the determinant for homogeneous ice nucleation in aqueous solutions, Nature, 406, 611–614, doi:10.1038/35020537, 2000.

Krämer, M., Schiller, C., Afchine, A., Bauer, R., Gensch, I., Mangold, A., Schlicht, S., Spelten, N., Sitnikov, N., Borrmann, S., de Reus, M., and Spichtinger, P.: Ice supersaturations and cirrus cloud crystal numbers, Atmos. Chem. Phys., 9, 3505–3522, doi:10.5194/acp-9-3505-2009, 2009.

Kunz, A., Spelten, N., Konopka, P., Müller, R., Forbes, R. M., and Wernli, H.: Comparison of Fast In situ Stratospheric Hygrometer (FISH) measurements of water vapor in the upper troposphere and lower stratosphere (UTLS) with ECMWF (re)analysis data, Atmos. Chem. Phys., 14, 10803–10822, doi:10.5194/acp-14-10803-2014, 2014.

Kärcher, B. and Burkhardt, U.: A cirrus cloud scheme for general circulation models, Q. J. Roy. Meteor. Soc., 134, 1439–1461, doi:10.1002/qj.301, 2008.

Lawson, R. P., Pilson, B., Baker, B., Mo, Q., Jensen, E., Pfister, L., and Bui, P.: Aircraft measurements of microphysical properties of subvisible cirrus in the tropical tropopause layer, Atmos. Chem. Phys., 8, 1609–1620, doi:10.5194/acp-8-1609-2008, 2008.

Liu, Y. S., Fueglistaler, S., and Haynes, P. H.: Advection-condensation paradigm for stratospheric water vapor, J. Geophys. Res.-Atmos., 115, 2156–2202, doi:10.1029/2010JD014352, 2010.

McFarquhar, G. M., Heymsfield, A. J., Spinhirne, J., and Hart, B.: Thin and subvisual tropopause tropical cirrus: Observations and radiative impacts, J. Atmos. Sci., 57, 1841–1853, 2000.

Mioche, G., Josset, D., Gayet, J.-F., Pelon, J., Garnier, A., Minikin, A., and Schwarzenboeck, A.: Validation of the CALIPSO-CALIOP extinction coefficients from in situ observations in midlatitude cirrus clouds during the CIRCLE-2 experiment, J. Geophys. Res.-Atmos., 115, 2156–2202, doi:10.1029/2009JD012376, 2010.

Morrison, H., Curry, J. A., and Khvorostyanov, V. I.: A New Double-Moment Microphysics Parameterization for Application in Cloud and Climate Models. Part I: Description, J. Atmos. Sci., 62, 1665–1677, doi:10.1175/JAS3446.1, 2005.

Muhlbauer, A., Berry, E., Comstock, J. M., and Mace, G. G.: Perturbed physics ensemble simulations of cirrus on the cloud system-resolving scale, J. Geophys. Res.-Atmos., 119, 4709–4735, doi:10.1002/2013JD020709, 2014.

Muhlbauer, A., Ackerman, T. P., Lawson, R. P., Xie, S., and Zhang, Y.: Evaluation of cloud-resolving model simulations of midlatitude cirrus with ARM and A-train observations, J. Geophys. Res.-Atmos., 120, 6597–6618, doi:10.1002/2014JD022570, 2015.

Murphy, D. M.: Rare temperature histories and cirrus ice number density in a parcel and a one-dimensional model, Atmos. Chem. Phys., 14, 13013–13022, doi:10.5194/acp-14-13013-2014, 2014.

Podglajen, A., Hertzog, A., Plougonven, R., and Žagar, N.: Assessment of the accuracy of (re)analyses in the equatorial lower stratosphere, J. Geophys. Res., 119, 11166–11188, doi:10.1002/2014JD021849, 2014.

Randel, W. J.: Upper Tropospheric Equatorial Waves In Ecmwf Analyses, Q. J. Roy. Meteor. Soc., 118, 365–394, doi:10.1002/qj.49711850409, 1992.

Riese, M., Ploeger, F., Rap, A., Vogel, B., Konopka, P., Dameris, M., and Forster, P.: Impact of uncertainties in atmospheric mixing on simulated UTLS composition and related radiative effects, J. Geophys. Res.-Atmos., 117, 2156–2202, doi:10.1029/2012JD017751, 2012.

Skamarock, W. C., Klemp, J. B., Dudhia, J., Gill, D. O., Barker, D. M., G., D. M., Huang, X.-Y., Wang, W., and Powers, J. G.: A description of the Advanced Research WRF Version 3., Tech. Rep., Natl. Cent. for Atmos. Res., 2008.

Spichtinger, P. and Krämer, M.: Tropical tropopause ice clouds: a dynamic approach to the mystery of low crystal numbers, Atmos. Chem. Phys., 13, 9801–9818, doi:10.5194/acp-13-9801-2013, 2013.

Stubenrauch, C. J., Cros, S., Guignard, A., and Lamquin, N.: A 6-year global cloud climatology from the Atmospheric InfraRed Sounder AIRS and a statistical analysis in synergy with CALIPSO and CloudSat, Atmos. Chem. Phys., 10, 7197–7214, doi:10.5194/acp-10-7197-2010, 2010.

Taylor, J. R., Randel, W. J., and Jensen, E. J.: Cirrus cloud-temperature interactions in the tropical tropopause layer: a case study, Atmos. Chem. Phys., 11, 10085–10095, doi:10.5194/acp-11-10085-2011, 2011.

Thompson, G. and Eidhammer, T.: A Study of Aerosol Impacts on Clouds and Precipitation Development in a Large Winter Cyclone, J. Atmos. Sci., 71, 3636–3658, doi:10.1175/JAS-D-13-0305.1, 2014.

Thompson, G., Rasmussen, R., and Manning, K.: Explicit Forecasts of winter precipitation using an improved bulk microphysics scheme. Part I: Description and sensitivity analysis., Mon. Weather Rev., 132, 519–542, 2004.

Thompson, G., Field, P. R., Rasmussen, R. M., and Hall, W. D.: Explicit Forecasts of Winter Precipitation Using an Improved Bulk Microphysics Scheme. Part II: Implementation of a New Snow Parameterization, Mon. Weather Rev., 136, 5095–5115, doi:10.1175/2008MWR2387.1, 2008.

Wang, B. and Xie, X.: Low-Frequency equatorial waves in vertically shear flow. Part I: Stable waves., J. Atmos. Sci., 53, 449–467, 1996.

Wang, P.-H., Minnis, P., McCormick, M. P., Kent, G. S., and Skeens, K. M.: A 6-year climatology of cloud occurrence frequency from Stratospheric Aerosol and Gas Experiment II observations (1985–1990), J. Geophys. Res., 101, 29407–29429, doi:10.1029/96JD01780, 1996.

Wang, T. and Dessler, A. E.: Analysis of cirrus in the tropical tropopause layer from CALIPSO and MLS data: A water perspective, J. Geophys. Res.-Atmos., 117, 2156–2202, doi:10.1029/2011JD016442, 2012.

Waugh, D. W. and Polvani, L. M.: Climatology of intrusions into the tropical upper troposphere, Geophys. Res. Lett., 27, 3857–3860, doi:10.1029/2000GL012250, 2000.

Wernli, H., Paulat, M., Hagen, M., and Frei, C.: Sal – a novel quality measure for the verification of quantitative pre-

cipitation forecasts., Mon. Weather Rev., 136, 4470–4487, doi:10.1175/2008MWR2415.1, 2008.

Winker, D. M., Hunt, W. H., and McGill, M. J.: Initial performance assessment of CALIOP, Geophys. Res. Lett., 34, 1944-8007, doi:10.1029/2007GL030135, 2007.

Wu, L., Su, H., Jiang, J. H., and Read, W. G.: Hydration or dehydration: competing effects of upper tropospheric cloud radiation on the TTL water vapor, Atmos. Chem. Phys., 12, 7727–7735, doi:10.5194/acp-12-7727-2012, 2012.

4.2.3 Discussion of the results and limits of the study

Important findings The main findings of the study are that:

1. The simulations compare reasonable well with the observations. Reproducing the observed cloud field required only limited tuning and modification of the default WRF set-up, and the sensitivity to model set-up was limited. This is especially encouraging since the event took place in a region with limited observational constraints feeding the analyses that provide the initial and boundary conditions (*Podglajen et al.*, 2014). In particular, the cloud is reproduced at the right location and timing even though the initial water vapor field is poorly constrained. *This suggests that temperature variability has a more important impact on TTL cirrus formation than the water vapor content.* This somehow surprising finding apparently contradicts recent studies that emphasized that the occurrence of clouds was associated with higher water vapor content than clear air, rather than with lower temperatures (*Diao et al.*, 2014). We explain our result by the predominance of vertical gradients, while the apparent contradiction with *Diao et al.* (2014) is probably due to the fact that those airborne measurements were carried at a fixed pressure level (and not on an isentrope). Indeed, assuming that a small adiabatic vertical displacement ζ is the reason for cloud formation (and neglecting the altitude variation of a pressure level), the change in relative humidity δRH_i on the fixed pressure level is

$$\delta RH_i = \underbrace{-\left(\frac{\partial RH_i}{\partial T}\right)\left(\frac{P}{P_0}\right)^{\kappa}\left(\frac{\partial \bar{\theta}}{\partial z}\right)\zeta}_{(\delta RH_i)_T} \underbrace{-\left(\frac{\partial RH_i}{\partial r}\right)\left(\frac{\partial \bar{r}}{\partial z}\right)\zeta}_{(\delta RH_i)_q} \tag{4.1}$$

where θ is the potential temperature, P the pressure, $\kappa = \frac{R}{C_p}$, $r = \frac{e}{P}$ the water vapor mixing ratio with e the water vapor partial pressure. $(\delta RH_i)_T$ and $(\delta RH_i)_q$ can be rewritten using Clausius Clapeyron equation, using the notation $r_{\text{sat}} = \frac{e_{\text{sat}}}{P}$:

$$(\delta RH_i)_T = RH_i \left(\frac{P}{P_0}\right)^{\kappa} \frac{L_s}{R_v T^2}\left(\frac{\partial \bar{\theta}}{\partial z}\right)\zeta \tag{4.2}$$

$$\begin{aligned}(\delta RH_i)_q &= -\frac{1}{\overline{r_{\text{sat}}}}\frac{\partial \bar{r}}{\partial z}\zeta \simeq -RH_i \frac{1}{\overline{r_{\text{sat}}}}\frac{\partial \overline{r_{\text{sat}}}}{\partial z}\zeta \\ &\simeq -RH_i \frac{1}{\overline{r_{\text{sat}}}}\frac{\partial \overline{r_{\text{sat}}}(T)}{\partial T}\left(\frac{\partial \bar{T}}{\partial z}\right)\zeta = -RH_i \frac{L_s}{R_v T^2}\left(\frac{\partial \bar{T}}{\partial z}\right)\zeta\end{aligned} \tag{4.3}$$

(4.4)

the changes in relative humidity due to temperature and water vapor mixing ratio variations, respectively. For $(\delta RH_i)_q$ we have neglected the vertical pressure variation that impact the relative humidity variations, since they are a factor of 5 or less smaller than the variations due to temperature changes. We also have considered a constant mean vertical profile of RH_i. Since the vertical temperature profile is usually closer to a dry adiabat than to an isotherm in the upper troposphere [2] $\left(\left|\left(\frac{P}{P_0}\right)^{\kappa}\frac{\partial \bar{\theta}}{\partial z}\right| < \left|\frac{\partial \bar{T}}{\partial z}\right|\right)$,

[2] Except very close to the tropopause where $\frac{\partial \bar{T}}{\partial z} = 0$.

this expression immediately shows that the variations of RH_i at constant pressure are more related to humidity variations than to pressure variations. However, the ultimate reason for the rise in relative humidity remains the large scale uplift and associated Lagrangian temperature variations. *Kärcher and Haag* (2004) have also argued that (Lagrangian) temperature variability is more important than water vapor variability. The main thing for accurate cloud simulations is to capture the (stronger) vertical water vapor gradient, which is reasonably well represented in the analyses.

2. Equatorial waves are crucial in controlling the occurrence of TTL cirrus, in particular in the Eastern Pacific region. This is consistent with observational findings (*Kim et al.*, 2016). Here, our study reveals this case as the first reported example of a large-scale Yanai wave influencing cirrus formation.

3. Although the region is favorable to cirrus formation, there is not one very long-lived cloud but a population of cirrus clouds that develop in the same region. A large-scale uplift induced by the Yanai wave is responsible for the clouds presence and controls the lifetime of the cloud ensemble. The uplift associated with the wave explains the low temperature anomalies (-5 K) and helps to make the cloud field persist against sedimentation (about 5 mm/s).

4. Cloud radiative effects are secondary in the life cycle of the cirrus. Ignoring cloud radiative effects does not change the evolution of the cloud field. We explain that conclusion by the fact that the Lagrangian cloud life time is shorter than the time scale τ for a cloud induced-radiative circulation to build. Indeed, τ can be expressed as (*Durran et al.*, 2009):

$$\tau \simeq \frac{\pi a}{DN} \tag{4.5}$$

with a the cloud size, D the cloud depth and N the background buoyancy frequency (we note the similarity with gravity wave dispersion relation). The cloud induced horizontal circulation scales as (*Durran et al.*, 2009):

$$u_{cs} \propto \frac{g\dot{T}}{T_0 N^2} \frac{\pi a}{2D} \tag{4.6}$$

From those two equations, it can be seen that clouds will induce significant circulations only if they are sufficiently large, in which case radiative circulations will take a significant amount of time to develop in a stable environment. To induce a significant circulation, a cloud of size of the order of a few hundred kilometers is required. Hence, for radiative heating rates $\dot{T}$ of the order of 3 K/day as expected in TTL cirrus, cloud circulations of a few m/s will require about a day to develop, which is more than twice longer than the typical Lagrangian cloud lifetime. The absence of radiative influence on the dynamics of thin TTL cirrus in the Eastern Pacific is thus expected. It is likely that only thicker TTL clouds forming in a low stability environment [3] may show radiatively-induced circulations.

[3] For instance, in the Western Pacific.

Advantages and limits Compared to previous approaches (Lagrangian models and idealized simulations), the real-case study conducted here has the advantage of being directly comparable to the observations. Compared to idealized simulations (e.g. *Dinh et al.*, 2010), it emphasizes the overwhelming impact on the cirrus field of background atmospheric variability and waves, rather than cloud radiatively-induced circulations. Compared to Lagrangian models, it allows for consistent picture of smaller scale motions and the response of the dynamics to the PV intrusion that is limited using in large-scale model fields using reanalysis.

The limited influence of nucleation assumptions on the cirrus field is the reason for the good agreement obtained between model and observations. However, it also stands as a major limitation. It is not possible with the limited remote-sensing observations to test microphysical hypotheses regarding cloud formation. Cloud-induced dynamics and microphysical processes, which ultimately matter for the equilibrium of the TTL, are only of secondary importance in front of external dynamical processes, at least at the scales considered here.

Implications *Regarding cirrus modeling* Water vapor horizontal distribution, a poorly constrained parameter, is not dramatically important for large-scale cirrus simulations. If small-scale microphysical observations are available, such a set-up can help evaluate the microphysics parameterizations used in the models. Especially, the absence of cloud-scale circulation emphasizes that, for thin TTL cirrus, realistic cloud fields and their impacts can be studied using a Lagrangian framework, without considering the secondary impacts of the cirrus on the flow. This is because the variability due to TTL wave motions is much larger than the variability induced by thin cirrus clouds. Radiative processes in thin clouds are important in a budget perspective, but they do not influence the evolution of one cloud field, at least in the case studied.

Regarding dehydration and transport Rehydration in the vicinity of the cirrus is a fundamental process which needs to be taken into account by models.

4.3 Conclusion

The study demonstrates that, despite uncertainties in the microphysical processes and in the water vapor field, mesoscale models initialized with large-scale analyses can successfully simulate TTL cirrus. The simulations are a useful tool to quantify cirrus-dynamics interactions. However, to get an insight into microphysical processes, in situ measurements are required, because the coarse resolution of satellite instruments (for water vapor and temperature) does not allow to investigate the relevant quantities at the fine microphysical scales.

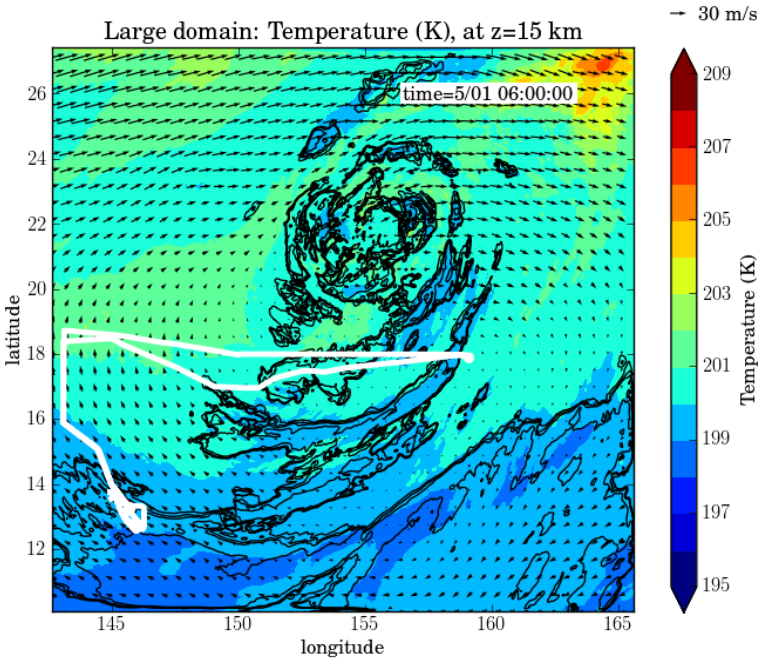

Figure 4.2 – Temperature (color) and cirrus cloud contours (black contours) at 15 km in the Western Pacific around tropical cyclone Faxai, on March 5 2014. The Global Hawk horizontal track is shown in white.

To illustrate the usefulness of mesoscale simulations for putting into context in situ observations, another case study has been recently undertaken of TTL cirrus observed during the ATTREX campaign in the vicinity of typhoon Faxai (see figure 4.2). The analysis is still underway at the time of the writing, but preliminary results are encouraging, e.g. the model shows cirrus bands developing in the TTL in the vicinity of the typhoon.

Chapter 5

Turbulence at the tropical tropopause and impact on vertical mixing

Sommaire

5.1 Introduction

This chapter focuses on the smallest scale fluctuations encountered in the TTL: turbulence. Turbulence is believed to be tightly linked to large-scale equatorial waves and to gravity waves, which generate dynamic instabilities when they break. Furthermore, small-scale fluctuations are responsible for mixing trace gases and might play a key role in their vertical transport. Turbulence is also important for the evolution of TTL cirrus clouds, by potentially entraining clear air within the clouds or modifying their structure.

Here, we use high frequency wind measurements from the Airborne Tropical TRopopause EXperiment (ATTREX) to analyze turbulence occurrence in the TTL and quantify its impact on vertical transport. In a first part, we recall some basic notions on turbulence and the turbulence inertial range. Then, we turn to the ATTREX dataset for a survey of turbulence occurrence and its relationship with the meteorological environment. The impact on mixing and vertical transport is also estimated; it is found smaller than the mean upwelling, so that in the average, the impact of turbulence is mainly to increase the diffusivity and homogenize the tracers.

5.2 Notions on turbulence

In this section, we review the basics of turbulence theory and formalism in order to outline the framework and objectives of the analysis in the article (next section). In particular, we introduce the impact of turbulence on mixing and transport of constituents. We also give a brief account on inertial range turbulence theory, which is used to estimate eddy dissipation rates.

5.2.1 Turbulence formalism and impact on the "mean state"

Reynolds decomposition and mean state equations A common starting point in the study of turbulence is Reynolds decomposition, which consists in artificially decomposing a flow between an average state and fluctuations around it. For that purpose, one introduces Reynolds averaging $\overline{(...)}$, an ensemble mean operator which, under the assumption of ergodicity[1], can be interpreted either as a space or a time average. For example, for a wind component u_j, we set:

$$u_j = \overline{u}_j + u'_j \tag{5.1}$$

In practice, when the decomposition is carried out in the governing equations of an atmospheric model, $\overline{(...)}$ corresponds to the resolved fields whereas the fluctuations correspond to subgrid-scale or unresolved perturbations.

The operator $\overline{(...)}$ commutes with the partial derivatives in the Navier-Stokes equations. With that property, the incompressible Navier-Stokes equations on the f-plan with Boussinesq approximation lead to the following equations for the evolution of each wind component $\bar{u}_j$, potential temperature $\bar{\theta}$ and passive tracer concentration $\bar{\chi}$:

[1] i.e. the time or space mean is also the ensemble mean, the statistical expectation

$$\frac{\bar{D}\bar{u}_j}{Dt} = \text{LS} \quad + \nu\frac{\partial^2\bar{u}_j}{\partial x_j^2} \; - \boxed{\frac{\partial\overline{u_i'u_j'}}{\partial x_j}} \tag{5.2}$$

$$\frac{\bar{D}\bar{\theta}}{Dt} = Q \quad + \nu_\theta\frac{\partial^2\bar{\theta}}{\partial x_j^2} \; - \boxed{\frac{\partial\overline{u_j'\theta'}}{\partial x_j}} \tag{5.3}$$

$$\frac{\bar{D}\bar{\chi}}{Dt} = P - L \; + \underbrace{\nu_\chi\frac{\partial^2\bar{\chi}}{\partial x_j^2}}_{\substack{\text{molecular}\\ \text{fluxes}}} - \underbrace{\boxed{\frac{\partial\overline{u_j'\chi'}}{\partial x_j}}}_{\text{eddy fluxes}} \tag{5.4}$$

where $\dfrac{\bar{D}}{Dt} = \dfrac{\partial}{\partial t} + \bar{u}_i\dfrac{\partial}{\partial x_i}$ is the mean state Lagrangian derivative[2], LS represent the large-scale forcing on the momentum equation (e.g. Coriolis, gravity and pressure gradient forces), Q is the diabatic heating (radiative and frictional heating since we neglect latent heat release), P and L are chemical production and loss terms. ν is the viscosity, ν_χ is the molecular diffusivity of the tracer and ν_θ is the thermal diffusivity. The assumption of incompressibility is not required but was made to simplify the formulas. In those equations, the boxed terms show the impact of turbulence on the mean state: $\overline{u_i'u_j'}$ is the Reynolds stress tensor, $\overline{u_i'\theta'}$ is the turbulent heat flux and $\overline{u_i'\chi'}$ is the turbulent tracer flux.

Turbulence closure By themselves, the previous equations are not helpful in solving the problem of the mean state evolution, since the mean fields also depend on quadratic terms involving the fluctuations. Additional equations can be obtained for the evolution of the quadratic terms but they themselves involve cubic terms, whose evolution depends on bi-quadratic terms, and so on. To advance on the problem, it is necessary to add a set of "closure equations" which relate the evolution of order-n fluctuation terms to the mean flow and lower order terms. The last order n for which the moments of the fluctuations are prognosed is the closure order. In the absence of coherent turbulent structure (i.e. looking at scales sufficiently small for local homogeneity), representing turbulent fluxes can be done through an order 1 closure assumption. A commonly used parameterization is the K-gradients method, which inspires from molecular diffusion:

$$\begin{aligned}
\overline{u_i'\theta'} &= -K_h\frac{\partial\bar{\theta}}{\partial x_i} \\
\overline{u_i'\chi'} &= -K_\chi\frac{\partial\bar{\chi}}{\partial x_i} \\
\overline{u_i'u_j'} &= -K_m\left(\frac{\partial\overline{u_i}}{\partial x_j} + \frac{\partial\overline{u_j}}{\partial x_i}\right)
\end{aligned} \tag{5.5}$$

[2]Note that in the equations there is the implicit convention to sum over the repeated indices in the products, so that $\bar{u}_i\dfrac{\partial}{\partial x_i} = \sum_{i=1}^{3}\bar{u}_i\dfrac{\partial}{\partial x_i}$ or $\dfrac{\partial^2\bar{u}_j}{\partial x_j^2} = \sum_{j=1}^{3}\dfrac{\partial^2\bar{u}_j}{\partial x_j^2}$.

with K_h, K_m and K_χ the turbulent diffusivities for momentum, heat and tracer. In general, it is assumed that $K_\chi = K_h$ [3].

In large-scale models, K_h and K_m are often expressed as functions of the mean flow only, as done in the ECMWF model (*Louis et al.*, 1982). That order 1 closure can be refined by making the diffusivity coefficients K_h and K_m depend on the turbulent kinetic energy $E_k = \frac{1}{2}(u'^2 + v'^2 + w'^2)$[4]. An additional equation is then required to prognose E_k evolution, and the closure is said to be of order 1.5 [5].

Turbulent energy equations Besides turbulent kinetic energy $E_k = \frac{1}{2}\overline{(u'^2 + v'^2 + w'^2)}$, one can define another quadratic quantity, the turbulent potential energy associated with buoyancy fluctuations in a stratified medium $E_p = \frac{1}{2}\frac{g^2}{N^2}\frac{\overline{\theta'^2}}{\bar{\theta}^2}$ (*Tennekes and Lumley*, 1972). Keeping in mind the application to the TTL, we neglect the moisture and latent heat release contributions to the buoyancy budget. With those approximations, the turbulent kinetic and potential energy budgets from the Boussinesq equations read:

$$\begin{aligned} \frac{\bar{D}E_k}{Dt} &= P - B - \epsilon_k - \nabla \cdot \mathbf{F_k} \\ \frac{\bar{D}E_p}{Dt} &= B - \epsilon_p - \nabla \cdot \mathbf{F_p} \end{aligned} \tag{5.6}$$

where

$(\mathbf{F_k})_j = \frac{1}{2}\overline{u_i'^2 u_j'} + \frac{1}{\bar{\rho}}\overline{p' u_j'}$ is the turbulent flux of E_k (neglecting the transport by viscous stress)

$(\mathbf{F_p})_j = \frac{1}{2}\frac{g^2}{(\bar{\theta}N)^2}\overline{\theta'^2 u_j'}$ is the turbulent flux of E_p

$B = -\frac{g}{\bar{\theta}}\overline{w'\theta'}$ is the turbulent buoyancy flux

$P = -\overline{u_i' u_j'}\frac{\partial \bar{u}_i}{\partial x_j} \simeq -\overline{w'u'}\frac{d\bar{u}}{dz} - \overline{w'v'}\frac{d\bar{v}}{dz}$ is the production of turbulent energy by shear

$\epsilon_k = \frac{\nu}{2}\overline{\left(\frac{\partial u_i'}{\partial x_j} + \frac{\partial u_j'}{\partial x_i}\right)^2} \simeq \nu\overline{\left(\frac{\partial u_i'}{\partial x_j}\right)\left(\frac{\partial u_i'}{\partial x_j}\right)}$ is the kinetic energy dissipation rate

$\epsilon_p = \nu_\theta \frac{g^2}{(\bar{\theta}N)^2}\overline{\left(\frac{\partial \theta'}{\partial x_j}\right)\left(\frac{\partial \theta'}{\partial x_j}\right)}$ is the dissipation rate of potential energy.

We will later focus on small-scale ($< 100\,\mathrm{m}$) turbulence, for which buoyancy forcing is less important. Equation 5.6 includes buoyancy terms and is valid also for scales larger than those examined in the following article.

With 1.5 order closures, such as those used in some Large Eddy Simulations models[6], the

[3] This is motivated by the molecular comparison and the conservation of θ and χ: turbulent diffusivity is due to the "random" motion of air parcels, which transport their potential temperature the same way they transport their tracer mixing ratio, i.e. $\frac{D\theta}{Dt} = 0$ and $\frac{D\chi}{Dt} = 0$ (the situation is different for the winds which are active tracers).

[4] strictly speaking, E_k is the turbulent kinetic energy per unit mass.

[5] It lies between order 1 and 2 since one second order moment (E_k) is prognosed but all other moments ($\overline{u_i' u_j'}$,$\overline{u_i'\theta'}$ ...) are diagnosed, for instance using K_m, K_h (see Equation (5.5)).

[6] Different orders are used depending on the model, 1.5 order, second order and 2.5 order (*Mellor and Yamada*, 1982) are frequently used options.

models do resolve budget equations for E_k and E_p similar to System (5.6). However, without going as far as resolving the full equations, one can note that the main balance is between the terms of production of turbulent energy by buoyancy B and shear P, and the terms of dissipation ϵ_p and ϵ_k. Rigorously, this is equivalent to assume homogeneity and stationarity to hold at each instant, and that the dissipation adjusts to the forcing. The turbulent diffusivity for heat $K_h = -\frac{\overline{w'\theta'}}{\frac{d\theta}{dz}}$ can then be related to the potential energy dissipation rate through (e.g., *Lilly et al.*, 1974):

$$K_h = \frac{\epsilon_p}{N^2} \tag{5.7}$$

this is the formula on which the mixing estimates are based in the following.

It is interesting to note that, under the previous assumptions, the scales for the generation of turbulent potential energy by buoyancy fluxes B can be distinct from the inertial scales through which energy transits towards even smaller scales, where it dissipates at rate ϵ_p. If there is a quasi-stationary balance between dissipation et forcing, then it is not required to know the scales or dynamical nature of the "turbulent" fluxes (B) in order to estimate their magnitude and to evaluate their impact. Making the quasi-stationary balance assumption, we obtain an integrated view of all irreversible fluxes, those who lead to molecular dissipation, irreversible mixing, and induce an irreversible change of the mean state. In other words, estimating $\overline{w'\theta'}$ through ϵ_p can be seen as filtering all "reversible" contributions (e.g., gravity waves) from $w'\theta'$, while keeping all contributions leading to cascading down to small scales and molecular mixing.

5.2.2 Inertial range turbulence and the energy cascade

Assumptions for inertial range turbulence Inertial range turbulence theory has its roots in the works of Richardson, Taylor, von Kármán, and Kolmogorov. It aims at explaining fluid motions at scales large enough so that viscosity can be neglected, but small enough so that buoyancy forcing of the motions can also be neglected. In terms of Froude number Fr[7] and Reynolds number Re[8] of the flow, this means that:

$$\mathrm{Fr} = \frac{U}{NL} \gg 1 \qquad\qquad \mathrm{Re} = \frac{LU}{\nu} \gg 1 \tag{5.8}$$

where U is the velocity scale and L the length scale of the flow and N the Brunt-Väisälä frequency (note that by extension the Rossby number $\mathrm{Ro} = \frac{N}{f}\mathrm{Fr} \gg 1$). In inertial range turbulence, the dominant terms in the horizontal and vertical momentum equations are thus the advective terms (and the pressure terms). If we also assume incompressibility of the flow, the governing equations for inertial range motions are:

$$\begin{aligned} &\partial_t \mathbf{u} + \mathbf{u}\cdot\nabla\mathbf{u} = -\frac{1}{\bar{\rho}}\nabla p \\ &\nabla\cdot\mathbf{u} = 0 \end{aligned} \tag{5.9}$$

Those equations are non linear and cannot be easily resolved; their solutions also show extensive sensitivity to the initial conditions. In that context, one way to progress is by looking

[7] Ratio of the advection term to the buoyancy term in the momentum equation.
[8] Ratio of the advection term to the viscous term in the momentum equation.

at the statistical properties of the flow rather than at a given flow field: this is the starting point of inertial range turbulence theory (*Monin and Yaglom*, 1977). Following *Kolmogorov* (1941), the assumptions usually made together are that of *local homogeneity*: there is a spatial domain over which the statistical properties of the flow do not depend on the position (the flow is invariant by translation), and of *local isotropy*: there is a spatial domain over which the statistical properties of the flow do not change if the axes are rotated.

The energy cascade From System (5.9), it can be shown that vorticity lines (the lines everywhere tangent to the vorticity vector) are also material lines: they are passively advected by the flow. Advection in 3-dimensions tilts those lines, creating smaller and smaller scales in the flow. The generation of smaller scales from a larger scale flow is named the turbulent cascade or also *Richardson's energy cascade*. Velocity gradients are created at smaller and smaller scales in the flow. Eventually, the gradients reach scales where viscosity cannot be neglected, momentum dissipation is efficient, and kinetic energy dissipates in thermal energy (heat). Under the assumption of isotropy[9], the rate of dissipation of kinetic energy, ϵ_k, simplifies in (*Batchelor*, 1947; *Tennekes and Lumley*, 1972):

$$\epsilon_k = \frac{15}{2}\nu\overline{\left(\frac{\partial u_2}{\partial x_1}\right)^2} = 15\nu\overline{\left(\frac{\partial u_1}{\partial x_1}\right)^2}. \tag{5.10}$$

With the assumption of stationarity (i.e. energy from the large scale is injected at a constant rate so that the statistical properties of the flow at small scales are constant) added to isotropy and homogeneity, *Kolmogorov* (1941) derived the famous $\frac{4}{5}$ law:

$$\overline{\delta u_l(r)^3} = -\frac{4}{5}\epsilon_k r \tag{5.11}$$

where $\overline{\delta u_l(r)^3} = \overline{(u_l(x+r) - u_l(x))^3}$ is the structure function of order 3 of the longitudinal wind u_l (i.e. the wind in the direction parallel to the direction along which the sampling is carried out), and r is the separation between the two points at which u_l is evaluated. It should be noted that the $\frac{4}{5}$ law is derived only from the homogeneity, isotropy and stationarity assumptions and the equations of motions above. It is one of the rare exact analytical results in inertial range turbulence.

Kolmogorov (1941) further introduced a similarity hypothesis, which states that the 1D-structure functions of order n of the winds S_n:

$$S_n(r) = \overline{\delta u_j(r)^n} \tag{5.12}$$

are proportional to $(\epsilon_k r)^{n/3}$:

$$S_n(r) \propto \epsilon_k^{\frac{n}{3}} r^{\frac{n}{3}} \tag{5.13}$$

Although this expression is consistent with the $\frac{4}{5}$ law (Equation (5.11)), it has not been demonstrated for any order other than order 3. For the special case of the second-order

[9]The momentum equations giving $\overline{\frac{\partial u_2}{\partial x_2}\frac{\partial u_3}{\partial x_3}} = \overline{\frac{\partial u_3}{\partial x_2}\frac{\partial u_2}{\partial x_3}}$.

structure function, Equation (5.13) gives:

$$S_2(r) \propto \epsilon_k^{\frac{2}{3}} r^{\frac{2}{3}} \tag{5.14}$$

Given the relation between 1D-structure functions and energy spectra[10], relationships can then be deduced for the power spectra of the velocity components. For instance, the energy spectrum of longitudinal wind Φ_l is:

$$\Phi_l(\kappa) = \alpha_k \epsilon_k^{\frac{2}{3}} \kappa^{-\frac{5}{3}} \tag{5.15}$$

where κ is the longitudinal wave number (in $\mathrm{rad\,m^{-1}}$) and $\alpha_k \simeq 0.5$ is a Kolmogorov constant. This relation can also be deduced directly from dimensional analysis. Under the assumption of isotropy, it can be shown that the power spectrum of any transverse wind component u_t is related to the power spectrum of longitudinal wind components:

$$\Phi_t(\kappa) = \frac{4}{3}\Phi_l(\kappa) = \frac{4}{3}\alpha_k \epsilon_k^{\frac{2}{3}} \kappa^{-\frac{5}{3}} \tag{5.16}$$

Relation (5.16) is used to analyze aircraft observations in the following section.

Due to the importance of the advective terms in the momentum and vorticity budget, Kolmogorov theory is generally used together with Taylor hypothesis, which states that turbulence is frozen within the mean flow: small vortices are passively advected by the mean wind and by larger vortices. Time variations at a given spatial location are then equivalent to space variations seen if the flow were frozen and the observer moving upstream at the same speed as the unfrozen wind.

Scales for inertial range in the atmosphere ? Up to now, we have been elusive regarding the scales actually involved in the inertial range. Its lower boundary corresponds to the scale at which viscosity is dissipating the eddies, more precisely the scale at which the molecular dissipation terms and the advection terms are of the same order. That scale, named the *inner scale*, relates to the strength of the eddies and to viscosity, and is defined by:

$$l_0 \simeq 11.35 \underbrace{\left(\frac{\nu^3}{\epsilon_k}\right)^{\frac{1}{4}}}_{l_\nu} \tag{5.17}$$

where l_ν is the Kolmogorov scale. In the upper troposphere and lower stratosphere, l_0 is generally much smaller than 1 m (1 cm).

The largest scale of the inertial range, the *outer scale* L_m, corresponds to the scale at which turbulence is affected by stratification. Stratification and the resulting buoyancy forces are playing against overturning by the eddies, so that the motions are not fully 3-dimensional.

[10] From Wiener–Khinchin theorem, $\overline{\delta u_j(r)^2} = \int_0^{+\infty} \Phi_j(\kappa)(1-\cos(\kappa r))\mathrm{d}\kappa$ with $\Phi_j(\kappa)$ the power spectrum of u_j and κ the wavenumber (in $\mathrm{rad\,s^{-1}}$)

Formally, the outer scale should write:

$$L_m = 2\pi\sqrt{\frac{\epsilon_p^{\frac{3}{2}}/\epsilon_k^{\frac{1}{2}}}{N^3}} \tag{5.18}$$

It is however justified to assume $\epsilon_p \propto \epsilon_k$ and thus to associate L_m with the Ozmidov scale $L_O = \sqrt{\frac{\epsilon_k}{N^3}}$, such that:

$$L_m \simeq \frac{2\pi}{C} L_O = \frac{2\pi}{C}\sqrt{\frac{\epsilon_k}{N^3}} \tag{5.19}$$

where C is a dimensionless number of order 1, which might be function of the mean state.

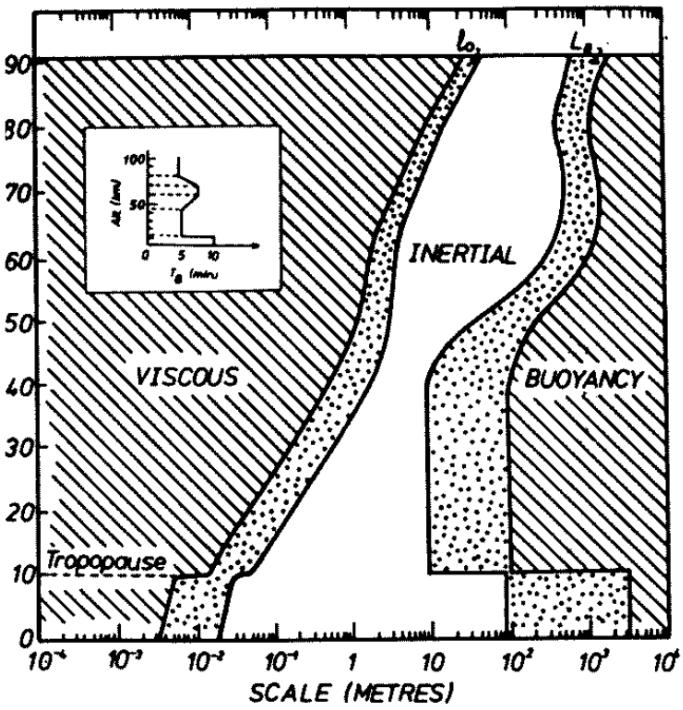

Figure 5.1 – Profile of typical upper and lower scale of the inertial range in the atmosphere, computed using Equation (5.19) and the profile of buoyancy period shown in the square and assuming eddy dissipation rates ϵ_k varying from 10^{-5} to $10^{-1}\mathrm{W\,kg^{-1}} = \mathrm{m^2\,s^{-3}}$. In the stratosphere, the dotted region corresponds to different values of ϵ_k between 10^{-5} and 10^{-3} $\mathrm{m^2\,s^{-3}}$ whereas in the troposphere they correspond to values between 10^{-4} and 10^{-1} $\mathrm{m^2\,s^{-3}}$. From *Hocking* (1985).

The Kolmogorov and Ozmidov scales vary by several order of magnitudes due to the variability of N and ϵ_k. The stratification jump near the tropopause imposes that the Ozmidov scale decreases from the troposphere to the stratosphere. Figure 5.1 shows the typical values of those scales where C is taken to be 0.62 (following *Weinstock*, 1978). In particular, Figure 5.1 suggests that in the altitude range we are interested in (14 to 19 km), there could be an inertial range between about 0.1 m to a few tens or hundreds of meters, depending on the local eddy dissipation rate.

Additional note: motions at scales larger than the inertial range At scales larger than the outer scale of the inertial range, shear and stratification come at play and one cannot consider that Fr $\gg 1$ anymore. It is less clear what processes govern the motions at those

scales; two theories have been invoked to explain the dynamics, gravity waves (e.g. *Dewan*, 1997) and stratified turbulence (e.g. *Lilly*, 1983; *Lindborg*, 1999). For both theories, authors have been arguing on a cascade (e.g. *Dewan*, 1997; *Lindborg*, 2006), and the horizontal velocity and horizontal kinetic energy power spectra should scale as:

$$E_{k_h}(\kappa) \propto \epsilon_k^{\frac{2}{3}} \kappa^{-\frac{5}{3}} \tag{5.20}$$

Hence, even outside the inertial, there are some theoretical support to evaluate the eddy dissipation rates from the horizontal power spectrum of horizontal velocities[11]. Differences in the value of the constants used might add additional errors, but they should be of order 1.

5.3 Article: Small-scale wind fluctuations in the tropical tropopause layer from aircraft measurements: occurrence, nature and impact on vertical mixing

This section corresponds to a paper in revision for the Journal of the Atmospheric Sciences: A. Podglajen,T. P. Bui, J. M. Dean-Day, L. Pfister, E. J. Jensen, M.J. Alexander, A. Hertzog, B. Kärcher, R. Plougonven, W.J. Randel (submitted,2017): Small-scale wind fluctuations in the tropical tropopause layer from aircraft measurements: occurrence, nature and impact on vertical mixing.

ABSTRACT

The contribution of turbulent mixing to heat and tracer transport in the Tropical Tropopause Layer (TTL) is poorly constrained, partly due to a lack of direct observations. Here, the authors use high-resolution airborne measurements to study the occurrence and properties of small-scale wind fluctuations in the TTL (14-19 km) over the tropical Pacific. The fluctuations are found to be highly intermittent and appear localized within shallow (100 m) patches. Furthermore, active turbulent events are more frequent at low altitude, near deep convection and within layers of low gradient Richardson number. A case study emphasizes the link between the turbulent events and the occurrence of inertio-gravity waves having small horizontal or vertical scale. In order to evaluate the impact of the observed fluctuations on mixing, their characteristics are examined. They are in broad agreement with inertial range turbulence theory : the motions are close to 3D-isotropic and the spectra follow the expected $-\frac{5}{3}$ power-law scaling. The diffusivity induced by turbulent bursts is estimated around 10^{-1} $\mathrm{m^2\,s^{-1}}$ and increases from the top to the bottom of the TTL ($\sim 2 \cdot 10^{-2}$ to $\sim 3 \cdot 10^{-1}$ $\mathrm{m^2\,s^{-1}}$). This is in reasonable agreement (about a factor of 3-4 lower) with the parametrized turbulent diffusivity in the ECMWF ERA-interim analysis but disagrees with other observational estimates from Radar and radiosondes. The magnitude of the consequent vertical transport depends on the altitude and the tracer; for the species considered, it is generally smaller than that induced by the mean tropical upwelling.

[11]It is different from the vertical spectrum which is expected to scale as $E_{k_h}(m) = C_1 \epsilon_k^{\frac{2}{3}} m^{-\frac{5}{3}} + C_2 N^2 m^{-3}$ where m is the vertical wavenumber and C_1 and C_2 are constants of order unity.

5.3.1 Introduction

The tropical tropopause layer (TTL, *Fueglistaler et al.*, 2009) is the transition region between the convectively influenced tropical troposphere and the radiatively-controlled tropical lower stratosphere. Hence, constituents in the TTL are believed to be vertically transported either by deep convection carrying air from the boundary layer or by the mean tropical upwelling associated with the lower branch of the Brewer-Dobson circulation. Similarly, latent heat release (negligible above 14-15 km) and radiative heating dominate the heat balance of the tropical UTLS, at least in reanalyses (*Wright and Fueglistaler*, 2013). However, for both the heat (*Wright and Fueglistaler*, 2013) and the tracer budget (*Mote et al.*, 1996, 1998), the effect of turbulent mixing and diffusion is highly uncertain. It might have a significant influence on the thermal and wind structure of the TTL (*Flannaghan and Fueglistaler*, 2014), on its water vapor and ice content (*Bardeen et al.*, 2013; *Ueyama et al.*, 2015) or on the vertical transport through that layer (*Konopka et al.*, 2007) to the stratosphere. Given the very slow mean upwelling (about 0.2 mm/s at 80 hPa), even weak turbulent mixing could indeed be sufficient to compete with advection. The uncertainty on the magnitude of turbulent diffusion limits our understanding of TTL processes and is a problem when modeling of its composition. This uncertainty comes from the computationnal unfeasability of direct numerical simulations of turbulence and its generation processes in the TTL, from the low level of theoritical understanding of turbulence generation, nature and life cycle, but it is also due to a lack of measurements of small-scale fluctuations.

Indeed, most estimates of turbulent diffusivity come from Radar or balloon measurements at specific tropical locations (*Rao et al.*, 2001; *Alappattu and Kunhikrishnan*, 2010). Turbulence intensity can be measured from commercial airplanes (*Cornman et al.*, 1995, 2004) and a fleet is now equipped to provide quantitative estimate of turbulence intensity (*Sharman et al.*, 2014). However, the sampling is still sparse outside the continental United States, and, in any case, those aircraft fly below the bottom of the TTL (14 km). At higher altitudes, precise measurements of meteorological parameters and turbulence have been carried in the past onboard scientific aircraft measuring platforms (e.g. *Lilly et al.*, 1974; *Chan et al.*, 1998; *Koch et al.*, 2005) but very few (and all unpublished to our knowledge) took place in the TTL. Recently, during the NASA Airborne Tropical Tropopause EXperiment (ATTREX) campaign (boreal winter 2013 and 2014), such measurements were acquired between 14 and 19 km over the tropical Pacific, providing a unique opportunity to quantify turbulence in the TTL.

In this work, we use the meteorological measurements from ATTREX to characterize the nature and occurrence of small-scale wind fluctuations in the TTL. The paper is organized as follows. subsection 5.3.2 introduces the ATTREX campaign and the data used. Then, in subsection 5.3.5, a specific case study is presented to illustrate the measured small-scale fluctuations and their relationship with waves. Next, we provide a systematic examination of the statistics and context of small-scale fluctuations occurrence in the whole dataset (subsection 5.3.6). In subsection 5.3.7, the characteristics of small-scale fluctuations are studied and compared with theoritical expectations for inertial range turbulence (isotropy, power-law scaling). Finally, subsection 5.3.8 presents an estimate of the eddy diffusivity from aircraft observations and compares with those derived from other measurements and those used in modern reanalyses systems. The results and conclusions are summarized in subsection 5.3.9.

5.3.2 Data and methods

5.3.2.1 Presentation of ATTREX campaign and MMS measurements

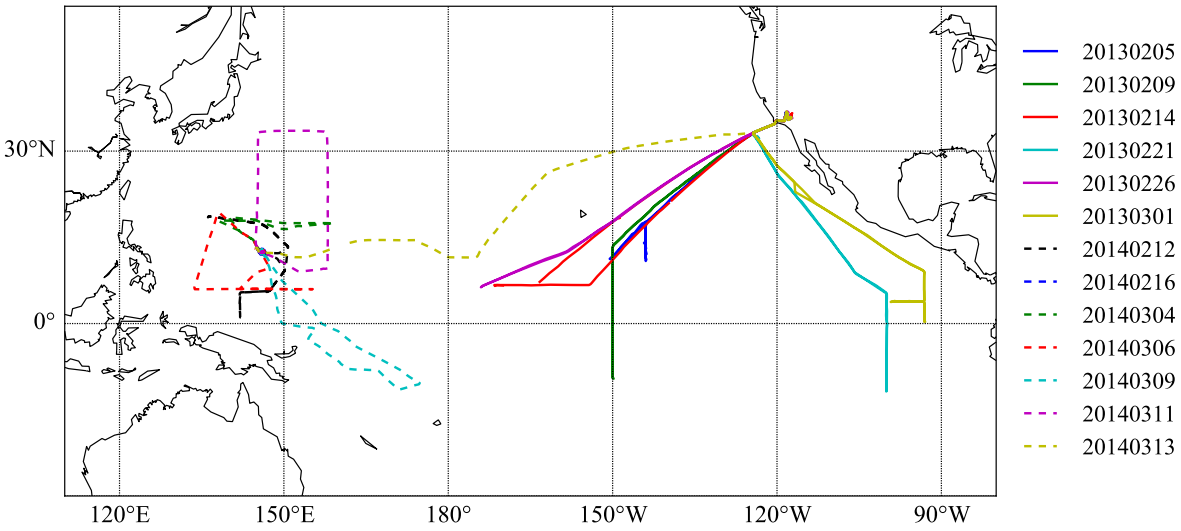

Figure 5.2 – Map of all ATTREX flights used in this study. Eastern Pacific flights were carried in February-March 2013, while Western Pacific ones flew in February-March 2014.

During the ATTREX campaign in boreal winters 2013 and 2014, the NASA Global Hawk unmanned aircraft flew through the Tropical tropopause layer (14-19 km) (*Jensen et al.*, 2015). It sampled the central and eastern Pacific in February-March 2013 from California, and the western Pacific in February-March 2014 from Guam. A map of all flights is displayed in figure 5.2. Combining both years, a reasonable sampling of the tropical Pacific region was achieved, with more data in the northern tropics. Since both 2013 and 2014 were nearly neutral ENSO years, the fact that the measurement were carried one year apart (2013 vs 2014) is probably of second order compared to the difference in geographic location (Eastern Pacific vs convective Western Pacific). This is confirmed by comparing the distribution of Richardson numbers from radiosonde observations in the Western Pacific between the two years (not shown).

Small-scale fluctuations are analyzed using ATTREX Meteorological Measurement System data (*Scott et al.*, 1990), which includes 3D-wind, temperature and pressure recorded at a frequency of 20 Hz (dataset produced by *Bui et al.*, 2014). The winds are deduced from the calculated pitch, roll and heading of the aircraft and from differential pressure sensors appropriately located on the aircraft fuselage (*Scott et al.*, 1990). The reported sensor precisions are 0.1 m/s for the longitudinal (along flight track) horizontal wind and 0.05 m/s for the vertical and horizontal-transverse to flight track winds. We stress that these different precisions between the longitudinal and the transverse and vertical winds mainly arise at the high frequencies. Indeed, the forward (ram) pressure sensor used to estimate the longitudinal wind needs to accommodate the large pressure value associated with the aircraft high true air speed, so that it is less sensitive to the small amplitude fluctuations at high frequencies than the differential pressure sensors used to measure u_t (the horizontal wind normal to track) and w (the vertical wind). Hence, quantitative observations of small-scales mainly rely on the high-frequency measurement of transverse and vertical wind.

The temperature sensor has a precision of 0.05 K while the pressure sensor precision is 0.3 Pa. Since we are interested in the very high frequencies (>1 Hz), the temperature sensor response time has a substantial impact. In the flight conditions of ATTREX, the response time of the Rosemount temperature sensor is estimated to be typically of 200 to 400 ms, so that it affects the high frequency measurements. Due to remaining uncertainties in the detailed high-frequency response of the sensor in flight conditions, only limited quantitative use of the temperature data is made in the paper.

5.3.3 Coordinate of the measurements and the Taylor hypothesis

Aircraft observations are recorded as a function of time along the plane trajectory. However, as emphasized by *Bacmeister et al.* (1996), they should be interpreted as instantaneous sections along the spatial coordinate of the aircraft position. For turbulence, the approximation holds when the plane speed is much larger than the wind speed. In this case, the determination of the spatial coordinate can be refined and extended using the True Air Speed (TAS), that is the air motion relative to the aircraft. The correction relies on the Taylor hypothesis which states that small turbulent eddies are stationary following the flow, i.e. they are just advected by the background wind and larger eddies.

In the paper, we assume the Taylor hypothesis and use the TAS to convert time scale to spatial scale. The Global Hawk TAS generally exceeds the ground relative wind speed by a factor of five and the TAS does not vary much during the flights, so that our methodology is similar to analyzing the observations in time with a constant TAS of about 170-180 m/s or directly in (ground relative) horizontal position. The variations of heading of the aircraft and its vertical ascent rate relative to the horizontal speed are neglected, as they only marginally affect the high frequencies.

5.3.4 Wavelet analysis and estimation of high frequency variance and eddy dissipation rates

As will be shown later in the paper, the small-scale fluctuations in wind and temperature are intermittent: aircraft observations show periods of high and low activity at high frequency. In order to quantify how activity at various frequencies varies with time, we used a continuous wavelet transform (e.g. *Torrence and Compo*, 1998) to perform time-frequency decomposition of the small-scale fluctuations.

In practice, we used a Morlet mother wavelet, applied in the time coordinate of the measurements. We retain the high frequencies (1-5 Hz band) of the wavelet transform to compute the evolution of the high frequency wind or temperature variance, σ_{HF}. Further discussion can be found in appendix C.1.

The eddy dissipation rate of kinetic energy ϵ_k is often used rather than the wind variance to quantify the intensity of turbulence (e.g. *Wilson*, 2004), specifically with the form $\epsilon_k^{\frac{1}{3}}$ (the "EDR") in the aviation turbulence literature (*Sharman et al.*, 2014). While ATTREX measurements in the 1-5 Hz range may not necessarily follow the expectations for Kolmogorov's inertial range (as will be discussed later), we assume a $-\frac{5}{3}$ spectral slope to derive ϵ_k from observations, following previous studies (e.g. *Lilly et al.*, 1974; *Chan et al.*, 1998). The power spectral densities of the longitudinal velocity component Φ_{u_l} and of the

vertical and transverse (normal to track) components, Φ_w and Φ_{u_t}, are assumed to follow:

$$\Phi_{u_l}(\kappa) = \alpha_k \epsilon_k^{\frac{2}{3}} \kappa^{-\frac{5}{3}} \text{ , and } \Phi_w(\kappa) = \Phi_{u_t}(\kappa) = \frac{4}{3}\alpha_k \epsilon_k^{\frac{2}{3}} \kappa^{-\frac{5}{3}} \text{ ,} \tag{5.21}$$

with κ the along-track angular wavenumber (in rad.m^{-1}) and α_k the "universal" Kolmogorov constant for high Reynolds number flows. $\alpha_k \simeq 0.5$ is a common value suggested, e.g., by *Sreenivasan* (1995).

To obtain estimates of ϵ_k, we chose to use the variance of vertical and transverse horizontal velocity since they are the most sensitive to high frequency fluctuations. The high frequency variance in those time series is integrated over the wavenumber range $[\kappa_1 - \kappa_2]$:

$$\epsilon_w = \left(\frac{\int_{\kappa_1}^{\kappa_2} \Phi_w(\kappa) d\kappa}{2\alpha_k \left(\kappa_1^{-2/3} - \kappa_2^{-2/3} \right)} \right)^{\frac{3}{2}} \text{ and } \epsilon_{u_t} = \left(\frac{\int_{\kappa_1}^{\kappa_2} \Phi_{u_t}(\kappa) d\kappa}{2\alpha_k \left(\kappa_1^{-2/3} - \kappa_2^{-2/3} \right)} \right)^{\frac{3}{2}} \text{ ,} \tag{5.22}$$

where $\int_{\kappa_1}^{\kappa_2} \Phi_{w,u_t}(\kappa) d\kappa = \sigma^2_{HF}$ is the estimate of the high frequency variance. In practice, $\kappa_1 = \dfrac{2\pi f_1}{V_a}$ and $\kappa_2 = \dfrac{2\pi f_2}{V_a}$ where V_a is the true air speed and f_1 =1 Hz and f_2 =5 Hz; assuming a true air speed close to 200 m/s, our frequency bounds f_1, f_2 correspond to frozen wavelengths of 200 and 40 m. The kinetic energy dissipation rate is then estimated as the geometric mean of the estimates from w and from u_t:

$$\epsilon_k = \sqrt{\epsilon_w \epsilon_{u_t}} \tag{5.23}$$

The noise level on ϵ_k arising from instrumental and quantization noise in the wind speed measurement is estimated to be around $3 \cdot 10^{-8} \text{m}^2\,\text{s}^{-3}$. No value can be measured below that noise level. The sampling precision of the derived ϵ_k is around 25% and the resolution is better than 7 seconds (appendix C.2).

In order to estimate ϵ_k, an alternative to the integrated variance approach used here is the maximum likelihood estimate from wind spectra (e.g. *Sharman et al.*, 2014). Both methods give similar results for our dataset (not shown), consistent with the conclusions of *Cornman* (2016).

5.3.5 A case-study of small-scale fluctuations occurrence

Due to a failure of the communications system for command and control, the Global Hawk remained within 2° of Guam (13°30'N, 144°48'E) during the second flight of ATTREX 2014 (2014/02/16). The aircraft track for this specific flight is shown on figure 5.3. 26 vertical profiles were acquired during that flight, allowing to precisely document the local TTL vertical wind and thermal stucture (*Kim and Alexander*, 2014), as well as the repartition of small-scale fluctuations. We examine the distribution of eddy dissipation rates and their repartition in the tropical tropopause layer during this well-documented period.

Figure 5.4 shows the time-altitude profiles of temperature and meridional and zonal winds, and eddy dissipation rates. A low-frequency Inertio-Gravity wave pattern can be identified through coherent oscillations in the wind and temperature fields. A slow descent of the wave phase during the flight can also be noticed, but overall the wave structure remained essentially

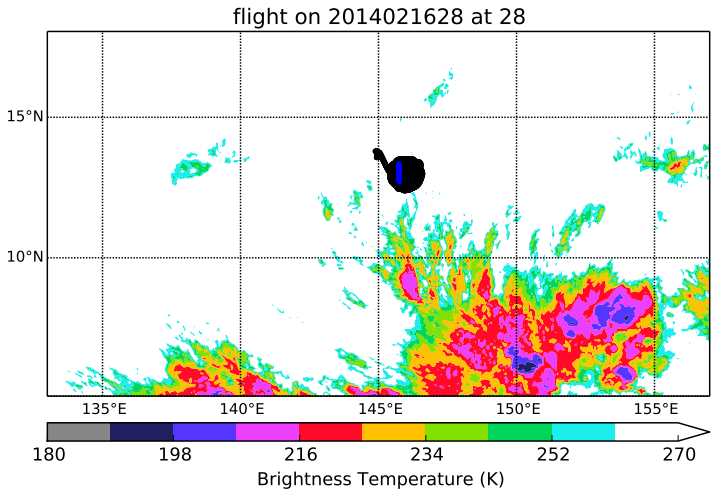

Figure 5.3 – ATTREX flight track on February 16$^{\text{th}}$-17$^{\text{th}}$ 2014 (black), when the Global Hawk remained near Guam. The brightness temperature of MTSAT window channel on February 17$^{\text{th}}$ at 5 am (UTC) is shown by the color scale and indicates the location of high altitude clouds. The location of the flight subsection presented in figure 5.6 is shown in blue.

stationary.

Figure 5.5 shows all vertical profiles of meridional wind v and potential temperature θ from that flight. As expected, it is apparent that the wave produces structures in the stability $\left(\frac{\partial\bar{\theta}}{\partial z}\right)$ and the vertical shear $\left(\frac{\partial\bar{u}}{\partial z}^2 + \frac{\partial\bar{v}}{\partial z}^2\right)$; it could thus drive dynamic instabilities, such as Kelvin-Helmholtz instability and structure turbulence occurrence (e.g. *Fritts et al.*, 2009b). Indeed, in figure 5.4, the profiles of ϵ_k show sporadic turbulence in the lower part of the TTL, but above 15.5 km high ϵ_k appear regrouped in two layers: one around 17 km active between 26 and 32 hours, and a weaker one at 16.2 km mainly active between 23 and 26 hours.

Figure 5.5 shows the mean gradient Richardson number (Ri_g) profile induced by the wave and the frequency of occurrence of turbulence as a function of altitude during the flights. Ri_g is defined by:

$$Ri_g = \frac{N^2}{\left(\frac{\partial\bar{u}}{\partial z}^2 + \frac{\partial\bar{v}}{\partial z}^2\right)} \tag{5.24}$$

Consistent with expectations from shear instabilities, figure 5.5 shows that turbulence preferentially occurs in the regions of low mean Richardson number.

Thus, figure 5.5 demonstrates that low frequency, small vertical wavelength (of the order of 2 km or less) waves play a key role in creating instabilities and enhancing the occurrence of turbulence in the tropics, as was already anticipated from the analysis of earlier aircraft observations by *Pfister et al.* (1986). Since equatorial waves with short vertical scales are often underestimated in current meteorological analyses and reanalyses (*Podglajen et al.*, 2014; *Kim and Alexander*, 2015), the fine-scale vertical structure of turbulence is probably missed by global weather and climate models, which have typical vertical resolution of 0.7 km at the most in the TTL and can hence only resolve waves with vertical wavelengths larger than about 3 km or more.

Besides the direct modulation of shear and stability, the large scale IGW also provides a

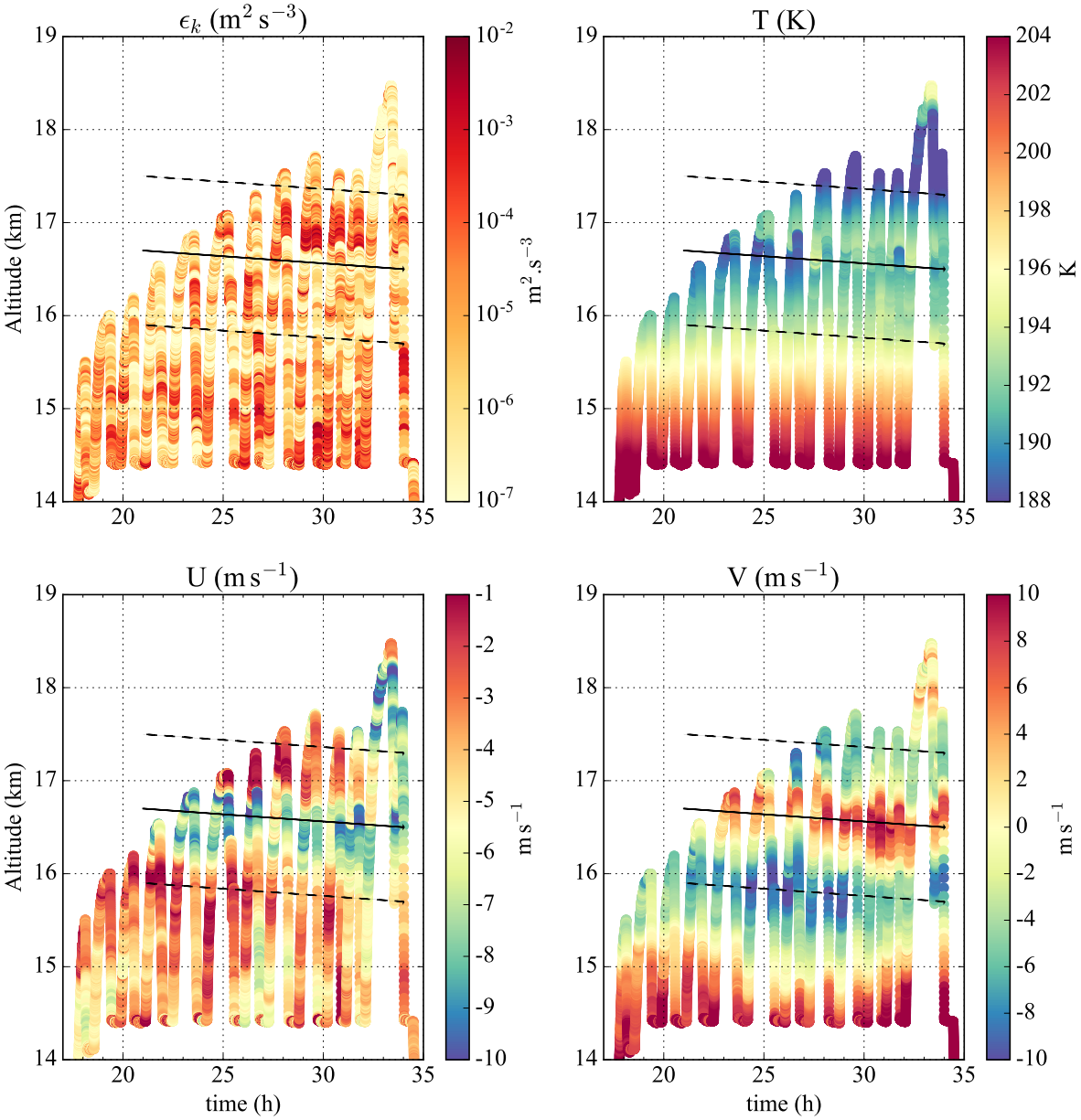

Figure 5.4 – On 2014/02/16, time altitude profiles of (top left) eddy dissipation rate ϵ_k (estimated from the winds using equations (5.23) and (5.22), (top right) temperature, (bottom left) zonal wind and (bottom right) meridional wind from aircraft observations showing the relationship of active layers with larger scale shear associated with an Inertio-Gravity Wave. The black lines emphasize the different wave phases of the Inertio-Gravity Wave: dashed lines correspond to negative meridional wind V anomalies due to the wave, whereas the continuous line corresponds to the positive meridional wind anomaly on the bottom right panel. The same lines have been added to the other panels in order to guide the eye in spotting the Inertio-Gravity Wave structure in U and T and its impact on ϵ_k layers.

background state in which shorter scale, higher frequency gravity waves propagate. Small-scale waves might also contribute to generating turbulence (*Pellacani and Lupini*, 1975; *Lane et al.*, 2012). Figure 5.6 shows that, before entering the turbulent layer near 17 km, the aircraft flew through a well defined monochromatic gravity wave packet of wavelength < 10 km (seen as consistent oscillations in potential temperature and vertical wind). However, it is difficult

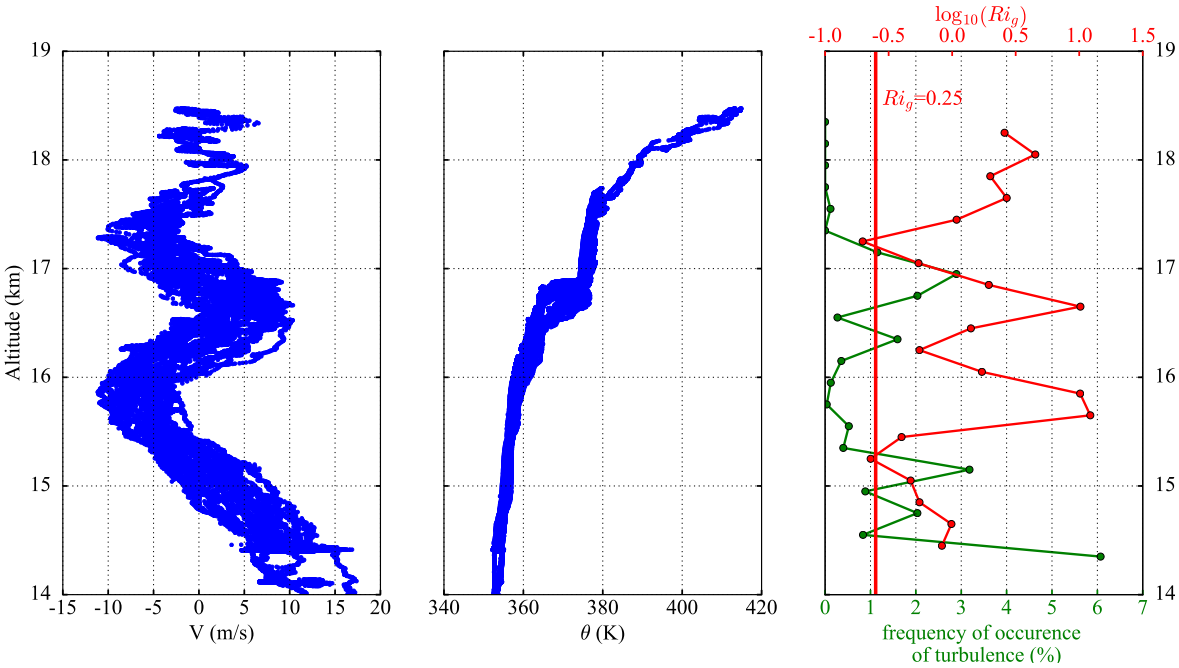

Figure 5.5 – Profiles of (left) meridional wind V, (middle) potential temperature θ and (right) gradient Richardson number Ri_g (red) and turbulence occurrence frequency (green), from the flight on 2014/02/16 during which the Global Hawk stayed near Guam (within 2°). The gradient Richardson number Ri_g and turbulence occurrence are estimated from all the average of the 26 profiles acquired on that day.

to demonstrate a mechanism between this gravity wave and the onset of turbulence from the observations only.

Nevertheless, this case-study shows that fine (vertical or horizontal) scale waves, which are unresolved in current global models, are important contributors to the driving of turbulence. Since a major source of gravity waves in the tropics is deep convection, this also suggests an important role of convectively-induced (clear-air) turbulence in the TTL. We will explore the influence of deep convection on turbulence occurrence in the next section.

5.3.6 Statistics of turbulence occurrence over the tropical Pacific during ATTREX

The previous subsection emphasized the role of both large and small scale gravity waves on turbulence occurrence. This subsection systematically examines the relationship between turbulence occurrence and its environment.

5.3.6.1 Definition of active events; distribution of eddy dissipation rates during all ATTREX flights

Figure 5.7 shows the distribution of eddy dissipation rates for all ATTREX flights, as well as for specific regions and altitude ranges. The lowest values are not geophysical (shaded gray area), as the observed peak around $3 \cdot 10^{-8}$ $\mathrm{m^2\,s^{-3}}$ corresponds to instrumental noise (see also appendix C.2). However, the highest branches of the distributions are well above the noise and vary by several orders of magnitude: typical values of ϵ_k range from below

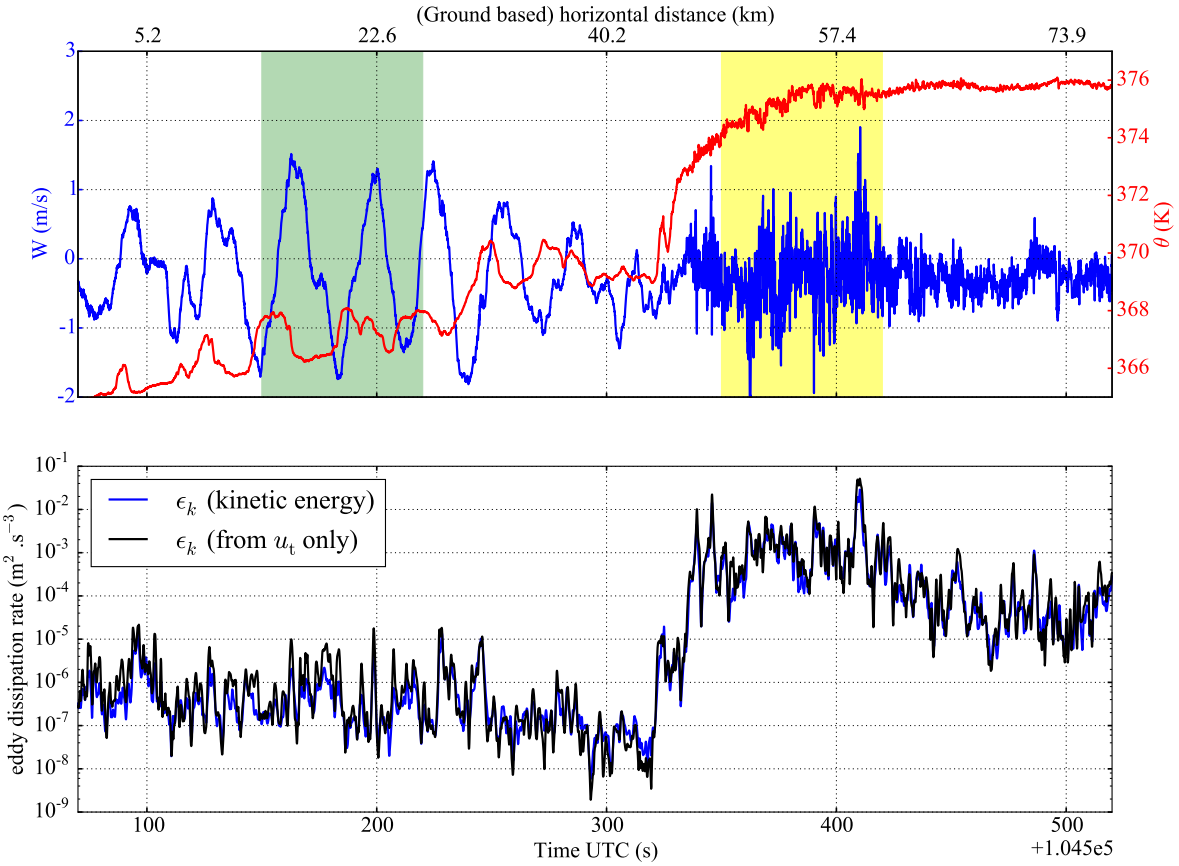

Figure 5.6 – (Top) Time series of vertical wind (W, m/s) and potential temperature (θ, K) along an aircraft climb on 2014/02/16 near Guam. A quiet period and a period with active small-scale fluctuations are emphasized with, respectively, green and yellow background. (Bottom) for the same time segment, time series of eddy dissipation rate of kinetic energy (blue) and kinetic energy estimated from transverse horizontal wind only (black).

10^{-7} to a few 10^{-1} $m^2\,s^{-3}$. We note that, even for the lowest of those typical values, the observed scale range (scales larger than 10 m) is well above the dissipation range starting below the Kolmogorov scale, which depends on the eddy dissipation rate ϵ_k and on the molecular viscosity ν: $l_\nu = \left(\frac{\nu^3}{\epsilon_k}\right)^{\frac{1}{4}}$ In typical TTL conditions, $l_\nu \ll 1$ m.

Figure 5.7 displays ϵ_k distribution in the Eastern-Central Pacific (ATTREX 2013) and Western Pacific (ATTREX 2014), and in the lower (below 15.5 km) and upper (above 15.5 km) TTL. High ϵ_k are more frequently observed over the convective Western Pacific than the Eastern Pacific, and they are generally more frequent in the lower TTL. For all the distributions, the high ϵ_k tail resembles a lognormal distribution, which is consistent with Radar (e.g. *Wilson et al.*, 2005) or other aircraft observations (e.g. *Sharman et al.*, 2014) and with Direct Numerical Simulations of turbulence generated by wave-breaking (*Fritts et al.*, 2009b).

The vertical black line in figure 5.7 corresponds to the threshold chosen to define "active" events. A measurement is considered to be part of an active event if its eddy dissipation rate is above a threshold of $\epsilon_{lim} = 10^{-3}$ $m^2\,s^{-3}$. This threshold (equivalent to $EDR = \epsilon_k^{1/3} = 0.1$ $m^{2/3}\,s^{-1}$) is similar in magnitude to thresholds taken to classify aviation turbulence (*Sharman et al.*, 2014). The fact that the different curves in figure 5.7 do not intersect each

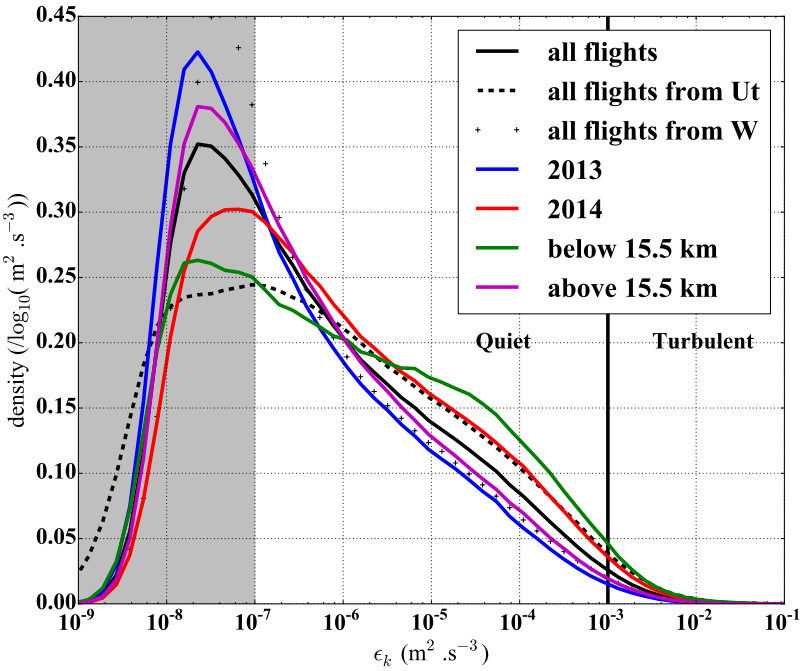

Figure 5.7 – Probability density function of kinetic energy eddy dissipation rates, for all ATTREX flights, 2013 Eastern Pacific flights, 2014 Western Pacific flights and for altitudes above and below 15.5 km. The vertical black line shows the threshold chosen to select occurrence of "active" events. The shaded grey area corresponds to values close to the estimated noise level of $3 \cdot 10^{-8}$ $m^2\,s^{-3}$

other for $\epsilon_k \geq 2 \cdot 10^{-6}$ $m^2\,s^{-3}$ suggests that the characterization of the environment of the "active" bursts will not be strongly sensitive to the threshold used to isolate them. Indeed, using different thresholds does not qualitatively affect the results.

5.3.6.2 Distribution of small-scale fluctuations with altitude and Richardson number

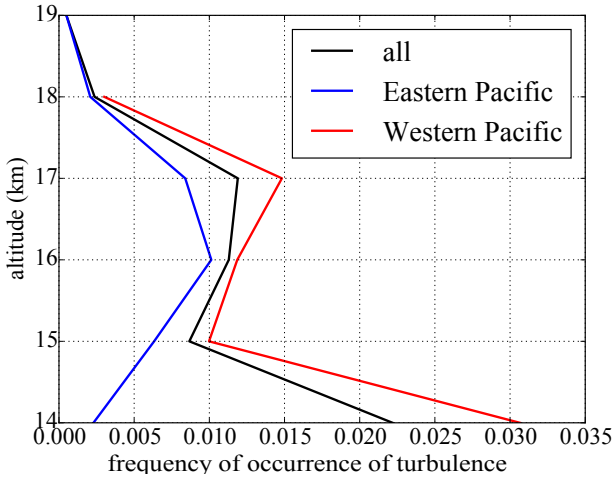

Figure 5.8 – Occurrence frequency of turbulence (defined by $\epsilon_k > 10^{-3}$ $m^2\,s^{-3}$) as a function of altitude, for all ATTREX flights (black), in the Eastern Pacific (boreal winter 2013, blue) and Western Pacific (boreal winter 2014, red). The frequency is computed from all obervations within 1 km layers.

As seen in the Guam case study, turbulence occurrence is related to shear and stability variations. In the TTL, both the stability and the shear strongly increase with altitude, at least over the tropical Pacific. They tend to balance one another, so that the distribution of the gradient Richardson number Ri_g does not vary too much with altitude, as indicated by radiosonde measurements (not shown, see also Figure 5.5). The stability effect is nevertheless dominant, so that the typical Ri_g slightly increases with altitude in the TTL. For this reason and because turbulence generating processes, such as deep convection, are more active in the lower TTL, turbulence occurrence is expected to depend on altitude. Figure 5.8 shows the profile of occurrence frequency of active events as a function of altitude in the whole dataset and for the Eastern and Western tropical flights separated. The vertical profiles show different behaviors, with a strong increase below 15 km in the tropical Western Pacific whereas in the Eastern Pacific turbulence occurrence seems to peak around 16 km altitude and then decreases when approaching the stratosphere. The frequency of turbulence occurrence is higher in the Western Pacific than in the Eastern Pacific at all altitudes, but we note that the difference is not so dramatic above about 15.5 km.

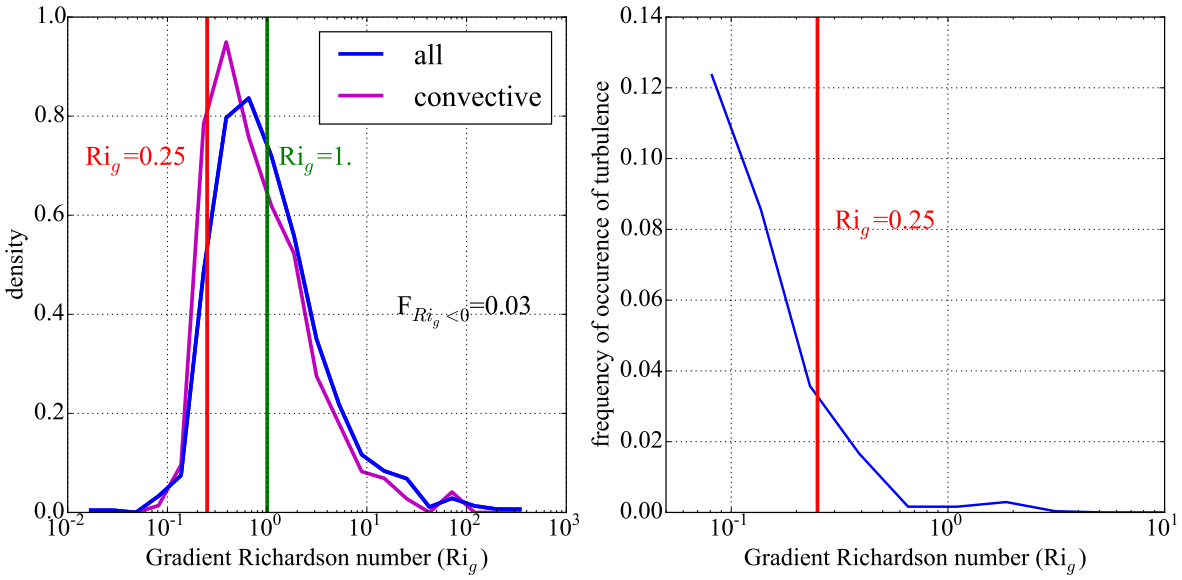

Figure 5.9 – (Left) Empirical distribution of the gradient Richardson number Ri_g from ATTREX descents, calculated over 200 m deep layers (blue curve). The magenta curve is the same, but for descents less than 100 km from convection. (Right) Frequency of occurrence of turbulence as a function of Ri_g.

The flight strategy used in ATTREX was such that most of the time the Global Hawk was climbing and descending through the TTL (see figure 5.4). During climbs, the horizontal speed of the aircraft is much bigger than its vertical ascent rate so that it is generally difficult to derive local estimates of the shear or of the Richardson number at the aircraft position. However, during descents, the vertical speed is larger (generally about 4-5 m/s). In the stratified TTL, descents can then be used to estimate the background wind vertical shear. We used 200 m vertical segments from the descents to obtain colocated measurements of the large-scale Ri_g and of turbulence occurrence frequency. Figure 5.9 shows the frequency distribution of Richardson number from the about 2000 segments of 200 m (blue curve). Highly stable layers are frequent, and the most frequent Ri_g are observed between 0.25 (the

onset of Kelvin-Helmholtz instability) and 1 (threshold for turbulence to be maintained). Rare occurences of Ri_g below 0.25 are found (about 12%), and about 3% show slightly negative N^2; those might not be strictly negative, since the soundings are not strictly vertical and in the case of low positive N^2 the small horizontal horizontal temperature gradients can affect this value. Figure 5.9 also shows the frequency of occurrence of turbulence as a function of Ri_g. As expected, turbulence is more frequent for low Richardson numbers, the occurrence frequency reaching about 10% for very low Ri_g (below 0.1). It should be noted here that the choice of the scale at which to calculate the wind shear and temperature lapse rate is somewhat arbitrary, as well as the threshold taken to select turbulent events, so that this figure should be taken as merely qualitative and illustrative of the effect of the background shear and stability. (We note that choosing another scale to compute Ri_g does not change the result qualitatively although there are some quantitative differences.) As emphasized in the case study, fine vertical scale waves modulate this vertical shear and stability.

5.3.6.3 Relationship between turbulence in the TTL and deep convection

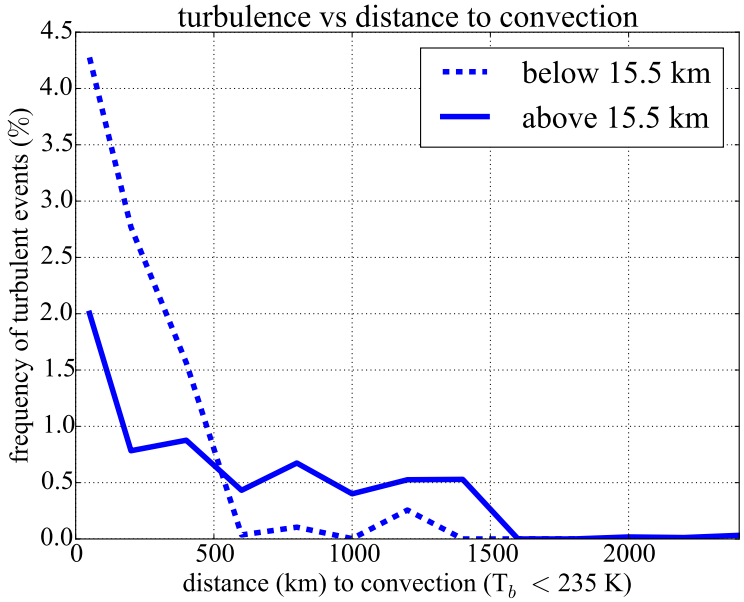

Figure 5.10 – Occurrence frequency of turbulent burst vs distance to convection (defined as regions with brightness temperature T_b <235 K).

The increased occurrence of turbulence in the vicinity (but out of) convective clouds has been the subject of much research due to the subsequent hazard it creates for aviation (*Lane et al.*, 2012). Is is often named CIT (Convectively Induced Turbulence) in this context. As emphasized by the Guam case-study, convectively-generated gravity waves are one of the processes linking turbulence to convective clouds. Thanks to the extended area sampled during ATTREX, it is possible to examine the effect of convection on an unprecedented spatial scale. Convection is here determined by examining the brightness temperature in the nearest-in-time geostationary image collected every 30 minutes by the Japanese Multifunctional Transport Satellites (MTSAT) or by the American Geostationary Operational Environmental Satellite-West (GOES-West). A pixel (about 4 km $\times$ 4 km) is considered convective if its brightness temperature T_b is lower than 235 K, following *Liu et al.* (2007). We note that the results

are not overly sensitive to the choice of this T_b-threshold. Figure 5.10 shows that, in the vicinity of convection, turbulence occurrence strongly increases. This is especially true at low altitudes (14-15.5 km) where the occurrence frequency can reach 8% or so, but higher altitude and data also follow this pattern. Since in the Western Pacific convection is more frequent than in the Eastern Pacific, figure 5.10 is consistent with figure 5.8 which showed more frequent turbulence over the Eastern Pacific, especially in the lower TTL. Figure 5.10 is similar in essence to figure 3 in *Lane et al.* (2012), who showed that distance to convection also controlled the distribution of turbulence occurrence in the UTLS but at a much finer scale (tens of kilometers). This figure suggests that deep convection is a key factor controlling (clear-sky) turbulence occurrence in the TTL. A number of studies (e.g., *Lane and Sharman*, 2006) have emphasized the role of convectively generated gravity waves as a link between deep convection and clear-air turbulence, through the enhancement of instabilities. Gravity wave activity is indeed generally enhanced near cold convective cloud tops (*Alexander et al.*, 2000). Consistently with that picture, figure 5.9 shows that low Ri_g, probably associated with wave activity, are more frequent in the vicinity of convection.

In addition to the relationship with convection, past studies have reported enhanced turbulence within thick mid-latitude cirrus (e.g. *Gultepe and Starr*, 1995; *Chan et al.*, 1998). During ATTREX, different relationships between clouds and turbulence were observed depending on the altitude and geographic location. In general, no correlation between thin TTL cirrus and turbulence was found in the upper part of the flights (above 15 km) but there were more occurrences of strong small-scale fluctuations within cirrus in the Western Pacific lower TTL (not shown). This suggests that the existence of enhanced turbulence within cirrus depends on cloud properties and their environment, similar to the impact of in-cloud radiative heating on cirrus evolution (*Jensen et al.*, 2011; *Podglajen et al.*, 2016a). Systematic examination of the cirrus-turbulence relation will be the subject of a dedicated follow-up study.

5.3.7 Nature of the small scale fluctuations

Small-scale motions encountered in the UTLS are generally referred to as turbulence. Such a framing implicitly brings to mind the Kolmogorov inertial range, but the exact nature of the observed motions, gravity waves or turbulence, is not always clear. This probably does not matter for aircraft safety, and in that context all fluctuations in the 100 m-2 km scale range perturbing commercial aircraft flights might be named "turbulent" (*Lane et al.*, 2012). However, knowledge of the nature of the fluctuations is important for estimating their impact on mixing processes. A spectrum of purely adiabatic, “linear" gravity waves would have vertical and horizontal scales too large (and gradients to weak) to induce significant molecular diffusion. On the contrary, inertial-range turbulence enhances tracer gradients down to the diffusion scale at which they are efficiently mixed by molecular diffusion; in that sense, inertial-range turbulence induces irreversible mixing. All formulations of small scale mixing, from Large Eddy Simulations to global models, assume some sort of inertial-range turbulence. Inertial-range turbulence indeed has the advantage that “universal” scaling laws can be statistically assumed in order to parameterize the effect of the unresolved scales on the small resolved scales.

Nevertheless, the nature of the observed motions is not obvious, partly due to an approx-

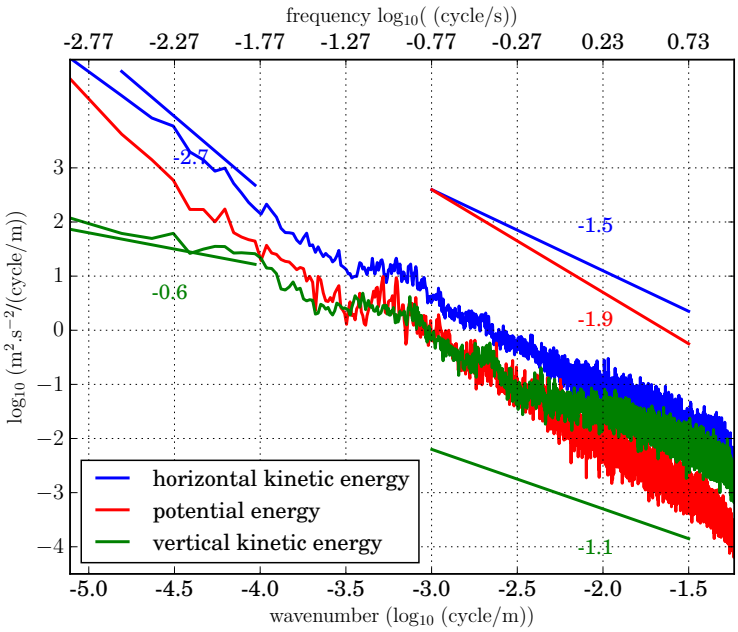

Figure 5.11 – Power spectral density of horizontal kinetic energy $E_{k_h}(k) = \frac{1}{2}(u'^2(k) + v'^2(k))$ (blue), vertical kinetic energy $E_{k_v}(k) = \frac{1}{2}w'^2(k)$ (green) and potential energy $E_p(k)$ (red)

imate $-\frac{5}{3}$ spectrum being present on a wide range of scales from the mesoscale hundreds of kilometers (*Nastrom and Gage*, 1985) to the very microscale (a few meters). Figure 5.11 shows power spectral density of horizontal and vertical kinetic energy and potential energy along a straight ATTREX flight segment obtained on March 6$^{\text{th}}$ 2014. Potential energy (and hence potential temperature) and horizontal kinetic energy spectra show approximate log-log linearity across the whole range, whereas the vertical wind spectrum is shallower at large scales and steepens at scales smaller than ∼10 km (*Gardner et al.*, 1993; *Bacmeister et al.*, 1996). The nature of the motions dominating the mesoscale part of the spectra (stratified turbulence or mixture of internal waves) has been and is still debated (e.g. *Lilly*, 1983; *Gage et al.*, 1986; *Bacmeister et al.*, 1996; *Lindborg*, 1999; *Callies et al.*, 2014). Regarding the subkilometer range (below 400 m or so), we note that the motions get closer to isotropy between vertical and horizontal kinetic energy and that the vertical kinetic energy (green curve) exceeds the potential energy (red curve); this suggests that motions at those fine scales resemble the 3D inertial-turbulence subrange. Even so, stratification and buoyancy forces are believed to play a major role in shaping the dynamics (*Weinstock*, 1978; *Lumley*, 1964). In this section, we examine the characteristics of small-scale motions and their consistency with inertial-range turbulence theory.

5.3.7.1 Characterization of an active layer

In Fig. 5.6, an active and quiet period are identified in the time series by the yellow and green shadings. Figure 5.12 shows the cross-wavelet amplitude and phase spectrum between w and θ. The integral across space and wavenumber of its real part corresponds to the heat flux $\overline{w'\theta'}$. The amplitude spectrum is represented by the colors (log-scale) while the arrows correspond to the phase. The active and quiet periods are clearly seen in the increase

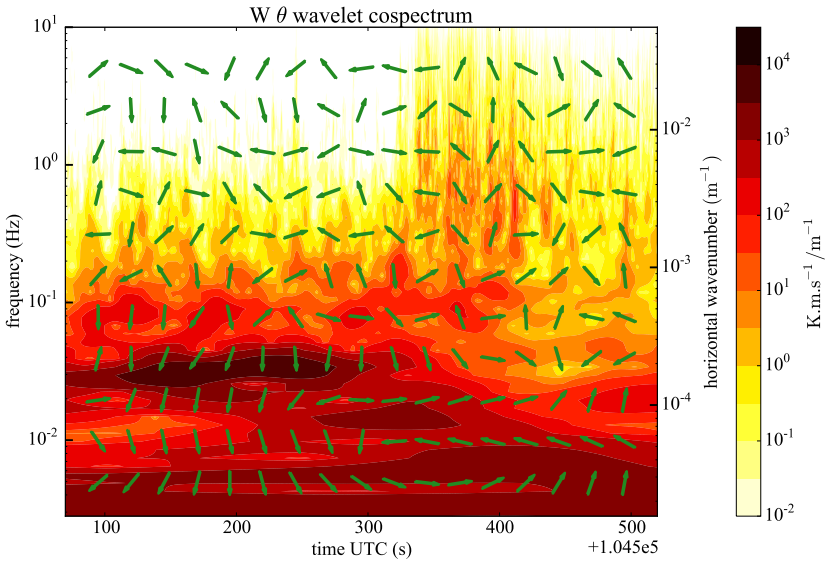

Figure 5.12 – Cross-wavelet amplitude (colors) and phase (arrows) spectrum of vertical wind W and potential temperature θ. Horizontal arrows directing towards the right (resp. left) indicate that the two fields are in phase (resp. out of phase), while the vertical arrows correspond to fields in quadrature.

of amplitude at small scales starting near 300 s. On top of the intermittency of the flux amplitude, the strong time and frequency variability of the phases during the active period can also be noticed, with no obvious polarization relation. This is in striking contrast with the low frequency signature of the gravity wave centered at 200 s and frequency $10^{-1.5}$ Hz, which indicates phase quadrature between temperature and vertical wind, as expected for a monochromatic gravity wave. Conversely, the absence of well-defined polarization relation at the high frequencies near 400 s supports the idea of "turbulent inertia" dominating at those scales (below 200 m).

Figure 5.13 shows the power spectral density of vertical, horizontal transverse and longitudinal velocity, and of potential energy $E_p(k)$ as a function of horizontal (linear) wavenumber $k = \dfrac{\kappa}{2\pi}$ (where κ is the angular wavenumber in rad.m^{-1}) during the active and quiet time sections. The power spectra $F(k)$ are defined such that $\int_0^\infty F(k)dk = \sigma_{\text{rms}}^2$ where σ_{rms} is the root mean-square of the variable. The potential energy spectra is calculated from the potential temperature spectra as

$$E_p(k) = \frac{1}{2}\frac{g^2}{N^2}\frac{\theta'^2(k)}{\bar{\theta}^2} \tag{5.25}$$

where N is estimated using the vertical temperature gradient inferred from the Microwave Temperature Profiler (MTP *Mahoney and Denning*, 2009) and averaged over the time section.

During the active period, both transverse velocities (vertical w and horizontal u_t) show a -1.5 to -1.6 slope, close to the expected $-\dfrac{5}{3} \simeq -1.66$ for inertial-range turbulence. Similarly, the second-order structure function has a $\dfrac{2}{3}$ slope (not shown). The longitudinal, along-track velocity spectrum drops quickly for scales below 500 m, which is a retrieval artifact as explained in section 5.3.2. Nevertheless, transverse wind speed w and u_t are at similar activity level, which again suggests nearly isotropic turbulence. The eddy dissipation rates

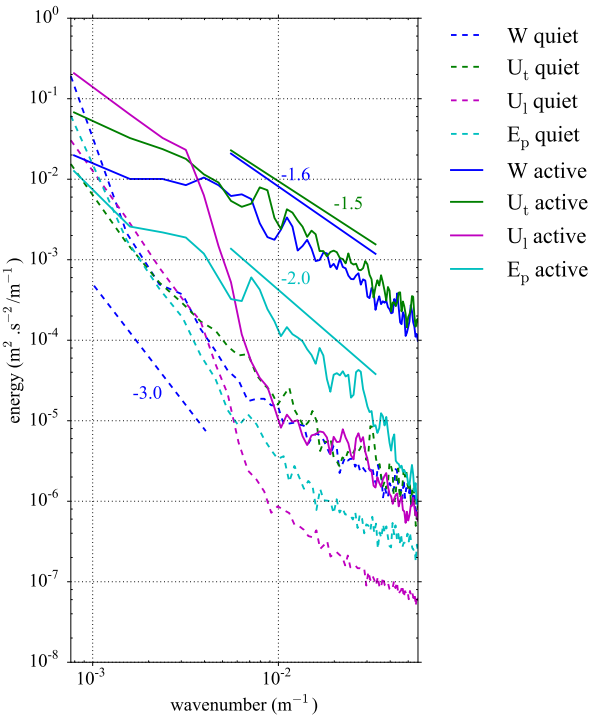

Figure 5.13 – Spectra of measured winds and temperature during a turbulent burst and a quiet period on 2014/02/16 near Guam.

inferred from vertical and horizontal wind speed only are also shown on figure 5.6; they are of close amplitude and also suggest nearly isotropic turbulence.

These observations (isotropy of winds and $-\frac{5}{3}$ slope) strongly suggest that we are observing inertial range turbulence. Indeed, the *outer* scale L_m of the inertial subrange of turbulence is related to the Ozmidov scale L_O:

$$L_m = \frac{2\pi}{C} L_O \,. \tag{5.26}$$

Weinstock (1978) suggested $C = 0.62$ for the dimensionless C constant, although later *Weinstock* (1992) argued that C was actually variable. The Ozmidov scale L_O is defined by

$$L_O = \sqrt{\frac{\epsilon_k}{N^3}} \tag{5.27}$$

so that L_m can be expressed as:

$$L_m = \frac{2\pi}{C}\sqrt{\frac{\epsilon_k}{N^3}} \simeq 10\sqrt{\frac{\epsilon_k}{N^3}} \,. \tag{5.28}$$

During the active period, $\epsilon_k \simeq 2 \cdot 10^{-3}$ m^2 s^{-3} (figure 5.6) and $N \simeq 10^{-2}$ rad s^{-1} so that $L_m \simeq 400$ m, which is roughly consistent with the scale at which the $-\frac{5}{3}$ slope starts in figure 5.13.

Regarding the potential energy (per unit mass) power spectral density, figure 5.13 shows that it exhibits somewhat different features than the velocities. Its magnitude is about 10 times smaller than that of the u_t wind speed; this disagrees with an interpretation in terms

of mid-frequency internal gravity waves for which there is an equipartition expected and observed between potential and total kinetic energy (see, e.g., figure 1 of *Podglajen et al.*, 2016b). However, an excess of turbulent kinetic energy compared to turbulent potential energy has been reported in the literature for inertial turbulence at the finest scales (*Wilson et al.*, 2014). In the figure, the slope of the potential energy spectrum with respect to horizontal wavenumber appears steeper than that of the wind spectra and than the $-\frac{5}{3}$ expected from theory. The steeper slope observed for E_P probably comes for the response time of the temperature sensor and the uncertainty in its correction, as explained in section 5.3.2.

The turbulence scaling and the statistics of energetics during all ATTREX turbulent burst are now explored more systematically in the following subsections.

5.3.7.2 Scaling of wind and temperature during turbulent bursts

An important prediction of inertial range turbulence theory, well verified in observations, is the $-\frac{5}{3}$ scaling of winds (the Kolmogorov spectrum). The power-law scaling slope s, i.e. the slope of the log-log linear energy spectrum: $E(k) \propto k^{-s}$, is expected to be close to $-\frac{5}{3} \simeq -1.66$. At larger scales, we note that theories suggesting different slopes exist: for instance, *Lumley* (1964) predicts -3 *buoyant subrange* and indeed there have been observations in the 200 m-20 km range of steeper slopes than $-\frac{5}{3}$, from -2.5 to -3 (e.g., *Nastrom et al.*, 1987; *Chan et al.*, 1998). Indeed, in figure 5.13 a steep slope (about -3) is observed for the quiet case at scales 100 m-1 km. Since ϵ_k is estimated assuming inertial range turbulence with $s = -\frac{5}{3}$, it is important to assess the validity of this assumption.

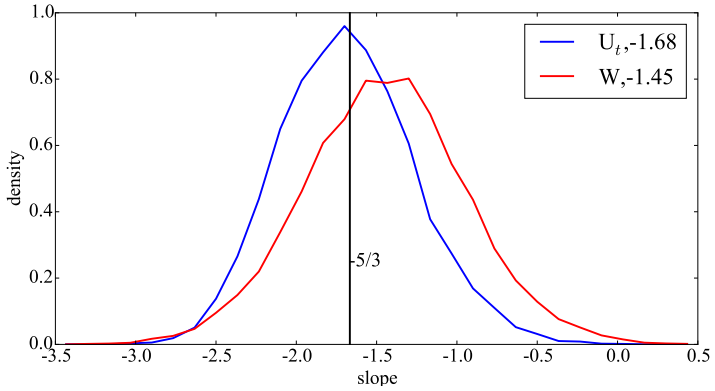

Figure 5.14 – PDF of spectral slopes of transverse horizontal wind (u_t) and vertical wind (w) during the turbulence bursts ($\epsilon_k > \epsilon_{lim}$) for frequencies between 1-5 Hz. It is usually close to $-\frac{5}{3}$.

Figure 5.14 shows the PDF of s observed during turbulent events. The slopes are computed from the logarithm of the ratio of wavelet power at scales of 1 s (180 m) and 0.2 s (36 m). While there is some variability, the $-\frac{5}{3}$ scaling is statistically well verified for transverse horizontal wind U_t. The vertical wind shows slightly shallower slope (-1.45), which is due to the 170 m scale being sometimes higher than the outer scale of the inertial range L_m, so that some of the flat low frequency part of the W spectrum is included in the slope

calculation. Nevertheless, the difference is small and figure 5.14 shows that a statistical $-\frac{5}{3}$ is verified for vertical and transverse wind. Some variability in the slope exists but a significant part of it can be attributed to sampling uncertainty.

5.3.7.3 Isotropy of small-scale motions

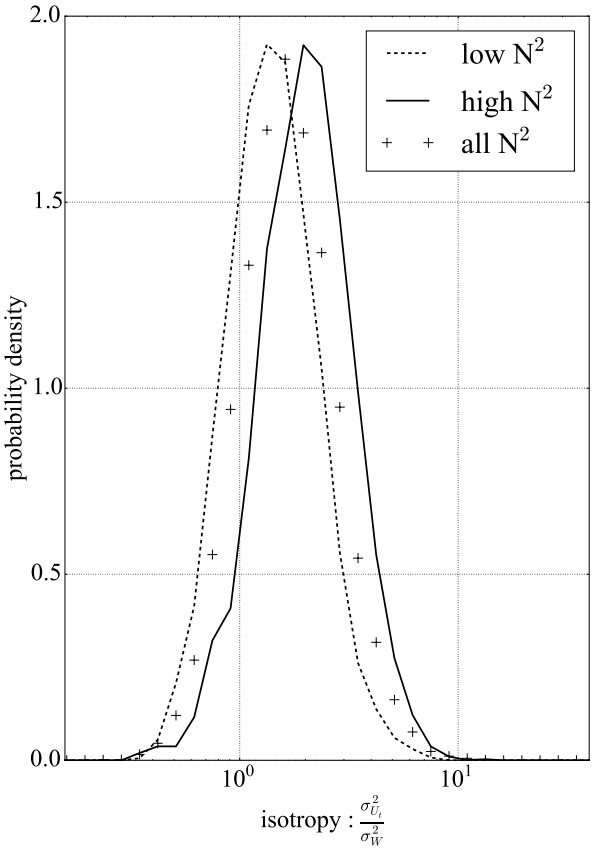

Figure 5.15 – Ratio of horizontal to vertical kinetic energy $\frac{\sigma^2_{u_t}}{\sigma^2_w}$ (black) for high ($N^2 > 4.10^{-4}$ s^{-1}, dashed), low ($N^2 < 10^{-4}$ s^{-1}, solid) and all (crosses) stability.

Figure 5.15 presents the distribution of the ratio between small-scale horizontal and vertical kinetic energy $\left(\frac{\sigma^2_{U_t}}{\sigma^2_W}\right)$ during turbulent bursts. Turbulent bursts are selected depending on the kinetic energy dissipation rate being over the chosen threshold for turbulence $\epsilon_{lim} = 10^{-3}\mathrm{m}^2\,\mathrm{s}^{-3}$. For those events, the motions appear statistically close to isotropy with nevertheless higher variance in the horizontal motions; this is related to our choice of ϵ_{lim}. Indeed, choosing $\epsilon_{lim} = 10^{-3}\mathrm{m}^2\,\mathrm{s}^{-3}$ generally places the outer scale L_m between 120 and 300 m, i.e. near the upper limit of the ∼40-200 m range used to estimate small-scale variance so that the motions are close to but not perfectly isotropic. Choosing a higher (resp. lower) threshold to select turbulent bursts increases (resp. decreases) their isotropy (not shown), in agreement with *Wroblewski et al.* (2010), who also found more isotropy associated with stronger turbulence in aircraft observations in the Southern Hemisphere Mid-Latitude UTLS. It should be noted that the sampling of high ϵ_k is necessary to obtain nearly statistical isotropy at our observing scales: for instance, *Schumann et al.* (1995) obtained strong

anisotropy $\left(\frac{\sigma^2_{U_t}}{\sigma^2_W} \simeq 10\right)$ but sampled much quieter air ($\epsilon_k \leq 10^{-7}\mathrm{m}^2\,\mathrm{s}^{-3}$).

If the motions appear almost isotropic on average in figure 5.15, there is a significant dispersion of the $\left(\frac{\sigma^2_{U_t}}{\sigma^2_W}\right)$ ratio from case to case. Direct Numerical Simulations (e.g. *Fritts et al.*, 2009b) and experiments (e.g. *Sreenivasan*, 1991) have reported significant anisotropy of turbulence arising in sheared and stratified flows. The numerous vertical profiles through the TTL acquired during the campaign allowed the sampling of a variety of stratification, which is important for the outer scale (Equation 5.28), so that the impact of this parameter can be tested. Figure 5.15 shows the distribution of $\frac{\sigma^2_{U_t}}{\sigma^2_W}$ for high and low stability N^2 ($N^2 > 4.10^{-4}$ s^{-1} and $N^2 < 10^{-4}$ s^{-1}). Higher N^2 are associated with a higher variance of the horizontal motions relative to vertical ones. This is intuitive: since the atmosphere is then more stratified, vertical motions are inhibited compared to horizontal ones. Furthermore, since the threshold for burst selection ϵ_{lim} is the same for the different N^2, the high N^2 correspond to smaller Ozmidov and outer scales. Thus, there is more contribution from anisotropic motions above the outer scale in the 40-200 m range. Consistently, taking the integration over smaller scales (20-100 m) to estimate the variance statistically shows more isotropic motions, i.e. a more important contribution of the vertical motions compared to horizontal ones (not shown). This has been noticed in high-resolution idealized LES simulations of turbulence near thunderstorms (*Lane and Sharman*, 2014).

5.3.7.4 Variability in turbulence activity

Figures 5.6 and 5.7 show that there is an order of magnitude variability in eddy dissipation rate. Turbulent events occur as a succession of bursts and the observed distribution of ϵ_k approximately follows a log-normal distribution (figure 5.7), as would be expected from Kolmogorov third hypothesis and is generally found in observations of dissipation rates (e.g. *Wilson*, 2004; *Sharman et al.*, 2014). Thus, the mean ϵ_k is dominated by rare, localized, intense events. This characteristic of turbulent bursts, sometimes referred to as intermittency, has important consequences for the effect on eddy mixing and should be quantified. Previous works have devoted much attention to the characterization of intermittency and multifractal properties of atmospheric turbulence (e.g. *Schmitt et al.*, 1994; *Lovejoy and Schertzer*, 2011). Here, we provide simple quantification of this intermittency.

One metric that quantifies inhomogeneity in a positive field is the Gini coefficient (*Gini*, 1921). Designed to diagnose inequalities of income, it has been previously used in atmospheric sciences to quantify variability in the momentum flux carried by gravity waves to the stratosphere (*Plougonven et al.*, 2013). It is expressed as:

$$G_{\epsilon_k} = \frac{\sum_{n=1}^{N} \left(n\overline{\epsilon_k} - \sum_{i=1}^{n} \left(\epsilon_k\right)_n\right)}{\sum_{n=1}^{N} n\overline{\epsilon_k}} \tag{5.29}$$

where $\left(\epsilon_k\right)_n$ is the n sample from the serie of ϵ_k measurements sorted in increasing order, N is the number of samples and $\overline{\epsilon_k} = \frac{1}{N}\sum_{i=1}^{N}\left(\epsilon_k\right)_n$ is the average eddy dissipation rate. G_{ϵ_k} quantifies statistical dispersion in the eddy dissipation rate, i.e. the relative importance of the tail of the PDF of ϵ_k on its integrated value. $G_{\epsilon_k} = 0$ corresponds to a constant

ϵ_k for which all measurements equally contribute to the sum. $G_{\epsilon_k} \to 1$ corresponds to a highly inhomogeneous turbulent field: a single measurement accounts for the total sum (all $(\epsilon_k)_n = 0$, except $(\epsilon_k)_N > 0$). For intermediate values, the exponential distribution for instance has $G_{\epsilon_k} = 0.5$. The Gini coefficient thus provides a quantitative measure of the relative contribution of the upper part of the tail to the average value.

Table 5.1 – Mean ϵ_k and Gini coefficient of ϵ_k in different regions and altitude range: all ATTREX flights, Eastern or Western Pacific flights only and upper (above 15.5 km) and lower (below 15.5 km) TTL.

	All ATTREX	East Pac	West Pac	upper TTL	lower TTL
$\overline{\epsilon_k}$ (10^{-5} m^2/s^{-3})	4.8	2.6	7.6	3.5	9.7
G_{ϵ_k}	0.96	0.96	0.95	0.96	0.95

The empirical G_{ϵ_k} obtained for different regions and altitude range are summarized in table 5.1. Contrary to regional averages, all values of the Gini coefficient are fairly similar, extremely high (close to 0.95), which emphasizes the dominant contribution of a few rare events to the average diffusivity. For comparison purposes, the highest typical Gini coefficients for income are lower than 0.7; gravity wave momentum flux in the lower stratosphere also have Gini coefficients lower than 0.7 (e.g. *Plougonven et al.*, 2013). Eddy dissipation rates in the TTL are therefore highly inhomogeneous.

5.3.7.5 Size of active “turbulent" patches

Turbulent activity is intermittent and localized in patches of limited size. This locality of turbulence is important to assess the level of the vertical eddy diffusion induced by turbulent patches (*Dewan*, 1981; *Alisse and Sidi*, 2000; *Vanneste*, 2004; *Osman et al.*, 2016).

Aircraft descents are used in order to infer the depth of the observed layers, a turbulent layer being defined as a continuous segment of $\epsilon_k \geq 10^{-4}$ m^2 s^{-3} containing at least one occurrence of $\epsilon_k \geq \epsilon_{lim} = 10^{-3}$ m^2 s^{-3}. As previously mentioned, there is a crude approximation in considering aircraft descents as strictly vertical profiles, given the huge horizontal speed of the plane compared to the vertical descent rate. This approximation is partly justified by the aspect ratio of the atmospheric flow in the TTL and its impact on the structure of turbulent layers, which are vertically thin and extend horizontally. The distribution of layer depths inferred from the 136 aircraft descents is presented in Figure 5.16. The descents are more than 2 km deep and generally 3-4 km deep (from 14 to 18 km), which limits the upper detectable depth of the encountered layers. However, figure 5.16 shows that the layers are found less than 500 m deep, and most of them have depth of the order a few 100 m or less. Furthermore, most observations of turbulence (95%) and of turbulent layers (93%) are within a layer with identified top and bottom. On the other hand, very few occurrence of layers narrower than a few tens of meter are found. This is probably due to the limit imposed by the minimum detectable depth, which is given by the time resolution of ϵ_k estimates (about 6 s, see appendix C.2), which at a descent rate higher than 1.5 m/s corresponds to about 10 m. Finding typical turbulent layers a few tens to a few hundred meters deep is roughly consistent with findings from radiosondes (*Wilson et al.*, 2011). We also note that this typical depth is also roughly consistent with the estimated outer scale of the turbulence studied

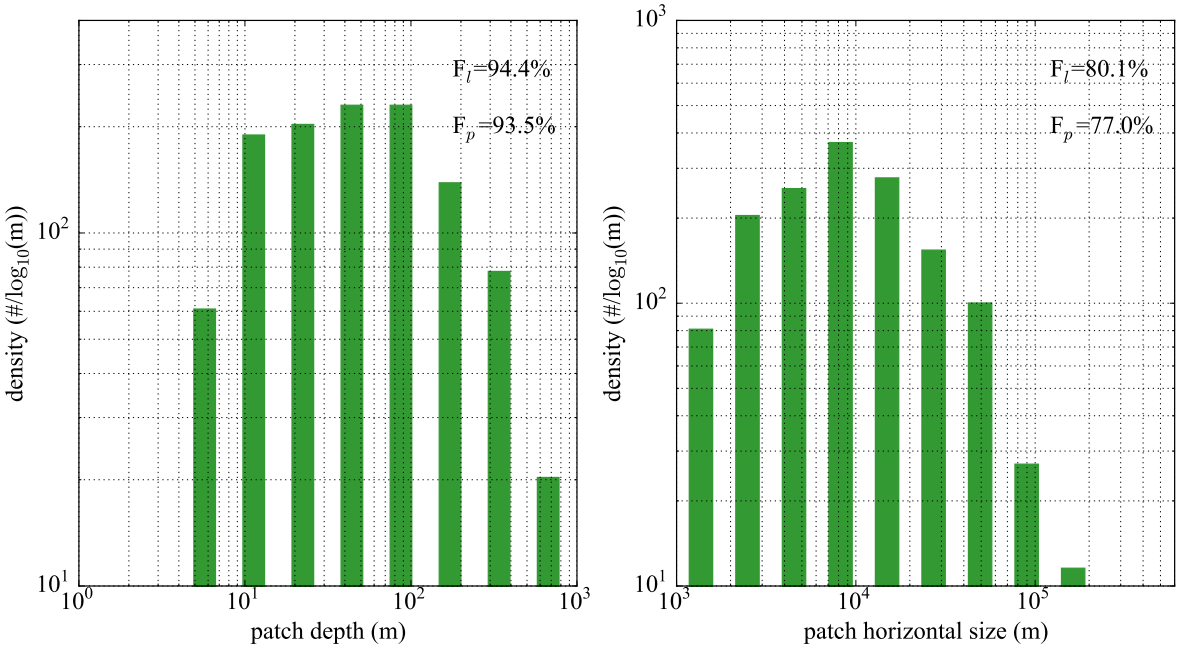

Figure 5.16 – Distribution (number of occurrence normalized by bin size) of turbulent patches depth (left) and horizontal size (right). Those are obtained from vertical descents of the aircraft and from straight horizontal scans, respectively, and patches are defined as continuous segments with $\epsilon_k \geq 10^{-4}$ m^2/s^3 and at least one occurrence of $\epsilon_k > \epsilon_{lim} = 10^{-3}$ m^2/s^3. The proportion of sampled patches F_l and of sampled turbulent points F_p entering in the statistics are indicated; they do not reach 100% because the bounds of the patches sometimes occur outside of the scans. F_u and F_p thus indicate the reliability of the presented size statictics.

(around 100 m); the outer scale of turbulence should indeed be no larger than the depth of the turbulent patches.

Figure 5.16 also shows the distribution of patches horizontal size, inferred from continuous straight horizontal aircraft segments. Typical patches are a few tens to hundreds of kilometer long, but the sampling of this distribution might be limited by the limited resolution and the typical size of straight segments during ATTREX (less than 200 km). Indeed, a little more than 20% of turbulent observations during those straight segments have their bounds outside of the sampled segment, so that the actual size of the associated turbulent patch cannot be determined. We also note that if turbulent patches are slightly tilted, the horizontal size will be underestimated. Hence, figure 5.16 only provides a lower estimate of horizontal sizes.

Finally, we note that the typical horizontal and vertical sizes might seem lower than those estimated by *Sharman et al.* (2014): this is probably mainly due to the fact that those authors quantified turbulence using thresholds on the peak EDR $\left(\epsilon_k^{\frac{1}{3}}\right)$ within 1 minute, rather than instantaneous EDR value as in our study.

5.3.8 Estimation of the impact on vertical mixing

Turbulence active patches have long been reckoned to control the vertical diffusion of constituents in the UTLS (*Dewan*, 1981; *Mote et al.*, 1996). However, the value of the effective diffusivity resulting from the activity of all patches remains a matter of debate. Assuming

perfect mixing inside the turbulent patches and no mixing out of them, *Dewan* (1981) deduced a typical mean diffusivity of the order of 0.2 $m^2\,s^{-1}$. This value is at odds with estimates derived from observed tracer evolution and structure: using the water vapor tape recorder in the tropical lower stratosphere, *Mote et al.* (1998) concluded that the typical value in that region should rather be of the order of 0.02-0.03 $m^2\,s^{-1}$. Generally, available estimates vary by a few order of magnitude (0.01 to 1 $m^2\,s^{-1}$ *Mote et al.*, 1998; *Legras et al.*, 2003; *Rao et al.*, 2001; *Sunilkumar et al.*, 2015; *Glanville and Birner*, 2016). Although particularly strong in the TTL, uncertainties in the magnitude of turbulent diffusivity are also found in other regions of the atmosphere (see table 1 of *Wilson*, 2004, for a review of diffusivity estimates in different regions).

5.3.8.1 Estimation of turbulent diffusivity from aircraft observations

The eddy diffusion coefficient for heat is defined as:

$$K_h = -\frac{\overline{w'\theta'}}{\frac{\mathrm{d}\overline{\theta}}{\mathrm{d}z}} \tag{5.30}$$

It is related to eddy diffusivity of the tracer of mixing ratio χ, K_χ, through the turbulent Lewis number L_e :

$$K_\chi = -\frac{\overline{w'\chi'}}{\frac{\mathrm{d}\overline{\chi}}{\mathrm{d}z}} = L_e K_h \quad , \tag{5.31}$$

L_e is generally assumed to be close to 1 in the free atmosphere, so that the heat diffusivity is the same as the diffusivity for tracer transport $K_\chi = K_h$.

Assuming spatial homogeneity and stationarity of the turbulence, K_h can be related to the potential energy dissipation rate (see, e.g. *Wilson*, 2004), following

$$K_h = \frac{\epsilon_p}{N^2} \quad . \tag{5.32}$$

It is also related to the kinetic energy dissipation rate:

$$K_h = \gamma \frac{\epsilon_k}{N^2} \quad , \tag{5.33}$$

where $\gamma = \frac{\epsilon_p}{\epsilon_k}$ is the dissipation rate ratio (*Wilson*, 2004). Under the hypotheses of homogeneity and stationarity, $\gamma = \frac{R_f}{1 - R_f}$ where R_f is the flux Richardson number. *Lilly et al.* (1974) suggest a canonical value of $R_f = 0.25$, based on *Thorpe* (1973), corresponding to $\gamma = \frac{1}{3}$. *Weinstock* (1978) argues for $\gamma \simeq 0.8$. Radar observations by *Dole et al.* (2001) show this ratio to be highly variable, dependent on the stability and approximately following a log-normal distribution. A typical value of γ from their study would be 0.2, not so different from $\frac{1}{3}$.

One method for estimating K_h consists in applying equation 5.33 using the estimated ϵ_k and the vertical stability from the Microwave Temperature Profiler (*Mahoney and Denning*, 2009) temperature lapse rate. It has been used by *Lilly et al.* (1974); *Schumann et al.* (1995).

The main uncertainty for this method comes from the poorly constrained parameter γ which, as just discussed, probably depends on various parameters (e.g., the stage of evolution of the turbulent layer).

Another method would consist in using the time series of w and θ to evaluate the flux $\overline{w'\theta'}$ from the covariance between w and θ using some spatial average and deduce the diffusivity using the vertical temperature gradient (*Kennedy and Shapiro*, 1975, 1980; *Pavelin et al.*, 2002). Apparently more direct, this method requires assuming: (1) the scale of the perturbations at which to calculate the flux and (2) the distance over which to average the flux. As $\overline{w'\theta'}$ is strongly intermittent (see Fig. 5.12), the output of this procedure is dependent on the scales chosen for averaging, which are difficult to physically justify. Tests led to very weak and upgradient potential temperature flux. Furthermore, given the intermittency of turbulence, it is not guaranteed that this approach will provide a reliable estimate of the ensemble average implied in the definition of K_h. For this reason and because of uncertainties in the high frequency temperature measurements, we use the first method to estimate K_h in the following with Lilly's value for γ, i.e. $\gamma = \frac{1}{3}$. This might induce a factor of uncertainty when compared to the empirical $\gamma \simeq 0.2$ found by *Dole et al.* (2001).

5.3.8.2 Impact on tracer transport : effective vertical eddy diffusivity

A natural approach to estimate the effect of the observed turbulent diffusion is to consider the average diffusivity. However, as recently reviewed by *Osman et al.* (2016), this overestimates the effect on tracer transport, which would be inferred from satellite observations of tracers (as in, e.g. *Mote et al.*, 1996). Indeed, turbulence appears within a limited number of shallow patches and the mixing is confined within those patches. In the extreme case of perfectly mixed but very small patches, the strong vertical mixing within the layer will not overcome the fact that no diffusion takes place out of the very shallow layer; one can thus get a large average diffusivity with virtually no impact on tracers. To estimate the impact of the finite size turbulent patches on the mixing properties, different authors (e.g. *Dewan*, 1981; *Alisse and Sidi*, 2000; *Vanneste*, 2004; *Osman et al.*, 2016) have introduced an effective diffusivity K_{eff}.

Alisse and Sidi (2000) and *Vanneste* (2004) propose the following expression for the effective diffusivity:

$$K_{eff} = F_t \frac{\overline{h_p^3}}{12\overline{h_p\tau_p}}(1-c), \quad c = \frac{96}{\pi^4\overline{h_p^3}} \sum_{n=0}^{\infty} \frac{\overline{h_p^3 \exp(-(2n+1)^2\delta_p)}}{(2n+1)^4} \tag{5.34}$$

where F_t is the so-called turbulent fraction, h_p is the depth of turbulent patch p, τ_p its lifetime, $\overline{(...)}$ is the ensemble average and $\delta_p = \frac{\pi^2 K_p \tau_p}{h_p^2}$ quantifies the intensity of mixing within the patches, with K_p the turbulent diffusivity within the patch. The parameter c is bounded ($0 \leq c \leq 1$) and quantifies the impact of small-scale mixing within the patches, $c = 0$ ($\delta_p \to \infty$) corresponding to perfect mixing while if $c = 1$ ($\delta_p = 0$) there is virtually no mixing. In the imperfect mixing limit ($\delta_p \ll 1$), *Vanneste* (2004) has shown that this expression can be simplified in :

$$K_{eff} = F_t \frac{\overline{h_p K_p \tau_p}}{\overline{h_p \tau_p}} \tag{5.35}$$

In that case, one recovers $K_{eff} = \overline{K}$, i.e. the ensemble average of the turbulent diffusivity (computed, e.g., from equation 5.33) is also the effective diffusivity seen by mean tracer transport. It can be noted that both equations 5.34 and 5.35 emphasize the prominent contribution of the deepest patches to the resulting effective diffusivity K_{eff}, which suggests that the vertical resolution of ATTREX observations is sufficient for vertical mixing estimates.

Equation 5.34 suggests that an upper bound on effective diffusivity may be written as $K_{eff}^{full} = F_t \frac{\overline{h_p^3}}{12\overline{h_p}\overline{\tau_p}}$. It is independant of turbulence strength within the patches, and corresponds to the fully mixed regime (as used by *Dewan*, 1981). Using the layer depth distribution derived in the previous subsection, and assuming a typical layer lifetime τ_p of 1 hour, as suggested by numerical simulations of turbulence (*Fritts et al.*, 2009b) and radar observations (*Wilson et al.*, 2005), we find $K_{eff}^{full} \simeq 0.32\ \mathrm{m^2\,s^{-1}}$. The estimated value of $K_{eff} \simeq 0.06\ \mathrm{m^2\,s^{-1}}$ is a factor of 5 lower than the full mixing estimate, so that the assumption of perfect tracer mixing within turbulent layers is probably not suitable for the TTL. The ensemble average estimate $\overline{K} \simeq 0.09\ \mathrm{m^2\,s^{-1}}$ still overestimates K_{eff}, but by no more than 50% (we note, however, that this will depend on the assumed lifetime τ_p). We therefore regard $\bar{K}$ as a reasonable practical approximation to K_{eff} since the resolution of aircraft observations gives access to the deepest, most active layers. Furthermore, the observations show that tracer variance is enhanced within turbulent patches, arguing against complete mixing (not shown). Finally, this estimate is natural and has practical advantages: it can be computed with better sampling since all data can be used, it is not restricted to aircraft descents nor does it require assumptions on the patch lifetime and turbulence structure. We therefore use this mean diffusivity in the following, and work in the imperfect mixing limit of *Vanneste* (2004).

5.3.8.3 Turbulent diffusivity in the tropical tropopause layer and comparison with ERA interim reanalysis and other observations

Figure 5.17 shows the average profile of turbulent diffusivity inferred from all ATTREX flights. Values appear to decrease from the bottom to the top of the TTL, consistent with the altitude distribution of turbulent events (figure 5.8). Typical values are between 0.02 and $0.1\ \mathrm{m^2\,s^{-1}}$. For comparison purposes, we consider here the average of all vertical diffusivity measurements within a fixed layer (about 1 km deep).

Figure 5.17 exhibits a strong decrease of turbulent diffusivity with increasing altitude. We note that this is in a small part biased by the fact that both 2014 and 2013 statistics are merged in this figure, and that 2014 was both more turbulent and had more flight segments in the lower TTL so that the increase at the lowest levels is mainly a 2014 feature (see also figure 5.8). However, this increase is also seen in the Eastern Pacific (though less strongly) because the computation of turbulent diffusivity involves the inverse of the stability (Equation 5.33), which decreases rapidly with altitude in both the Eastern and Western Pacific TTL.

In figure 5.17, the estimated vertical profile is compared with the turbulent diffusion from the ECMWF ERA-interim reanalysis (*ECMWF*, 2009) interpolated along the flight tracks. While the strong decrease of diffusivity with altitude is a common feature of the observations and the analysis, the discrepancy in magnitude is as much as a factor of 3. We emphasize that our estimate might be biased due to the *ad hoc* parameter γ; however, the observations of *Dole et al.* (2001) suggest that we overestimate it rather than underestimate it. The

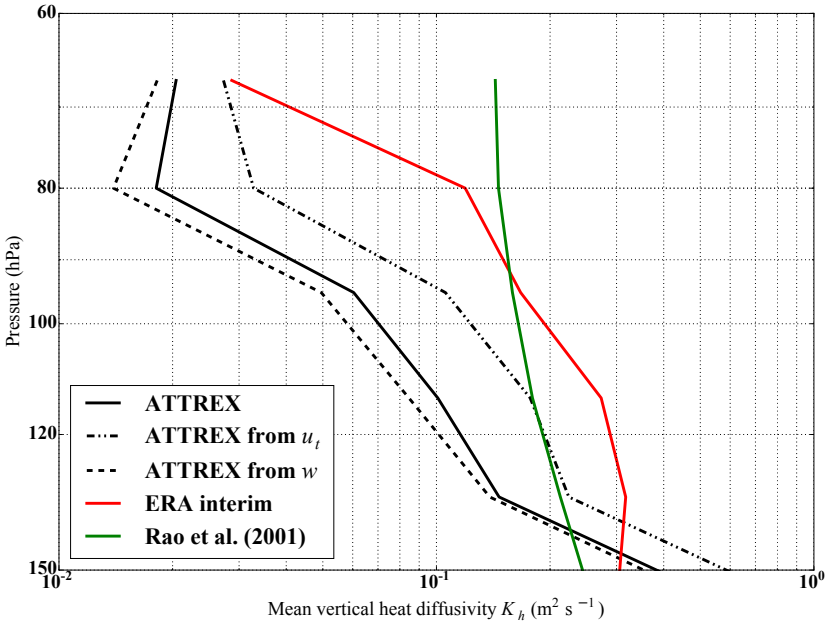

Figure 5.17 – Vertical profile of eddy diffusivity inferred from ATTREX observations using $K_h = \frac{1}{3}\left(\frac{\epsilon_k}{N^2}\right)$ and from the ERA interim along the aircraft trajectory. The ERA interim profile is not significantly different from the mean profile over the tropical Pacific, showing the reasonable sampling obtained with the aircraft.

amplitude of this discrepancy is then a major concern. Still, it should be noted that order of magnitude differences in the average vertical diffusivity are commonly observed between models. For instance, in the General Circulation Model CAM, *Bardeen et al.* (2013) showed that the change of the PBL scheme (which is applied over the whole atmosphere for the parameterization of turbulent processes) between CAM 4 and CAM 5 resulted in a more than two orders of magnitude change in the vertical diffusivity. This caused major issues for the water vapor budget of the tropical UTLS and the diffusivity had to be artificially reduced to avoid an unrealistically wet lower stratosphere. Thus, it may not be possible to attribute with certainty the discrepancy of our estimate with ERA-interim either to model or observations deficiencies. However, we note that, using a completely different approach based on the water vapor tape recorder signal in the lower stratosphere, *Glanville and Birner* (2016) also suggested an overestimated vertical diffusivity in ERA interim analyses, with a tape recorder water vapor signal ascending faster and being attenuated more rapidly than in satellite observations.

Comparing with other observational estimates, we note that ATTREX values are also generally below typical estimates from Radar observations over Japan or India. Using MU-Radar measurements, *Fukao et al.* (1994) over Japan and *Rao et al.* (2001) over Gadanki (India) report median vertical diffusivity values of the order of respectively $10^{-1} - 10^{0}$ and $10^{-1} - 3.10^{-1} \mathrm{m^2\,s^{-1}}$ in our altitude range. The typical median data reported by *Rao et al.* (2001) for the year 1995-1996 are also represented on figure 5.17, showing that they exceed our estimates by a factor of 6 at the upper levels while being in closer agreement at lower levels. The values reported by *Rao et al.* (2001) do not exhibit as strong an altitude dependence. While the fact that those authors represent the median (rather than the mean) value of their estimated K_h might bias the comparison, this is clearly not sufficient to explain the

discrepancy, which is a factor of 5-6 in the upper TTL. *Rao et al.* (2001) emphasized more active turbulence during the Monsoon period (a factor of 2 or more) and diffusivity a factor 2 smaller in the ENSO year 1998, so that part of the observed difference might rather come from this seasonal, interannual and geographical variability. Generally, our values are well below those reported by *Fukao et al.* (1994), but closer and compatible with those reported by *Rao et al.* (2001).

Alappattu and Kunhikrishnan (2010) estimated vertical diffusivity from high-resolution radiosonde observations over the Bay of Bengal and the Arabian Sea, and also found a decrease of about one order of magnitude from the bottom to the top of the TTL. However, they obtained values about one order of magnitude higher than those estimated from ATTREX (a few 10^{-1} to about 10^{1} $\mathrm{m^2\,s^{-1}}$). Using similar observations, *Sunilkumar et al.* (2015) evaluated vertical diffusivity over Gadanki and Trivarandum, India, and found values about two orders of magnitude higher than those found in our study (10^{0} to 10^{1} $\mathrm{m^2\,s^{-1}}$). The decrease of K_h by one order of magnitude from the bottom to the top of the TTL is also found in their study, but there is no agreement on the magnitude. The different regions and period are probably insufficient to explain the discrepancy of ATTREX values with those studies. However, *Sunilkumar et al.* (2015) noted that the values obtained in their study were much higher than obtained in other works, which might come from the uncertainties in some poorly known coefficients used in estimating K_h from radiosondes.

5.3.8.4 Impact on some TTL tracers: O_3, CO, H_2O

The impact of small-scale turbulent diffusivity on vertical tracer transport in the TTL and lower stratosphere can be compared with the impact of the mean vertical transport by tropical upwelling. It should be noted, however, that small-scale turbulent diffusivity is also important in controlling the exchange with the extratropics, by diluting the large-scale extratropical intrusions that arise due to breaking Rossby waves. For the purpose of comparing turbulent diffusivity with vertical advection by tropical upwelling, we derive an equivalent vertical speed for different tracers. The vertical flux of the tracer χ is

$$\overline{w'\chi'} = -K_h \frac{\partial \overline{\chi}}{\partial z} = \overline{w}_{\chi_{eq}} \overline{\chi} \quad . \tag{5.36}$$

The equivalent vertical speed is $\overline{w}_{\chi_{eq}} = -K_h \dfrac{\dfrac{\partial \overline{\chi}}{\partial z}}{\overline{\chi}} = \dfrac{K_h}{D_\chi}$ where

$$D_\chi(z) = -\frac{1}{\dfrac{\mathrm{d}\ln(\bar{\chi})}{\mathrm{d}z}}$$

is the length of exponential decay (increase) with altitude z of the tracer mixing ratio.

The exponential lengths $D_\chi(z)$ are estimated from multi-year tropical mean profiles derived from the Aura Microwave Limb Sounder, published in *Randel et al.* (2007) for O_3 and CO and *Fueglistaler et al.* (2009) for H_2O. They are given in table 5.2, together with the typical equivalent vertical speed in the upper and lower TTL obtained from our estimate of turbulent diffusivity. In the upper TTL and lower stratosphere, the equivalent vertical speed associated with turbulent diffusivity is generally one order of magnitude lower than

Table 5.2 – Exponential length D_χ and equivalent vertical speed $w_{\chi_{eq}}$ induced by vertical eddy-mixing, in the upper TTL (near 80-90 hPa) and in the lower TTL (near 150 hPa). Those should be compared to the dynamical upwelling speed, which is about 2.10^{-4} m/s at 80 hPa.

	tracer	O_3	CO	H_2O
upper TTL	D_χ (km)	-1.25	3.4	3.8
	$w_{\chi_{eq}}$ (10^{-4} m/s)	-0.16	0.06	0.05
lower TTL	D_χ (km)	-10.	15.	1.1
	$w_{\chi_{eq}}$ (10^{-4} m/s)	-0.40	0.27	3.6

the mean upwelling speed (typically $2{\cdot}10^{-4}$ m/s in the upper TTL). This agrees with previous studies that showed that for those tracers the variability was dominated by the variability in mean tropical upwelling (e.g. *Randel et al.*, 2007; *Abalos et al.*, 2013). Ozone is the examined constituent for which the estimated $\overline{w}_{\chi_{eq}}$ is the strongest in the upper TTL, but it is less than 10% of the annual mean upwelling (which is itself lower than the winter value when the annual cycle peaks). In the lower TTL, the equivalent speeds are higher due to higher diffusion, especially for species with strong vertical gradients such as water vapor; however at these altitudes, direct convective injection, mixing between convective overshoots and their environment, and higher mean upwelling (*Randel et al.*, 2008) probably dominate the vertical transport. The impact of vertical diffusion on vertical transport may be larger for other short lived tropospheric species who have stronger gradients in the lower TTL. However, these calculations suggest that the major role of turbulent diffusion is probably not as much in its impact on vertical transport as in the mixing impact, such as the dilution of the tape recorder signal in water vapor or in the mixing of intrusions from the midlatitudes.

5.3.9 Summary and conclusions

This paper characterized the occurrence of small-scale (40-200 m) wind and temperature fluctuations in the tropical tropopause layer over the tropical Pacific from aircraft observations. The fluctuations are found more frequently at the bottom of the TTL and in the Western Pacific. They are correlated with shear and low static stability, as quantified by the gradient Richardson number. Since they modify the background wind shear and stability, both inertia-gravity and small-scale gravity waves play a role in turbulence occurrence, as illustrated in a case study. Furthermore, closeness to deep convective clouds, which might generate convective gravity waves, was found to be favorable for the occurrence of turbulence.

The small-scale fluctuations appear consistent with 'inertial range' turbulence *à la Kolmogorov*. They typically exhibit a $-\frac{5}{3}$ spectrum for the winds, and show approximate isotropy between horizontal and vertical directions. An important property of turbulence in the tropical UTLS is its intermittency: a few rare bursts dominate the variance at small scales, as quantified by the typical value of the Gini coefficient (0.95). Strong turbulence is confined within patches of a few tens to hundreds of meters vertically, a few tens of kilometers horizontally.

Using the approach of *Lilly et al.* (1974), we used the measured eddy dissipation rate to estimate the diffusivity K_h induced by those turbulent encounters. The average value of K_h

in the TTL is typically of the order of 0.1 $m^2.s^{-1}$, but shows a strong gradient (one order of magnitude) from the bottom (a few 0.1 $m^2\,s^{-1}$) to the top of the TTL (a few 0.01 $m^2\,s^{-1}$). Interestingly, those values are compatible, within a factor of 3 to 4, with the average diffusivity parameterized in the ERA interim reanalysis. This result has important implications for numerical models. Although these models typically do not capture small-horizontal scale and fine vertical-scale waves, the formulation used could be adapted to better represent the mean effect of turbulent burst on the heat transfer. Despite the relative agreement with ERA-interim, there is a discrepancy of about an order of magnitude or more between aircraft observations and previous estimates from Radar or radiosonde observations, which might come from geographic and seasonal differences, but probably also from some poorly constrained coefficients in K_h estimates.

The observed turbulent diffusion might have a significant impact on vertical tracer transport, depending on the vertical profile of the specie considered, but its effect is generally lower than the mean tropical upwelling. In the lower TTL, turbulent diffusion may be of secondary importance when compared to convective detrainment, although some modeling studies suggest that it might control the vertical transport of tracers up to the level of zero radiative heating (LZRH) (*Konopka et al.*, 2007). Furthermore, in both the lower stratosphere and the TTL, turbulent diffusion ultimately controls dilution and mixing with the extra-tropics. Turbulent diffusion might also prove important to simulating cloud properties; the dilution of newly nucleated ice particles after nucleation contributes to modifying cirrus volume and extent, which, in turn impacts their dehydration efficiency and greenhouse effect. Given the importance of TTL turbulence and the uncertainty of its parameterization in models, further observations are required to assess its magnitude and its seasonal and geographic dependency.

The statistics on turbulence in the TTL presented in this paper will be of use for modelers. They can serve to assess the diffusion schemes used in global climate, which is crucial for an accurate representation of the heat and tracer budgets. Such statistics will also prove useful for Lagrangian models; they provide a way to assess the importance of the parameterized diffusion process, which controls tracer mixing.

5.4 Specific discussion: "mixed layers" in the TTL

We provide below some further discussion on one point mentioned in the article: the quasi adiabatic layer seen in the case study and its relationship with tracers.

The quasi-adiabatic layer presented in the case study (subsection 3 of the article) bears special "historical" interest regarding the study of mixing and turbulence in the TTL. Indeed, the quasi-constant θ profile closely resembles the "well mixed layers" from which *Danielsen* (1993) argued about the hydration potential of deep convection (see Chapter 1 and Figure 5.18). Such layers have been repeatedly described in radiosonde measurements of water vapor and ozone (e.g. *Vömel et al.*, 1995; *Teitelbaum et al.*, 1999; *Moustaoui et al.*, 2004). Observed mainly over the Western Pacific, and not the Eastern Pacific, these layers have been associated with deep convection. More precisely, they were attributed to turbulent mixing generated by the breaking of gravity waves near their critical levels. Equatorial Kelvin waves can also generate that type of structure, as noticed by *Fujiwara et al.* (2001) and shown in Figure 5.19.

The quasi-adiabatic layer discussed above is in many aspects similar to the "well mixed

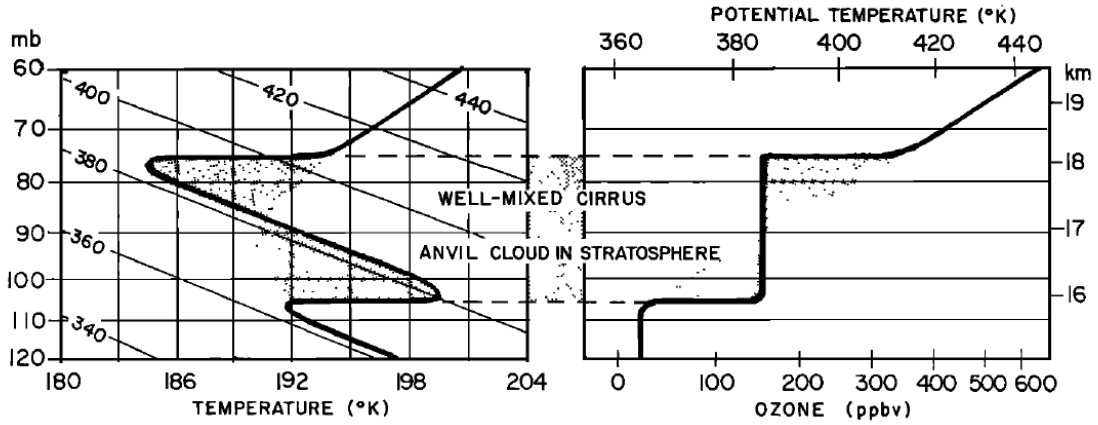

Figure 5.18 – Schematic of altitude-potential temperature-ozone profiles showing "well mixed cirrus layers" observed during STEP (Stratosphere Troposphere Exchange Processes) (*Danielsen*, 1993).

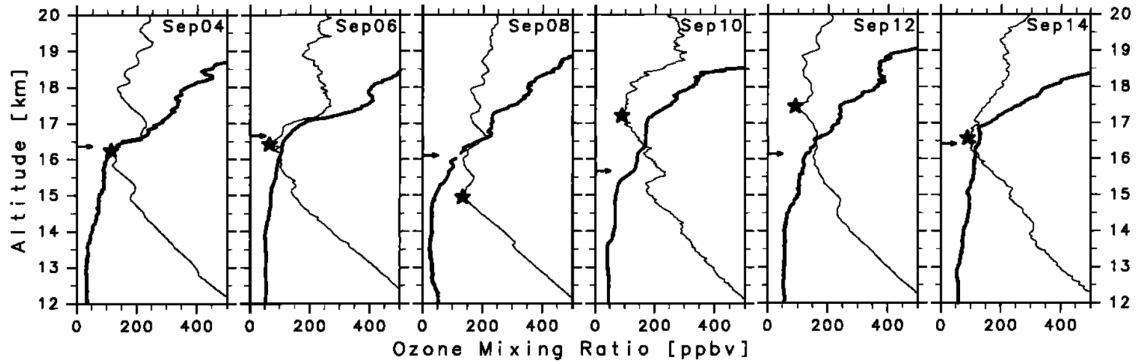

Figure 5.19 – Altitude profiles of temperature (thin line) and ozone (thick line), showing "mixed layers" associated with equatorial Kelvin waves, observed above Galapagos islands. From *Fujiwara et al.* (2001).

layers" of those previous works. Besides (dry) potential temperature, Figure 5.20 shows the profiles of several tracers including water vapor and ozone. On those, it can clearly be spotted that the "quasi-adiabatic layer" is also characterized by nearly constant water vapor and ozone. With tracer observations only, it is however difficult to distinguish a "well mixed layer" due to irreversible turbulent mixing from reversible wave-induced vertical displacement. Indeed, just by virtue of the reversible wave displacement, the layers where the isentrope surfaces are apart from one another $\left(\text{low } \frac{\partial\theta}{\partial z}\right)$ is also the layer where the isopleths are apart $\left(\text{low } \frac{\partial\chi}{\partial z}\right)$. The wave displacement alone enhances gradients in certain layers and diminishes them in others; the effect is then similar to turbulent mixing which suppresses vertical gradients in the mixed layer only to increase them at the layer boundaries.

Between the two possibilities (mixing or reversible wave motions), previous studies have favored the turbulent mixing interpretation and discussed the triggering of turbulence due to the breaking of the wave. With our coincident turbulence measurement, we can provide insights on this problem. The colors in Figure 5.20 correspond to the estimated eddy dissipation rates at the same point as the tracer and temperature measurements. Only the lower part of the quasi-adiabatic layer shows enhanced turbulence, whereas the upper part

of the profile is rather quiet. It is possible that the upper part was previously mixed by active turbulence that has stopped since. However, since the wave alone is able to create the observed features and since no turbulence is detected in the upper part of the profile, it seems reasonable to assume that most of the observed structure just results from reversible wave motions. Nevertheless, ATTREX observations do show that turbulence is induced in the lower part of the profiles, where it contributes to irreversible mixing.

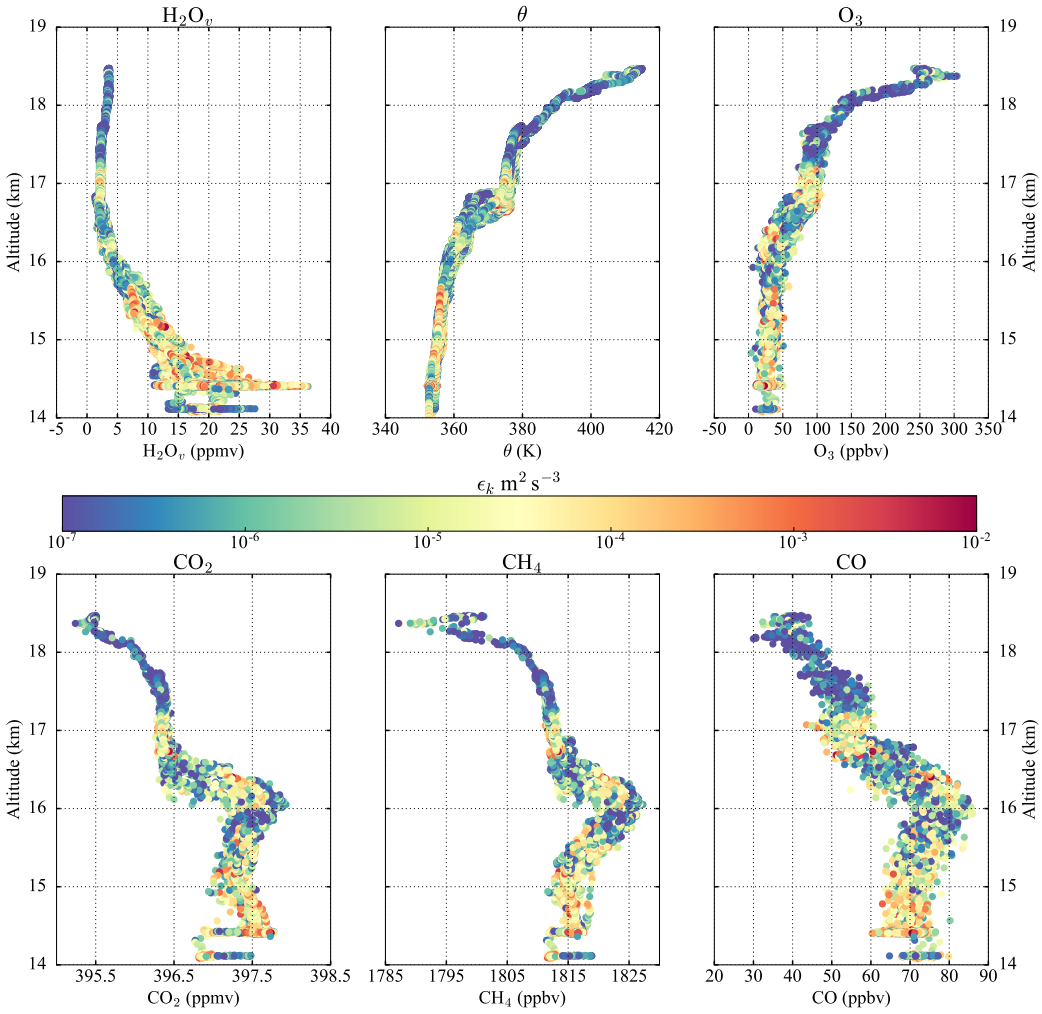

Figure 5.20 – Profiles of potential temperature θ and tracers from a Global Hawk flight near Guam (13°N 146°E) on February 16 2014. The colors correspond to the value of the estimated eddy dissipation rate ϵ_k. The quasi adiabatic layer can be noticed from about 16.9 to 17.7 km, and is characterized low vertical gradients for the different tracers, but only its lower part is turbulent and has high ϵ_k. On this figure, one can also note that lower in the profiles, a maximum concentration of tropospheric tracers (CO, CO_2 and CH_4) seems indicative of boundary layer air detrained from convection. That air mass might have traveled significant horizontal distances, being transported horizontally by the wave horizontal wind field (*Kim and Alexander*, 2014).

5.5 Conclusions and outlook

The above study was the first to provide a survey of turbulence in the Tropical Tropopause Layer over wide regions of the tropical Pacific. Although limited to a specific time period, it brings essential constraints for the parameterization of turbulence in global models. In particular, the diffusivity values obtained, of the order of $0.1\,m^2\,s^{-1}$, will be a useful information for modelers. Future studies should benefit from recent campaigns to extend the dataset to other latitudes, and to other regions of the tropics. For instance, a more precise evaluation of turbulence intensity in the vicinity of and above convective clouds will help constrain the overall impact of turbulent mixing on transport.

Given the discrepancies between our work and previous literature, it appears essential to compare the diffusivity estimates obtained using different measurements and methods. In particular, a direct comparison between estimates from aircraft wind measurements and from radiosonde temperature measurements using the Thorpe method is needed to better characterize the uncertainties. Indirect methods based on observed tracer gradients and diffusive backward trajectory calculations (e.g. *Legras et al.*, 2005) also provide an integrated view of the impact of turbulent diffusivity. They can serve as a benchmark to evaluate diffusivity estimates from turbulence measurements.

Finally, an interesting perspective of this work is to evaluate and improve the statistical representation of turbulent mixing in atmospheric models. Turbulence impact in the free troposphere is generally computed with the same scheme as in the planetary boundary layer (PBL). However, the relative importance of different mechanisms driving turbulence, such as gravity waves, varies between the PBL and the free atmosphere. Hence, the current approach might create biases in the transport of chemical species. Furthermore, gravity wave parameterizations in the free atmosphere are essentially designed to account for momentum transfer when breaking, but pay less attention to tracer transport. Hence, it is critical to evaluate the intensity of turbulent diffusion in models versus observations, in order to improve the representation of UTLS chemical and microphysical processes. Our results and comparison with ERA-interim parameterization are a first step in that direction.

Chapter 6

Conclusions and outlook

The main purpose of this thesis is to contribute to a better knowledge of mesoscale and small-scale dynamics at the tropical tropopause and to a better understanding of its impact on the microphysics of cold cirrus clouds. The work is based on the analysis of in situ observations, theoretical modeling and numerical modeling (WRF model). In the following, we recall the main results and propose some perspectives.

Temperature and vertical wind fluctuations in the Tropical Tropopause Layer

The first chapter of the thesis was dedicated to the quantification and characterization of temperature fluctuations in the TTL. One of the issues was the distribution of the fluctuations' variance as a function of intrinsic frequency $\hat{\omega}$. For periods between 1 day and 20 minutes, the temperature fluctuations have a $\hat{\omega}^{-2}$ spectral shape. The variability of temperature is dominated by the "low frequencies". On the contrary, vertical velocity fluctuations are mainly induced by high frequency waves: their power spectrum is similar to that of a white noise ($\hat{\omega}^0$), at least up to the Brunt-Väisälä frequency N. At very high frequencies near the buoyancy frequency N, superpressure balloons furthermore suggest an enhancement in vertical wind variability.

Low frequency fluctuations (period 1 day) responsible for the temperature variability seem nearly ubiquitous in the TTL, and correspondingly the distribution of temperature perturbations is nearly Gaussian. The amplitude of the associated waves does not seem significantly larger near convection. On the contrary, high frequency fluctuations (period of about 30 minutes or less) responsible for vertical wind perturbations are more intermittent and are larger near convection. The PDF of vertical velocity fluctuations hence shows larger tails than that of the temperature, and is close to a Laplace distribution. Since low frequency gravity waves propagate horizontally further away from their sources than high frequency ones, the different behavior between low and high frequency waves suggests that the variability of vertical wind and temperature fluctuations in the TTL results from a combination of the propagation properties of gravity waves and of the distribution of their sources. Vertical propagation of gravity waves, rather than a cascade from low to high frequency waves, could then be responsible for the shape of the intrinsic frequency spectrum of the fluctuations.

The observations of vertical wind fluctuations were also compared to atmospheric analyses. Not unexpectedly, the magnitude of vertical winds is highly underestimated in global

weather models. Other characteristics, such as the decrease with altitude of vertical velocity variance, also depart from the observations. The fluctuations hence need to be parameterized, which can be done efficiently using a Markov process with adjustments accounting for the non Gaussianity of the fluctuations. The magnitude of the parameterized fluctuations can be matched to the observations, but might also be deduced from outputs of gravity wave parameterizations developed to represent the wave drag on the mean flow.

Even though the analysis of observations presented has largely improved our knowledge of temperature fluctuations in the TTL, uncertainties remain. This thesis pointed out the limits of our current understanding of the balloon response to atmospheric motions at high frequencies. Another (smaller) limitation was due to the fact that the balloons flew above the top of the TTL, at altitudes higher than the tropical tropopause cold point. On those two aspects, an exciting perspective is the planned future balloon campaign, called "Stratéole 2", which will consist in 45 ballons launched during one test campaign (2018-2019) and two main campaigns (2020 and 2023) and will provide extensive coverage of the TTL, with a lower altitude level of flight near 18 km near the cold point tropopasue. It will be interesting to use the methodology developed in this work to anayze the new dataset. Futhermore, one of the two planned flight levels will be in the TTL, which will allow to directly obtain Lagrangian fluctuations in the TTL. Adding measurements of the vertical wind relative to the balloon would further help with the interpretation of the variability observed at high frequencies.

Impacts of waves on cirrus microphysics

In the second chapter, taking advantage of the improved knowledge of T fluctuations gained from the balloon measurements, some impacts of atmospheric waves on microphysical processes were investigated using simplified models. Accounting for high frequency waves has a dramatic impact on homogeneous ice nucleation. Statistically, the waves appear to increase the Ice Crystal Number (ICN) after nucleation due to increased vertical wind speeds. However, in agreement with previous studies, we find that the common assumption of constant vertical velocity during nucleation does not hold. When realistic changes of vertical wind during nucleation are taken into account, the ICN nucleated through homogeneous nucleation is very sensitive to the initial water vapor content, which might create the spikes of high ICN recently observed in TTL cirrus clouds. The properties of newly nucleated clouds are highly dependent on wave-nucleation interactions. Parameterizations of homogeneous nucleation should account for that effect, and we provide analytical formulas that could serve that purpose.

A second impact of waves on microphysics is on the transport of ice by wave advection. Since ice crystals are not purely Lagrangian, but fall relative to the mean flow, interesting interactions can arise when the sedimentation speed of the crystal is close to the wave vertical phase speed. The average effect (deduced both from theoretical considerations and from aircraft observations) appears to be slowing down the sedimentation of ice crystals, which diminishes the efficiency of dehydration by TTL cirrus. This interaction may also explain the wave-cirrus relationships recently observed in aircraft data (*Kim et al.*, 2016). Low frequency ($\sim$ 1 day), small vertical wavelength ($\sim$4 km or less) waves thus have direct impact on cirrus beyond their impact on temperature. This is another interaction currently neglected in large-scale models.

On both the sedimentation and the nucleation aspects, the wave impacts on microphysics were analyzed here focusing on cirrus clouds and ice particles. Other aerosols are present in the TTL. For instance, the rate of sulfuric aerosols nucleation from H_2SO_4 and H_2O is highly sensitive to temperature and relative humidity (e.g. *Yu*, 2010) and will hence be sensitive to the temperature fluctuations described above. An interesting perspective of this work would be to examine the impact of the temperature fluctuations on aerosol nucleation. Another prospect is related to the upcoming "Stratéole 2" campaign, during which high resolution profiles of temperature, water vapor and aerosols will be obtained up to 2 km below the superpressure balloon (RACHuTS instrument). This will allow to investigate more precisely the wave-sedimentation interaction, since both stability and cloud presence will be measured. Finally, it would be interesting to implement the interactions in larger scale models, such as climate models, to investigate how they influence climate sensitivity and the climate impact of cirrus and aerosols.

Impact of equatorial waves on large-scale cirrus properties

The third chapter studied the formation and structure of a large-scale cirrus in the TTL, and used a limited area model to reproduce the cloud field observed by satellite. Although cirrus and microphysics exhibit small-scale structures and are sensitive to small-scale dynamical features, the study shows that large-scale dynamics is the main driver of TTL cirrus formation, life cycle and large-scale structure. Especially, the modeled cirrus cloud field is sensitive to the "dynamics" initial and boundary conditions, but much less to details in the water vapor field. The sensitivity to microphysical processes (Ice nuclei concentration) is partly masked by the impact of the uncertainties in the dynamics, so that remote sensing observations alone provide only limited constraint. Radiative effects have only a minor impact on the evolution of the thin cirrus cloud field, which responds more to the superposition of waves of different scales present in the simulations.

The study demonstrates that mesoscale simulations are an appropriate tool to study TTL cirrus, even with uncertainties in the initialization of the wind, temperature and water vapor fields. They provide a realistic setting to investigate the impact of microphysics and radiative assumptions on the cloud field. For that purpose, they can best be combined with in situ observations, which they will put in the local perspective of the flow. A natural extension of our study is to perform similar simulations for a case where in situ observations are available. Such a work has been started with data from the NASA AiRborne Tropical Tropopause EXperiment (ATTREX), to understand the formation of TTL cirrus surrounding deep convection. The future campaigns "Stratoclim" and "Stratéole 2" will also provide interesting datasets in which to investigate those issues.

Small-scale fluctuations and their impact on mixing

The last chapter of the dissertation was devoted to the study of turbulence in the tropical Upper Troposphere-Lower Stratosphere using in situ observations from ATTREX. Turbulent bursts were found tightly linked to convection and wave activity which modulates the background Richardson number. The turbulent diffusivity K_h was found to be of the order of $0.1\,\mathrm{m^2\,s^{-1}}$, but highly variable between the top and the bottom of the TTL (an order of magnitude). Such values largely disagree with the rare previous estimates from indirect

methods. Intercomparisons of estimates from different instruments are needed in order to better understand turbulence and its impact on mixing and transport of constituents.

In the future, the analysis method used here can be extended to other recent aircraft campaigns to increase the dataset and investigate turbulence in regions near deep convective clouds, in order to obtain a more complete statistical picture. The results will also be very useful to evaluate and improve subgrid-scale turbulence schemes in large-scale models, at moderate to high resolutions (down to Large Eddy Simulations). Finally, "Stratéole 2" will provide an interesting dataset in which to investigate turbulence and its impact on vertical mixing, with high resolution vertical temperature profiles.

Context

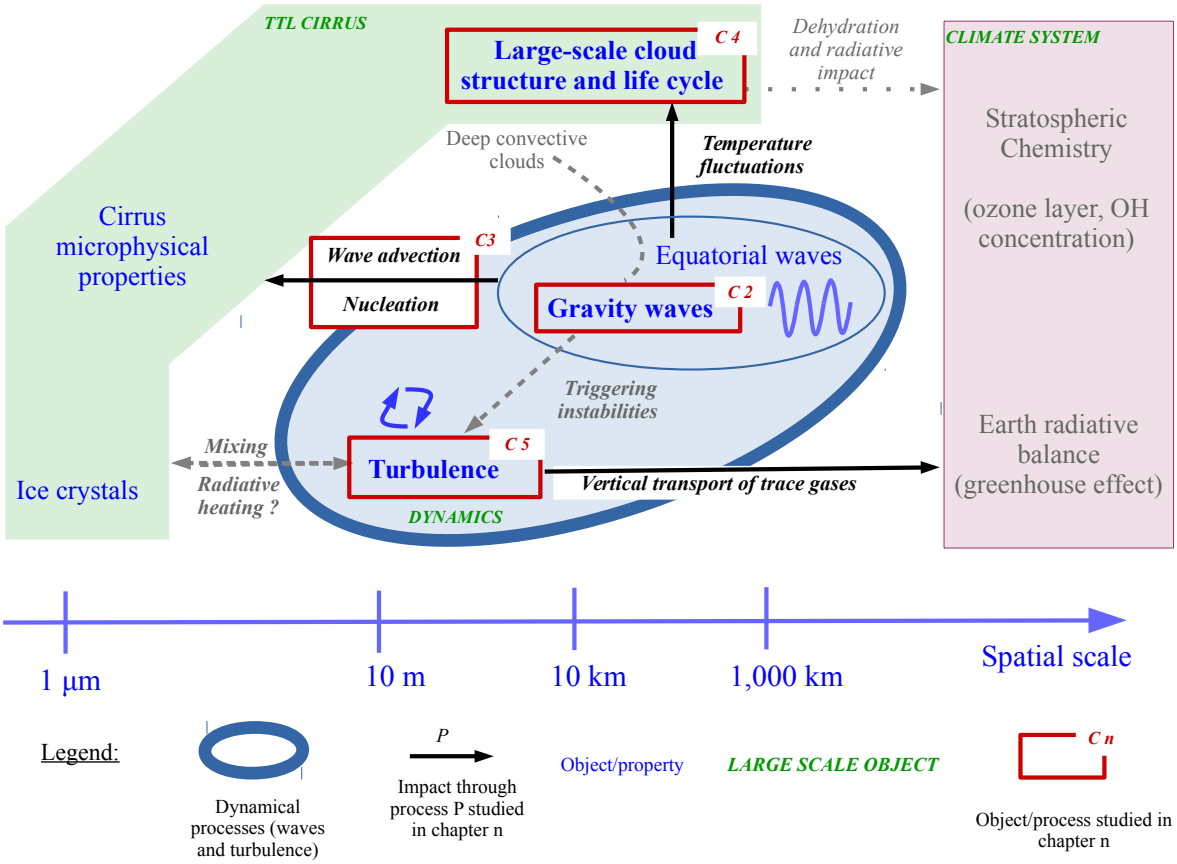

Figure 6.1 – Schematic of the objects and processes studied in this work and their spatial scale. In blue are represented microphysical or dynamical objects whereas black arrows represent the processes through which they interact. Full line arrows correspond to the processes studied in this work while gray and dashed lines are for other processes briefly mentioned or motivating the work. The red squares indicate the chapters where the processes/objects are studied.

In conclusion, Figure 6.1 summarizes the connection between the objects and processes investigated in the thesis, and their larger context and impacts on stratospheric chemistry and climate. Small-scale waves and turbulence have been characterized and quantified in unprecedented datasets, and evaluated in large-scale models. Parameterizations of the fluctuations for transport and microphysics have been discussed. Some of the impacts of realistic waves on cirrus, wave advection and impact on ice nucleation, have been investigated and de-

scribed using theoretical and realistic models. The main contributions of the thesis reside in the characterization of wave fluctuations appropriate for microphysics modeling, in the study of their impact, and in the quantification of turbulence in the TTL. Those will be useful to increase our knowledge and understanding of TTL processes and improve their representation in limited area and global models. One major motivation to study those processes is their influence on the composition of the atmosphere, and thus on stratospheric chemistry and climate.

Chapitre 7

Résumé et perspectives (en français)

Sommaire

L'objectif de cette thèse est d'améliorer notre connaissance des fluctuations dynamiques de méso et petite échelle à la tropopause tropicale (entre 14 et 18,5 km) et notre compréhension de leurs impacts sur la microphysique des cirrus. Les études présentées sont basées sur l'analyse d'observations *in situ*, sur des approches théoriques et sur de la modélisation numérique. Nous résumons dans la suite les principaux résultats et proposons des perspectives aux travaux effectués.

7.1 Fluctuations de température et de vent vertical à la tropopause tropicale

Le premier chapitre de la thèse est dédié à la quantification des fluctuations de température (proportionnelles au déplacement vertical ζ des masses d'air dans l'approximation adiabatique : $T' = -\frac{g}{C_p}\zeta$) et de vent vertical dans la couche de la tropopause tropicale (TTL), ceci afin de pouvoir contraindre leur impact sur la formation des cirrus. Une des questions posées concerne la distribution de l'amplitude des fluctuations en fonction de leur fréquence intrinsèque $\hat{\omega}$, c'est-à-dire la fréquence mesurée par un observateur suivant les masses d'air au cours de leurs déplacements. Pour répondre à cette question, nous avons utilisé les mesures de deux ballons stratosphériques longue durée, lancés par le CNES en février 2010 et qui ont volé pendant 3 mois dans la basse stratosphère équatoriale (à environ 20 km d'altitude). Ces ballons se déplacent en suivant les vents horizontaux et fournissent donc des séries temporelles de perturbations de vent et de température comparables à celles que subissent les masses d'air. On parle de séries temporelles (quasi-)lagrangiennes.

Les observations montrent que, dans une gamme de fréquences intrinsèques allant de 1 à 150 cycles par jour environ (périodes de 20 minutes à un jour), l'écart-type associé aux fluctuations de température (ou de déplacement) est de l'ordre de 1 K (ou 100 m). Le spectre des fluctuations de déplacement vertical ζ a une forme en $\hat{\omega}^{-2}$ (représenté sur la figure 7.1) : la variance des fluctuations de température et de déplacement est donc concentrée dans les « basses fréquences ». Au contraire, les vitesses verticales, dérivées temporelles du déplacement : $w = \frac{D\zeta}{Dt}$, sont principalement induites par des ondes de haute fréquence. D'amplitude typique 0.1 m/s, leur spectre de puissance se rapproche de celui d'un bruit blanc ($\hat{\omega}^0$) dans la gamme de fréquence étudiée. Aux fréquences les plus hautes, proches de la fréquence de Brunt-Väisälä, les mesures ballon suggèrent un maximum local, un pic de variance pour les fluctuations de vent vertical. Cependant, il est difficile de quantifier l'amplitude de ce maximum, à cause d'incertitudes concernant la réponse du ballon au forçage atmosphérique.

Une analyse en ondelettes des séries temporelles issues des ballons montre que les ondes de basse fréquence (1 jour) qui génèrent les fluctuations de température sont omniprésentes dans la TTL. Leur amplitude varie peu en fonction de la localisation géographique (du moins au cours des trois mois de la campagne ballon). En particulier, elles ne semblent pas particulièrement reliées à l'activité convective. En accord avec cette observation, la distribution des perturbations de température est proche d'une loi normale. Les ondes de haute fréquence induisant des perturbations de vent vertical sont, elles, plus intermittentes. Elles ont des amplitudes plus importantes près de la convection profonde. Ainsi, les fluctuations de vi-

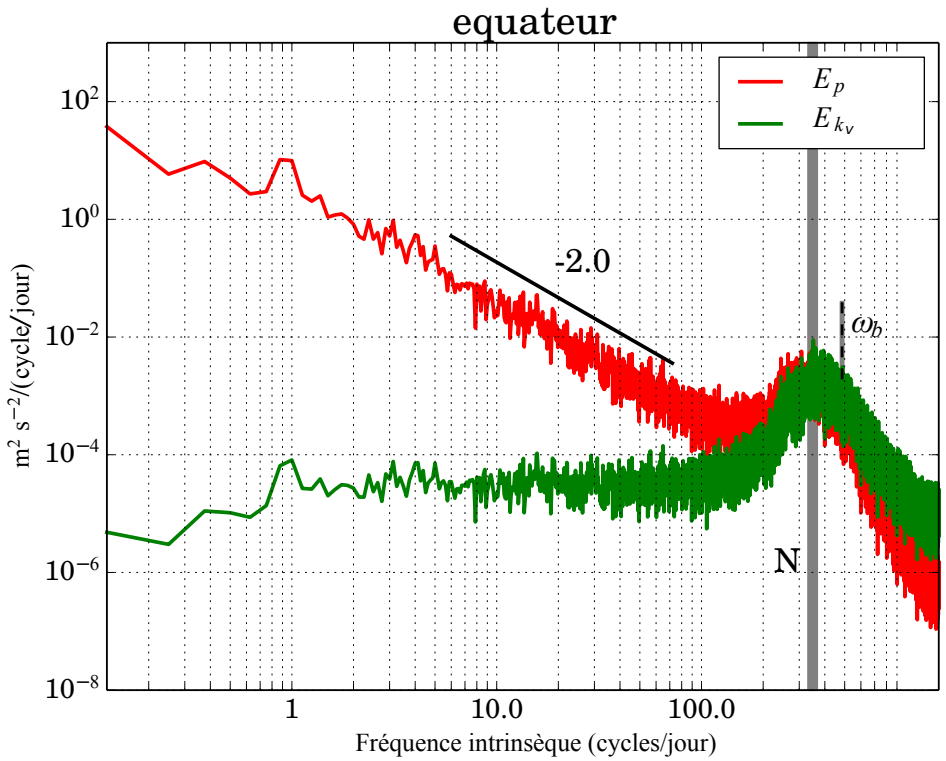

FIGURE 7.1 – Spectres d'énergie cinétique verticale E_{k_v} (reliée aux vitesses verticales, $E_{k_v} = \frac{1}{2}w^2$) et d'énergie potentielle E_p (reliée aux anomalies lagrangiennes de température ou de déplacement vertical $E_p = \frac{1}{2}N^2\zeta^2$) estimés d'après les observations ballon dans les tropiques en février-mai 2010. N est la fréquence de Brunt-Väisälä.

tesse verticale ont des queues de PDF plus larges, et sont plus proches d'une distribution de Laplace (double exponentielle). Cette observation de fluctuations plus intermittentes à plus haute fréquence est cohérente avec la théorie des ondes de gravité : les paquets d'ondes de haute fréquence se propagent sur de plus longues distances horizontales que ceux de basse fréquence, qui se propagent plus verticalement et sont localisés près de leurs sources. Ceci tend à suggérer que ce sont les propriétés de propagation des ondes depuis leur source en troposphère qui sont à l'origine du spectre de fluctuations observé (forme en $\hat{\omega}^{-2}$), plutôt qu'une cascade transférant l'énergie depuis les basses vers les hautes fréquences.

Les fluctuations de vitesse verticale observées ont été comparées à celles résolues par des modèles globaux de prévision numérique du temps, ceux du centre européen de prévisions météorologiques à moyen terme (ECMWF, leur modèle opérationnel et la réanalyse ERA-interim), de la NASA (MERRA2) et de l'agence météorologique japonaise (JRA 55). Comme on pouvait s'y attendre, les amplitudes des fluctuations présentes dans ces modèles sont très inférieures à celles observées (un facteur 5 à 10). Plus étonnant, la diminution de l'amplitude des fluctuations avec l'altitude est plus importante dans les modèles considérés que celle suggérée par les observations de la campagne ATTREX. Les fluctuations doivent donc être paramétrées ; une procédure simple et efficace permettant de reproduire les propriétés observées des fluctuations de vent vertical et de température a été proposée. Il s'agit de générer un processus de Markov (bruit rouge) ajusté pour prendre en compte la non-gaussianité des fluctuations. L'amplitude des fluctuations peut être choisie pour correspondre aux observations

au niveau de vol du ballon. Cette paramétrisation peut être facilement étendue à d'autres altitudes via des hypothèses sur l'évolution de l'amplitude avec l'altitude, par exemple en supposant une propagation conservative des ondes. On pourrait aussi s'appuyer sur les paramétrisations développées pour représenter l'effet des ondes de gravité sur l'écoulement moyen, qui prennent en compte l'effet des processus non conservatifs (saturation et déferlement) sur l'amplitude des ondes.

Les analyses d'observations effectuées lors de la thèse ont permis d'améliorer grandement notre connaissance des fluctuations de température et de vent vertical dans la TTL. Cependant, différents points restent à éclaircir. Une incertitude importante dans notre analyse est due à la méconnaissance de la réponse du ballon au forçage atmosphérique à haute fréquence. Une autre limite du jeu de données employé vient du fait que les observations ont été effectuées juste au-dessus du sommet de la TTL, à des altitudes plus élevées que celle du point froid. Sur ces deux aspects, la future campagne ballon « Stratéole 2 » offre des perspectives intéressantes : deux niveaux de vol seront déployés, le plus bas situé à 18 km, proche du point froid de la tropopause (CPT). Répéter l'analyse développée dans la thèse sur ces observations permettra d'étendre nos connaissances sur les fluctuations lagrangiennes de température à d'autres altitudes et de vérifier les prédictions théoriques, d'augmenter l'échantillonage pour mieux caractériser l'intermittence, et éventuellement d'en étudier la variabilité interannuelle. Afin de réduire les incertitudes associées à la réponse du ballon à haute fréquence, il serait souhaitable d'ajouter des mesures de vent vertical relatif au ballon.

7.2 Impacts des ondes sur la microphysique des cirrus

Dans le second chapitre de la thèse, deux impacts des fluctuations de température ont été examinés à l'aide d'approches théoriques et d'un modèle numérique de microphysique de la glace. La prise en compte d'ondes de gravité de haute fréquence réalistes et des fluctuations de vitesse verticale associées a un impact considérable sur la nucléation homogène des cristaux de glace. En général, la présence d'ondes de haute fréquence a pour effet d'augmenter le nombre de cristaux de glace, à cause de vitesses verticales plus importantes. Néanmoins, en accord avec des études antérieures, nous avons montré que l'hypothèse communément admise d'une vitesse verticale quasi-constante au cours de la nucléation[1] pouvait mener à des résultats erronés. En effet, en incluant des variations réalistes du vent vertical, il est possible que celui-ci varie voire change de signe au cours de la nucléation, stoppant ainsi la formation des cristaux de glace et limitant leur nombre. Deux régimes de nucléation existent donc. Le premier à vitesse verticale quasi-constante, pour lequel la nucléation est limitée par la chute de la sursaturation due à la consommation de vapeur d'eau par les cristaux de glace nouvellement formés. C'est le régime traditionnellement pris en compte dans les modèles, pour lequel le nombre de cristaux de glace est surtout fonction de la vitesse verticale au moment de la nucléation. Le second régime est associé à une variation de vitesse verticale lors de la nucléation, changement qui entraîne une augmentation de température et une diminution de la sursaturation qui vient stopper la nucléation et limiter le nombre de cristaux. Dans ce

[1] On utilise ici le terme nucléation en remplacement de celui de nucléation homogène.

régime, le nombre de cristaux est moins dépendant des vitesses verticales. Par contre, il est très sensible au contenu initial en vapeur d'eau. On propose que cette extrême sensibité à la quantité initiale de vapeur d'eau soit la cause des fortes hétérogénéités de la concentration en cristaux de glace observées dans certains cirrus tropicaux. Ce travail montre que les propriétés microphysiques des nuages de glace nouvellement formés sont très dépendantes des interactions entre ondes de gravité et nucléation. Pour davantage de réalisme, les paramétrisations de la nucléation homogène devraient prendre ce processus en compte. Nous établissons des relations analytiques permettant de prédire le nombre de cristaux nucléés qui pourraient servir à cet effet.

Un autre impact des ondes sur la microphysique exploré dans la thèse est celui du transport de glace. À notre connaissance, cet effet n'a pas été étudié auparavant. Comme les cristaux de glace ne sont pas purement lagrangiens mais sédimentent par rapport à l'écoulement, les anomalies de vent induites par l'onde peuvent avoir un impact moyen (qui ne s'annule pas au bout d'une période). Cet effet est d'autant plus important que la vitesse de sédimentation des cristaux est proche de la vitesse de phase verticale de l'onde. Les cristaux peuvent alors rester « bloqués » dans une phase particulière de l'onde, et subissent une anomalie de vent constante. L'impact moyen, déduit à partir d'une analyse théorique du problème comme des observations ATTREX, est de ralentir le flux de sédimentation des cristaux de glace, ce qui diminue l'efficacité de la déshydratation par les cirrus. Par ailleurs, notre étude propose une explication aux observations récentes de relations ondes-cirrus : *Kim et al.* (2016) ont observé que les nuages se rencontraient préférentiellement dans les phases des ondes pour lesquelles l'anomalie de température était négative $T' < 0$ (Pacifique Est), mais aussi dans les phases pour lesquelles l'anomalie de gradient vertical de température était négative : $\frac{\partial T'}{\partial z} < 0$ (Pacifique ouest). Notre étude suggère que cela soit dû à l'effet des anomalies de température et de vent se propageant verticalement sur la croissance et la chute des cristaux de glace. Du fait de ces processus, les cristaux ont tendance à se regrouper dans certaines phases spécifiques de l'onde, en fonction de l'humidité relative moyenne : ce sont les phases d'anomalie de température négative en environnement sec ou les phases d'anomalie de gradient vertical de température négatif en environnement plus humide. Ainsi, les ondes équatoriales de basse fréquence (périodes de $\sim$ 1 jour ou plus), de petite longueurs d'onde verticales ($\sim$4 km ou moins), ont un impact sur les processus microphysiques qui va au-delà de leur impact sur la température. Il s'agit ici d'une autre interaction ondes-cirrus absente des modèles de grande échelle, qui souvent ne représentent pas les ondes équatoriales de fine échelle près de la tropopause tropicale à cause d'une résolution verticale insuffisante.

Sur ces aspects de nucléation et de sédimentation-transport, nos études se sont focalisées sur les particules de glace constituant les cirrus. D'autres aérosols, de différentes natures, sont présents dans la TTL, et sont probablement affectés par les ondes. Par exemple, le taux de nucléation des aérosols sulfatés à partir de H_2SO_4 et H_2O en phase gazeuse est très sensible à la température et à l'humidité relative (e.g. *Yu*, 2010) ; les fluctuations rapides de température ont donc très certainement un impact sur ce processus, qu'il serait intéressant d'étudier. Une autre perspective de ce travail est à nouveau associée à la campagne ballon « Stratéole 2 », au cours de laquelle des profils de température, de vapeur d'eau et d'aérosols

seront mesurés jusque 2 km sous certains ballons longue durée (instrument RACHuTS). Cela permettra d'analyser l'interaction entre ondes et sédimentation dans un cadre quasi-Lagrangien, puisque à la fois la température, son gradient vertical et la présence de nuages seront mesurés. Enfin, une dernière perspective serait d'implémenter ce type d'interactions dans un modèle à plus grande échelle voire dans la partie atmosphérique d'un modèle de climat, afin d'évaluer comment ces processus influent sur la chimie et la sensibilité climatique et d'étudier leurs impacts sur l'effet indirect des aérosols anthropiques sur les nuages de glace.

7.3 Modélisation d'un cirrus de grande échelle

Le troisième chapitre de la thèse s'intéresse à comprendre la formation et l'évolution d'un cirrus de grande échelle observé dans le Pacifique est. Pour ce faire, un modèle météorologique à méso-échelle, à aire limitée (le modèle WRF), a été utilisé afin de reproduire les observations nuageuses par satellite effectuées par l'instrument CALIOP. Bien que les cirrus présentent des structures de petite échelle et que leurs propriétés microphysiques soient sensibles aux ondes de gravité, l'étude montre que ce sont avant tout des ondes équatoriales de grande échelle qui contrôlent la formation, la durée de vie et les propriétés de grande échelle (500 km) du cirrus étudié. En particulier, les simulations sont sensibles aux conditions initiales en vent et température dues aux ondes, bien plus qu'aux détails du champ initial de vapeur d'eau. La sensibilité du champ nuageux à la représentation des processus microphysiques est masquée en partie par ces incertitudes sur la dynamique, de telle sorte que les observations par télédétection à elles seules ne sont pas suffisantes pour contraindre la représentation des processus microphysiques. Pour ce cas d'étude, les simulations montrent également que le chauffage radiatif dans le champ de nuages fins, bien que relativement important (quelques K/jour), reste trop faible pour avoir un impact majeur sur l'évolution du cirrus ; celle-ci répond davantage au champ d'ondes de différentes échelles présentes dans la simulation.

Bien que la modélisation à méso-échelle d'un cas d'étude réaliste soit associée à des incertitudes importantes concernant l'initialisation en vent, en température et en vapeur d'eau, ce travail montre qu'elle constitue un outil approprié et intéressant pour l'étude des cirrus dans la TTL. Les simulations fournissent un contexte aux observations, indispensable à leur interprétation (par exemple concernant le temps de vie du cirrus). Elles fournissent également une représentation réaliste de l'environnement atmosphérique dans lequel évolue le cirrus et permettent donc d'évaluer l'impact réel de différents processus (radiatifs, microphysiques), et leur importance par rapport à la variabilité atmosphérique présente par ailleurs. Dans l'optique d'améliorer notre compréhension des processus, ce type de simulations présente tout son intérêt lorsqu'il est combiné à des observations in situ. Un tel travail a été commencé à partir d'un cas d'étude lors de la campagne ATTREX, afin de mieux comprendre la formation des cirrus entourant la convection profonde. La future campagne « Stratéole 2 » et la très prochaine campagne « Stratoclim », fourniront également une série de cas d'étude dans lesquels ces problématiques pourront être étudiées.

7.4 Fluctuations de petite échelle (< 100 m) et leur impact sur le mélange

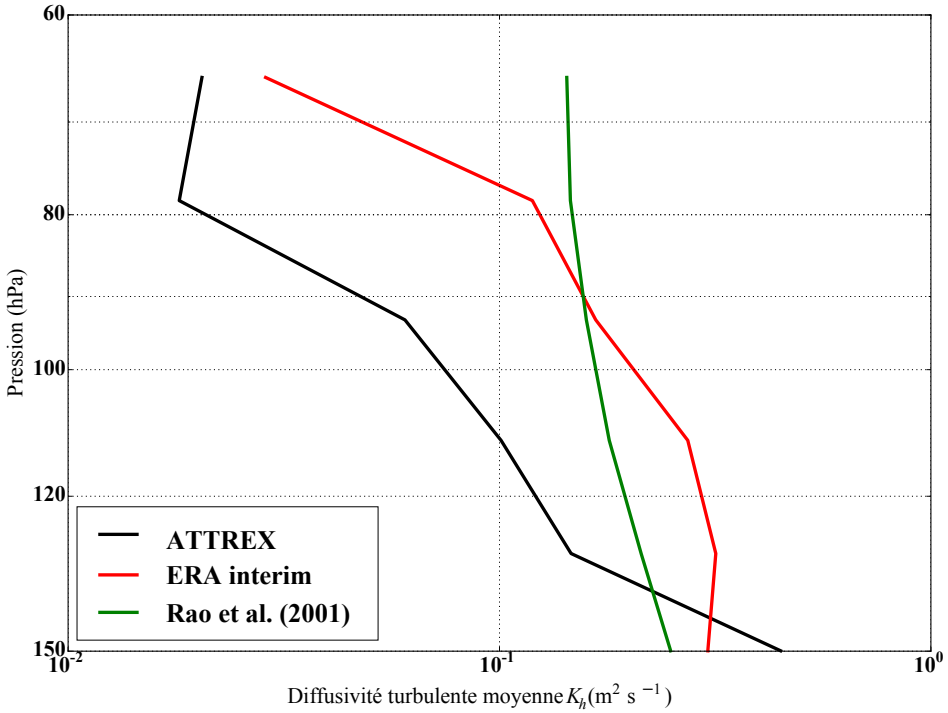

FIGURE 7.2 – Profil de diffusivité turbulence K_h estimée d'après les observations de la campagne ATTREX dans le Pacifique tropical, durant l'hiver boréal (en noir). Pour comparaison, le profil déduit par une étude précédente est illustré en vert, ainsi que le profil de diffusivité turbulente paramétré dans le modèle utilisé pour la réanalyse ERA interim (en rouge).

Le dernier chapitre de la thèse est consacré à l'étude de la turbulence de « petite échelle » dans la haute troposphère-basse stratosphère tropicale, à partir des observations avion de la campagne ATTREX au-dessus du Pacifique. On a montré que les poches de turbulence présentes dans la TTL étaient fortement liées à la convection profonde et aux ondes, qui modulent le nombre de Richardson. Ces poches turbulentes induisent du mélange et de la diffusivité turbulente K_h pour les traceurs et la chaleur. À partir des observations, K_h est évalué à environ $0.1\,\mathrm{m^2\,s^{-1}}$ mais présente un gradient vertical marqué (un ordre de grandeur de différence) entre la base de la TTL (14 km) et son sommet (18,5 km). Le profil de K_h estimé à partir des observations est présenté dans la figure 7.2. Les valeurs estimées d'après les observations ATTREX sont en désaccord avec les (rares) autres estimations disponibles, issues de méthodes plus indirectes. Une intercomparaison entre les différentes méthodes et les différents instruments semble nécessaire afin de mieux comprendre la turbulence et son impact sur le mélange et le transport de constituants dans la TTL mais aussi dans d'autres régions de l'atmosphère.

La méthodologie employée dans notre étude peut être étendue à d'autres campagnes récentes, afin d'inclure notamment des régions plus convectives. En effet, le drone Global Hawk, plateforme utilisée lors de la campagne ATTREX, n'était autorisé à voler qu'à distance de la convection profonde ; le jeu de données présenté est donc légèrement biaisé vers les régions

« peu convectives ». Une autre campagne récente, POSIDON, menée dans le Pacifique ouest à l'automne 2016, permettra de compléter cette lacune. Les résultats présentés seront utiles afin d'évaluer et d'améliorer la paramétrisation de la diffusivité turbulente dans les modèles atmosphériques globaux ou la représentation des processus turbulents dans des simulations à plus haute résolution (LES par exemple). Enfin, à nouveau, la campagne « Stratéole 2 » fournira un jeu de données intéressant pour examiner la turbulence et son impact sur le mélange vertical, à partir des profils de température à haute résolution obtenus.

7.5 Contexte

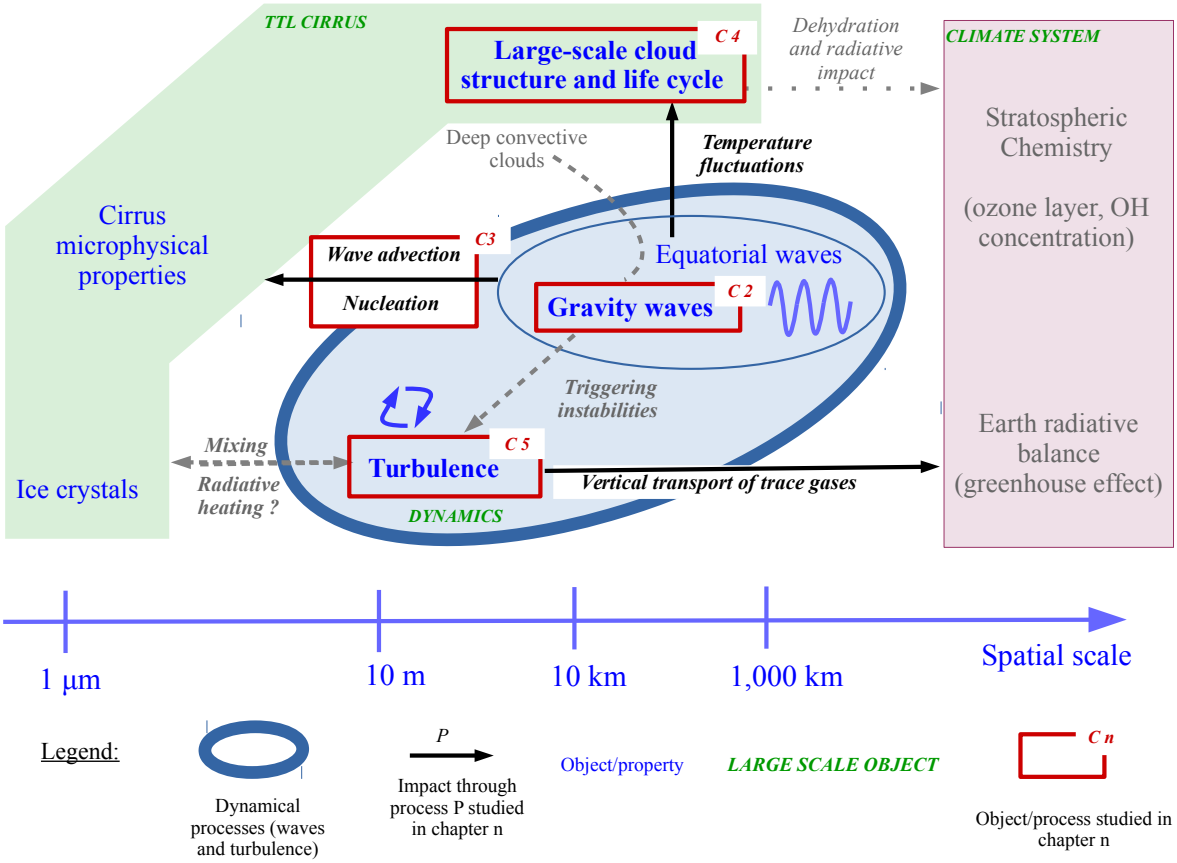

FIGURE 7.3 – Schéma des objets et processus étudiés dans ce travail de thèse, et des échelles spatiales associées. En bleu sont représentés différents objets d'étude, microphysiques ou dynamiques ; les flèches noires représentent les processus par lesquels ils interagissent. Les interactions étudiées dans cette thèse sont représentées par des flèches pleines, alors que les les flèches en pointillés correspondent à d'autres processus qui n'ont été mentionnés que brièvement ou qui motivent le travail dans un contexte plus large.

En conclusion, la figure 7.3 résume le contexte de ce travail de thèse. Elle comprend les différents objets et processus étudiés ainsi que leur place dans la TTL, le système climatique et leurs impacts sur la chimie stratosphérique et le climat. Les ondes atmosphériques et la turbulence ont été caractérisées et quantifiées dans des jeux inédits de mesures in situ, et comparées aux champs représentés et paramétrés dans les modèles atmosphériques. La para-

métrisation de ces fluctuations et de leurs impacts sur le transport et la microphysique a été discutée. Certains des impacts d'un champ d'ondes réaliste sur la microphysique des cirrus ont été examinés à l'aide de modèles théoriques et réalistes, en particulier l'impact de l'advection par le champ d'onde sur le transport des cristaux de glace et l'impact des ondes de haute fréquence sur la nucléation de ces cristaux. La contribution principale de la thèse réside d'une part dans la caractérisation, de façon appropriée pour la modélisation microphysique, des fluctuations dues aux ondes de gravité, d'autre part dans l'analyse de leurs impacts en lien avec les observations de cirrus, et enfin dans la quantification jusqu'alors inédite de la turbulence dans la TTL. Ces études ont amélioré notre connaissance de ces processus. Elles constituent une étape vers l'amélioration de leur représentation dans les modèles météorologiques à aire limitée et globaux, avec pour motivation d'établir leur rôle dans la composition de l'atmosphère et leur impact sur la chimie stratosphérique et sur le climat.

Appendices

Appendix A

Appendix to Chapter 2

A.1 Reflected waves and the polarization relations in the monochromatic case

When reflected waves are present, constructive interferences occur so that the polarization relations (e.g. equation (3) of the letter) are not valid for the superposition of waves with the same intrinsic frequency but different vertical wavenumbers. Boussinesq approximation is used here to simplify the algebra; the example is meant to be illustrative of the limits of the polarization relations encountered at high frequency and near a stratification jump.

We suppose a transition at altitude $z = 0$ between two media A below and B above, with a jump in horizontal winds ($\bar{u}_1$, $\bar{v}_1$ vs $\bar{u}_2$, $\bar{v}_2$) and stratification (N_1 vs N_2). Waves are radiated from the troposphere, so that we suppose an incident wave (subscript i) from medium A below of horizontal wavenumber k, l and frequency ω. That incident wave excites a reflected wave (r) in medium A and a transmitted one (t) in medium B.

The continuity of vertical and horizontal wind speeds at the interface between the two media (A) and (B) at altitude $z = 0$ imposes that $w_A(x, y, z, t) = w_B(x, y, z, t)$ and $\frac{\partial w_A}{\partial z}(x, y, z, t) = \frac{\partial w_B}{\partial z}(x, y, z, t)$ (from the continuity equation $\partial_x u + \partial_y v + \partial_z w = 0$ and the continuity of u and v). In particular, this imposes that $(k_i =)k = k_r = k_t$, $(l_i =)l = l_r = l_t$, $(\omega_i =)\omega = \omega_r = \omega_t$. In general, the intrinsic frequency $\hat{\omega} = \omega - k\bar{u} - l\bar{v}$ will be different for the incident, reflected and refracted waves. The superposition of the incident, reflected and refracted wave fields then give the velocities in the two media:

$$w_A = Re\left((\hat{w}_i e^{im_1 z} + \hat{w}_r e^{-im_1 z})e^{i\Psi}\right) \tag{A.1}$$

$$w_B = Re\left(\hat{w}_t e^{im_2 z} e^{i\Psi}\right) \tag{A.2}$$

where $\Psi = kx + ly - \omega t$, $m_1 < 0$ (for the upward propagating incident wave) and $m_2 < 0$. The Boussinesq dispersion relation gives that:

$$r = \frac{m_2}{m_1} = \sqrt{\left(\frac{N_2^2 - \hat{\omega}_2^2}{N_1^2 - \hat{\omega}_2^1}\right)\left(\frac{\hat{\omega}_1^2 - f^2}{\hat{\omega}_2^2 - f^2}\right)} \tag{A.3}$$

and the continuity of w and $\frac{\partial w}{\partial z}$ at the interface implies

$$\hat{w}_r = \frac{1-r}{1+r}\hat{w}_i \text{ and } \hat{w}_t = \frac{2}{1+r}\hat{w}_i\,. \tag{A.4}$$

If r is real, we note that there is a systematic phase relationship (either in phase or in opposition) between that of the incident and reflected wave. Even with ensemble averaging over different phases of the incident wave, that phase relationship is imposed by the reflection and will be preserved.

In that case, the relation between vertical kinetic energy at frequency $\hat{\omega} = \hat{\omega}_1$ in domain A reads:

$$E_{k_v}(\hat{\omega}, z) = \frac{1}{2}|\hat{W}_A(\hat{\omega}, z)|^2 = \frac{1}{2}\left(|\hat{w}_i|^2 + |\hat{w}_r|^2 + 2|\hat{w}_i|^2\frac{1-r}{1+r}\text{sign}(1-r)\cos(2m_1 z)\right) \tag{A.5}$$

and from the linearized equations it can be shown that, if r is real:

$$E_{k_v}(\hat{\omega}, z) = \frac{\hat{\omega}^2}{N^2-\hat{\omega}^2}\frac{\hat{\omega}^2-f^2}{\hat{\omega}^2+f^2}E_{k_h}(\hat{\omega}, z) + 4|\hat{w}_i|^2\text{sign}(1-r)\cos(2m_1 z) \tag{A.6}$$

which differs from the monochromatic polarization relation due to the interference fringes term $\cos(2m_1 z)$.

For hydrostatic and mid-frequency waves, we have $r \simeq \frac{N_2}{N_1}$. Thus, for those waves, reflection and related interferences are probably negligible at the balloon level since it is above the major jump in stratification at the tropopause ($r \simeq 1$ and $\hat{w}_r \simeq 0$). It might not be the case for future balloon campaigns. On the contrary, for high-frequency waves ($\hat{\omega} \sim N$), even moderate wind shears can induce $r \ll 1$ or $r \gg 1$ or even imaginary r and the associated ducted or trapped waves. The effect of interferences between the reflected and incident waves might be partially suppressed when averaging if the shear variability is sufficient so that there will be more variability in the phase difference between $\hat{w}_i$ and $\hat{w}_r$ and the interference terms might cancel out. It can also be averaged out if,

1. in the case of a monochromatic incident wave, measurements are carried out at different altitudes z from the reflector, so that phase averaging along the interference fringes is possible; this can be efficient only for mid-frequency waves for which stratification changes dominate r and the main reflector is the tropopause.

2. in the case of a superposition of incident waves with uncorrelated vertical wavenumbers, the interference term will be canceled out if the measurements are away from the reflector $z < 0$.

Both possibilities will arise for mid-frequency waves, even below the tropopause, provided that the measurements are taken at different altitudes sufficiently below the stratification jump. This will limit the impact of interferences in that range so that the polarization relation holds statistically. However, for high frequency waves, even moderate wind shears are sufficient to create close-by reflectors so that $z \simeq 0$ always. The only averaging-out can arise from waves with the same intrinsic frequency in medium A but different wavenumbers,

which is unlikely in the essentially zonal background wind of the lower stratosphere. Thus, in Figure 2.4, the disagreement between observed and expected polarization relations arising at high frequencies is mainly due to non isopycnic balloon response but also partly due to the reflected wave packets.

A final note should be made on the analysis of high frequency waves. Since incident and reflected wave packets are likely to be present at the same time, this limits the possibility of time-frequency wavepacket decomposition and analysis at those frequencies.

A.2 Proposed parameterization of Lagrangian temperature fluctuations

Generation of synthetic time series To generate synthetic time series of gravity-wave vertical displacements ζ', we have used an Auto-Regressive Integrated Moving Average (ARIMA) model.

For the tropical dataset, the simplest model that enables us to reproduce the observed $\hat{\omega}^{-2}$ power law of the vertical-displacement spectrum (see Figure 1 in the article) is the autoregressive process of order 1 (Markov process). The synthetic vertical-displacement time series is thus obtained through:

$$\zeta'_{t+dt} = \zeta'_t + W \cdot dt \tag{A.7}$$

where W is a white noise process that corresponds to the vertical velocity, and dt is the time step between two values of the time series. We choose $dt = 2.5$ min so that the Nyquist frequency of the synthetic time series roughly coincides with N in the stratosphere, and we use a Laplace (or double exponential) distribution with a standard deviation of 0.12 m/2.5 min for W. Note that due to uncertainties in the balloon response for frequencies above $\frac{N}{2}$, we do not include the observed peak at frequency N. Furthermore, we apply a fifth order high-pass Butterworth filter to the generated time series to remove frequencies lower than 2 day^{-1}, corresponding to longer waves. Also note that we have chosen an Infinite Impulse Response filter in order to only rely on past values of the time series in the filtering computation. This causes a phase delay in the filtered time series, which has no practical consequence for our purpose.

As in the letter, converting this Lagrangian vertical displacement to temperature disturbance is computed through: $T'_l = -\frac{g}{C_P}\zeta'$ where g is the gravitational acceleration and C_P the heat capacity of air at constant pressure. As previously mentioned, this whole procedure allows to fit the observed PDFs of temperature and cooling rates in the lower stratosphere, as well as their spectrum up to $\frac{N}{2}$.

The synthetic time series can be interpolated at higher frequency if needed. A higher frequency noise representing perturbations above $\frac{N}{2}$ could also be added (using for instance the mid-point displacement method to match a theoretically expected slope, or adding a small number of well-chosen harmonics close to N to reproduce a peak). In practice, we refrain from adding this noise here because of uncertainties of the balloon observations at those frequencies and because we target more the tropical tropopause layer where the Brunt-Väisälä frequency is half its value in the tropical stratosphere. Hence frequencies above the stratospheric $\frac{N}{2}$ will correspond to the turbulence frequency range in the tropical upper troposphere.

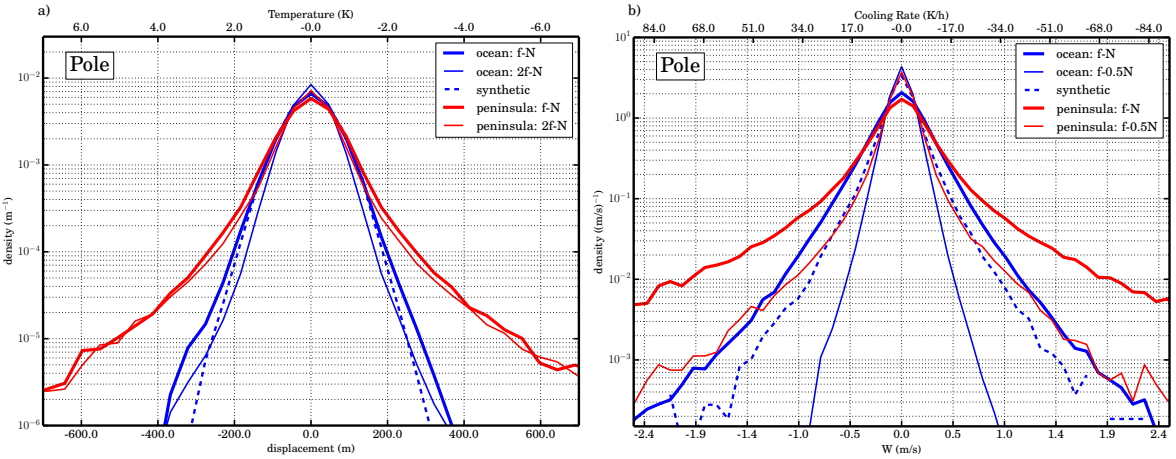

Figure A.1 – (Left) Temperature (or vertical-displacement) PDF inferred from balloon observations during the Concordiasi campaign, screened according to the geographical regions (polar ocean and Antarctic peninsula). (Right) Same, but for the cooling-rate (or vertical-velocity) PDF. The dotted lines correspond to time series synthesized using the method introduced in this appendix. This figure illustrates the importance of (intermittent) mountain waves in generating extreme wave events in both temperature and vertical velocity.

For the polar case, reproducing time series similar to the observations is less straightforward due to the intermittency associated with mountain waves, which cause large wings in the temperature PDF. As shown in Figure S3, these intermittent events are clearly important in the region of the Antarctic peninsula, but much less over oceanic regions where the temperature PDF is closer to a Gaussian. We have developped a simple parameterization to describe the background variability encountered in those high latitude oceanic regions. The highly intermittent variability linked to mountain waves probably needs a specific parameterisation, as emphasized by *Bacmeister et al.* (1999).

The parameterization once again consists in an ARIMA model that fits the observed -1.8 slope of the spectrum. As for the tropical case, we use a time step of $dt = 2.5$ min, but a white noise W, which this time follows a symmetric stretched exponential distribution. More precisely, its PDF $f_W(w)$ is of the form:

$$f_W(w) = Ae^{-\left(\frac{|w|}{\beta}\right)^{\alpha}} \tag{A.8}$$

where A is an integration constant. To match the observations, we have used $\alpha = 0.6$ and $\beta = 0.038$ m/2.5 min. The corresponding PDFs of temperature and vertical velocity are also shown on figure S3, while the spectrum follows a $\hat{\omega}^{-1.8}$ power law. As for the tropical case, we did not try to fit the balloon observed peak at N because of its uncertainty.

Extension to other altitudes than the balloon level To examine how the wave-induced Lagrangian temperature disturbances could be extended to other altitudes than the balloon flight level, we consider the conservation of the wave pseudomomentum flux, which is valid at second order in the stationary and conservative (no dissipation, no thermal forcing) limits (e.g., *Fritts and Alexander*, 2003). Similar results could be obtained with wave action.

Namely, for the zonal component:

$$\frac{\partial}{\partial z}\left[\bar{\rho}(z)\left(1-\frac{f^2}{\hat{\omega}^2}\right)\overline{u'w'}\right]=0 \tag{A.9}$$

where $\bar{\rho}(z)=\rho_0\exp(-z/H)$ is the background atmospheric density and H the density scale height, and with the same notations than in the letter otherwise. Close to the equator ($f\to 0$), or alternatively in the mid or high-frequency approximation ($f\ll\hat{\omega}$), this equation reduces to:

$$\frac{\partial}{\partial z}\left[\overline{u'w'}\,\exp(-z/H)\right]=0 \tag{A.10}$$

Manipulating gravity-wave polarization relations (*Fritts and Alexander*, 2003), one obtains:

$$\overline{u'w'}=-\frac{N^2-\hat{\omega}^2}{\hat{\omega}^2-f^2}\,\frac{\left(\hat{\omega}km+\frac{fl}{2H}\right)}{\hat{\omega}\left(m^2+\frac{1}{4H^2}\right)}\,\overline{w'^2} \tag{A.11}$$

where k, l and m are respectively the zonal, meridional and vertical wave numbers. Letting once again $f\to 0$, and assuming furthermore that $m^2\gg 1/4H^2$, which typically corresponds to vertical wavelengths smaller than 20 km, one can make use of the gravity-wave simplified dispersion relation:

$$m^2=\frac{N^2-\hat{\omega}^2}{\hat{\omega}^2}\,k_h^2 \tag{A.12}$$

where $k_h=\sqrt{k^2+l^2}$ to rewrite (A.11) as:

$$|\,\overline{u'w'}\,|=\frac{\sqrt{N^2-\hat{\omega}^2}}{\hat{\omega}}\,\overline{w'^2} \tag{A.13}$$

To obtain this latter equation, we have assumed for simplicity and without loss of generality that the wave packet propagates in the zonal direction, i.e. $l=0$.

Consequently, (A.10) now writes:

$$\frac{\sqrt{N^2-\hat{\omega}^2}}{\hat{\omega}}\,\rho(z)\,\overline{w'^2}=\text{constant} \tag{A.14}$$

which is the same as equation (13) in *Alexander* (1996). Since N is larger in the stratosphere than in the troposphere, the $\sqrt{N^2-\hat{\omega}^2}$ factor in this equation implies an enhancement in the tropospheric vertical-velocity power when $\hat{\omega}\sim N$. At lower frequencies ($\hat{\omega}^2\ll N^2$), Equation (A.14) further simplifies into:

$$\frac{N}{\hat{\omega}}\,\rho(z)\,\overline{w'^2}=\text{constant} \tag{A.15}$$

or equivalently, for the amplitudes W_1 and W_2 of the wave-induced vertical-velocity disturbances at two different altitudes z_1 and z_2, respectively associated with two different Brunt-Väisälä frequencies N_1 and N_2:

$$\frac{N_2}{\hat{\omega}_2}\rho_2 W_2^2=\frac{N_1}{\hat{\omega}_1}\,\rho_1\,W_1^2 \tag{A.16}$$

Those two last equations are similar to those derived, in the context of stratospheric mountain waves by *Bacmeister et al.* (1994) [1]. Note that near the tropical tropopause, the variation of the Brunt-Väisälä frequency tends to compensate that of the density $\frac{\rho_1}{\rho_2} = \exp\left(\frac{z_2 - z_1}{H}\right)$. Hence, for a typical N variation of a factor 2 across the tropopause, the vertical-velocity amplitudes remain roughly constant over an altitude range of $\Delta z \sim H \ln 2$, i.e. about 4 km. In other words, the statistics of the wave-induced vertical-velocity disturbances derived from the balloon observations in the tropical lower stratosphere, as well as those of the Lagrangian temperature (T'_l), which are directly linked to the wave-induced vertical displacement, likely apply fairly well over the whole tropical tropopause layer for the low frequencies. In contrast, the amplitude of the Eulerian temperature disturbances (T') increases by a factor 4 over the same 4-km altitude range encompassing the tropopause, since T' scales as $N^2\zeta'$, and thus has an additional dependence on N.

[1] For stationary waves, it further simplifies in: $W_2^2 = \frac{U_2}{U_1}\frac{\rho_1 N_1}{\rho_2 N_2} W_1^2$, so that the vertical wind scales with the square root of the mean horizontal wind.

Appendix B

Appendix to Chapter 3

B.1 Observed spikes in the ice crystal number and sensitivity homogeneous nucleation to the initial water content

This appendix examines different possible explanations for the high ICN spikes shown on Figure 3.5. It is argued that the most likely explanation for their existence is that they are formed by quenched nucleation events superimposed on a (small) initial variability in the water vapor content.

The high ICN spikes (Figure 3.5) are thin vertical layers of high ICN (although they are more extensive horizontally, since the plane moves about 100 times faster on the horizontal than on the vertical). As a consequence of the disparities in ICN, there are also small-scale heterogeneities in the water vapor content because within high ICN spikes the supersaturation relaxation time scale is small and water is efficiently driven near saturation by the ice crystals, whereas in the near-by environment with low ICN, the ICN is too low for rapid relaxation toward saturation to take place. However, if the water vapor is variable, the total water is not, so that before the nucleation event the humidities were close. Then there is the question of how those layers formed and why are they so localized?

Due to the high ICN, *Jensen et al.* (2010) argue that the formation of the ice crystals in those layers can only be due to homogeneous nucleation, since there are probably no such high heterogeneous ice nuclei concentrations in the TTL, and since there is no sign of convective influence near the observations. However, the nucleation event must have happened upstream of the observations, since at the observation point the supersaturation in the environment is below the threshold for homogeneous nucleation ($S_i \simeq 1.3$ versus 1.6 for homogeneous nucleation at that temperature).

The total water content appears not so different between the high ICN cloud layers and their environment, so that before homogeneous nucleation took place, the air parcels that have experienced nucleation and the surrounding ones had similar but slightly different humidity contents. They should have experienced nucleation at close-by temperatures. In the constant updraft framework, the heterogeneities in the nucleated ICN for a similar nucleation temperature are governed by heterogeneities in the vertical velocity w (see Figure 3.2). At that temperature, the different ICNs correspond to differences in vertical velocity Δw of about 0.2 m/s at the most over less than 20 m. The heterogeneities in Δw are roughly given

by:

$$\Delta w = \epsilon_k^{\frac{1}{3}} l^{\frac{1}{3}} \tag{B.1}$$

where ϵ_k is the eddy dissipation rate. To induce such a Δw over the 200 m aircraft resolution, the required ϵ_k should be of the order of about $4\,10^{-4}\mathrm{m}^2\,\mathrm{s}^{-3}$. This is high and rare, but possible in the TTL (see Chapter 5). However, vertical velocity fluctuations are generally smaller than that. It seems unlikely that differences in vertical velocity due to turbulence are responsible for the observed heterogeneities of ICN.

The heterogeneities and high gradient of ICN observed might also have been increased by the horizontal strain in the TTL. However, typical horizontal strain values are of the order of $10^{-5}\,\mathrm{s}^{-1}$ so that doubling the horizontal gradient requires time scales of the order of a day, even larger than the expected life time of small ice crystals cirrus clouds (about ten hours, see *Jensen et al.*, 2011). The implied vertical scales are so small (< 2 m) that vertical strain cannot have created those features. Furthermore, the total water content gradients seem to remain fairly small in the region, while there are several spikes seen in the ICN. The fact that only the ICN appears affected does not preach in favor of advection-enhanced gradients.

The conclusion of the previous paragraph is that it appears difficult to reconcile the very high gradients in the ICN observed by (*Jensen et al.*, 2013) with either

- constant-w nucleation combined with heterogeneities in cooling rates, due for instance to turbulence
- vertical shear or horizontal strain

The only remaining explanation relies on time variations of w due to the waves.

In liquid water clouds, the sharp edges of the clouds are due to the relative humidity getting over the 100% threshold for water droplets formation at a specific point. To explain the heterogeneities observed in ICN, the only simple solution is by assuming a similar threshold behavior is responsible for the observations: the high ICN regions experienced homogeneous nucleation and went over the nucleation threshold while the others did not. However, the vertical velocity required to create $> 10,000$ #/L crystals is larger than 0.1 m/s. In the likely absence of strong differences in vertical velocities at such scales (tens of meters), as discussed above, and given the relatively low differences in total water before nucleation, we expect that, at a constant w, less than 100 s would have been sufficient for the close points that did not nucleate to also cross the nucleation threshold and experience homogeneous nucleation. Since they did not, the cooling must have stopped during the one-two minutes following the first near-by nucleation event. This stopped cooling has created probably generated temperature-limit nucleation events. Combined with small-scale fluctuations of the water content of fairly small amplitude present prior to nucleation, the temperature-limit nucleation may be responsible for the heterogeneities in ICN as we show in the paper. The existence of this temperature limit homogeneous nucleation regime thus allows to explain the ICN spikes through small heterogeneities in the water vapor field prior to nucleation.

In one-dimensional simulations, *Murphy* (2014) also found that the presence of high frequency temperature fluctuations could induce very large differences in homogeneously nucleated ice crystal numbers. However, *Murphy* (2014) attributed this to the different temperature histories followed by different near-by parcels, whereas we point out the importance of prior small vapor fluctuations. This different interpretation comes from the setup chosen

by *Murphy* (2014), who imposed large temperature variability over relatively shallow region (more than 1 K over 100 m for the temperature fluctuations), thus imposing strong small scale disparities in RH_i through the temperature field while the vapor was chosen nearly uniform. This set-up is different from the observations in Figure 3.5 who show nearly constant T in the region of interest. However, we show that water vapor fluctuations are a good candidate together with quenched nucleation to explain the heterogeneities.

B.2 Note on wave stability

To avoid strongly overestimating the effect of wave driven vertical transport on sedimentation, it is important to recall that the wave amplitude is limited by a stability requirement. Shear and convective breaking of monochromatic gravity waves have been treated in a number of studies (e.g. *Lindzen*, 1981), and we adapt those considerations to our notations, to highlight where our two wave parameters ($\frac{\omega}{m}$ and W) intervene.

We take the criterion that the Richardson number Ri must be larger than a critical value Ri_c. Miles-Howard stability criterion suggests $Ri_c \simeq \frac{1}{4}$, and a more conservative choice would be $Ri_c \simeq 1$. For simplicity, we ignore background shear; then the Richardson number induced by the monochromatic wave field is:

$$Ri = \frac{\frac{g}{\bar{\theta}}\frac{\partial\theta}{\partial z}}{\left(\frac{\partial u}{\partial z}\right)^2} = \frac{\bar{N}^2(1+\frac{W}{\omega}\cos(\Phi))}{\frac{m^4}{k^2}W^2\sin^2(\Phi)} = \left(\frac{\omega}{mW}\right)^2 \frac{1+\frac{W}{\omega}\cos(\Phi)}{1-\cos^2(\Phi)} = \frac{1}{a^2}\frac{1+a\cos(\Phi)}{1-\cos^2(\Phi)} \tag{B.2}$$

with $a = \frac{W}{\frac{\omega}{m}}$ ($a < 0$ since we are interested in upward propagating waves).

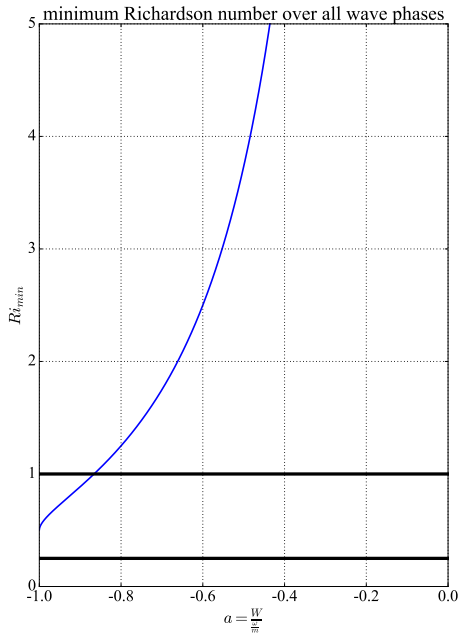

Minimum Richardson number over all wave phases, as a function of the amplitude

parameter $\frac{W}{\frac{\omega}{m}}$.

The figure above represents the minimum Richardson number over all wave phases in our configuration. Examination of the figure or of Equation B.2 shows that for $a \geq -1$, $Ri \geq 0.5$. The condition $Ri > \frac{1}{4}$ is equivalent for the monochromatic upward propagating wave to the condition for convective stability, i.e. $Ri > 0$ or $|a| < 1$. The condition $Ri > 1$ is a bit more restrictive and requires $0 \geq a >\sim -0.82$. We will then restrict the chosen wave amplitude so that the minimum Ri remains above 1, i.e. $|a| < 0.82$. Wave breaking and the generated turbulence probably has an important impact on vertical mixing and vertical transport of ice and water in the TTL (see Chapter 5), but this is not considered in our configuration which focuses on sedimentation.

Appendix C

Appendix to Chapter 5

C.1 Wavelet estimate of high frequency variance

For aircraft observations time series of N measurements separated by a sampling time step $\delta t = 0.05$ s, the (redundant) scales of the wavelet analysis s_j are given by:

$$s_j = s_0 2^{j\delta t},\ j = 1, ..., J$$

with $J = \delta j^{-1} \log_2(N\delta t/s_0)$. Here we have chosen $\delta j = 0.2$ and checked the accuracy of the corresponding wavelet reconstruction.

Although Morlet wavelets are non orthogonal, the redundancy of the continuous wavelet transform allows an approximate time-frequency decomposition of the variance associated with the fluctuations. Indeed, the obtained time series of wavelet coefficients at different scales $W_n(s_j) = W(s_j, t_n)$ approximately verify *Parseval*'s identity:

$$\sigma^2 \simeq \frac{\delta j \delta t}{C_\delta N} \sum_{n=0}^{N-1} \sum_{j=0}^{J} \frac{|W_n(s_j)|^2}{s_j}$$

(within 1%), where σ^2 is the variance of the time series and $C_\delta = 0.776$ for the Morlet wavelet (*Torrence and Compo*, 1998). Time series of the high frequency variance σ_{HF} can also be derived as

$$\sigma^2_{HF}(t_n) \simeq \frac{\delta j \delta t}{C_\delta N} \sum_{j=j_1}^{j_2} \frac{|W_n(s_j)|^2}{s_j}$$

where only the time scales between s_{j_1} and s_{j_2} have been selected. Unless stated otherwise, we have used $s_{j_1} = 0.2$ s and $s_{j_2} = 1$ s for estimating the high frequency variance.

C.2 Uncertainty in eddy dissipation rate estimate

In this appendix we discuss the precision and accuracy of the Eddy Dissipation Rate estimates derived from ATTREX MMS observations. The formulas are taken from *Scott et al.* (1990).

The vertical wind measured by the aircraft is approximately given by (*Scott et al.*, 1990):

$$W = -V_a \sin(\theta - \alpha) + \dot{Z}$$

where V_a is the True airspeed measured with Pitot sondes (around 170-180 m/s for the Global Hawk), θ the pitch of the aircraft measured with the inertial system and α the angle of attack (AOA) measured using the radome differential pressure sensors, and $\dot{Z}$ the aircraft ascent rate, determined from the GPS and the inertial system. In practice, given the atmospheric variability in vertical wind, the dominant term (generally by one order of magnitude) for measuring W at high frequency is the variation of the AOA, α. Due to this one term dominating the others rather than having comparable terms that cancel one another, the measurements are actually the most reliable at those high frequencies. The accuracy in the retrieval of $V_a\alpha$ at high frequency controls the accuracy of ϵ_w estimated in the 1-5 Hz frequency band. In the following we evaluate the uncertainty in W *in that specific frequency range*.

The accuracy of high frequency vertical velocity measurements is $\frac{\delta W}{W} = \frac{\delta V_a}{V_a} + \frac{\delta \alpha}{\alpha}$. α is retrieved from the radome system vertical differential pressure sensor ΔP using the relation $\alpha = a\Delta P(q)^{-1}$ where a is the airflow angle sensitivity factor, taken to be $a = \frac{1}{0.07854^\circ}$, and $q = \frac{1}{2}\rho V_a^2$ (hPa) is the compressible dynamic pressure, which is evaluated from the difference between total pressure and static pressure.

Regarding the noise level, pitch and AOA are retrieved with a resolution of 0.01°, so that the quantization noise is $\sigma_\theta \simeq \sigma_\alpha \simeq 0.03^\circ$. In the 1-5 Hz frequency band, the noise level on the vertical velocity variance is of the order of

$$\sigma_W^2 \simeq \frac{4}{10} V_a^2(\sigma_\alpha^2 + \sigma_\theta^2) \simeq 6 \cdot 10^{-6} \mathrm{m}^2\,\mathrm{s}^{-2}$$

. The corresponding noise level on ϵ_w is $\sigma_{\epsilon_w} = \left(\frac{\sigma_W^2}{\alpha_k(\kappa_1^{-2/3} - \kappa_2^{-2/3})}\right)^{\frac{3}{2}} \simeq 3 \cdot 10^{-8} \mathrm{m}^2\,\mathrm{s}^{-3}$.

The transverse wind measured by the aircraft is approximately given by *Scott et al.* (1990):

$$U_t = V_a \sin(\beta) + \dot{Y}_t$$

where β is the yaw angle and $\dot{Y}_t$ the aircraft ground relative speed in the rasverse direction. The yaw being retrieved similarly to the AOA, the corresponding noise level and accuracy of the transverse horizontal wind are similar to the vertical wind, except that the pitch noise does not intervene. We then have $\sigma_{\epsilon_{u_t}} \simeq 1.2 \cdot 10^{-8} \mathrm{m}^2\,\mathrm{s}^{-3}$.

Finally, the estimate of the eddy dissipation rate relies on wavelet transforms obtained with a limited sampling. *Torrence and Compo* (1998) explain how to derive the corresponding uncertainty and we shall follow their methodology. The high frequency variance was estimated by averaging over wavelet scales:

$$(\sigma_{est})^2 \simeq \frac{\delta j \delta t}{C_\delta N} \sum_{j=j_1}^{j_2} \frac{|W_n(s_j)|^2}{s_j}$$

. The confidence interval of the true high-frequency variance σ^2 is then:

$$\frac{\nu}{\chi_\nu^2(1-p/2)} \leq \frac{\sigma^2}{\sigma_{est}^2} \leq \frac{\nu}{\chi_\nu^2(p/2)}$$

where χ_ν^2 is the value of the chi-square distribution with ν degrees of freedom. For continuous

wavelet transforms, the number of degrees of freedom ν can be modelled as (*Torrence and Compo*, 1998, equation 28):

$$\nu \simeq \frac{2n_a S_{\text{avg}}}{S_{\text{mid}}} \sqrt{1 + \left(\frac{n_a \delta j}{\delta j_0}\right)^2}$$

where n_a is the number of scales used for averaging, $S_{\text{avg}} = \sum_{j=j_1}^{j_2} (s_j)^{-1}$ and $S_{\text{mid}} = s_0 2^{0.5(j_1+j_2)\delta j}$, and $\delta j_0 = 0.6$ for the Morlet wavelet. For ATTREX MMS data, we have used $\delta j = 0.2$ and $n_a = 12$ so that $\nu \simeq 4$. The 95 % confidence interval for the variance is then $]0.85\,;1.16]$, so that the sampling uncertainty is 15 % for the variance and less than 25 % on the eddy dissipation rate.

The estimate of ϵ_k is provided at 20 Hz, the frequency of wind observations; however, the wavelet coefficients have an autocorrelation of time of $\sqrt{2}s$. The largest scale used for the ϵ_k estimation is $s = 6 * 1$ seconds so the resolution is about 7 seconds, i.e. about 1.2 km on the horizontal and less than 30 m on the vertical.

Bibliography

Abalos, M., W. J. Randel, D. E. Kinnison, and E. Serrano (2013), Quantifying tracer transport in the tropical lower stratosphere using waccm, *Atmospheric Chemistry and Physics*, *13*(21), 10,591–10,607, doi:10.5194/acp-13-10591-2013. 197

Alappattu, D. P., and P. K. Kunhikrishnan (2010), First observations of turbulence parameters in the troposphere over the bay of bengal and the arabian sea using radiosonde, *Journal of Geophysical Research: Atmospheres*, *115*(D6), n/a–n/a, doi:10.1029/2009JD012916. xi, 36, 37, 38, 172, 196

Alexander, M., T. Tsuda, and R. A. Vincent (2002), Latitudinal variations observed in gravity waves with short vertical wavelengths, *Journal of the Atmospheric Sciences*, *59*(8), 1394–1404, doi:10.1175/1520-0469(2002)059<1394:LVOIGW>2.0.CO;2. x, 16, 78, 79

Alexander, M. J. (1996), A simulated spectrum of convectively generated gravity waves: Propagation from the tropopause to the mesopause and effects on the middle atmosphere, *J. Geophys. Res.: Atmos.*, *101*(D1), 1571–1588, doi:10.1029/95JD02046. 225

Alexander, M. J., and C. Barnet (2007), Using satellite observations to constrain parameterizations of gravity wave effects for global models, *Journal of the Atmospheric Sciences*, *64*(5), 1652–1665, doi:10.1175/JAS3897.1. 78

Alexander, M. J., and T. J. Dunkerton (1999), A spectral parameterization of mean-flow forcing due to breaking gravity waves, *Journal of the Atmospheric Sciences*, *56*(24), 4167–4182, doi:10.1175/1520-0469(1999)056<4167:ASPOMF>2.0.CO;2. 15

Alexander, M. J., J. H. Beres, and L. Pfister (2000), Tropical stratospheric gravity wave activity and relationships to clouds, *Journal of Geophysical Research: Atmospheres*, *105*(D17), 22,299–22,309, doi:10.1029/2000JD900326. 16, 17, 75, 183

Alexander, M. J., D. A. Ortland, A. W. Grimsdell, and K. J.-E. (2017), A model study of tropical gravity wave changes with El Nino and La Nina conditions and wave forcing of the quasibiennial oscillation, *J. Atmos. Sci., submitted.* 13

Alisse, J.-R., and C. Sidi (2000), Experimental probability density functions of small-scale fluctuations in the stably stratified atmosphere, *JFM*, *402*(402), 137–162, doi:10.1175/1520-0450(1974)013\%3C0488:SMEFHA\%3E2.0.CO;2. 35, 190, 193

Andrews, D., J. Holton, and C. Leovy (1987), *Middle Atmosphere Dynamics*, International geophysics series, Academic Press. 19, 113

Augier, P., and E. Lindborg (2013), A new formulation of the spectral energy budget of the atmosphere, with application to two high-resolution general circulation models, *Journal of the Atmospheric Sciences*, *70*(7), 2293–2308, doi:10.1175/JAS-D-12-0281.1. 81

Bacmeister, J. T., P. A. Newman, B. L. Gary, and K. R. Chan (1994), An algorithm for forecasting mountain wave–related turbulence in the stratosphere, *Wea. Forecast.*, *9*, 241–253, doi:10.1175/1520-0434. 226

Bacmeister, J. T., S. D. Eckermann, P. A. Newman, L. Lait, K. R. Chan, M. Loewenstein, M. H. Proffitt, and B. L. Gary (1996), Stratospheric horizontal wavenumber spectra of winds, potential temperature, and atmospheric tracers observed by high-altitude aircraft, *Journal of Geophysical Research: Atmospheres*, *101*(D5), 9441–9470, doi:10.1029/95JD03835. 75, 82, 174, 184

Bacmeister, J. T., S. D. Eckermann, A. Tsias, K. S. Carslaw, and T. Peter (1999), Mesoscale temperature fluctuations induced by a spectrum of gravity waves: A comparison of parameterizations and their impact on stratospheric microphysics, *J. Atmos. Sci.*, *56*, 1913–1924, doi:10.1175/1520-0469. 86, 224

Baldwin, M. P., et al. (2001), The quasi-biennial oscillation, *Rev. Geophys.*, *39*(2), 179–229, doi:10.1029/1999RG000073. ix, 6, 20

Barahona, D., and A. Nenes (2011), Dynamical states of low temperature cirrus, *Atmos. Chem. Phys.*, *11*(8), 3757–3771, doi:10.5194/acp-11-3757-2011. 95

Barahona, D., A. Molod, J. Bacmeister, A. Nenes, A. Gettelman, H. Morrison, V. Phillips, and A. Eichmann (2014), Development of two-moment cloud microphysics for liquid and ice within the nasa goddard earth observing system model (geos-5), *Geoscientific Model Development*, *7*(4), 1733–1766, doi:10.5194/gmd-7-1733-2014. 87, 88

Barahona, D., A. Molod, and H. Kalesse (2017), Direct estimation of the vertical velocity distribution in cirrus and implications for the aerosol indirect effect, in *EGU general assembly*, Vienna, Austria. 90

Bardeen, C. G., A. Gettelman, E. J. Jensen, A. Heymsfield, A. J. Conley, J. Delanoë, M. Deng, and O. B. Toon (2013), Improved cirrus simulations in a general circulation model using CARMA sectional microphysics, *Journal of Geophysical Research: Atmospheres*, *118*(20), 11,679–11,697, doi:10.1002/2013JD020193. xi, 37, 38, 172, 195

Batchelor, G. K. (1947), Kolmogoroff's theory of locally isotropic turbulence, *Mathematical Proceedings of the Cambridge Philosophical Society*, *43*(4), 533–559, doi:10.1017/S0305004100023793. 168

Beres, J. H., M. J. Alexander, and J. Holton (2004), A method of specifying the gravity wave spectrum above convection based on latent heating properties and background wind, *Journal of the Atmospheric Sciences*, *61*(3), 324–337, doi:10.1175/1520-0469(2004)061<0324:AMOSTG>2.0.CO;2. 13

Bergman, J. W., E. J. Jensen, L. Pfister, L. L. Pan, and S. Honomichl (2014), Analyzing dynamical circulations in the tropical tropopause layer through empirical predictions of

cirrus cloud distributions, *Journal of Geophysical Research: Atmospheres*, *119*(6), 2831–2845, doi:10.1002/2013JD021295. x, 18

Bergman, J. W., E. J. Jensen, L. Pfister, and T. V. Bui (2016), Air parcel trajectory dispersion near the tropical tropopause, *Journal of Geophysical Research: Atmospheres*, *121*(8), 3759–3775, doi:10.1002/2015JD024320. 87

Boehm, M. T., and J. Verlinde (2000), Stratospheric influence on upper tropospheric tropical cirrus, *Geophys. Res. Lett.*, *27*(19), 3209–3212, doi:10.1029/2000GL011678. x, 23

Bonazzola, M., and P. H. Haynes (2004), A trajectory-based study of the tropical tropopause region, *Journal of Geophysical Research: Atmospheres*, *109*(D20), n/a–n/a, doi:10.1029/2003JD004356. 18

Bony, S., B. Stevens, D. Coppin, T. Becker, K. A. Reed, A. Voigt, and B. Medeiros (2016), Thermodynamic control of anvil cloud amount, *Proceedings of the National Academy of Sciences*, *113*(32), 8927–8932, doi:10.1073/pnas.1601472113. 5

Brewer, A. W. (1949), Evidence for a world circulation provided by the measurements of helium and water vapour distribution in the stratosphere, *Q. J. Roy. Meteor. Soc.*, *75*(326), 351–363, doi:10.1002/qj.49707532603. v, ix, 3, 4

Bühler, O. (2003), Equatorward propagation of inertia–gravity waves due to steady and intermittent wave sources, *Journal of the Atmospheric Sciences*, *60*(11), 1410–1419, doi:10.1175/1520-0469(2003)060<1410:EPOIWD>2.0.CO;2. 79

Bui, T., J. Dean-Day, and coauthors (2014), ATTREX meteorological measurement system data, https://espoarchive.nasa.gov/archive/browse/attrex, accessed 9 September 2016. 173

Callies, J., R. Ferrari, and O. Bühler (2014), Transition from geostrophic turbulence to inertia–gravity waves in the atmospheric energy spectrum, *Proceedings of the National Academy of Sciences*, *111*(48), 17,033–17,038, doi:10.1073/pnas.1410772111. 184

Chaboureau, J.-P., J.-P. Cammas, J. Duron, P. J. Mascart, N. M. Sitnikov, and H.-J. Voessing (2007), A numerical study of tropical cross-tropopause transport by convective overshoots, *Atmospheric Chemistry and Physics*, *7*(7), 1731–1740, doi:10.5194/acp-7-1731-2007. 32

Chan, K. R., J. Dean-Day, S. W. Bowen, and T. P. Bui (1998), Turbulence measurements by the dc-8 meteorological measurement system, *Geophysical Research Letters*, *25*(9), 1355–1358, doi:10.1029/97GL03590. 30, 172, 174, 183, 187

Cornman, L. B. (2016), *Airborne In Situ Measurements of Turbulence*, pp. 97–120, Springer International Publishing, Cham, doi:10.1007/978-3-319-23630-8_5. 175

Cornman, L. B., C. S. Morse, and G. Cunning (1995), Real-time estimation of atmospheric turbulence severity from in-situ aircraft measurements, *Journal of Aircraft*, *32*(1), 171–177, doi:10.2514/3.46697. 172

Cornman, L. B., G. Meymaris, and M. Limber (2004), An update on the faa aviation weather research program's in situ turbulence measurement and report system., in *11th Conf. on Aviation, Range, and Aerospace Meteorology*, Hyannis, MA. 172

Corti, T., B. P. Luo, Q. Fu, H. Vömel, and T. Peter (2006), The impact of cirrus clouds on tropical troposphere-to-stratosphere transport, *Atmos. Chem. Phys.*, *6*(9), 2539–2547, doi:10.5194/acp-6-2539-2006. 6

Corti, T., et al. (2008), Unprecedented evidence for deep convection hydrating the tropical stratosphere, *Geophysical Research Letters*, *35*(10), n/a–n/a, doi:10.1029/2008GL033641. xi, 32, 33

Coy, L., D. C. Fritts, and J. Weinstock (1986), The stokes drift due to vertically propagating internal gravity waves in a compressible atmosphere, *Journal of the Atmospheric Sciences*, *43*(22), 2636–2643, doi:10.1175/1520-0469(1986)043<2636:TSDDTV>2.0.CO;2. 113

Cziczo, D. J., K. D. Froyd, C. Hoose, E. J. Jensen, M. Diao, M. A. Zondlo, J. B. Smith, C. H. Twohy, and D. M. Murphy (2013), Clarifying the dominant sources and mechanisms of cirrus cloud formation., *Science*, *340*(6138), 1320–1324, doi:10.1126/science.1234145. 25, 95

Danielsen, E. F. (1982), A dehydration mechanism for the stratosphere, *Geophysical Research Letters*, *9*(6), 605–608, doi:10.1029/GL009i006p00605. xi, 32, 33

Danielsen, E. F. (1993), In situ evidence of rapid, vertical, irreversible transport of lower tropospheric air into the lower tropical stratosphere by convective cloud turrets and by larger-scale upwelling in tropical cyclones, *Journal of Geophysical Research: Atmospheres*, *98*(D5), 8665–8681, doi:10.1029/92JD02954. xviii, 32, 198, 199

Dauhut, T., J.-P. Chaboureau, J. Escobar, and P. Mascart (2016), Giga-les of hector the convector and its two tallest updrafts up to the stratosphere, *Journal of the Atmospheric Sciences*, *73*(12), 5041–5060, doi:10.1175/JAS-D-16-0083.1. 32, 33

Davis, A., A. Marshak, W. Wiscombe, and R. Cahalan (1994), Multifractal characterizations of nonstationarity and intermittency in geophysical fields: Observed, retrieved, or simulated, *Journal of Geophysical Research: Atmospheres*, *99*(D4), 8055–8072, doi:10.1029/94JD00219. 71

Davis, S. M., C. K. Liang, and K. H. Rosenlof (2013), Interannual variability of tropical tropopause layer clouds, *Geophysical Research Letters*, *40*(11), 2862–2866, doi:10.1002/grl.50512. x, 20, 21

De Reus, M., et al. (2009), Evidence for ice particles in the tropical stratosphere from in-situ measurements, *Atmos. Chem. Phys*, *9*, 6775–6792. 32

Dewan, E. (1981), Turbulent vertical transport due to thin intermittent mixing layers in the stratosphere and other stable fluids, *Science*, *211*, 1041–1042, doi:10.1126/science.211.4486.1041. 35, 190, 191, 192, 193, 194

Dewan, E. (1997), Saturated-cascade similitude theory of gravity wave spectra, *Journal of Geophysical Research: Atmospheres*, *102*(D25), 29,799–29,817, doi:10.1029/97JD02151. 77, 78, 171

Diao, M., M. A. Zondlo, A. J. Heymsfield, L. M. Avallone, M. E. Paige, S. P. Beaton, T. Campos, and D. C. Rogers (2014), Cloud-scale ice-supersaturated regions spatially correlate with high water vapor heterogeneities, *Atmospheric Chemistry and Physics*, *14*(5), 2639–2656, doi:10.5194/acp-14-2639-2014. 159

Dinh, T., D. R. Durran, and T. Ackerman (2010), Maintenance of tropical tropopause layer cirrus, *J. Geophys. Res.*, *115*, D02,104, doi:10.1029/2009JD012735. 31, 135, 161

Dinh, T., A. Podglajen, A. Hertzog, B. Legras, and R. Plougonven (2016), Effect of gravity wave temperature fluctuations on homogeneous ice nucleation in the tropical tropopause layer, *Atmos. Chem. Phys.*, *16*, 35–46, doi:10.5194/acp-16-35-2016. 110

Dobbie, S., and P. Jonas (2001), Radiative influences on the structure and lifetime of cirrus clouds, *Quarterly Journal of the Royal Meteorological Society*, *127*(578), 2663–2682, doi:10.1002/qj.49712757808. 30

Dole, J., R. Wilson, F. Dalaudier, and C. Sidi (2001), Energetics of small scale turbulence in the lower stratosphere from high resolution radar measurements, *Annales Geophysicae*, *19*(8), 945–952, doi:10.5194/angeo-19-945-2001. 192, 193, 194

Durran, D. R., T. Dinh, M. Ammerman, and T. Ackerman (2009), The mesoscale dynamics of thin tropical tropopause cirrus, *J. Atmos. Sci.*, *66*(9), 2859–2873, doi:10.1175/2009JAS3046.1. 135, 160

ECMWF (2009), ERA-Interim project., ECMWF data archive, accessed 20 September 2016, doi:10.5065/D6CR5RD9. 194

Evan, S., M. J. Alexander, and J. Dudhia (2012), WRF simulations of convectively generated gravity waves in opposite QBO phases, *J. Geophys. Res.*, *117*(D12), doi:10.1029/2011JD017302. 16

Evan, S., K. H. Rosenlof, T. Thornberry, A. Rollins, and S. Khaykin (2015), TTL cooling and drying during the january 2013 stratospheric sudden warming, *Quarterly Journal of the Royal Meteorological Society*, *141*(693), 3030–3039, doi:10.1002/qj.2587. 20

Fahey, D. W., et al. (2014), The AquaVIT-1 intercomparison of atmospheric water vapor measurement techniques, *Atmos. Meas. Tech.*, *7*(9), 3177–3213, doi:10.5194/amt-7-3177-2014. 95

Fels, S. (1984), The radiative damping of short vertical scale waves in the mesosphere, *Journal of the Atmospheric Sciences*, *41*(10), 1755–1764, doi:10.1175/1520-0469(1984)041<1755:TRDOSV>2.0.CO;2. 15

Flannaghan, T. J., and S. Fueglistaler (2011), Kelvin waves and shear-flow turbulent mixing in the ttl in (re-)analysis data, *Geophysical Research Letters*, *38*(2), n/a–n/a, doi:10.1029/2010GL045524. 34

Flannaghan, T. J., and S. Fueglistaler (2013), The importance of the tropical tropopause layer for equatorial kelvin wave propagation, *Journal of Geophysical Research: Atmospheres*, *118*(11), 5160–5175, doi:10.1002/jgrd.50418. 10

Flannaghan, T. J., and S. Fueglistaler (2014), Vertical mixing and the temperature and wind structure of the tropical tropopause layer, *Journal of the Atmospheric Sciences*, *71*(5), 1609–1622, doi:10.1175/JAS-D-13-0321.1. 37, 172

Forster, P. M. d. F., and K. P. Shine (2002), Assessing the climate impact of trends in stratospheric water vapor, *Geophys. Res. Lett.*, *29*(6), 1086, doi:10.1029/2001GL013909. 5

Fovell, R., D. Durran, and J. R. Holton (1992), Numerical Simulations of Convectively Generated Stratospheric Gravity Waves, *J. Atmos. Sci.*, *49*(16), 1427–1442. ix, 13, 14

Frey, W., R. Schofield, P. Hoor, D. Kunkel, F. Ravegnani, A. Ulanovsky, S. Viciani, F. D'Amato, and T. P. Lane (2015), The impact of overshooting deep convection on local transport and mixing in the tropical upper troposphere/lower stratosphere (utls), *Atmospheric Chemistry and Physics*, *15*(11), 6467–6486, doi:10.5194/acp-15-6467-2015. 32, 33

Fritts, D. C., and M. J. Alexander (2003), Gravity wave dynamics and effects in the middle atmosphere, *Rev. Geophys.*, *41*(1), n/a–n/a, doi:10.1029/2001RG000106. 11, 15, 52, 114, 224, 225

Fritts, D. C., L. Wang, J. Werne, T. Lund, and K. Wan (2009a), Gravity wave instability dynamics at high reynolds numbers. part i: Wave field evolution at large amplitudes and high frequencies, *Journal of the Atmospheric Sciences*, *66*(5), 1126–1148, doi:10.1175/2008JAS2726.1. 28

Fritts, D. C., L. Wang, J. Werne, T. Lund, and K. Wan (2009b), Gravity wave instability dynamics at high reynolds numbers. part ii: Turbulence evolution, structure, and anisotropy, *Journal of the Atmospheric Sciences*, *66*(5), 1149–1171, doi:10.1175/2008JAS2727.1. 28, 176, 179, 189, 194

Froyd, K. D., D. M. Murphy, T. J. Sanford, D. S. Thomson, J. C. Wilson, L. Pfister, and L. Lait (2009), Aerosol composition of the tropical upper troposphere, *Atmospheric Chemistry and Physics*, *9*(13), 4363–4385, doi:10.5194/acp-9-4363-2009. 95

Froyd, K. D., D. M. Murphy, P. Lawson, D. Baumgardner, and R. L. Herman (2010), Aerosols that form subvisible cirrus at the tropical tropopause, *Atmospheric Chemistry and Physics*, *10*(1), 209–218, doi:10.5194/acp-10-209-2010. 92, 95

Fu, Q., S. K. Krueger, and K. N. Liou (1995), Interactions of radiation and convection in simulated tropical cloud clusters, *Journal of the Atmospheric Sciences*, *52*(9), 1310–1328, doi:10.1175/1520-0469(1995)052<1310:IORACI>2.0.CO;2. 30

Fueglistaler, S., and M. B. Baker (2006), A modelling study of the impact of cirrus clouds on the moisture budget of the upper troposphere, *Atmospheric Chemistry and Physics*, *6*(5), 1425–1434, doi:10.5194/acp-6-1425-2006. 22, 23, 131

Fueglistaler, S., M. Bonazzola, P. H. Haynes, and T. Peter (2005), Stratospheric water vapor predicted from the Lagrangian temperature history of air entering the stratosphere in the tropics, *J. Geophys. Res.*, *110*, D08,107, doi:10.1029/2004JD005516. 18

Fueglistaler, S., A. E. Dessler, T. J. Dunkerton, I. Folkins, Q. Fu, and P. W. Mote (2009), Tropical tropopause layer, *Rev. Geophys.*, *47*, RG1004, doi:10.1029/2008RG000267. ix, xi, 2, 5, 6, 33, 172, 196

Fujita, T. T. (1982), Principle of stereoscopic height computations and their applications to stratospheric cirrus over severe thunderstorms, *Journal of the Meteorological Society of Japan. Ser. II*, *60*(1), 355–368. 22

Fujiwara, M., K. Kita, and T. Ogawa (1998), Stratosphere-troposphere exchange of ozone associated with the equatorial kelvin wave as observed with ozonesondes and rawinsondes, *Journal of Geophysical Research: Atmospheres*, *103*(D15), 19,173–19,182, doi:10.1029/98JD01419. 34

Fujiwara, M., F. Hasebe, M. Shiotani, N. Nishi, H. Vömel, and S. J. Oltmans (2001), Water vapor control at the tropopause by equatorial kelvin waves observed over the galápagos, *Geophysical Research Letters*, *28*(16), 3143–3146, doi:10.1029/2001GL013310. xviii, 34, 198, 199

Fujiwara, M., M. K. Yamamoto, H. Hashiguchi, T. Horinouchi, and S. Fukao (2003), Turbulence at the tropopause due to breaking kelvin waves observed by the equatorial atmosphere radar, *Geophysical Research Letters*, *30*(4), n/a–n/a, doi:10.1029/2002GL016278. 23, 29

Fujiwara, M., et al. (2009), Cirrus observations in the tropical tropopause layer over the western Pacific, *J. Geophys. Res.*, *114*, D09,304, doi:10.1029/2008JD011040. 23

Fujiwara, M., et al. (2017), Introduction to the sparc reanalysis intercomparison project (s-rip) and overview of the reanalysis systems, *Atmospheric Chemistry and Physics*, *17*(2), 1417–1452, doi:10.5194/acp-17-1417-2017. xxi, 81

Fukao, S., M. D. Yamanaka, N. Ao, W. K. Hocking, T. Sato, M. Yamamoto, T. Nakamura, T. Tsuda, and S. Kato (1994), Seasonal variability of vertical eddy diffusivity in the middle atmosphere: 1. three-year observations by the middle and upper atmosphere radar, *Journal of Geophysical Research: Atmospheres*, *99*(D9), 18,973–18,987, doi:10.1029/94JD00911. 195, 196

Gage, K. S., B. B. Balsley, and R. Garello (1986), Comparisons of horizontal and vertical velocity spectra in the mesosphere, stratosphere and troposphere: Observations and theory, *Geophys. Res. Lett.*, *13*(11), 1125–1128, doi:10.1029/GL013i011p01125. 184

Gardner, C. S. (1994), Diffusive filtering theory of gravity wave spectra in the atmosphere, *Journal of Geophysical Research: Atmospheres*, *99*(D10), 20,601–20,622, doi:10.1029/94JD00819. 77

Gardner, C. S., C. A. Hostetler, and S. J. Franke (1993), Gravity wave models for the horizontal wave number spectra of atmospheric velocity and density fluctuations, *Journal of Geophysical Research: Atmospheres*, *98*(D1), 1035–1049, doi:10.1029/92JD02051. 184

Gettelman, A., and C. Chen (2013), The climate impact of aviation aerosols, *Geophysical Research Letters*, *40*(11), 2785–2789, doi:10.1002/grl.50520. 90

Gill, A. E. (1980), Some simple solutions for heat-induced tropical circulation, *Q. J. Roy. Meteor. Soc.*, *106*(449), 447–462. 24

Gini, C. (1921), Measurement of inequality of incomes, *The Economic Journal*, *31*(121), 124–126, doi:10.2307/2223319. 72, 189

Glanville, A. A., and T. Birner (2016), Role of vertical and horizontal mixing in the tape recorder signal near the tropical tropopause, *Atmospheric Chemistry and Physics Discussions*, *2016*, 1–24, doi:10.5194/acp-2016-312. x, 19, 35, 37, 192, 195

Grooß, J.-U., and R. Müller (2007), Simulation of ozone loss in Arctic winter 2004/2005, *Geophys. Res. Lett.*, *34*(5), doi:10.1029/2006GL028901, l05804. 131

Gultepe, I., and D. O. Starr (1995), Dynamical structure and turbulence in cirrus clouds: Aircraft observations during fire, *Journal of the Atmospheric Sciences*, *52*(23), 4159–4182, doi:10.1175/1520-0469(1995)052<4159:DSATIC>2.0.CO;2. 30, 183

Hanisco, T. F., et al. (2007), Observations of deep convective influence on stratospheric water vapor and its isotopic composition, *Geophysical Research Letters*, *34*(4), n/a–n/a, doi:10.1029/2006GL027899. 33

Hankinson, M. C. N., M. J. Reeder, and T. P. Lane (2014a), Gravity waves generated by convection during twp-ice: I. inertia-gravity waves, *Journal of Geophysical Research: Atmospheres*, *119*(9), 5269–5282, doi:10.1002/2013JD020724. 16

Hankinson, M. C. N., M. J. Reeder, and T. P. Lane (2014b), Gravity waves generated by convection during twp-ice: 2. high-frequency gravity waves, *Journal of Geophysical Research: Atmospheres*, *119*(9), 5257–5268, doi:10.1002/2013JD020726. 16, 17

Hardiman, S. C., et al. (2015), Processes controlling tropical tropopause temperature and stratospheric water vapor in climate models, *Journal of Climate*, *28*(16), 6516–6535, doi:10.1175/JCLI-D-15-0075.1. v

Hassim, M. E. E., and T. P. Lane (2010), A model study on the influence of overshooting convection on ttl water vapour, *Atmospheric Chemistry and Physics*, *10*(20), 9833–9849, doi:10.5194/acp-10-9833-2010. 32, 34

Haynes, P., and E. Shuckburgh (2000), Effective diffusivity as a diagnostic of atmospheric transport: 2. troposphere and lower stratosphere, *Journal of Geophysical Research: Atmospheres*, *105*(D18), 22,795–22,810, doi:10.1029/2000JD900092. 2

Hertzog, A., F. Vial, C. R. Mechoso, C. Basdevant, and P. Cocquerez (2002), Quasi-lagrangian measurements in the lower stratosphere reveal an energy peak associated with near-inertial waves, *Geophys. Res. Lett.*, *29*(8), 70–1–70–4, doi:10.1029/2001GL014083. 16, 17, 44, 71, 86

Heymsfield, A. J., and C. D. Westbrook (2010), Advances in the estimation of ice particle fall speeds using laboratory and field measurements, *Journal of the Atmospheric Sciences*, *67*(8), 2469–2482, doi:10.1175/2010JAS3379.1. xvi, 131

Hocking, W. K. (1985), Measurement of turbulent energy dissipation rates in the middle atmosphere by radar techniques: A review, *Radio Science*, *20*(6), 1403–1422, doi:10.1029/RS020i006p01403. xvi, 170

Holton, J., and R. Lindzen (1968), A note on "kelvin" waves in the atmosphere, *Monthly Weather Review*, *96*(6), 385–386, doi:10.1175/1520-0493(1968)096<0385:ANOKWI>2.0.CO;2. v

Holton, J. R., and A. Gettelman (2001), Horizontal transport and the dehydration of the stratosphere, *Geophys. Res. Lett.*, *28*(14), 2799–2802, doi:10.1029/2001GL013148. 18

Holton, J. R., P. H. Haynes, M. E. McIntyre, A. R. Douglass, R. B. Rood, and L. Pfister (1995), Stratosphere-troposphere exchange, *Reviews of Geophysics*, *33*(4), 403–439, doi:10.1029/95RG02097. ix, 4

Holton, J. R., J. H. Beres, and X. Zhou (2002), On the vertical scale of gravity waves excited by localized thermal forcing, *Journal of the Atmospheric Sciences*, *59*(12), 2019–2023, doi:10.1175/1520-0469(2002)059<2019:OTVSOG>2.0.CO;2. 13

Hoskins, B. J., M. E. McIntyre, and A. W. Robertson (1985), On the use and significance of isentropic potential vorticity maps, *Quarterly Journal of the Royal Meteorological Society*, *111*(470), 877–946, doi:10.1002/qj.49711147002. 135

Immler, F., K. Krüger, M. Fujiwara, G. Verver, M. Rex, and O. Schrems (2008), Correlation between equatorial Kelvin waves and the occurrence of extremely thin ice clouds at the tropical tropopause, *Atmos. Chem. Phys.*, *8*(14), 4019–4026, doi:10.5194/acp-8-4019-2008. 23

Jensen, E., and L. Pfister (2004), Transport and freeze-drying in the tropical tropopause layer, *J. Geophys. Res.: Atmos.*, *109*(D2), n/a–n/a, doi:10.1029/2003JD004022. xiii, xiv, 23, 86, 87, 96, 110, 112, 113, 131

Jensen, E. J., and O. B. Toon (1994), Ice nucleation in the upper troposphere: Sensitivity to aerosol number density, temperature, and cooling rate, *Geophysical Research Letters*, *21*(18), 2019–2022, doi:10.1029/94GL01287. 26, 93

Jensen, E. J., O. B. Toon, L. Pfister, and H. B. Selkirk (1996), Dehydration of the upper troposphere and lower stratosphere by subvisible cirrus clouds near the tropical tropopause, *Geophys. Res. Lett.*, *23*(8), 825–828, doi:10.1029/96GL00722. 22, 25

Jensen, E. J., et al. (2005), Ice supersaturations exceeding 100% at the cold tropical tropopause: implications for cirrus formation and dehydration, *Atmos. Chem. Phys.*, *5*, 851–862, doi:10.5194/acp-5-851-2005. 44, 95

Jensen, E. J., A. S. Ackerman, and J. A. Smith (2007), Can overshooting convection dehydrate the tropical tropopause layer?, *Journal of Geophysical Research: Atmospheres*, *112*(D11), n/a–n/a, doi:10.1029/2006JD007943. 32, 131

Jensen, E. J., L. Pfister, T.-P. Bui, P. Lawson, and D. Baumgardner (2010), Ice nucleation and cloud microphysical properties in tropical tropopause layer cirrus, *Atmos. Chem. Phys.*, *10*(3), 1369–1384, doi:10.5194/acp-10-1369-2010. 92, 93, 95, 227

Jensen, E. J., L. Pfister, and O. B. Toon (2011), Impact of radiative heating, wind shear, temperature variability, and microphysical processes on the structure and evolution of thin cirrus in the tropical tropopause layer, *J. Geophys. Res.*, *116*(D12209), doi:10.1029/2010JD015417. 31, 135, 183, 228

Jensen, E. J., L. Pfister, and T. P. Bui (2012), Physical processes controlling ice concentrations in cold cirrus near the tropical tropopause, *J. Geophys. Res.*, *117*(D11), D11,205, doi:10.1029/2011JD017319. 95, 96, 110

Jensen, E. J., et al. (2013), Ice nucleation and dehydration in the Tropical Tropopause Layer, *Proc. Nat. Acad. Sci.*, *110*(6), 2041–2046, doi:10.1073/pnas.1217104110. xiv, 110, 112, 117, 228

Jensen, E. J., et al. (2015), The nasa airborne tropical tropopause experiment (attrex): High-altitude aircraft measurements in the tropical western pacific, *Bulletin of the American Meteorological Society*, *0*(0), null, doi:10.1175/BAMS-D-14-00263.1. 173

Jensen, E. J., et al. (2016), High-frequency gravity waves and homogeneous ice nucleation in tropical tropopause layer cirrus, *Geophysical Research Letters*, *43*(12), 6629–6635, doi:10.1002/2016GL069426. xiii, xiv, 90, 110, 112, 113

Jensen, E. J., et al. (2017), The nasa airborne tropical tropopause experiment: High-altitude aircraft measurements in the tropical western pacific, *Bulletin of the American Meteorological Society*, *98*(1), 129–143, doi:10.1175/BAMS-D-14-00263.1. 95

Jewtoukoff, V., A. Hertzog, R. Plougonven, A. de la Cámara, and F. Lott (2015), Comparison of gravity waves in the southern hemisphere derived from balloon observations and the ecmwf analyses, *Journal of the Atmospheric Sciences*, *72*(9), 3449–3468, doi:10.1175/JAS-D-14-0324.1. 81, 82

Joos, H., P. Spichtinger, U. Lohmann, J.-F. Gayet, and A. Minikin (2008), Orographic cirrus in the global climate model echam5, *Journal of Geophysical Research: Atmospheres*, *113*(D18), n/a–n/a, doi:10.1029/2007JD009605. 88

Kärcher, B., and W. Haag (2004), Factors controlling upper tropospheric relative humidity, *Annales Geophysicae*, *22*(3), 705–715, doi:10.5194/angeo-22-705-2004. 160

Kärcher, B., and U. Lohmann (2002), A parameterization of cirrus cloud formation: Homogeneous freezing of supercooled aerosols, *J. Geophys. Res.*, *107*, D2, doi:10.1029/2001JD000470. 25, 26, 93, 116

Kärcher, B., A. Dörnback, and Sölch (2014), Supersaturation variability and cirrus ice crystal size distributions, *Journal of the Atmospheric Sciences*, *71*(8), 2905–2926, doi:10.1175/JAS-D-13-0404.1. 129

Kay, J. E., and R. Wood (2008), Timescale analysis of aerosol sensitivity during homogeneous freezing and implications for upper tropospheric water vapor budgets, *Geophys. Res. Lett.*, *35*(L10809), doi:10.1029/2007GL032628. 116

Kennedy, P. J., and M. A. Shapiro (1975), The energy budget in a clear air turbulence zone as observed by aircraft, *Monthly Weather Review*, *103*(7), 650–654, doi:10.1175/1520-0493(1975)103<0650:TEBIAC>2.0.CO;2. 193

Kennedy, P. J., and M. A. Shapiro (1980), Further encounters with clear air turbulence in research aircraft, *Journal of the Atmospheric Sciences*, *37*(5), 986–993, doi:10.1175/1520-0469(1980)037<0986:FEWCAT>2.0.CO;2. 193

Kiladis, G. N., M. C. Wheeler, P. T. Haertel, K. H. Straub, and P. E. Roundy (2009), Convectively coupled equatorial waves, *Reviews of Geophysics*, *47*(2), n/a–n/a, doi:10.1029/2008RG000266. ix, 9

Kim, J.-E., and M. J. Alexander (2013), A new wave scheme for trajectory simulations of stratospheric water vapor, *Geophysical Research Letters*, *40*(19), 5286–5290, doi:10.1002/grl.50963. 10, 25, 84, 119

Kim, J.-E., and M. J. Alexander (2014), A fine vertical wave structure and its relation with trace gas transport, in *ATTREX science team meeting*, Boulder, Colorado. xviii, 175, 201

Kim, J.-E., and M. J. Alexander (2015), Direct impacts of waves on tropical cold point tropopause temperature, *Geophys. Res. Lett.*, *42*(5), 1584–1592, doi:10.1002/2014GL062737. ix, x, 11, 22, 115, 176

Kim, J.-E., M. J. Alexander, T. P. Bui, J. M. Dean-Day, R. P. Lawson, S. Woods, D. Hlavka, L. Pfister, and E. J. Jensen (2016), Ubiquitous influence of waves on tropical high cirrus clouds, *Geophysical Research Letters*, *43*(11), 5895–5901, doi:10.1002/2016GL069293. x, 23, 24, 25, 92, 120, 126, 127, 132, 160, 204, 213

Koch, S. E., et al. (2005), Turbulence and gravity waves within an upper-level front, *Journal of the Atmospheric Sciences*, *62*(11), 3885–3908, doi:10.1175/JAS3574.1. 28, 172

Kolmogorov, A. (1941), The Local Structure of Turbulence in Incompressible Viscous Fluid for Very Large Reynolds' Numbers, *Akademiia Nauk SSSR Doklady*, *30*, 301–305. 168

Konopka, P., et al. (2007), Contribution of mixing to upward transport across the tropical tropopause layer (TTL), *Atmospheric Chemistry and Physics*, *7*(12), 3285–3308, doi:10.5194/acp-7-3285-2007. 172, 198

Koop, T., B. Luo, A. Tsias, and T. Peter (2000), Water activity as the determinant for homogeneous ice nucleation in aqueous solutions, *Nature*, *406*(6796), 611–614, doi:10.1038/35020537. x, xiii, 26, 93, 94, 95

Korolev, A., and I. Mazin (2003), Supersaturation of water vapor in clouds, *Journal of the Atmospheric Sciences*, *60*(24), 2957–2974, doi:10.1175/1520-0469(2003)060<2957:SOWVIC>2.0.CO;2. 129

Krämer, M., et al. (2009), Ice supersaturations and cirrus cloud crystal numbers, *Atmospheric Chemistry and Physics*, *9*(11), 3505–3522, doi:10.5194/acp-9-3505-2009. xiv, 26, 95, 96, 117, 128, 129

Krämer, M., et al. (2016), A microphysics guide to cirrus clouds – part 1: Cirrus types, *Atmospheric Chemistry and Physics*, *16*(5), 3463–3483, doi:10.5194/acp-16-3463-2016. 92

Lane, T. P., and R. D. Sharman (2006), Gravity wave breaking, secondary wave generation, and mixing above deep convection in a three-dimensional cloud model, *Geophysical Research Letters*, *33*(23), n/a–n/a, doi:10.1029/2006GL027988. x, 29, 34, 183

Lane, T. P., and R. D. Sharman (2014), Intensity of thunderstorm-generated turbulence revealed by large-eddy simulation, *Geophysical Research Letters*, *41*(6), 2221–2227, doi:10.1002/2014GL059299. 189

Lane, T. P., M. J. Reeder, and T. L. Clark (2001), Numerical modeling of gravity wave generation by deep tropical convection, *Journal of the Atmospheric Sciences*, *58*(10), 1249–1274, doi:10.1175/1520-0469(2001)058<1249:NMOGWG>2.0.CO;2. 12, 13

Lane, T. P., R. D. Sharman, T. L. Clark, and H.-M. Hsu (2003a), An investigation of turbulence generation mechanisms above deep convection, *Journal of the Atmospheric Sciences*, *60*(10), 1297–1321, doi:10.1175/1520-0469(2003)60<1297:AIOTGM>2.0.CO;2. xi, 29, 31

Lane, T. P., M. J. Reeder, and F. M. Guest (2003b), Convectively generated gravity waves observed from radiosonde data taken during mctex, *Quarterly Journal of the Royal Meteorological Society*, *129*(590), 1731–1740, doi:10.1256/qj.02.196. 16

Lane, T. P., J. D. Doyle, R. Plougonven, M. A. Shapiro, and R. D. Sharman (2004), Observations and numerical simulations of inertia–gravity waves and shearing instabilities in the vicinity of a jet stream, *Journal of the Atmospheric Sciences*, *61*(22), 2692–2706, doi:10.1175/JAS3305.1. 28

Lane, T. P., R. D. Sharman, S. B. Trier, R. G. Fovell, and J. K. Williams (2012), Recent advances in the understanding of near-cloud turbulence, *Bulletin of the American Meteorological Society*, *93*(4), 499–515, doi:10.1175/BAMS-D-11-00062.1. x, 30, 177, 182, 183

Legras, B., B. Joseph, and F. Lefèvre (2003), Vertical diffusivity in the lower stratosphere from Lagrangian back-trajectory reconstructions of ozone profiles, *Journal of Geophysical Research: Atmospheres*, *108*(D18), n/a–n/a, doi:10.1029/2002JD003045. 192

Legras, B., I. Pisso, G. Berthet, and F. Lefèvre (2005), Variability of the lagrangian turbulent diffusion in the lower stratosphere, *Atmospheric Chemistry and Physics*, *5*(6), 1605–1622, doi:10.5194/acp-5-1605-2005. 202

Lilly, D. K. (1983), Stratified turbulence and the mesoscale variability of the atmosphere, *Journal of the Atmospheric Sciences*, *40*(3), 749–761, doi:10.1175/1520-0469(1983)040<0749:STATMV>2.0.CO;2. 171, 184

Lilly, D. K., D. E. Waco, and S. I. Adelfang (1974), Stratospheric mixing estimated from high-altitude turbulence measurements., *JAM*, *13*(13), 488–493, doi:10.1175/1520-0450(1974)013\%3C0488:SMEFHA\%3E2.0.CO;2. 167, 172, 174, 192, 197

Lindborg, E. (1999), Can the atmospheric kinetic energy spectrum be explained by two-dimensional turbulence?, *JFM*, (388), 259–288, doi:10.1017/S0022112099004851. 171, 184

Lindborg, E. (2006), The energy cascade in a strongly stratified fluid, *Journal of Fluid Mechanics*, *550*, 207–242, doi:10.1017/S0022112005008128. 171

Lindzen, R. S. (1981), Turbulence and stress owing to gravity wave and tidal breakdown, *Journal of Geophysical Research: Oceans*, *86*(C10), 9707–9714, doi:10.1029/JC086iC10p09707. 15, 88, 229

Lindzen, R. S., M.-D. Chou, and A. Y. Hou (2001), Does the earth have an adaptive infrared iris?, *Bulletin of the American Meteorological Society*, *82*(3), 417–432, doi:10.1175/1520-0477(2001)082<0417:DTEHAA>2.3.CO;2. 5

Liu, C., and E. J. Zipser (2005), Global distribution of convection penetrating the tropical tropopause, *J. Geophys. Res.*, *110*(D23), D23,104, doi:10.1029/2005JD006063. 32, 75

Liu, C., E. J. Zipser, and S. W. Nesbitt (2007), Global distribution of tropical deep convection: Different perspectives from trmm infrared and radar data, *Journal of Climate*, *20*(3), 489–503, doi:10.1175/JCLI4023.1. 182

Louis, J. F., M. Tiedtke, and J.-F. Geleyn (1982), A short history of the operational pbl parametrization at ECMWF. 166

Lovejoy, S., and D. Schertzer (2011), Space-time cascades and the scaling of ecmwf reanalyses: Fluxes and fields, *Journal of Geophysical Research: Atmospheres*, *116*(D14), n/a–n/a, doi:10.1029/2011JD015654. 189

Lumley, J. L. (1964), The spectrum of nearly inertial turbulence in a stably stratified fluid, *Journal of the Atmospheric Sciences*, *21*(1), 99–102, doi:10.1175/1520-0469(1964)021<0099:TSONIT>2.0.CO;2. 184, 187

Magee, N., A. M. Moyle, and D. Lamb (2006), Experimental determination of the deposition coefficient of small cirrus-like ice crystals near −50 celsius, *Geophys. Res. Lett.*, *33*, L17,813, doi:10.1029/2006GL026665. 116

Mahoney, M. J., and R. Denning (2009), A state-of-the-art airborne microwave temperature profiler (MTP), in *Proceedings of the 33rd International Symposium on the Remote Sensing of the Environment*, Stresa, Italy. 185, 192

Malardel, S., and N. P. Wedi (2016), How does subgrid-scale parametrization influence nonlinear spectral energy fluxes in global nwp models?, *Journal of Geophysical Research: Atmospheres*, *121*(10), 5395–5410, doi:10.1002/2015JD023970. 81

Malardel, S., N. Wedi, M. Deconinck, Willem Diamankatis, C. Kühlein, G. MOZDZYNSKI, M. Hamrud, and P. Smolarkeiwicz (2015-2016), A new grid for the IFS, *ECMWF Newsletter*, *146*(146), 23–16. 89

Massman, W. J. (1978), On the nature of vertical oscillations of constant volume balloons, *J. Appl. Meteor.*, *17*, 1351–1356, doi:10.1175/1520-0450(1978)017<1351:OTNOVO>2.0.CO;2. 52

Matsuno, T. (1966), Quasi-geostrophic motions in the equatorial area, *Journal of the Meteorological Society of Japan. Ser. II*, *44*(1), 25–43. v, 7

Mellor, G. L., and T. Yamada (1982), Development of a turbulence closure model for geophysical fluid problems, *Reviews of Geophysics*, *20*(4), 851–875, doi:10.1029/RG020i004p00851. 166

Monin, A., and A. Yaglom (1977), *Statistical Fluid Mechanics: Mechanics of Turbulence. : Vol.: 1*, MIT Press. 71, 168

Mote, P. W., et al. (1996), An atmospheric tape recorder: The imprint of tropical tropopause temperatures on stratospheric water vapor, *J. Geophys. Res.*, *101*(D2), 3989–4006, doi:10.1029/95JD03422. 20, 34, 35, 172, 191, 193

Mote, P. W., T. J. Dunkerton, M. E. McIntyre, E. A. Ray, P. H. Haynes, and J. M. Russell (1998), Vertical velocity, vertical diffusion, and dilution by midlatitude air in the tropical lower stratosphere, *Journal of Geophysical Research: Atmospheres*, *103*(D8), 8651–8666, doi:10.1029/98JD00203. xi, 34, 35, 172, 192

Moustaoui, M., B. Joseph, and H. Teitelbaum (2004), Mixing layer formation near the tropopause due to gravity wave–critical level interactions in a cloud-resolving model, *Journal of the Atmospheric Sciences*, *61*(24), 3112–3124, doi:10.1175/JAS-3289.1. 198

Moyer, E. J., F. W. Irion, Y. L. Yung, and M. R. Gunson (1996), Atmos stratospheric deuterated water and implications for troposphere-stratosphere transport, *Geophysical Research Letters*, *23*(17), 2385–2388, doi:10.1029/96GL01489. 33

Murphy, D. M. (2014), Rare temperature histories and cirrus ice number density in a parcel and a one-dimensional model, *Atmos. Chem. Phys.*, *14*(23), 13,013–13,022, doi:10.5194/acp-14-13013-2014. xiv, 95, 110, 111, 228, 229

Murphy, D. M., and T. Koop (2005), Review of the vapour pressures of ice and supercooled water for atmospheric applications, *Quarterly Journal of the Royal Meteorological Society*, *131*(608), 1539–1565, doi:10.1256/qj.04.94. 17

Murray, B. J., et al. (2010), Heterogeneous nucleation of ice particles on glassy aerosols under cirrus conditions, *Nat. Geosci.*, *3*(4), 233–237, doi:10.1038/ngeo817. 92

Nastrom, G. D. (1980), The response of superpressure balloons to gravity waves, *J. Appl. Meteor.*, *19*, 1013–1019, doi:10.1175/1520-0450(1980)019<1013:TROSBT>2.0.CO;2. 47, 48, 50, 51

Nastrom, G. D., and K. S. Gage (1985), A climatology of atmospheric wavenumber spectra of wind and temperature observed by commercial aircraft, *Journal of the Atmospheric Sciences*, *42*(9), 950–960, doi:10.1175/1520-0469(1985)042<0950:ACOAWS>2.0.CO;2. 81, 184

Nastrom, G. D., D. C. Fritts, and K. S. Gage (1987), An investigation of terrain effects on the mesoscale spectrum of atmospheric motions, *Journal of the Atmospheric Sciences*, *44*(20), 3087–3096, doi:10.1175/1520-0469(1987)044<3087:AIOTEO>2.0.CO;2. 187

Ortland, D. A., M. J. Alexander, and A. W. Grimsdell (2011), On the wave spectrum generated by tropical heating, *Journal of the Atmospheric Sciences*, *68*(9), 2042–2060, doi: 10.1175/2011JAS3718.1. 13, 20

Osman, M., W. Hocking, and D. Tarasick (2016), Parameterization of large-scale turbulent diffusion in the presence of both well-mixed and weakly mixed patchy layers, *Journal of Atmospheric and Solar-Terrestrial Physics*, *143–144*, 14 – 36, doi:http://dx.doi.org/10.1016/j.jastp.2016.02.025. 35, 190, 193

Pavelin, E., J. A. Whiteway, R. Busen, and J. Hacker (2002), Airborne observations of turbulence, mixing, and gravity waves in the tropopause region, *Journal of Geophysical Research: Atmospheres*, *107*(D10), ACL 8–1–ACL 8–6, doi:10.1029/2001JD000775. 28, 193

Pellacani, C., and R. Lupini (1975), Resonant trapped gravity waves and turbulent patches in an inversion layer, *Boundary-Layer Meteorology*, *9*(2), 205–215, doi:10.1007/BF00215640. 177

Penner, J. E., Y. Chen, M. Wang, and X. Liu (2009), Possible influence of anthropogenic aerosols on cirrus clouds and anthropogenic forcing, *Atmospheric Chemistry and Physics*, *9*(3), 879–896, doi:10.5194/acp-9-879-2009. 90

Peter, T., C. Marcolli, P. Spichtinger, T. Corti, M. B. Baker, and T. Koop (2006), When dry air is too humid, *Science*, *314*(5804), 1399–1402, doi:10.1126/science.1135199. 95

Pfister, L., W. Starr, R. Craig, M. Loewenstein, and M. Legg (1986), Small-scale motions observed by aircraft in the tropical lower stratosphere: Evidence for mixing and its relationship to large-scale flows, *Journal of the Atmospheric Sciences*, *43*(24), 3210–3225, doi:10.1175/1520-0469(1986)043<3210:SSMOBA>2.0.CO;2. 176

Pfister, L., K. R. Chan, T. P. Bui, S. Bowen, M. Legg, B. Gary, K. Kelly, M. Proffitt, and W. Starr (1993), Gravity waves generated by a tropical cyclone during the step tropical field program: A case study, *Journal of Geophysical Research: Atmospheres*, *98*(D5), 8611–8638, doi:10.1029/92JD01679. 14, 16

Pfister, L., et al. (2001), Aircraft observations of thin cirrus clouds near the tropical tropopause, *Journal of Geophysical Research: Atmospheres*, *106*(D9), 9765–9786, doi: 10.1029/2000JD900648. 23

Plougonven, R., A. Hertzog, and L. Guez (2013), Gravity waves over antarctica and the southern ocean: consistent momentum fluxes in mesoscale simulations and stratospheric balloon observations, *Quarterly Journal of the Royal Meteorological Society*, *139*(670), 101–118, doi:10.1002/qj.1965. 73, 189, 190

Plougonven, R., V. Jewtoukoff, A. de la Cámara, F. Lott, and A. Hertzog (2017), On the relation between gravity waves and wind speed in the lower stratosphere over the southern ocean, *Journal of the Atmospheric Sciences*, *74*(4), 1075–1093, doi:10.1175/JAS-D-16-0096.1. 75

Podglajen, A., A. Hertzog, R. Plougonven, and N. Žagar (2014), Assessment of the accuracy of (re)analyses in the equatorial lower stratosphere, *J. Geophys. Res.*, *119*, 11,166–11,188, doi:10.1002/2014JD021849. 10, 130, 159, 176

Podglajen, A., R. Plougonven, A. Hertzog, and B. Legras (2016a), A modelling case study of a large-scale cirrus in the tropical tropopause layer, *Atmospheric Chemistry and Physics*, *16*(6), 3881–3902, doi:10.5194/acp-16-3881-2016. 136, 183

Podglajen, A., A. Hertzog, R. Plougonven, and B. Legras (2016b), Lagrangian temperature and vertical velocity fluctuations due to gravity waves in the lower stratosphere, *Geophysical Research Letters*, *43*(7), 3543–3553, doi:10.1002/2016GL068148. 187

Potter, B. E., and J. R. Holton (1995), The role of monsoon convection in the dehydration of the lower tropical stratosphere, *Journal of the Atmospheric Sciences*, *52*(8), 1034–1050, doi:10.1175/1520-0469(1995)052<1034:TROMCI>2.0.CO;2. 22, 23

Pruppacher, H. R., and J. D. Klett (1978), *Microphysics of clouds and precipitation*, D. Reidel Publishing Company, Dordrecht, Holland. 116, 117

Randel, W. J., and E. J. Jensen (2013), Physical processes in the tropical tropopause layer and their roles in a changing climate, *Nat. Geosci.*, *6*(3), 169–176, doi:10.1038/ngeo1733. v, x, 20, 21

Randel, W. J., and F. Wu (2005), Kelvin wave variability near the equatorial tropopause observed in gps radio occultation measurements, *Journal of Geophysical Research: Atmospheres*, *110*(D3), n/a–n/a, doi:10.1029/2004JD005006. x, 21

Randel, W. J., and F. Wu (2015), Variability of zonal mean tropical temperatures derived from a decade of gps radio occultation data, *Journal of the Atmospheric Sciences*, *72*(3), 1261–1275, doi:10.1175/JAS-D-14-0216.1. 20

Randel, W. J., R. R. Garcia, and F. Wu (2002), Time-Dependent Upwelling in the Tropical Lower Stratosphere Estimated from the Zonal-Mean Momentum Budget, *J. Atmos. Sci.*, *59*(13), 2141–2152, doi:10.1175/1520-0469(2002)059<2141:TDUITT>2.0.CO;2. 19, 20

Randel, W. J., M. Park, F. Wu, and N. Livesey (2007), A large annual cycle in ozone above the tropical tropopause linked to the brewer–dobson circulation, *Journal of the Atmospheric Sciences*, *64*(12), 4479–4488, doi:10.1175/2007JAS2409.1. 196, 197

Randel, W. J., R. Garcia, and F. Wu (2008), Dynamical balances and tropical stratospheric upwelling, *Journal of the Atmospheric Sciences*, *65*(11), 3584–3595, doi:10.1175/2008JAS2756.1. 197

Rao, D. N., T. N. Rao, M. Venkataratnam, S. Thulasiraman, S. V. B. Rao, P. Srinivasulu, and P. B. Rao (2001), Diurnal and seasonal variability of turbulence parameters observed with indian mesosphere-stratosphere-troposphere radar, *Radio Science*, *36*(6), 1439–1457, doi:10.1029/2000RS002316. xi, 36, 172, 192, 195, 196

Riese, M., F. Ploeger, A. Rap, B. Vogel, P. Konopka, M. Dameris, and P. Forster (2012), Impact of uncertainties in atmospheric mixing on simulated UTLS composition and related radiative effects, *J. Geophys. Res.: Atmos.*, *117*(D16), doi:10.1029/2012JD017751. v, ix, 5

Rollins, A. W., T. D. Thornberry, R. S. Gao, S. Woods, R. P. Lawson, T. P. Bui, E. J. Jensen, and D. W. Fahey (2016), Observational constraints on the efficiency of dehydration mechanisms in the tropical tropopause layer, *Geophysical Research Letters*, *43*(6), 2912–2918, doi:10.1002/2016GL067972. 128

Salby, M. L., and R. R. Garcia (1987), Transient response to localized episodic heating in the tropics. part i: Excitation and short-time near-field behavior, *Journal of the Atmospheric Sciences*, *44*(2), 458–498, doi:10.1175/1520-0469(1987)044<0458:TRTLEH>2.0.CO;2. 13

Schmitt, F., D. Schertzer, S. Lovejoy, and Y. Brunet (1994), Empirical study of multifractal phase transitions in atmospheric turbulence, *Nonlinear Processes in Geophysics*, *1*(2/3), 95–104, doi:10.5194/npg-1-95-1994. 189

Schoeberl, M., A. Dessler, H. Ye, T. Wang, M. Avery, and E. Jensen (2016), The impact of gravity waves and cloud nucleation threshold on stratospheric water and tropical tropospheric cloud fraction, *Earth and Space Science*, *3*(8), 295–305, doi:10.1002/2016EA000180. 23

Schoeberl, M., E. Jensen, A. Podglajen, L. Coy, C. Lodha, S. Candido, and R. Carver (2017), Gravity wave spectra in the lower stratosphere diagnosed from project loon balloon trajectories, *Journal of Geophysical Research: Atmospheres*, *In revision*, n/a–n/a. 89

Schoeberl, M. R., D. F. Strobel, and J. P. Apruzese (1983), A numerical model of gravity wave breaking and stress in the mesosphere, *Journal of Geophysical Research: Oceans*, *88*(C9), 5249–5259, doi:10.1029/JC088iC09p05249. 15

Schumann, U., P. Konopka, R. Baumann, R. Busen, T. Gerz, H. Schlager, P. Schulte, and H. Volkert (1995), Estimate of diffusion parameters of aircraft exhaust plumes near the tropopause from nitric oxide and turbulence measurements, *Journal of Geophysical Research: Atmospheres*, *100*(D7), 14,147–14,162, doi:10.1029/95JD01277. 188, 192

Scott, S. G., T. P. Bui, K. R. Chan, and S. W. Bowen (1990), The meteorological measurement system on the nasa er-2 aircraft, *Journal of Atmospheric and Oceanic Technology*, *7*(4), 525–540, doi:10.1175/1520-0426(1990)007<0525:TMMSOT>2.0.CO;2. 39, 173, 231, 232

Sharman, R., and T. Lane (2016), *Aviation Turbulence: Processes, Detection, Prediction*, Springer International Publishing. 27

Sharman, R. D., L. B. Cornman, G. Meymaris, J. Pearson, and T. Farrar (2014), Description and derived climatologies of automated in situ eddy-dissipation-rate reports of atmospheric turbulence, *Journal of Applied Meteorology and Climatology*, *53*(6), 1416–1432, doi:10.1175/JAMC-D-13-0329.1. 172, 174, 175, 179, 189, 191

Sherwood, S. C., and A. E. Dessler (2000), On the control of stratospheric humidity, *Geophysical Research Letters*, *27*(16), 2513–2516, doi:10.1029/2000GL011438. 32

Sherwood, S. C., and A. E. Dessler (2001), A model for transport across the tropical tropopause, *J. Atmos. Sci.*, *58*(7), 765–779. 32

Skrotzki, J., P. Connolly, M. Schnaiter, H. Saathoff, O. Möhler, R. Wagner, M. Niemand, V. Ebert, and T. Leisner (2013), The accommodation coefficient of water molecules on ice – cirrus cloud studies at the AIDA simulation chamber, *Atmos. Chem. Phys.*, *13*(8), 4451–4466, doi:10.5194/acp-13-4451-2013. 116

Solomon, S., K. H. Rosenlof, R. W. Portmann, J. S. Daniel, S. M. Davis, T. J. Sanford, and G.-K. Plattner (2010), Contributions of stratospheric water vapor to decadal changes in the rate of global warming, *Science*, *327*(5970), 1219–1223, doi:10.1126/science.1182488. v, 5

Spichtinger, P., and D. J. Cziczo (2010), Impact of heterogeneous ice nuclei on homogeneous freezing events in cirrus clouds, *Journal of Geophysical Research: Atmospheres*, *115*(D14), n/a–n/a, doi:10.1029/2009JD012168. 95, 131

Spichtinger, P., and M. Krämer (2013), Tropical tropopause ice clouds: a dynamic approach to the mystery of low crystal numbers, *Atmos. Chem. Phys.*, *13*(19), 9801–9818, doi:10.5194/acp-13-9801-2013. x, xiii, 26, 92, 93, 94, 95, 96

Sreenivasan, K. R. (1991), On local isotropy of passive scalars in turbulent shear flows, *Proc. Roy. Soc. London*, *8*(434A), 165–182. 189

Sreenivasan, K. R. (1995), On the universality of the kolmogorov constant, *Physics of Fluids*, *7*(11), 2778–2784, doi:http://dx.doi.org/10.1063/1.868656. 175

Stohl, A., C. Forster, A. Frank, P. Seibert, and G. Wotawa (2005), Technical note: The lagrangian particle dispersion model flexpart version 6.2, *Atmospheric Chemistry and Physics*, *5*(9), 2461–2474, doi:10.5194/acp-5-2461-2005. 87

Sunilkumar, S., et al. (2015), Characteristics of turbulence in the troposphere and lower stratosphere over the indian peninsula, *Journal of Atmospheric and Solar-Terrestrial Physics*, *133*, 36 – 53, doi:http://dx.doi.org/10.1016/j.jastp.2015.07.015. xi, 36, 192, 196

Taylor, J. R., W. J. Randel, and E. J. Jensen (2011), Cirrus cloud-temperature interactions in the tropical tropopause layer: a case study, *Atmos. Chem. Phys.*, *11*(19), 10,085–10,095, doi:10.5194/acp-11-10085-2011. xvi, 18, 134, 135

Teitelbaum, H., M. Moustaoui, R. Sadourny, and F. Lott (1999), Critical levels and mixing layers induced by convectively generated gravity waves during cepex, *Quarterly Journal of the Royal Meteorological Society*, *125*(557), 1715–1734, doi:10.1002/qj.49712555712. 198

Tennekes, H., and J. Lumley (1972), *A First Course in Turbulence*, MIT Press. 166, 168

Thornberry, T. D., A. W. Rollins, R. S. Gao, L. A. Watts, S. J. Ciciora, R. J. McLaughlin, and D. W. Fahey (2015), A two-channel, tunable diode laser-based hygrometer for measurement of water vapor and cirrus cloud ice water content in the upper troposphere and lower stratosphere, *Atmospheric Measurement Techniques*, *8*(1), 211–224, doi:10.5194/amt-8-211-2015. 39

Thorpe, S. A. (1973), Turbulence in stably stratified fluids: A review of laboratory experiments, *Boundary-Layer Meteorology*, *5*(1), 95–119, doi:10.1007/BF02188314. 192

Torrence, C., and G. P. Compo (1998), A practical guide to wavelet analysis, *Bulletin of the American Meteorological Society*, *79*(1), 61–78, doi:10.1175/1520-0477(1998)079<0061:APGTWA>2.0.CO;2. 71, 174, 231, 232, 233

Ueyama, R., E. J. Jensen, L. Pfister, and J.-E. Kim (2015), Dynamical, convective, and microphysical control on wintertime distributions of water vapor and clouds in the tropical tropopause layer, *Journal of Geophysical Research: Atmospheres*, *120*(19), 10,483–10,500, doi:10.1002/2015JD023318. 23, 131, 172

Vanneste, J. (2004), Small-scale mixing, large-scale advection, and stratospheric tracer distributions, *Journal of the Atmospheric Sciences*, *61*(22), 2749–2761, doi:10.1175/JAS3303.1. 35, 190, 193, 194

Vial, F., A. Hertzog, C. R. Mechoso, C. Basdevant, P. Cocquerez, V. Dubourg, and F. Nouel (2001), A study of the dynamics of the equatorial lower stratosphere by use of ultra-long-duration balloons: 1. planetary scales, *J. Geophys. Res.: Atmos.*, *106*(D19), 22,725–22,743, doi:10.1029/2000JD000241. 46

Vincent, R. A., and A. Hertzog (2014), The response of superpressure balloons to gravity wave motions, *Atmos. Meas. Tech.*, *7*, 1043–1055, doi:10.5194/amt-7-1043-2014. xi, 48, 49, 50

Virts, K. S., and J. M. Wallace (2010), Annual, interannual, and intraseasonal variability of tropical tropopause transition layer cirrus, *Journal of the Atmospheric Sciences*, *67*(10), 3097–3112, doi:10.1175/2010JAS3413.1. x, 19

Vömel, H., S. J. Oltmans, D. Kley, and P. J. Crutzen (1995), New evidence for the stratospheric dehydration mechanism in the equatorial pacific, *Geophysical Research Letters*, *22*(23), 3235–3238, doi:10.1029/95GL02940. 198

Wallace, J., and V. E. Kousky (1968), Observational evidence of kelvin waves in the tropical stratosphere, *Journal of the Atmospheric Sciences*, *25*(5), 900–907, doi:10.1175/1520-0469(1968)025<0900:OEOKWI>2.0.CO;2. v

Wang, P.-H., P. Minnis, M. P. McCormick, G. S. Kent, and K. M. Skeens (1996), A 6-year climatology of cloud occurrence frequency from Stratospheric Aerosol and Gas Experiment II observations (1985–1990), *J. Geophys. Res.*, *101*(D23), 29,407–29,429, doi:10.1029/96JD01780. 134

Wang, P. K. (2004), A cloud model interpretation of jumping cirrus above storm top, *Geophysical Research Letters*, *31*(18), n/a–n/a, doi:10.1029/2004GL020787. 22, 34

Weinstock, J. (1978), On the theory of turbulence in the buoyancy subrange of stably stratified flows, *Journal of the Atmospheric Sciences*, *35*(4), 634–649, doi:10.1175/1520-0469(1978)035<0634:OTTOTI>2.0.CO;2. 170, 184, 186, 192

Weinstock, J. (1992), Vertical diffusivity and overturning length in stably stratified turbulence, *Journal of Geophysical Research: Oceans*, *97*(C8), 12,653–12,658, doi:10.1029/92JC01099. 186

Wilson, R. (2004), Turbulent diffusivity in the free atmosphere inferred from mst radar measurements: a review, *Annales Geophysicae*, *22*(11), 3869–3887, doi:10.5194/angeo-22-3869-2004. 174, 189, 192

Wilson, R., F. Dalaudier, and F. Bertin (2005), Estimation of the turbulent fraction in the free atmosphere from mst radar measurements, *Journal of Atmospheric and Oceanic Technology*, *22*(9), 1326–1339, doi:10.1175/JTECH1783.1. 179, 194

Wilson, R., F. Dalaudier, and H. Luce (2011), Can one detect small-scale turbulence from standard meteorological radiosondes?, *Atmospheric Measurement Techniques*, *4*(5), 795–804, doi:10.5194/amt-4-795-2011. 36, 190

Wilson, R., H. Luce, H. Hashiguchi, N. Nishi, and Y. Yabuki (2014), Energetics of persistent turbulent layers underneath mid-level clouds estimated from concurrent radar and radiosonde data, *Journal of Atmospheric and Solar-Terrestrial Physics*, *118, Part A*, 78 – 89, doi:http://dx.doi.org/10.1016/j.jastp.2014.01.005, recent progress from networked studies based around {MST} radar. 187

Wright, J. S., and S. Fueglistaler (2013), Large differences in reanalyses of diabatic heating in the tropical upper troposphere and lower stratosphere, *Atmospheric Chemistry and Physics*, *13*(18), 9565–9576, doi:10.5194/acp-13-9565-2013. v, 172

Wroblewski, D. E., O. R. Coté, J. M. Hacker, and R. J. Dobosy (2010), Velocity and temperature structure functions in the upper troposphere and lower stratosphere from high-resolution aircraft measurements, *Journal of the Atmospheric Sciences*, *67*(4), 1157–1170, doi:10.1175/2009JAS3108.1. 188

Yu, F. (2010), Ion-mediated nucleation in the atmosphere: Key controlling parameters, implications, and look-up table, *Journal of Geophysical Research: Atmospheres*, *115*(D3), n/a–n/a, doi:10.1029/2009JD012630. 205, 213

Zelinka, M. D., and D. L. Hartmann (2010), Why is longwave cloud feedback positive?, *Journal of Geophysical Research: Atmospheres*, *115*(D16), n/a–n/a, doi:10.1029/2010JD013817. 5

Résumé

Cette thèse s'intéresse aux ondes de gravité et à la turbulence dans la région de la tropopause tropicale (TTL pour Tropical Tropopause Layer, entre 14 et 18 km d'altitude), et à leurs impacts sur les cirrus.

Dans un premier temps, les fluctuations de température et de vent vertical induites par les ondes de gravité sont caractérisées à partir de mesures provenant de ballons stratosphériques longue durée. Les perturbations observées sont comparées à celles résolues par différents modèles atmosphériques globaux. À la lumière de ces observations, différentes méthodes de paramétrisation des fluctuations de température sont discutées.

Dans un second temps, l'influence des ondes équatoriales et de gravité sur la microphysique des cirrus est étudiée. On considère d'abord l'impact des ondes de gravité de haute fréquence sur la nucléation des cristaux de glace. Ensuite, l'effet des ondes de basse fréquence sur le transport de la glace est examiné, puis quantifié à l'aide d'observations in situ. Enfin, on étudie la formation et l'évolution d'un cirrus de grande échelle à l'aide de simulations numériques. Parmi les différents processus en jeu, on montre l'importance d'une onde équatoriale de grande échelle dans la structuration du champ nuageux.

Dans une dernière partie, les fluctuations de vent de petite échelle, interprétées comme de la turbulence, sont étudiées à partir des observations avion de la campagne ATTREX dans la TTL au-dessus de l'océan Pacifique. Leur impact sur le transport vertical de différents traceurs est quantifié. Il est inférieur à l'impact de l'upwelling équatorial de grande échelle mais néanmoins significatif.

Mots Clés

Tropopause tropicale (TTL), ondes de gravité, cirrus, turbulence, mélange, modélisation méso-échelle, microphysique, ballons longue durée

Abstract

Atmospheric waves and turbulence and their impacts on cirrus clouds in the Tropical Tropopause Layer (TTL, 14-18 km above sea level) are studied using in situ observations, numerical simulations and theoretical approaches.

First, long-duration stratospheric balloon measurements are used to analyze Lagrangian temperature and vertical wind fluctuations induced by gravity waves at the tropical tropopause. The amplitude and intermittency of wave fluctuations are assessed, and the observations are compared with resolved wave fluctuations in atmospheric models. Methods to parameterize Lagrangian temperature fluctuations are then discussed.

Then, some impacts of waves on cirrus cloud microphysics are examined. We first consider the influence of high-frequency gravity waves on the ice nucleation process. Next, we explore the interplay between the sedimentation of the ice crystals and their advection by wave-induced wind perturbations. Last, we use numerical simulations to investigate the formation of a large-scale cirrus in the TTL. We demonstrate the role of large-scale equatorial waves and quantify the impact of different processes (dynamics, radiative heating, microphysics) on the cloud field.

Finally, small-scale wind fluctuations, interpreted as turbulent bursts, are characterized using aircraft measurements from the ATTREX campaign in the tropical Pacific. The impacts of the fluctuations on vertical mixing and on the TTL tracer budget are quantified. The vertical transport induced by turbulent mixing is found to be smaller than the one induced by mean tropical upwelling, but nonetheless significant.

Key words

Tropical tropopause layer (TTL), gravity waves, cirrus clouds, turbulence, mixing, mesoscale modeling, cirrus microphysics, superpressure balloons